Rectangular Hollow Sections with circular web openings

Fundamental behaviour in torsion, bending and shear

by D.J.Ridley-Ellis, B.Eng. M.Res.

Thesis submitted to the University of Nottingham

for the degree of Doctor of Philosophy, October 2000

Since men were of an imitative and teachable nature, they boasted of their inventions as they daily showed their various achievements in building, and thus, exercising their talents in rivalry, were rendered of better judgement daily.

Vitruvius, circa 27 B.C.E.
De Architectura, (Liber Secundus, I)
(Granger Translation, University College Nottingham, 1931)

Table of contents

Table of contents iii
List of figures vii
List of tables xiii
Abstract (long version) xv
Abstract (short version) xviii
Acknowledgements xx
Author's declaration xxi
Notation and symbols xxii
List of abbreviations and trademarks xxviii
1 Introduction and background 1-1
1.1 Introduction 1-1
1.2 Background 1-1
1.2.1 An outline of the slim floor method of construction 1-1
1.2.2 Slimdek 1-4
1.2.3 Slim floor edge beams 1-5
1.3 Methodology 1-9
1.4 Scope of study and dimensions of cross-section 1-10
1.5 The contents of this Thesis 1-13
2 Relevant knowledge and theory 2-1
2.1 Introduction 2-1
2.2 The stress-strain behaviour of hot finished steel 2-2
2.2.1 Introduction 2-2
2.2.2 The stress-strain behaviour of hot finished steel and BS EN 10002-1 2-3
2.2.3 A mathematical model of stress-strain behaviour 2-5
2.2.4 Applying the mathematical approximation to experimental data 2-8
2.2.4.1 Applying the mathematical approximation to a single coupon result 2-8
2.2.4.2 Measuring the suitability of the fit 2-11
2.2.4.3 Applying the mathematical model to a group of coupon results 2-15
2.2.5 Multi-linear approximations 2-16
2.3 Finite Element analysis 2-17
2.3.1 Introduction 2-17
2.3.2 The Finite Element approach 2-17
2.3.3 Good practice 2-19
2.3.4 Stress accuracy 2-21
2.3.5 Non-linear problems 2-22
2.3.6 Shell elements 2-23
2.3.7 The ABAQUS Finite Element analysis program 2-24
2.4 Experimental strain and stress measurement 2-25
2.4.1 Introduction 2-25
2.4.2 The components of stress 2-26
2.4.3 The components of strain 2-29
2.4.4 Strain measurement 2-32
2.4.4.1 Introduction 2-32
2.4.4.2 Electrical resistance strain gauges 2-34

2.4.4.3 Brittle coatings 2-38
2.5 Torsion theory 2-41
2.5.1 Introduction 2-41
2.5.2 Basic torsion theory 2-41
2.5.3 Warping 2-48
2.5.4 Calculation of torsional capacity 2-53
2.5.4.1 Expressions for elastic and plastic capacity 2-53
2.5.4.2 The shear yield stress and tensile yield stress 2-54
2.5.4.3 Experimental measurement of the shear yield stress for hot finished steel 2-56
2.5.5 Experimental studies of the torsional properties of tubes 2-59
2.6 Summary 2-60
3 Bending (four-point loading) 3-1
3.1 Introduction 3-1
3.2 A description of the apparatus and testing procedure 3-2
3.2.1 The four-point bending test apparatus 3-2
3.2.2 The four-point bending test specimens 3-5
3.2.3 Instrumentation 3-6
3.2.3.1 Measurement of bending moment 3-6
3.2.3.2 Measurement of curvature 3-6
3.2.3.3 Measurement of strain 3-7
3.2.3.4 Other measurements 3-9
3.2.4 Testing procedure 3-9
3.3 Specimen types, dimensions and properties 3-10
3.3.1 Specimens tested 3-10
3.3.2 Material properties 3-11
3.3.3 Dimensions and geometrical properties 3-12
3.4 The experimental results 3-14
3.5 A comparison of experimental results and analytical predictions 3-20
3.6 Concluding remarks 3-32
4 Shear (three-point loading) 4-1
4.1 Introduction 4-1
4.2 A description of the apparatus and testing procedure 4-2
4.2.1 The three-point bending test apparatus 4-2
4.2.2 The three-point bending test specimens 4-4
4.2.3 Instrumentation 4-5
4.2.3.1 Measurement of shear force and bending moment 4-5
4.2.3.2 Measurement of deflection 4-5
4.2.3.3 Measurement of strain 4-6
4.2.3.4 Other measurements 4-7
4.2.4 Testing procedure 4-8
4.3 Specimen types, dimensions and properties 4-9
4.3.1 Specimens tested 4-9
4.3.2 Material properties 4-9
4.3.3 Dimensions and geometrical properties 4-10
4.4 The experimental results 4-12
4.5 A comparison of experimental results and analytical predictions 4-19
4.6 Concluding remarks 4-28
5 Full-scale torsion 5-1
5.1 Introduction 5-1
5.2 A description of the apparatus and testing procedure 5-1
5.2.1 The torsion test apparatus 5-1
5.2.2 The torsion test specimens 5-4
5.2.3 Connection of the specimen and rig 5-5
5.2.4 Instrumentation 5-6
5.2.4.1 Measurement of torque 5-6
5.2.4.2 Measurement of rotation 5-9
5.2.4.3 Measurement of strain 5-10
5.2.4.4 Other measurements 5-12

5.2.5 Testing procedure 5-12
5.3 Specimen types, dimensions and properties 5-13
5.3.1 Specimens tested 5-13
5.3.2 Material properties 5-14
5.3.3 Dimensions and geometrical properties 5-14
5.4 The experimental results 5-16
5.5 A comparison of experimental results and analytical predictions 5-21
5.6 The validity of the experimental findings 5-32
5.6.1 Introduction 5-32
5.6.2 Measurement of rotation 5-32
5.6.3 Measurement of torque 5-34
5.6.4 Measurement of strain 5-35
5.6.5 Repeatability of experimental results 5-36
5.6.6 Accuracy of the data measurement and logging system 5-36
5.6.7 Additional loads on the specimen 5-37
5.6.8 The validity of the theoretical and analytical predictions 5-38
5.6.8.1 Introduction 5-38
5.6.8.2 Boundary conditions 5-38
5.6.8.3 Cross-section dimensions 5-40
5.6.8.4 Material properties 5-40
5.6.9 Marshall's results 5-48
5.6.10 Summary 5-51
5.7 Suitable schemes for further investigation 5-52
5.8 Concluding remarks 5-52
6 Small-scale torsion 6-1
6.1 Introduction 6-1
6.2 A description of the apparatus and testing procedure 6-2
6.2.1 The torsion test apparatus and specimens 6-2
6.2.2 Types of specimen and scope of study 6-4
6.3 The experimental results 6-10
6.3.1 Measured torque-rotation relationships 6-10
6.3.2 Mechanisms of failure 6-14
6.4 A comparison of experimental results and analytical predictions 6-17
6.4.1 Introduction 6-17
6.4.2 Deformed shapes 6-18
6.4.3 Torque-rotation relationships 6-20
6.5 Stress distributions 6-25
6.6 Concluding remarks 6-27
7 Parametric study and design recommendations 7-1
7.1 Introduction 7-1
7.2 Scope and limitations 7-2
7.3 General design procedure 7-5
7.4 The parametric Finite Element study 7-8
7.5 Bending 7-13
7.5.1 Introduction 7-13
7.5.2 Concentration factors for elastic stress 7-17
7.5.3 Resistance 7-24
7.5.4 Deflection 7-37
7.5.5 Zone of influence 7-40
7.5.6 Design recommendation for calculation of resistance 7-41
7.6 Shear 7-43
7.6.1 Introduction 7-43
7.6.2 Concentration factors for elastic stress 7-46
7.6.3 Resistance 7-50
7.6.4 Deflection 7-56
7.6.5 Zone of influence 7-58
7.6.6 Design recommendation for calculation of resistance 7-58
7.7 Torsion 7-60
7.7.1 Introduction 7-60

7.7.2 Concentration factors for elastic stress 7-62
7.7.3 Resistance 7-66
7.7.4 Deflection 7-72
7.7.5 Zone of influence 7-75
7.7.6 Design recommendation for calculation of resistance 7-76
7.8 Combinations 7-77
7.8.1 Introduction 7-77
7.8.2 Design recommendation for calculation of resistance 7-78
7.9 Concluding remarks 7-81
8 Conclusions 8-1
8.1 Introduction 8-1
8.2 Laboratory testing and calibration of Finite Element models 8-1
8.2.1 Four-point bending (bending) 8-1
8.2.2 Three-point bending (shear) 8-2
8.2.3 Full-scale torsion 8-3
8.2.4 Small-scale torsion 8-4
8.3 The parametric Finite Element study 8-5
8.3.1 Bending 8-5
8.3.2 Shear 8-6
8.3.3 Torsion 8-7
8.4 Concluding remarks 8-8
8.5 Lists of conclusions 8-9
8.5.1 Bending of perforated RHS (without elastic instability) 8-9
8.5.2 Shearing of perforated RHS (without elastic instability) 8-10
8.5.3 Torsion of perforated RHS (without elastic instability) 8-11
Appendices I
Table of contents II
List of figures III
List of tables IV
A. Calibration of the Avery torsion testing machine VI
B. Sensitivity of sectional properties XVII
C. Formulae for the calculation of the properties of cross-section XXV
D. Material properties XXIX
E. Stress concentration factors (Finite Element) LII
F. Calibration of testing equipment LVIII
References LX
Standards and technical design documents LXVI
Papers and project reports LXVIII
Errata LXIX

List of figures

Figure 1-1: Slim floor and conventional construction 1-3
Figure 1-2: Nineteenth century ‘slim floor’ construction 1-3
Figure 1-3: Examples of internal slim floor beams 1-4
Figure 1-4: The Slimdek internal beam (ASB) 1-5
Figure 1-5: Composite and non-composite edge beam construction 1-7
Figure 1-6: Slim floor edge beam construction 1-8
Figure 1-7: Slim floor components 1-8
Figure 1-8: Perforations 1-11
Figure 1-9: Dimensions (cross-section and corner profile) 1-12
Figure 1-10: Dimensions (web opening) 1-12
Figure 2-1: The stress-strain behaviour of steel from hot finished RHS 2-4
Figure 2-2: The yield plateau 2-5
Figure 2-3: The mathematical model 2-7
Figure 2-4: Evaluating the difference between two functions using area 2-13
Figure 2-5: The difference between the approximation and the experimental data 2-14
Figure 2-6: The mathematical approximation and the yield plateau 2-14
Figure 2-7: The mathematical approximation and the experimental data 2-15
Figure 2-8: A multi-linear model 2-17
Figure 2-9: Components of stress acting on a small cubic element 2-28
Figure 2-10: A rotation of the coordinate system 2-29
Figure 2-11: Mohr’s circle for stress (two-dimensions) 2-29
Figure 2-12: Mohr’s circle for strain (two-dimensions) 2-32
Figure 2-13: An electrical resistance strain gauge 2-37
Figure 2-14: A three-element strain gauge rosette 2-38
Figure 2-15: Measurements of strain on a three-element strain gauge rosette 2-38
Figure 2-16: Three types of yield lines in brittle coatings 2-40
Figure 2-17: Yield lines in a brittle coating due to bending 2-40
Figure 2-18: Stress distributions around web openings (yield line patterns) 2-41
Figure 2-19: Torsional inertia constant (Marshall and BS EN 10210 calculations) 2-46
Figure 2-20: Torsional modulus constant (Marshall and BS EN 10210 calculations) 2-46
Figure 2-21: Torsional inertia constant (thin and thick wall calculations) 2-47
Figure 2-22: Torsional modulus constant (thin and thick wall calculations) 2-47
Figure 2-23: Warping of rectangular cross-sections 2-51

Figure 2-24: Warping of RHS in torsion (theory and FE) 2-52
Figure 2-25: The effect of end restraint on torsional behaviour of RHS 2-52
Figure 2-26: Warping at an unrestrained end adjacent to a torsional buckle 2-53
Figure 2-27: The von Mises and Tresca failure envelopes 2-56
Figure 2-28: The shear testing coupon 2-58
Figure 2-29: Shear testing coupon results 2-58
Figure 3-1: Schematic of the four-point bending test 3-3
Figure 3-2: The four-point loading test apparatus 3-3
Figure 3-3: The supports (rocker and fixed) 3-4
Figure 3-4: A dual axis rocker bearing 3-4
Figure 3-5: Four-point bending test specimen 3-5
Figure 3-6: Measurement of curvature with linear potentiometers 3-6
Figure 3-7: Strain gauge pattern (not REPEAT1, REPEAT4, DREB1 and DREB2) 3-7
Figure 3-8: Strain gauge pattern (tests DREB1 and DREB2) 3-8
Figure 3-9: Strain gauge pattern (test REPEAT4) 3-8
Figure 3-10: Experimental results RHS 200x100x8 no holes 3-17
Figure 3-11: Experimental results RHS 250x250x10 no holes 3-17
Figure 3-12: Experimental results RHS 200x100x8 one hole 165 mm dia 3-18
Figure 3-13: Experimental results RHS 250x250x10 one hole 165 mm dia 3-18
Figure 3-14: Experimental results RHS 200x100x8 two holes 165 mm dia 3-19
Figure 3-15: Experimental results RHS 250x250x10 two holes 165 mm dia 3-19
Figure 3-16: FE and experimental (tests REPEAT1 and REPEAT5) 3-25
Figure 3-17: FE and experimental (tests REPEAT3 and REPEAT4) 3-25
Figure 3-18: FE and experimental (test TEST6) 3-26
Figure 3-19: FE and experimental (test DREB1) 3-26
Figure 3-20: FE and experimental (tests TEST5A and TEST5B) 3-27
Figure 3-21: FE and experimental (test DREB2) 3-27
Figure 3-22: Displaced shape RHS 200x100x8 no holes 3-28
Figure 3-23: Displaced shape RHS 200x100x8 one hole 3-28
Figure 3-24: Displaced shape RHS 200x100x8 two holes 3-28
Figure 3-25: Displaced shape RHS 250x250x10 no holes 3-29
Figure 3-26: Displaced shape RHS 250x250x10 one hole 3-29
Figure 3-27: Displaced shape RHS 250x250x10 two holes 3-29
Figure 3-28: Displaced shape RHS 200x100x8 two holes (superposition) 3-30
Figure 3-29: Longitudinal strain for RHS 250x250x10 unperforated (REPEAT4) 3-30
Figure 3-30: Principal strains for RHS 250x250x10 one hole (unperforated web) 3-31
Figure 3-31: Principal strains for RHS 250x250x10 one hole (perforated web) 3-31
Figure 4-1: Schematic of the three-point bending test 4-3
Figure 4-2: The three-point bending test apparatus 4-3
Figure 4-3: Three-point bending test specimen 4-4

Figure 4-4: Measurement of vertical displacement with linear potentiometers 4-5
Figure 4-5: Strain gauge pattern (all tests) 4-6
Figure 4-6: Inclinometers for measurement of twist 4-7
Figure 4-7: Measurement of twist at the rocker support 4-8
Figure 4-8: Experimental results RHS 200x100x8 4-14
Figure 4-9: Experimental results RHS 250x250x10 4-14
Figure 4-10: Shear force-displacement relationship RHS 200x100x8 no holes 4-15
Figure 4-11: Displacement profiles RHS 200x100x8 no holes 4-15
Figure 4-12: Shear force-displacement relationship RHS 200x100x8 one hole 4-16
Figure 4-13: Displacement profiles RHS 200x100x8 one hole (perforated web) 4-17
Figure 4-14: Displacement profiles RHS 200x100x8 one hole (unperforated web) 4-17
Figure 4-15: Shear force-displacement relationship RHS 200x100x8 two holes 4-18
Figure 4-16: Displacement profiles RHS 200x100x8 two holes 4-18
Figure 4-17: FE and experimental (test TESTS1) 4-22
Figure 4-18: FE and experimental (test TESTS4) 4-22
Figure 4-19: FE and experimental (test TESTS3) 4-23
Figure 4-20: FE and experimental (test TESTS6) 4-23
Figure 4-21: FE and experimental (test TESTS2) 4-24
Figure 4-22: FE and experimental (test TESTS5) 4-24
Figure 4-23: FE and experimental (twist of TESTS3) 4-25
Figure 4-24: FE and experimental (twist of TESTS6) 4-25
Figure 4-25: Displaced shapes (Finite Element, perforated) 4-26
Figure 4-26: Displaced shapes (experimental, perforated) 4-26
Figure 4-27: Displaced shapes (Finite Element, unperforated) 4-27
Figure 4-28: Displaced shapes (Experimental, unperforated) 4-27
Figure 4-29: Displaced shape RHS 200x100x8 two holes (superposition) 4-28
Figure 5-1: The torsion testing apparatus (schematic) 5-3
Figure 5-2: The torsion testing apparatus 5-3
Figure 5-3: Torsion test specimen 5-4
Figure 5-4: The connecting plates and bolting arrangement 5-6
Figure 5-5: The calibration shaft 5-7
Figure 5-6: Calibration data 5-8
Figure 5-7: Calibration data (averaged measurements) 5-8
Figure 5-8: Calibration of the load-indicating shaft 5-9
Figure 5-9: Inclinometers for measurement of rotation 5-10
Figure 5-10: Inclinometer locations 5-10
Figure 5-11: Strain gauge pattern (tests TT1-TT6) 5-11
Figure 5-12: Strain gauge pattern (test TT7) 5-11
Figure 5-13: Experimental results RHS 200x100x8 no holes 5-18
Figure 5-14: Experimental results RHS 150x150x6.3 no holes 5-18

Figure 5-15: Experimental results RHS 200x100x8 one hole 165 mm dia 5-19
Figure 5-16: Experimental results RHS 150x150x6.3 one hole 99 mm dia 5-19
Figure 5-17: Experimental results RHS 200x100x8 two holes 165 mm dia 5-20
Figure 5-18: Experimental results RHS 150x150x6.3 two holes 99 mm dia 5-20
Figure 5-19: Experimental result RHS 150x150x6.3 two holes 38.1 mm dia 5-21
Figure 5-20: FE and experimental (test TT4) 5-25
Figure 5-21: FE and experimental (test TT3) 5-25
Figure 5-22: FE and experimental (test TT6) 5-26
Figure 5-23: FE and experimental (test TT5) 5-26
Figure 5-24: FE and experimental (test TT2) 5-27
Figure 5-25: FE and experimental (test TT1) 5-27
Figure 5-26: FE and experimental (tests TT7 and TT14) 5-28
Figure 5-27: FE and experimental (test TT8) 5-28
Figure 5-28: FE and experimental (test TT12) 5-29
Figure 5-29: FE and experimental (test TT13) 5-29
Figure 5-30: FE and experimental (test TT9) 5-30
Figure 5-31: FE and experimental (test TT10) 5-30
Figure 5-32: FE and experimental (test TT11) 5-31
Figure 5-33: Displaced shape RHS 150x150x6.3 one hole 99 mm dia 5-31
Figure 5-34: Displaced shape RHS 200x100x8 two holes 165 mm dia 5-32
Figure 5-35: Rotation measurements 5-33
Figure 5-36: Load measurements 5-35
Figure 5-37: Boundary conditions RHS 200x100x8 grade S275J2H 1 hole 5-39
Figure 5-38: Boundary conditions RHS 150x150x6.3 grade S275J2H 1 hole 5-39
Figure 5-39: Reduced yield RHS 200x100x8 grade S275J2H no holes 5-44
Figure 5-40: Reduced yield RHS 150x150x6.3 grade S275J2H no holes 5-44
Figure 5-41: Reduced yield RHS 200x100x8 grade S275J2H one hole 5-45
Figure 5-42: Reduced yield RHS 150x150x6.3 grade S275J2H one hole 5-45
Figure 5-43: Reduced yield RHS 200x100x8 grade S275J2H two holes 5-46
Figure 5-44: Reduced yield RHS 150x150x6.3 grade S275J2H two holes 5-46
Figure 5-45: Strain measurements (test TT4 south web) 5-47
Figure 5-46: Strain measurements (test TT4 north web) 5-47
Figure 5-47: Measurements and predictions of torque at yield (unperforated) 5-51
Figure 6-1: The small-scale torsion rig 6-3
Figure 6-2: Small-scale torsion test specimen 6-3
Figure 6-3: The inserts and clamping plates 6-4
Figure 6-4: Types of specimen (developed views) 6-7
Figure 6-5: Stress-strain relationship from tensile tests 6-7
Figure 6-6: Stress-strain relationship for cold-formed and hot finished steel (1%) 6-9
Figure 6-7: Stress-strain relationship for cold-formed and hot finished steel 6-9

Figure 6-8: Torque rotation curves – One hole (Type II) 6-12
Figure 6-9: Torque rotation curves – Two holes facing (Type III) 6-12
Figure 6-10: Peak torque and hole diameter – Types I, II & III 6-13
Figure 6-11: Torque-rotation curves for type IV specimens 6-13
Figure 6-12: Peak torque and hole separation (Type IV) 6-14
Figure 6-13: Post-yield failure by buckling 6-16
Figure 6-14: Failure of type II specimens 6-16
Figure 6-15: Failure of type III specimens 6-16
Figure 6-16: Failure of type IV specimens 6-17
Figure 6-17: Regions of high tensile stress around the hole 6-17
Figure 6-18: Displaced shape (type I) 6-18
Figure 6-19: Displaced shape (type II 10 mm dia) 6-18
Figure 6-20: Displaced shape (type II 30 mm dia) 6-19
Figure 6-21: Displaced shape (type III 20 mm dia) 6-19
Figure 6-22: Displaced shape (type III 30 mm dia) 6-19
Figure 6-23: FE and experimental for type I specimens (no holes) 6-23
Figure 6-24: FE and Experimental for type II specimens (one hole) 6-23
Figure 6-25: FE and experimental for type III specimens (two holes facing) 6-24
Figure 6-26: The influence of boundary conditions 6-25
Figure 6-27: Concentration factors for Von Mises stress around a small hole 6-26
Figure 6-28: Concentration factors for Von Mises stress around a large hole 6-27
Figure 7-1: Perforated and unperforated sub-members 7-7
Figure 7-2: Locations for stress concentration 7-7
Figure 7-3: Model coordinate axes 7-12
Figure 7-4: Finite Element meshes for parametric investigation 7-12
Figure 7-5: Cross-section classifications and moment-rotation relationship 7-17
Figure 7-6: Distribution of elastic bending stress 7-21
Figure 7-7: Distribution of von Mises stress for RHS 250x250x10 in bending 7-22
Figure 7-8: Parametric sampling for bending 7-23
Figure 7-9: Stress concentration factors for bending 7-23
Figure 7-10: Critical hole size ratio for bending 7-24
Figure 7-11: Elastic moment capacity 7-29
Figure 7-12: The significance of strain hardening for beam ductility 7-30
Figure 7-13: Distortions under the action of bending (two holes) 7-31
Figure 7-14: Distortions under the action of bending (one hole) 7-31
Figure 7-15: Moment-curvature relationship for RHS 250x250x10 one hole 7-32
Figure 7-16: Moment-curvature relationship for RHS 250x250x10 two holes 7-32
Figure 7-17: Moment-curvature relationship for RHS 300x200x12 one hole 7-33
Figure 7-18: Moment-curvature relationship for RHS 300x200x12 two holes 7-33
Figure 7-19: Moment-curvature relationship for RHS 200x100x8 one hole 7-34

Figure 7-20: Moment-curvature relationship for RHS 200x100x8 two holes 7-34
Figure 7-21: Yield in bending for sections with one hole (FE and design) 7-35
Figure 7-22: Yield in bending for sections with two holes (FE and design) 7-35
Figure 7-23: Maximum moment for sections with one hole (FE and design) 7-36
Figure 7-24: Maximum moment for sections with two holes (FE and design) 7-36
Figure 7-25: Maximum moment without strain hardening 7-37
Figure 7-26: Bending displacement of RHS 200x100x8 two holes 140.8 mm dia 7-40
Figure 7-27: Critical cantilever length for shear 7-45
Figure 7-28: Distribution of elastic shear stress 7-48
Figure 7-29: Parametric sampling for shear 7-48
Figure 7-30: Distribution of von Mises stress for RHS 200x100x8 in shear 7-49
Figure 7-31: Stress concentration factors for shear 7-50
Figure 7-32: Shear force-shearing angle relationship for RHS 250x250x10 one hole 7-53
Figure 7-33: Shear force-shearing angle relationship for RHS 250x250x10 two holes 7-53
Figure 7-34: Shear force-shearing angle relationship for RHS 300x200x12 one hole 7-54
Figure 7-35: Shear force-shearing angle relationship for RHS 300x200x12 two holes 7-54
Figure 7-36: Shear force-shearing angle relationship for RHS 200x100x8 one hole 7-55
Figure 7-37: Shear force-shearing angle relationship for RHS 200x100x8 two holes 7-55
Figure 7-38: The vierendeel mechanism of shear failure 7-56
Figure 7-39: Distortions under the action of shear 7-57
Figure 7-40: Shear displacement of RHS 200x100x8 two holes 140.8 mm dia 7-57
Figure 7-41: Parametric sampling for torsion 7-64
Figure 7-42: Stress concentration factors for torsion 7-64
Figure 7-43: Distribution of von Mises stress for RHS 250x250x10 in torsion 7-65
Figure 7-44: Torque-rotation relationship for RHS 250x250x10 one hole 7-68
Figure 7-45: Torque-rotation relationship for RHS 250x250x10 two holes 7-68
Figure 7-46: Torque-rotation relationship for RHS 300x200x12 one hole 7-69
Figure 7-47: Torque-rotation relationship for RHS 300x200x12 two holes 7-69
Figure 7-48: Torque-rotation relationship for RHS 200x100x8 one hole 7-70
Figure 7-49: Torque-rotation relationship for RHS 200x100x8 two holes 7-70
Figure 7-50: Maximum torque for RHS 250x250x10 7-71
Figure 7-51: Maximum torque for RHS 200x100x8 7-71
Figure 7-52: Distortions under the action of torsion 7-73
Figure 7-53: Torsional twist of RHS 250x250x10 two holes 7-74
Figure 7-54: Torsional twist of RHS 200x100x8 two holes 7-74
Figure 7-55: Stiffness reduction factors for torsion 7-75
Figure 7-56: Contours of bending capacity with coexistent shear and torsion 7-80
Figure 7-57: Bending capacity with coexistent shear or torsion 7-80
Figure 7-58: Possible stiffening or reinforcement of web openings 7-83

List of tables

Table 3-1: Specimens tested 3-11
Table 3-2: Material models 3-12
Table 3-3: Dimensions of cross-section (measured) 3-13
Table 3-4: Properties of cross-section (from measured dimensions) 3-13
Table 3-5: Sectional properties (measured dims and material props, theoretical) 3-13
Table 3-6: Sectional properties (nominal, theoretical) 3-14
Table 3-7: Experimental results – stiffness and maximum bending moment 3-16
Table 3-8: Experimental results and theory– stiffness and max bending moment 3-16
Table 3-9: Finite Element results – stiffness and maximum bending moment 3-23
Table 3-10: Experimental and FE results – stiffness and maximum bending moment 3-24
Table 4-1: Specimens tested 4-9
Table 4-2: Material models 4-10
Table 4-3: Dimensions of cross-section (measured) 4-11
Table 4-4: Properties of cross-section (from measured dimensions) 4-11
Table 4-5: Sectional properties (measured dims and material props, theoretical) 4-11
Table 4-6: Sectional properties (nominal, theoretical) 4-11
Table 4-7: Experimental results – stiffness and maximum shear force 4-13
Table 4-8: Finite Element results – stiffness and maximum shear force 4-21
Table 4-9: Experimental and FE results – stiffness and maximum shear force 4-21
Table 5-1: Specimens tested 5-13
Table 5-2: Material models 5-14
Table 5-3: Dimensions of cross-section (measured) 5-15
Table 5-4: Properties of cross-section (from measured dimensions) 5-15
Table 5-5: Sectional properties (measured dims and material props, theoretical) 5-15
Table 5-6: Sectional properties (nominal, theoretical) 5-15
Table 5-7: Experimental results – stiffness and maximum torque 5-17
Table 5-8: Measurements of torsional shear strain in unperforated sections 5-17
Table 5-9: Finite Element results – stiffness and maximum torque 5-23
Table 5-10: Experimental and FE results – stiffness and maximum torque 5-24
Table 5-11: Dimensions and material properties of Marshall's torsion test specimens 5-49
Table 5-12: Properties of cross-section for Marshall's torsion test specimens 5-49
Table 5-13: Theoretical plastic torque and torque at yield for Marshall's torsion tests 5-50
Table 5-14: Plastic torque and torque at yield measured by Marshall 5-50

Table 6-1: Specimens tested 6-6
Table 6-2: ABAQUS material models for cold-formed tube 6-8
Table 6-3: Dimensions of cross-section (measured) 6-8
Table 6-4: Properties of cross-section (from measured dimensions) 6-8
Table 6-5: Sectional properties (measured dims and material props, theoretical) 6-8
Table 6-6: Maximum torque (average experimental and FE) 6-22
Table 6-7: Elastic stiffness from Finite Element (average over 240 mm length) 6-22
Table 6-8: Concentration factors for Von Mises stress 6-26
Table 7-1: Equivalence of material grades for design 7-2
Table 7-2: RHS in the European Standard range 7-5
Table 7-3: Material model for parametric study 7-11
Table 7-4: ABAQUS material model for parametric study 7-11
Table 7-5: Boundary conditions for parametric FE models 7-11
Table 7-6: Deflection in bending 7-39
Table 7-7: Stress concentration factors for bending, $\psi_{bending}$ 7-43
Table 7-8: Critical hole size ratio for bending, Φ_{cr} 7-43
Table 7-9: Stress concentration factors for shear, ψ_{shear} 7-59
Table 7-10: Stress concentration factors for torsion, $\psi_{torsion}$ 7-77

Abstract (long version)

The use of Rectangular Hollow Sections (RHS) as edge beams in steel frame building construction is becoming increasingly common. Edge beams are subject to out of balance loads and RHS members are usually specified to take advantage of their comparatively high torsional rigidity. Although the tubular nature of the RHS offers an ideal opportunity for improved service integration, the influence of an opening in the web upon the structural performance of the section has been found to be significant.

The primary aim of the project was to develop the basis for a set of rules to be used in the design of RHS slim floor edge beams with web openings. However, since the research is fundamental in nature, the findings are also applicable to other situations where it may be advantageous to cut holes in load bearing tubular members of rectangular cross-section.

The study considered the influence of the number and size of holes upon resistance and stiffness in bending, shear, and torsion and combined analytical Finite Element modelling with large and small scale pseudo-static (short-time static loading) laboratory testing.

Large web openings were found to cause a significant reduction in both the torsional capacity (up to 60%) and stiffness (up to 40%). The reduction in stiffness was due to the perforated zone being much more flexible than the unperforated beam and severe deformations in this zone were observed. The reduction in capacity was

found to be comparable to the reduction in the cross-sectional area of the perforated web.

The reduction in the shear capacity due to large web openings was found to be as much as 85%, and the shear stiffness of the perforated zone was also reduced significantly. The reduction in the shear capacity was found to be comparable to the reduction in the cross-sectional area of the webs at the location of the hole.

The reduction in the bending capacity due to large web openings was found to be as much as 30%, but the reduction in elastic stiffness was slight (less than 5%). The reduction in the bending capacity was found to be comparable to the reduction in the elastic and plastic section moduli at the location of the hole. In some cases, web openings were observed to decrease the plastic stability of the cross-section causing a reduction in the rotation capacity.

In all but one category of tests (see below), good agreement was achieved between experimentally measured quantities (such as capacities, deflections and strains) and the corresponding Finite Element predictions, allowing parametric investigations to be conducted with calibrated analytical models. Generally, the predictions of elastic and plastic capacities were within 15% of the measured quantities and predictions of elastic stiffness within 20%.

Preliminary design recommendations are presented based on the results of the parametric study and laboratory tests. The design advice was developed with regard to existing recommendations for the design of perforated I-beams, and was produced in a form that allows integration with modern limit state design codes. Aspects of behaviour requiring further investigation have been identified and categorised.

Torsion tests on full-scale RHS without web openings yielded some unexpected results. Elastic and plastic capacities measured in the laboratory were significantly lower (12–20%) than those predicted by the Finite Element models and the thick walled torsion theory used as the basis of the British and European design procedures. Attempts were made to determine the cause of this behaviour and a number of possibilities were eliminated. Although the anomalous results have not been fully explained, evidence of similar behaviour in previous full-scale testing was discovered.

Abstract (short version)

The primary aim of the project was to develop the basis for a set of rules to be used in the design of RHS slim floor edge beams with web openings. However, since the research is fundamental in nature, the findings are also applicable to other situations where it may be advantageous to cut holes in load bearing tubular members of rectangular cross-section.

The study considered the influence of the number and size of holes upon resistance and stiffness in bending, shear, and torsion and combined analytical Finite Element modelling with large and small scale pseudo-static (short-time static loading) laboratory testing.

In all but one category of tests (see below), good agreement was achieved between experimentally measured quantities (such as capacities, deflections and strains) and the corresponding Finite Element predictions, allowing parametric investigations to be conducted with calibrated analytical models.

Preliminary design recommendations are presented based on the results of the parametric study and laboratory tests. The design advice was developed with regard to existing recommendations for the design of perforated I-beams, and was produced in a form that allows integration with modern limit state design codes. Aspects of behaviour requiring further investigation have been identified and categorised.

Torsion tests on full scale RHS without web openings yielded some unexpected results. Elastic and plastic capacities measured in the laboratory were significantly lower (12–20%) than those predicted by the Finite Element models and the thick walled torsion theory used as the basis of the British and European design procedures. Attempts were made to determine the cause of this behaviour and a number of possibilities were eliminated. Although the anomalous results have not been fully explained, evidence of similar behaviour in previous full-scale testing was discovered.

Acknowledgements

I would like to offer my thanks for the invaluable support, guidance and motivation provided by my supervisors, Dr. Gwynne Davies and Dr. John Owen, of the University of Nottingham and by my project advisors, Eddie Hole and Noel Yeomans of British Steel Tubes and Pipes plc (now known as Corus Tubes). Thanks are also due to Gordon Hardy, Gary Hayes, Geoff Mitchell, Bal Loyla, Brian Whitehouse, Nigel Rook and Bob Collins for their expedient and proficient technical assistance, and to the University for the use of its facilities. I would also like to thank everyone else who has helped me on the way, most notably my parents for their continuing patience.

Funding for this research was provided jointly and graciously by the University of Nottingham and by British Steel Tubes and Pipes plc.

Author's declaration

I declare that, unless otherwise stated in the text, the contents of this thesis are the results of my own work conducted under the guidance of my supervisors.

Daniel James Ridley-Ellis

Signature
Not Verified

Daniel
Ridley-Ellis

Digitally signed by
Daniel Ridley-Ellis
DN: cn=Daniel
Ridley-Ellis, o=University
of Nottingham,
ou=School of Civil
Engineering, c=GB
Date: 2001.09.17
15:45:43 Z

Notation and symbols

Latin

a	Horizontal semi axis of the strain hardening ellipse
A	Area (of cross-section)
A_h	Area enclosed by mean perimeter
A_v	Shear area
A_ζ	Intermediate quantity (BS EN 10210-2:1997)
A_ξ	Intermediate quantity (BS EN 10210-2:1997)
b	Length of the shorter side of a Rectangular Hollow Section (width)
b	Vertical semi axis of the strain hardening ellipse
C_t	Torsional modulus constant
D	The diameter of a circular web opening
E	Young's modulus
$E_{plateau}$	Stiffness of the yield plateau
f_u	Ultimate (material) strength
f_y	Yield strength
f_{y1}	Yield strength (mathematical model)
f_{y2}	Stress at onset of strain hardening
$f_{y,reduced}$	Reduced yield strength allowing for shear and/or torsion
G	Shear modulus
h	Length of the longer side of a Rectangular Hollow Section (height)
h_c	Mean perimeter
h_ζ	Intermediate quantity (BS EN 10210-2:1997)
h_ξ	Intermediate quantity (BS EN 10210-2:1997)
i_y	Radius of gyration (axis parallel to flanges)
I_t	Torsional inertia constant
$I_{t,unperf}$	Torsional inertia constant for an unperforated section
I_y	Second moment of area (axis parallel to flanges)
$I_{y,unperf}$	Second moment of area for an unperforated section (axis parallel to flanges)
$l_{V,cr}$	Critical cantilever length for shear

$I_{\zeta\zeta}$	Intermediate quantity (BS EN 10210-2:1997)
$I_{\xi\xi}$	Intermediate quantity (BS EN 10210-2:1997)
K	The suitability of fit (total energy error proportion)
K	Intermediate quantity (BS EN 10210-2:1997)
K_{ends}	The stiffness of the small-scale torsion testing machine
l	Separation of strain gauges
l_{cr}	Critical cantilever length for shear
L	Length of a member
M	Bending moment
$M_{c,y,Rd}$	Design moment of resistance (bending about axis parallel to flanges)
M_e	Elastic moment
$M_{el,y}$	Moment at yield (bending about axis parallel to flanges)
$M_{el,y,Rd,1hole}$	Moment at yield for a section with one opening (design value)
$M_{el,y,Rd,2holes}$	Moment at yield for a section with two openings (design value)
$M_{el,y,Rd,unperf}$	Moment at yield for an unperforated section (design value)
M_p	Full plastic moment
$M_{pl,y}$	Full plastic moment (bending about axis parallel to flanges)
$M_{pl,y,Rd,1hole}$	Moment of resistance for a section with one opening (design value)
$M_{pl,y,Rd,2holes}$	Moment of resistance for a section with two openings (design value)
$M_{pl,y,Rd,unperf}$	Moment of resistance for an unperforated section (design value)
$M_{y,Sd}$	Applied moment (about axis parallel to flanges)
n	Number of openings
r	Radius of web opening (not r_o as in EC3 Annex N)
r	Radius of a circular bar
r	Radius to a strain gauge from the centre of an opening
r_o	External corner radius
r_i	Internal corner radius
R	Rotation capacity
R_c	Mean corner radius
R_{eH}	Upper yield strength as defined by BS EN 10002-1:1990
R_{eL}	Lower yield strength as defined by BS EN 10002-1:1990
R_m	Tensile strength as defined by BS EN 10002-1:1990
s	The distance between two openings in the same web
s	x-coordinate of the centre of the strain hardening ellipse
t	Wall thickness
t	y-coordinate of the centre of the strain hardening ellipse

T	Torque (torsional moment)
T_{el}	Torque at yield
$T_{el,Rd,1hole}$	Torque at yield for a section with one opening (design value)
$T_{el,Rd,2holes}$	Torque at yield for a section with two openings (design value)
$T_{el,Rd,unperf}$	Torque at yield for an unperforated section (design value)
T_{pl}	Torque of resistance
$T_{pl,Rd,1hole}$	Torque of resistance for a section with one opening (design value)
$T_{pl,Rd,2holes}$	Torque of resistance for a section with two openings (design value)
$T_{pl,Rd,unperf}$	Torque of resistance for an unperforated section (design value)
T_{Sd}	Applied torque
$V_{el,y,Rd,1hole}$	Design shear resistance for a section with one opening (yield limited)
$V_{el,y,Rd,2holes}$	Design shear resistance for a section with two openings (yield limited)
$V_{pl,y,Rd,unperf}$	Design shear resistance for an unperforated section (plastic)
V_y	Shear resistance (the product of the shear area and the shear yield stress)
$V_{y,Sd}$	Applied shear force (parallel to webs)
w	Longitudinal warping distortion at the corners of an RHS
$W_{el,y}$	Elastic section modulus (axis parallel to flanges)
$W_{el,y,1hole}$	Elastic section modulus for an RHS with one hole (axis parallel to flanges)
$W_{el,y,2holes}$	Elastic section modulus for an RHS with two holes (axis parallel to flanges)
$W_{el,y,unperf}$	Elastic section modulus for an unperforated section (axis parallel to flanges)
$W_{pl,y}$	Plastic section modulus (axis parallel to flanges)
$W_{pl,y,1hole}$	Plastic section modulus for an RHS with one hole (axis parallel to flanges)
$W_{pl,y,2holes}$	Plastic section modulus for an RHS with two holes (axis parallel to flanges)
$W_{pl,y,unperf}$	Plastic section modulus for an unperforated section (axis parallel to flanges)
x	Rectangular coordinate
x'	Rectangular coordinate (rotated)
xx	Axis along the member
y	Rectangular coordinate
y'	Rectangular coordinate (rotated)
yy	Axis of the cross-section (parallel to flanges, normally the major axis)
z	Rectangular coordinate
zz	Axis of the cross-section (parallel to webs)

Standard Greek

α	Aspect ratio
γ	Partial safety factor
γ	Shear strain
γ_{M0}	Material partial factor
γ_{MBen1}	Material partial factor for bending of perforated RHS
γ_{MBen2}	Material partial factor for bending of perforated RHS
γ_{MShe1}	Material partial factor for shear of perforated RHS
γ_{MShe2}	Material partial factor for shear of perforated RHS
γ_{MTor1}	Material partial factor for torsion of perforated RHS
γ_{MTor2}	Material partial factor for torsion of perforated RHS
γ_{xy}	Shear strain in the y-direction on a plane perpendicular to the x-axis
γ_{yz}	Shear strain in the z-direction on a plane perpendicular to the y-axis
γ_{zx}	Shear strain in the x-direction on a plane perpendicular to the z-axis
ε	Engineering (normal) strain
ε_1	Maximum principal strain
ε_2	Minimum principal strain
ε_A	Normal strain in the A direction
ε_B	Normal strain in the B direction
ε_C	Normal strain in the C direction
ε_T	True (normal) strain
ε_u	Total elongation at maximum stress
ε_{xx}	Normal strain in the x-direction on a plane perpendicular to the x-axis
ε_{y1}	Total normal strain at yield
ε_{y2}	Total normal strain at onset of strain hardening
ε_{yy}	Normal strain in the y-direction on a plane perpendicular to the y-axis
ε_{zz}	Normal strain in the z-direction on a plane perpendicular to the z-axis
θ	Rotation of a Finite Element node or twist of a beam in torsion
θ_A	Inclination of the A direction
θ_B	Inclination of the B direction
θ_C	Inclination of the C direction
θ_{el}	Rotation at yield
κ	Curvature

κ_e	Curvature at elastic moment
κ_p	Curvature at plastic moment (assuming elastic flexural rigidity)
λ_{ESHF}	Elliptical strain hardening factor
λ_{flange}	Flange slenderness
$\lambda_{plateau}$	Plateau ratio
$\lambda_{strength}$	Strength ratio
λ_{web}	Web slenderness
ν	Poisson's ratio
π	Pi (3.14159265359)
$\rho_{torsion}$	Stiffness reduction factor for torsion
σ	Direct stress
σ	Engineering stress
σ_1	Maximum principal stress
σ_2	Minimum principal stress
σ_{xx}	Direct stress in the x-direction on a plane perpendicular to the x-axis
$\sigma_{x'x'}$	Direct stress in the x'-direction on a plane perpendicular to the x'-axis
σ_{yy}	Direct stress in the y-direction on a plane perpendicular to the y-axis
$\sigma_{y'y'}$	Direct stress in the y'-direction on a plane perpendicular to the y'-axis
σ_{zz}	Direct stress in the z-direction on a plane perpendicular to the z-axis
$\sigma_{Mises,Max}$	The maximum von Mises stress
σ_T	True stress
τ	Shear stress
τ_i	Shear stress at the internal surface
τ_{Max}	Maximum shear stress
τ_o	Shear stress at the external surface
τ_{xy}	Shear stress in the y-direction on a plane perpendicular to the x-axis
$\tau_{x'y'}$	Shear stress in the y'-direction on a plane perpendicular to the x'-axis
τ_{xz}	Shear stress in the z-direction on a plane perpendicular to the x-axis
τ_y	Shear stress at yield
τ_{yx}	Shear stress in the x-direction on a plane perpendicular to the y-axis
τ_{yz}	Shear stress in the z-direction on a plane perpendicular to the y-axis
τ_{zx}	Shear stress in the x-direction on a plane perpendicular to the z-axis
τ_{zy}	Shear stress in the y-direction on a plane perpendicular to the z-axis
ϕ	Angle of principal strain

Φ	Hole size ratio
Φ_{cr}	Critical hole size ratio for bending
$\psi_{bending}$	Stress concentration factor for bending
ψ_{shear}	Stress concentration factor for shear
$\psi_{torsion}$	Stress concentration factor for torsion

List of abbreviations and trademarks

ASB	Asymmetric Slimflor Beam
CF210	ComFlor 210 mm deep profiled steel deck
ESHF	Elliptical Strain Hardening Factor
FE	Finite Element
FEA	Finite Element Analysis
RHS	Rectangular Hollow Section
RHSFB	Rectangular Hollow Slimflor beam
SD225	225 mm deep profiled steel deck for Slimdek
UK	United Kingdom

1 Introduction and background

1.1 Introduction

This Thesis describes an investigation into the fundamental behaviour of Rectangular Hollow Sections (RHS), with circular web cut-outs, under the actions of bending, shear and torsion. Full and small-scale laboratory tests were conducted, and the results compared with Finite Element (FE) models and other theoretical predictions, in order to develop the basis for design recommendations. The application in mind initially was that of RHS edge beams with web openings for simple services in steel framed buildings of slim floor construction, but, since the research is fundamental in nature, the results have a more general applicability.

1.2 Background

1.2.1 An outline of the slim floor method of construction

Slim floor is a method of construction for multi-storey steel-framed buildings in which the structural depth of each floor is minimised by incorporating the steel floor beams within the depth of the concrete floor slab. Conventional steel-frame construction places the floor slab above the (downstand) beam such that the structural floor depth is the sum of the slab depth and the depth of the beam. The slim floor approach permits a more efficient use of vertical space, which can result

in a significant reduction in building height and a corresponding reduction in cladding costs. Since the slim floor beams are integrated into the floor structure there are no downstand beams and the floor can be prepared with either a flat soffit, or a false ceiling with no obstructions for service runs.

Floor slabs may comprise of pre-cast concrete units or in-situ concrete placed on profiled metal decking. The use of a composite deck can reduce the weight of the floor and allows the accommodation of minor services in the voids between the ribs of the deck.

Like many innovations, the technique was not entirely new and forms similar to slim floor (Figure 1-2) can be seen in a number of nineteenth century buildings. One such example is Salt's Mill (a textile mill built by Lockwood and Mawson in the early 1850s) at Saltaire near Bradford.

The modern slim floor technique was originally developed in Scandinavia during the 1980s where it has markedly increased the market share for steel framed multi-storey buildings (Lawson and Mullett (1993)). The original Scandinavian beams were termed 'hat' or 'top hat' beams because of their shape, but slim floor beams have since developed into a number of alternative configurations. Figure 1-3 is a schematic illustration of several typical internal beams.

Method (a) is the classic hat shape and consists of four plates welded to form a box. This form has been used previously in the UK. Method (b) uses tee-sections. This and similar forms are common in Norway and Finland. Method (c) is marketed by ConstrucThor plc and is a patented system used in the UK and Scandinavia. Method (d) makes use of a Universal Column (UC) section. The floor units are pre-cast planks and are supported by the bottom flange. Method (e) is British Steel's Slimflor and uses a UC section welded to a bottom plate. This system involves

more fabrication than method (d), but allows easier construction and the use of composite deep deck slabs (principally CF210). Method (f) is British Steel's Slimdek system, incorporating a special asymmetric rolled I-beam, and is described in detail in the following Section.

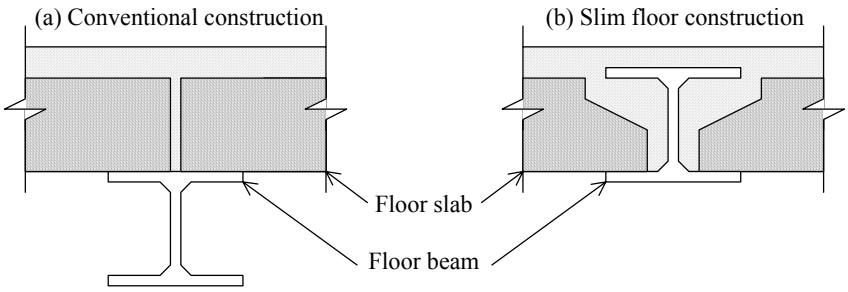

Figure 1-1: Slim floor and conventional construction

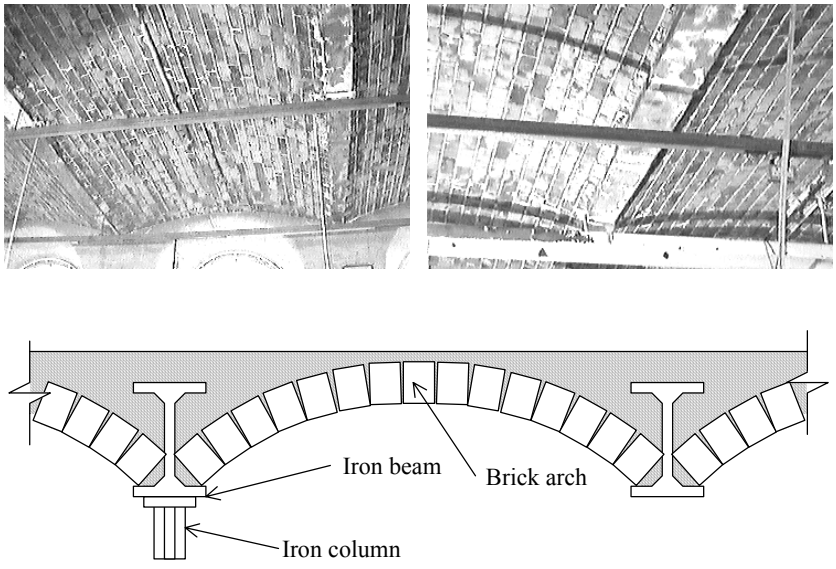

Figure 1-2: Nineteenth century 'slim floor' construction

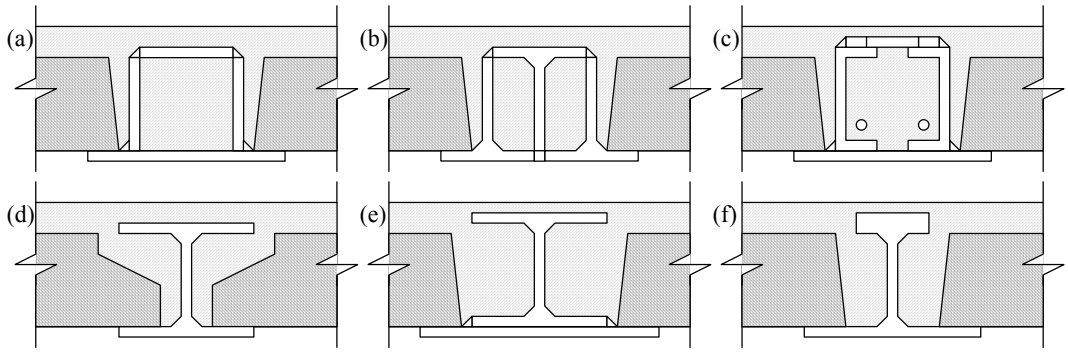

Figure 1-3: Examples of internal slim floor beams

1.2.2 Slimdek

British Steel markets a proprietary slim floor system under the registered trademark Slimdek. Slimdek is a development of the Slimflor beam with new elements specifically designed for slim floor construction. The complete Slimdek system consists of the 'Asymmetric Slimflor Beam' (ASB) used in conjunction with a composite slab of in-situ concrete placed on a profiled metal deck (Figure 1-4).

The asymmetric beam can be up to 25% lighter than conventional Slimflor beams (Lawson et al 1997), and will permit larger openings (up to 160 mm diameter) for services in the web. An embossed diamond pattern rolled on to the beam during manufacture is said to provide composite action with the floor slab without the need for welded shear connectors (Lawson et al 1997). ASB sections are designed for use only with deep deck composite slabs, and an improved deck profile (SD225) was developed to be part of the Slimdek system. The SD225 deck has a greater load carrying capacity and a longer span range than the old CF210 system. It also has an improved ceiling fixing and service integration capability.

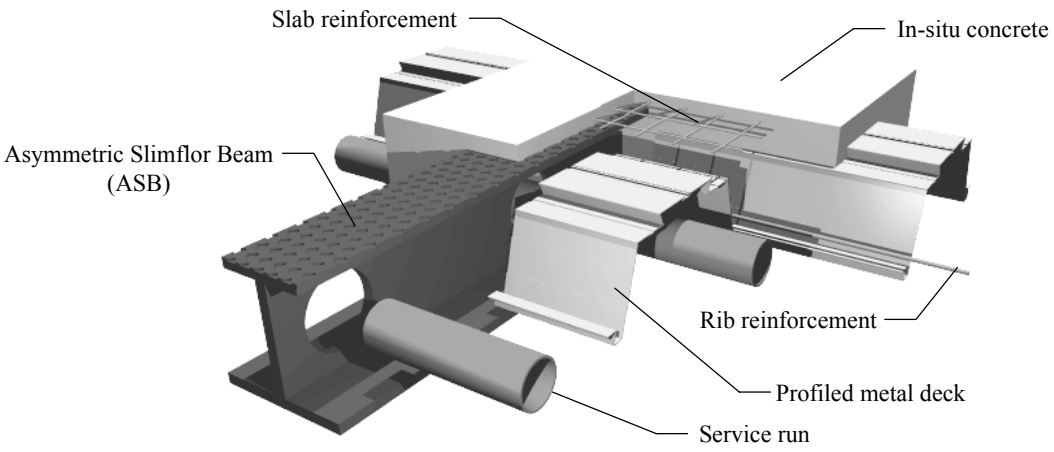

Figure 1-4: The Slimdek internal beam (ASB)

1.2.3 Slim floor edge beams

Beams on the perimeter of a building are loaded, chiefly, on one side only. The ASB and similar open section beams are generally inefficient when subjected to out of balance (combined flexure and torsion) loads. If used inappropriately, they may develop high degrees of rotational twist, causing damage to the building finishes and cladding. For this reason, the Steel Construction Institute recommends the use of an RHS based edge beam (Mullett 1997). In addition to the advantages afforded by the superior torsional rigidity, preliminary studies (Mullett et al 1995) have shown that there is sufficient weight saving to compensate for the higher steel basis cost. RHS edge beams also offer architectural advantages over downstand beam alternatives (Mullett 1997).

The Rectangular Hollow Slimflor beam (RHSFB) consists of a hot finished RHS welded to a 15 mm thick steel flange plate (Figure 1-5). The plate projects on one side to support the floor slab, and usually projects a small amount on the other to permit welding of the section without the need for turning. RHS used in edge beam applications are normally between 200 and 300 mm deep, with wall thicknesses in the range: 6.3 mm to 16 mm (Mullett 1997). Beams are usually of grade S355J2H steel (BS EN 10210-1:1994), but grade S275J2H can be more economical in situations when design is governed by serviceability

The RHSFB may be designed to act compositely or non-compositely with the floor slab depending on the level of structural performance required (Figure 1-5). Composite action requires the use of shear studs tied to the reinforcement mesh in the in-situ concrete. Composite edge beam construction requires an RHS of sufficient wall thickness (8 mm) to prevent burn-through when attaching the shear studs, but torsional loads on the beam are reduced as a result of the composite action. Design advice is available from the Steel Construction Institute (Mullett 1997). Figure 1-6 shows the main elements of slim floor construction using deep decking and an RHS edge beam.

One of the main features of the Slimdek system is the improved service integration capability made possible by the new internal beam and deck profile. The ability to incorporate basic building services in the structural zone capitalises on the principal advantage of the slim floor method by introducing a further economy of vertical space. At the perimeter of the building, such services may be required to pass through the edge beam to the exterior of the building or to pass within the void of the edge beam itself (Figure 1-7). In both instances, openings are required in the webs of the RHS forming the edge beam.

Although the flexural behaviour of I-beams with web openings has been well researched and procedures exist for design (e.g. Annex N of Eurocode 3), there has been little study of the effects of holes in the webs of RHS. The primary aim of this project was to study, experimentally and analytically, the behaviour of RHS with web openings, and to develop the basis for a set of rules for the design of perforated RHS edge beams (presented in Chapter 7). However, since the research is fundamental in nature, the findings are also applicable to other situations where it may be advantageous to cut holes in the webs of load bearing tubular members of rectangular cross-section.

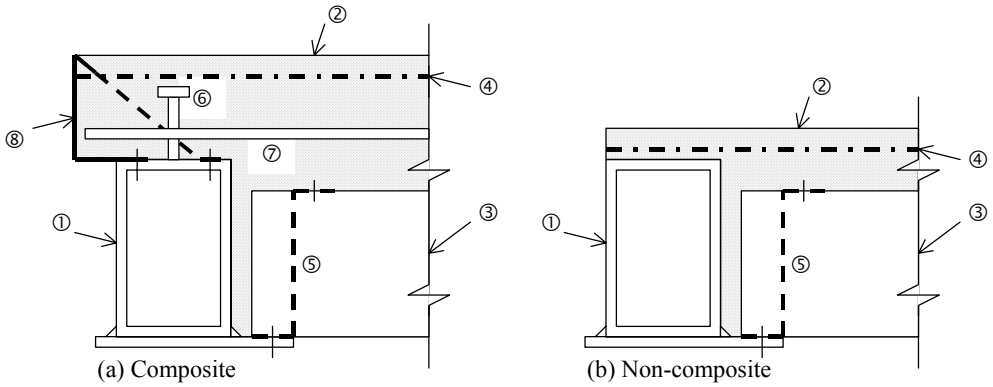

Figure 1-5: Composite and non-composite edge beam construction

Figure based on illustrations in reference Mullett 1997

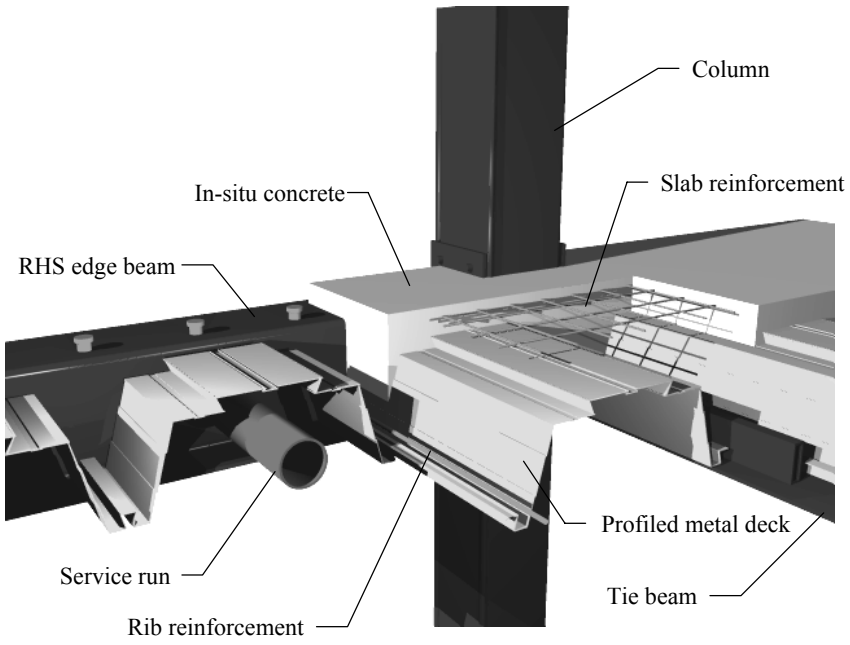

Figure 1-6: Slim floor edge beam construction

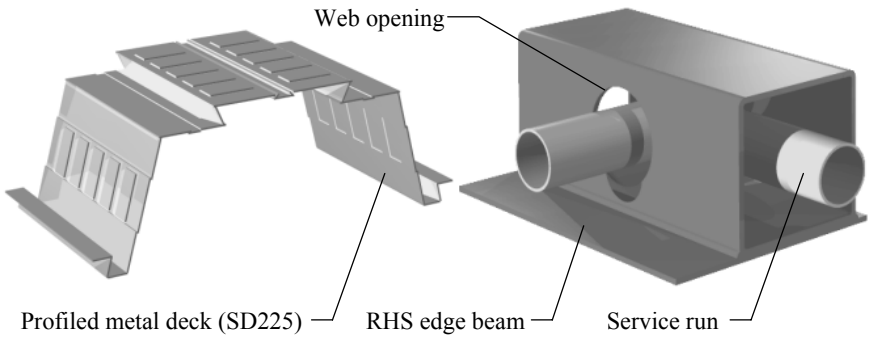

Figure 1-7: Slim floor components

1.3 Methodology

As stated above, the primary aim of this project was to study the behaviour of RHS with web openings, and to develop the basis for a set of design rules for perforated RHS edge beams. To this end, the fundamental structural behaviour of RHS with web openings was examined by an investigation that combined analytical study with both small and full-scale testing. Representative laboratory tests were conducted to provide sufficient data for FE models to be calibrated. The FE models were then used to study the behaviour in greater detail, over a wider range of parameters.

Laboratory testing compared the performance of perforated RHS with that of unperforated control specimens. Three types of full-scale test were used to investigate each of three actions: bending (Chapter 3), shear (Chapter 4) and torsion (Chapter 5). The full-scale tests were conducted on sizes of RHS similar to those used in slim floor construction (Section 1.2.3). A preliminary study, consisting of small-scale torsion testing (Chapter 6), was used to aid the design of the full-scale tests, and the results were also used to augment the calibration of the FE models.

Once the FE models were shown to predict the experimental response to a sufficiently accurate and reliable degree, they were used in a parametric investigation to study the importance of variables such as hole diameter and web slenderness. The FE models were used to obtain information that would have been impractical to obtain from laboratory testing alone, and the results, combined with the experimental observations, were used to develop the basis for the design rules (Chapter 7).

1.4 Scope of study and dimensions of cross-section

The scope of the research is limited to tubes of constant wall thickness, with circular holes (also referred to as 'perforations', 'web openings' and 'cut-outs') placed at mid-depth in the webs. Two cases of perforated section are considered, depending on whether or not both webs contain holes (Figure 1-8). In the case of the doubly perforated RHS, the two holes are of equal diameter, and are situated symmetrically with one in each web.

Standard section sizes for hot-finished RHS are specified by BS EN 10210-2:1997. The three primary dimensions: depth (h), width (b) and wall thickness (t), are defined by BS EN 10210-2:1997 as shown in Figure 1-9. Web and flange slenderness (λ_{web} and λ_{flange}) are defined by Equation 1-1 and Equation 1-2. An additional dimensionless parameter, the hole size ratio (Φ), is used here to indicate the size of the perforation (Equation 1-3 and Figure 1-10).

$$\lambda_{web} = (h - 3t)/t$$

Equation 1-1

$$\lambda_{flange} = (b - 3t)/t$$

Equation 1-2

$$\Phi = 2r/(h - 3t)$$

Equation 1-3

BS EN 10210-2:1997 prescribes a standard nominal corner profile, which relates the internal and external radii to the section thickness. Although most producers roll their own corner profiles (within the permitted tolerances), the section properties quoted in technical documents are calculated from the nominal corner profile. Section properties quoted in this Thesis are based on measured corner profiles, as are FE models of the laboratory tests.

The formulae in Annex A of BS EN 10210-2:1997 for the calculation of the geometrical properties of RHS are also given in Appendix C of this Thesis.

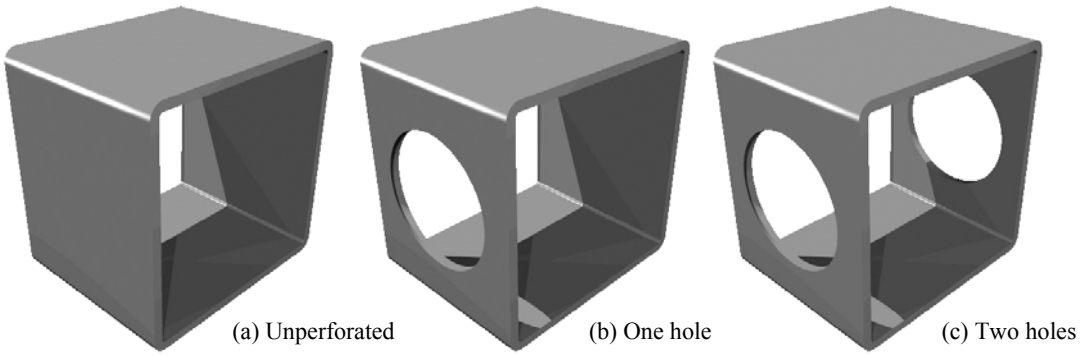

Figure 1-8: Perforations

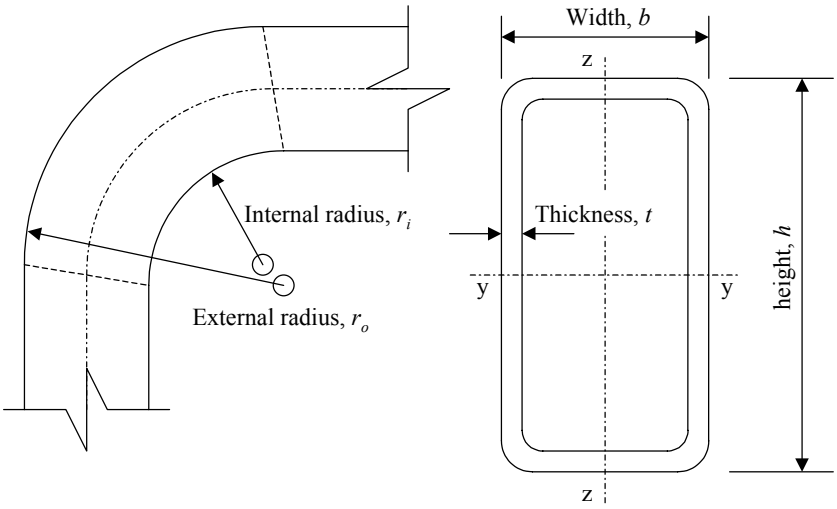

Figure 1-9: Dimensions (cross-section and corner profile)

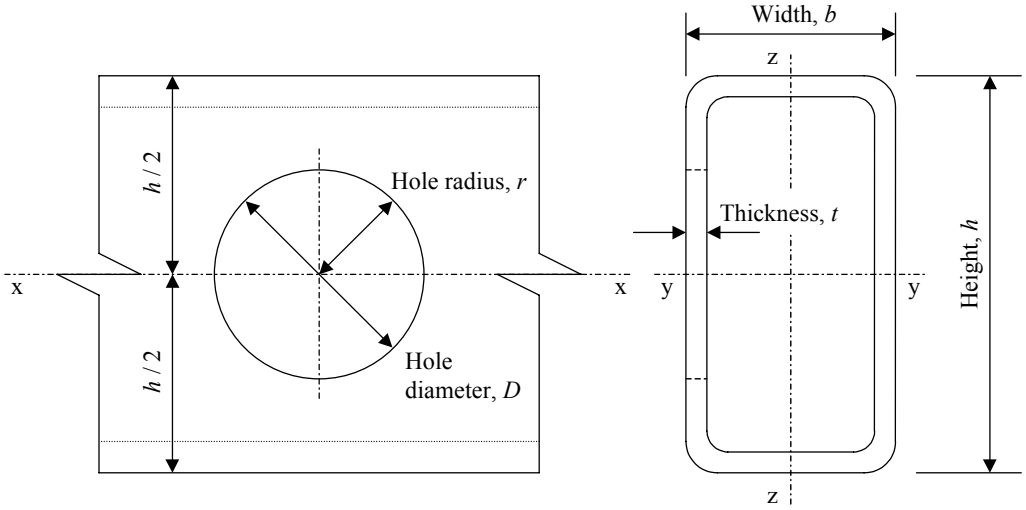

Figure 1-10: Dimensions (web opening)

1.5 The contents of this Thesis

The Thesis began with an introduction to the project and the methodology employed. The slim floor method of construction was briefly described with particular emphasis towards edge beams, design and the British Steel Slimdek system (of which, edge beams based on RHS are an integrated element).

The following Chapter contains a review of the existing knowledge and theory relevant to this research. Discussion is limited to factors that are of greatest relevance to the main body of the thesis and those which are most likely to be unfamiliar to the reader. Consequently, the theories of torsion are discussed in particular detail, while a sound understanding of the theories of flexure is presumed.

The experimental results and complementary FE work are described in four chapters, that are grouped according to the test series to which they belong. In each case, the Chapter begins with a description of the experimental procedure, before discussing the results and the theoretical and FE predictions. The four laboratory test series are: full-scale four-point bending (bending), full-scale three-point bending (shear), full-scale torsion and small-scale torsion.

The penultimate and largest Chapter contains the principal conclusions of the research in the form of design recommendations. The recommendations were developed following the calibrated FE parametric study, which is also described. The justifications for the recommendations are outlined with reference to the analytical and experimental data.

The final Chapter summarises the conclusions that were drawn at each stage of the project and ends with a brief critical analysis of the project as a whole.

2 Relevant knowledge and theory

2.1 Introduction

The aim of this project, as stated in the previous chapter, was to study the behaviour of Rectangular Hollow Sections (RHS) with web openings, and to develop the basis for a set of design rules for perforated RHS beams in flexure and torsion. To this end, the fundamental structural behaviour of RHS with web openings was examined by an investigation that combined analytical study with laboratory testing. This Chapter is a review of the existing knowledge and theory pertinent to this research. Discussion is limited to factors that are of greatest relevance to the main body of the Thesis and those which are most likely to be unfamiliar to the reader.

Section 2.2 discusses the stress-strain behaviour of hot finished steel as measured by tensile testing. The features of the stress-strain curve are described with reference to the representation of material non-linearity in analytical models. The material model used in the course of this research is explained and the various parameters that are used to describe the properties of the material are defined.

In this study, the analytical modelling was performed using a commercial Finite Element (FE) program and the underlying principles of the FE method are outlined in Section 2.3. The FE method has certain inherent imperfections, and predictions that are both reliable and accurate can only be obtained if the method is

used correctly. The Section contains a discussion of what is normally regarded as good practice, and concludes by summarising the rationale behind the various decisions that were made regarding the analytical component of the research.

The topic of strain measurement is discussed in Section 2.4 with particular emphasis on electrical resistance strain gauges of the type used in the experimental investigation. The strengths and limitations of the technique are outlined with reference to the validation of theoretical and analytical predictions.

The theories of torsion are introduced in Section 2.5. Discussion focuses on torsion of closed sections and describes the development of torsion theory from classical thin wall theory to the sophisticated thick wall theory used in design today. The differences between the various approaches are quantified with reference to experimental torsion studies conducted by other investigators.

Issues relating specifically to the design of beams in flexure and torsion are discussed in Chapter 7, which presents the findings of the parametric FE study in the form of recommendations for the design of RHS with web openings.

2.2 The stress-strain behaviour of hot finished steel

2.2.1 Introduction

This Section describes a mathematical approximation, suitable for modelling the stress-strain behaviour of hot finished steel, for use in FE analysis. It describes how a material can be modelled using data obtained from tensile tests, and proposes a quantitative measure of the similarity between the experimental data and the approximation. The approximation is compared to standard measures of material properties as defined by BS EN 10002-1:1990.

2.2.2 The stress-strain behaviour of hot finished steel and BS EN 10002-1

Figure 2-1 shows a typical stress-strain curve for hot finished steel, when tested at ambient temperature in accordance with BS EN 10002-1:1990. The figure shows four distinct regions of behaviour:

1) The elastic region: Stress is proportional to strain and all deformation is elastic and recoverable.
2) The yield plateau (also known as 'Lüder's extension'): At yield the stress reaches a local peak (the upper yield strength), before decreasing rapidly to fluctuate above a lower value (the lower yield strength). This region has a lower average stiffness (which may be negative) than the elastic region (Figure 2-2). Occasionally an apparent reduction in strain will follow the upper yield peak (as in Figure 2-2). This will occur if the location of first yield lies outside the gauge length of the extensometer and is a consequence of the upper and lower yield behaviour of the steel.
3) Strain hardening: Engineering stress increases with increasing strain to reach a maximum value (the ultimate tensile strength). The stiffness at any value of strain within the strain hardening region decreases with increasing strain and is zero at the maximum value of stress.
4) Necking and fracture: Engineering stress falls with increasing strain as the material thins and eventually fractures.

BS EN 10002-1:1990 provides definitions of upper yield strength (R_{eH}) lower yield strength (R_{eL}) and tensile strength (R_m) (Figure 2-1):

1) Upper yield strength: 'The value of [engineering] stress at the moment when the first decrease in force is observed.'
2) Lower yield strength: 'The lowest value of [engineering] stress during plastic yielding, ignoring any transient effects.' This value may correspond to different locations in the yield plateau depending on the shape of the plateau.
3) Tensile strength: 'The [engineering] stress corresponding to the maximum force.' The maximum force is defined as 'the greater force which the test piece withstands during the test once the yield point has been passed.'

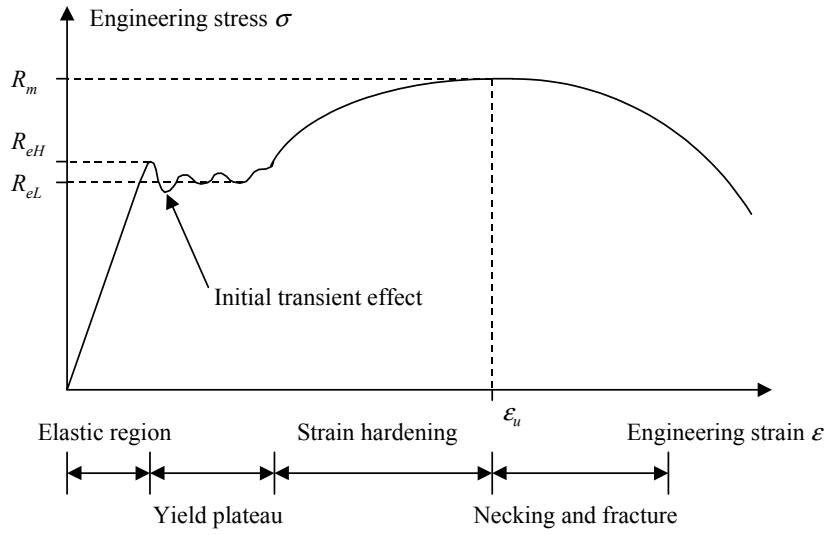

Figure 2-1: The stress-strain behaviour of steel from hot finished RHS

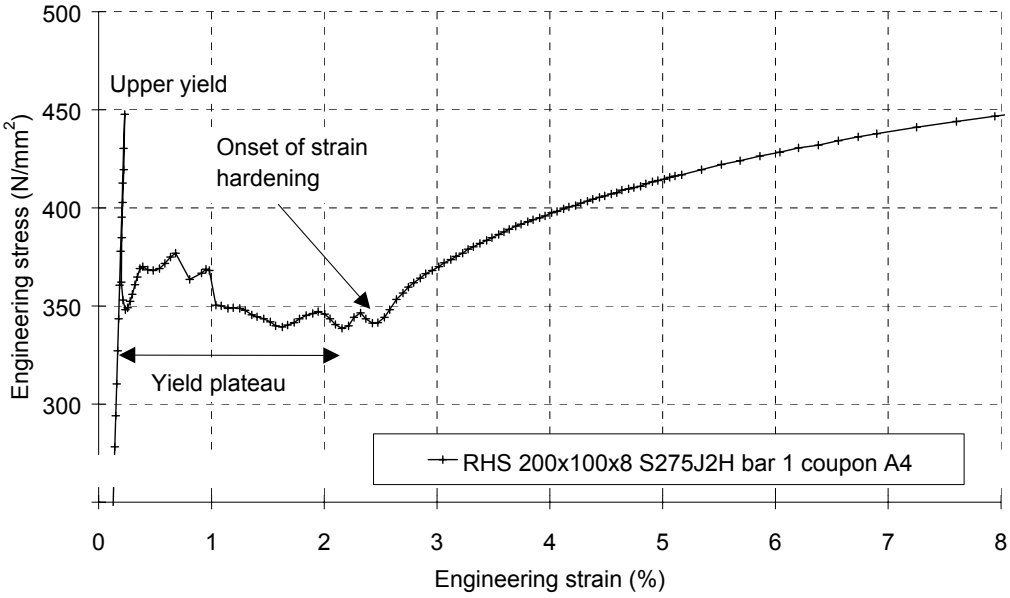

Figure 2-2: The yield plateau

2.2.3 A mathematical model of stress-strain behaviour

The author proposes that a stress-strain relationship of the type discussed in Section 2.2.2 can be represented by the mathematical approximation shown in Figure 2-3. The approximation uses simple geometric shapes to model the experimental curve, and is therefore a way of expressing, in a simple form, the behaviour as measured by a tensile test (it is not model of material behaviour per se).

The elastic region can be represented by a straight line up to a value of yield stress (f_{y1}). This is consistent with the assumption that hot finished steel is a perfectly elastic material in this range. The modulus of elasticity or Young's modulus (E) is defined as the ratio of yield stress (f_{y1}) and yield strain (ε_{y1}) as given in Equation 2-1.

$$E = \frac{f_{y1}}{\varepsilon_{y1}}$$

Equation 2-1

The initial upper yield peak and the yield plateau are the most variable of all the aspects of the stress-strain behaviour. These parameters are sensitive to the nature and quantity of impurities in the metal, and the shape, temperature, loading rate and stress history of the coupon (Nádai 1931). The upper and lower yield strengths and the oscillation of the plateau can vary significantly between different tests of the same batch of material.

The average stress-strain relationship for the whole yield plateau can be approximated by a second straight line to a second value of yield stress (f_{y2}) and yield strain (ε_{y2}). The values of the first and second yield stress (f_{y1} and f_{y2}) do not necessarily correspond to the values of upper and lower yield (R_{eH} and R_{eL}) as defined by BS EN 10002-1:1990. The definition of lower yield can vary depending on the shape of the yield plateau and upper yield is highly variable, and is not appropriate for use in material models for many applications.

The first yield stress (f_{y1}) is the stress at which the elastic line meets the plateau line and is a simplification of true yield behaviour that removes the variability of transient effects (the upper yield spike and the subsequent downward spike). The second yield point (f_{y2} , ε_{y2}) marks the end of the yield plateau and the onset of strain hardening. This point is often well defined in experimental stress-strain curves.

The strain hardening behaviour can be approximated by a segment of an ellipse up to the tensile strength (f_u) and total strain at maximum stress (ε_u). The

strain hardening segment of the ellipse will always terminate at the apex, but may begin at different locations depending on the material. The location of the ellipse is defined by its centre (*s* , *t*) and the size of its semi axes (*a* and *b*). The strain at maximum stress (ε_u) defines the x-coordinate of the strain hardening ellipse (*s*) as stated in Equation 2-2.

$$s = \varepsilon_u$$

Equation 2-2

The final part of the stress-strain curve is difficult to model since the coupon necks and fractures over a small portion of the gauge length. Engineering stress may be assumed to remain at a constant value (that of the tensile strength) for increasing strain provided this assumption is valid in respect to the end use of the material model.

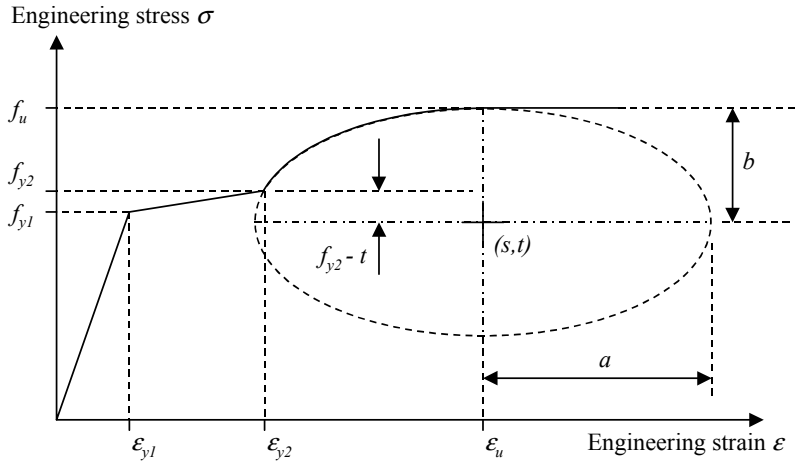

Figure 2-3: The mathematical model

2.2.4 Applying the mathematical approximation to experimental data

2.2.4.1 Applying the mathematical approximation to a single coupon result

The mathematical approximation described in Section 2.2.3 can be applied to a single coupon result by inspection if sufficient fixed points (such as yield stress, Young's modulus and tensile strength) are obtained by established methods. If a more scientific approach is required, the approximation can be applied as detailed below.

The function defining the approximated stress-strain relationship can be defined by four equations. The elastic region is defined by Equation 2-3. The yield plateau is defined by Equation 2-4. The strain hardening function is defined by Equation 2-5 and the final portion of the curve can be defined by Equation 2-6 if appropriate.

$$\sigma = \frac{f_{y1}}{\varepsilon_{y1}}\varepsilon \qquad 0 \le \varepsilon < \varepsilon_{y1}$$

Equation 2-3

$$\sigma = f_{y1} + \left(\frac{f_{y2} - f_{y1}}{\varepsilon_{y2} - \varepsilon_{y1}}\right)\left(\varepsilon - \varepsilon_{y1}\right) \qquad \varepsilon_{y1} \le \varepsilon < \varepsilon_{y2}$$

Equation 2-4

$$\sigma = \left(f_u - t\right)\sqrt{1 - \frac{\left(\varepsilon - \varepsilon_u\right)^2}{a^2}} + t \qquad \varepsilon_{y2} \le \varepsilon < \varepsilon_u$$

Equation 2-5

$$\sigma = f_u \qquad \varepsilon_u \le \varepsilon$$

Equation 2-6

The semi axes of the ellipse (a and b) are determined by the onset of strain hardening, as defined by the point (f_{y2} , ε_{y2}). Equation 2-7 and Equation 2-8 express a and b explicitly.

$$a = \sqrt{\frac{(\varepsilon_{y2} - \varepsilon_u)^2 (f_u - t)^2}{(f_u - t)^2 - (f_{y2} - t)^2}}$$

Equation 2-7

$$b = f_u - t$$

Equation 2-8

The tensile strength (f_u) can be determined directly from the coupon results and will correspond to the tensile strength as defined by BS EN 10002-1:1990. The six remaining variables can be determined by minimising the difference between the coupon data and the approximation. It may be possible to determine the total strain at maximum stress (ε_u) in advance, if the precise value is apparent from the experimental data.

A possible measure of the suitability of the fit is introduced in the following section. The calculation is computationally intensive, but can be performed easily on a computer. The approximation should be visually compared to the original data to confirm the appropriateness of the fit.

The variables are (as defined earlier):

f_{y1} Yield stress

ε_{y1} Total strain at yield

f_{y2} Stress at onset of strain hardening

ε_{y2} Total strain at onset of strain hardening

t y-coordinate of the centre of the strain hardening ellipse

ε_u Total elongation at maximum stress

These six variables together with the tensile strength (f_u) are sufficient to define the complete stress-strain relationship (with the exception of necking and fracture). They may be used to determine the following quantities, which provide a more immediate understanding of the stress-strain behaviour:

f_{y1} Yield stress

E Young's modulus (Equation 2-1)

$E_{plateau}$ Stiffness of the yield plateau (Equation 2-9)

$\lambda_{plateau}$ Plateau ratio (Equation 2-10)

λ_{ESHF} Elliptical strain hardening factor (Equation 2-11)

ε_u Total elongation at maximum stress

and either

f_u Tensile strength

or

$\lambda_{strength}$ Strength ratio (Equation 2-12)

The plateau ratio ($\lambda_{plateau}$) is a measure of the length of the yield plateau compared to the length of the elastic region. The elliptical strain hardening factor (λ_{ESHF}) is a measure of the initial gradient of the strain hardening effect. A value close to zero indicates a marked onset of strain hardening while a larger value indicates a less well defined boundary.

$$E_{plateau} = \frac{f_{y2} - f_{y1}}{\varepsilon_{y2} - \varepsilon_{y1}}$$

Equation 2-9

$$\lambda_{plateau} = \frac{\varepsilon_{y1} - \varepsilon_{y2}}{\varepsilon_{y1}}$$

Equation 2-10

$$\lambda_{ESHF} = \frac{f_{y2} - t}{f_u - t}$$

Equation 2-11

$$\lambda_{strength} = \frac{f_u}{f_{y1}}$$

Equation 2-12

2.2.4.2 Measuring the suitability of the fit

In order to determine the parameters that define the best approximation to an experimental coupon result, it is necessary to define what is meant by ‘best’. If the experimental data consists of a series of stress-strain coordinates then it is possible, using the equations in Section 2.2.4.1, to sum up the differences between the

experimental stresses, and the stresses calculated at the corresponding strains using the approximation. The sum of these differences can be minimised to find a best fit. This method can be adversely biased by the distribution of data points and by transient effects such as a sharp upper yield spike. A more stable solution, which is not influenced by such aspects to the same degree, is explained below.

The difference between two functions, *f(x)* and *g(x)*, can be quantified in terms of the sum of the areas between them in *xy* space as indicated by the shaded region in Figure 2-4. In the case of a stress-strain curve, the area below the curve represents the energy required to strain a unit volume of material. The area between two curves is the difference between them in terms of strain energy. This area, or strain energy, measurement of fit is not biased by the distribution of data points (e.g. between A and B in Figure 2-4) or, if the functions are expressed by a sufficient number of points, by transient effects (e.g. point C), since they do not represent significant energy features.

If the two functions can be evaluated at the same values of *x*, then the error area can be calculated by applying the trapezium rule to the modulus of the difference between the functions. The total area difference has the dimensions $[M_{ass}/L_{ength}T_{ime}^2]$ and can be non-dimensionalised by expressing it as a percentage of the area below the experimental curve.

In this Thesis, the quantitative measure of the suitability of fit of the mathematical approximation to the experimental curve is given the symbol *K*. The suitability of fit is the sum of the areas between the mathematical approximation and the experimental curve (calculated to the strain at maximum stress) expressed as a percentage of the area below the experimental curve (to the same strain).

When the best fit solution is found by minimising the energy error (K) the difference between the stress predicted by the mathematical approximation and that observed in the laboratory is greatest in the yield plateau region as shown by example in Figure 2-5, Figure 2-6 and Figure 2-7.

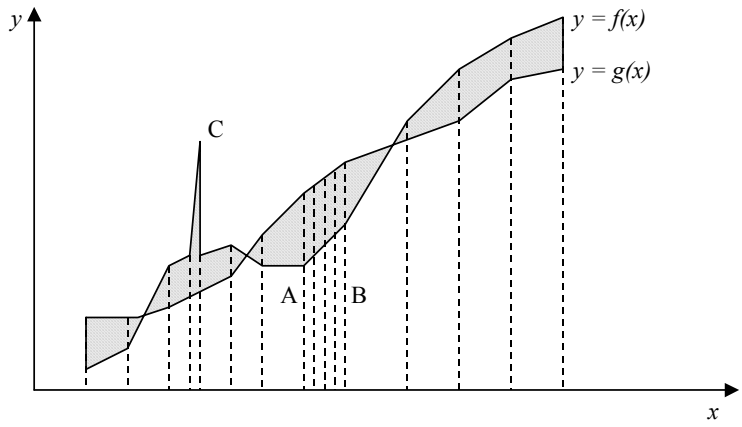

Figure 2-4: Evaluating the difference between two functions using area

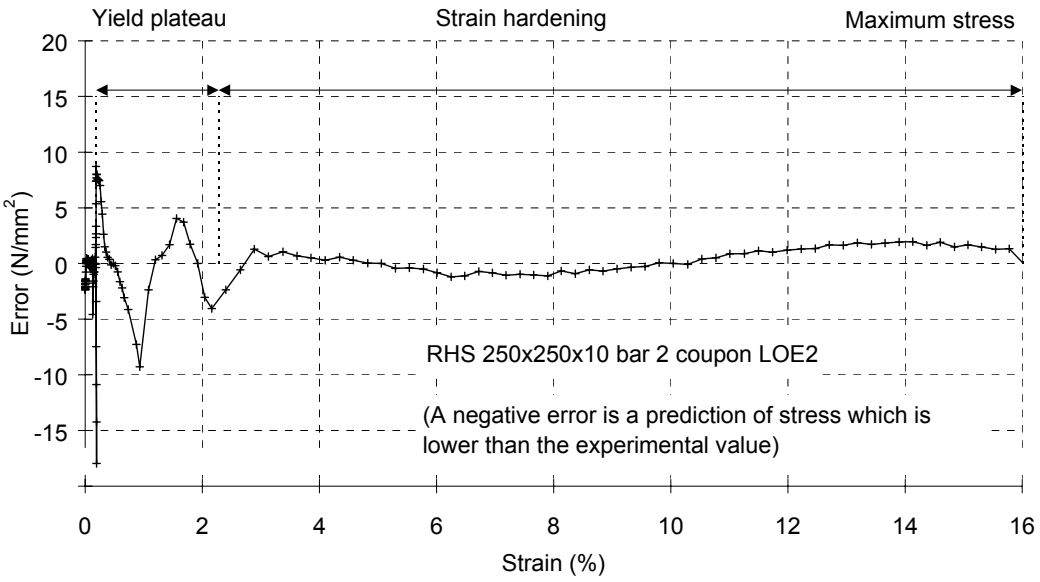

Figure 2-5: The difference between the approximation and the experimental data

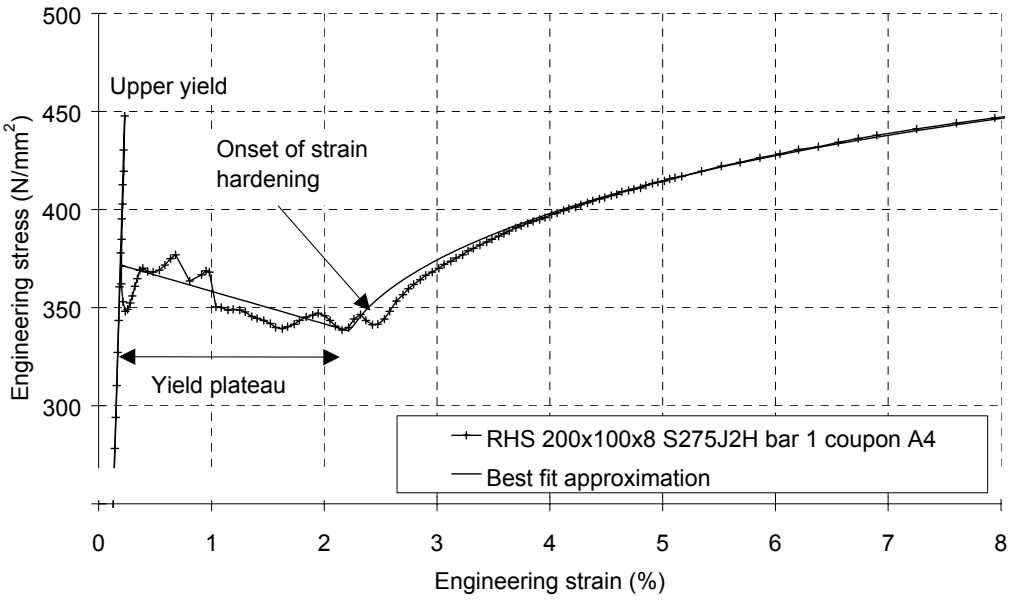

Figure 2-6: The mathematical approximation and the yield plateau

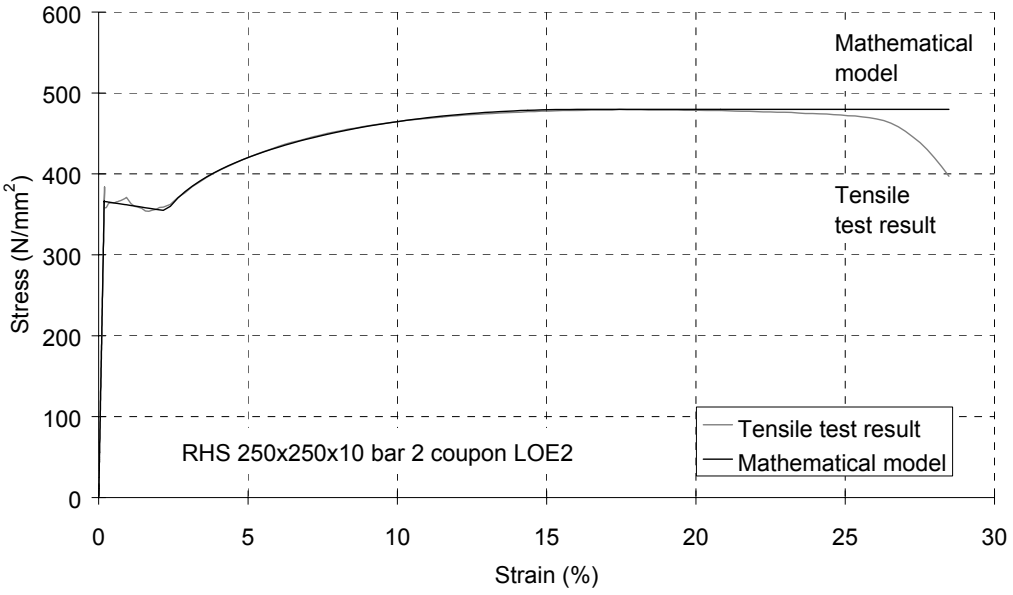

Figure 2-7: The mathematical approximation and the experimental data

2.2.4.3 Applying the mathematical model to a group of coupon results

A best fit for a series of coupon results can be obtained by averaging the seven parameters of the best fit for each individual stress-strain curve (as defined earlier):

f_{y1} Yield stress

E Young's modulus

$E_{plateau}$ Stiffness of the yield plateau

$\lambda_{plateau}$ Plateau ratio

λ_{ESHF} Elliptical strain hardening factor

ε_u Total elongation at maximum stress

and either one of:

f_u Tensile strength

$\lambda_{strength}$ Strength ratio

A quantitative measure of the suitability of the fit can be obtained in the same way as for the individual results by averaging the sums of the areas between all the experimental curves and the averaged approximation. There may be other material parameters that give a lower energy error (K) but they may not be realistic values.

2.2.5 Multi-linear approximations

For some applications, the stress-strain behaviour of a material must be expressed as a series of straight lines. It is possible to divide the strain hardening ellipse into linear regions. One such scheme results in total of six lines by splitting the ellipse into three straight lines at 5%, 20% and 50% of the distance between the strain at the onset of strain hardening and the strain at maximum force (Figure 2-8).

A multi-linear approximation can be converted from engineering stress and strain (ε and σ) to true stress and strain (ε_T and σ_T) using Equation 2-13 and Equation 2-14.

$$\varepsilon_T = \ln(1+\varepsilon)$$

Equation 2-13

$$\sigma_T = \sigma(1+\varepsilon)$$

Equation 2-14

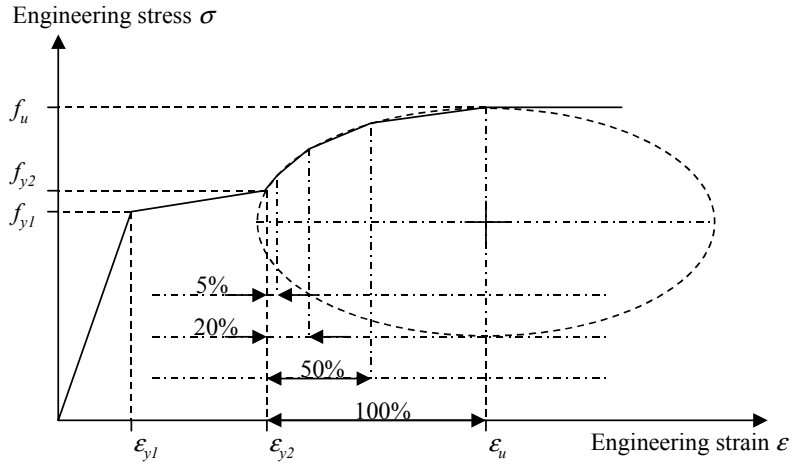

Figure 2-8: A multi-linear model

2.3 Finite Element analysis

2.3.1 Introduction

This Section is a brief introduction to the FE method that summarises the various decisions that were made regarding the analytical component of the research. Comprehensive discussions of topics relating to the FE technique can be found in such works as Cook et al (1988), Zienkiewicz et al (1994) and Rockey et al (1986).

2.3.2 The Finite Element approach

Most numerical techniques in continuum mechanics are based on the principle that it is possible to describe the behaviour of a complex body, with a reasonable degree of accuracy, by dividing the body into a large number of small, but not infinitesimal, parts. Predictions about the body as a whole can be made by describing how each part acts individually, and by deriving the relationships that

link the parts together. The techniques can be classified broadly as belonging to one of three categories (discussion here is limited to the Finite Element method):

1) Finite Difference
2) Boundary Element
3) Finite Element (FE)

In the FE approach, the body is described by a number of small units known as 'elements'. Each element is described separately by a set of mathematical equations, and is linked to neighbouring elements by relationships considering equilibrium of forces and continuity of the body. The FE method is well suited to many engineering problems since it offers versatility in the choice of the mesh and is able to cope with complex geometry.

The FE procedure requires manipulation of large sparsely populated matrices. Consequently, the major part of the development of the theory coincided with the introduction of digital computers. Much of the initial work was conducted within the aerospace industry, but the technique gained widespread recognition after it was shown to have a sound mathematical foundation in the mid 1960s.

FE models were initially constructed on an ad hoc basis, but large general-purpose FE computer programs were beginning to emerge by the late 1960s. Programs such as ANSYS and NASTRAN included several different types of elements for performing different types of problem. The development of pre-processors (for data input) and post processors (for evaluation of results) coincided with the boom in computer graphics technology in the early 1980s.

Modern FE packages offer a wide variety of different element types for use in different types of problem. Each type of element can vary in complexity

according to parameters such as the number of nodes, the number of integration points, and the active degrees of freedom. Much of the skill involved in FE analysis, using a standard package, lies in the choice of element and the formation of the mesh. The following Section discusses good practice in the use of FE analysis.

2.3.3 Good practice

FE solutions are not exact and the predictions, at best, are only an approximation to the true situation. Generally, there are three main sources of error in an FE solution:

1) Modelling errors: Errors due to geometry not being accurately modelled or boundary conditions not being properly applied
2) Mesh errors: Errors due to 'bad mesh' (including poor element formulation)
3) Numerical errors: Rounding errors in computations, errors in numerical integration techniques, and errors due to an ill-conditioned solution matrix

These errors can be minimised by good practice, but the solutions should, whenever possible, be compared with data obtained by other methods (such as laboratory experimentation). It is generally agreed among experienced users of FE analysis that the following general guidelines constitute, at least in part, good practice:

1) Choose the most appropriate element for the task
2) Use a 'good mesh'
3) Use a fine mesh in regions where stress is of particular interest
4) Start with a relatively course mesh and refine in stages until there is little change in the solution

5) Check there are no significant discontinuities in the stress values between elements
6) Check that the externally applied forces are consistent with the reactions at the restrained nodes
7) Prevent rigid body motion unless it is required as part of the problem
8) Before attempting a new analysis, use a 'benchmark' to test the accuracy of the FE package

Precisely what constitutes a 'good mesh' will depend on the program being used. General pointers are:

1) Use the most appropriate element type
2) Ensure a good fit to the boundary
3) Use higher mesh densities in regions where the loading, internal stresses, or geometry change rapidly
4) Ensure a gradual change in size between neighbouring elements
5) Ensure the correct connectivity between neighbouring elements
6) Ensure the elements have suitable aspect ratios

FE programs use a displacement-based formulation that gives an upper bound solution to the true stiffness matrix. Displacements and stresses are therefore under-estimated, and the error in a correctly formulated FE problem will always be negative. As the density of the mesh increases, the FE solution will approach the exact solution from below. In this research, the sensitivity of the solutions to mesh types and densities was carefully studied to make sure that the FE predictions were

close to the exact analytical solution. Ultimately, the complexity and computational overhead of the problem must be balanced against the level of precision required.

2.3.4 Stress accuracy

In FE solutions, the internal stresses are calculated from the nodal displacements by considering each element as an individual entity. These stresses are not continuous across element boundaries and may not necessarily satisfy equilibrium between elements. Most commercial FE programs calculate the stress at a node in one of three ways:

1) Stress at a node is an average taking into consideration all elements connected to the node
2) Stresses at the nodes are calculated by a combination of extrapolation and interpolation between the Gaussian integration points
3) Stresses at the nodes are calculated by a combination of extrapolation and interpolation between points identified as being appropriate for the element type

Increasing the number of integration points in an element increases the accuracy of the stress calculation, but adds to the complexity of the problem being solved. For some problems (particularly non-linear problems), it is advisable to use fewer integration points ('reduced integration elements') rather than more ('full integration elements') because a better displacement solution can be obtained. Since the FE method always underestimates the stresses, the loss in accuracy associated with reduced integration is compensated by an improvement in the modelling of overall behaviour. However, a numerical instability problem known as 'hourglassing' may occur if reduced integration elements are used unwisely.

2.3.5 Non-linear problems

There are four categories of non-linear problem:

1) Material non-linearity: The stress-strain relationship is non-linear, but the strain-displacement relationship remains linear (eg elasto-plastic material behaviour in a metal)
2) Geometric non-linearity: The strain-displacement relationship is non-linear, but the stress-strain relationship remains linear (eg elastic buckling)
3) Combined geometric and material non-linearity: The stress-strain relationship and the strain-displacement relationship are both non-linear (eg plastic collapse)
4) Boundary non-linearity: Deformations and stresses are not linearly dependent on the applied loads (eg contact problems)

Most modern commercial FE packages arrive at a final solution in a non-linear problem by a combination of incremental and iterative procedures. Incremental procedures treat non-linearity in a 'piecewise linear' manner by dividing the total load applied into a number of smaller steps (or 'increments'). An iterative procedure applies the full load or deformation in the first step and calculates the correction to be applied in the next (the 'unbalanced' portion). The iteration proceeds until the unbalanced forces and deformations are within acceptable limits.

By using a combination of increments and iterations, a more reliable and accurate solution can be obtained. This usually occurs at the expense of higher computation time and greater computational effort. Incremental and iterative procedures both require numerical search techniques. The exact method by which FE solvers arrive at the solution to a non-linear problem is one of the biggest differences between modern commercial FE packages. Certain solution techniques

are more suited to certain types of problems and particular FE programs will be better at some types of problem than others, even when the same types of elements are used.

2.3.6 Shell elements

Shell elements are used to model structures where the thickness is significantly smaller than the other dimensions, and the stresses in the direction of the thickness are negligible. Shells normally fall into one of two categories depending on whether or not they model transverse shear deformation. Shells that model shear flexibility are known as 'thick shells' and those that do not are known as 'thin shells'.

In addition to the different shear characteristics of shells, there are also variations in the calculation of membrane strains. In geometrically non-linear analysis (Section 2.3.5), certain types of shell are able to model the changes in thickness that result from extreme deformation. Shells in which thickness changes are neglected are known as 'small strain shells' and are not recommended for use in situations where strains exceed 5%.

A further distinction between different shell types lies in the number of nodes and integration points, both of which lie on the shell's reference surface. Shells with mid-side nodes have quadratic shape functions are able to model curved surfaces more accurately than shells without mid-side nodes, which have linear shape functions. Shells are able to model variations in stress through the thickness by including additional calculation points known as 'section points'. Section points exist at each integration point and are positioned at various levels in the shell thickness.

2.3.7 The ABAQUS Finite Element analysis program

The FE models used in this research were created and solved using the general purpose ABAQUS/Standard program marketed by Hibbitt, Karlsson & Sorensen Inc. Early models were solved using version 5.5.1 running on a VAX/VMS system, while later models were solved using version 5.8.1 running on a newer and better-equipped UNIX system. In the context of this research, the two versions of the code were functionally identical and gave identical results when presented with the same problem.

The FE models included full material and geometric non-linearity, which were both necessary for accurate modelling of the large displacements and high strains present in the laboratory tests. Material non-linearity was provided by a classical metal plasticity model of the type recommended for time-independent stress analysis at relatively low temperatures. In ABAQUS, the isotropic metal plasticity model uses the standard von Mises yield surface and is defined by giving the uniaxial yield stress as a function of the uniaxial equivalent plastic strain.

The elastic region is defined by the Young's modulus (N/mm^2) and Poisson's ratio in the card following the keyword, *ELASTIC. The post-yield behaviour is approximated by a series of straight lines defined by a set of cards following the keyword, *PLASTIC. The first figure in each card is the true plastic strain and the second figure is the true stress (N/mm^2). The program assumes a constant response outside the range defined by the input data.

ABAQUS provides a number of different shell elements, but only one shell type combines the ability to model finite membrane strain, and transverse shear deformation. The shell is of the reduced integration type with four nodes known by

the designation ‘S4R’. Since four noded shells are formulated by a linear shape function, a large number were required to accurately model the curved surfaces of circular openings and corner radii.

2.4 Experimental strain and stress measurement

2.4.1 Introduction

This Section summarises the equilibrium based stress relationships, and displacement based strain relationships, that are used commonly to interpret experimental measurements of surface strain using electrical resistance gauges. Detailed discussion of various strain measurement techniques, and the theories behind them, can be found in reference Dally and Riley (1991). Derivations of the fundamental elastic theories of stress and strain can be found in reference Timoshenko and Goodier (1970).

The following analyses are based on the assumption that the magnitudes of the strains are small enough to assume that, over a small distance, planes remain plane during deformation (the products and squares of the strain gradients may be neglected). This assumption is valid for the working range of the basic types of electrical resistance strain gauges. For such strains, the magnitudes of true and engineering strain (Equation 2-13) are sufficiently similar for them to be treated as being equal, as are the values of true and engineering stress (Equation 2-14).

The following equations for stress (Section 2.4.2) are based on consideration of equilibrium and are valid for strains outside the elastic range of the material. Similarly, the equations for strain (Section 2.4.3) are based on consideration of the geometrical limitations on displacement, and are also valid for strains outside the

elastic range. However, the expressions that relate the components of stress to the components of strain are only valid in the elastic range and for isotropic and homogeneous materials.

2.4.2 The components of stress

The stresses acting on the surfaces of a small cubic element of a body, the faces of which are normal to an arbitrarily chosen system of rectangular coordinates (x, y and z), can be resolved into Cartesian stress components as shown in Figure 2-9. Vector components of direct, or normal, stress (σ) act normal to the six faces of the cube and components of shear stress (τ) act in the planes of the six faces, in the directions of the axes.

The sign convention is such that, if the outer normal defining the cube face is in the direction of increasing x, y or z, then the associated direct and shear stresses are also in the direction of positive x, y, z. If the direction of the outer normal is negative, then the stresses are in the direction of decreasing x, y, z. In Figure 2-9 and the following discussion, the first subscript refers to the outer normal that defines the face upon which the stress component acts, and the second subscript indicates the direction. For normal stresses, positive magnitudes indicate tension and negative magnitudes indicate compression.

If the cube is small enough to neglect any spatial variation in the stress system, consideration of equilibrium indicates that only six of the components are necessary to describe the three-dimensional system of stress at a point. For translational equilibrium to be maintained, the three components acting on each face must be equal in magnitude and opposite in direction to the corresponding components on the opposite face. Similarly, the shear stresses on adjacent faces must be consistent with rotational equilibrium (Equation 2-15).

$$\tau_{xy} = \tau_{yx} \quad , \quad \tau_{xz} = \tau_{zx} \quad , \quad \tau_{yz} = \tau_{zy}$$

Equation 2-15

For the most part, strain gauges are limited to measuring strains on a free surface, where the two-dimensional state of stress that exists, can be expressed in terms of the three non-zero Cartesian vector components of stress (σ_{xx}, σ_{yy} and τ_{xy}). The magnitudes and directions of these components depend on the orientation of the coordinate system. The expressions for the components, for a rotation (θ) of the coordinate system (Figure 2-10) are given in Equation 2-16, Equation 2-17 and Equation 2-18. These relationships, that govern the transformation of one coordinate system to another, can be represented graphically by a Mohr's circle of stress (Figure 2-11).

$$\sigma_{x'x'} = \frac{\sigma_{xx} + \sigma_{yy}}{2} + \frac{\sigma_{xx} - \sigma_{yy}}{2}\cos(2\theta) + \tau_{xy}\sin(\theta)$$

Equation 2-16

$$\sigma_{y'y'} = \frac{\sigma_{yy} + \sigma_{xx}}{2} + \frac{\sigma_{yy} - \sigma_{xx}}{2}\cos(2\theta) - \tau_{xy}\sin(\theta)$$

Equation 2-17

$$\tau_{x'y'} = \frac{\sigma_{yy} - \sigma_{xx}}{2}\sin(2\theta) + \tau_{xy}\cos(2\theta)$$

Equation 2-18

For a two-dimensional state of stress, there exist two mutually perpendicular principal stresses (σ_1 and σ_2), given by Equation 2-19 and Equation 2-20, and a single value of maximum shear stress (τ_{Max}), given by Equation 2-21. An additional

coordinate independent value of stress, the von Mises stress, is extremely useful in relating a three-dimensional stress system to material properties measured in a one-dimensional tensile test (Section 2.5.4.2). The von Mises stress, for a two dimensional system of stress, is given by Equation 2-22.

$$\sigma_1 = \frac{\sigma_{xx} + \sigma_{yy}}{2} + \sqrt{\left(\frac{\sigma_{xx} - \sigma_{yy}}{2}\right)^2 + \tau_{xy}^2}$$

Equation 2-19

$$\sigma_2 = \frac{\sigma_{xx} + \sigma_{yy}}{2} - \sqrt{\left(\frac{\sigma_{xx} - \sigma_{yy}}{2}\right)^2 + \tau_{xy}^2}$$

Equation 2-20

$$\tau_{Max} = \frac{\sigma_1 - \sigma_2}{2}$$

Equation 2-21

$$\sigma_{Mises} = \sqrt{\sigma_1^2 - \sigma_1\sigma_2 + \sigma_2^2} = \sqrt{\sigma_{xx}^2 - \sigma_{xx}\sigma_{yy} + \sigma_{yy}^2 + 3\tau_{xy}^2}$$

Equation 2-22

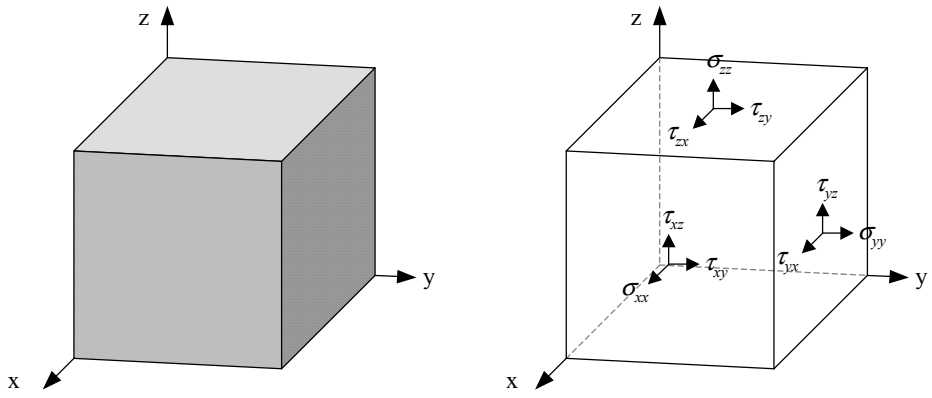

Figure 2-9: Components of stress acting on a small cubic element

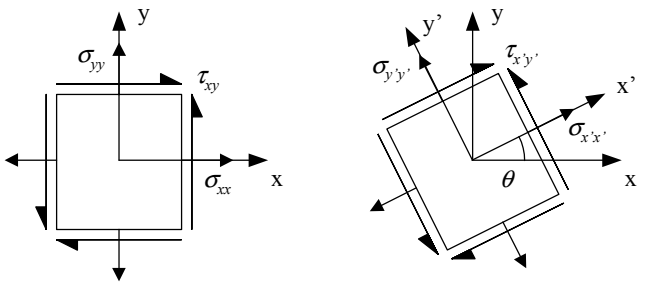

Figure 2-10: A rotation of the coordinate system

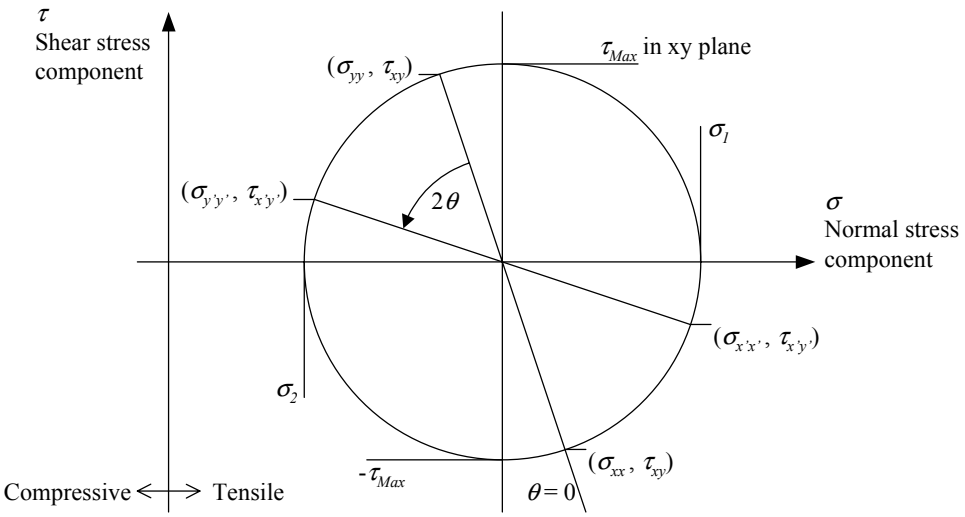

Figure 2-11: Mohr's circle for stress (two-dimensions)

2.4.3 The components of strain

Each of the six vector components of stress, that describe a three-dimensional state of stress, is associated with a co-directional vector component of strain. In the elastic range, the three components of normal strain (ε_{xx}, ε_{yy} and ε_{zz}) are related to the three direct stresses (σ_{xx}, σ_{yy} and σ_{zz}) as described by generalised Hooke's law (Equation 2-23). The components of shear stress (τ_{xy}, τ_{xz} and τ_{yz}) are

proportional to the corresponding components of shear strain (γ_{xy}, γ_{xz} and γ_{yz}) and shear modulus (G) of the material (Equation 2-24). The Young's modulus (E) and the shear modulus (also known as 'modulus of rigidity' and 'modulus of elasticity in shear') are two of the five elastic constants used in engineering to describe the elastic properties of isotropic, homogenous materials. The other three elastic constants are Lamé's constant, bulk modulus and Poisson's ratio (ν). However, although there are five elastic constants, there are only two independent values. The shear modulus can be related to the Young's modulus and Poisson's ratio (approximately 0.3 for steel) by the expression given in Equation 2-25.

$$\varepsilon_{xx} = \frac{\left(\sigma_{xx} - \nu\left(\sigma_{yy} + \sigma_{zz}\right)\right)}{E}$$
$$\varepsilon_{yy} = \frac{\left(\sigma_{yy} - \nu\left(\sigma_{xx} + \sigma_{zz}\right)\right)}{E}$$
$$\varepsilon_{zz} = \frac{\left(\sigma_{zz} - \nu\left(\sigma_{xx} + \sigma_{zz}\right)\right)}{E}$$

Equation 2-23

$$\gamma_{xy} = \frac{1}{G}\tau_{xy} \quad , \quad \gamma_{xz} = \frac{1}{G}\tau_{xz} \quad , \quad \gamma_{yz} = \frac{1}{G}\tau_{yz}$$

Equation 2-24

$$G = \frac{E}{2\left(1 + \upsilon\right)}$$

Equation 2-25

As is the case for stress, the magnitudes of the components of normal and shear strain are dependent on the choice of coordinate system. For a two-dimensional state of stress, the expressions for the three components of strain, for a rotation (θ) of the coordinate system (Figure 2-10) are given in Equation 2-26,

Equation 2-27 and Equation 2-28. The Mohr's circle for strain (Figure 2-12) is similar to that for stress, but requires half the shear strain component to be plotted on the ordinate axis.

$$\varepsilon_{x'x'} = \frac{\varepsilon_{xx} + \varepsilon_{yy}}{2} + \frac{\varepsilon_{xx} - \varepsilon_{yy}}{2}\cos(2\theta) + \frac{\gamma_{xy}\sin(\theta)}{2}$$

Equation 2-26

$$\varepsilon_{y'y'} = \frac{\varepsilon_{yy} + \varepsilon_{xx}}{2} + \frac{\varepsilon_{yy} - \varepsilon_{xx}}{2}\cos(2\theta) - \frac{\gamma_{xy}\sin(\theta)}{2}$$

Equation 2-27

$$\gamma_{x'y'} = (\varepsilon_{yy} - \varepsilon_{xx})\sin(2\theta) + \gamma_{xy}\cos(2\theta)$$

Equation 2-28

For a two-dimensional state of stress, there exist two mutually perpendicular principal strains (ε_1 and ε_2), given by Equation 2-29 and Equation 2-30, and a single value of maximum shear strain (γ_{Max}), given by Equation 2-31.

$$\varepsilon_1 = \frac{\varepsilon_{xx} + \varepsilon_{yy}}{2} + \sqrt{\left(\frac{\varepsilon_{xx} - \varepsilon_{yy}}{2}\right)^2 + \frac{\gamma_{xy}^2}{2}}$$

Equation 2-29

$$\varepsilon_2 = \frac{\varepsilon_{xx} + \varepsilon_{yy}}{2} - \sqrt{\left(\frac{\varepsilon_{xx} - \varepsilon_{yy}}{2}\right)^2 + \frac{\gamma_{xy}^2}{2}}$$

Equation 2-30

$$\gamma_{Max} = \varepsilon_1 - \varepsilon_2$$

Equation 2-31

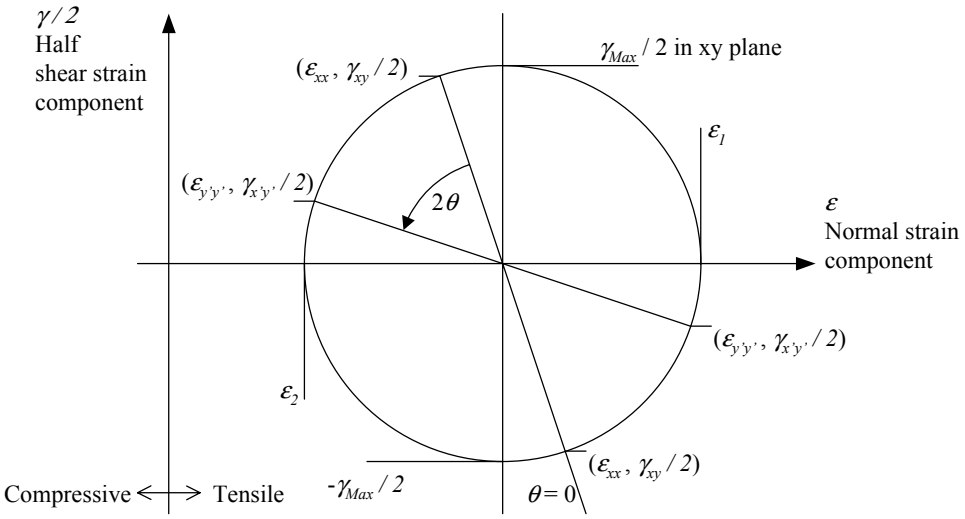

Figure 2-12: Mohr's circle for strain (two-dimensions)

2.4.4 Strain measurement

2.4.4.1 Introduction

For the most part, strain gauges are limited to measurements on a free surface, where the two dimensional system of strains can be represented by the three Cartesian strain components (ε_{xx}, ε_{yy} and γ_{xy}). Most types of strain gauge measure one component of normal strain over a small region of the body, known as the 'gauge length'. Since the measurement is made over a finite length, rather than at a point, the measurement is not exact for non-uniform strain fields. The error depends on the gauge length and the variation of the strain gradient over this distance. If the material is perfectly homogenous and isotropic, the measurement error can be reduced by using a strain gauge with as small a gauge length as possible. However, metallurgical study of steel reveals that, at a microscopic scale, it is composed of a number of different types of crystal, and is far from homogeneous and isotropic over small distances.

The error due to variations in the strain gradient over the gauge length must be balanced against the need to take measurements over lengths large enough to average out the variations in strain due to small scale features of the steel. Once the steel begins to yield, it becomes highly variable at the small end of the macroscopic scale (Section 2.4.4.3) and it becomes extremely difficult to take accurate measurements of strain with small gauge length strain gauges. When strain measurements are to be used in the calibration of FE models, it is wisest to make measurements of strain where the stress distribution is governed by the property under examination, but is expected to be nearly uniform over the gauge length. Measurements of strain after yielding are unlikely to match those predicted by FE models due to small-scale variations in the steel, but qualitative comparisons and quantitative comparisons based on the average of several strain measurements are still possible.

There are many different types of strain gauge, but no single type of gauge is without shortcomings and the choice of gauge depends largely on the requirements of the experiment. The electrical resistance strain gauge (Section 2.4.4.2) currently dominates the strain gauge market, but there are a number of alternative gauges based on a variety of different principals:

1) Mechanical
2) Optical
3) Piezoresistive
4) Acoustic
5) Pneumatic
6) Electrical (resistance, inductance and capacitance)

2.4.4.2 Electrical resistance strain gauges

Although, there are many different types of strain gauge, there is no single measurement device that possesses all the characteristics required for optimum performance. However, the electrical resistance strain gauge (Figure 2-13) has proved to be extremely successful as it enables precise results of surface strain to be obtained quickly, using relatively simple and inexpensive equipment. Electrical resistance strain gauges are also widely used as the principal measurement device in sensors such as load cells and extensometers.

The electrical resistance strain gauge is based on the principle that the electrical resistance of metal wire changes with strain. They have been in use for some 60 years, and have developed into a versatile, robust and easy to use device. Gauges come in a large number of different configurations, but normally consist of a length of conductive foil or wire of suitable resistance (frequently 120 Ω or 350 Ω) wound back and forth over a short gauge length. The most frequently employed gauges in current use consist of an etched foil grid, bonded to a thin insulating substrate that can be glued to the surface of the test specimen. The sensitivity of the gauge, normally specified in the accompanying documentation, is dependent on the choice of alloy for the gauge wire and the configuration of the gauge.

In order to obtain accurate strain measurements, it is necessary to handle the gauges carefully and follow the mounting procedures specified in the gauge documentation. After the adhesive has cured, it is good practice to inspect the quality of the bond, and replace the gauge if it is found to be damaged, or improperly attached to the specimen. If possible, it is also advisable to monitor the

performance of the gauge while applying a small number of elastic load cycles to the specimen, prior to the actual test.

The maximum strain that can be measured with an electrical resistance strain gauge is known as the 'elongation limit' or 'strain limit'. After this limit, the linearity of the gauge readout is likely to be reduced by damage to the foil grid, or substrate material. The types of gauges employed in this project were of the 'low strain' type, which had elongation limits between about 3% and 5%. However, it is possible for a gauge, or adhesive bond, to become damaged before the elongation limit quoted by the manufacturer is achieved, and careful inspection of the gauges throughout a test is necessary to ensure the results are not contaminated by spurious data. During the experimental component of this research, it was observed that gauges were particularly prone to early de-bonding when used in situations with high biaxial shear (such as torsion).

Gauges can be configured to measure strain in single direction (known as 'linear gauges'), but are also available with stacked or in-plane grids for measuring strain in more than one direction at a single location (known as a 'rosette'). The three-element rectangular rosette (Figure 2-14) is commonly used configuration, as the three strain measurements (ε_A, ε_B and ε_C) at 0^o, 45^o and 90^o (Figure 2-15) can be used to calculate the two-dimensional system of strain that exists at the surface with a simple set of equations based on those quoted in Section 2.4.3. The three Cartesian strain components (ε_{xx}, ε_{yy} and γ_{xy}) can be calculated using Equation 2-32, Equation 2-33 and Equation 2-34.

$$\varepsilon_{xx} = \varepsilon_A$$

Equation 2-32

$$\varepsilon_{yy} = \varepsilon_C$$

Equation 2-33

$$\gamma_{xy} = 2\varepsilon_B - \varepsilon_A - \varepsilon_C$$

Equation 2-34

The principal strains (ε_1 and ε_2) can be calculated from Equation 2-35 and Equation 2-36. The angle between the x-axis and the principal strain directions, known at the principal angle (ϕ) can be calculated using Equation 2-37.

$$\varepsilon_1 = \frac{\varepsilon_A + \varepsilon_C}{2} + \frac{1}{2}\sqrt{(\varepsilon_A - \varepsilon_C)^2 + (2\varepsilon_B - \varepsilon_A - \varepsilon_C)^2}$$

Equation 2-35

$$\varepsilon_2 = \frac{\varepsilon_A + \varepsilon_C}{2} - \frac{1}{2}\sqrt{(\varepsilon_A - \varepsilon_C)^2 + (2\varepsilon_B - \varepsilon_A - \varepsilon_C)^2}$$

Equation 2-36

$$\phi = \frac{1}{2}\text{atan}\left(\frac{2\varepsilon_B - \varepsilon_A - \varepsilon_C}{\varepsilon_A - \varepsilon_C}\right)$$

Equation 2-37

In the elastic range, the two principal stresses can be calculated using generalised Hooke's law (Equation 2-23) using Equation 2-38 and Equation 2-39.

$$\sigma_1 = E\left(\frac{\varepsilon_A + \varepsilon_C}{2(1+\upsilon)} + \frac{1}{2(1+\upsilon)}\sqrt{(\varepsilon_A - \varepsilon_C)^2 + (2\varepsilon_B - \varepsilon_A - \varepsilon_C)^2}\right)$$

Equation 2-38

$$\sigma_2 = E\left(\frac{\varepsilon_A + \varepsilon_C}{2(1+\upsilon)} - \frac{1}{2(1+\upsilon)}\sqrt{(\varepsilon_A - \varepsilon_C)^2 + (2\varepsilon_B - \varepsilon_A - \varepsilon_C)^2}\right)$$

Equation 2-39

In the full-scale experimental component of this research, strain gauges manufactured by Tokyo Sokki Kenkyujo and by Kyowa Electronic Instruments were used to measure surface strains and provide data for the calibration of FE models. Linear strain gauges, with gauge lengths ranging from 5 mm to 20 mm, were used to measure strains on the flanges, while three-element rosettes, with gauge lengths of 5 mm and 6 mm, were used to measure the more complex strains in the webs. Torque gauges (two grids used to measure shear strain) with a gauge length of 2 mm were used to measure the applied torque in the full-scale torsion tests (Chapter 5), and a small number of 30 mm sandwich gauges (two parallel linear grids between a thick substrate) were used measure bending strain in the four-point loading tests (Chapter 3).

Figure 2-13: An electrical resistance strain gauge

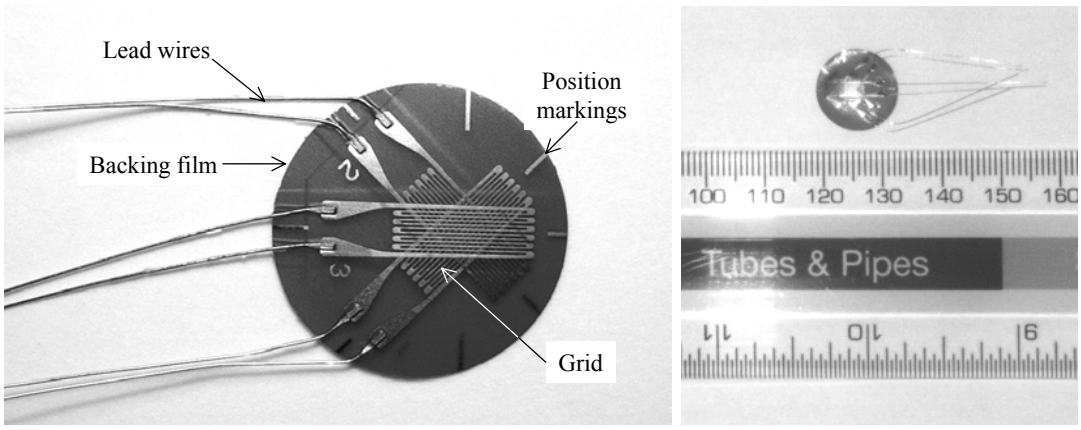

Figure 2-14: A three-element strain gauge rosette

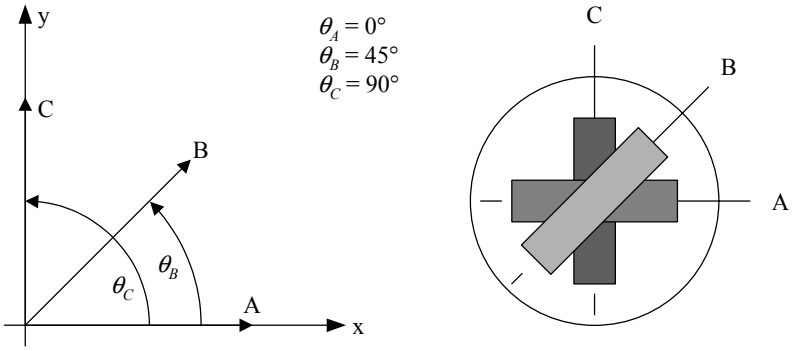

Figure 2-15: Measurements of strain on a three-element strain gauge rosette

2.4.4.3 Brittle coatings

A brittle coating is a thin layer of material applied to the surface of the body being tested. The coating is bonded to the surface and the strains in the body are transmitted to the coating. The patterns of cracks that form in the coating are observed in order to make deductions about the distribution of stress at the surface of the body.

Although brittle coating analysis can be highly advanced, an extremely effective, if primitive, coating can be used at very little cost and without the need for special materials and surface treatments. It is common practice, when testing hot finished steel, to make use of the brittle oxide coating (mill-scale) that forms on the surface of the steel during manufacture. The oxide coating fails by flaking and cracking when the base material yields. To improve the visibility of the yield lines, the steel is often coated with a lime wash (also a primitive form of brittle coating) so that the dark coloured lines show up against the white background. In this project, all of the full-scale test specimens were painted with a lime wash consisting of, approximately, four parts of hydrated lime (by volume) to three parts water.

In this investigation, three, individually distinct, types of yield line were observed in the lime wash/mill-scale coating. The most common type was the shear slip line, collectively known as Lüder's lines, that forms in the direction of maximum shear stress (Figure 2-16a). Lines due to high compressive strain in the direction of the maximum principal stress were also observed at 45 degrees to the Lüder's lines (Figure 2-16b). A third, but much less common category of lines was observed that arose as a result of high tensile strain (Figure 2-16c). Lüder's lines and compression yield lines can be seen in Figure 2-17 (four-point bending test: RHS 250x250x10 no holes).

The yield line pattern provides information about the distribution of plastic stress within the steel at all stages of the test, and can be compared with FE predictions of the directions of the principal stresses. Example yield line patterns are presented in Figure 2-18a (torsion test: RHS 150x150x6.3 with two holes of 38.1 mm diameter) and Figure 2-18b (four-point bending test: RHS 250x250x10 with two holes of 165 mm diameter).

Lüder's lines represent the intersection of the surface of the body with planes on which shear stress has produced plastic slip or gliding. In hot finished steel, it is possible for the material between the Lüder's lines to remain elastic, because of the yield plateau behaviour of the steel (Section 2.2.2). It is also possible for material on either side of a Lüder's line to have very different systems of strain. Over small distances, the steel ceases to be homogenous and information gained from the brittle coating may help to interpret the information gained from strain gauges.

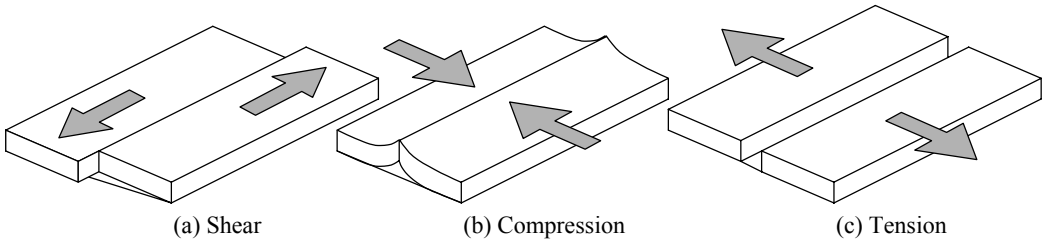

Figure 2-16: Three types of yield lines in brittle coatings

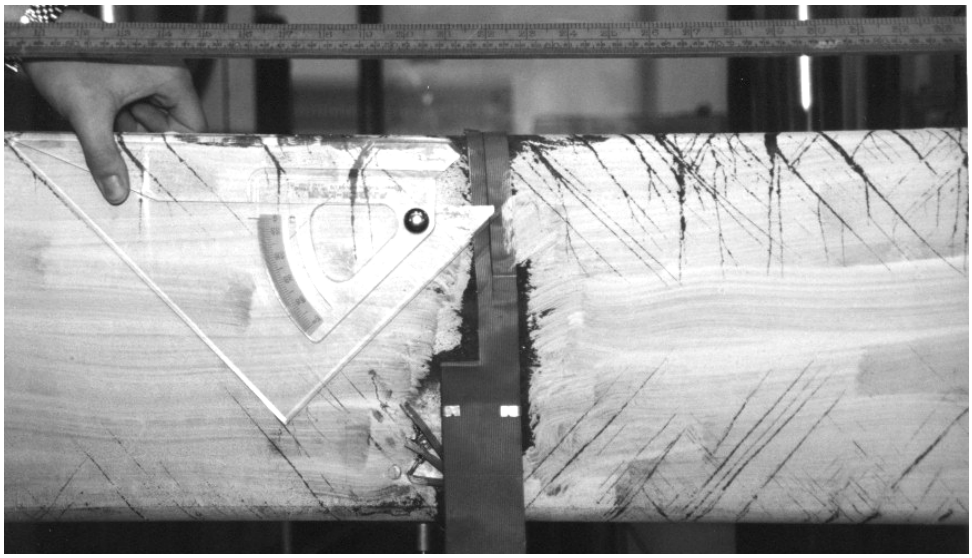

Figure 2-17: Yield lines in a brittle coating due to bending

(a) 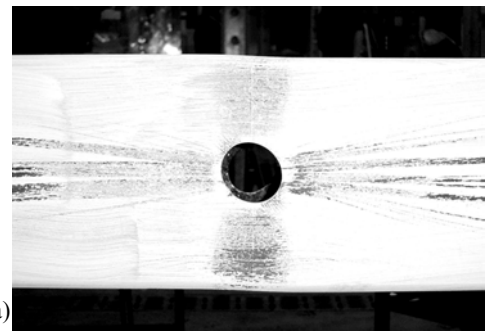 (b) 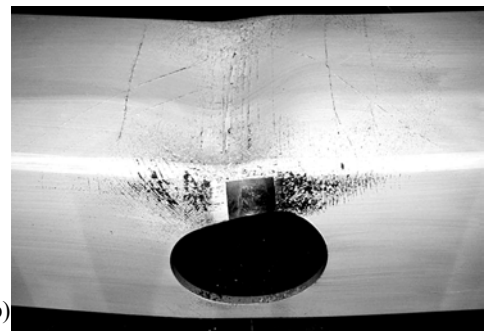

Figure 2-18: Stress distributions around web openings (yield line patterns)

2.5 Torsion theory

2.5.1 Introduction

This Section is a summary of the torsion theory relevant to this research. It covers both thin and thick-wall treatments of RHS and describes how stiffness and resistance can be calculated by both methods. The effect of warping restraint is discussed, with reference to theoretical and FE predictions. Finally, the findings of previous experimental investigations are summarised.

2.5.2 Basic torsion theory

The first advances in torsion theory were made during the Industrial Revolution, mainly as a consequence of the introduction of steam power and the development of iron and steel as structural materials. Coulomb (1787) established the relationship between the torque and angle of twist of a solid bar of circular section, and the theory was developed to cover bars of non-circular section by Navier (1826 and 1864) and Saint-Venant (1855).

For a circular bar, the angle of twist (θ) is dependent on the applied torque (T), the length of the member (L), the second polar moment of area (J) and the shear

modulus of the material (G), as described by Equation 2-43. The shear stress at the surface of the member, due to the torque, is proportional to the applied torque and the radius of the bar (r), and is inversely proportional to the second polar moment of area, as described by Equation 2-50. For a circular bar, the second polar moment of area (sometimes called the polar moment of inertia) is given by Equation 2-42.

$$\theta = \frac{TL}{GJ}$$

Equation 2-40

$$\tau_o = Tr/J$$

Equation 2-41

$$J = \frac{1}{2}\pi r^4$$

Equation 2-42

The torsional properties of a prismatic bar with a non-circular cross-section are governed by a shape dependent parameter known as the 'torsional inertia constant' (I_t), which is never greater than the second polar moment of area. If the member is free to warp at both ends without restraint (Section 2.5.3), then the angle of twist can be described by Equation 2-43 and the shear stress at the external surface by Equation 2-44. In Equation 2-44, the relationship between the torque and shear stress is described by a shorthand parameter known as the 'torsional modulus constant' (C_t). The torsional modulus constant is related to the torsional inertia constant and analogous to the elastic section modulus in bending theory.

$$\theta = \frac{TL}{GI_t}$$

Equation 2-43

$$\tau_o = T/C_t$$

Equation 2-44

The values of the torsional constants are usually estimated by approximate mathematical methods based on the 'stress function' or 'membrane analogy' proposed by Prandtl (1903), and developed by Brendt (1896) and Griffith and Taylor (1917). In summary, the function describing the variation in the shear stress, in a member of constant cross-section, is represented by an imaginary homogeneous membrane supported at the edges, and capped by rigid weightless plates over any internal voids. The shear stress is represented by the slope of the membrane and the torque is represented by twice the volume enclosed. The ratio of the pressure under the membrane to the membrane tension represents twice the product of the angle of twist and the shear modulus. Early investigators studied the torsion of bars with non-circular cross-sections by measuring soap films (e.g. Trayer and March 1930), but the development of computers allowed later investigators to use more accurate methods, such as Finite Difference (e.g. Marshall 1971) and Finite Element (e.g. Schultz and Filippou 1998), to evaluate the stress function directly.

For a tubular cross-section, such as an RHS, the shear stress due to torsion is greatest at the outside surface and decreases through the thickness. Estimates of the torsional constants fall into two categories depending on how the variation of shear stress through the thickness is treated, viz 'thin wall' and 'thick wall'.

Thin wall theories are simple to apply, but are only accurate when the thickness is small because they assume that the shear stress is uniform through the thickness. The classic thin wall theory is that of Brent, restated here in Equation 2-45 (see also Timoshenko and Goodier 1970). The expressions given in Table 20 of Roark's Formulas (Young 1989) for an RHS with sharp re-entrant corners are based on Brent's formula and are therefore thin wall estimates. Roark's expressions are given in Equation 2-46 and Equation 2-47, where the width (b), depth (h), and thickness (t), are as defined in Figure 1-9.

$$I_{t,Brent} = \frac{4A_h^2 t}{h_c}$$

Equation 2-45

Where:

A_h = Area enclosed by mean perimeter

h_c = Mean perimeter

$$I_{t,no\,radii,Roark} = \frac{2t(b-t)^2(h-t)^2}{b+h-2t}$$

Equation 2-46

$$C_{t,no\,radii} = 2t(h-t)(b-t)$$

Equation 2-47

Thick wall theories are those which attempt to account for the variation in shear stress through the thickness and, perhaps, at the corners. Abramyan (1951), developed accurate numerical series solutions for boxes with walls of finite thickness that were significant improvements upon the foregoing semi-empirical formulae, but were complicated to implement. A decade later, Byrne and Carré

(1962) were able to apply computer technology to solve the more accurate, but mathematically cumbersome problem, of box sections with (very tight) internal corner radii. Byrne and Carré found that localised high stresses are present at the internal radii, which are potentially higher than those on the external surface. This observation is also made by Marshall (1971 and 1972) who confidently states that the measured behaviour of RHS in the laboratory has shown that thin-walled theory is inappropriate for design. Marshall's values of torsional inertia constant and torsional modulus constant, calculated by the application of the Finite Difference method, are practically identical to those calculated from the formulae[1] in Annex A of BS EN 10210-2:1997 (Figure 2-19 and Figure 2-20). Close inspection of the formulae in Annex A reveals that they are based on the approximate formulae proposed by Marshall (1970), with an allowance for the corner radii. Design, however, does not take into account the raised stresses at internal radii that, according to Marshall, can be significantly higher (up to 30% for typical radii) than elsewhere. This may not be important as Marshall also states that the area of concentrated stress does not exceed 0.6% of the total area of cross-section.

Values of torsional inertia constant calculated by thin wall theory are, for typical sizes of RHS, between 5% and 1% lower than values calculated by thick wall theory (Figure 2-21). Values of torsional modulus constant calculated by thin wall theory are, for typical sizes of RHS between 5% and 25% higher those calculated by thick wall theory (Figure 2-22).

[1] The formulae in BS EN 10210-2:1997 are also given in Appendix C of this Thesis.

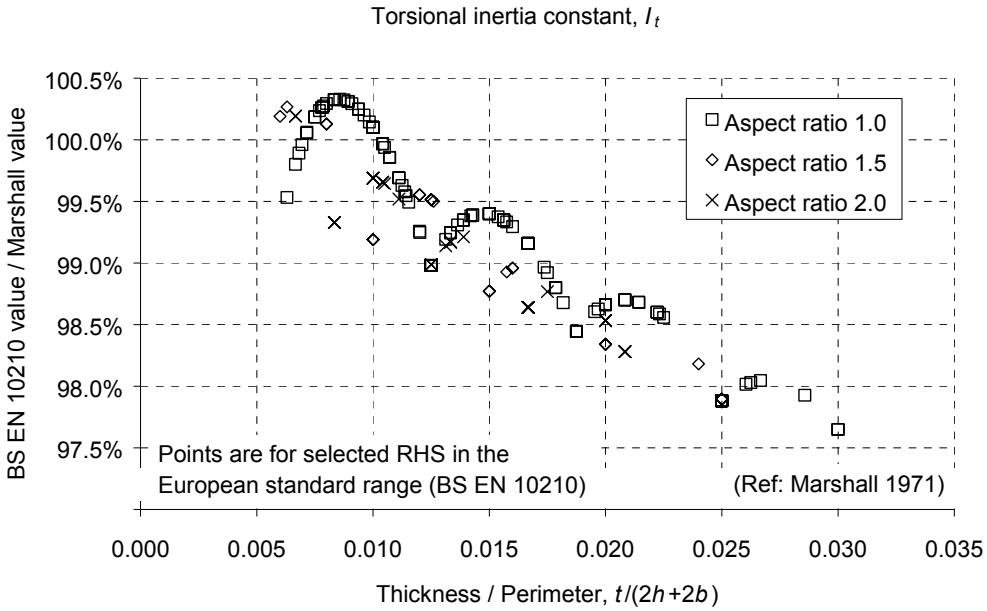

Figure 2-19: Torsional inertia constant (Marshall and BS EN 10210 calculations)

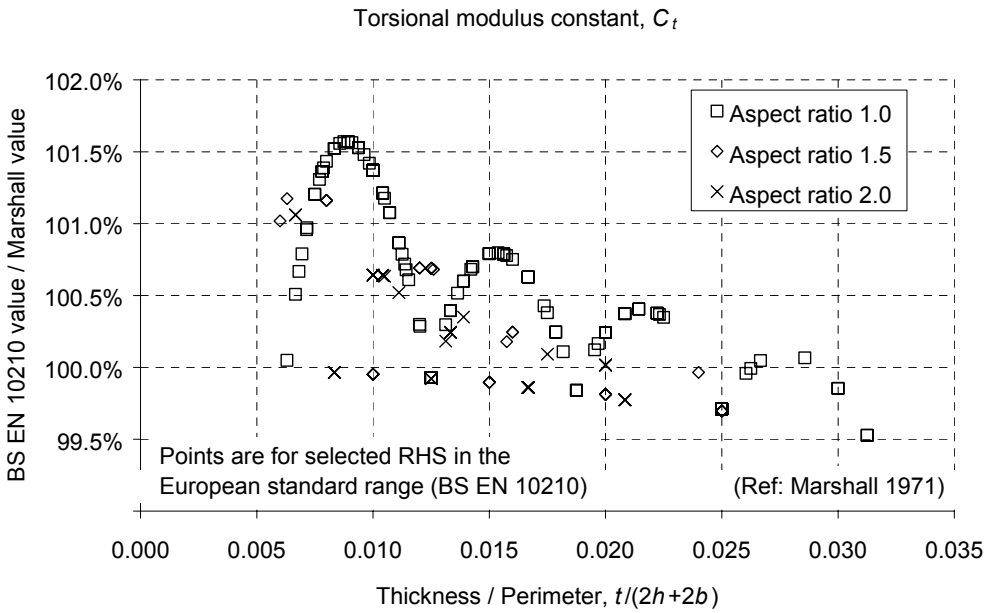

Figure 2-20: Torsional modulus constant (Marshall and BS EN 10210 calculations)

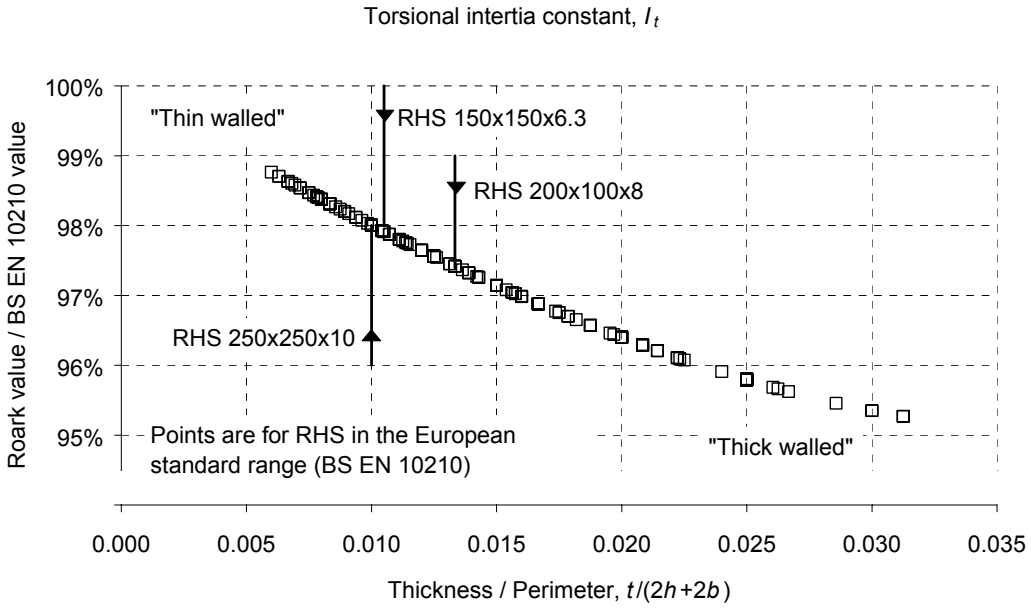

Figure 2-21: Torsional inertia constant (thin and thick wall calculations)

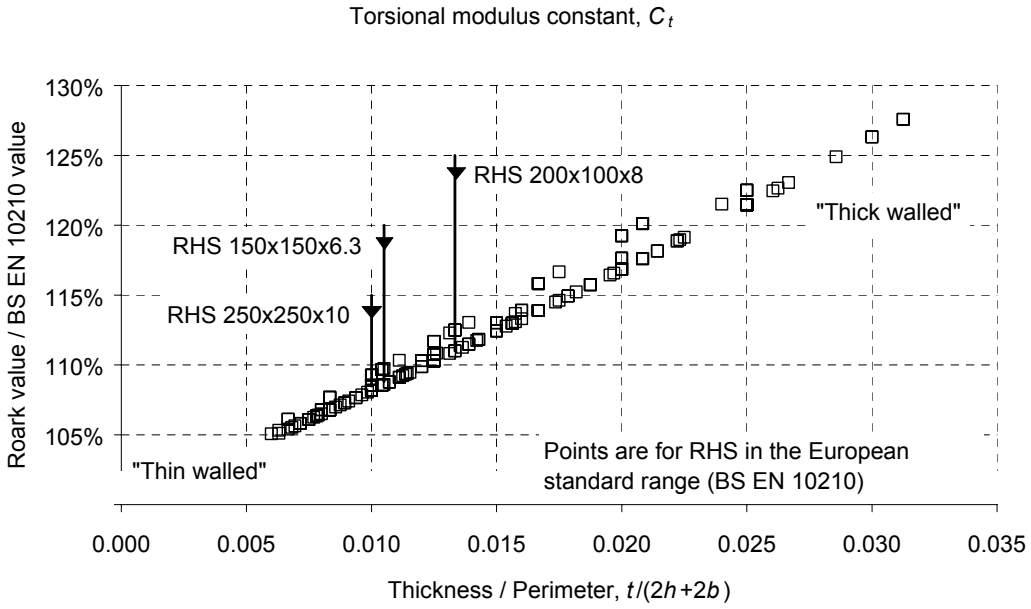

Figure 2-22: Torsional modulus constant (thin and thick wall calculations)

2.5.3 Warping

The numerous symmetries of a circle imply certain constraints on the torsional deformation of members with solid circular, and concentrically hollow, cross-sections:

1) All sections must remain circular and rotate around their centres: By symmetry, all radial lines are equivalent and the deformation along those lines must be identical for all radii
2) Cross-sections remain plane: Longitudinal displacement would be in violation of the symmetry of all cross-sections
3) Radial lines must remain straight during deformation: Curvature of radial lines would be in violation of the symmetry about the sectional plane
4) The angle between any two radial lines remains constant with twist: Any change in this angle would be in violation of the rotational symmetry about the longitudinal axis

These assumptions formed the basis for Coulomb's theory for the torsion of circular shafts (Coulomb (1789)), and were later applied by Navier (1826), when he expanded the theory to cover prismatic bars of non-circular cross-section. However, the above statements cannot be made for a general shape, and Navier's analysis was erroneous, implying a solution that is in violation of equilibrium at the boundary of the cross-section. Saint-Venant modified Navier's approach to include the possibility of longitudinal, or warping, distortion of cross-sections (Saint-Venant (1855) and Navier (1864)).

The warping of cross-sections in torsion becomes important when it is suppressed, as warping restraint induces longitudinal direct stresses that act in addition to the 'Saint-Venant' shear stresses. The portion of the externally applied torque carried by these longitudinal stresses is known as the 'warping torsion' and the portion of the externally applied torque resisted by the shear stresses is known as the 'Saint-Venant torsion'. In open sections, the warping torsion is a significant proportion of the externally applied torque, but for tubular sections the warping torsion is extremely small and usually represents less than 1% of the applied torque. For a prismatic bar, warping restraint can take one or more of the following forms:

1) Forces are present that resist the longitudinal displacement of the cross-section at particular locations e.g. the end of a beam, welded to a stiff foundation or joint
2) The applied torque varies along the beam: Adjacent cross-sections subject to different torsional moments will attempt to warp by different amounts and provide a degree of restraint to one another e.g. a beam loaded by an eccentric distributed load
3) The rate twist changes along the beam: Adjacent cross-sections subject to different rates of twist will attempt to warp by different amounts and provide a degree of restraint to one another e.g. formation of a torsional buckle in a thin walled tube

The effect of warping restraint, in members such as RHS, is slight (see below), and it is usually neglected in practical applications. For this reason, the majority of the textbooks that discuss torsion of structural sections choose to ignore warping in tubes, and concentrate instead on open-sections where consideration of warping is more important. However, a commentary on the theory of warping in hollow box sections can be found in references: Young (1982), Megson (1990), and

Trahair and Bradford (1998). The theory was originally proposed by von Kármán and Chien (1946), who studied torsion of aircraft boxes (thin webs between longitudinal stringers) and was later developed to cover heavy box beams (similar to RHS) used in the construction of earth moving machinery (Thomas (1969), Smith et al (1970), Nitzsche and Miller (1976), and Just and Walley (1978)).

In contrast to the warping of members with solid rectangular cross-sections (Figure 2-23a), the warping distortion in an RHS is linear across the four faces, and takes the form shown in Figure 2-23b. Consideration of the symmetry of an RHS implies the following:

1) If warping is not restrained, the distribution is identical at all cross-sections
2) Warping is zero at all points where the cross-section meets a transverse axis of symmetry
3) The warping distortion at diametrically opposite corners is equal and opposite
4) The warping distortion at the corners of square cross-sections is zero

The longitudinal warping distortion (w) at the corner of an RHS is proportional to the applied torque and is given by Equation 2-48. When the section depth (h) equals the width (b), the longitudinal corner warp predicted by Equation 2-48 is zero. Closed section beams that do not warp in torsion are known as 'Neuber beams' and a square tube with a constant wall thickness is one example. The theoretical prediction of the warping distortion is very close to that observed in FE models (Figure 2-24).

$$w = \frac{T \times (h - b)}{8hbtG}$$

Equation 2-48

When warping is restrained in an RHS, the warping shear and normal stresses reduce to zero within a short distance of the point of restraint (approximately twice the section depth), where the warping distortion returns to the unrestrained distribution (Thomas (1969) and Smith et al (1970)). Warping restraint increases the von Mises stress at the ends (by 8% for RHS 200x100x8), where it also increases the torsional stiffness slightly, but it has little effect on the performance of the whole member (unless it is very short). Figure 2-24 shows the torque-rotation behaviour for three FE models: one for which warping is restrained at both ends, one for which warping and longitudinal movement (shortening) are restrained at both ends, and one for which warping is restrained at one end and free at the other. The Figure shows that elastic stiffness and torsional capacity are not sensitive to the effects of warping and longitudinal restraint, and that differences are only noticeable at high values of twist. The decrease in torque at high plastic twist was caused by the formation of a torsional buckle, which resulted in shortening and additional warping of the cross-section (Figure 2-26).

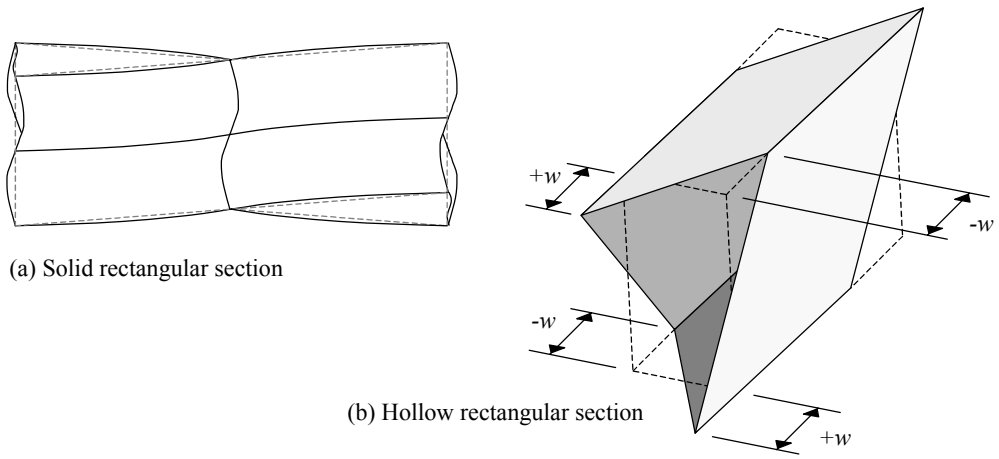

(a) Solid rectangular section

(b) Hollow rectangular section

Figure 2-23: Warping of rectangular cross-sections

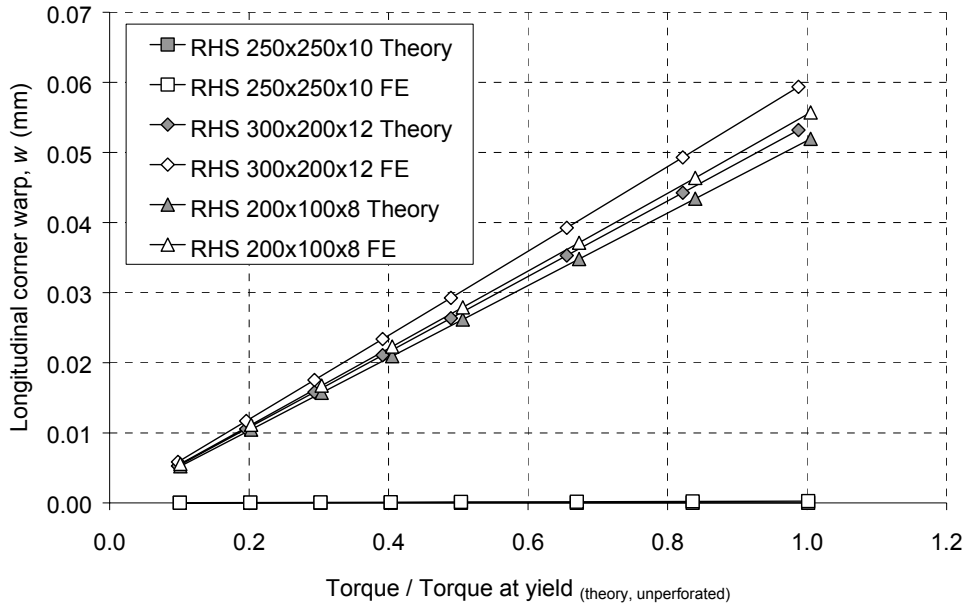

Figure 2-24: Warping of RHS in torsion (theory and FE)

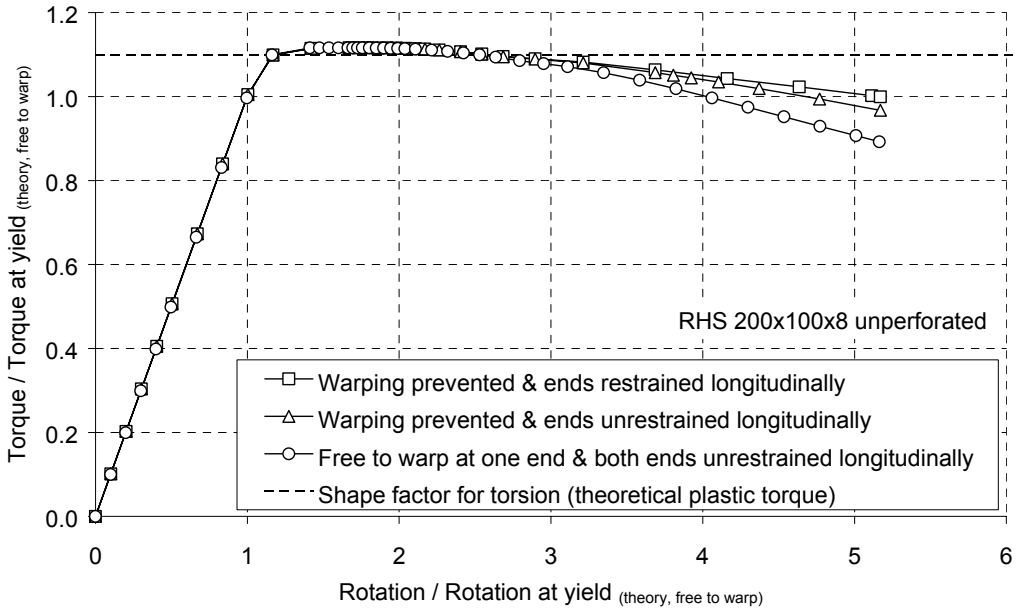

Figure 2-25: The effect of end restraint on torsional behaviour of RHS

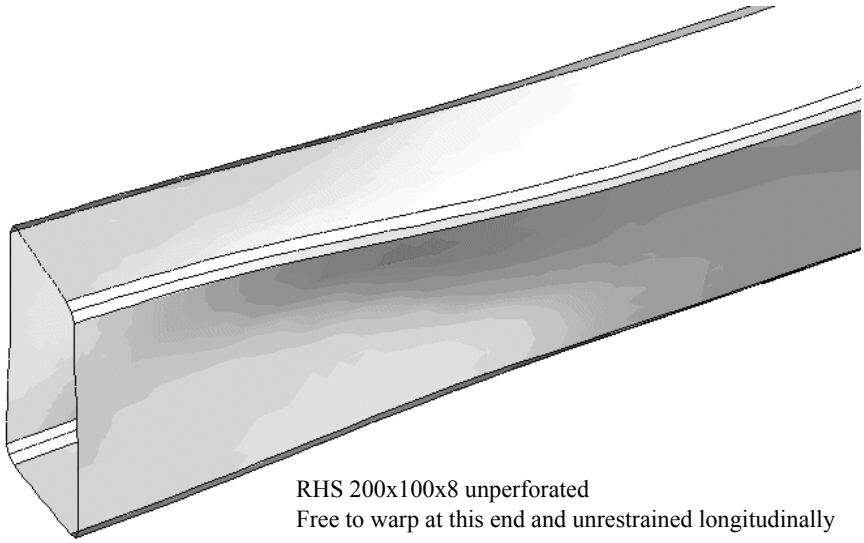

Figure 2-26: Warping at an unrestrained end adjacent to a torsional buckle

2.5.4 Calculation of torsional capacity

2.5.4.1 Expressions for elastic and plastic capacity

As implied by Equation 2-44, the elastic torsional capacity (T_{el}) is proportional to the torsional modulus constant and can be calculated from the shear yield stress (τ_y) as shown in Equation 2-49. The elastic torsional capacity is the torque at which the shear stress at the external surface begins to yield. The calculation does not account for the stress concentrations at the inside surface of sharp corners.

The plastic torsional capacity (T_{pl}) can be calculated by considering the flow of plastic shear around the cross-section (Equation 2-50). The plastic torsional capacity does not account for strain hardened shear stresses, which may permit a higher ultimate torque than the plastic torsional capacity.

$$T_{el} = \tau_y C_t$$

Equation 2-49

$$T_{pl} = \frac{A\tau_y}{2(b+h)}(h(b-t)+b(h-t))$$

Equation 2-50

2.5.4.2 The shear yield stress and tensile yield stress

Calculations of both the elastic and torsional capacities require knowledge of the shear yield stress. When direct measurements are required, the shear yield stress of materials is usually calculated from torsion tests. However, the American Society for Metals (ASM 1985) lists two methods of direct measurement, in addition to the torsion test and those reserved for sheet blanking and testing of fasteners:

1) The Miyauchi shear test (Miyauchi 1984)
2) The Marciniak in-plane sheet torsion test (Marciniak 1973)

These shear tests require special testing equipment and are normally reserved for specialist applications. In practice, the shear properties of structural grade steels are usually inferred from the results of uniaxial tensile testing and the various methods by which this can be achieved are discussed by Timoshenko and Goodier (1970). The two principal methods of calculating the shear yield stress from the uniaxial tensile yield strength, commonly referred to as 'von Mises' and 'Tresca' (Figure 2-27), are summarised below.

The ratio between the uniaxial yield stress (σ_y) and the shear stress at yield (τ_y) can be estimated in a number of different ways, by the various material failure

models that describe yield for arbitrary systems of stresses. Current practice favours the von Mises failure criterion (Mises 1913 and Huber 1904), which is based on strain energy. In brief, the strain energy is split into two portions: strain energy due to volume change and strain energy due to distortion. Failure is determined by the strain energy due to distortion and, for pure shear, gives the familiar ratio expressed in Equation 2-51.

$$\tau_y = \sigma_y \big/ \sqrt{3} = 0.577 \times \sigma_y$$

Equation 2-51

Experimental work in combined axial load and torsion by investigators such as Lode (1926 and 1928), Taylor and Quinney (1928), and Hohenemser and Prager (1932) have shown that the von Mises failure criterion is particularly successful at modelling the behaviour of structural grade steels. The same ratio was also deduced (apparently independently) from shear strain measurements by experimental torsion investigators Stang et al (1937). Timoshenko (1955) summarises the results of various investigators in the statement that, for steel, the experimentally determined ratio usually lies between 0.55 and 0.60 (See also Willems et al (1981).

For metals, the main alternative to the von Mises yield criterion is the Tresca, or 'principal shear stress theory', which assumes that the effect of all the shear stresses within the material is proportional to the maximum shear stress. The criterion is very easy to implement, but, as Shanley (1957) points out, is based on assumptions that are least valid for the situation of pure shear. The Tresca criterion can be applied in a number of different ways, but usually relates the shear yield stress to the uniaxial yield stress by a factor of one half.

Knowledge of the relationship between the shear yield stress and the uniaxial yield stress was critical for the full-scale torsion testing component of this research (Chapter 5). For this reason, an attempt was made to experimentally determine the ratio for the hot finished steel of the RHS, without recourse to applications of torsion theory. The method by which this was achieved and the results are described in the following Section.

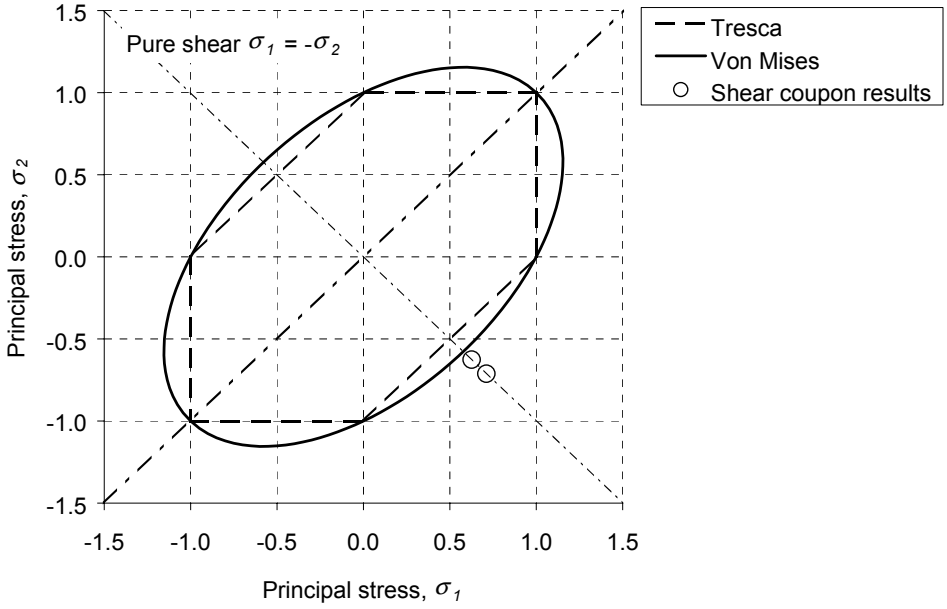

Figure 2-27: The von Mises and Tresca failure envelopes

2.5.4.3 Experimental measurement of the shear yield stress for hot finished steel

A specially designed tensile test coupon was used to study the failure of the steel in pure shear (Figure 2-28). Shear failure occurred in the middle of the coupon where the transverse and longitudinal legs of the cross meet. Strains in this region, on both sides of the coupon, were measured using strain gauges (Section 2.4). The

thickness of the coupon was sufficient to prevent buckling of the transverse (compression) legs.

Two coupons were made from the webs of untested RHS 150x150x6.3 grade S275J2H material from the same bar used in the full-scale torsion tests (Chapter 5). When tested, the coupons indicated yielding in shear at a stress slightly higher (approximately 16%) than that predicted by the von Mises yield criterion (Figure 2-27 and Figure 2-29). This measurement is consistent with the findings of the experimental studies mentioned in the previous Section.

The two coupons measured different values of shear yield stress, which suggests variability in the material. A torsion test subjects the whole tube to pure shear and failure would occur first where the steel is weakest. However, it is not possible to make any assessment about the range of the variability in the tube with just two measurements.

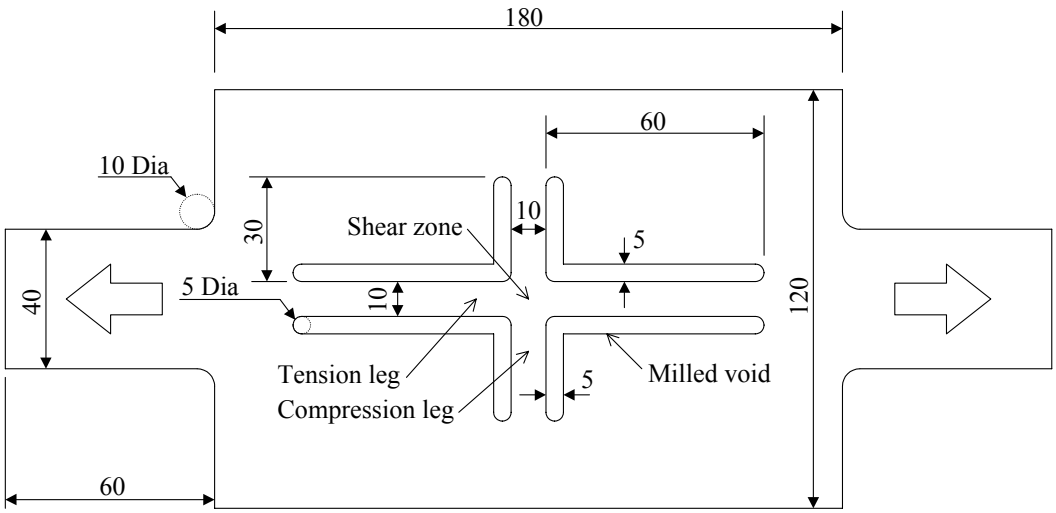

Figure 2-28: The shear testing coupon

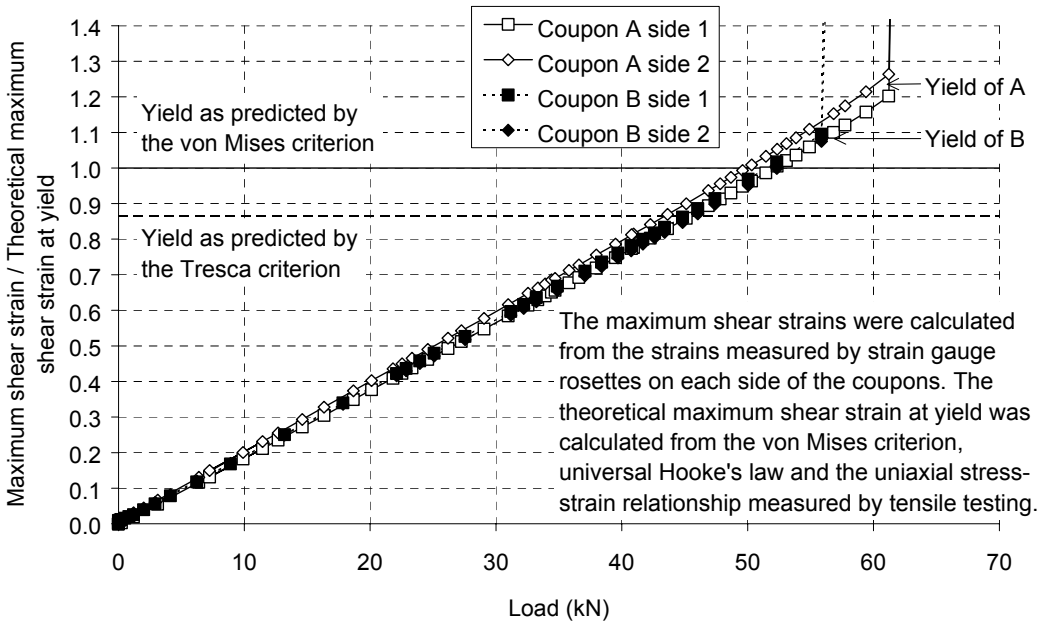

Figure 2-29: Shear testing coupon results

2.5.5 Experimental studies of the torsional properties of tubes

Many of the experimental studies of the torsional properties of tubes were conducted in the years leading to and during the Second World War. At the time, thin tubes of various cross-sections were used to transmit torques to the control surfaces of aircraft. One such series of tests was commissioned by the National Advisory Committee for Aeronautics (now known as the National Aeronautics and Space Administration Federal Agency). Stang et al (1937) tested steel and aluminium tubes of circular cross-section and concluded that relationships between torque, twist and shear stress could be adequately described by the basic torsion theory expressed by Equation 2-40 through Equation 2-42. Later, Moore (Moore and Paul 1943, and Moore 1947) tested tubes of various materials and concluded that torsional stiffness, maximum shear stress and torsional capacity could be adequately described by the formulae quoted by well-known sources such as Roark (1938) and Timoshenko (1941b). Both Stang et al and Moore observed the ratio of uniaxial stress to shear stress expressed by Equation 2-51.

Extensive torsion tests on I and H-sections were conducted by Darwish and Johnson (1965) and the results were compared favourably with soap film predictions made by Lyse and Johnson (1936). In the discussion following the paper, Roop and Letherbury described torsion tests of thick walled square tube, but their understanding of the fundamental theory was flawed (in assuming that the tube could be analysed by an inappropriate adaptation of the theory for solid sections) and their conclusions were of limited value.

Tests on hot finished RHS, of sizes similar to those used in this study (Chapter 5), were conducted by Marshall (1972), who compared the results to the

predictions made by his thick wall torsion theory (Section 2.5.2). Marshall measured shear stresses on the internal and external surfaces of the RHS in addition to torque and twist, and concluded that torsional stiffness and shear stress were adequately predicted by his theoretical expressions. Marshall also measured the elastic and plastic torsional capacities, but chose to use the Tresca yield criterion rather than the von Mises criterion (Section 2.5.4.2) in his theoretical calculations. Marshall's decision is curious[2] as, in the same document, he references the second edition of Timoshenko's 'Strength of materials' (Timoshenko 1941a and 1941b). Marshall briefly discusses alternative yield criteria, but does not mention von Mises, and justifies the use of the Tresca criterion with an obscure reference to an old technical paper (Marin 1937). The implications of Marshall's theoretical treatment of torsional capacity are discussed in Section 5.6.9 in relation to the results of the full-scale torsion testing component of this research.

2.6 Summary

This Chapter began with a discussion of the stress-strain behaviour of hot-finished steel (Section 2.2). The various features of the stress-strain curve were described, and since they have a direct influence on the behaviour of perforated and unperforated RHS, will be referred to later in the Thesis.

The topics of FE analysis, and experimental strain measurement, were introduced in Sections 2.3 and 2.4. Data from strain gauge measurements and the

[2] Timoshenko (1941b) also references Marin (1937) and states that Tresca is often used in machine design (as it is both easy to use and conservative), but goes on to discuss von Mises and the good agreement with experimental observations (Lode (1926) and (1928)).

observation of brittle coatings were used in the calibration of the FE models, which were later used in the parametric study (Chapter 7). However, as discussed above, there are limitations in both the strain measurement technique and the FE method, which meant that comparisons of FE predictions and measurements of strain were expected to diverge with increasing plastic strain. Nevertheless, quantitative comparisons of measured and predicted strains in the elastic range, and at low plastic strain were expected to be reliable and therefore suitable for use in the calibration of FE models.

The theories of torsion were discussed in some detail in Section 2.5. During the project, it was observed that some of the experimental results contradicted the accepted theoretical model. As a consequence, the various aspects of torsion theory are referred to later, in the Chapter concerned with the full-scale torsion tests (Chapter 5).

The experimental results and complementary FE work are described in the following four Chapters, grouped according to the test series to which they belong. In each case, the Chapter begins with a description of the experimental procedure, before discussing the results and the theoretical and FE predictions. The discussion of the experimental investigation begins with the four-point bending tests.

3 Bending (four-point loading)

3.1 Introduction

This Chapter contains a description of the full-scale four-point loading flexural testing component of the project. The testing apparatus and procedure are described, and the details of the test specimens are listed. The tests were conducted to investigate the behaviour of perforated Rectangular Hollow Sections (RHS) in uniform bending (no externally applied shear). The full-scale three-point loading flexural testing programme, which was used to investigate the behaviour of perforated RHS in combined shear and bending, is described in Chapter 4. The full-scale and small-scale torsion testing programmes are described in Chapters 5 and 6 respectively.

In this Chapter, the experimental results of the four-point bending tests are summarised, as are the comparisons with conventional beam bending theory and Finite Element (FE) predictions. The FE models that were calibrated, using the data from the four-point loading tests, were later used in a parametric study to investigate the influence of hole diameter, and section size, on the flexural performance of perforated RHS (Section 7.5).

3.2 A description of the apparatus and testing procedure

3.2.1 The four-point bending test apparatus

The set-up for the four-point bending tests, which were performed in a 2MN Instron universal testing machine, is shown in Figure 3-1 and Figure 3-2. The beams were supported on semi-cylindrical bearings (Figure 3-3) with a span of 1750 mm. Nylon pads were used to reduce friction between the specimen and supports.

The load was applied vertically by the hydraulic actuator through a heavily reinforced spreader beam, and a pair of rocker bearings placed 1000 mm apart on the compression flange. Each rocker bearing (Figure 3-4) consisted of a roller bearing that was free to rotate about (and slide along) its longitudinal axis. The cradle, housing the roller bearing, was free to rotate, within its base, about an axis perpendicular to (and in-plane with) the axis of the roller.

The rocker bearings, together with a rocker support (Figure 3-3a), allowed twisting and lozenging of the specimens to occur, without restraint, during the test. This precaution was necessary because specimens may have been caused to twist or lozenge under load as a result of any asymmetry of the web openings (intentional or otherwise), or any distortions present in the specimens as manufactured.

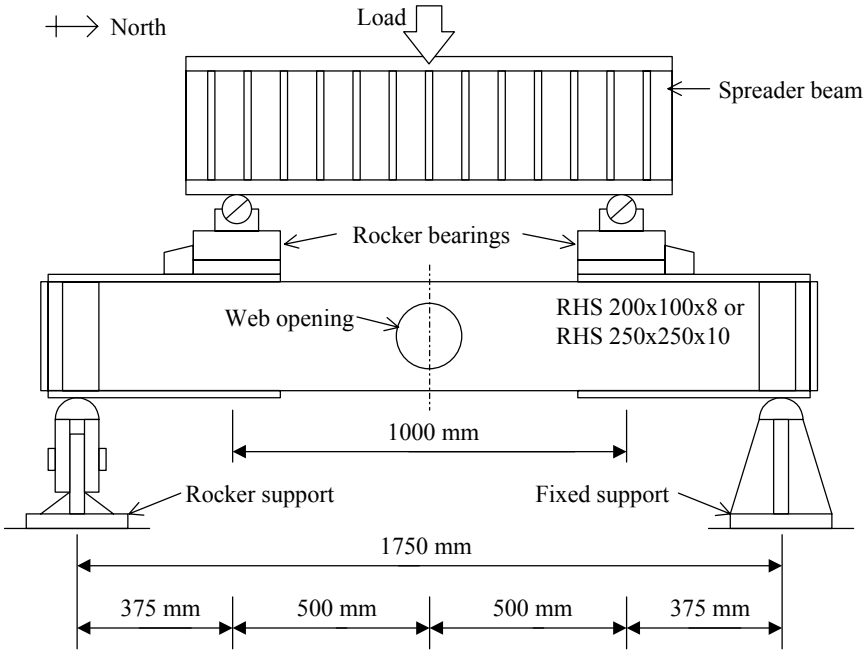

Figure 3-1: Schematic of the four-point bending test

Figure 3-2: The four-point loading test apparatus

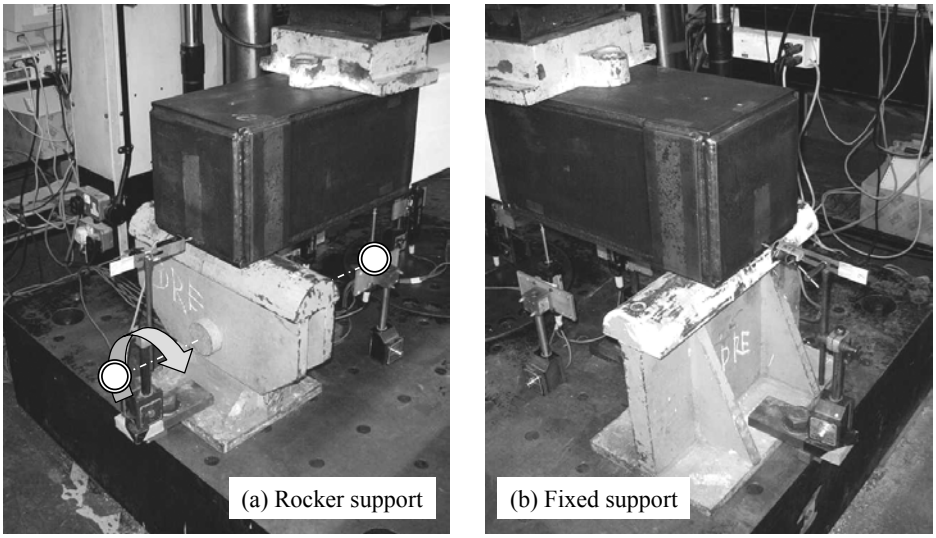

Figure 3-3: The supports (rocker and fixed)

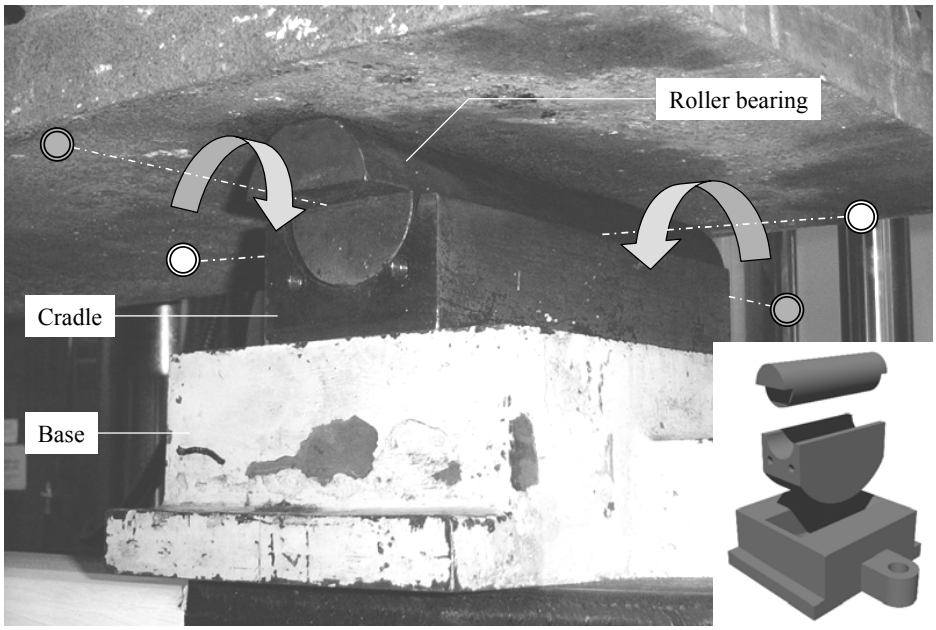

Figure 3-4: A dual axis rocker bearing

3.2.2 The four-point bending test specimens

Each four-point loading test specimen comprised of a 1.9 m length of RHS as shown in Figure 3-1 and Figure 3-5. Steel plates were welded to the flanges, in the shear span, to prevent failure in combined flexure and shear. Sealing plates and bearing stiffeners were added to prevent bearing failure at the supports and load points. The web openings were cold cut to a tolerance of ±0.1 mm in shape and ±0.1 mm in position. Further details of the specimens are given in Section 3.3.

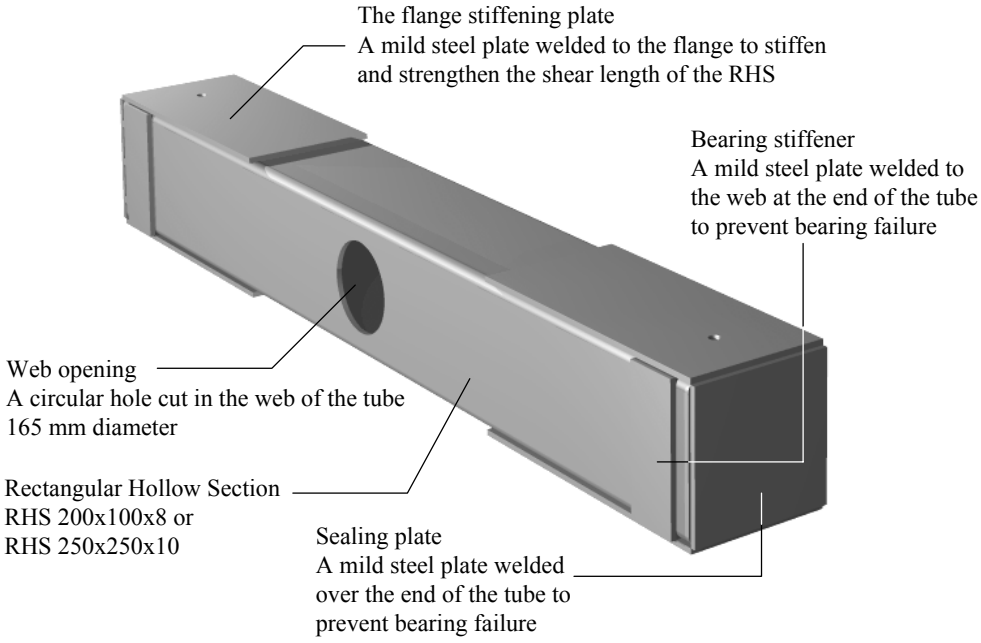

Figure 3-5: Four-point bending test specimen

3.2.3 Instrumentation

3.2.3.1 Measurement of bending moment

The vertical load was measured using the load cell of the Instron machine which had been rated as a grade 0.5 device in compression to BS 1610-1:1992 (Appendix F). The bending moment was calculated from the applied vertical load and the magnitude of the shear span lever arm (375 mm). Preliminary calculations (including FE analysis) had shown that the change in the shear span lever arm with increasing curvature was small enough to be neglected.

3.2.3.2 Measurement of curvature

The average curvature of the central span was calculated from the measured vertical displacement, of the tension flange, at the loading points and in the middle of the central span. Vertical displacements were measured by linear potentiometers and the layout of the instrumentation is shown in Figure 3-6.

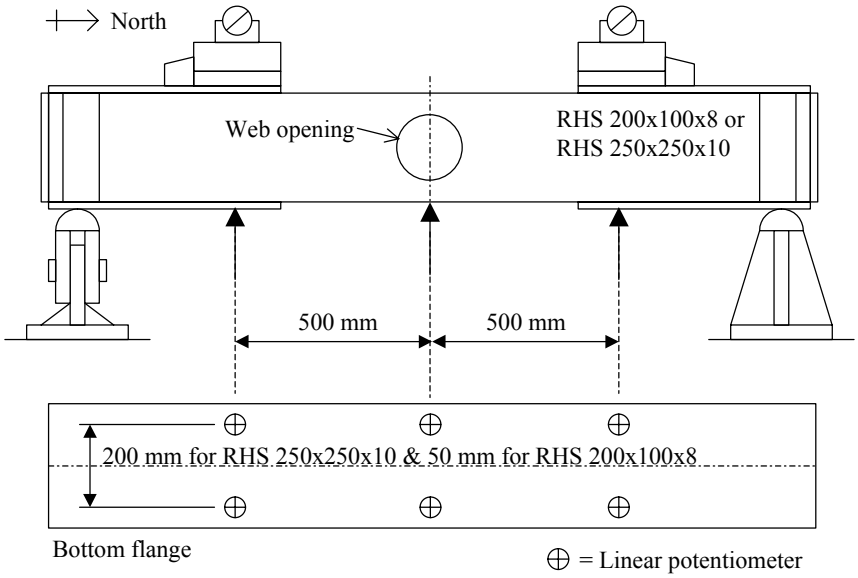

Figure 3-6: Measurement of curvature with linear potentiometers

3.2.3.3 Measurement of strain

Several of the bending test specimens were instrumented with electrical resistance strain gauges of the type shown in Figure 2-13 and Figure 2-14. The layouts are shown in Figure 3-7, Figure 3-8 and Figure 3-9.

All specimens were painted with a brittle lime wash to increase the visibility of slip lines in the steel and mill scale (Section 2.4.4.3). Examination of the formation of the slip line patterns provided information about the onset of yield and the distribution of plastic shear.

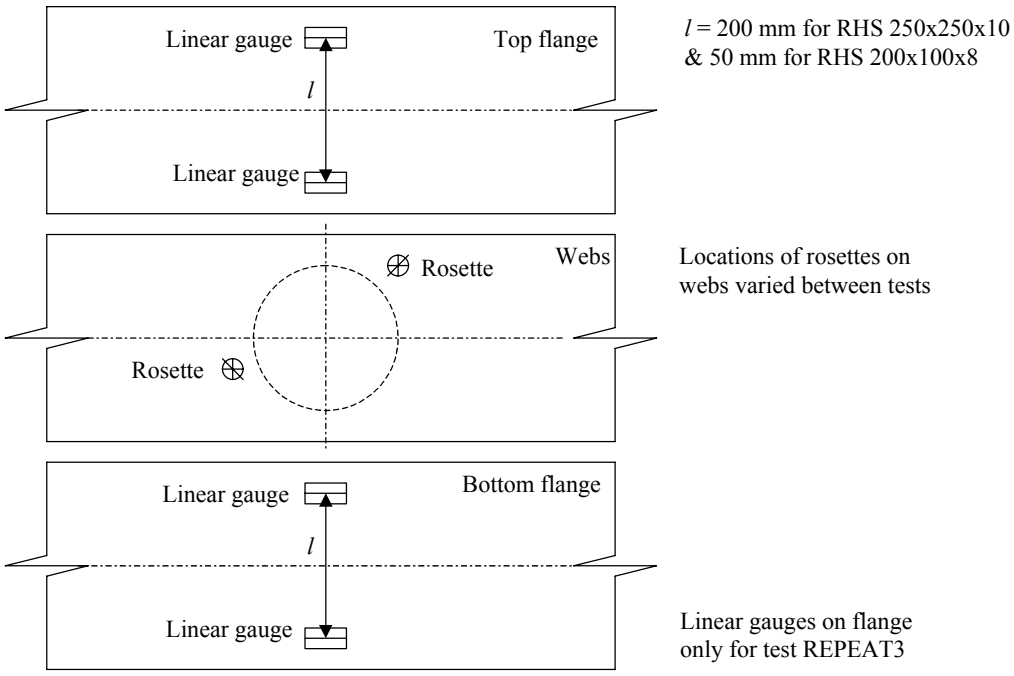

Figure 3-7: Strain gauge pattern (not REPEAT1, REPEAT4, DREB1 and DREB2)

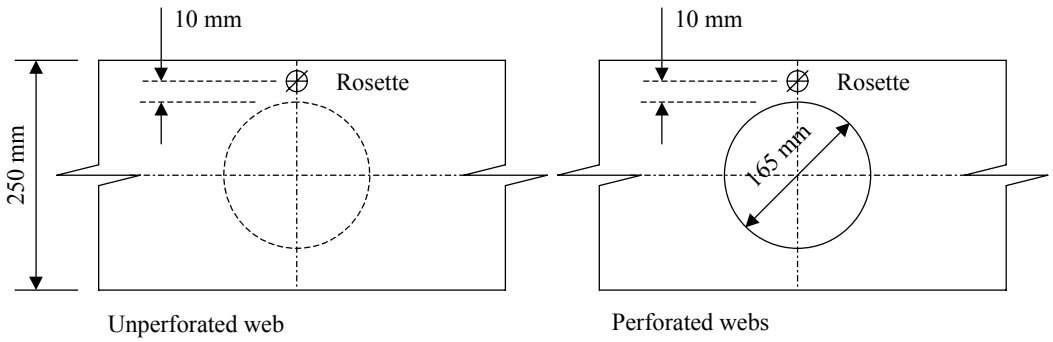

Figure 3-8: Strain gauge pattern (tests DREB1 and DREB2)

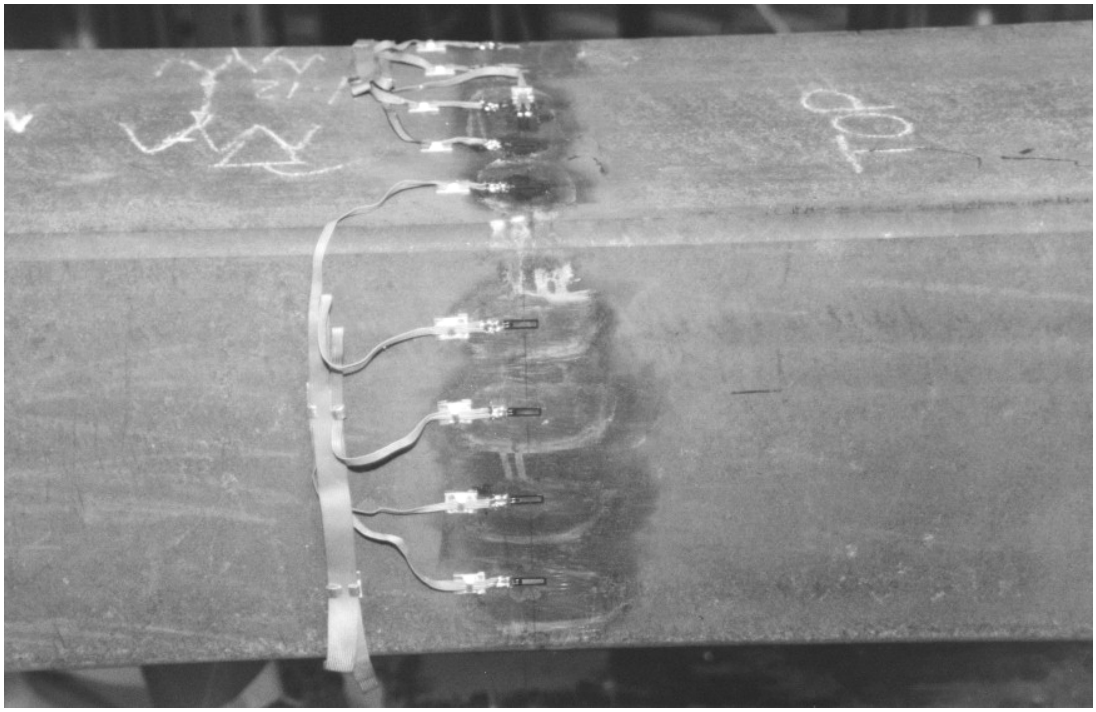

Figure 3-9: Strain gauge pattern (test REPEAT4)

3.2.3.4 Other measurements

In the tests of the specimens with single web openings (i.e. asymmetric), gravity inclinometers (measuring rotation) and additional linear potentiometers were used in an attempt measure secondary structural responses, such as twisting about the longitudinal axis and bending about the secondary transverse axis. No measurable twisting or secondary bending was observed, although the RHS 200x100x8 one hole specimen was observed to lozenge at high curvature.

In every test, linear potentiometers (which can be seen in Figure 3-3) were used to measure the horizontal movement of the specimen at the supports as the bottom flange lengthened with increasing curvature. The measurements confirmed the efficacy of the precautionary procedures aimed at ensuring that significant additional loads were not placed on the specimens by excessive friction.

3.2.4 Testing procedure

Testing proceeded as outlined below. In all cases, elastic tests were performed by repeated loading and unloading within the elastic range. One test (REPEAT1) was conducted in load control rather than displacement control.

1) The specimen was inserted into the loading apparatus and carefully positioned
2) The strain gauges were initialised (zeroed) using the data logger
3) A reading was taken at zero load
4) The spreader beam was lowered onto the specimen, and its weight (7.137 kN) included in the calculation of the applied load
5) A reading was taken

6) An increment of displacement was applied (either manually, or automatically using a predefined ramp)
7) A reading was taken
8) Steps 6 and 7 were repeated until the desired curvature was achieved
9) The specimen was unloaded in increments and readings were taken at each
10) The spreader beam was removed and a reading was taken at zero load
11) The specimen was removed from the loading apparatus

3.3 Specimen types, dimensions and properties

3.3.1 Specimens tested

The specimens tested are listed in Table 3-1. Five different hot finished bars were used in the manufacture of the specimens (two section sizes of grade S275J2H). The material was provided and manufactured by British Steel (now Corus).

Unfortunately, an intermittent valve servo fault in the hydraulic control system of the testing machine caused large errors in the measurement of load for a number of the tests; particularly those involving the highest loads. The results of tests TEST1, TEST2, TEST3 and TEST4 were affected by the fault, which became known when it caused the accidental uncontrolled premature destruction of test REPEAT2. Additional tests were conducted to replace those affected, and the results are presented here in lieu of the originals. However, measurements of elastic stiffness and elastic strain were unaffected by the fault, and those measurements were made use of in the calibration of the FE models.

Table 3-1: Specimens tested

ID Code	Date tested	Section size	Material grade [Bar number]	Number of holes	Hole diameter (mm)	Hole size ratio, Φ
TEST4	06/02/1998	RHS 200x100x8	S275J2H [#1]	0	-	-
REPEAT1	11/09/1998	RHS 200x100x8	S275J2H [#1]	0	-	-
REPEAT2	17/09/1998	RHS 200x100x8	S275J2H [#1]	0	-	-
REPEAT5	21/01/1999	RHS 200x100x8	S275J2H [#2]	0	-	-
TEST6	11/03/1998	RHS 200x100x8	S275J2H [#2]	1	165.0	0.94
TEST5A	12/02/1998	RHS 200x100x8	S275J2H [#1]	2	165.0	0.94
TEST5B	23/02/1998	RHS 200x100x8	S275J2H [#1]	2	165.0	0.94
TEST1	24/10/1997	RHS 250x250x10	S275J2H [#1]	0	-	-
REPEAT3	07/10/1998	RHS 250x250x10	S275J2H [#2]	0	-	-
REPEAT4	20/10/1999	RHS 250x250x10	S275J2H [#2]	0	-	-
TEST3	25/11/1997	RHS 250x250x10	S275J2H [#1]	1	165.0	0.75
DREB1	24/01/2000	RHS 250x250x10	S275J2H [#3]	1	165.0	0.75
TEST2	20/11/1997	RHS 250x250x10	S275J2H [#1]	2	165.0	0.75
DREB2	19/01/2000	RHS 250x250x10	S275J2H [#3]	2	165.0	0.75

Note 1: Results of tests TEST1, TEST2, TEST3 and TEST4 affected by testing machine fault
Note 2: Test REPEAT2 destroyed by failure of the hydraulic control system of the testing machine
Note 3: The hole size ratio (Φ) is defined by Equation 1-3
Note 4: Test REPEAT1 tested in load control (all others tested in displacement control)

3.3.2 Material properties

The properties of the five bars are summarised in Table 3-2. The results of the individual tensile tests are given in Appendix D. The definitions of the parameters used can be found in Section 2.2 and BS EN 10002-1:1990.

Table 3-2: Material models

Section size Grade [Bar no]	K (%)	f_{y1} (N/mm^2)	E (kN/mm^2)	$\lambda_{plateau}$	$E_{plateau}$ (kN/mm^2)	λ_{ESHF}	f_u (N/mm^2)	ε_u (%)
RHS 200x100x8 S275J2H [#1]	1.21	355.4	199.5	13.4	-0.07	0.17	477.4	16.2
RHS 200x100x8 S275J2H [#2]	2.53	335.1	182.0	11.7	0.50	0.21	475.5	16.0
RHS 250x250x10 S275J2H [#1]	1.48	347.7	210.0	14.8	0.52	0.24	463.8	15.6
RHS 250x250x10 S275J2H [#2]	3.16	343.2	197.6	12.9	0.21	0.22	468.0	15.9
RHS 250x250x10 S275J2H [#3]	1.23	364.1	204.0	11.0	0.31	0.27	490.0	15.0

Note: Refer to Section 2.2

3.3.3 Dimensions and geometrical properties

The measured dimensions of the five bars, used in the manufacture of the test specimens, are given in Table 3-3. Dimensions are as defined by BS EN 10210-2:1997 (Figure 1-9). The geometrical properties, obtained using the formulae given in BS EN 10210-2:1997 (Appendix C), are listed in Table 3-4.

Sectional properties, based on measured material properties and dimensions, are given in Table 3-5. The theoretical shear capacities of the bars are also listed (for completeness) and the method by which they were calculated is explained in Section 4.3.3. For comparison, the nominal section properties are given in Table 3-6.

Table 3-3: Dimensions of cross-section (measured)

Section size	Material grade [Bar number]	Height h (mm)	Width b (mm)	Thickness t (mm)	Corner radius (mm) Internal	External
RHS 200x100x8	S275J2H [#1]	197.5	100.0	7.79	5.0	12.5
RHS 200x100x8	S275J2H [#2]	198.0	100.0	7.73	5.0	12.5
RHS 250x250x10	S275J2H [#1]	250.0	250.0	9.70	8.0	15.0
RHS 250x250x10	S275J2H [#2]	249.5	249.5	9.74	8.0	15.0
RHS 250x250x10	S275J2H [#3]	250.5	251.0	10.22	8.0	15.0

Table 3-4: Properties of cross-section (from measured dimensions)

Section size	Material grade [Bar number]	Shear area A_v (cm^2)	Second moment of area I_y (cm^4)	Elastic section Modulus $W_{el,y}$ (cm^4)	Plastic section Modulus $W_{pl,y}$ (cm^3)
RHS 200x100x8	S275J2H [#1]	28.38	2074	210	265
RHS 200x100x8	S275J2H [#2]	28.25	2074	209	265
RHS 250x250x10	S275J2H [#1]	45.66	8699	696	817
RHS 250x250x10	S275J2H [#2]	45.74	8675	695	817
RHS 250x250x10	S275J2H [#3]	48.11	9179	733	862

Note: Shear area calculated as in Table 5.16 of Eurocode 3 and Clause 4.2.3d of BS 5950

Table 3-5: Sectional properties (measured dims and material props, theoretical)

Section size	Material grade [Bar number]	Curvature at yield κ_e (km^{-1})	Elastic moment $M_{el,y}$ (kNm)	Plastic moment $M_{pl,y}$ (kNm)	Shape factor $M_{pl,y}$ / $M_{el,y}$	Shear resistance V_y (kN)
RHS 200x100x8	S275J2H [#1]	18.02	74.78	94.47	1.26	583
RHS 200x100x8	S275J2H [#2]	18.58	70.32	88.81	1.26	548
RHS 250x250x10	S275J2H [#1]	13.24	242.4	284.6	1.17	918
RHS 250x250x10	S275J2H [#2]	13.91	239.1	280.8	1.17	908
RHS 250x250x10	S275J2H [#3]	14.24	267.3	314.4	1.18	1013

Note: Shear resistance calculated as in Eurocode 3 (Clause 5.5.1) and BS 5950 (Clause 4.2.3)

Table 3-6: Sectional properties (nominal, theoretical)

Section size	Material grade [Bar number]	Curvature at yield (km^{-1})	Elastic moment (kNm)	Plastic moment (kNm)	Shape factor	Shear resistance (kN)
RHS 200x100x8	S275J2H [1]	13.10 (73%)	61.42 (82%)	77.54 (82%)	1.26 (100%)	438 (75%)
RHS 200x100x8	S275J2H [2]	13.10 (71%)	61.42 (87%)	77.54 (87%)	1.26 (100%)	438 (80%)
RHS 250x250x10	S275J2H [1]	10.48 (79%)	199.2 (82%)	233.9 (82%)	1.17 (100%)	754 (82%)
RHS 250x250x10	S275J2H [2]	10.48 (75%)	199.2 (83%)	233.9 (83%)	1.17 (100%)	754 (83%)
RHS 250x250x10	S275J2H [3]	10.48 (74%)	199.2 (75%)	233.9 (74%)	1.17 (99%)	754 (74%)

Note 1: The percentages in parentheses denote the nominal value as a percentage of the measured
Note 2: Shear resistance calculated as in Eurocode 3 (Clause 5.5.1) and BS 5950 (Clause 4.2.3)

3.4 The experimental results

Measured elastic stiffnesses and maximum bending moments are listed in Table 3-7. The full moment-curvature relationships are presented in Figure 3-10 through Figure 3-15. The bending moment and curvature have been non-dimensionalised against the theoretical moment and curvature at yield for the corresponding unperforated section. The curvature is the average value over the uniform bending length (1000 mm).

The theoretical moments and curvatures were calculated using conventional (Euler-Bernoulli-Parent) beam bending theory and were based on measured dimensions and material properties. The shape factor is also plotted on the Figures, and is shown as a horizontal dashed line. The shape factor is the ratio of the elastic and plastic section moduli and, in this instance, represents the theoretical plastic capacity of the corresponding unperforated section.

The unperforated sections behaved as predicted by conventional bending theory, although the RHS 250x250x10 specimens showed limited plastic rotation capacity due to compression flange buckling. Calculation of the slenderness ratio of the flange indicated that the RHS 250x250x10 section was at the very limit of the

Eurocode 3 (Clause 5.3) and BS 5950 (Clause 3.5) class 1 definition, and although the measured rotation capacities were sufficient for plastic design (Section 7.5.1), plastic buckling at high curvature was not unexpected.

The presence of the web openings was observed to decrease the stability of the compression elements of the perforated zone, and inelastic buckling in this region was observed in all the tests of perforated sections. The destabilising effect of the web openings is discussed further in Sections 3.5 and 7.5.

Measurements of elastic stiffness and maximum bending moment are compared to the theoretical values of the corresponding unperforated sections in Table 3-9. The measurements show that the unperforated specimens were able to achieve capacities slightly higher (up to 10%) than the plastic moment of resistance. This is likely to be the result of strain hardening at the location of the plastic hinge.

In the case of the RHS 200x100x8 with two holes, the capacity was reduced by around 30%, but in the case of the RHS 250x250x10, the reduction was around 5%. A qualitative difference of this type was expected, as, in the case of the RHS 250x250x10 beam, the holes were smaller in relation to the section depth, and the webs contributed a smaller proportion of the section modulus.

No conclusions could be drawn, from the experimental results alone, about the effect of the web openings on stiffness, as the measurements showed a relatively large amount of variability, even for unperforated specimens. This is because the effect of web openings on bending stiffness, discussed further in Sections 3.5 and 7.5.4, is slight.

In the cases where duplicate tests were performed, comparisons of the complete moment-curvature relationships indicated good repeatability, implying good reliability of the testing method.

Table 3-7: Experimental results – stiffness and maximum bending moment

ID Code	Section size	Material grade [Bar number]	Number of holes	Hole diameter (mm)	Stiffness (MNm^2)	Moment (kNm)	@
TEST4	RHS 200x100x8	S275J2H [#1]	0	-	4.59	-	-
REPEAT1	RHS 200x100x8	S275J2H [#1]	0	-	4.18	94.3	Max
REPEAT5	RHS 200x100x8	S275J2H [#2]	0	-	4.33	91.2	Max
TEST6	RHS 200x100x8	S275J2H [#2]	1	165.0	4.22	81.4	Max
TEST5A	RHS 200x100x8	S275J2H [#1]	2	165.0	4.33	71.5	Max
TEST5B	RHS 200x100x8	S275J2H [#1]	2	165.0	4.57	70.1	Max
TEST1	RHS 250x250x10	S275J2H [#1]	0	-	19.1	-	-
REPEAT3	RHS 250x250x10	S275J2H [#2]	0	-	18.2	303	Max
REPEAT4	RHS 250x250x10	S275J2H [#2]	0	-	17.4	291	Max
TEST3	RHS 250x250x10	S275J2H [#1]	1	165.0	18.0	-	-
DREB1	RHS 250x250x10	S275J2H [#3]	1	165.0	17.8	309	Max
TEST2	RHS 250x250x10	S275J2H [#1]	2	165.0	18.4	-	-
DREB2	RHS 250x250x10	S275J2H [#3]	2	165.0	17.9	298	Max

Table 3-8: Experimental results and theory– stiffness and max bending moment

ID Code	Section size	Material grade [Bar number]	Number of holes	Hole diameter (mm)	Stiffness (% of theory)	Moment (% of theory)
TEST4	RHS 200x100x8	S275J2H [#1]	0	-	110.6%	-
REPEAT1	RHS 200x100x8	S275J2H [#1]	0	-	100.7%	99.8%
REPEAT5	RHS 200x100x8	S275J2H [#2]	0	-	114.4%	102.7%
TEST6	RHS 200x100x8	S275J2H [#2]	1	165.0	111.5%	91.7%
TEST5A	RHS 200x100x8	S275J2H [#1]	2	165.0	104.3%	75.7%
TEST5B	RHS 200x100x8	S275J2H [#1]	2	165.0	110.1%	74.2%
TEST1	RHS 250x250x10	S275J2H [#1]	0	-	104.3%	-
REPEAT3	RHS 250x250x10	S275J2H [#2]	0	-	105.9%	107.9%
REPEAT4	RHS 250x250x10	S275J2H [#2]	0	-	101.2%	103.6%
TEST3	RHS 250x250x10	S275J2H [#1]	1	165.0	98.3%	-
DREB1	RHS 250x250x10	S275J2H [#3]	1	165.0	94.8%	98.3%
TEST2	RHS 250x250x10	S275J2H [#1]	2	165.0	100.5%	-
DREB2	RHS 250x250x10	S275J2H [#3]	2	165.0	95.4%	94.8%

Note: Theoretical quantities are for the corresponding unperforated section

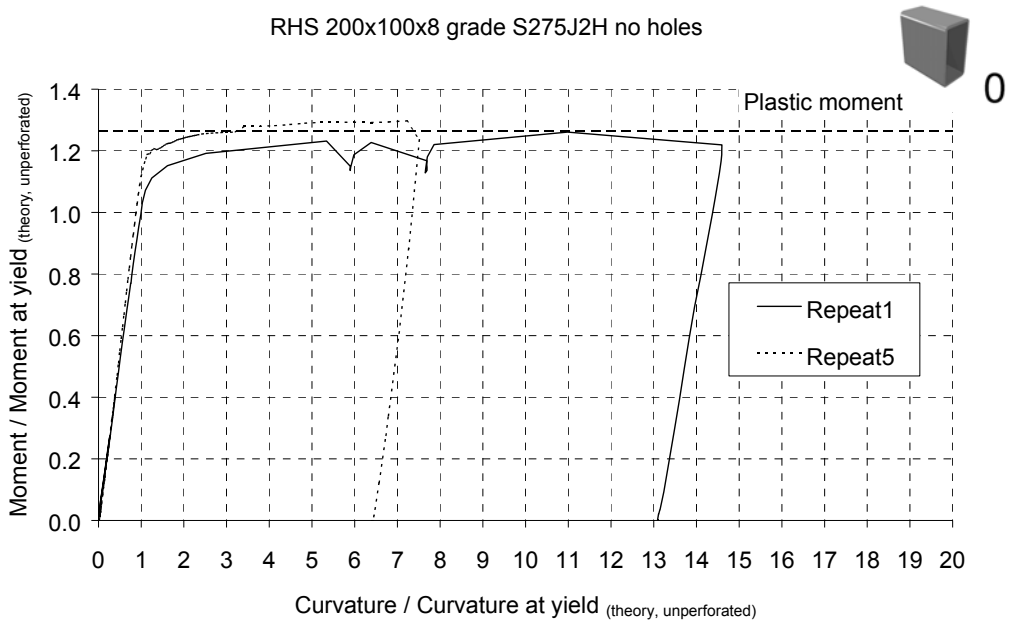

Figure 3-10: Experimental results RHS 200x100x8 no holes

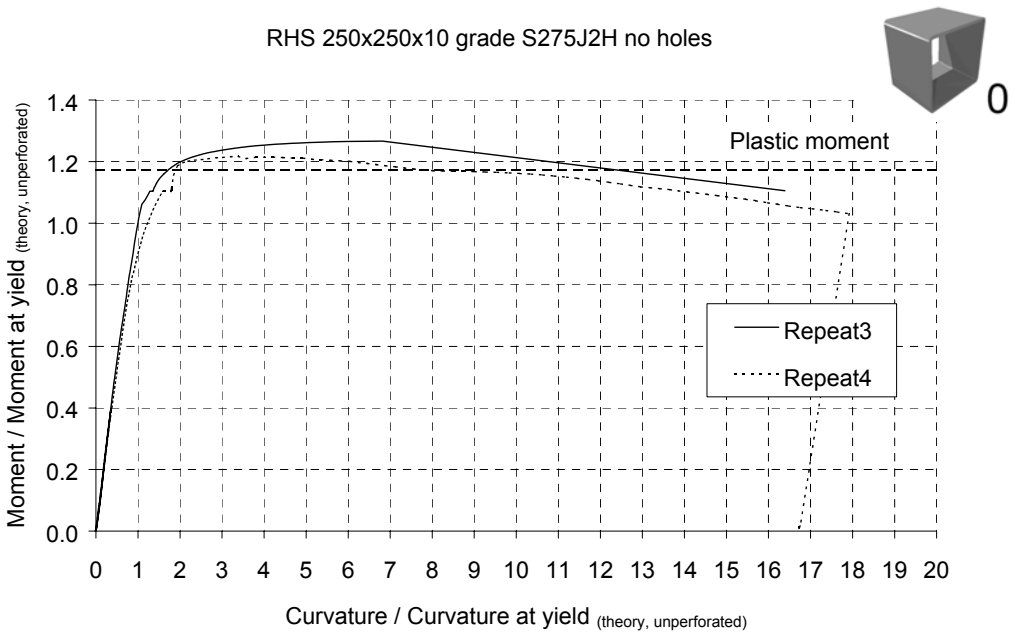

Figure 3-11: Experimental results RHS 250x250x10 no holes

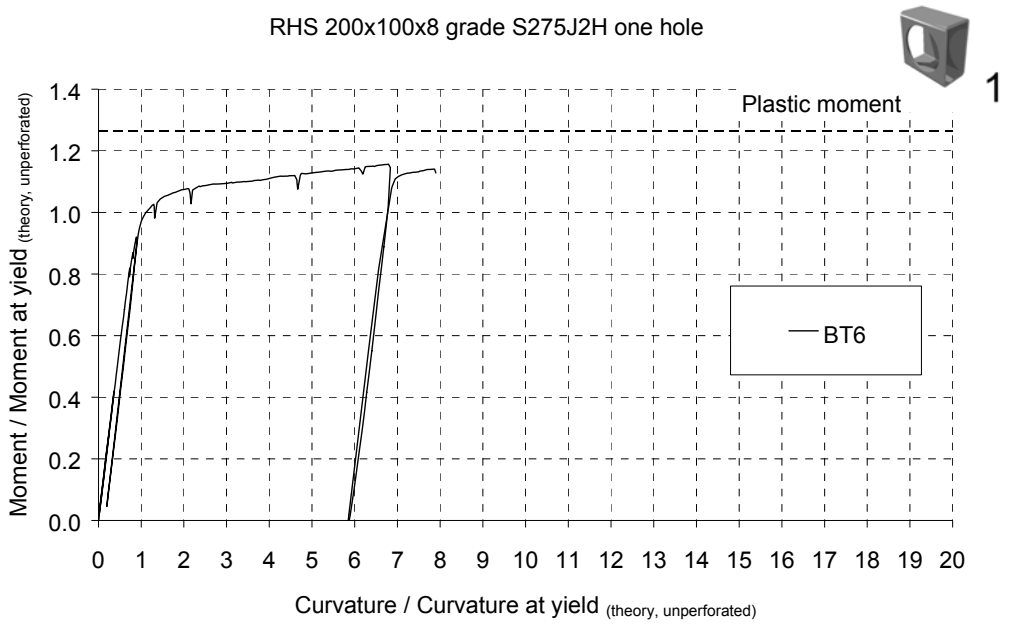

Figure 3-12: Experimental results RHS 200x100x8 one hole 165 mm dia

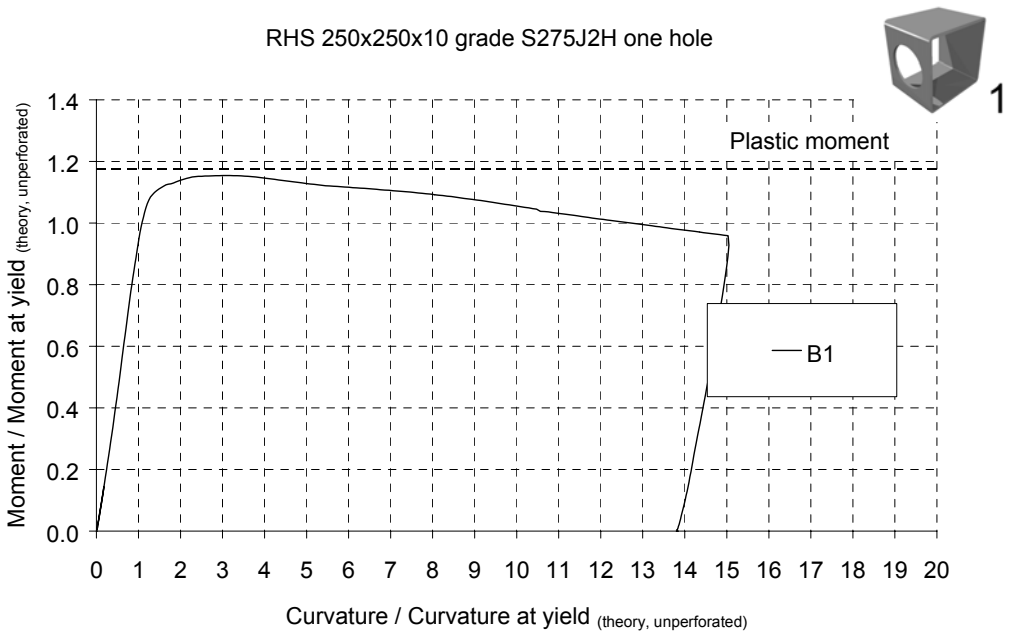

Figure 3-13: Experimental results RHS 250x250x10 one hole 165 mm dia

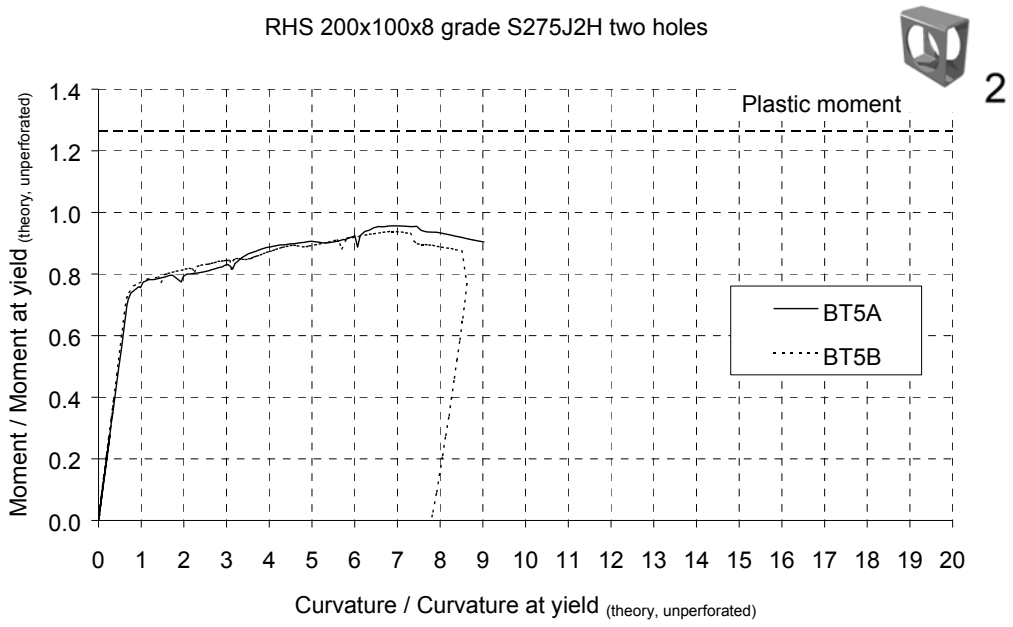

Figure 3-14: Experimental results RHS 200x100x8 two holes 165 mm dia

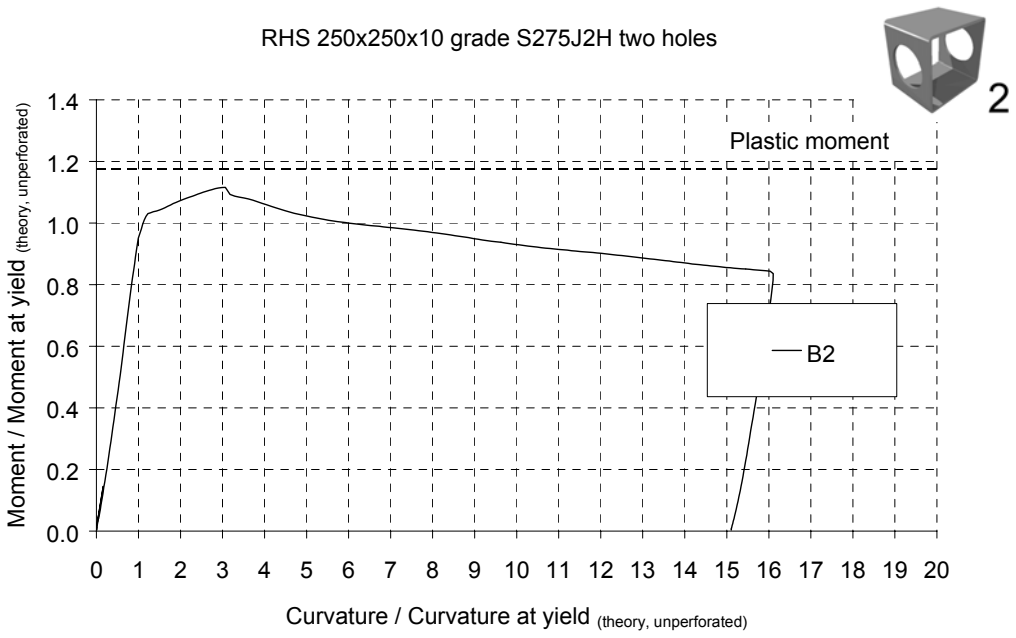

Figure 3-15: Experimental results RHS 250x250x10 two holes 165 mm dia

3.5 A comparison of experimental results and analytical predictions

The laboratory tests were modelled using the ABAQUS FEA program (versions 5.5.1 and 5.8.1) and the experimental results were compared with the FE predictions. Models included both material and geometric non-linearity and contained between 4200 and 5800 four-noded shell elements (S4R). These elements were chosen to create the models because they allowed changes in thickness at high strains to be modelled (Section 2.3.6). The FE models were based on the actual measured dimensions of the test specimens and included the corner radii of the tube. The stiffening and strengthening plates were also included, and were modelled by locally increasing the thickness of the elements. The support conditions and bearings at the loading points were modelled by defining constraint equations to describe the permitted displacements in the nodal degrees of freedom.

The initial stiffnesses and maximum bending moments predicted by the FE models are listed in Table 3-9. The differences between the experimental values (Table 3-7) and the FE predictions are listed in Table 3-10.

The complete moment-curvature relationships are presented in Figure 3-16 through Figure 3-21. The bending moment and curvature have been non-dimensionalised against the theoretical moment and curvature at yield of the corresponding unperforated section (Table 3-5). The moment-curvature relationships predicted by the FE models matched those measured in the laboratory, and the FE was able to correctly model the negative stiffness in the collapse stage.

The FE models tended to under-predict the maximum bending resistance by around 10%. Predictions of elastic stiffness were within 14% of those measured experimentally. However, this difference in elastic stiffness is accounted for, in

part, by the difficulty in obtaining accurate measurements of Young's modulus from tensile tests.

The FE models of the unperforated sections failed to achieve the full theoretical plastic capacity due to the long yield plateau in the material model and the large curvature required to achieve yield in the entire cross-section. In the laboratory tests, the plastic deformation was concentrated over a short length (a plastic hinge) where strain hardened stresses were able to develop. However, in the FE models, the homogeneity of the material meant that plastic strain occurred uniformly over the whole bending length of the beam, and strains were too small to result in strain hardened stresses.

The FE predictions of the elastic stiffness for the unperforated sections were close to those predicted by bending theory, although, in the case of the RHS 250x250x10 sections, the FE predictions were slightly lower (around 3%). The FE models of the perforated sections indicated that the reduction in stiffness, due to the presence of the hole, was small (less than 5% in the case of the RHS 200x100x8 and less than 1% in the case of the RHS 250x250x10). The effect of the web openings on the elastic stiffness is discussed further in Section 7.5.4.

As was the case with the laboratory tests, the FE model of the RHS250x250x10 unperforated section showed limited ductility due to compression flange buckling. The natural tendency of the compression flange in the FE model was to buckle outwards, while inward buckles were observed in the laboratory. A slight imperfection (0.05% of the section width) was introduced into the flange of the FE model used in the calibration, in order to induce an inward buckle. A parametric investigation showed that the ultimate resistance of the beam was insensitive to the size of the imperfection, although the rotation capacity could be

increased (up to 20%) by balancing the imperfection with the natural tendency of the flange to buckle outwards.

The FE models matched closely the deformed shapes observed in the laboratory (Figure 3-22 through Figure 3-27). The deformation in the perforated zone was modelled extremely well, as can be seen in Figure 3-28, which shows a deformed FE mesh superimposed on a photograph of the deformed test specimen (RHS 200x100x8 with two holes).

In the perforated sections, the presence of the web openings reduced the plastic stability of the compression elements in the perforated zone. In the case of the RHS 200x100x8 sections, plastic collapse of the section occurred through arching of the cee-shaped compression zone above the hole (Figure 3-23, Figure 3-24 and Figure 3-28). In the case of the RHS 250x250x10 sections, plastic collapse of the section occurred through buckling of the compression flange because the perforation(s) reduced the stabilising influence of the webs (Figure 3-26 and Figure 3-27). For the RHS 250x250x10 sections, the buckle in the compression flange was slightly off-centre, in both the FE models and the laboratory tests (Figure 3-26 and Figure 3-27).

In the elastic range, the theoretical and FE predictions of surface strain for unperforated sections were close to those measured in the laboratory. However, the measurements and predictions diverged with increasing strain (this is explained in Section 2.6). Figure 3-29 shows a comparison of the longitudinal strain-curvature gradient for various points around the circumference of an unperforated RHS 250x250x10 specimen (test REPEAT4, Figure 3-9). In this case, the measurements of the bending strain in the webs were close to those predicted by conventional beam bending theory, but measurements of bending strain in the flanges were slightly

lower (15%). It is possible that this difference is a result of shear lag, although no shear lag was observed in the FE models.

In the elastic range, the FE predictions of surface strain for perforated sections were also close to those measured in the laboratory. As was the case with the perforated sections, the measurements and predictions diverged with increasing strain (this is explained in Section 2.6). In this respect, the comparisons of measured strains and FE predictions, for an RHS 250x250x10 with one hole (test DREB1), shown in Figure 3-30 and Figure 3-31 are typical. The Figures show the maximum and minimum principal strains for a point 10 mm above the top of the hole, for the perforated (Figure 3-31) and unperforated (Figure 3-30) webs (see also Figure 3-8). The effect of the perforation on the stress distribution in the beam, evident in these results, is discussed further in Section 7.5.2.

Table 3-9: Finite Element results – stiffness and maximum bending moment

ID Code	Section size	Material grade [Bar number]	Number of holes	Hole diameter (mm)	Stiffness (MNm^2)	Moment @ (kNm)	
TEST4	RHS 200x100x8	S275J2H [#1]	0	-	4.16	-	-
REPEAT1	RHS 200x100x8	S275J2H [#1]	0	-	4.16	91.5	Max
REPEAT5	RHS 200x100x8	S275J2H [#2]	0	-	3.80	86.1	Max
TEST6	RHS 200x100x8	S275J2H [#2]	1	165.0	3.72	74.0	Max
TEST5A	RHS 200x100x8	S275J2H [#1]	2	165.0	3.96	63.0	Max
TEST5B	RHS 200x100x8	S275J2H [#1]	2	165.0	3.96	63.0	Max
TEST1	RHS 250x250x10	S275J2H [#1]	0	-	17.8	-	-
REPEAT3	RHS 250x250x10	S275J2H [#2]	0	-	16.7	275	Max
REPEAT4	RHS 250x250x10	S275J2H [#2]	0	-	16.7	275	Max
TEST3	RHS 250x250x10	S275J2H [#1]	1	165.0	17.8	-	-
DREB1	RHS 250x250x10	S275J2H [#3]	1	165.0	18.1	287	Max
TEST2	RHS 250x250x10	S275J2H [#1]	2	165.0	17.8	-	-
DREB2	RHS 250x250x10	S275J2H [#3]	2	165.0	18.1	271	Max

Table 3-10: Experimental and FE results – stiffness and maximum bending moment

ID Code	Section size	Material grade [Bar number]	Number of holes	Hole diameter (mm)	Difference stiffness (%)	Difference moment (%)
TEST4	RHS 200x100x8	S275J2H [#1]	0	-	10.4	-
REPEAT1	RHS 200x100x8	S275J2H [#1]	0	-	0.35	3.00
REPEAT5	RHS 200x100x8	S275J2H [#2]	0	-	14.1	6.02
TEST6	RHS 200x100x8	S275J2H [#2]	1	165.0	13.5	9.87
TEST5A	RHS 200x100x8	S275J2H [#1]	2	165.0	9.20	13.5
TEST5B	RHS 200x100x8	S275J2H [#1]	2	165.0	15.2	11.3
TEST1	RHS 250x250x10	S275J2H [#1]	0	-	7.42	-
REPEAT3	RHS 250x250x10	S275J2H [#2]	0	-	8.41	10.0
REPEAT4	RHS 250x250x10	S275J2H [#2]	0	-	4.11	5.66
TEST3	RHS 250x250x10	S275J2H [#1]	1	165.0	0.71	-
DREB1	RHS 250x250x10	S275J2H [#3]	1	165.0	-1.34	7.47
TEST2	RHS 250x250x10	S275J2H [#1]	2	165.0	3.62	-
DREB2	RHS 250x250x10	S275J2H [#3]	2	165.0	-0.79	10.2

Note: A negative percentage indicates experimental values lower than Finite Element values

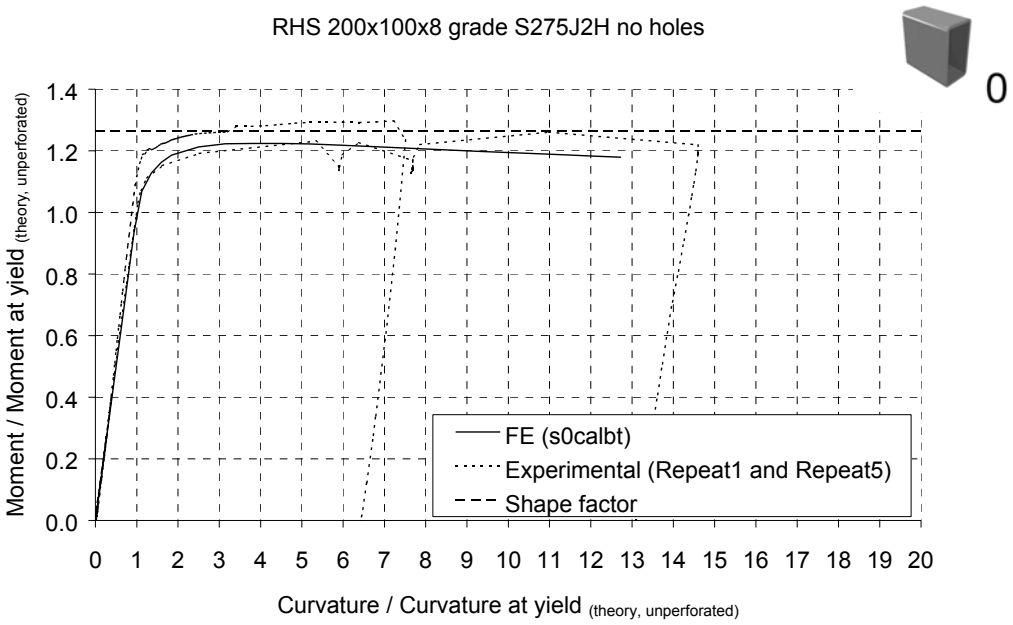

Figure 3-16: FE and experimental (tests REPEAT1 and REPEAT5)

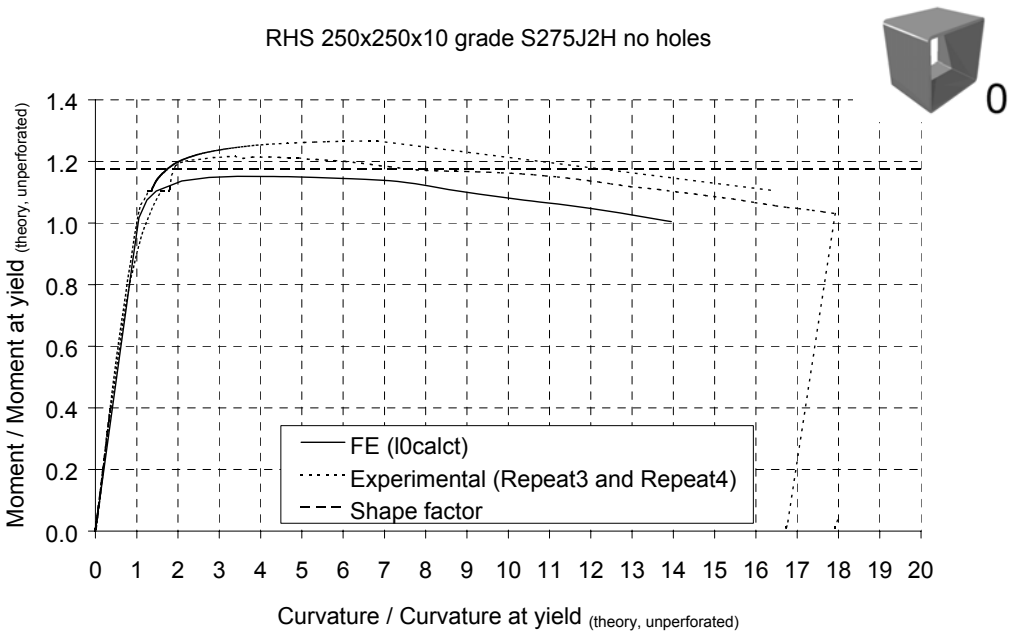

Figure 3-17: FE and experimental (tests REPEAT3 and REPEAT4)

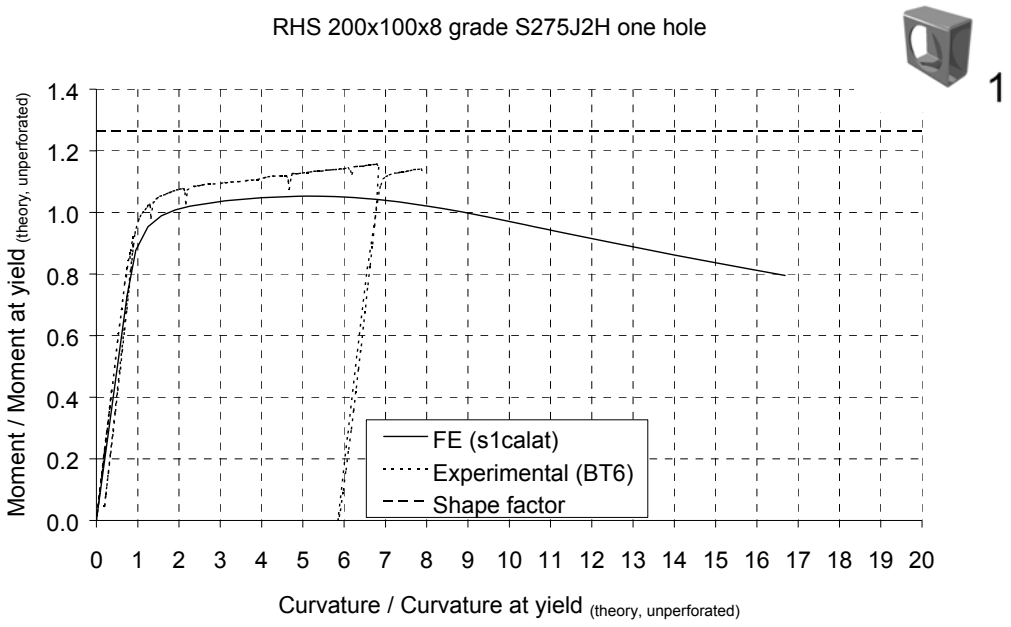

Figure 3-18: FE and experimental (test TEST6)

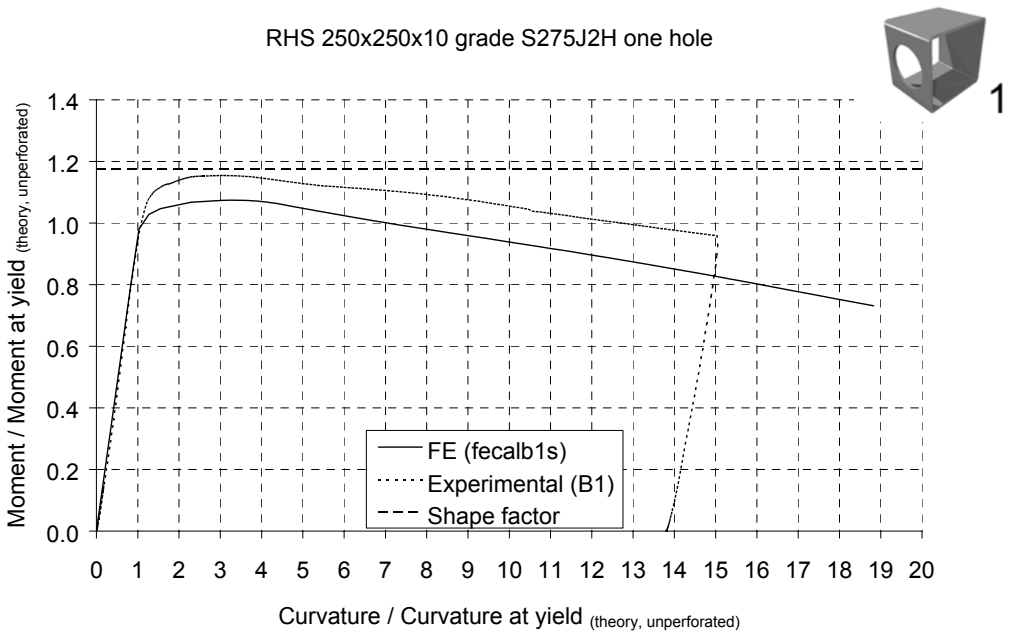

Figure 3-19: FE and experimental (test DREB1)

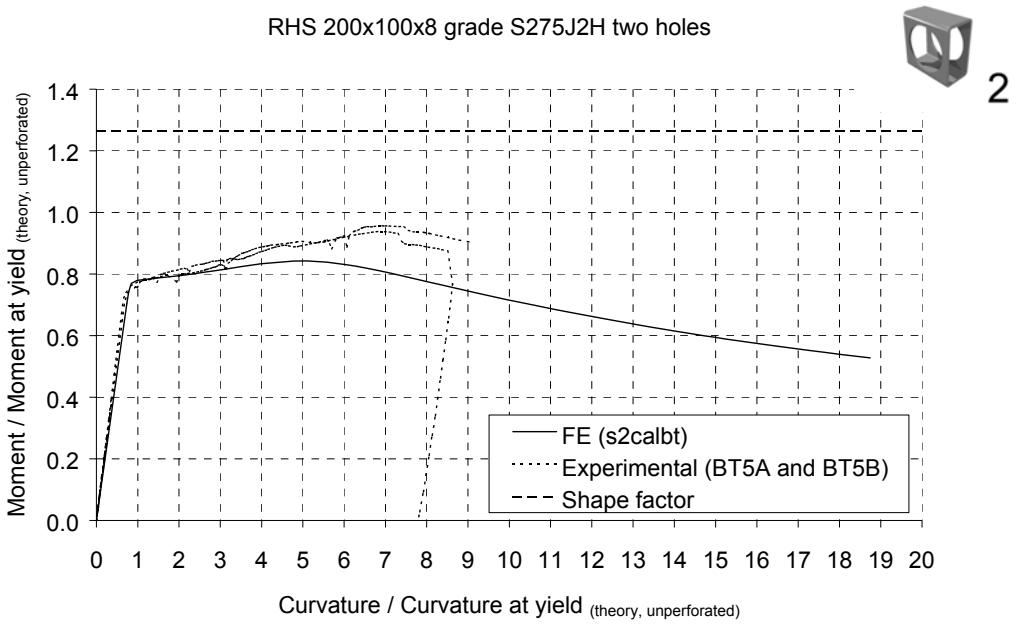

Figure 3-20: FE and experimental (tests TEST5A and TEST5B)

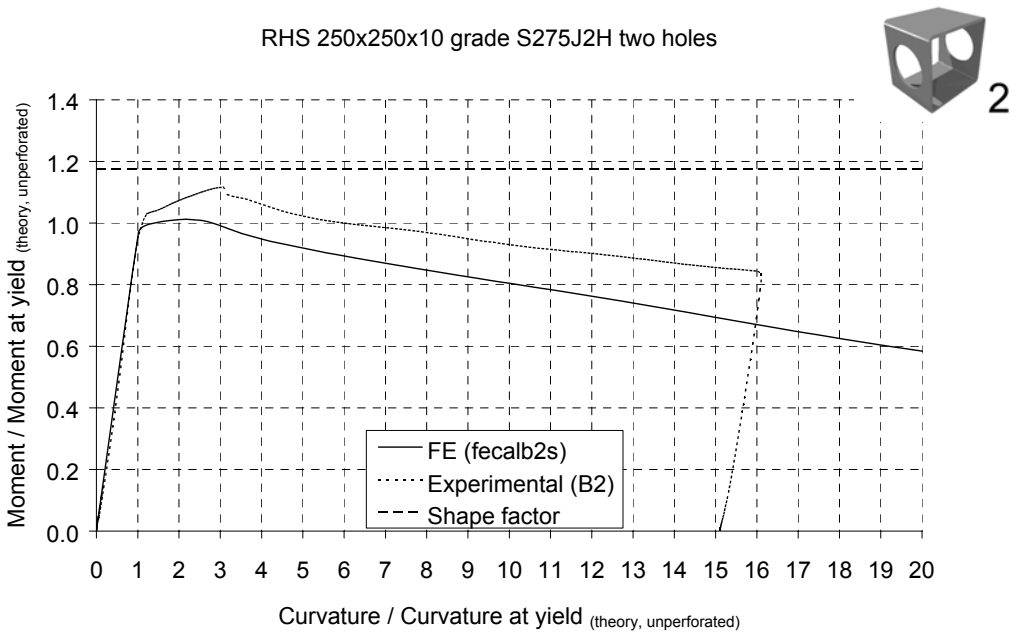

Figure 3-21: FE and experimental (test DREB2)

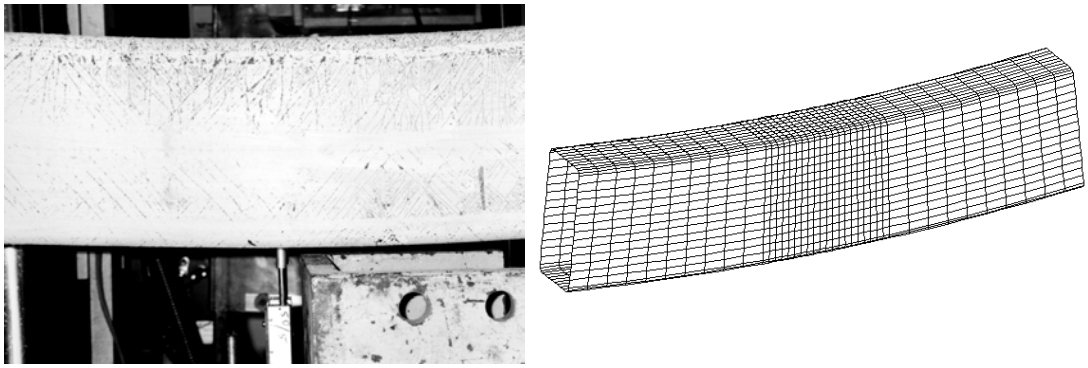

Figure 3-22: Displaced shape RHS 200x100x8 no holes

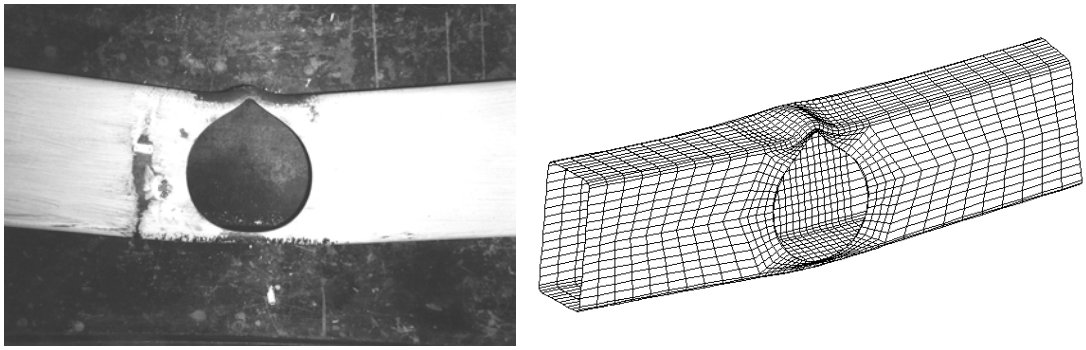

Figure 3-23: Displaced shape RHS 200x100x8 one hole

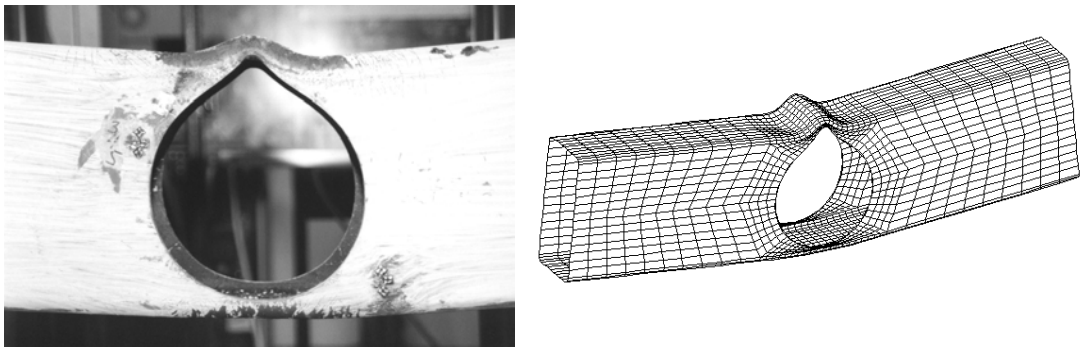

Figure 3-24: Displaced shape RHS 200x100x8 two holes

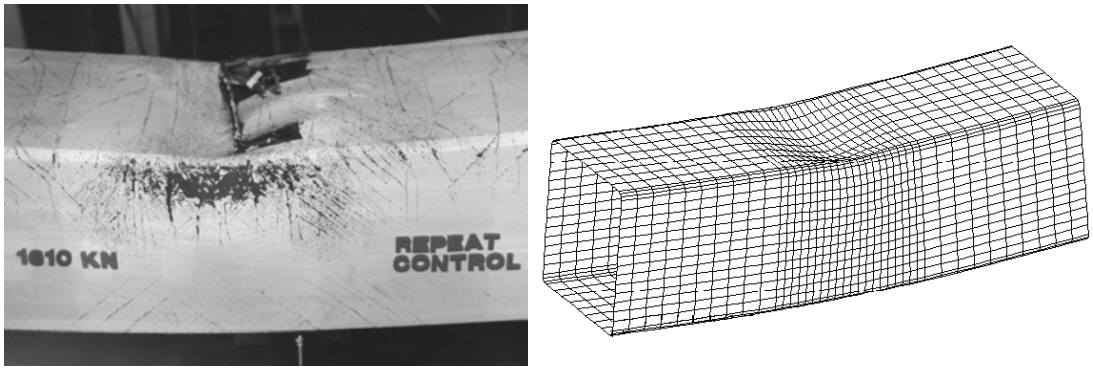

Figure 3-25: Displaced shape RHS 250x250x10 no holes

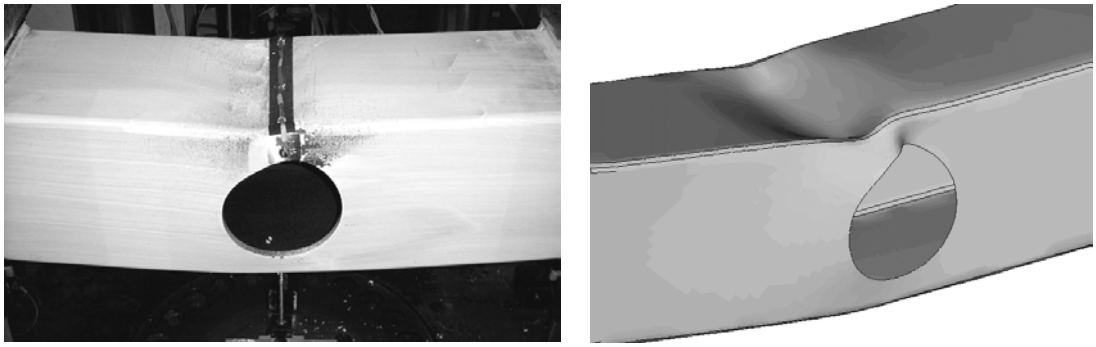

Figure 3-26: Displaced shape RHS 250x250x10 one hole

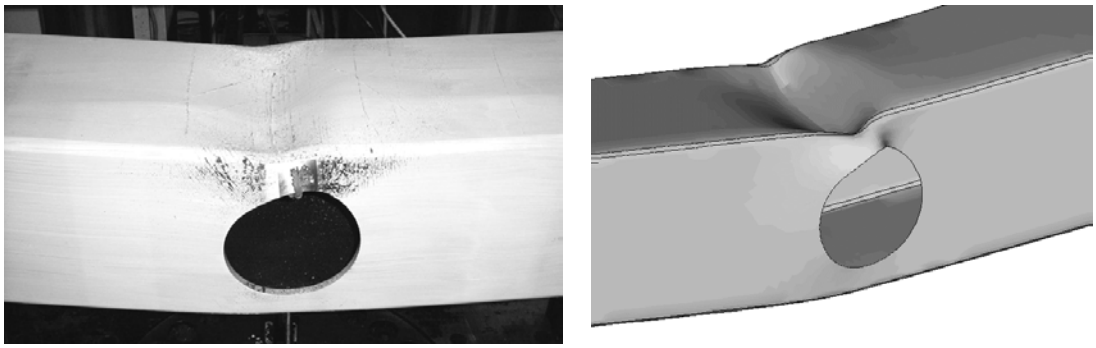

Figure 3-27: Displaced shape RHS 250x250x10 two holes

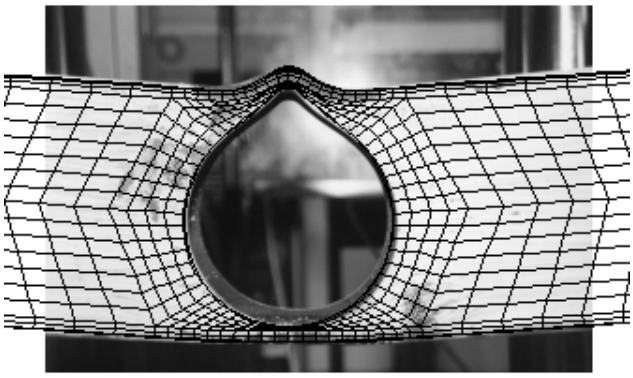

Figure 3-28: Displaced shape RHS 200x100x8 two holes (superposition)

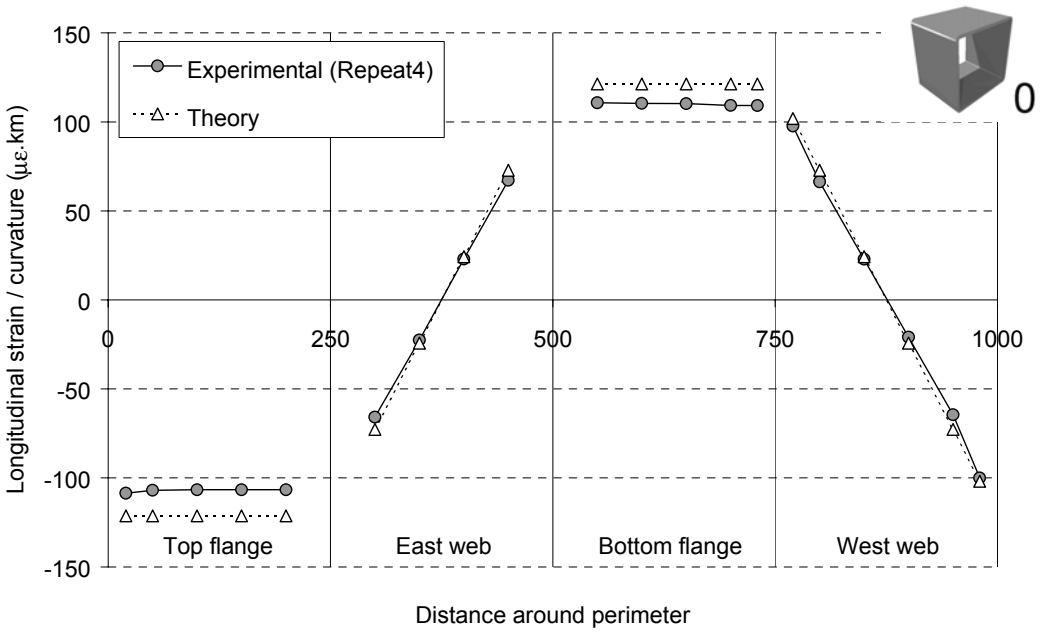

Figure 3-29: Longitudinal strain for RHS 250x250x10 unperforated (REPEAT4)

(Distance around perimeter in millimetres)

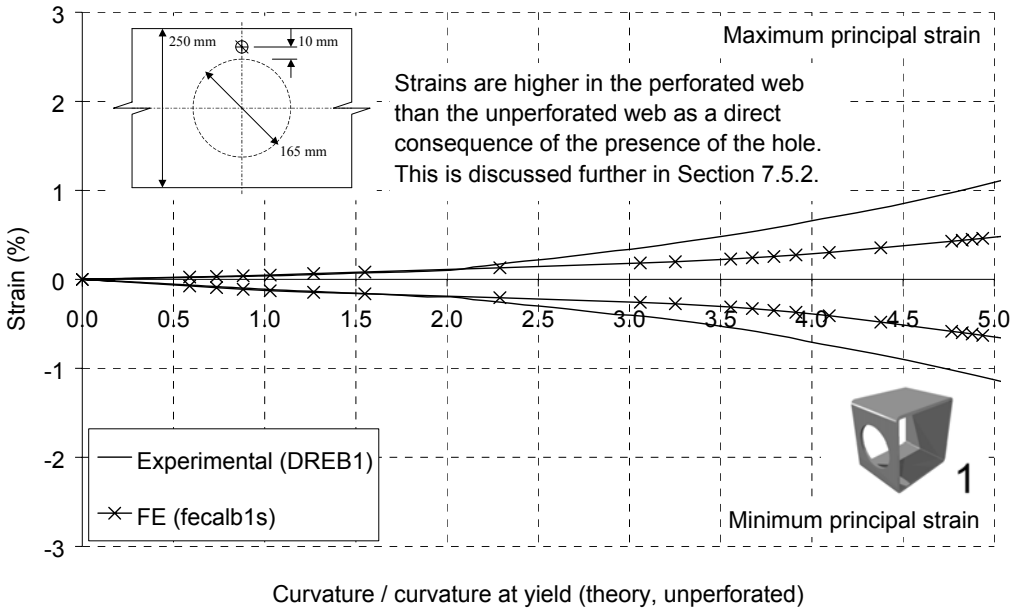

Figure 3-30: Principal strains for RHS 250x250x10 one hole (unperforated web)

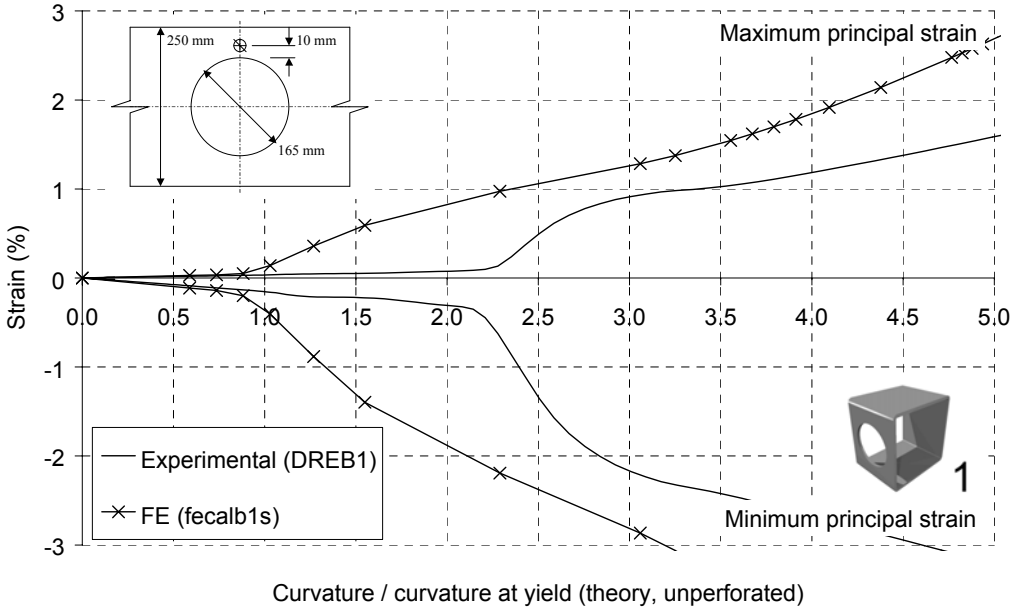

Figure 3-31: Principal strains for RHS 250x250x10 one hole (perforated web)

3.6 Concluding remarks

A series of 13 full-scale four-point bending tests were conducted on two sizes of RHS to assess the effect of web openings upon structural performance in uniform bending. During the tests, the moment and average curvature were measured. In 12 of the tests, strains on the external surface of the flanges and webs were also measured.

The results of the tests showed that the reduction in the bending capacity due to the web openings was as much as 30%, and that the openings caused no measurable reduction in elastic stiffness. It was also observed that the presence of the web openings reduced the plastic stability of the compression elements in the perforated zone, causing a decrease in the rotation capacity.

The experimental results were compared with FE predictions and a close agreement was observed in terms of displaced shapes, elastic stiffnesses and strains in the elastic range. The experimental moment-curvature relationships matched those predicted by the FE models, although the FE tended to under-predict the bending resistance by around 10%.

The FE models of the perforated sections indicated that the reduction in elastic stiffness, due to the presence of the hole, was small. The reduction was less than 5% in the case of the RHS 200x100x8 and less than 1% in the case of the RHS 250x250x10.

The full-scale three-point loading flexural testing programme, which was used to investigate the behaviour of perforated RHS in combined shear and bending, is described in the following Chapter.

4 Shear (three-point loading)

4.1 Introduction

This Chapter contains a description of the full-scale three-point loading flexural testing component of the project. The testing apparatus and procedure are described, and the details of the test specimens are listed. The tests were conducted to investigate the behaviour of perforated Rectangular Hollow Sections (RHS) in combined bending and shear. The high shear resistance of the RHS prevented the beams being tested under the action of shear in the absence of significant bending forces. The full-scale four-point loading flexural testing programme (bending without shear) is described in Chapter 3, and the full-scale and small-scale torsion testing programmes are described in Chapters 5 and 6 respectively.

In this Chapter, the experimental results of the three-point loading tests are summarised, as are the comparisons with conventional beam bending theory and Finite Element (FE) predictions. The FE models that were calibrated, using the data from the three-point loading tests, were later used in a parametric study to investigate the influence of hole diameter, and section size, on the shear resistance of perforated RHS (Section 7.6).

4.2 A description of the apparatus and testing procedure

4.2.1 The three-point bending test apparatus

The set-up for the three-point bending tests, which were performed in the same 2MN Instron universal testing machine as the four-point loading tests (Chapter 3), is shown in Figure 4-1 and Figure 4-2. The beams were supported on semi-cylindrical bearings (Figure 3-3) with a span of 1750 mm. Nylon pads were used to reduce friction between the specimen and supports.

The load was applied vertically by the hydraulic actuator through a single rocker bearing (Figure 3-4) placed centrally on the compression flange. The web openings were placed at a distance of 500 mm from the loading point and were subject to combined shear and bending moment.

The rocker bearings, together with a rocker support (Figure 3-3a), allowed twisting and lozenging of the specimens to occur, without restraint, during the test. This precaution was necessary because specimens may have been caused to twist or lozenge under load as a result of any asymmetry of the web openings (intentional or otherwise), or any distortions present in the specimens as manufactured.

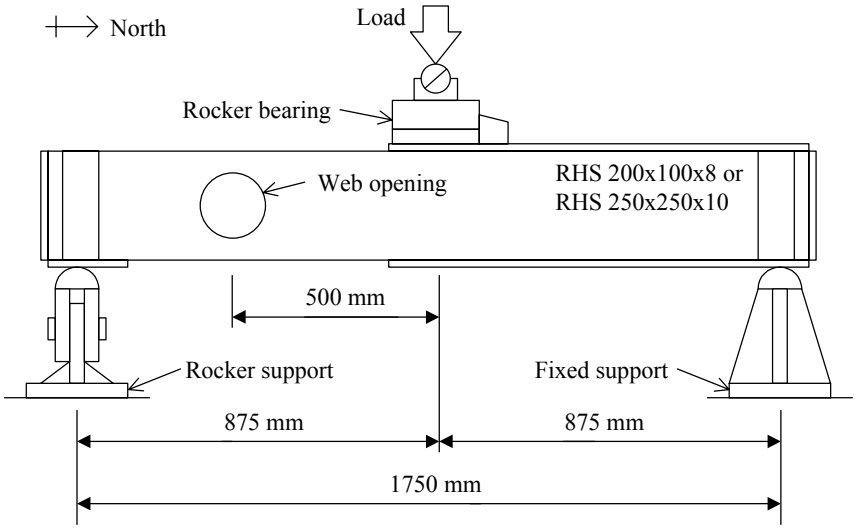

Figure 4-1: Schematic of the three-point bending test

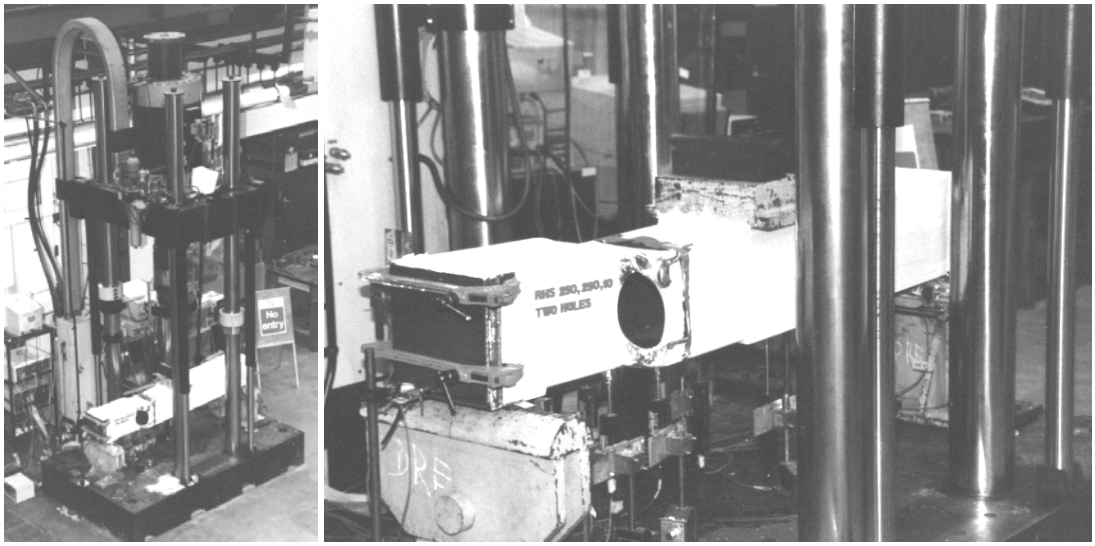

Figure 4-2: The three-point bending test apparatus

4.2.2 The three-point bending test specimens

Each three-point bending test specimen comprised of a 1.9 m length of RHS, as shown in Figure 4-1 and Figure 4-3. Steel plates were welded to the flanges in the supporting span to ensure failure occurred in the 875 mm span containing the web opening. In addition, sealing plates and bearing stiffeners were added to prevent bearing failure at the supports and load points. The web openings were cold cut to a tolerance of ±0.1 mm in shape and ±0.5 mm in position. Further details of the specimens are given in Section 4.3. Unperforated beams, which failed in bending close to the load point, were included in the testing programme to aid in the calibration of the FE models.

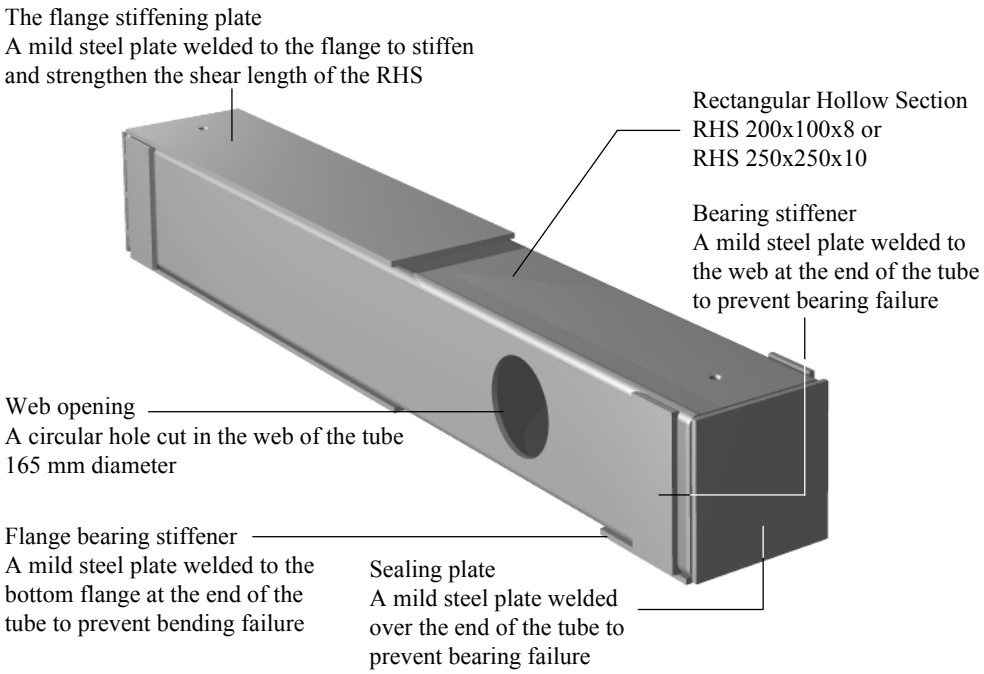

Figure 4-3: Three-point bending test specimen

4.2.3 Instrumentation

4.2.3.1 Measurement of shear force and bending moment

The shear force and bending moment were calculated from the vertical load, which was measured using the load cell of the Instron machine (rated as a grade 0.5 device in compression to BS 1610-1:1992, see Appendix F).

4.2.3.2 Measurement of deflection

The total central deflection of the beam was calculated from the measured vertical displacement of the tension flange at the load point and at the supports (settlement). Vertical deflections of the tension flange were also measured at each side of the web opening to measure shear deformation. The layout of the linear potentiometers, used to measure these vertical deflections, is shown in Figure 4-4.

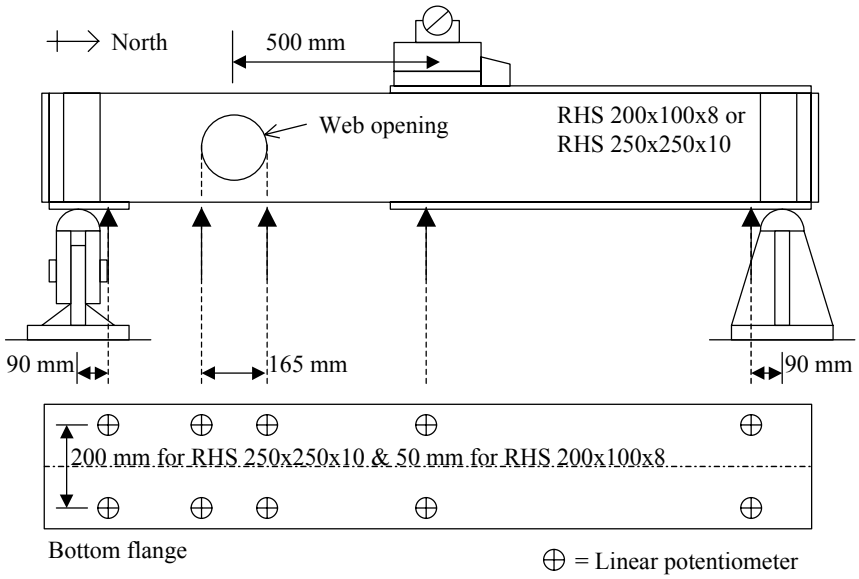

Figure 4-4: Measurement of vertical displacement with linear potentiometers

4.2.3.3 Measurement of strain

The test specimens were instrumented with electrical resistance strain gauges of the type shown in Figure 2-13 and Figure 2-14. The layouts are shown in Figure 4-5. The specimens were also painted with a brittle lime wash to increase the visibility of slip lines in the steel and mill scale (Section 2.4.4.3). Examination of the formation of the slip line patterns provided information about the onset of yield and the distribution of plastic shear.

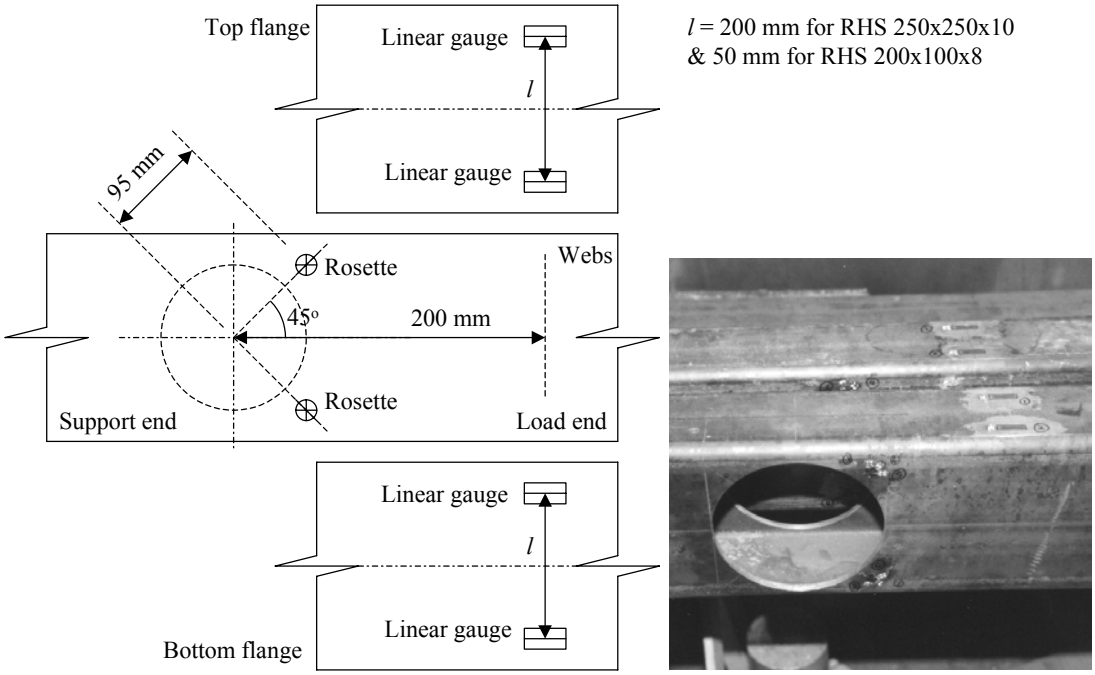

Figure 4-5: Strain gauge pattern (all tests)

4.2.3.4 Other measurements

In all the tests, gravity inclinometers (measuring rotation) were used to measure twisting about the longitudinal axis. The inclinometers (Figure 4-6 and Figure 4-7) were placed at the ends of the specimens in order to measure the total twist along the whole length (although most of this twist occurred in the perforated zone).

In addition, linear potentiometers were used to measure the horizontal movement of the specimen at the supports as the bottom flange lengthened with increasing curvature. The measurements confirmed the efficacy of the precautionary procedures aimed at ensuring that significant additional loads were not placed on the specimens by excessive friction.

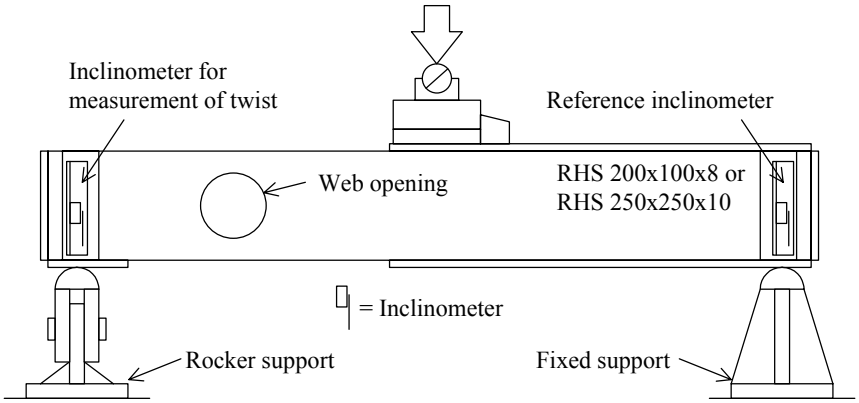

Figure 4-6: Inclinometers for measurement of twist

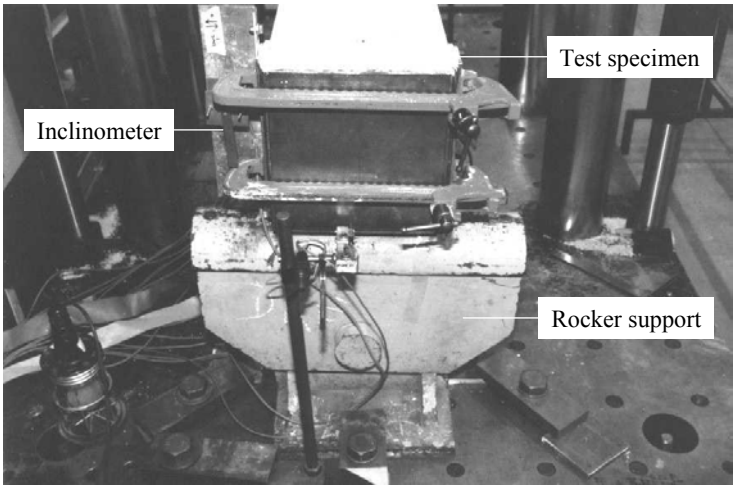

Figure 4-7: Measurement of twist at the rocker support

4.2.4 Testing procedure

Testing proceeded as outlined below. In some cases, elastic tests were performed by repeated loading and unloading within the elastic range.

1) The specimen was inserted into the loading apparatus and carefully positioned
2) The strain gauges were initialised (zeroed) using the data logger
3) A reading was taken at zero load
4) An increment of displacement was applied (either manually, or automatically using a predefined ramp)
5) A reading was taken
6) Steps 4 and 5 were repeated until the desired central displacement was achieved
7) The specimen was unloaded in increments and readings were taken at each
8) A reading was taken at zero load
9) The specimen was removed from the loading apparatus

4.3 Specimen types, dimensions and properties

4.3.1 Specimens tested

The specimens tested are listed in Table 4-1. Three different hot finished bars were used in the manufacture of the specimens (two section sizes of grade S275J2H). The material was provided and manufactured by British Steel (now Corus).

Table 4-1: Specimens tested

ID Code	Date tested	Section size	Material grade [Bar number]	Number of holes	Hole diameter (mm)	Hole size ratio, Φ
TESTS1	07/12/1998	RHS 200x100x8	S275J2H [#2]	0	-	-
TESTS3	14/12/1998	RHS 200x100x8	S275J2H [#2]	1	165.0	0.94
TESTS2	09/12/1998	RHS 200x100x8	S275J2H [#2]	2	165.0	0.94
TESTS4	16/12/1998	RHS 250x250x10	S275J2H [#2]	0	-	-
TESTS6	13/01/1999	RHS 250x250x10	S275J2H [#2]	1	165.0	0.75
TESTS5	19/01/1999	RHS 250x250x10	S275J2H [#1]	2	165.0	0.75

Note: The hole size ratio (Φ) is defined by Equation 1-3

4.3.2 Material properties

The properties of the three bars are summarised in Table 4-2. The results of the individual tensile tests are given in Appendix D. The definitions of the parameters used can be found in Section 2.2 and BS EN 10002-1:1990.

Table 4-2: Material models

Section size Grade [Bar no]	K (%)	f_{y1} (N/mm^2)	E (kN/mm^2)	$\lambda_{plateau}$	$E_{plateau}$ (kN/mm^2)	λ_{ESHF}	f_u (N/mm^2)	ε_u (%)
RHS 200x100x8 S275J2H [#2]	2.53	335.1	182.0	11.7	0.50	0.21	475.5	16.0
RHS 250x250x10 S275J2H [#1]	1.48	347.7	210.0	14.8	0.52	0.24	463.8	15.6
RHS 250x250x10 S275J2H [#2]	3.16	343.2	197.6	12.9	0.21	0.22	468.0	15.9

Note: Refer to Section 2.2

4.3.3 Dimensions and geometrical properties

The measured dimensions of the three bars, used in the manufacture of the test specimens, are given in Table 4-3. Dimensions are as defined by BS EN 10210-2:1997 (Figure 1-9). The geometrical properties, obtained using the formulae given in BS EN 10210-2:1997 (Appendix C), are listed in Table 4-4. The shear area was calculated as specified in Table 5.16 of Eurocode 3 and Clause 4.2.3d of BS 5950.

Sectional properties, based on measured material properties and dimensions, are given in Table 4-5. The theoretical shear capacity was calculated from the product of the shear yield stress and the shear area. The shear yield stress was calculated from the yield stress, as measured from direct tensile testing, and the von Mises failure criterion (Section 2.5.4.2). This method of calculating the shear capacity is the same as that used by the Eurocode 3 (Clause 5.5.1) and BS 5950 (Clause 4.2.3) design procedures. For comparison, the nominal section properties are given in Table 4-6.

Table 4-3: Dimensions of cross-section (measured)

Section size	Material grade [Bar number]	Height h (mm)	Width b (mm)	Thickness t (mm)	Corner radius (mm) Internal	External
RHS 200x100x8	S275J2H [#2]	198.0	100.0	7.73	5.0	12.5
RHS 250x250x10	S275J2H [#1]	250.0	250.0	9.70	8.0	15.0
RHS 250x250x10	S275J2H [#2]	249.5	249.5	9.74	8.0	15.0

Table 4-4: Properties of cross-section (from measured dimensions)

Section size	Material grade [Bar number]	Shear area A_v (cm^2)	Second moment of area I_y (cm^4)	Elastic section Modulus $W_{el,y}$ (cm^4)	Plastic section Modulus $W_{pl,y}$ (cm^3)
RHS 200x100x8	S275J2H [#2]	28.25	2074	209	265
RHS 250x250x10	S275J2H [#1]	45.66	8699	696	817
RHS 250x250x10	S275J2H [#2]	45.74	8675	695	817

Note: Shear area calculated as in Table 5.16 of Eurocode 3 and Clause 4.2.3d of BS 5950

Table 4-5: Sectional properties (measured dims and material props, theoretical)

Section size	Material grade [Bar number]	Curvature at yield κ_e (km^{-1})	Elastic moment $M_{el,y}$ (kNm)	Plastic moment $M_{pl,y}$ (kNm)	Shape factor $M_{pl,y}$ / $M_{el,y}$	Shear resistance V_y (kN)
RHS 200x100x8	S275J2H [#2]	18.58	70.32	88.81	1.26	548
RHS 250x250x10	S275J2H [#1]	13.24	242.4	284.6	1.17	918
RHS 250x250x10	S275J2H [#2]	13.91	239.1	280.8	1.17	908

Note: Shear resistance calculated as in Eurocode 3 (Clause 5.5.1) and BS 5950 (Clause 4.2.3)

Table 4-6: Sectional properties (nominal, theoretical)

Section size	Material grade [Bar number]	Curvature at yield (km^{-1})	Elastic moment (kNm)	Plastic moment (kNm)	Shape factor	Shear resistance (kN)
RHS 200x100x8	S275J2H [#2]	13.10 (71%)	61.42 (87%)	77.54 (87%)	1.26 (100%)	438 (80%)
RHS 250x250x10	S275J2H [#1]	10.48 (79%)	199.2 (82%)	233.9 (82%)	1.17 (100%)	754 (82%)
RHS 250x250x10	S275J2H [#2]	10.48 (75%)	199.2 (83%)	233.9 (83%)	1.17 (100%)	754 (83%)

Note 1: The percentages in parentheses denote the nominal value as a percentage of the measured
Note 2: Shear resistance calculated as in Eurocode 3 (Clause 5.5.1) and BS 5950 (Clause 4.2.3)

4.4 The experimental results

Measured elastic stiffnesses and maximum shear forces are listed in Table 4-7. The full shear force-central displacement relationships are presented in Figure 4-8 and Figure 4-9. The shear force has been non-dimensionalised against the theoretical shear capacity of the corresponding unperforated section (Section 4.3.3). The central displacement has been non-dimensionalised against the theoretical central displacement at which the corresponding unperforated section begins to yield, in bending, at the load point (calculated using conventional beam bending theory).

The unperforated sections failed in bending rather than shear on the unstrengthened side of the loading point where the bending moment was largest. The shear forces corresponding to the theoretical moments required to cause bending failure at the load point are plotted, in Figure 4-8 and Figure 4-9, as horizontal dotted lines, which are labelled 'Bending failure elastic' and 'Bending failure plastic' corresponding to the theoretical elastic and plastic moment capacities. The unperforated sections behaved as predicted by beam bending theory, and were able to resist loads higher than the theoretical plastic moment capacity due to high (strain hardening) strains at the hinge location. The unperforated RHS250x250x10 specimen reached a maximum load when buckling of the compression flange occurred.

The sections with web openings failed in shear in the perforated zone, although significant bending forces were also present at this location. The results of the tests showed that the reduction in the shear capacity due to the web openings was as much as 85%, and that the openings caused a significant reduction in the

shear stiffness of the perforated zone. The reductions in the shear resistance of the RHS 250x250x10 specimens (around 70%) were less than those for the RHS 200x100x8 specimens (around 80%) because the holes were smaller in relation to the section depth. Asymmetry of the web openings caused twisting and lozenging of the sections due to unbalanced shear deformation of the perforated and unperforated webs. Symmetrical sections (unperforated and two holes) did not twist or lozenge.

Displacement profiles, for the RHS 200x100x8 specimens, are shown in Figure 4-10 through Figure 4-16. The measurements were made using the linear potentiometers shown in Figure 4-4. In the symmetrical cases (no holes and two holes), the profile shown is the average of the measured profiles of the two webs. In the unsymmetrical case (one hole), the profiles of the perforated and unperforated webs are shown separately. The numbered symbols on the profiles relate to the numbered symbols on the corresponding shear force-displacement plots. The Figures illustrate the modes of failure discussed above.

Table 4-7: Experimental results – stiffness and maximum shear force

ID Code	Section size	Material grade [Bar number]	Number of holes	Hole diameter (mm)	Stiffness (kN/mm)	Shear force @ (kN)	
TESTS1	RHS 200x100x8	S275J2H [#2]	0	-	29.7	291	25 mm
TESTS3	RHS 200x100x8	S275J2H [#2]	1	165.0	26.0	224	Max
TESTS2	RHS 200x100x8	S275J2H [#2]	2	165.0	23.9	150	Max
TESTS4	RHS 250x250x10	S275J2H [#2]	0	-	112.2	803	Max
TESTS6	RHS 250x250x10	S275J2H [#2]	1	165.0	99.0	762	Max
TESTS5	RHS 250x250x10	S275J2H [#1]	2	165.0	95.0	661	Max

Note: Unperforated sections failed in bending rather than shear

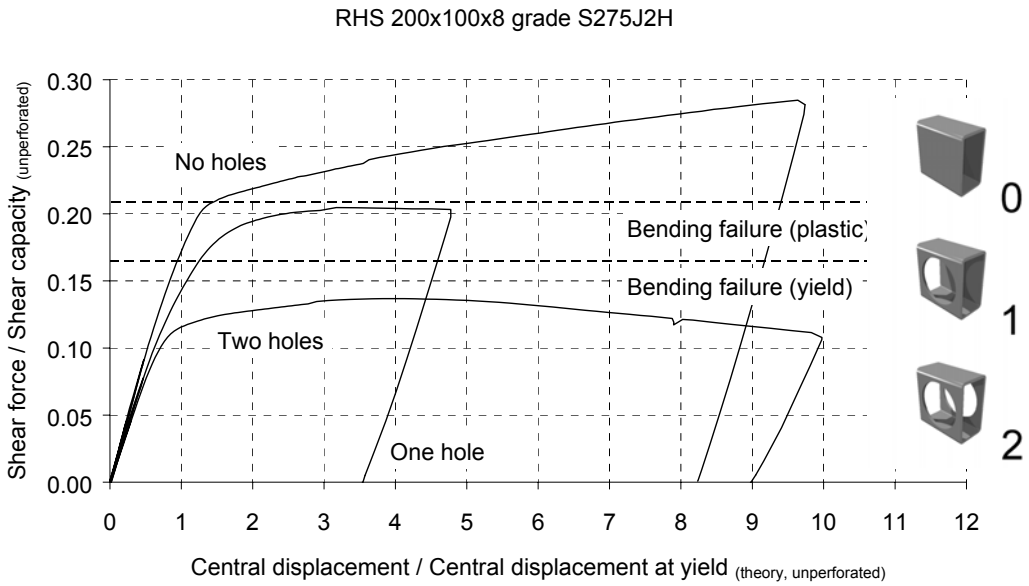

Figure 4-8: Experimental results RHS 200x100x8

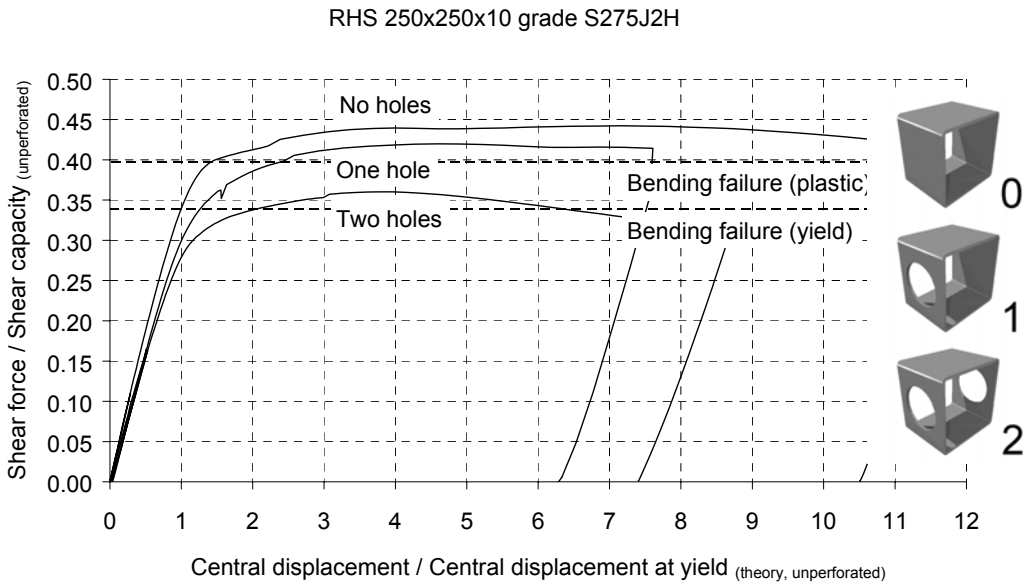

Figure 4-9: Experimental results RHS 250x250x10

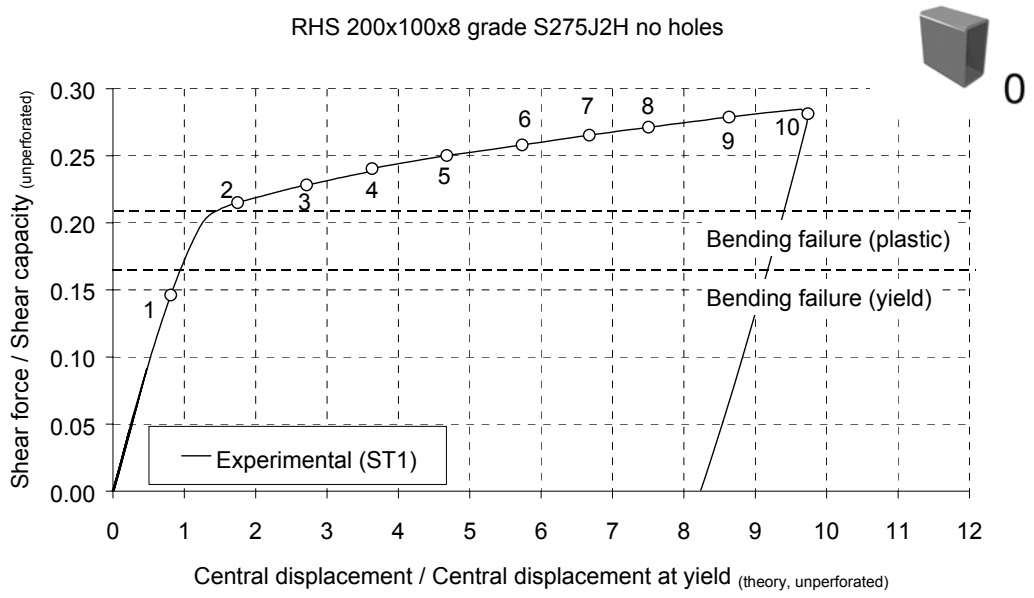

Figure 4-10: Shear force-displacement relationship RHS 200x100x8 no holes

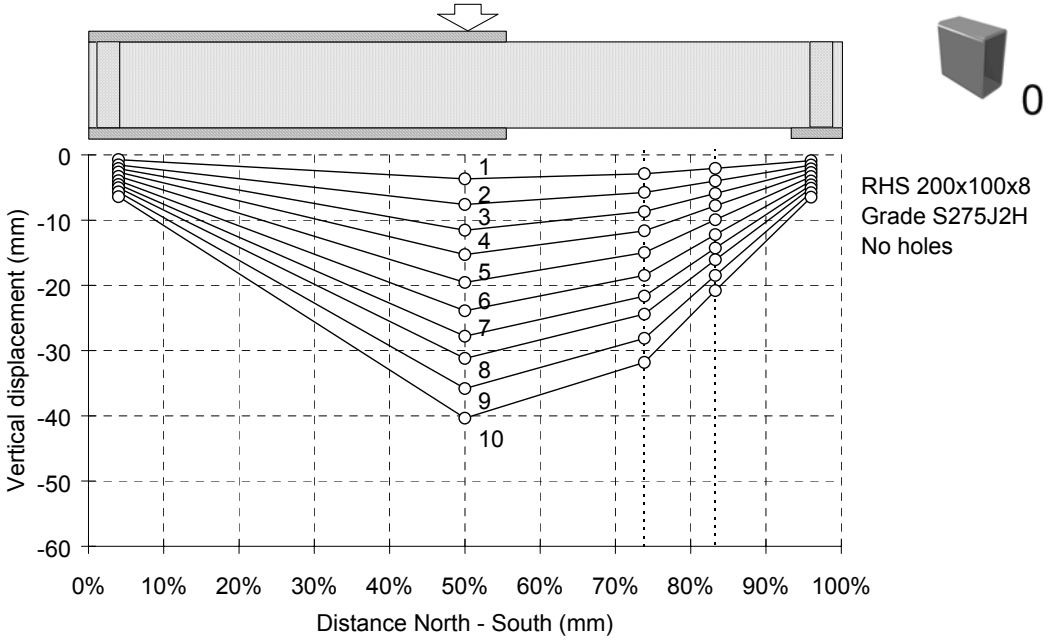

Figure 4-11: Displacement profiles RHS 200x100x8 no holes

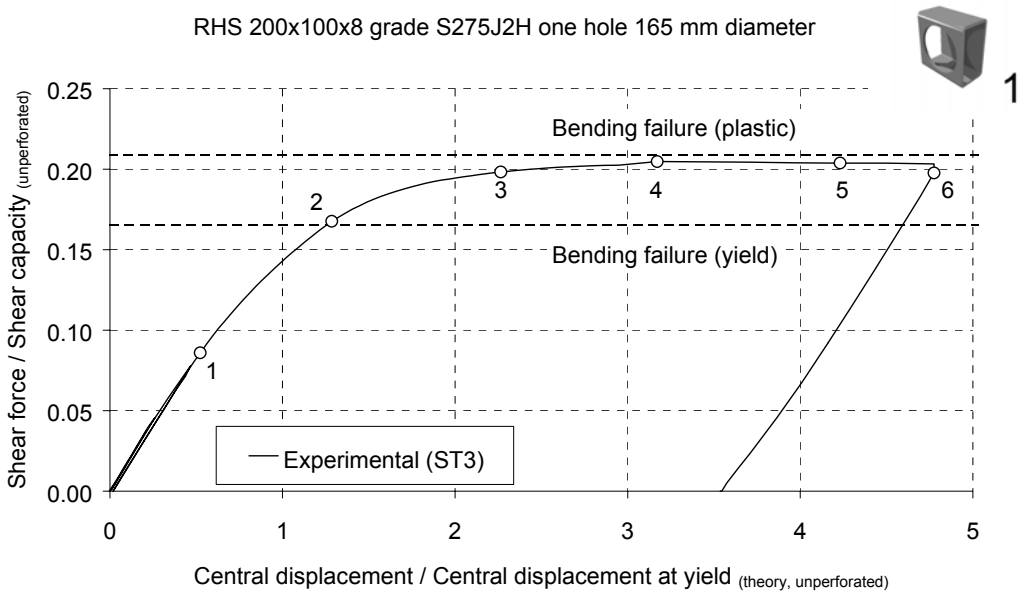

Figure 4-12: Shear force-displacement relationship RHS 200x100x8 one hole

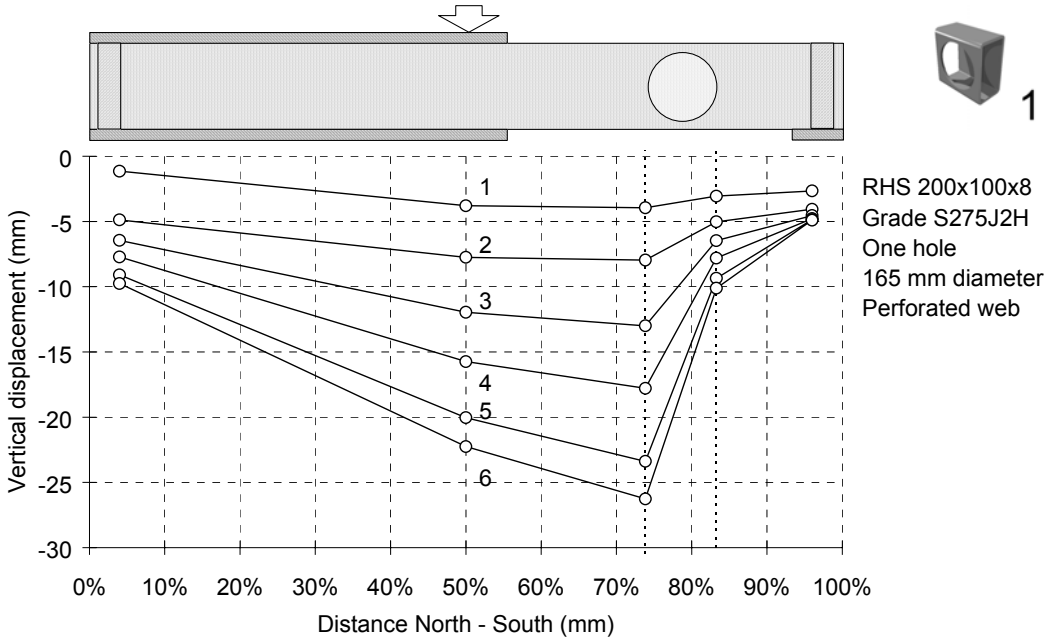

Figure 4-13: Displacement profiles RHS 200x100x8 one hole (perforated web)

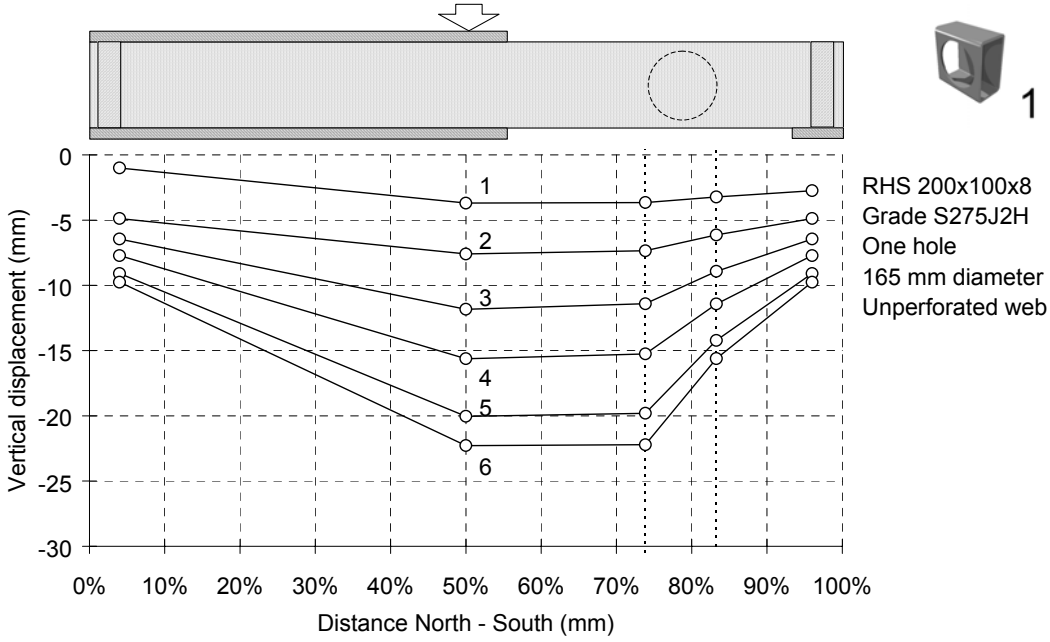

Figure 4-14: Displacement profiles RHS 200x100x8 one hole (unperforated web)

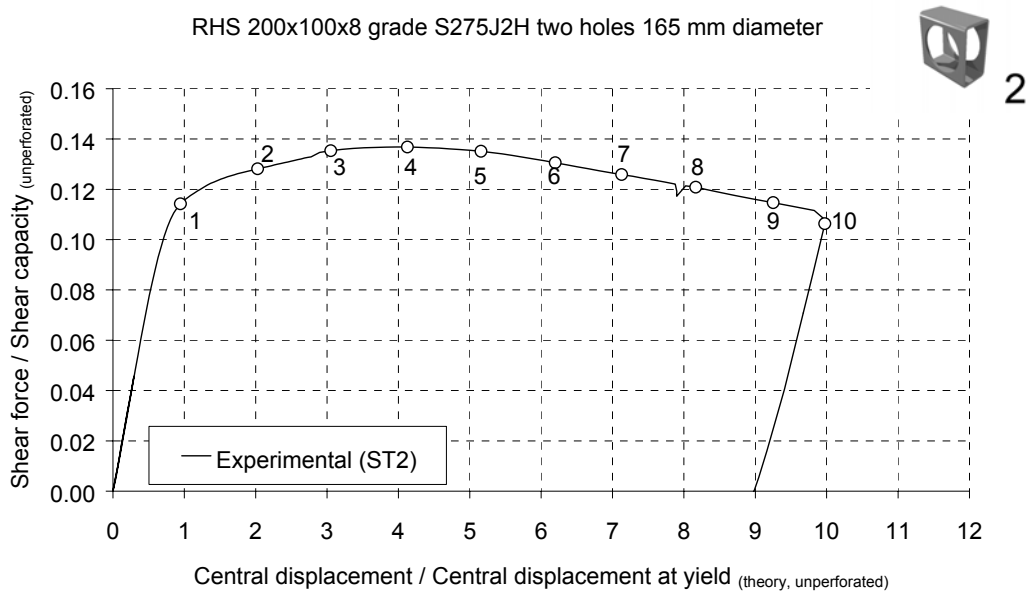

Figure 4-15: Shear force-displacement relationship RHS 200x100x8 two holes

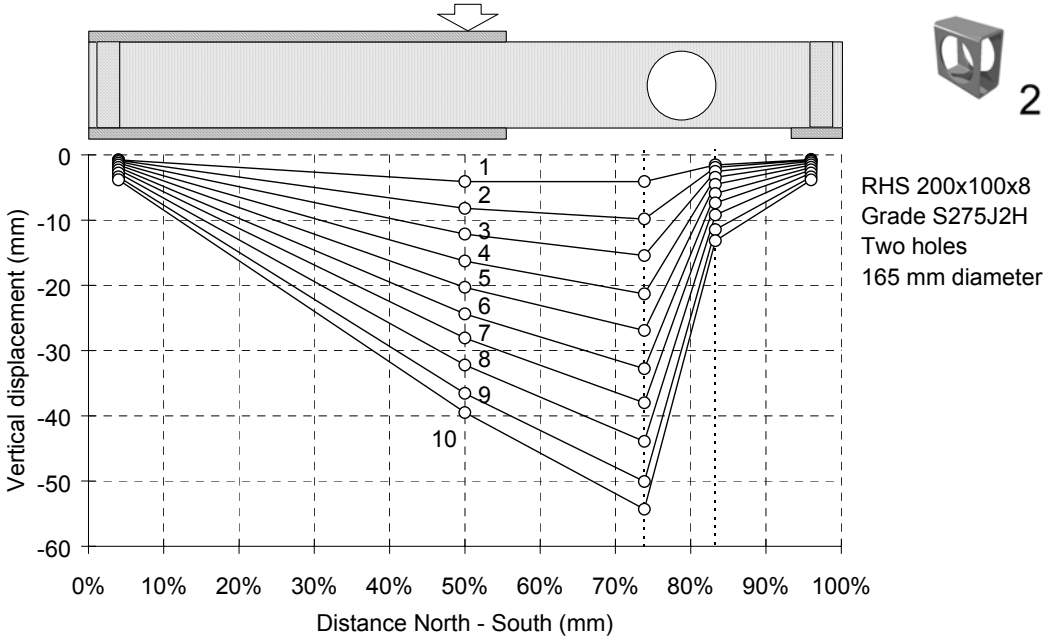

Figure 4-16: Displacement profiles RHS 200x100x8 two holes

4.5 A comparison of experimental results and analytical predictions

The experimental tests were modelled using the ABAQUS v5.5.1 FEA program and the experimental results were compared with the FE predictions. Models included both material and geometric non-linearity and contained between 6700 and 7600 four-noded shell elements (S4R). These elements were chosen to create the models because they allowed changes in thickness at high strains to be modelled (Section 2.3.6). The FE models were based on the actual measured dimensions of the test specimens and included the corner radii of the tube. The stiffening and strengthening plates were also included, and were modelled by locally increasing the thickness of the elements. The support conditions and bearings at the loading points were modelled by defining constraint equations to describe the permitted displacements in the nodal degrees of freedom.

The initial stiffnesses and maximum shear forces predicted by the FE models are listed in Table 4-8. The differences between the experimental values (Table 4-7) and the FE predictions are listed in Table 4-9.

The full shear force-central displacement relationships are presented in Figure 4-17 through Figure 4-22. The shear force has been non-dimensionalised against the theoretical shear capacity of the corresponding unperforated section (Section 4.3.3). The central displacement has been non-dimensionalised against the theoretical central displacement at which the corresponding unperforated section begins to yield, in bending, at the load point (calculated using conventional beam bending theory). The shear force-displacement relationships predicted by the FE models closely matched those measured in the laboratory.

In contrast to the four-point bending (Section 3.5), the FE models tended to over-predict the maximum resistance, but by no more than 5%. Predictions of elastic stiffness were less accurate, but within 17% of those measured experimentally. However, this difference in elastic stiffness is accounted for, in part, by the difficulty in obtaining accurate measurements of Young's modulus from tensile tests.

As was the case for the laboratory tests, the FE models of the unperforated sections behaved as predicted by beam bending theory, and were able to resist loads higher than the theoretical plastic moment capacity due to high (strain hardening) strains at the hinge location. The unperforated RHS250x250x10 specimen reached a maximum load when buckling of the compression flange occurred. However, the buckle predicted by the FE model was a slightly different shape to that observed experimentally (see below).

In the case of the RHS 200x100x8 specimen with one hole, the FE model was able to correctly predict the twisting of the beam with increasing shear displacement (Figure 4-23). The prediction of twisting for the RHS 250x250x10 specimen with one hole was less successful, although the twist was correctly predicted for shear deformations in the elastic range (Figure 4-24).

The FE models matched closely the deformed shapes observed in the laboratory (Figure 4-25 through Figure 4-28). The deformation in the perforated zone was modelled extremely well, as can be seen in Figure 4-29, which shows a deformed FE mesh superimposed on a photograph of the deformed test specimen (RHS 200x100x8 with two holes). However, in the case of the unperforated RHS 250x250x10 (Figure 4-27 and Figure 4-28), the buckle predicted by the FE model (outwards) was a slightly different shape to that observed experimentally (inwards).

In the elastic range, the theoretical and FE predictions of surface strain were close to those measured in the laboratory. However, the measurements and predictions diverged with increasing strain (this is explained in Section 2.6).

Table 4-8: Finite Element results – stiffness and maximum shear force

ID Code	Section size	Material grade [Bar number]	Number of holes	Hole diameter (mm)	Stiffness (kN/mm)	Shear force @ (kN)	
TESTS1	RHS 200x100x8	S275J2H [#2]	0	-	25.5	294	25 mm
TESTS3	RHS 200x100x8	S275J2H [#2]	1	165.0	23.1	236	Max
TESTS2	RHS 200x100x8	S275J2H [#2]	2	165.0	20.5	154	Max
TESTS4	RHS 250x250x10	S275J2H [#2]	0	-	99.4	808	Max
TESTS6	RHS 250x250x10	S275J2H [#2]	1	165.0	95.2	763	Max
TESTS5	RHS 250x250x10	S275J2H [#1]	2	165.0	95.0	682	Max

Note: Unperforated sections failed in bending rather than shear

Table 4-9: Experimental and FE results – stiffness and maximum shear force

ID Code	Section size	Material grade [Bar number]	Number of holes	Hole diameter (mm)	Difference stiffness (%)	Difference Shear force (%)
TESTS1	RHS 200x100x8	S275J2H [#2]	0	-	16.5	-0.95
TESTS3	RHS 200x100x8	S275J2H [#2]	1	165.0	12.9	-4.86
TESTS2	RHS 200x100x8	S275J2H [#2]	2	165.0	16.5	-2.90
TESTS4	RHS 250x250x10	S275J2H [#2]	0	-	12.9	-0.56
TESTS6	RHS 250x250x10	S275J2H [#2]	1	165.0	3.99	-0.10
TESTS5	RHS 250x250x10	S275J2H [#1]	2	165.0	0.04	-3.00

Note 1: A negative percentage indicates experimental values lower than Finite Element values
Note 2: Unperforated sections failed in bending rather than shear

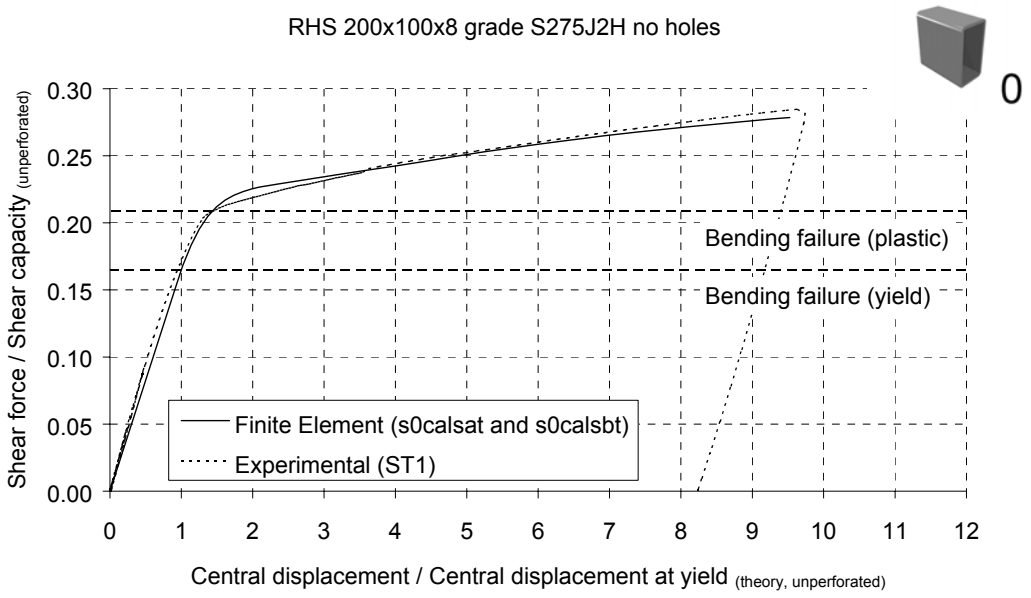

Figure 4-17: FE and experimental (test TESTS1)

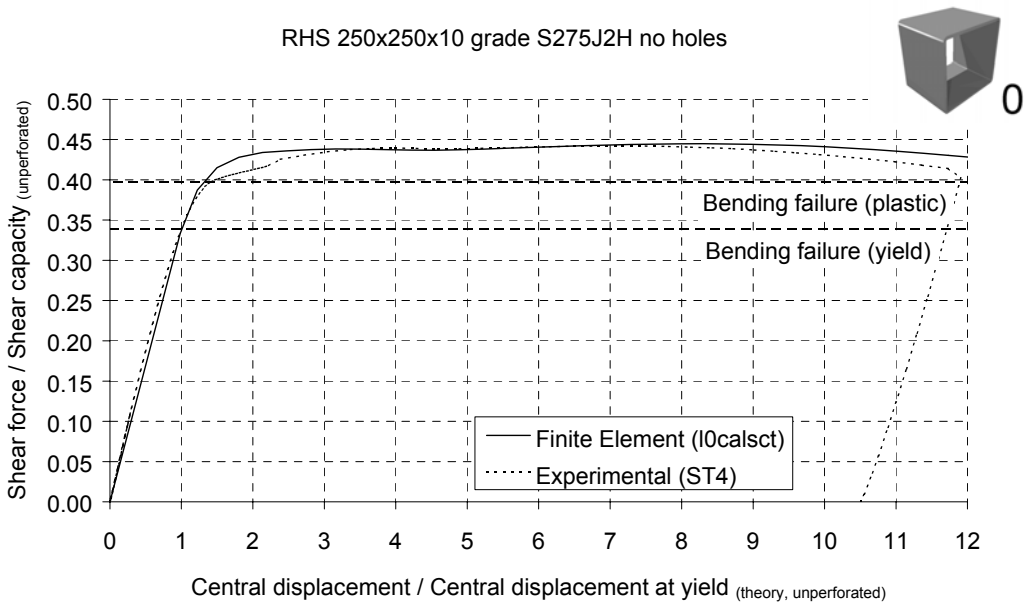

Figure 4-18: FE and experimental (test TESTS4)

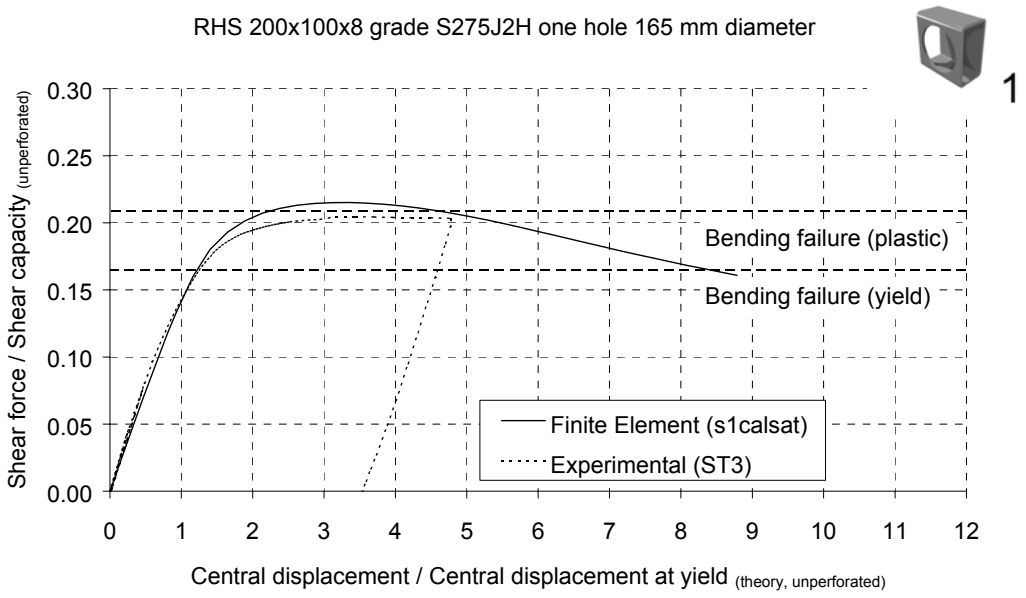

Figure 4-19: FE and experimental (test TESTS3)

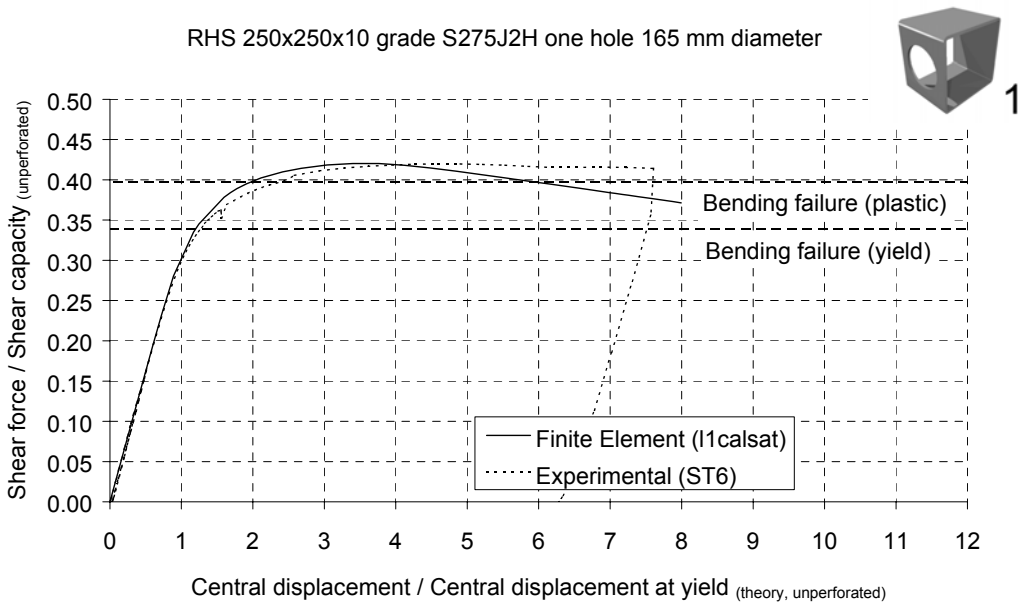

Figure 4-20: FE and experimental (test TESTS6)

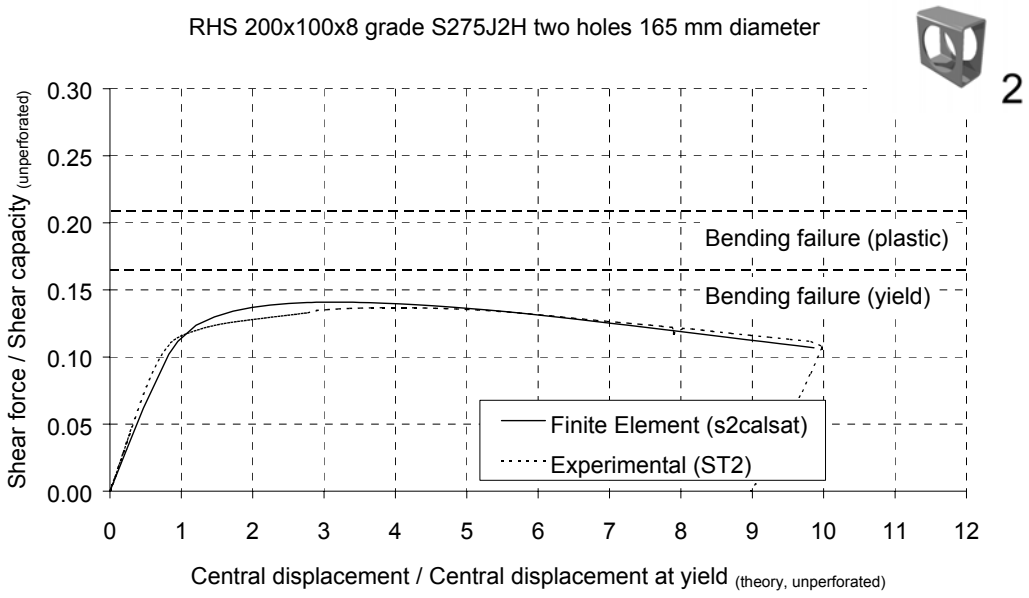

Figure 4-21: FE and experimental (test TESTS2)

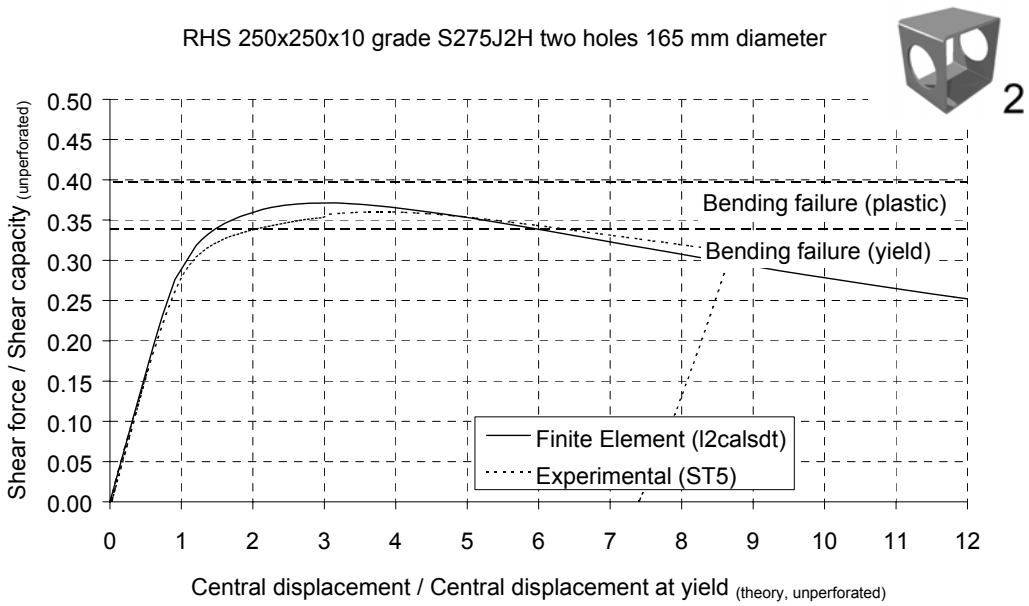

Figure 4-22: FE and experimental (test TESTS5)

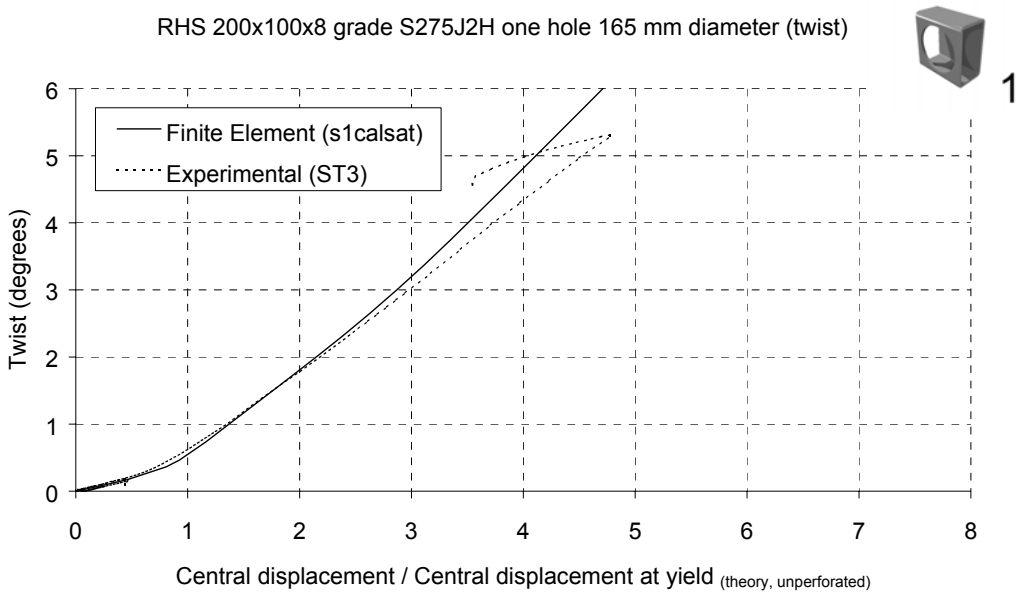

Figure 4-23: FE and experimental (twist of TESTS3)

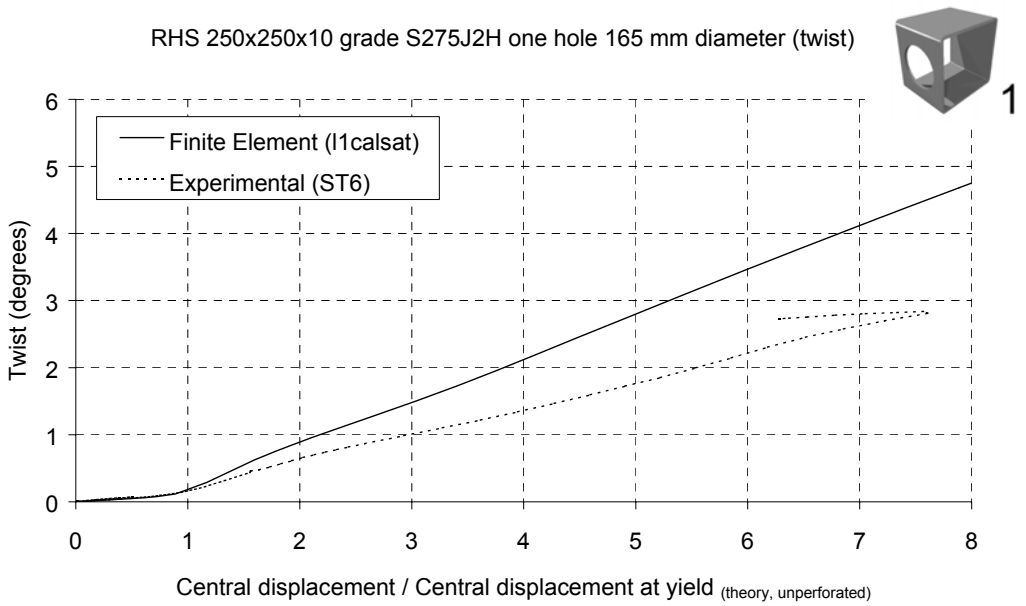

Figure 4-24: FE and experimental (twist of TESTS6)

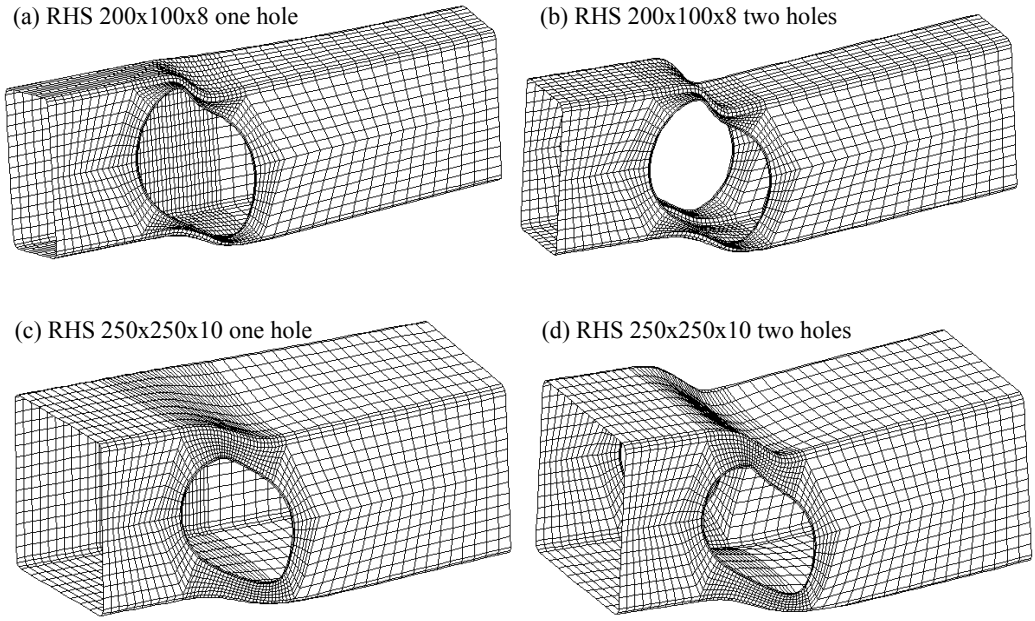

Figure 4-25: Displaced shapes (Finite Element, perforated)

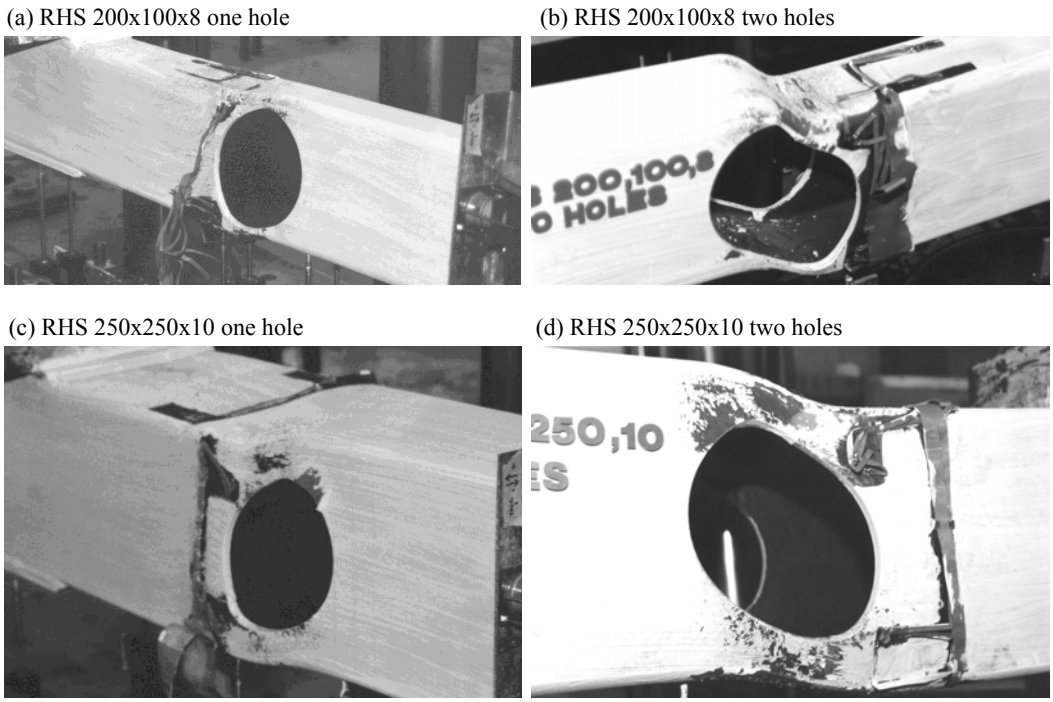

Figure 4-26: Displaced shapes (experimental, perforated)

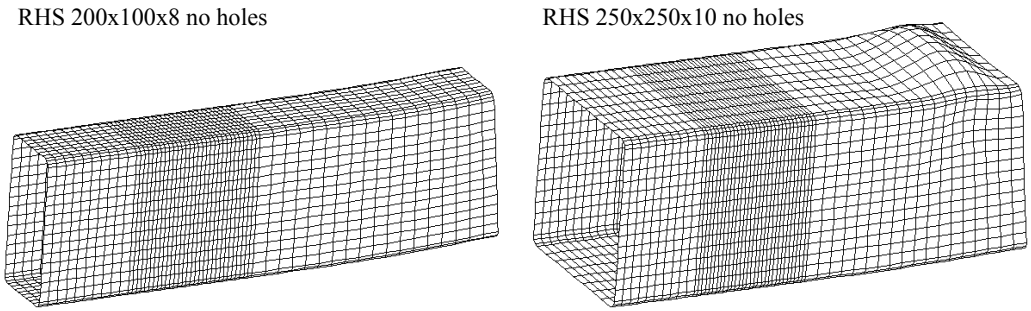

Figure 4-27: Displaced shapes (Finite Element, unperforated)

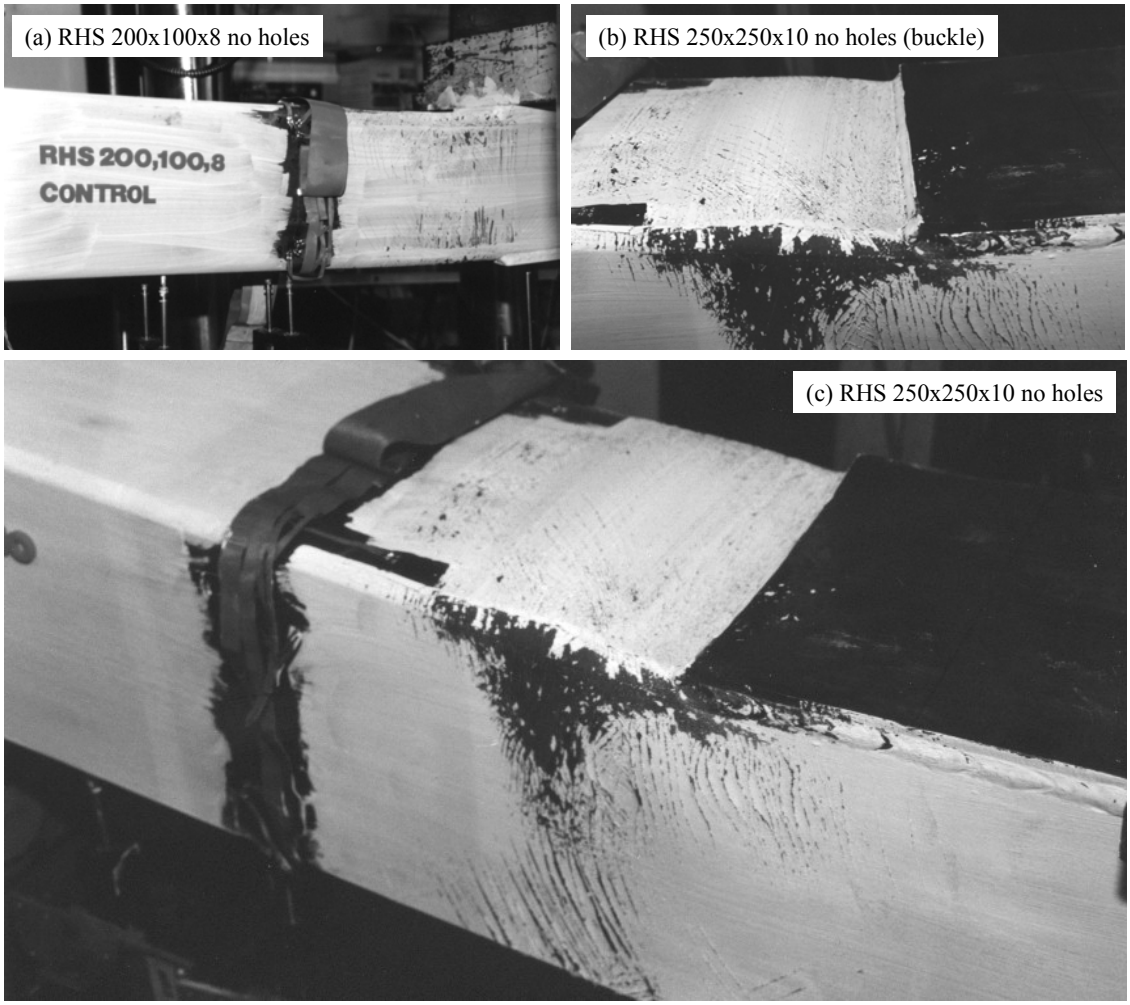

Figure 4-28: Displaced shapes (Experimental, unperforated)

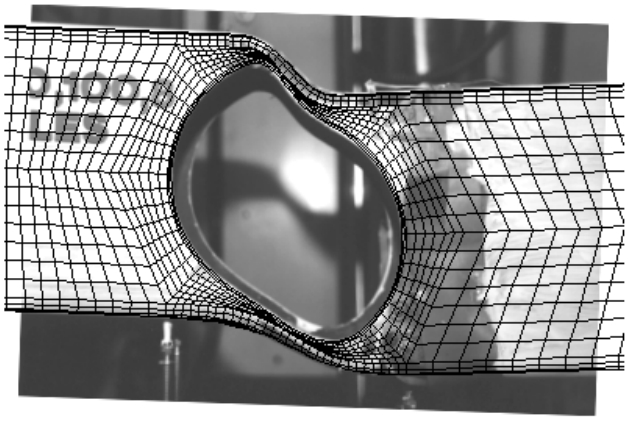

Figure 4-29: Displaced shape RHS 200x100x8 two holes (superposition)

4.6 Concluding remarks

A series of six full-scale three-point bending tests were conducted on two sizes of RHS to assess the effect of web openings upon structural performance in combined shear and bending. During the tests, the shear force, bending moment and displacement were measured. In all six tests, strains on the external surface of the flanges and webs were also measured.

The results of the tests showed that the reduction in the shear capacity due to the web openings was as much as 85%, and that the openings caused a significant reduction in the shear stiffness of the perforated zone.

The experimental results were compared with FE predictions and a close agreement was observed in terms of displaced shapes, elastic stiffnesses and strains in the elastic range. The experimental shear force-displacement relationships closely matched those predicted by the FE models with a maximum difference of only 5%.

The full-scale torsion testing programme, which was used to investigate the behaviour of perforated RHS in torsion, is described in the following Chapter.

5 Full-scale torsion

5.1 Introduction

This Chapter contains a description of the full-scale torsion testing component of the project. The testing apparatus and procedure are described, and the details of the test specimens are listed. The small-scale torsion testing programme is described in Chapter 6, and the full-scale bending and shear testing programmes are described in Chapters 3 and 4.

The experimental results are summarised and compared with conventional torsion theory (Section 2.5) and Finite Element (FE) predictions. Differences between the experimental observations and theoretical and analytical models were found, and arguments supporting the validity of the experimental data are discussed. A possible explanation of the differences is proposed and suitable schemes for further investigation are suggested.

5.2 A description of the apparatus and testing procedure

5.2.1 The torsion test apparatus

The torsion testing rig comprised of a fixed reaction beam and a pivoted rotating beam, between which a length of Rectangular Hollow Section (RHS) could be caused to twist about its longitudinal axis (Figure 5-1 and Figure 5-2). The apparatus was designed to function correctly and safely up to a torque of 100 kNm.

The tee-shaped fixed reaction beam was held in place by two sets of columns bolted to a structural strong floor. A crosspiece of grade S275J2H RHS 250x250x10 resisted the torque by bearing vertically on the columns and a short shaft consisting of doubled-up grade S275J2H RHS 200x100x8 transmitted the torque from the specimen to the crosspiece.

The torsional action was applied through the rotation of a further grade S275J2H RHS 250x250x10 crosspiece. This beam was supported on the axis of the rig by a 50 mm diameter mild steel bar and a bearing block. The bearing was held in place by a pair of columns bolted to the strong floor. Excessive movement of the rotating beam out of the vertical plane was prevented by two sets of guide columns, also bolted to the strong floor.

The rotating end of the specimen was connected to the rotating beam through a 500 mm length of grade S355J2H Circular Hollow Section. This length of circular shaft was used to measure the torque and was machined internally and externally to an external diameter of 242.5 mm and a thickness of 10.5 mm, with a tolerance of ±0.05 mm.

The torque was created by a matched pair of double acting hydraulic cylinders mounted on the guide columns. Each cylinder was operated from a separate oil source allowing the two loads to be balanced manually during the test. Control over the unloading of the specimens was achieved by the regulation of the out-flowing oil through a pair of needle valves.

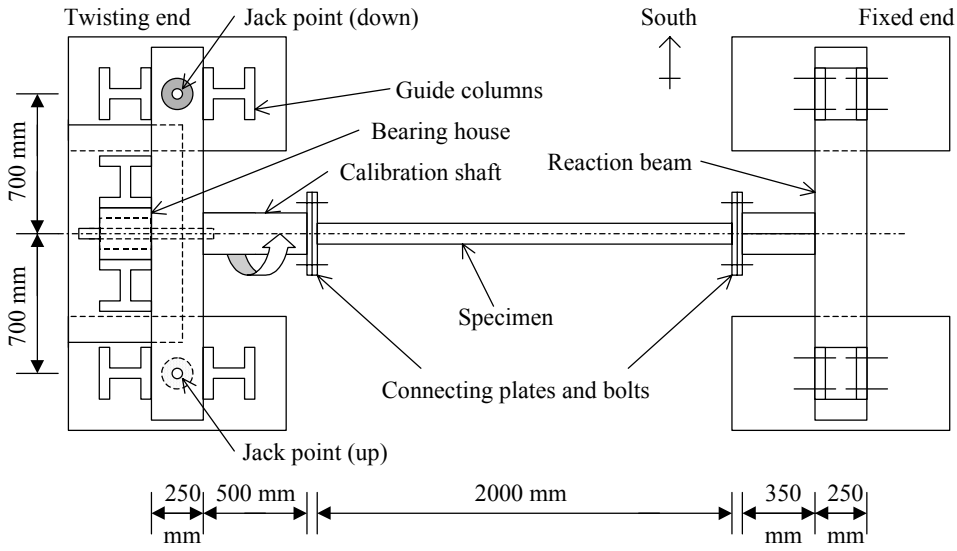

Figure 5-1: The torsion testing apparatus (schematic)

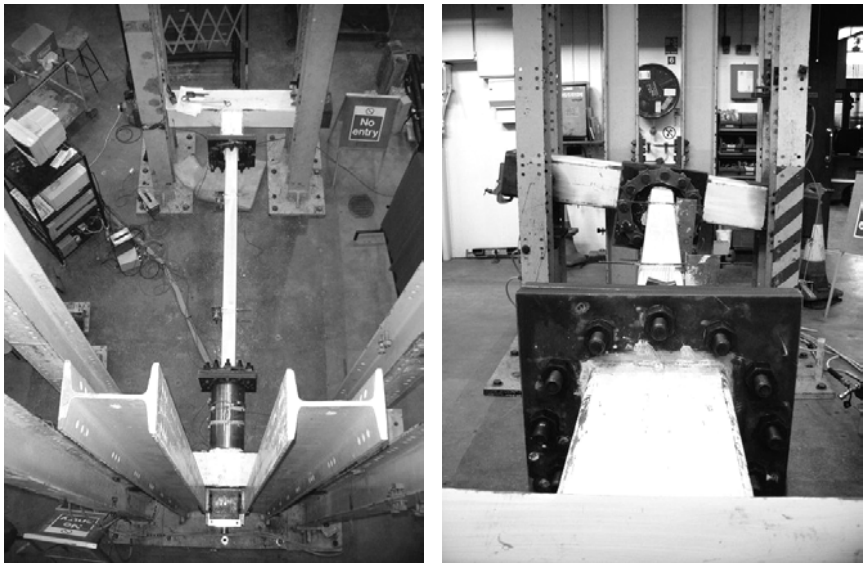

Figure 5-2: The torsion testing apparatus

5.2.2 The torsion test specimens

Each torsion test specimen comprised of a two-metre length of RHS as shown in Figure 5-3. The details of the specimens, which were tested with the plane of the major axis horizontal, are given in Section 5.3. The web openings were cold cut to a tolerance of ±0.1 mm in shape and ±0.1 mm in position, and the overall length of the specimens was controlled to ±0.5 mm. The torsional action from the loading apparatus was transmitted to the specimen through bolted connections at both ends.

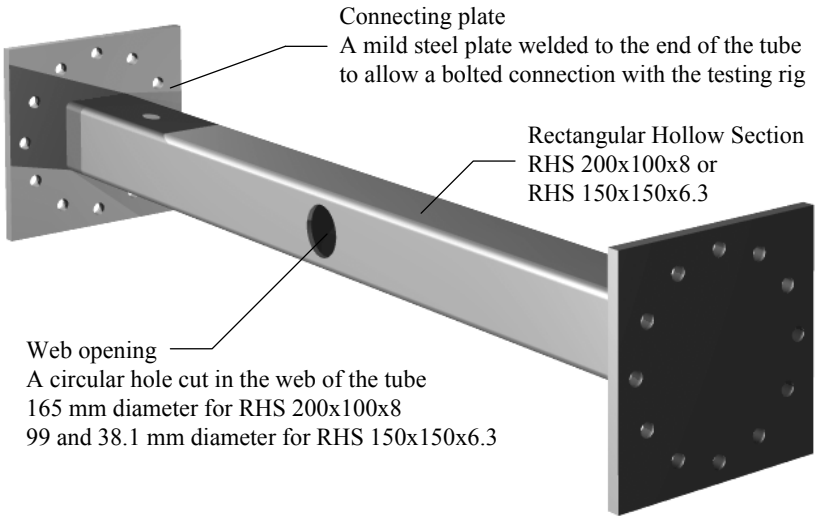

Figure 5-3: Torsion test specimen

5.2.3 Connection of the specimen and rig

Connectivity of the specimens with the testing apparatus was provided by 410 mm square mild steel plates, which were joined to the rig shafts and specimens by single bevel full penetration butt welds. The plates were machined from a thickness of 30 mm to 25 mm to insure the mating surfaces were both flat and perpendicular to the axis of the testing rig. Each plate contained 12 equally spaced holes of 26 mm diameter, at a radius of 170 mm from the axis of the rig. The connecting plates on the specimen and the rig were bolted together with M24x150 mm high strength friction grip bolts. A chain-like series of 12 mild steel links provided additional support to the specimen-side connecting plates (Figure 5-4). The bolts were manually tightened to a torque of 550 Nm after the free movement due to the oversized holes was taken up. This torque was not sufficient to generate the full design bolt pre-load required for 'friction grip', but was sufficient to prevent slippage of the connection. The bolts were tightened in an alternating sequence to avoid uneven fixity.

Figure 5-4: The connecting plates and bolting arrangement

5.2.4 Instrumentation

5.2.4.1 Measurement of torque

Measurement of the torque was achieved by monitoring the shear strain on the outside surface of the circular shaft (Figure 5-5). Six evenly spaced shear strain (or torsion) gauges (Section 2.4.4.2) provided an unbiased measure of average shear strain (Figure 5-6 and Figure 5-7). Measurement of the torque in this way ensured that the measurement was unaffected by friction and the change in the lever arm with rotation. The slight difference between the measured shear strains and the theoretical shear strains in Figure 5-6 and Figure 5-7 is due to the assumptions made about the Young's modulus and Poisson's ratio of the shaft (no direct measurements were made).

The circular shaft was calibrated, prior to the torsion tests, by comparing the output from the shear strain gauges with applied torques of known magnitude. The shaft was calibrated in a vertical position (Figure 5-8), by suspending the rotating beam from the fixed reaction beam. The torque was applied through the action of two hydraulic cylinders placed at equal distances from the vertical axis. The magnitude of the torque was calculated from the forces measured by two load cells, mounted on spherical seatings between the hydraulic cylinders and the rotating beam. The fixed reaction beam resisted the torque applied to the calibration shaft by bearing on two sets of columns that were bolted to the strong floor. Under this arrangement, the rotating beam was freely suspended and was in contact solely with the jacks and reaction beam. The applied torque was not diminished by friction, and the high stiffness of the apparatus minimised the effect of rotation on the torque calculation. The shaft was calibrated to a torque of 90 kNm and linear behaviour was confirmed over this range (Figure 5-7).

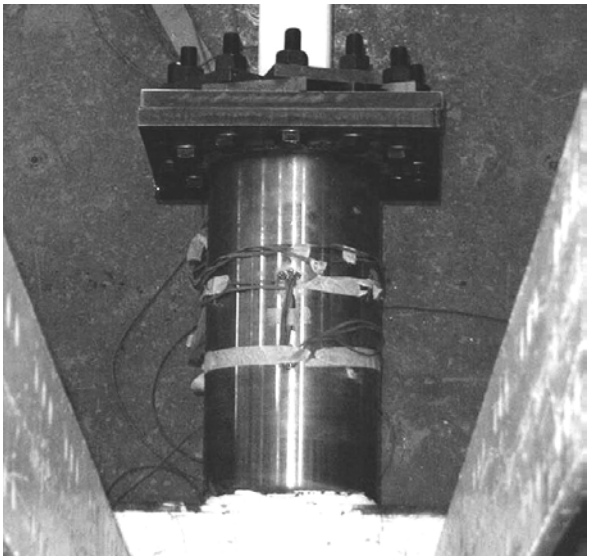

Figure 5-5: The calibration shaft

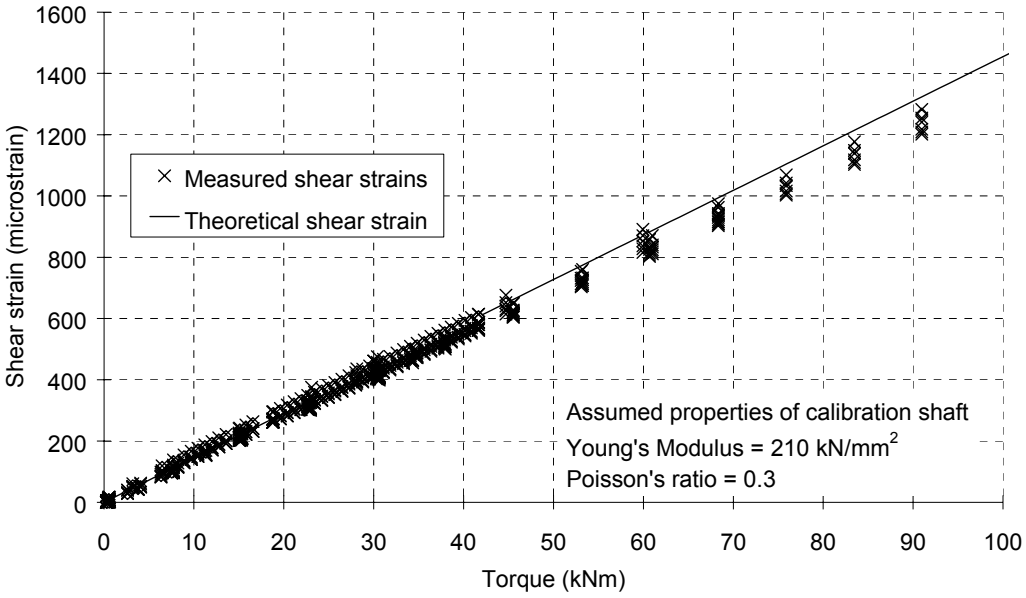

Figure 5-6: Calibration data

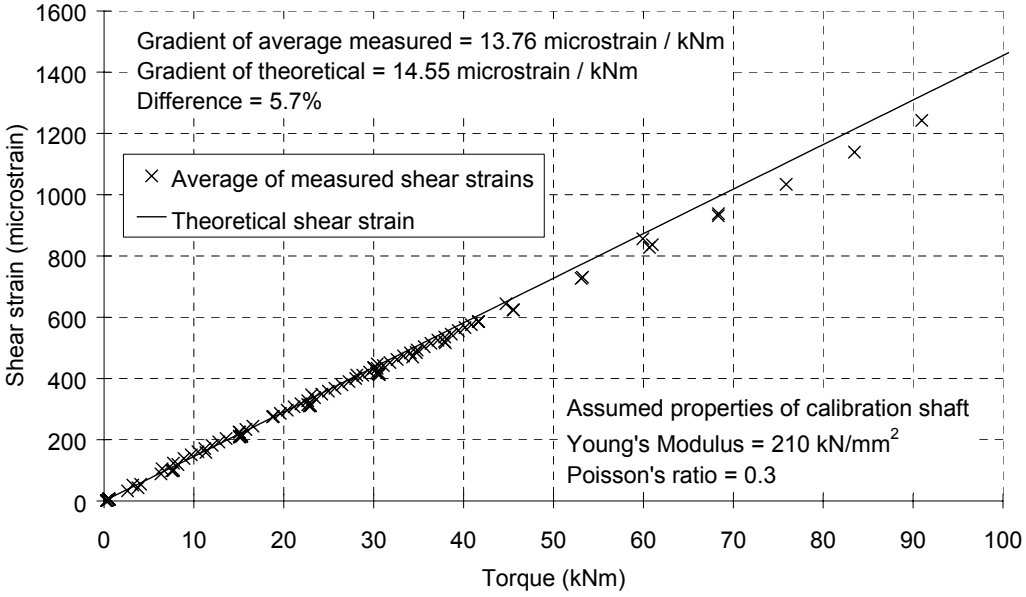

Figure 5-7: Calibration data (averaged measurements)

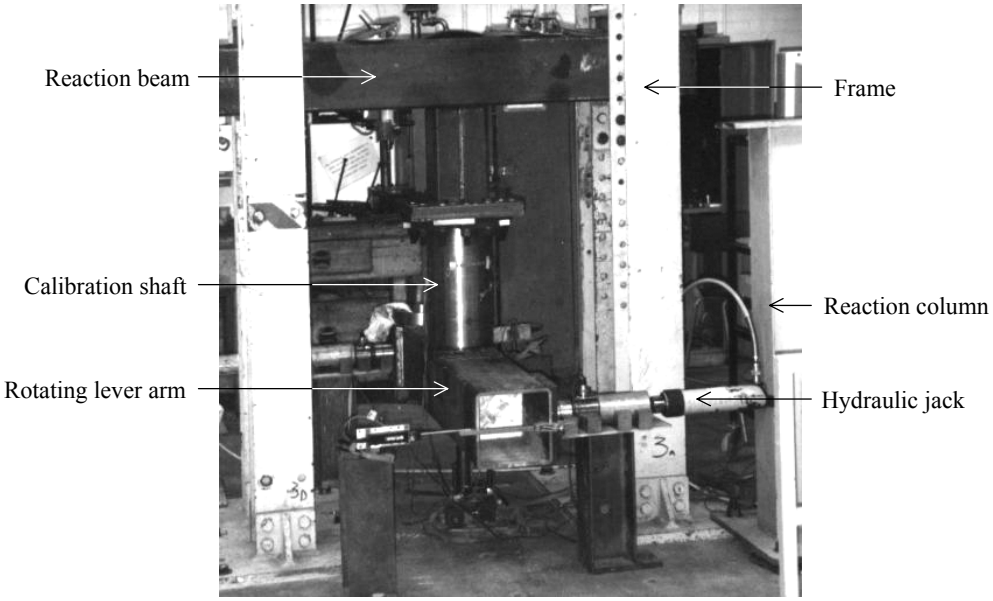

Figure 5-8: Calibration of the load-indicating shaft

5.2.4.2 Measurement of rotation

Rotation was measured at each end of the specimen using gravity inclinometers (Figure 5-9) mounted on the connecting plates. Two additional inclinometers measured the rotation at the quarterpoints of the specimen. The twist was calculated by referencing the rotations measured at locations 1, 2 and 3 (Figure 5-10) to the fiduciary rotation at the fixed end, location 4. Measurement of the twist in this way was independent of the stiffness of the testing apparatus and bolted connections.

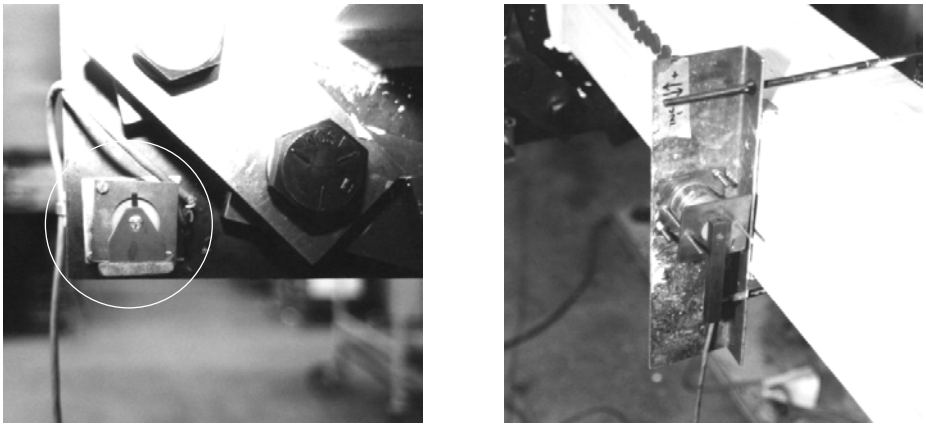

Figure 5-9: Inclinometers for measurement of rotation

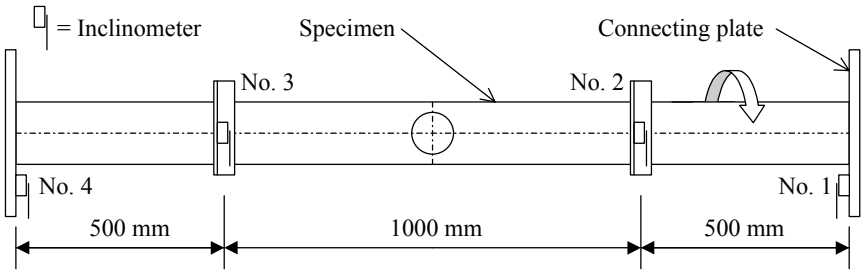

Figure 5-10: Inclinometer locations

5.2.4.3 Measurement of strain

Several of the torsion specimens were instrumented with electrical resistance strain gauges of the type shown in Figure 2-14. The layouts are shown in Figure 5-11 and Figure 5-12. The strain gauges provided data for use in the calibration of the FE models, which were later used in the parametric study (Chapter 7). The arrangement, shown in Figure 5-12, was used to study the variation in torsional shear stress along the length of the specimen.

All specimens were painted with a brittle lime wash to increase the visibility of slip lines in the steel and mill scale (Section 2.4.4.3). Examination of the

formation of the slip line patterns provided information about the onset of yield and the distribution of plastic shear.

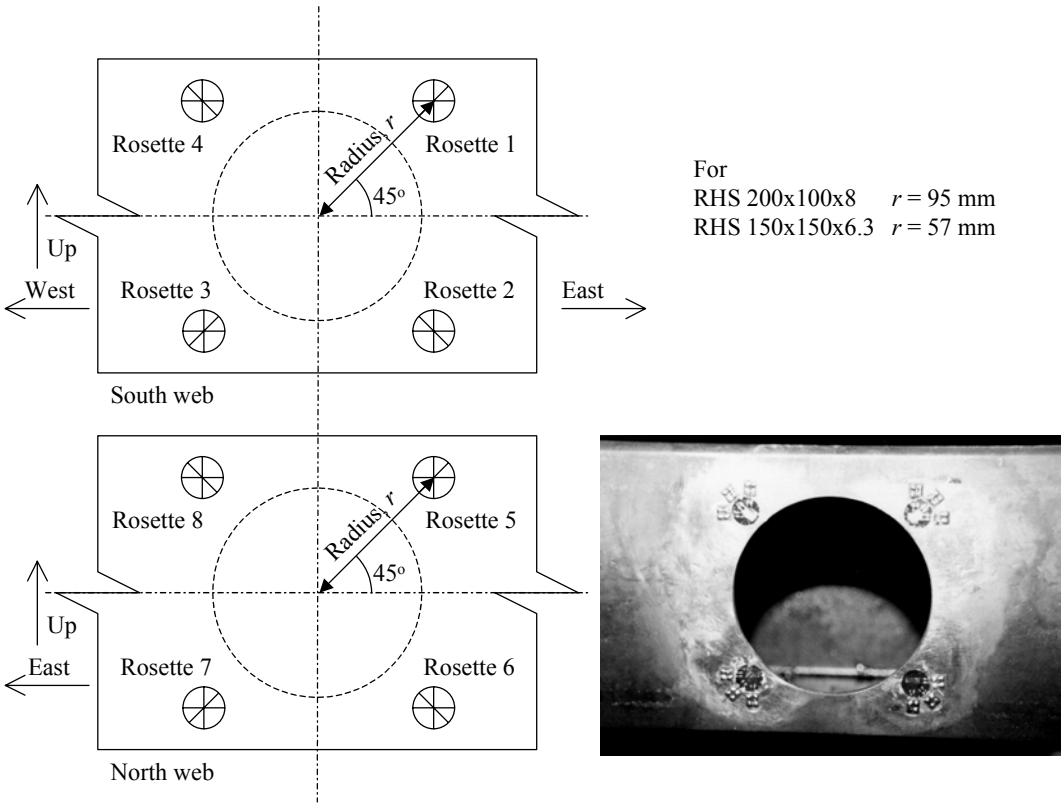

Figure 5-11: Strain gauge pattern (tests TT1-TT6)

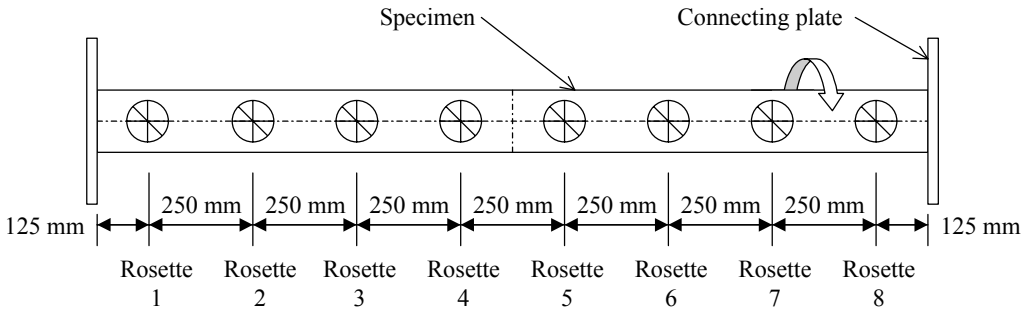

Figure 5-12: Strain gauge pattern (test TT7)

5.2.4.4 Other measurements

The loads applied by the hydraulic jacks were measured by load cells to aid in the balancing of the vertical forces. The movement of the end of the rotating beam was measured by a linear potentiometer to assist in the determination of the loading increments. These devices also provided secondary, but less reliable, measurements of torque and rotation.

5.2.5 Testing procedure

Testing proceeded as outlined below. In some cases, elastic tests were performed by repeated loading and unloading within the elastic range.

1) The specimen was inserted into the loading apparatus. The bolts were inserted, but not tightened.
2) The strain gauges were initialised (zeroed) using the data logger.
3) The specimen was rotated by the hydraulic jacks until a small torque was measured by the load cells. This procedure removed the rotation due to the oversized holes in the connecting plates. The load was then released.
4) The bolts were tightened in alternating sequence.
5) The strain gauge output was reviewed to verify that there was no load on the specimen.
6) A reading was taken at zero load.
7) An increment of displacement was applied.
8) A reading was taken.
9) Steps 7 and 8 were repeated until the desired total rotation was achieved.
10) The specimen was unloaded in increments and readings were taken at each.

11) A reading was taken at zero load.

12) The specimen was de-mounted.

5.3 Specimen types, dimensions and properties

5.3.1 Specimens tested

The specimens tested are listed in Table 5-1. Four different hot finished bars were used in the manufacture of the specimens (two section sizes each of two different grades). The grade S275J2H material was provided and manufactured by British Steel (now Corus). The grade S355J2H material was provided by British Steel and manufactured by Vallourec and Mannesmann Tubes, Germany.

Table 5-1: Specimens tested

ID code	Date tested	Section size	Material grade [Bar number]	Number of holes	Hole diameter (mm)	Hole size ratio, Φ
TT4	12/08/1999	RHS 200x100x8	S275J2H [#3]	0	-	-
TT6	19/08/1999	RHS 200x100x8	S275J2H [#3]	1	165.0	0.94
TT2	03/08/1999	RHS 200x100x8	S275J2H [#3]	2	165.0	0.94
TT3	09/08/1999	RHS 150x150x6.3	S275J2H [#1]	0	-	-
TT5	17/08/1999	RHS 150x150x6.3	S275J2H [#1]	1	99.0	0.76
TT1	27/07/1999	RHS 150x150x6.3	S275J2H [#1]	2	99.0	0.76
TT7	03/03/2000	RHS 200x100x8	S355J2H [#1]	0	-	-
TT14	16/03/2000	RHS 200x100x8	S355J2H [#1]	0	-	-
TT12	14/03/2000	RHS 200x100x8	S355J2H [#1]	1	165.0	0.94
TT9	08/03/2000	RHS 200x100x8	S355J2H [#1]	2	165.0	0.94
TT8	07/03/2000	RHS 150x150x6.3	S355J2H [#1]	0	-	-
TT13	15/03/2000	RHS 150x150x6.3	S355J2H [#1]	1	99.0	0.76
TT11	13/03/2000	RHS 150x150x6.3	S355J2H [#1]	2	38.1	0.29
TT10	10/03/2000	RHS 150x150x6.3	S355J2H [#1]	2	99.0	0.75

Note 1: Only one hydraulic cylinder used for TT1 (acting upwards)
Note 2: The hole size ratio (Φ) is defined by Equation 1-3

5.3.2 Material properties

The properties of the four bars are summarised in Table 5-2. The results of individual tensile tests are given in Appendix D. The definitions of the parameters used can be found in Section 2.2 and BS EN 10002-1:1990.

Table 5-2: Material models

Section size Grade [Bar no]	K (%)	f_{y1} (N/mm^2)	E (kN/mm^2)	$\lambda_{plateau}$	$E_{plateau}$ (kN/mm^2)	λ_{ESHF}	f_u (N/mm^2)	ε_u (%)
RHS 200x100x8 S275J2H [#3]	0.96	344.4	195.2	13.7	0.71	0.25	476.2	16.2
RHS 150x150x6.3 S275J2H [#1]	1.02	329.3	195.2	16.7	-0.16	0.14	457.0	17.9
RHS 200x100x8 S355J2H [#1]	0.71	380.9	203.1	7.0	-0.09	0.24	523.7	12.9
RHS 150x150x6.3 S355J2H [#1]	0.98	404.7	199.9	7.1	0.13	0.34	544.7	13.1

Note: Refer to Section 2.2

5.3.3 Dimensions and geometrical properties

The measured dimensions of the four bars, used in the manufacture of the test specimens, are given in Table 5-3. Dimensions are as defined by BS EN 10210-2:1997 (Figure 1-9). The geometrical properties, obtained using the formulae given in BS EN 10210-2:1997 (Appendix C), are listed in Table 5-4. Sectional properties, based on measured material properties and dimensions, are given in Table 5-5. Plastic torque was calculated by considering the flow of plastic shear strain around a simplified cross-section (Equation 2-50), and the torque and rotation at yield were calculated as in BS EN 10210-2:1997. For comparison, the nominal section properties are given in Table 5-6.

Table 5-3: Dimensions of cross-section (measured)

Section size	Material grade [Bar number]	Height h (mm)	Width b (mm)	Thickness t (mm)	Corner radius (mm) Internal	External
RHS 200x100x8	S275J2H [#3]	197.5	99.5	7.79	5.0	12.5
RHS 150x150x6.3	S275J2H [#1]	149.0	149.0	6.09	5.0	11.0
RHS 200x100x8	S355J2H [#1]	199.0	100.0	7.93	5.0	12.5
RHS 150x150x6.3	S355J2H [#1]	149.5	149.5	5.79	5.0	11.0

Table 5-4: Properties of cross-section (from measured dimensions)

Section size	Material grade [Bar number]	Cross-sectional area A (cm^2)	Torsional inertia constant, I_t (cm^4)	Torsional modulus constant, C_t (cm^3)
RHS 200x100x8	S275J2H [#3]	42.7	1717	242
RHS 150x150x6.3	S275J2H [#1]	34.0	1816	230
RHS 200x100x8	S355J2H [#1]	43.7	1777	248
RHS 150x150x6.3	S355J2H [#1]	32.5	1755	222

Table 5-5: Sectional properties (measured dims and material props, theoretical)

Section size	Material grade [Bar number]	Rotation at yield, θ_{el} (^{o}/m)	Torque at yield, T_{el} (kNm)	Plastic torque T_{pl} (kNm)	Shape factor for torsion T_{pl} / T_{el}
RHS 200x100x8	S275J2H [#3]	2.13	48.1	52.9	1.10
RHS 150x150x6.3	S275J2H [#1]	1.83	43.7	46.2	1.06
RHS 200x100x8	S355J2H [#1]	2.25	54.7	60.3	1.10
RHS 150x150x6.3	S355J2H [#1]	2.20	51.9	54.7	1.05

Table 5-6: Sectional properties (nominal, theoretical)

Section size	Material grade [Bar number]	Rotation at yield (^{o}/m)	Torque at yield (kNm)	Plastic torque (kNm)	Shape factor for torsion
RHS 200x100x8	S275J2H [#3]	1.61 (76%)	39.9 (83%)	44.5 (84%)	1.12 (102%)
RHS 150x150x6.3	S275J2H [#1]	1.45 (79%)	38.0 (87%)	40.8 (88%)	1.07 (101%)
RHS 200x100x8	S355J2H [#1]	2.07 (92%)	51.5 (94%)	57.5 (95%)	1.12 (102%)
RHS 150x150x6.3	S355J2H [#1]	1.87 (85%)	49.1 (95%)	52.7 (96%)	1.07 (102%)

Note: The percentages in parentheses denote the nominal value as a percentage of the measured

5.4 The experimental results

Measured initial stiffnesses and maximum torques are listed in Table 5-7. In cases where no maximum was reached during the test, the torque is quoted for a particular value of twist. The complete torque-rotation relationships are presented in Figure 5-13 through Figure 5-19. Torque and rotation have been non-dimensionalised against the theoretical torque and rotation at yield of the corresponding unperforated section (Table 5-5).

The results indicated that large openings in the webs caused a significant reduction in both the torsional stiffness and capacity. The reduction in stiffness (an average measurement over the whole length of the specimen) was due to the perforated zone being much more flexible than the unperforated beam, and severe rotational deformations were observed around the openings. A slight reverse twist was observed in the beam at either side of the opening due warping and lozenging of the cross-section. The reduction in stiffness was less severe for the specimens with square cross-sections than for the specimens with rectangular cross-sections, as, in the former, the webs contributed a smaller proportion toward the total resistance of the cross-section to the applied torque.

Observation of the Lüders lines in the steel indicated that yielding occurred at low magnitudes of torque, due to stress concentrations around the web openings. However, perforated sections were able to resist torques much higher than those at the onset of yield, but at the expense of plastic deformation around the hole (hence the hysteresis in the unloading curves).

The results also indicated that the unperforated sections were unable to achieve the theoretical torsional capacity (Section 2.5.4), although the experimental

measurements of torsional stiffness and shear strain (Table 5-8) in the elastic range were close the theoretical predictions. The contradictions between the experimental observations and the theoretical predictions are discussed later in this Chapter.

Table 5-7: Experimental results – stiffness and maximum torque

ID Code	Section size	Material grade [Bar number]	Number of holes	Hole diameter (mm)	Stiffness (kNm/^{o})	Torque (kNm)	@
TT4	RHS 200x100x8	S275J2H [#3]	0	-	12.6	43.1	Max
TT6	RHS 200x100x8	S275J2H [#3]	1	165	8.32	20.8	10^o
TT2	RHS 200x100x8	S275J2H [#3]	2	165	7.33	16.2	10^o
TT3	RHS 150x150x6.3	S275J2H [#1]	0	-	13.4	38.8	Max
TT5	RHS 150x150x6.3	S275J2H [#1]	1	99	12.0	24.3	7^o
TT1	RHS 150x150x6.3	S275J2H [#1]	2	99	10.2	23.3	Max
TT7	RHS 200x100x8	S355J2H [#1]	0	-	12.3	53.2	Max
TT14	RHS 200x100x8	S355J2H [#1]	0	-	13.1	53.6	Max
TT12	RHS 200x100x8	S355J2H [#1]	1	165	9.44	26.4	10^o
TT9	RHS 200x100x8	S355J2H [#1]	2	165	6.87	23.2	Max
TT8	RHS 150x150x6.3	S355J2H [#1]	0	-	11.9	49.6	Max
TT13	RHS 150x150x6.3	S355J2H [#1]	1	99	11.0	32.1	10^o
TT11	RHS 150x150x6.3	S355J2H [#1]	2	38.1	12.6	49.2	7^o
TT10	RHS 150x150x6.3	S355J2H [#1]	2	99	10.5	28.1	Max

Table 5-8: Measurements of torsional shear strain in unperforated sections

ID code	Section size Material grade [Bar]	Torsional modulus constant, *Ct* Measured (cm^3)	% of theory	Shear stress / twist % of theory
TT4	RHS 200x100x8 S275J2H [#3]	270.8	112.1	99.9
TT3	RHS 150x150x6.3 S275J2H [#1]	259.3	113.0	99.5
TT7	RHS 200x100x8 S355J2H [#1]	269.15	108.3	92.4

Note: Measured values obtained from strain gauges on the specimens

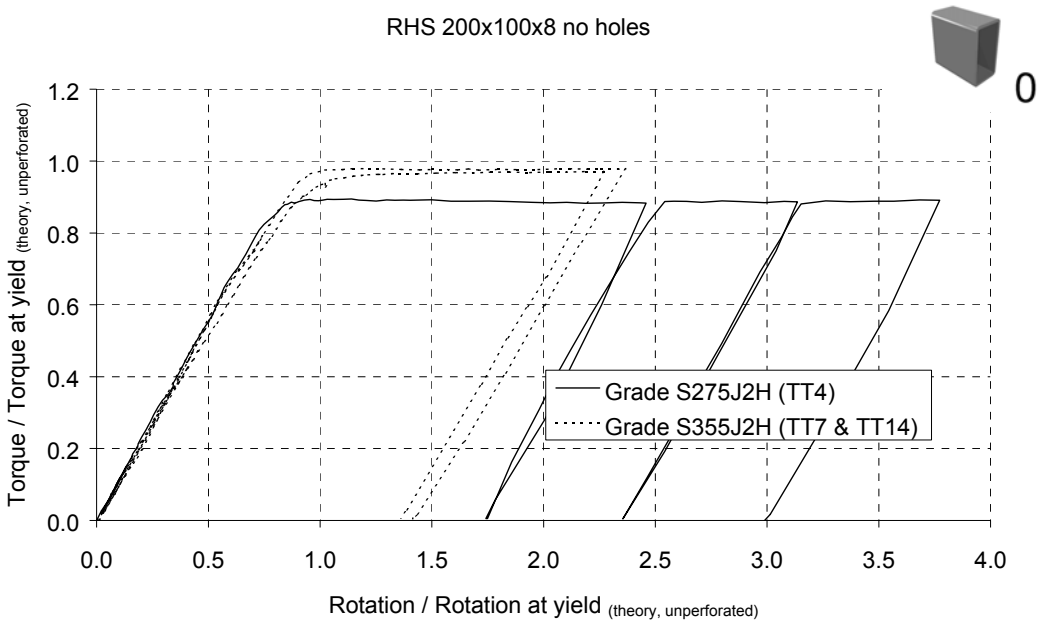

Figure 5-13: Experimental results RHS 200x100x8 no holes

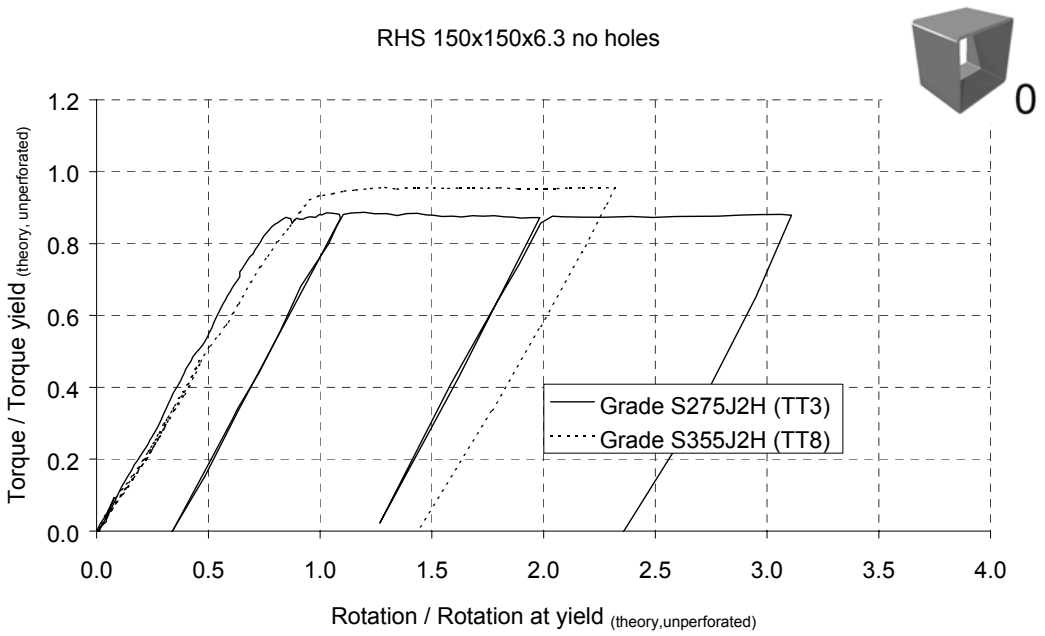

Figure 5-14: Experimental results RHS 150x150x6.3 no holes

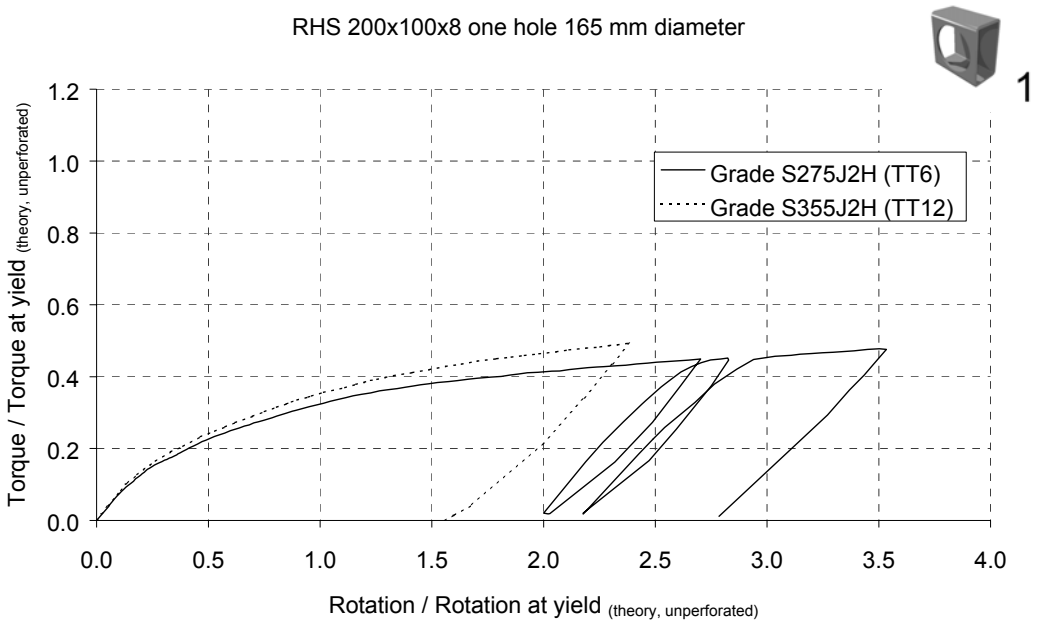

Figure 5-15: Experimental results RHS 200x100x8 one hole 165 mm dia

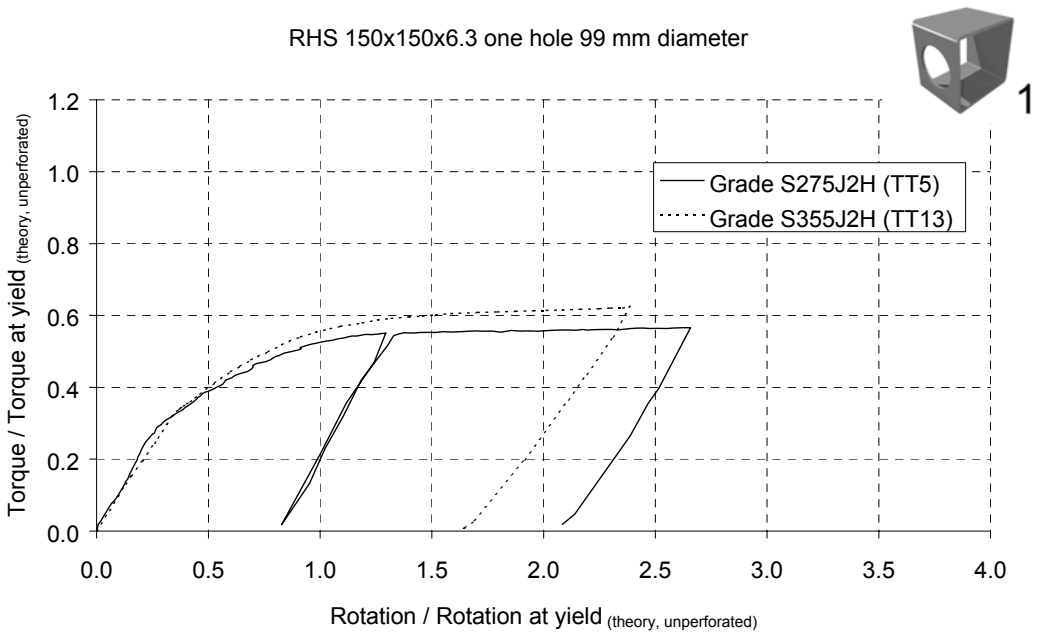

Figure 5-16: Experimental results RHS 150x150x6.3 one hole 99 mm dia

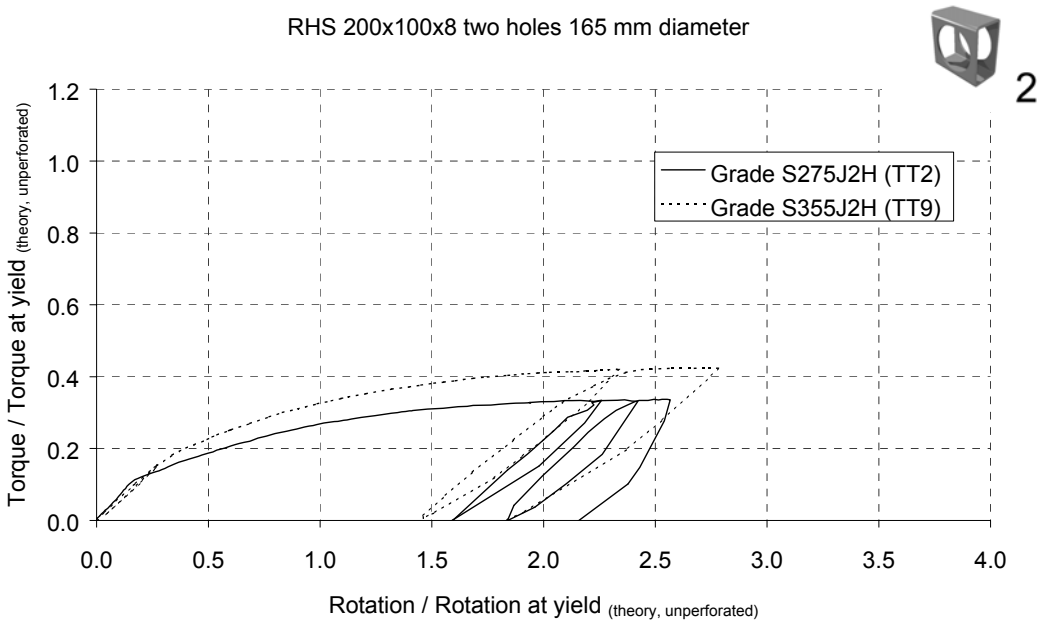

Figure 5-17: Experimental results RHS 200x100x8 two holes 165 mm dia

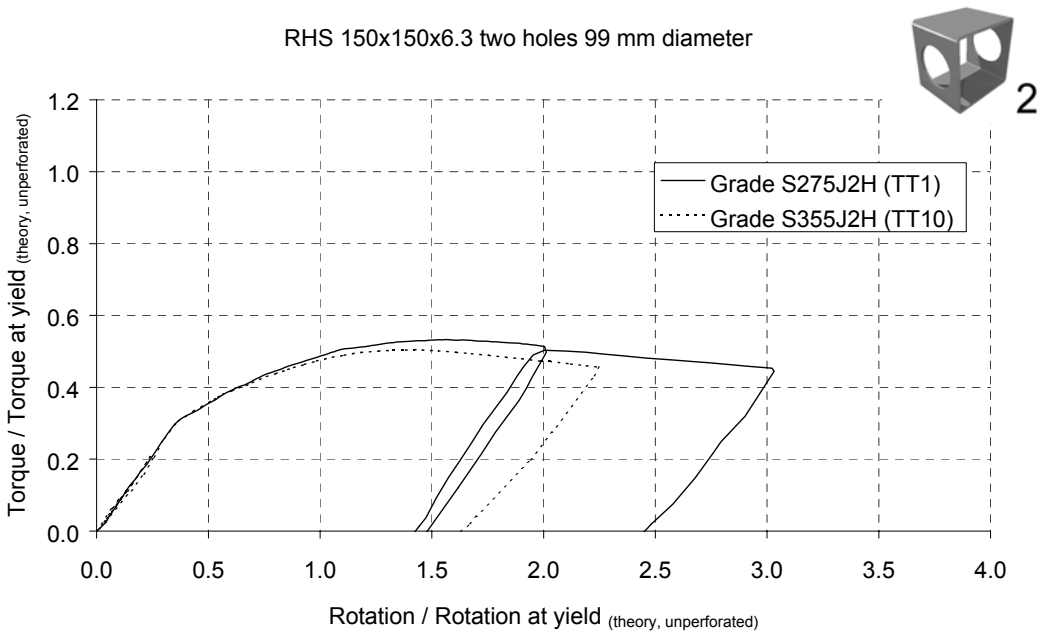

Figure 5-18: Experimental results RHS 150x150x6.3 two holes 99 mm dia

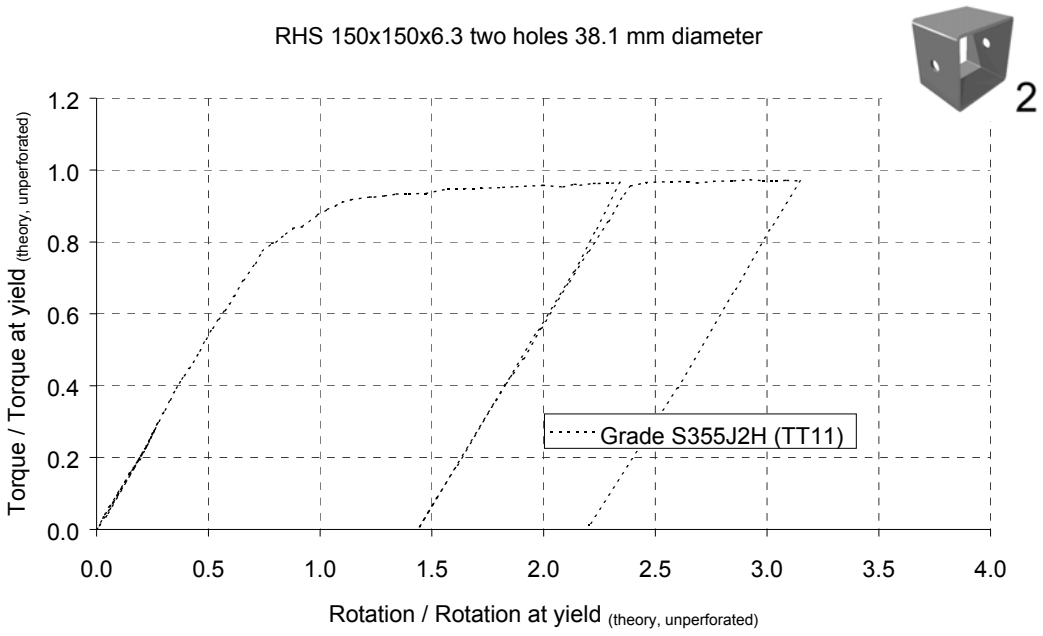

Figure 5-19: Experimental result RHS 150x150x6.3 two holes 38.1 mm dia

5.5 A comparison of experimental results and analytical predictions

The laboratory tests were modelled using the ABAQUS v5.8.1 FEA program (Section 2.3). Models included both material and geometric non-linearity and contained between 6200 and 8300 four-noded shell elements (S4R). These elements were chosen to create the models because they allowed changes in thickness at high strains to be modelled (Section 2.3.6). The FE models were based on the actual measured dimensions of the test specimens and included the corner radii of the tube. The connecting plates were also included, and the support conditions were modelled by defining constraint equations to describe the permitted displacements in the nodal degrees of freedom.

The initial stiffnesses and maximum torques predicted by the FE models are listed in Table 5-9. In cases where no maximum was reached during the test, the torque is quoted for the same value of twist as in Table 5-7. The differences between the experimental values and the FE predictions are listed in Table 5-10.

The complete torque-rotation relationships are presented in Figure 5-20 through Figure 5-32. Torque and rotation have been non-dimensionalised against the theoretical torque and rotation at yield of the corresponding unperforated section (Table 5-5).

Although the FE models matched the displaced shapes observed experimentally (e.g. Figure 5-33 and Figure 5-34), in some instances the torque-rotation relationships were not good matches. For an unperforated section in particular, the simplicity of the testing arrangement should lead to good agreement with standard theory and FE predictions. A difference in excess of 10% is indicative of an important aspect of behaviour that is missing from the analytical models. FE models of unperforated sections agreed almost exactly with standard theory, but not with the behaviour observed in the laboratory.

In most cases, the elastic stiffnesses predicted by FE were close to those measured experimentally. Stiffness is proportional to the Young's modulus of the steel, which is difficult to measure accurately with tensile tests. For perforated sections, the elastic range was very small and is likely to have been affected by the loads imposed on the specimens during manufacturing and handling.

Yielding occurred at small rotations for sections with large openings. The post-yield stiffness is governed by the yield stress and, to a lesser extent, strain hardening. In the case of the grade S355J2H material with large openings, FE predictions and experimental results agreed closely over the full range of rotation.

In the case of the grade S275J2H RHS 200x100x8, the specimens were less stiff and weaker than predicted. For the grade S275J2H RHS 150x150x6.3 with one hole, post-yield stiffness was similar to the FE prediction in the early stages of the test, but the maximum torque was lower. For two holes the experimental result and FE prediction are similar.

Despite the poor agreement with accepted torsion theory, tests TT7 and TT14 gave near identical results indicating good experimental repeatability.

Table 5-9: Finite Element results – stiffness and maximum torque

ID code	Section size	Material grade [Bar number]	Number of holes	Hole diameter (mm)	Stiffness (kNm/^{o})	Torque (kNm)	@
TT4	RHS 200x100x8	S275J2H [#3]	0	-	11.3	54.0	Max
TT6	RHS 200x100x8	S275J2H [#3]	1	165	7.59	23.2	10^o
TT2	RHS 200x100x8	S275J2H [#3]	2	165	6.02	20.0	10^o
TT3	RHS 150x150x6.3	S275J2H [#1]	0	-	11.9	47.4	Max
TT5	RHS 150x150x6.3	S275J2H [#1]	1	99	11.2	27.1	7^o
TT1	RHS 150x150x6.3	S275J2H [#1]	2	99	10.4	23.7	Max
TT7	RHS 200x100x8	S355J2H [#1]	0	-	12.1	61.2	Max
TT14	RHS 200x100x8	S355J2H [#1]	0	-	12.1	61.2	Max
TT12	RHS 200x100x8	S355J2H [#1]	1	165	8.29	26.7	10^o
TT9	RHS 200x100x8	S355J2H [#1]	2	165	6.67	23.5	Max
TT8	RHS 150x150x6.3	S355J2H [#1]	0	-	11.9	56.3	Max
TT13	RHS 150x150x6.3	S355J2H [#1]	1	99	11.2	32.4	10^o
TT11	RHS 150x150x6.3	S355J2H [#1]	2	38.1	11.8	53.6	7^o
TT10	RHS 150x150x6.3	S355J2H [#1]	2	99	10.2	27.7	Max

Table 5-10: Experimental and FE results – stiffness and maximum torque

ID code	Section size	Material grade [Bar number]	Number of holes	Hole diameter (mm)	Difference stiffness (%)	Difference torque (%)
TT4	RHS 200x100x8	S275J2H [#3]	0	-	12.2	-20.2
TT6	RHS 200x100x8	S275J2H [#3]	1	165	9.66	-10.3
TT2	RHS 200x100x8	S275J2H [#3]	2	165	21.7	-19.2
TT3	RHS 150x150x6.3	S275J2H [#1]	0	-	12.3	-18.2
TT5	RHS 150x150x6.3	S275J2H [#1]	1	99	7.76	-10.2
TT1	RHS 150x150x6.3	S275J2H [#1]	2	99	-2.49	-1.84
TT7	RHS 200x100x8	S355J2H [#1]	0	-	1.96	-13.1
TT14	RHS 200x100x8	S355J2H [#1]	0	-	8.70	-12.4
TT12	RHS 200x100x8	S355J2H [#1]	1	165	13.9	-1.09
TT9	RHS 200x100x8	S355J2H [#1]	2	165	3.04	-1.03
TT8	RHS 150x150x6.3	S355J2H [#1]	0	-	-0.65	-11.9
TT13	RHS 150x150x6.3	S355J2H [#1]	1	99	-1.39	-0.76
TT11	RHS 150x150x6.3	S355J2H [#1]	2	38.1	6.31	-8.24
TT10	RHS 150x150x6.3	S355J2H [#1]	2	99	2.48	1.49

Note: A negative percentage indicates experimental values lower than Finite Element values

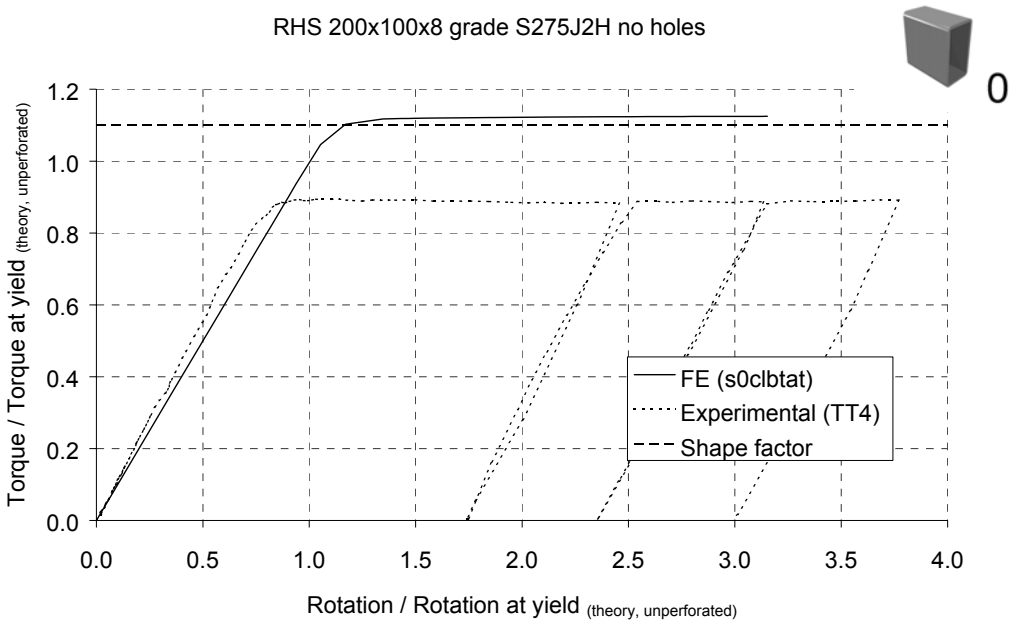

Figure 5-20: FE and experimental (test TT4)

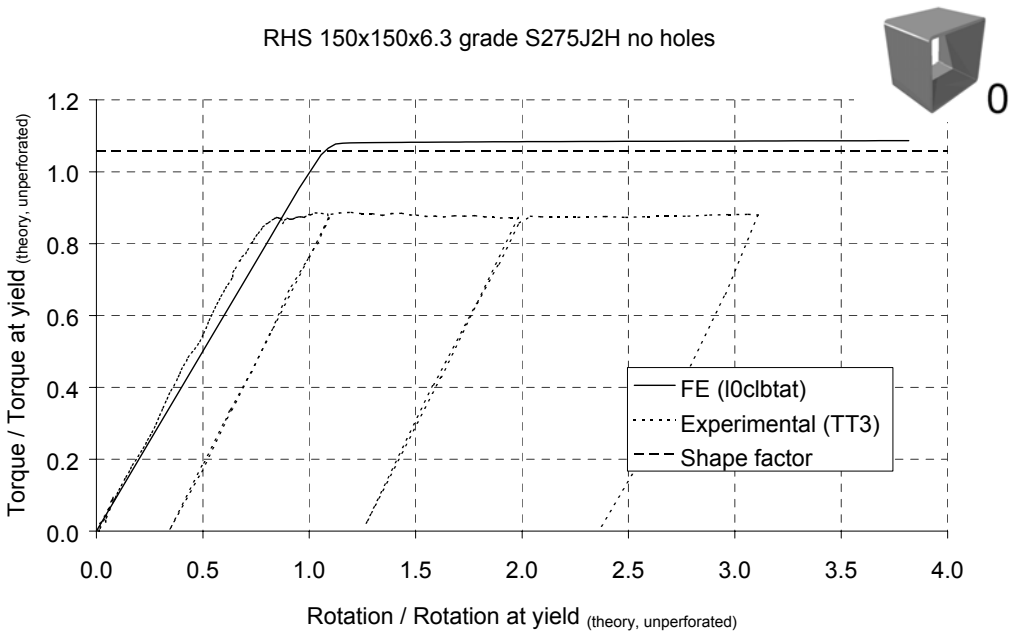

Figure 5-21: FE and experimental (test TT3)

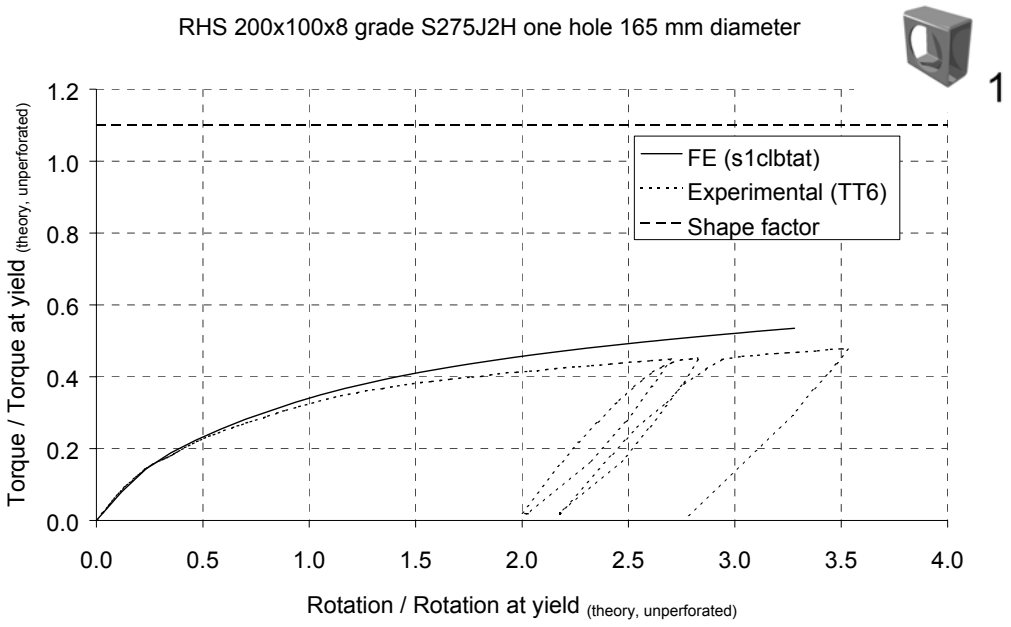

Figure 5-22: FE and experimental (test TT6)

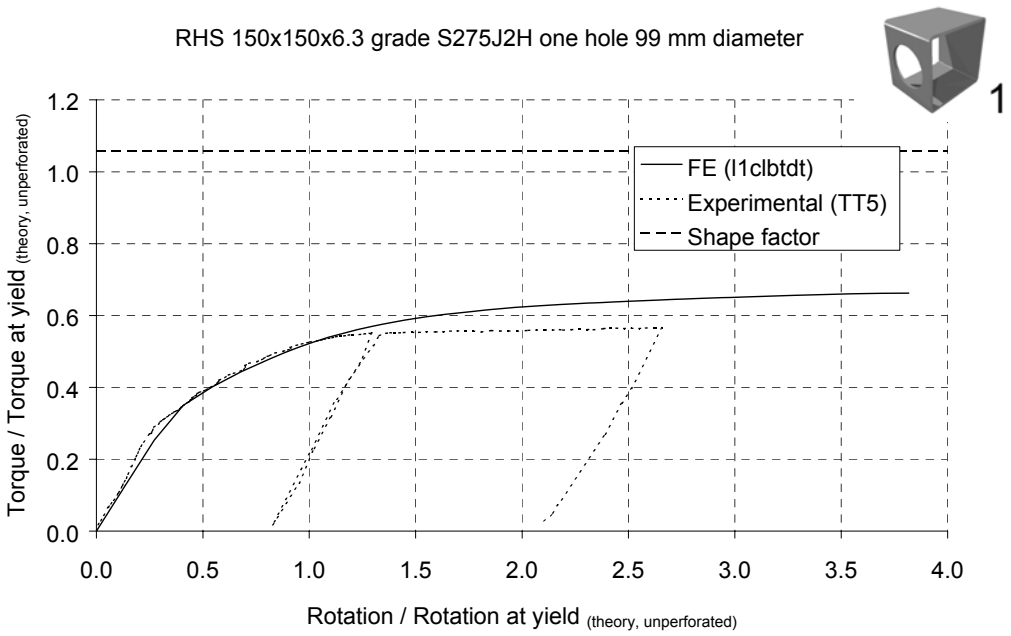

Figure 5-23: FE and experimental (test TT5)

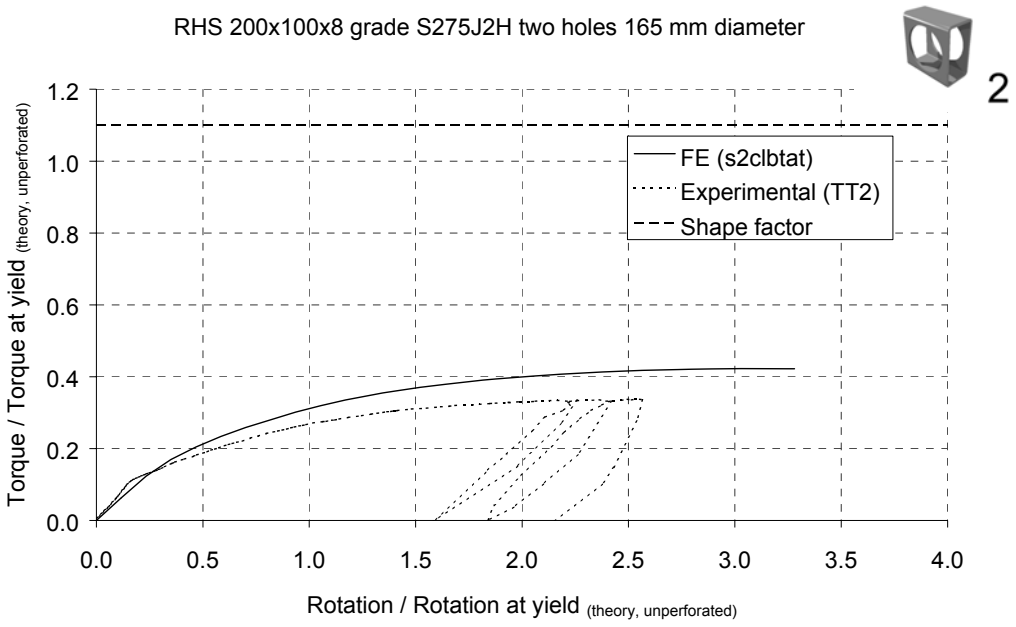

Figure 5-24: FE and experimental (test TT2)

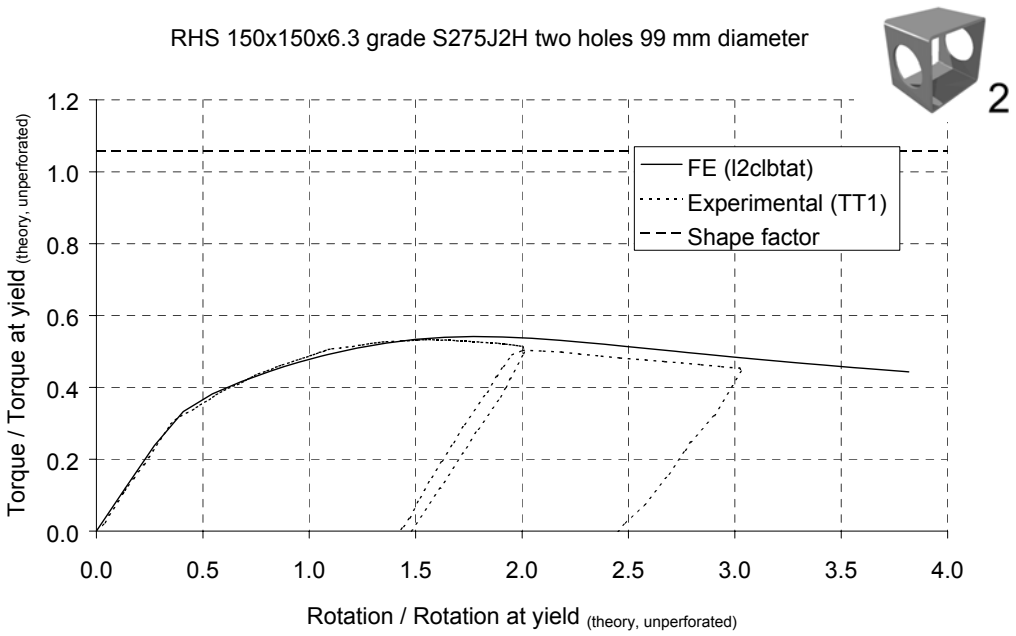

Figure 5-25: FE and experimental (test TT1)

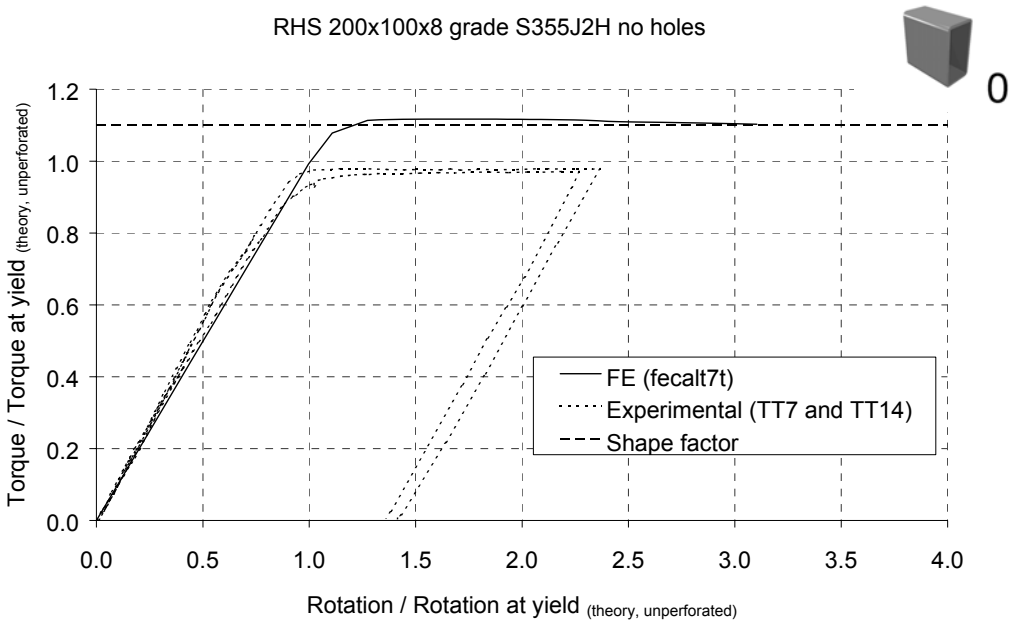

Figure 5-26: FE and experimental (tests TT7 and TT14)

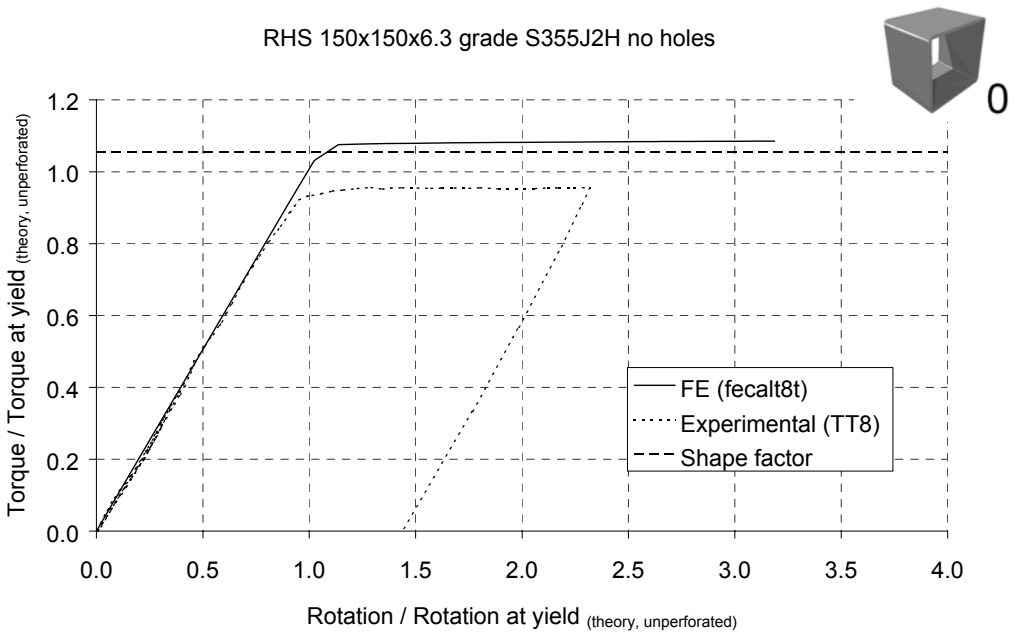

Figure 5-27: FE and experimental (test TT8)

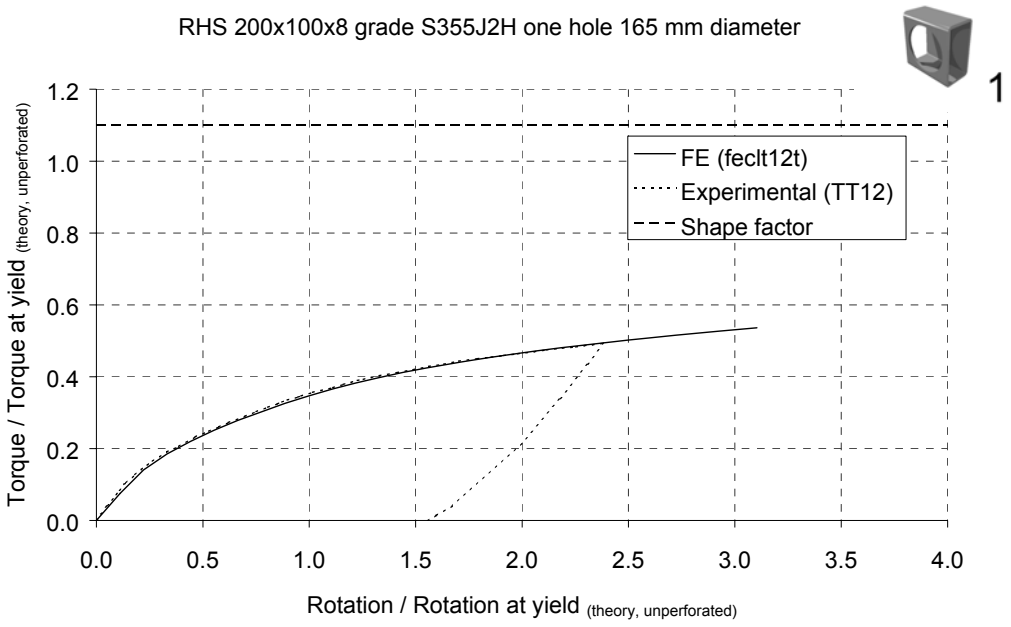

Figure 5-28: FE and experimental (test TT12)

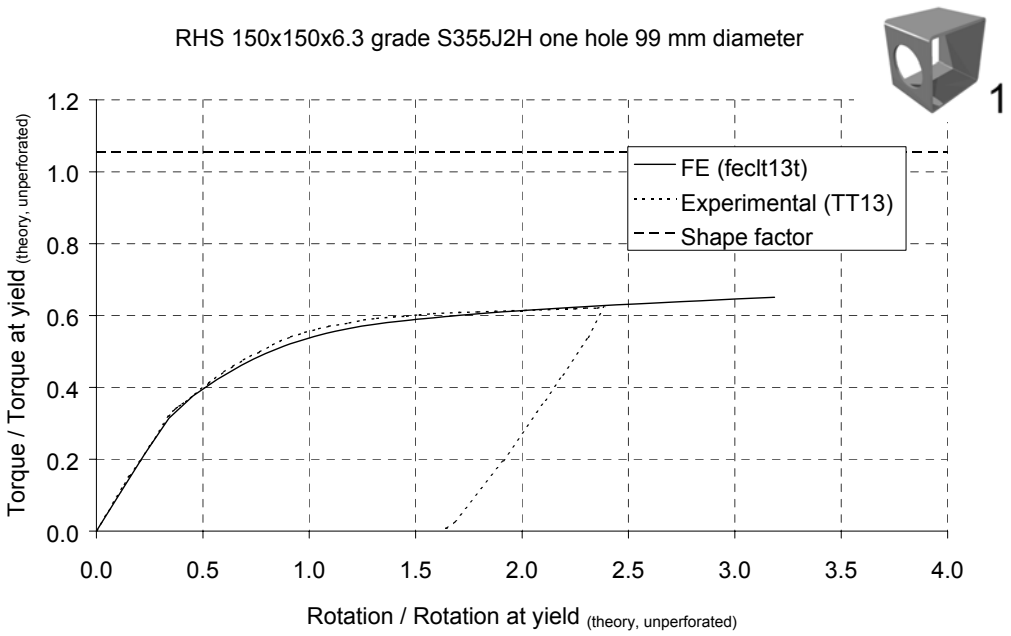

Figure 5-29: FE and experimental (test TT13)

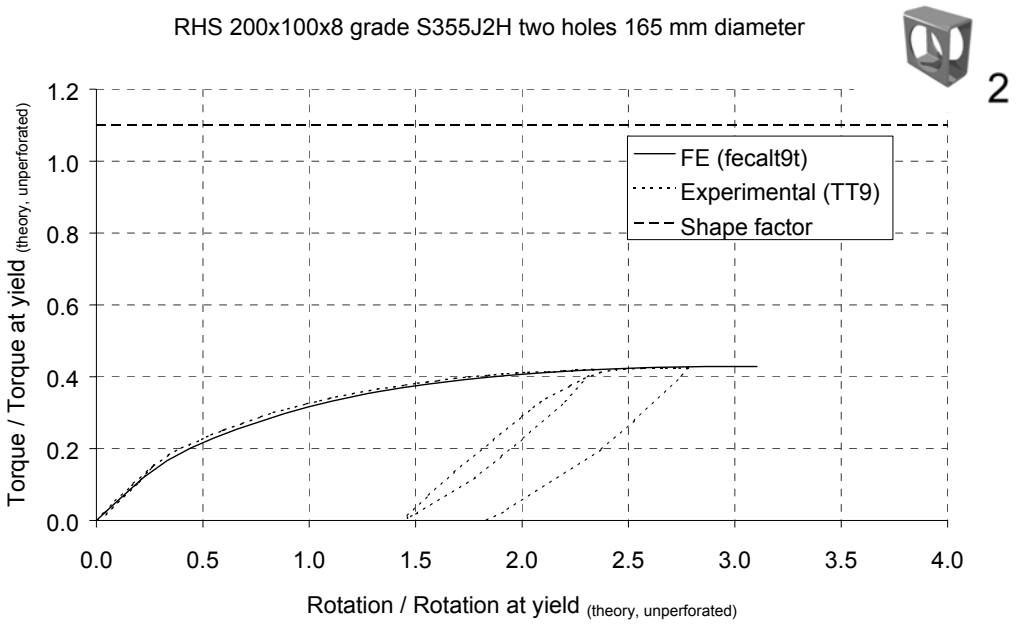

Figure 5-30: FE and experimental (test TT9)

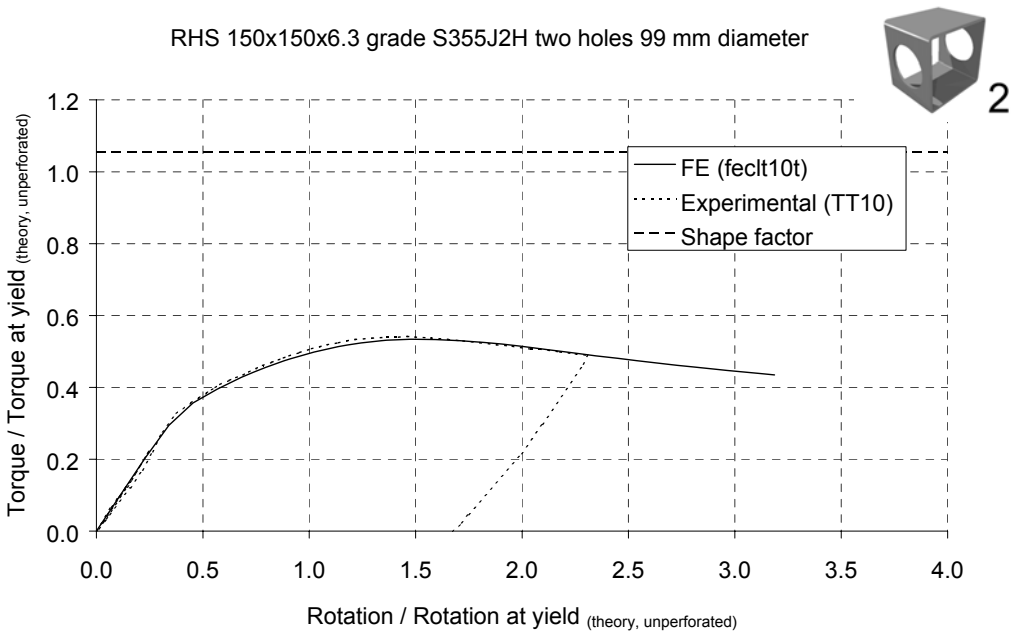

Figure 5-31: FE and experimental (test TT10)

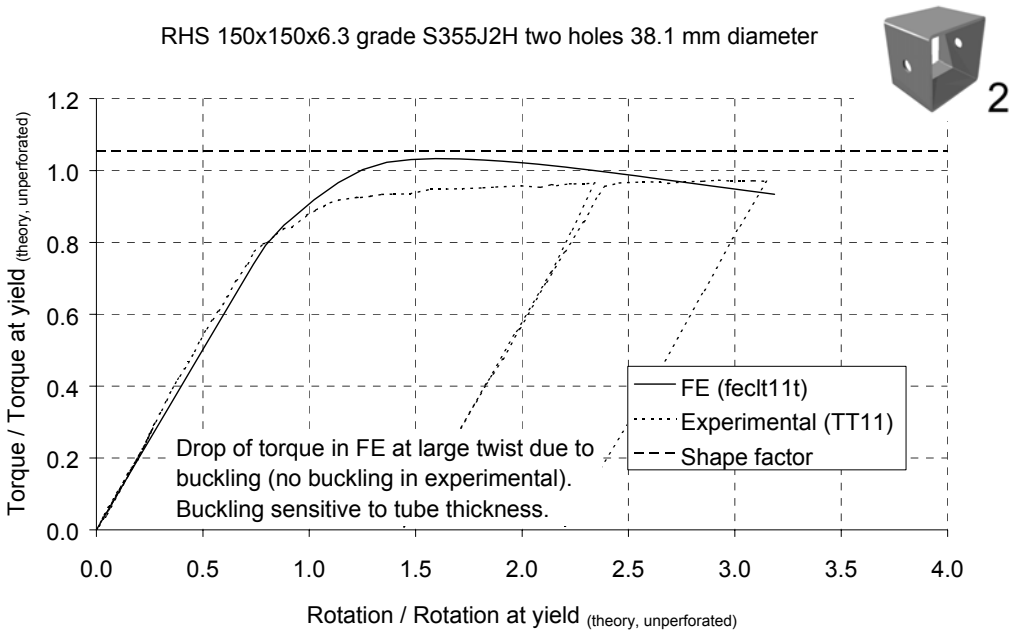

Figure 5-32: FE and experimental (test TT11)

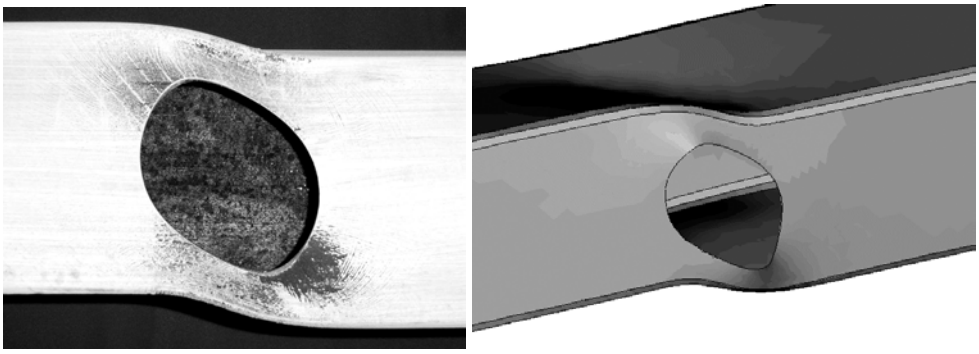

Figure 5-33: Displaced shape RHS 150x150x6.3 one hole 99 mm dia

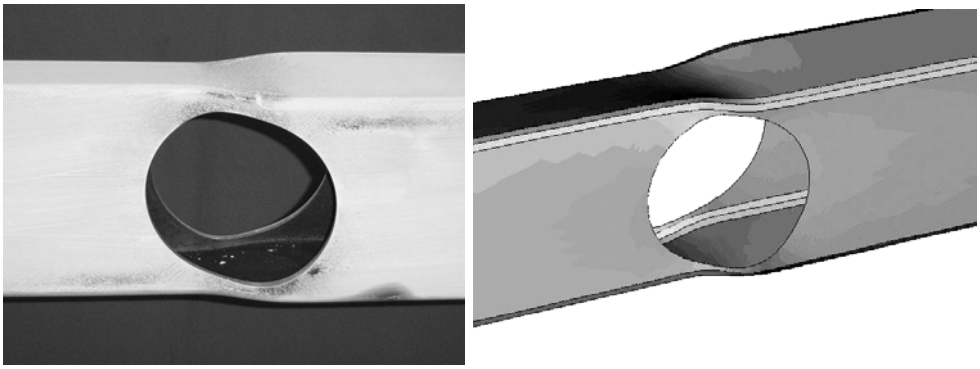

Figure 5-34: Displaced shape RHS 200x100x8 two holes 165 mm dia

5.6 The validity of the experimental findings

5.6.1 Introduction

The experimental method was thoroughly examined in an attempt to provide an explanation for the differences between the measured torsional behaviour and that predicted by FE and standard torsion theory. The validity of the experimental results is discussed in detail in Project Report SC2000-010, but the main points are summarised in the following Sections.

5.6.2 Measurement of rotation

Measurement of rotation was achieved using gravity inclinometers. These devices were particularly susceptible to external influences such as the stability of the input voltage, vibration and draughts. These influences had a random effect on the instrument output, which appeared as noise on the channel. The accuracy of the inclinometers quoted by the manufacturer was compromised by these, relatively large, random external influences. Observation of their performance in the laboratory suggested the following statistics:

Reliability	(inspection of experimental results)	better than ±0.05°
Precision	(observation of data logger performance)	around 0.001°
Accuracy	(calibration against known quantities)	better than ±0.1°

Although the inclinometers were not being used to their full potential, their performance was adequate for the purposes of the torsion tests. Furthermore, in every test, the rotation calculated from the vertical movement of the lever arm was consistent with the rotation measured by the inclinometers (Figure 5-35 is a typical example).

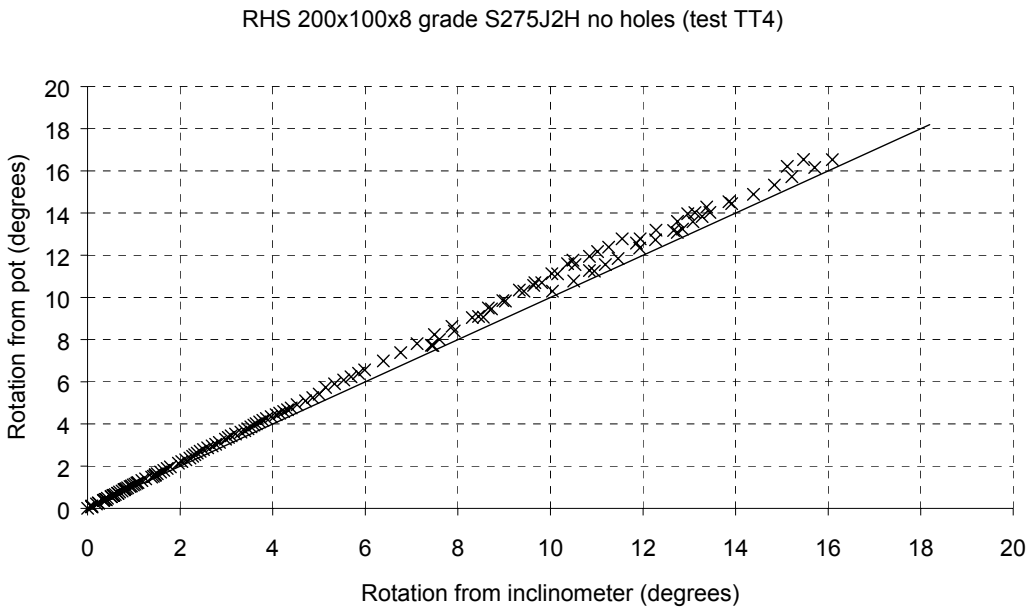

Figure 5-35: Rotation measurements

5.6.3 Measurement of torque

In the tests, the torque was measured by monitoring the shear strain on the external surface of the calibration shaft (Figure 5-5). Six electrical resistance shear strain gauges (Section 2.4.4.2) were used for this purpose, giving six separate measurements of torque. In all the tests, the difference between the lowest and highest indicated torque (the six measurements before averaging) was never more than 2.5 kNm. Furthermore, a three-element strain gauge rosette, also placed on the shaft, confirmed that the orientation of the principal strain axes was consistent with pure torsion in the shaft. Observation of the performance of the calibration shaft in the laboratory suggested the following statistics for the averaged indicated torque:

Reliability	(inspection of experimental results)	better than ±0.5 kNm
Precision	(observation of data logger performance)	around 0.1 kNm
Accuracy	(calibration against known quantities)	better than ±0.5 kNm

The performance of the calibration shaft was adequate for the purposes of the torsion tests. Inaccurate measurement of torque is unlikely to be the cause of the disparity between the laboratory measurements and the predictions of theory and FE for the following reasons:

1) In the cases of the grade S355J2H material with large openings, the experimental torque agreed very closely with the FE predictions. In the other cases, the elastic stiffness was close to that predicted by FE and theory
2) A corresponding error in the measurement of rotation would be necessary to maintain the agreement with the measured stiffnesses, and those predicted by FE and theory (Section 5.6.2)

3) The shear strains measured at the surface of the calibration shaft were similar to those predicted by standard torsion theory (Figure 5-7)
4) The jack forces measured during the tests corresponded to the torque measured by the calibration shaft (Figure 5-36 is a typical example)
5) In the elastic range, the strains measured on the surface of the specimen were consistent with those expected for the measured value of torque

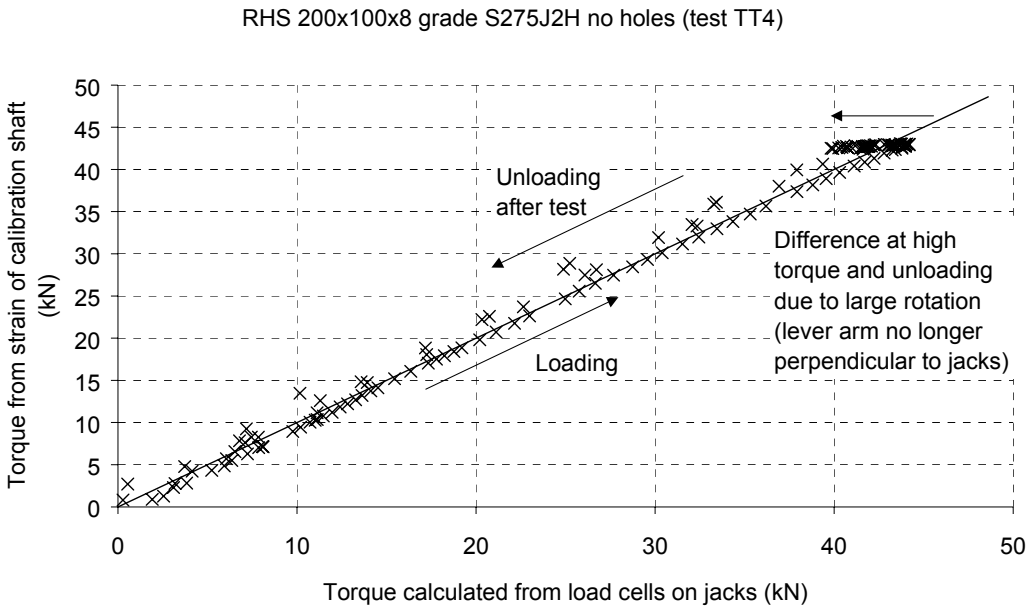

Figure 5-36: Load measurements

5.6.4 Measurement of strain

Inspection of the experimental results suggested a reliability and precision in the order of ±0.1 microstrain. The manufacturer's documentation quotes an accuracy of ±1 % for strains less than 0.04. This level of accuracy is only possible if the gauges are used correctly.

5.6.5 Repeatability of experimental results

Repeatability of results is necessary to prove the reliability of the testing method. Two unperforated specimens cut from the same length of RHS 200x100x8 S355J2H (tests TT7 and TT14) gave very similar results (Figure 5-13) indicating good repeatability and hence good reliability of the testing method. Good reliability can also be inferred from the good repeatability within individual tests (elastic tests and unloading-reloading after plastic deformation).

5.6.6 Accuracy of the data measurement and logging system

An error introduced by the data measurement and logging equipment could affect all the experimental measurements, but is unlikely to be the cause of the disparity between the experimental measurements and the predictions of FE and theory for the following reasons:

1) The measurements would have to be changed in different directions to result in an error of this type, while still maintaining consistency between strain, rotation and torque in the elastic range
2) An error in the measurement and logging equipment would be likely to affect all tests equally, but the differences between the experimental measurements and FE predictions were not equal for all tests
3) The equipment was in frequent use for other work and no problems were reported

4) The accuracy of the measurement and logging equipment was checked with known voltages, loads and displacements, and was found to be well within acceptable limits

5.6.7 Additional loads on the specimen

Additional loads on the specimens could have caused them to fail at lower torques than those predicted by the FE models, if those additional loads were not included in the FE models. Potentially, these loads may have resulted from friction, out-of-balance hydraulic jacks, warping restraint, bending due to asymmetry, and/or axial restraint. However, this is an unlikely explanation for the disparity between the experimental measurements and the predictions of FE and theory for the following reasons:

1) The elastic strains measured on the specimens do not indicate anything other than pure torsional shear
2) According to accepted theory, the reduction in the torsional capacity due to warping stresses in box sections is so small it may be neglected (Section 2.5.3)
3) Warping restraint is included in the FE models
4) Square cross-sections do not warp, but produced similar results to the rectangular cross-sections
5) Friction between the rotating beam and the guide columns would not have affected the torque measured on the calibration shaft
6) The rig structure was too flexible to exert the enormous bending and axial forces required to reduce the torsional capacity by 10%
7) External forces would also have affected the linearity of the elastic response of the unperforated specimens

8) FE models, of unperforated beams with axial restraint, predicted identical capacities to the FE models without axial restraint (since changes in length due to deformation were very small e.g. Figure 2-25)

When the unperforated specimens were tested, Lüders lines were first observed at the corners where the RHS was welded to the connecting plates. Localised effects due to captured thermal stresses, warping, and heat induced metallurgical changes are likely to be responsible for this effect, but they do not explain the differences between the measured torque-rotation response and the FE predictions. At maximum torque, all the unperforated specimens exhibited plastic deformation along the whole length. Perforated specimens formed plastic hinges around the holes without plastic deformation at the ends.

5.6.8 The validity of the theoretical and analytical predictions

5.6.8.1 Introduction

It is possible that the experimental measurements were correct, but that theoretical and FE models may have been incorrectly applied.

5.6.8.2 Boundary conditions

Correct identification of the boundary conditions in particular has been found to be an important aspect of the FE modelling. In an FE model, the ends of the specimen may, or may not be, restrained from rotating about the major and minor axes of the cross-section. For an asymmetric case (one hole), a pinned boundary condition results in a lower capacity than a fixed boundary condition (Figure 5-37 and Figure 5-38). However, boundary conditions have no effect on the response of the symmetric cases.

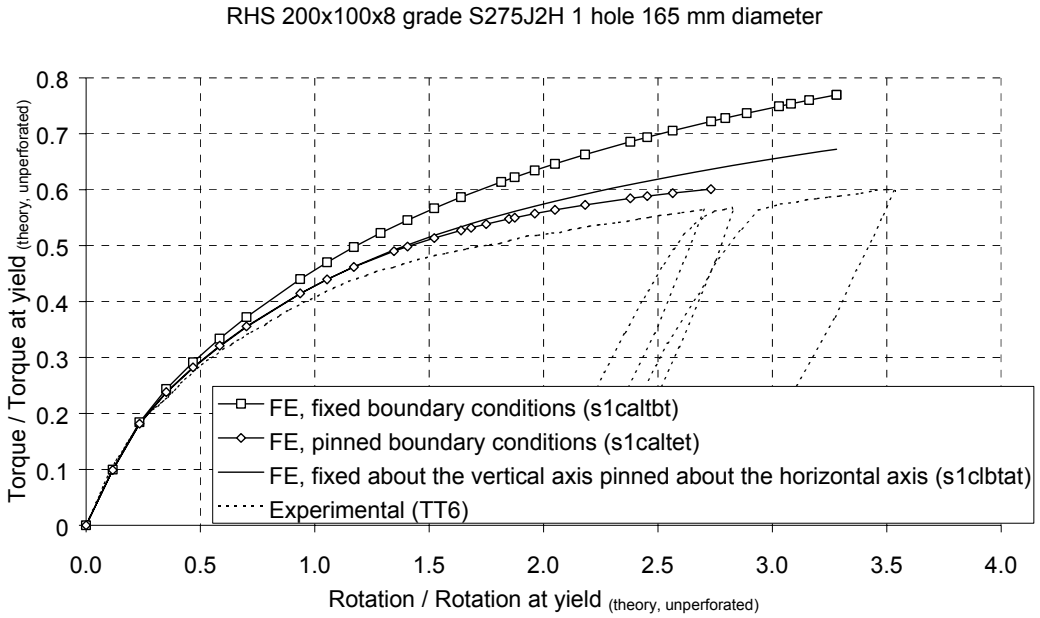

Figure 5-37: Boundary conditions RHS 200x100x8 grade S275J2H 1 hole

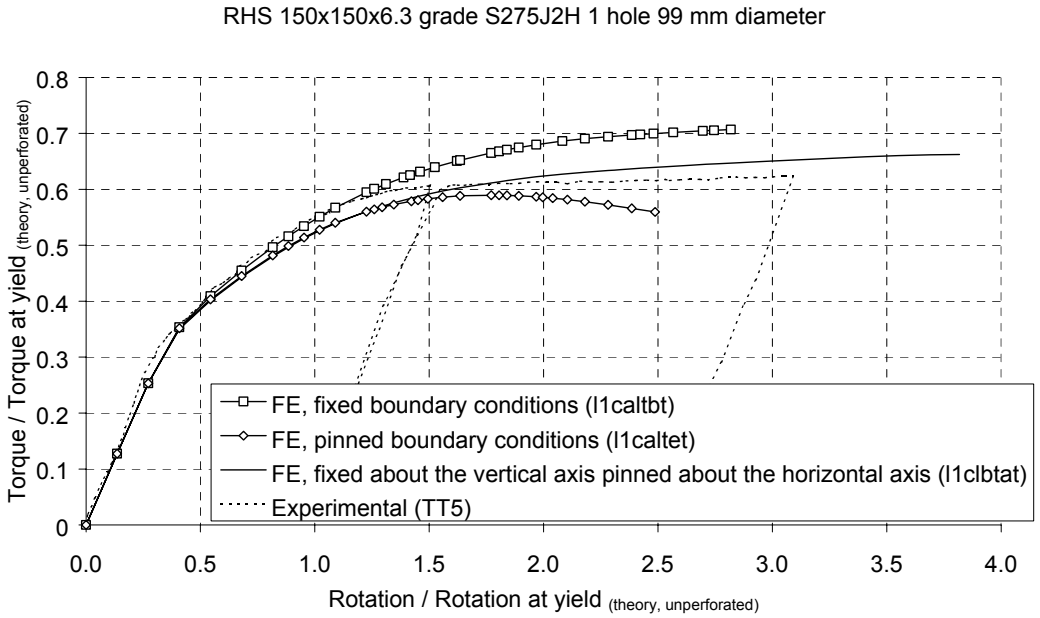

Figure 5-38: Boundary conditions RHS 150x150x6.3 grade S275J2H 1 hole

5.6.8.3 Cross-section dimensions

If incorrect dimensions had been used in the calculations, then the FE and theoretical predictions would be in error. Consideration of the theoretical equations governing behaviour of an unperforated RHS in torsion allowed the sensitivity of the theoretical torsional properties to changes in the dimensions to be quantified (Appendix B). However, the use of erroneous dimensions is an unlikely explanation for the disparity between the experimental measurements and the predictions of FE and theory for the following reasons:

1) No single parameter affects behaviour in the correct way, and unfeasibly large changes are required to reduce torsional capacity by 10%
2) Grade S355J2H specimens with large holes agreed with FE, yet they have the same cross-section dimensions as the unperforated specimens
3) Specimens were re-measured after the tests and the dimensions were found to be correct

5.6.8.4 Material properties

If incorrect material properties had been used in the calculations, then the FE and theoretical predictions would be in error. Consideration of the theoretical equations governing behaviour of an unperforated RHS in torsion allowed the sensitivity of the theoretical torsional properties to changes in the material properties to be quantified (Appendix B).

Yield stress influences torsional capacity, without changing stiffness, but is easy to measure accurately with tensile tests. Young's modulus is difficult to

measure accurately with tensile tests, but does not influence capacity, unless there is instability. The value of poisson's ratio used in the analysis (0.3) is an assumed rather than a measured quantity, but only influences stiffness. Residual stresses in hot formed steel tubes are small and do not reduce plastic capacity when they are present.

It is possible that the use of erroneous values of yield stress, in the theoretical and FE calculations, is the cause of the disparity between the predictions of torsional capacity and the experimental measurements. The following evidence supports this conjecture:

1) Some of the theoretical and FE predictions can be made to match the experimental results by using a lower yield stress (see below)
2) Experimental observations of strain in the specimen indicate plastic strain occurring when measured material properties predict elastic behaviour (see below)

However, there is also evidence that suggests that the correct value of yield stress was used in the theoretical and FE calculations:

1) The material properties were measured by a large number of tensile tests in accordance with BS EN 10002 (Appendix D)
2) The variation in yield stress as measured by tensile testing of coupons from individual bars was small, indicating homogeneity and good experimental repeatability (Appendix D)
3) FE predictions of grade S355J2H specimens with large holes matched the experimental results when the measured material properties were used

4) Similar RHS were tested in three and four point bending, and measured material properties were consistent with experimental results (Chapters 3 and 4)
5) Two coupons, inclined to the axis of the tube were tested in an attempt to measure anisotropy, but no anisotropy was observed (Appendix D)
6) One coupon was tested at a very low strain rate, but no difference was observed when compared with the BS EN 10002 coupons (Appendix D)
7) Special coupons, designed to investigate the shear yield behaviour of the steel, indicated that the correct values of shear yield stress were used in the calculations (Section 2.5.4.3)

Despite the numerous arguments against the 'reduced yield' explanation, it remains a feasible mechanism that explains how torsional capacity could potentially have been reduced, without affecting the elastic response.

When a yield stress of 275 N/mm^2 was used in an FE model of the RHS 200x100x8 grade S275J2H no holes specimen, the torque-rotation relationship matched the experimental result (Figure 5-39). When a yield stress of 267 N/mm^2 was used in an FE model of the RHS 150x150x6.3 grade S275J2H no holes specimen, a similar match was achieved (Figure 5-40). When these reduced yield stresses were applied to the specimens with holes, the torque-rotation relationships matched for the RHS 200x100x8 case, but not for the RHS 150x150x6.3 (Figure 5-41 through Figure 5-44).

Similar reductions in yield stress for the unperforated grade S355J2H specimens were used to match the FE predictions with the experimental results, but no reductions were required to match the behaviour of the specimens with large holes.

When the strain gauge data was examined for the unperforated specimens, it showed behaviour similar to the examples shown in Figure 5-45 and Figure 5-46. At low twist, strains were uniform and linear and matched those predicted by FE and theory. However, a departure from linearity occurred at strains that should have been elastic. In the examples here, the strain was, at first, maintained at a constant level indicating that failure was occurring at some other location in the specimen. With more rotation, the strains began to separate and increase, indicating that plastic deformation was occurring at the location of the gauges.

The difference between the experimentally measured torque and the torque calculated, using torsion theory, from the experimentally measured strains in the specimen can be used to back-calculate a yield stress from the torsion test. The yield stresses back-calculated from strain data were the same as the reduced yield stresses necessary to match experimental and FE torque-rotation relationships.

It appears from the observations that the steel does not obey the von Mises failure criterion, but this is contrary to the results of previous investigators (Section 2.5.4.2) and the results of attempts to measure the shear yield stress directly (Section 2.5.4.3). It is unclear why some specimens behaved as predicted using measured yield stresses, and why some specimens behaved as predicted using reduced yield stresses. It is possible that this could be a result of variability within the steel, but no evidence is available to support this suggestion.

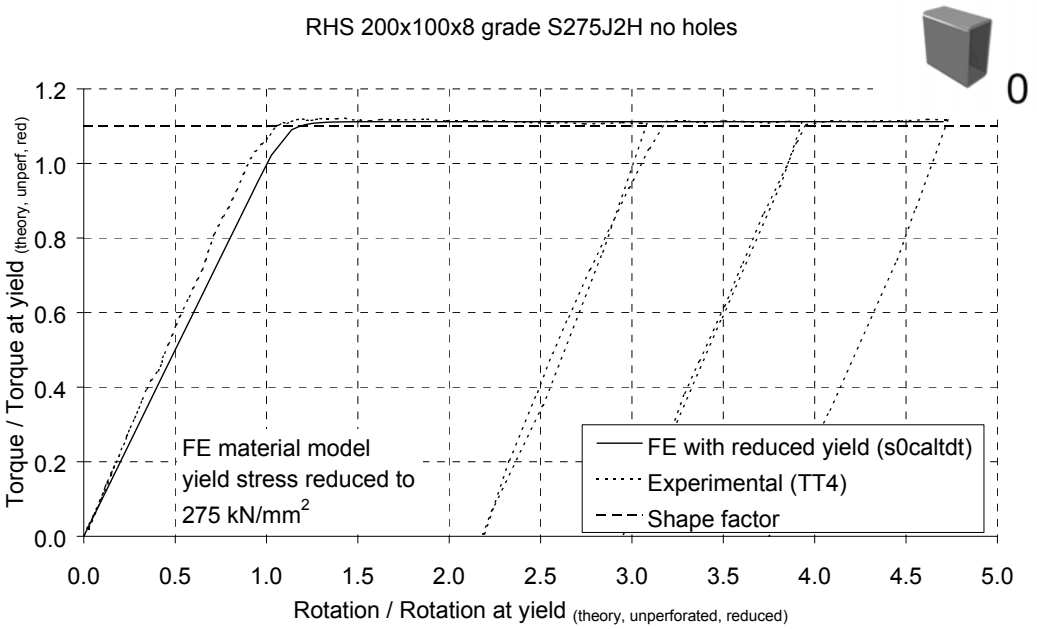

Figure 5-39: Reduced yield RHS 200x100x8 grade S275J2H no holes

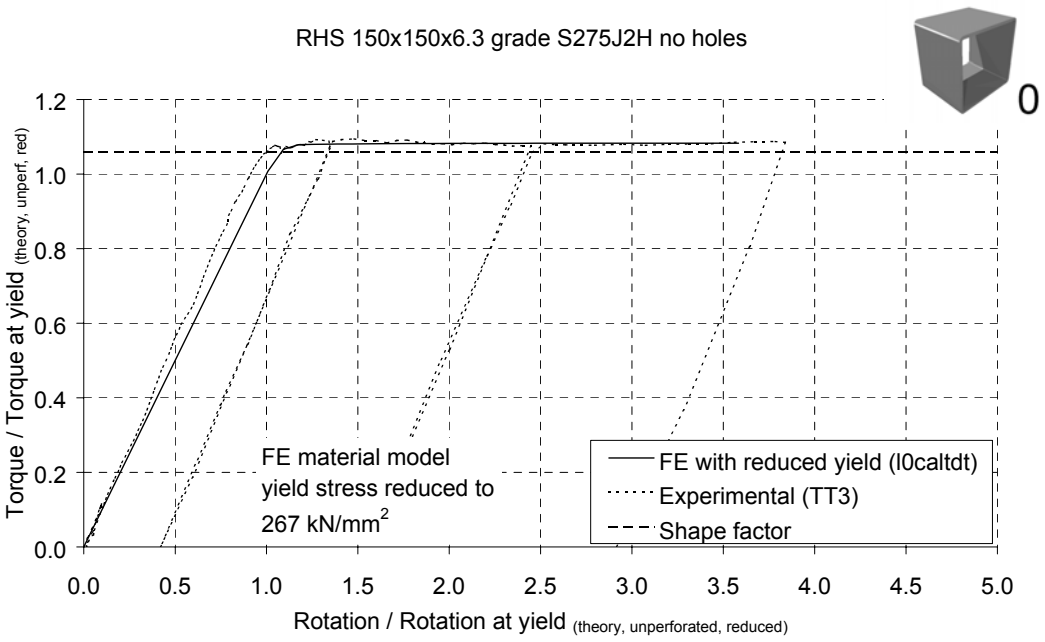

Figure 5-40: Reduced yield RHS 150x150x6.3 grade S275J2H no holes

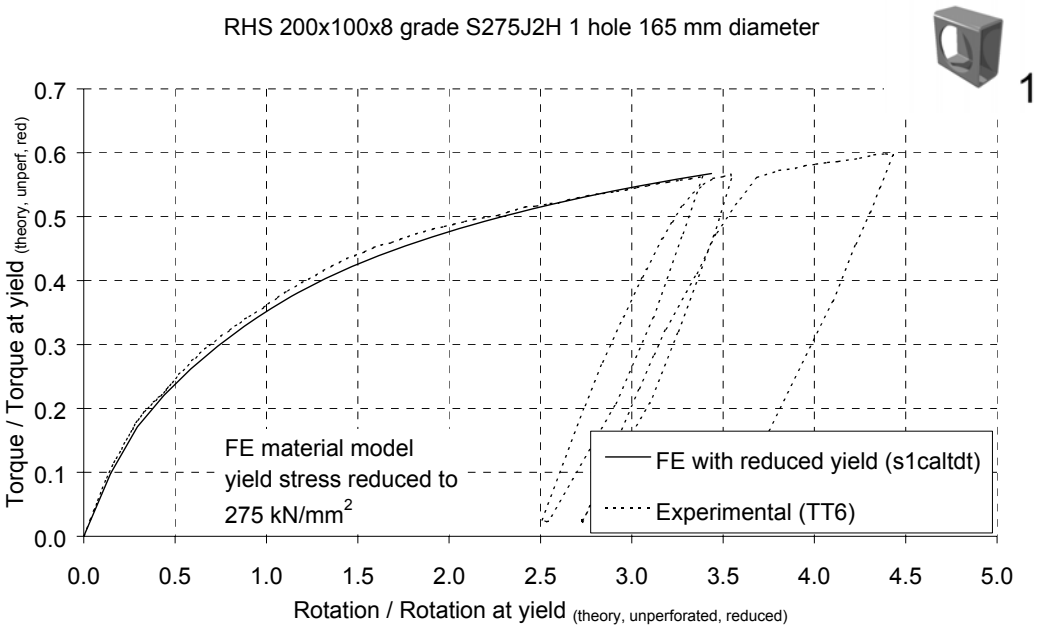

Figure 5-41: Reduced yield RHS 200x100x8 grade S275J2H one hole

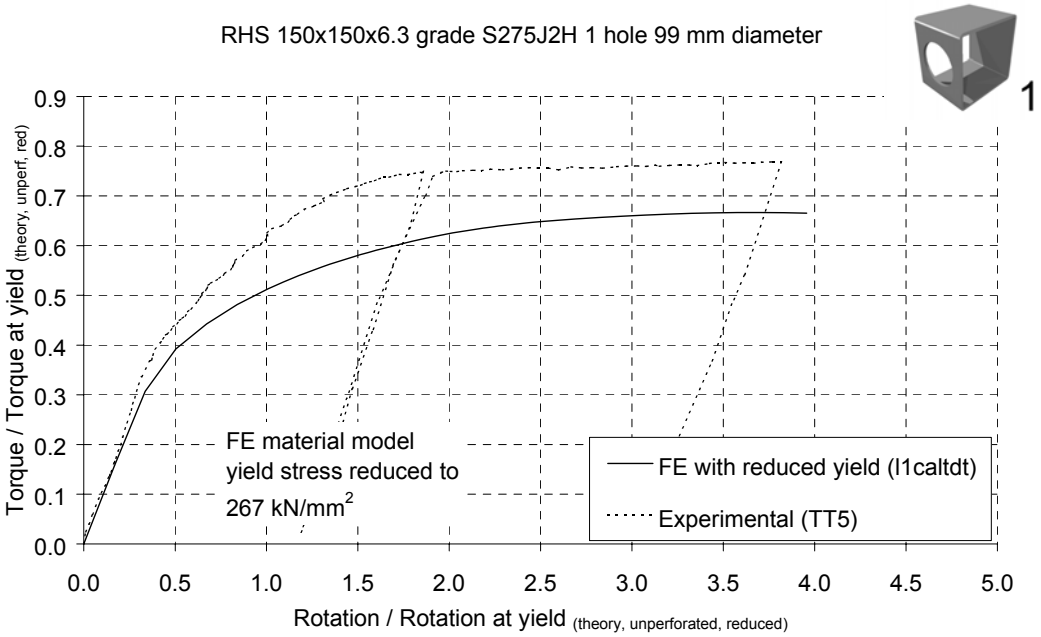

Figure 5-42: Reduced yield RHS 150x150x6.3 grade S275J2H one hole

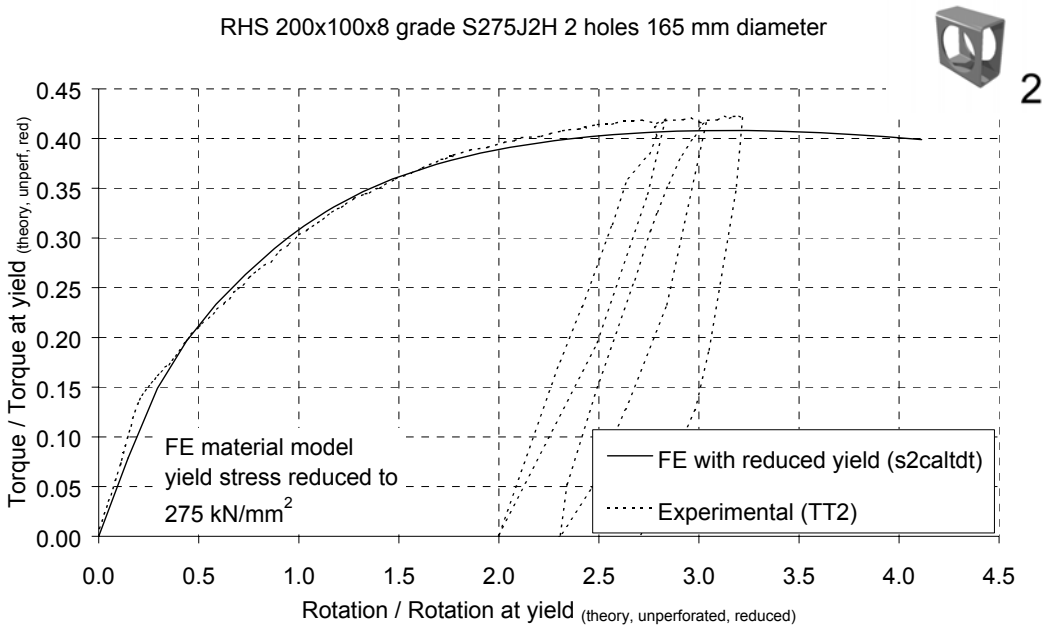

Figure 5-43: Reduced yield RHS 200x100x8 grade S275J2H two holes

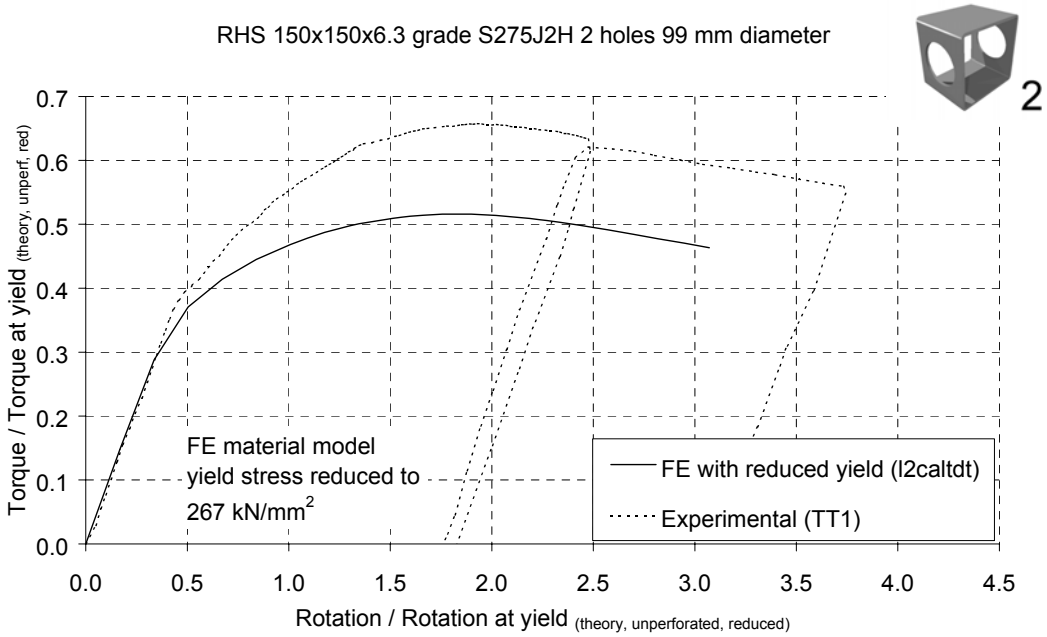

Figure 5-44: Reduced yield RHS 150x150x6.3 grade S275J2H two holes

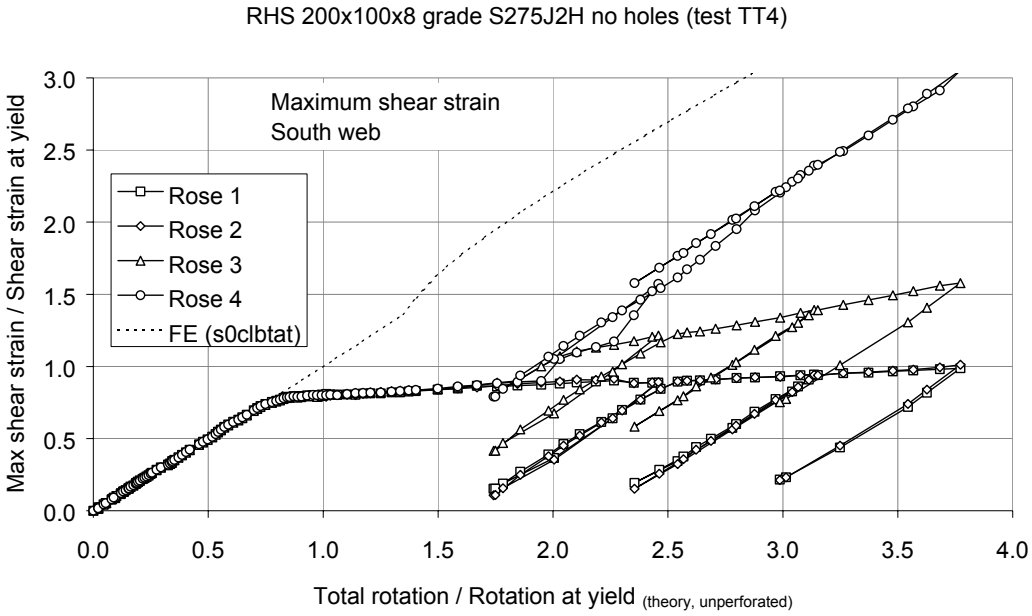

Figure 5-45: Strain measurements (test TT4 south web)

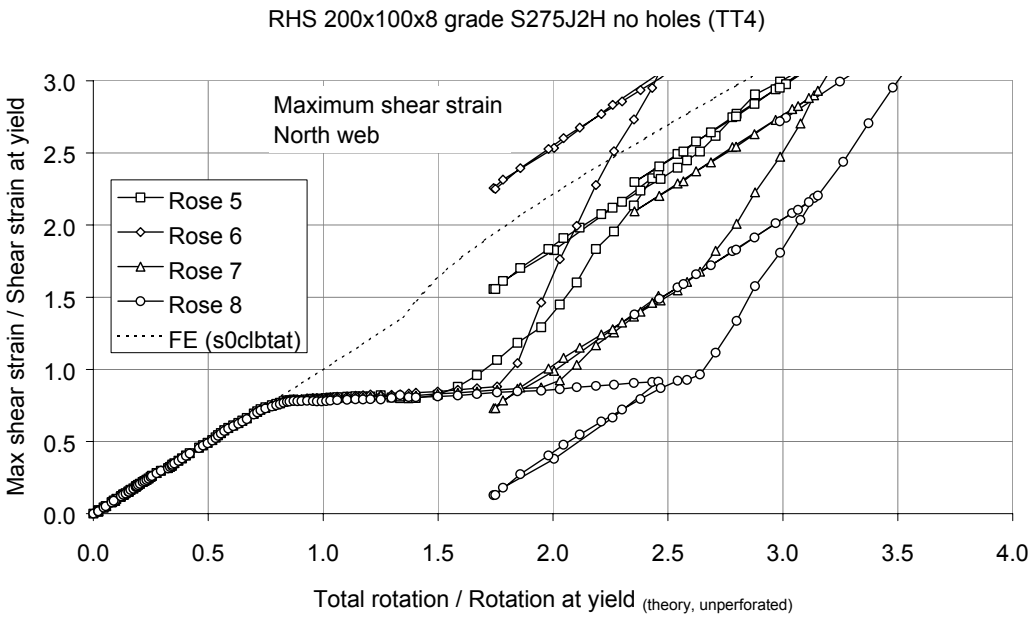

Figure 5-46: Strain measurements (test TT4 north web)

5.6.9 Marshall's results

Torsion tests on unperforated hot finished RHS, of sizes similar to those used in this study, were conducted by Marshall (1972), who compared the results to the predictions made by his thick wall torsion theory (Section 2.5.2). As is the case with the unperforated sections tested in this project, Marshall achieved good agreement between the theoretical predictions (of shear strain and torsional stiffness) in the elastic range and the experimentally measured values.

However, when Marshall compared his measurements of elastic and plastic torsional capacities, he chose to use the Tresca yield criterion rather than the von Mises criterion (Sections 2.5.4.2 and 2.5.5) in his theoretical calculations. As a result, his theoretical predictions of the torsional capacities were 15% lower than they would have been if he had used the von Mises criterion, which is widely regarded as the more appropriate criterion for such calculations. When Marshall's test data was re-examined, using the theoretical treatments employed to analyse torsional behaviour in this project, the results showed evidence of behaviour similar to that observed in the full-scale torsion testing component of this research.

The dimensions and material properties of Marshall's test specimens, as quoted in reference Marshall (1972), are listed in Table 5-11. The torsional constants, calculated from these dimensions, are listed in Table 5-12, and the theoretical torsional capacities (using the von Mises criterion) are listed in Table 5-13. Marshall's measurements of the torsional capacities are listed in Table 5-14, and compared with the theoretical predictions. The calculations indicate that the experimental measurements were up to 18% lower than the theoretical predictions, and typically 10% lower for the larger sections (Figure 5-47).

Table 5-11: Dimensions and material properties of Marshall's torsion test specimens

Test	Height h (mm)	Width b (mm)	Thickness t (mm)	Yield stress f_{y1} (N/mm2)	Young's modulus E (kN/mm2)	Poisson's ratio ν
A	50.8	50.8	4.9	307.3	211.6	0.29
B	63.5	63.5	4.9	307.3	211.6	0.29
C	76.2	76.2	4.9	432.4	211.6	0.29
D	101.6	101.6	6.4	307.3	211.6	0.29
E	101.6	101.6	4.1	307.3	211.6	0.29
F	127.0	50.8	6.4	307.3	211.6	0.29
G	76.2	38.1	4.1	307.3	211.6	0.29
H	76.2	50.8	3.3	307.3	211.6	0.29
I	101.6	50.8	3.3	307.3	211.6	0.29

Note: Data obtained from reference Marshall (1972)

Table 5-12: Properties of cross-section for Marshall's torsion test specimens

Test	Cross sectional area A (cm^2)	Torsional inertia constant I_t (cm^4)	Torsional modulus constant C_t (cm^3)
A	8.70	49.25	17.1
B	11.2	102.0	28.9
C	13.7	182.4	43.8
D	23.8	565.5	102
E	15.7	384.8	71.5
F	20.5	228.8	57.4
G	8.44	47.66	17.1
H	7.72	66.58	20.3
I	9.37	99.57	27.7

Note 1: Calculations based on data obtained from reference Marshall (1972)
Note 2: Calculations made using equations in BS EN 10210-2:1997 (Also in Appendix C)

Table 5-13: Theoretical plastic torque and torque at yield for Marshall's torsion tests

Test	Rotation at yield θ_{el} (°/m)	Torque at yield T_{el} (kNm)	Plastic torque T_{pl} (kNm)	Shape Factor for torsion T_{pl} / T_{el}
A	4.30	3.03	3.55	1.17
B	3.51	5.13	5.83	1.14
C	4.19	10.9	12.2	1.11
D	2.24	18.1	20.1	1.11
E	2.30	12.7	13.6	1.07
F	3.11	10.2	12.1	1.19
G	4.43	3.02	3.50	1.16
H	3.78	3.60	3.95	1.10
I	3.44	4.91	5.36	1.09

Note 1: Calculations based on data obtained from reference Marshall (1972)
Note 2: Calculations made using equations in BS EN 10210-2:1997 (Also in Appendix C)
Note 3: Plastic torque calculated using Equation 2-50

Table 5-14: Plastic torque and torque at yield measured by Marshall

Test	Marshall's measurements		Difference measured - theory	
	Torque at yield T_y (kNm)	Plastic torque T_{pl} (kNm)	Torque at yield (% of theory)	Plastic torque (% of theory)
A	2.78	3.67	-8.10	3.50
B	4.56	5.31	-11.2	-8.80
C	9.36	10.2	-14.3	-15.7
D	15.9	17.7	-11.9	-11.8
E	11.6	12.0	-8.20	-11.4
F	8.35	10.4	-18.0	-14.0
G	2.78	3.29	-8.00	-6.00
H	3.54	3.75	-1.70	-5.30
I	4.56	4.81	-7.20	-10.3

Note 1: Data obtained from reference Marshall (1972)
Note 2: A negative percentage indicates experimental values lower than theoretical values

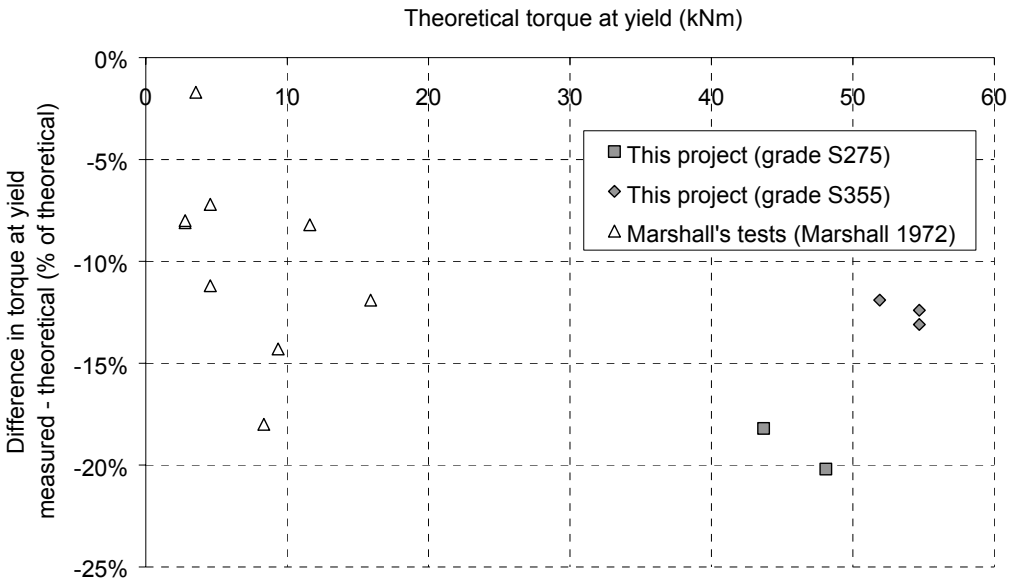

Figure 5-47: Measurements and predictions of torque at yield (unperforated)

5.6.10 Summary

Some torsional capacities measured in the laboratory were significantly lower than the theoretical and FE predictions. The validity of the experimental findings has been verified leading to the conclusion that there is some unknown aspect of behaviour, which is not included in the theoretical and FE models. One explanation (that appears to fit most of the available evidence) is that the steel does not always comply with the von Mises failure criterion. Evidence of similar behaviour is present in the results of full-scale testing of hot-finished RHS by Marshall (1972).

5.7 Suitable schemes for further investigation

Further experimental work is necessary if the differences between the experimental results, and the theoretical and FE predictions, are to be explained. The following schemes are suitable:

1) Additional torsion tests of unperforated tubes of different sizes and grades
2) Torsion tests of Circular Hollow Sections – to investigate the response of the steel to pure shear without the complications of shape
3) Torsion tests of cold formed or aluminium tubes – to investigate the torsional behaviour of box sections made from different materials
4) Additional shear testing of the remaining material – to investigate the variability of the shear yield stress (Section 2.5.4.3)

5.8 Concluding remarks

A series of 14 torsion tests were performed on two sizes and grades of RHS with and without circular openings. For each test, the torque and twist were measured. In half the tests, strains on the external surface of the RHS were also measured.

When the experimental results were compared with FE predictions, good matches were observed in terms of displaced shapes, elastic stiffness and strains in the elastic range. Torque-rotation relationships and torsional resistances matched FE predictions for some cases, but were significantly different in others. The largest difference occurred for the unperforated sections where the best agreement was anticipated.

The experimental measurements were re-examined and found to be valid. One explanation for the differences between measured and predicted behaviour, that fits most of the available evidence, is that the steel did not always comply with the von Mises failure criterion. Attempts were made to measure this effect, but without success (Section 2.5.4.3).

Although the anomalous results have not been fully explained, evidence of similar behaviour in previous full-scale tests, conducted by Marshall (1972), was discovered. Paradoxically, the torsional capacities measured by the small-scale torsion tests, discussed in the following Chapter, agree extremely well with the predictions of FE and theory.

6 Small-scale torsion

6.1 Introduction

The full-scale torsion tests described in the previous Chapter required the preparation of large and expensive testing equipment, with consequent time penalties. The availability of a small-scale torsion testing machine (Figure 6-1), used usually for undergraduate teaching, enabled an extensive series of tests to be carried out during the preliminary stages of the project.

The small-scale study indicated some notable similarities and differences when compared to the behaviour observed in the full-scale torsion study (Chapter 5). In addition to providing valuable insights into the nature of torsional behaviour at both scales, it acted as an additional source of experimental data for calibration of the Finite Element (FE) models. The small-scale torsion study was presented in a conference paper (Ridley-Ellis et al (1998)) shortly after it was conducted. However, this Chapter contains substantial additional discussion and analysis, which extends the published research.

In the small-scale torsion testing series, a large number of tests on cold-formed steel tube in torsion revealed the effects of various arrangements of circular cut-outs on torsional capacity and modes of failure. The tests provided an understanding of how the diameter of the circular openings can influence both torsional resistance and stiffness. Comparison of the experimental results with FE predictions indicated good agreement over the whole range of hole diameters.

6.2 A description of the apparatus and testing procedure

6.2.1 The torsion test apparatus and specimens

The small-scale torsion tests were conducted on lengths of square section cold-formed steel tube, the dimensions of which are shown in Figure 6-2. The cross-section of the tube was close to being geometrically similar to the RHS 250x250x10 used in the three and four-point testing programmes (Chapters 3 and 4) and the RHS 150x150x6.3 used in the full-scale torsion study (Chapter 5). The small tube had a web slenderness of 23.6 compared with 22.0 for the RHS 250x250x10 and 20.8 for the RHS 150x150x6.3. The specimens were 300 mm in length, but were restrained at the ends by solid metal inserts and stiff clamping plates (Figure 6-2 and Figure 6-3). The inserts provided connectivity with the testing rig (Figure 6-1).

In all the tests described in this Chapter, the length of the portion of the specimen that was free to twist under load was 240 mm. A number of sections of different lengths, but without holes, were also tested as part of an exercise to determine the stiffness of the testing machine (Appendix A). In all cases, the torque (T) was applied at a constant rate of twist ($3^1/_3$ degrees per minute).

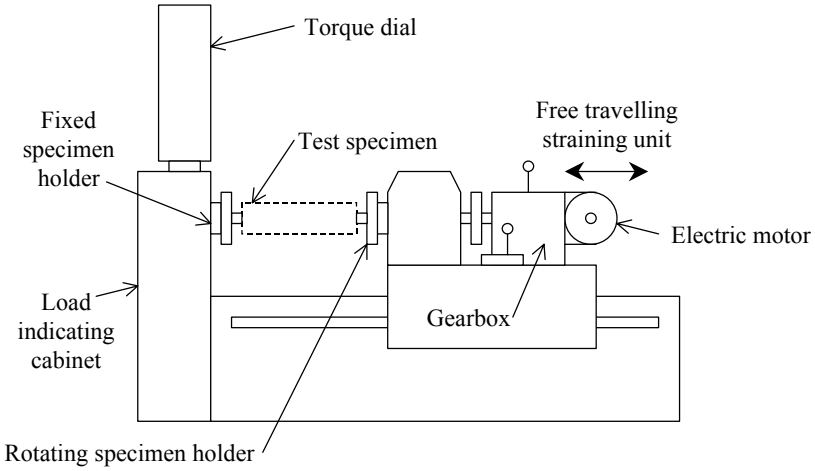

Figure 6-1: The small-scale torsion rig

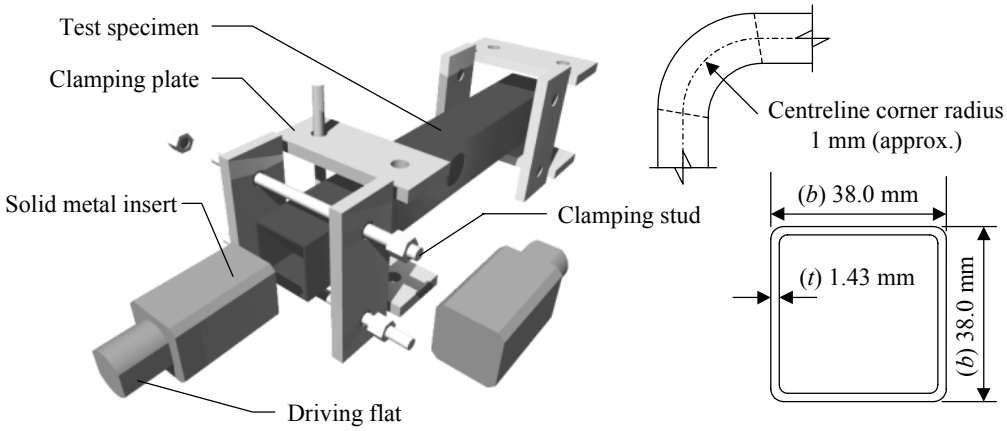

Figure 6-2: Small-scale torsion test specimen

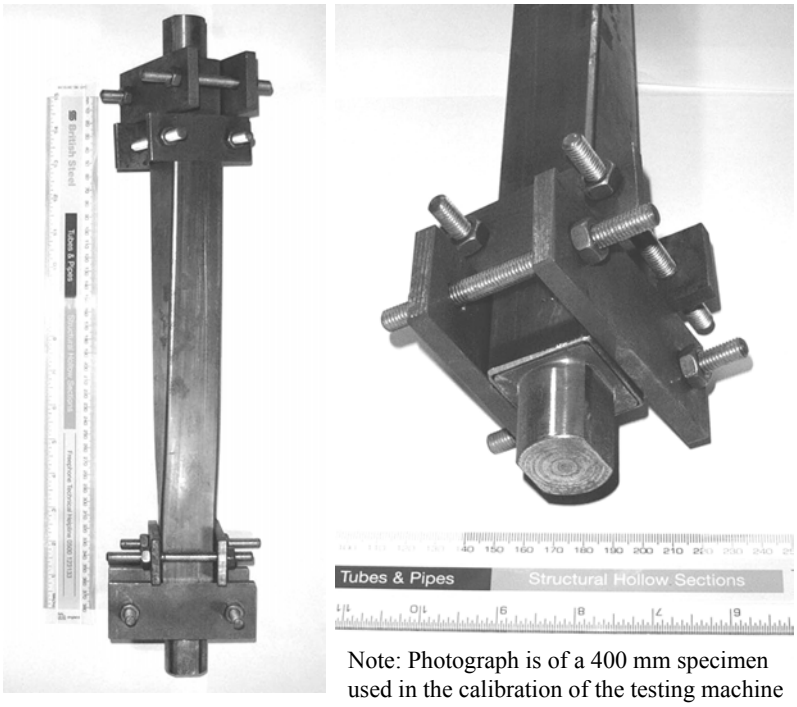

Note: Photograph is of a 400 mm specimen used in the calibration of the testing machine

Figure 6-3: The inserts and clamping plates

6.2.2 Types of specimen and scope of study

The test specimens were classified according to the number and position of holes. Figure 6-4 shows the types of test pieces. The figure shows all four faces of the tube as if it was opened out; the dotted lines represent the corners and the tube is such that the lines labelled AB coincide. Table 6-1 is a summary of the dimensions of the specimens tested.

Specimens of type I formed the control group. They had no holes and their torsional resistance and stiffness could therefore be predicted by established formulae (Section 2.5). The behaviour of the specimens with web openings was compared directly with the behaviour of the control group to quantify the influence of the hole(s).

Specimens of type II had a single circular hole. The diameter (D) varied, but the hole was always placed centrally in one face. Specimens of type III had two circular holes. The diameter varied, but the holes were always placed centrally in opposing faces. Specimens of type IV had two circular holes. The holes are placed symmetrically in the same face at a series of different separations (s).

The material properties of the test pieces were determined from direct tensile testing of coupons cut from the walls of the tube. Tensile test piece dimensions were specified in accordance with BS EN 10002–1:1990. The results of the materials tests are shown in Figure 6-5. The torsion specimens were cut from one of three bars, with similar material properties. Material models for FE calibration were based on the coupon results for the corresponding bar (Table 6-2).

The dimensions of the tube are listed in Table 6-3 and the properties of the cross-section are listed in Table 6-4. Sectional properties based on the average material properties of the three bars are listed in Table 6-5. Sectional properties were calculated using the formulae in BS EN 10210 (Appendix C) with the exception of plastic torque, which was calculated from Equation 2-50.

The nature of the stress-strain relationship for the cold-formed steel meant that unperforated specimens were able to generate a maximum torque significantly higher (23%) than the theoretical plastic torque. The cold-formed steel exhibited two regions of strain hardening. The first region consisted of a rapid gain in stress immediately following the yield point, in contrast to the very long flat yield plateau in the hot finished RHS (Figure 6-6). The second, more gradual, strain hardening region was much shorter than the strain hardening region for the hot finished RHS. The tensile strength (engineering stress) was reached at 4% strain in contrast to 16% strain for the hot finished RHS. The strains generated in the small and full-scale

torsion tests were of similar magnitude, but the relatively rapid and early onset of strain hardening in the cold-formed tube meant that strain hardening played a much more significant role in the small-scale tests. Table 6-5 contains a theoretical estimate of the maximum torque based on a plastic shear stress flow equivalent to the 0.5% proof stress. The theoretical maximum torque (T_{max}) was calculated using Equation 2-50 substituting the 0.5% proof stress for the yield stress.

Table 6-1: Specimens tested

Type	Number of specimens tested	Hole diameter			Hole separation	
		Diameter D (mm)	Hole size ratio, Φ	D/h (%)	Separation s (mm)	s/D (%)
I	6	-	-	-	-	-
II	2	5	0.15	13.1	-	-
	2	10	0.30	26.3	-	-
	2	15	0.44	39.5	-	-
	2	20	0.59	52.6	-	-
	2	25	0.74	65.8	-	-
	2	30	0.89	78.9	-	-
III	2	5	0.15	13.1	-	-
	2	10	0.30	26.3	-	-
	2	15	0.44	39.5	-	-
	2	20	0.59	52.6	-	-
	2	25	0.74	65.8	-	-
	2	30	0.89	78.9	-	-
IV	1	20	0.59	52.6	5	25
	1	20	0.59	52.6	10	50
	1	20	0.59	52.6	15	75
	1	20	0.59	52.6	20	100
	1	20	0.59	52.6	25	125

Note: The hole size ratio (Φ) is the ratio of the hole diameter to h-3t (refer to Figure 1-9)

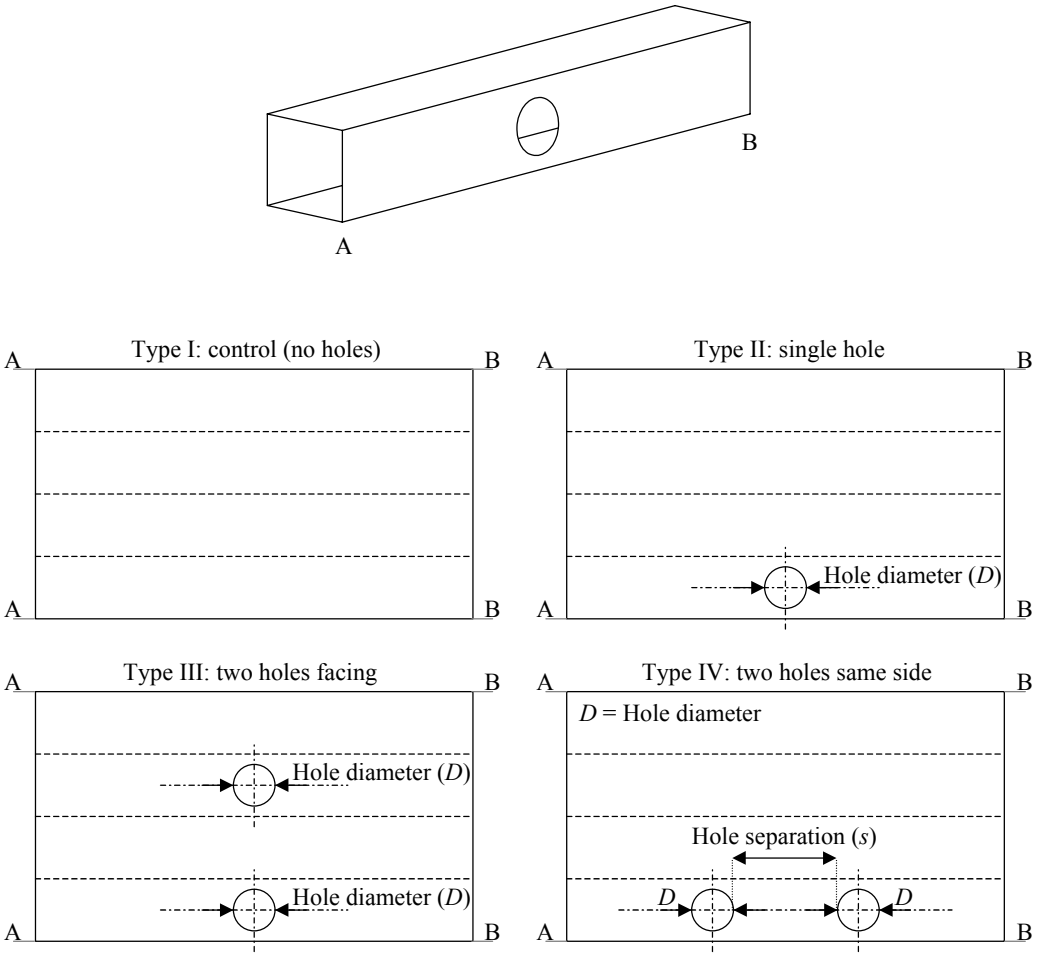

Figure 6-4: Types of specimen (developed views)

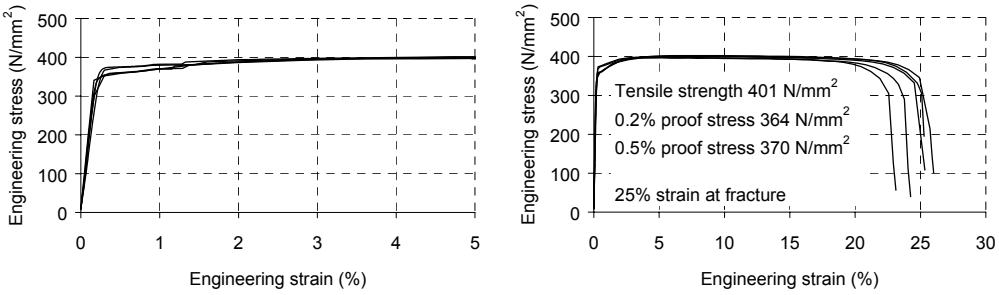

Figure 6-5: Stress-strain relationship from tensile tests

Table 6-2: ABAQUS material models for cold-formed tube

Bar 1		Bar 2		Bar 3	
*ELASTIC		*ELASTIC		*ELASTIC	
169902.2 ,	0.3	197231.9 ,	0.3	181362.6 ,	0.3
*PLASTIC		*PLASTIC		*PLASTIC	
305.55 ,	0	305.47 ,	0	291.76 ,	0
350.82 ,	0.000282	340.61 ,	0.000071	332.15 ,	0.000256
371.11 ,	0.000811	350.70 ,	0.000220	353.16 ,	0.001008
375.38 ,	0.001484	357.07 ,	0.001185	387.02 ,	0.012055
393.82 ,	0.012571	387.73 ,	0.012923	407.00 ,	0.027315
404.88 ,	0.022310	404.52 ,	0.025564	422.20 ,	0.050426
411.41 ,	0.031980	420.53 ,	0.046658	440.55 ,	0.092881
451.95 ,	0.137102	457.70 ,	0.137441	457.70 ,	0.137238

Note: Refer to Sections 2.2.5 & 2.3.7

Table 6-3: Dimensions of cross-section (measured)

Section	Height	Width	Thickness	Corner radius (mm)	
	h (mm)	b (mm)	t (mm)	Internal	External
Cold formed tube	38.0	38.0	1.43	0.3	1.7

Table 6-4: Properties of cross-section (from measured dimensions)

Section	Cross-sectional area, A (cm^2)	Torsional inertia constant, I_t (cm^4)	Torsional modulus constant, C_t (cm^3)
Cold formed tube	2.07	7.082	3.56

Table 6-5: Sectional properties (measured dims and material props, theoretical)

Section	Rotation at yield, θ_{el} (^{o}/m)	Torque at yield, T_{el} (kNm)	Plastic torque, T_{pl} (kNm)	Shape factor for torsion T_{pl} / T_{el}	Maximum torque, T_{max} (kNm)
Cold formed tube	7.13	0.618	0.657	1.06	0.807

Note: Maximum torque is plastic torque based on 0.5% proof stress rather than yield

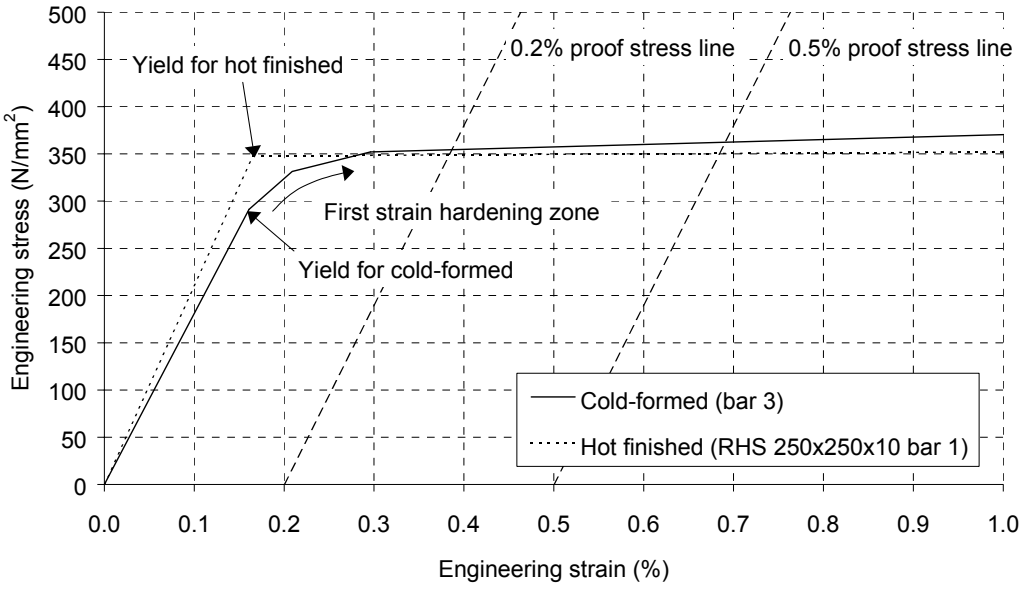

Figure 6-6: Stress-strain relationship for cold-formed and hot finished steel (1%)

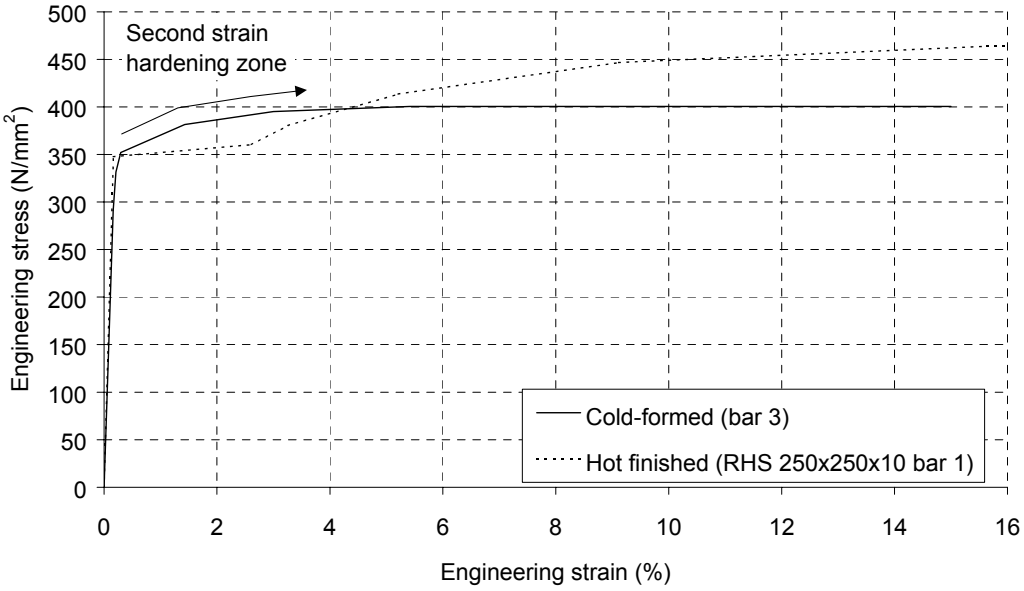

Figure 6-7: Stress-strain relationship for cold-formed and hot finished steel

6.3 The experimental results

6.3.1 Measured torque-rotation relationships

The measured torque-rotation histories for the one and two hole specimens (type II and type III) are shown in Figure 6-8 and Figure 6-9. In the figures, the torque is non-dimensionalised against the theoretical torque at yield of the unperforated tube (T_{el}), and rotation is non-dimensionalised against the theoretical rotation at yield (θ_{el}). The theoretical maximum torque (T_{max}) is also plotted.

These two figures also include the torque-rotation histories for the control specimens (type I). The initial elastic behaviour is followed by extensive plastic deformation (10 to 15 times the elastic rotation). The plastic deformation shows marginally positive stiffness that is associated with strain hardening and the effects of large deflection. This is followed by a significant drop in torque, associated with large out-of-plane distortion of the walls near the ends of the tube adjacent to the ends of the metal inserts. Although the full cross-section was observed to reach the yield stress, the sections failed by buckling before the full strain hardened tensile strength observed in the coupon tests could develop.

Figure 6-8 also shows the behaviour of specimens with single holes (type II). The effect of the diameter of the hole was seen to be important: small holes had little effect on the overall resistance but decreased the extent of plastic behaviour. However, for larger holes (Φ greater than 0.3) the reduction in resistance was seen to be significant. For large holes, the subsequent negative stiffness, associated with collapse at the location of the opening, was seen to be reduced, and hardly existed for Φ greater than 0.7.

The onset of non-linearity was seen to be more pronounced in the specimens with larger holes. As in the full-scale torsion tests (Chapter 5), this is due to stress concentrations and rotational displacements that were concentrated over a short length around the hole. It was not possible to identify the point at which permanent damage first occurred from the experimental results alone, but the FE study (Section 6.4) was used examine the distribution of stress indirectly.

The web openings reduced the initial stiffness of the section, although the reduction was less pronounced for a hole of small diameter than for one of large diameter. The stiffness described here is an average value, since the rotation is measured over the full 240 mm length of the specimen.

Figure 6-9 shows the torque-rotation histories for the control specimens (type I) and the specimens with two holes facing (type III). As in the full-scale torsion testing study (Chapter 5), the results showed the double holes influencing torsional performance in a similar way to the single holes. A double hole was found to have a similar effect to that of a single hole of equal diameter (Figure 6-10). However, the negative stiffness effect as shown in Figure 6-9 remained strong for all the specimens tested compared with the single sided holes shown in Figure 6-8.

The complete torque-rotation relationship for type IV specimens (two holes in the same side) is shown in Figure 6-11. Figure 6-12 shows how the distance between the holes affected the peak torque. For large separations the capacity was similar to that of a specimen with a single hole of equal diameter. For smaller separations, interaction between the holes resulted in a reduction in capacity. Type IV specimens also show a greater rotation before the peak torque was reached and reduced subsequent negative stiffness, as the distortion was shared between the two openings.

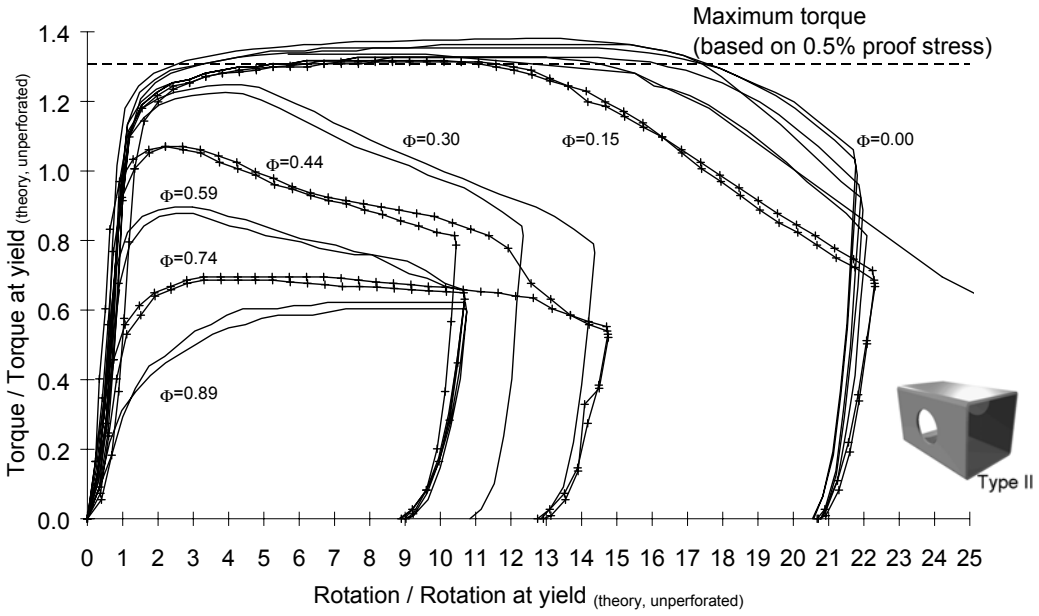

Figure 6-8: Torque rotation curves – One hole (Type II)

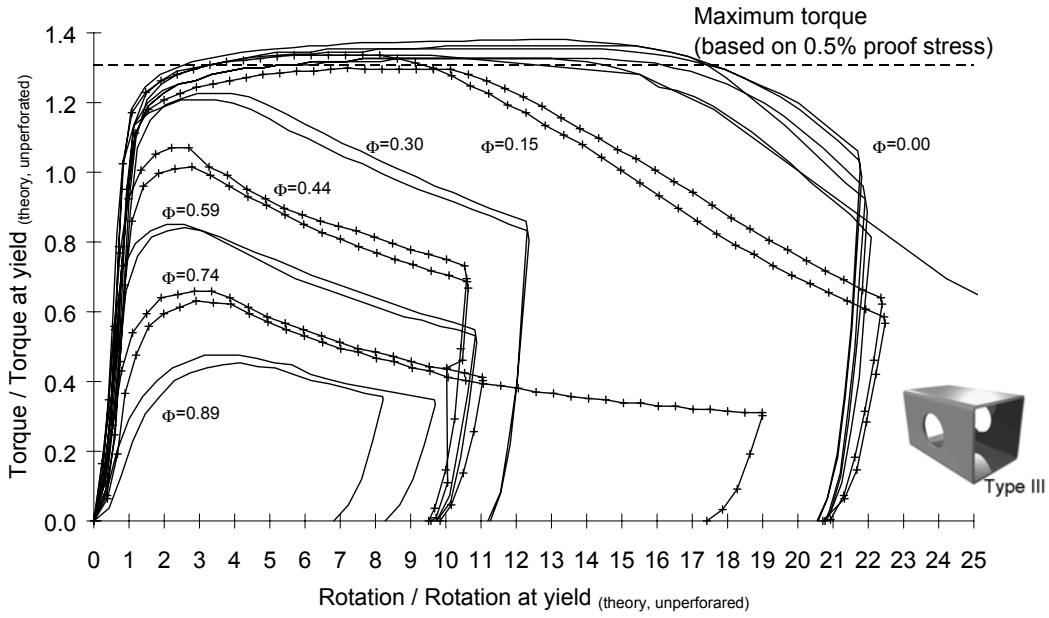

Figure 6-9: Torque rotation curves – Two holes facing (Type III)

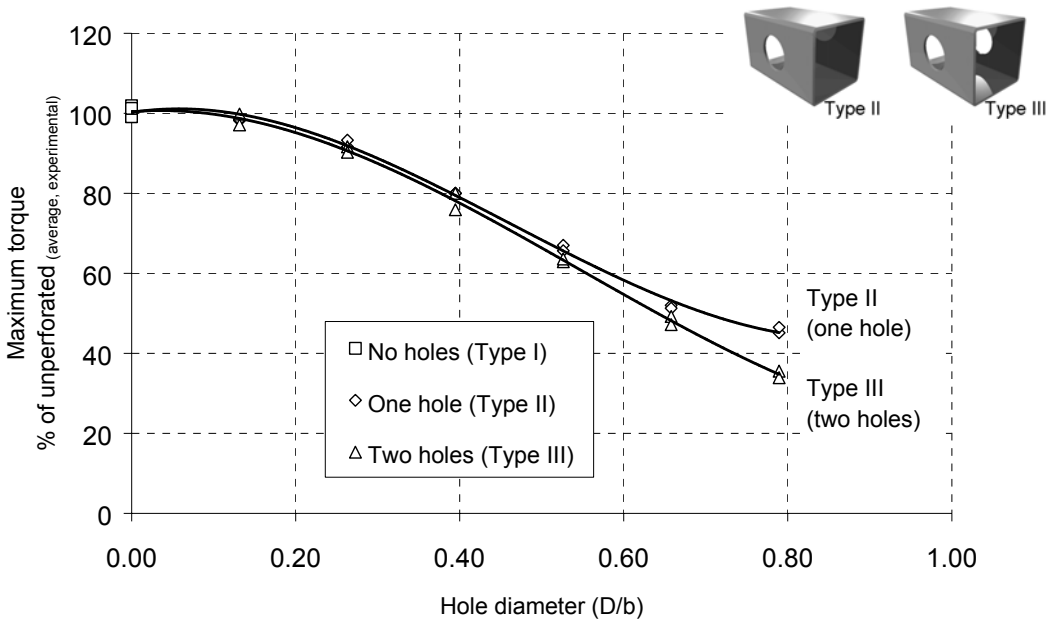

Figure 6-10: Peak torque and hole diameter – Types I, II & III

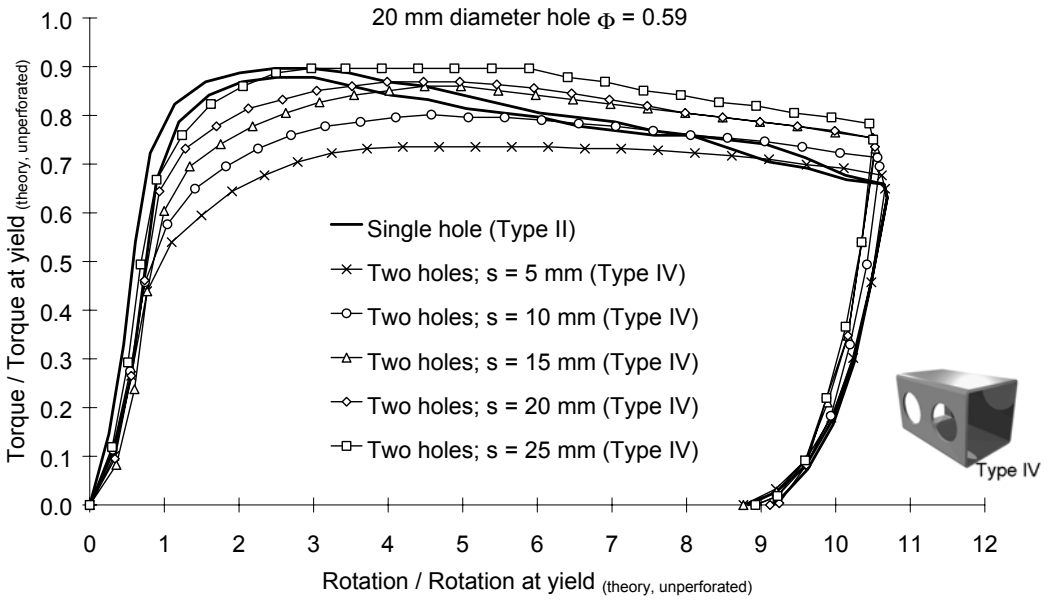

Figure 6-11: Torque-rotation curves for type IV specimens

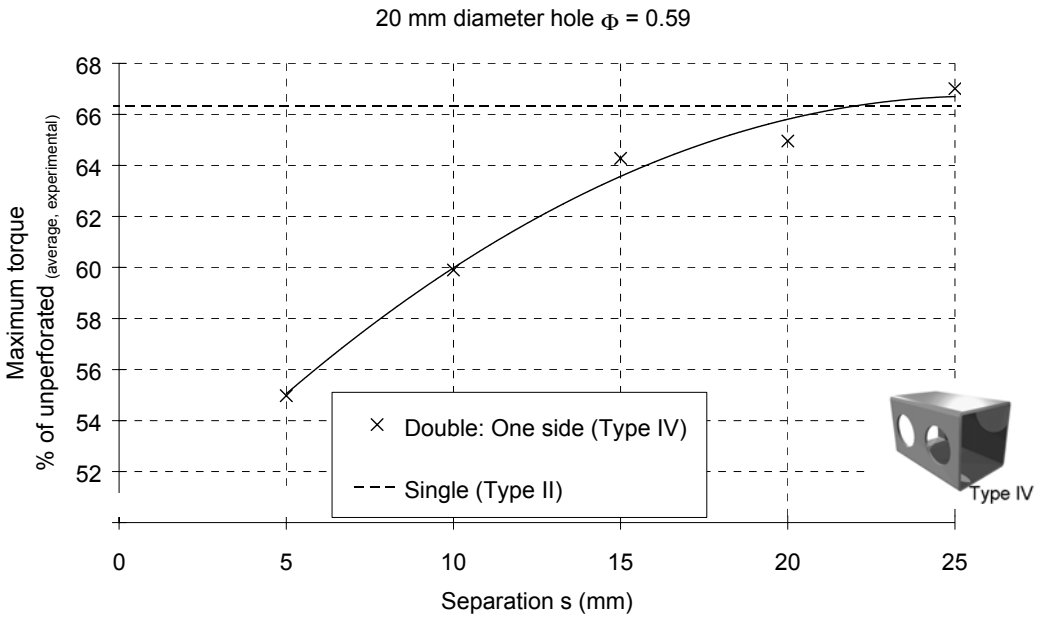

Figure 6-12: Peak torque and hole separation (Type IV)

6.3.2 Mechanisms of failure

The specimens all failed in one of two ways: either a local end failure after global plastic strain, or a local failure in the region of the hole due to the weakening influence of the perforation.

The failure of the stronger sections (those without holes or with Φ less than 0.2) was accompanied by the formation of a buckle on each of the four faces at 45^{o} to the longitudinal axis of the section as shown in Figure 6-13. Sections with larger holes failed in the region of the hole in the manner shown in Figure 6-14 (Type II) & Figure 6-15 (Type III). The failure mode of the type IV specimens is shown in Figure 6-16.

Figure 6-13 shows local failure initiated adjacent to the metal insert and clamp. Plastic strain occurred along the whole length of the specimens that failed in this manner indicating that such sections had developed the full plastic (non-strain-hardened) torsional capacity prior to the formation of the buckle.

In type II specimens (unsymmetrical) most of the rotation took place in the region of the hole and was about an axis parallel to, but offset from the longitudinal axis of the section. The face opposite the perforation remained essentially plane, which resulted in bending of the section. It was observed that the unsymmetrical mode of failure caused the cross-section to lozenge (Figure 6-14).

In type III specimens (symmetrical, two holes facing. Figure 6-15) the rotation took place about the longitudinal axis of the section, and there was no bending or lozenging effect.

The mode of failure for type IV specimens seen in Figure 6-16 strongly resembles that of the type II specimens, but with a shearing of the material between the holes. Initial plastic deformation was observed to occur at equal rates at both holes before the diagonal inward buckles formed around the (marginally) weaker of the two cut-outs.

A feature common to all the modes of failure in the local region around the hole was the sudden change in curvature at the distorted corners of the section marked with an asterisk in the Figures. This zone was associated with the high tensile stresses that developed around the hole (Figure 6-17). Necking and even tearing could be seen in this region in the specimens with larger holes.

The test showed that web openings could have a profound effect on the torsional performance of the specimens. They also showed failure by several different mechanisms depending on the number, diameter and position of the holes.

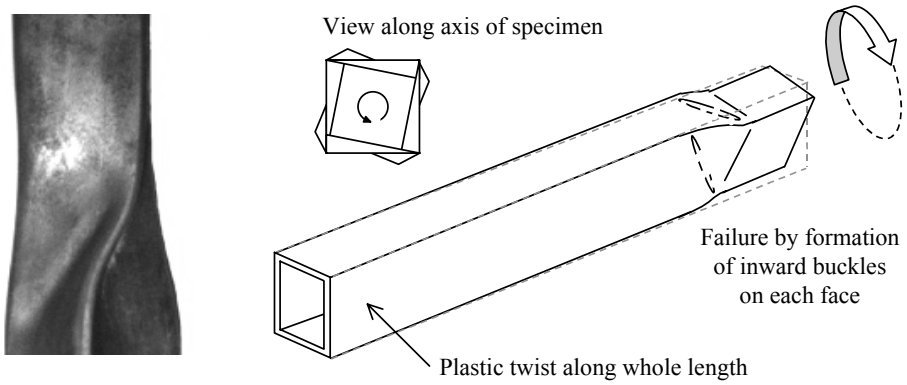

Figure 6-13: Post-yield failure by buckling

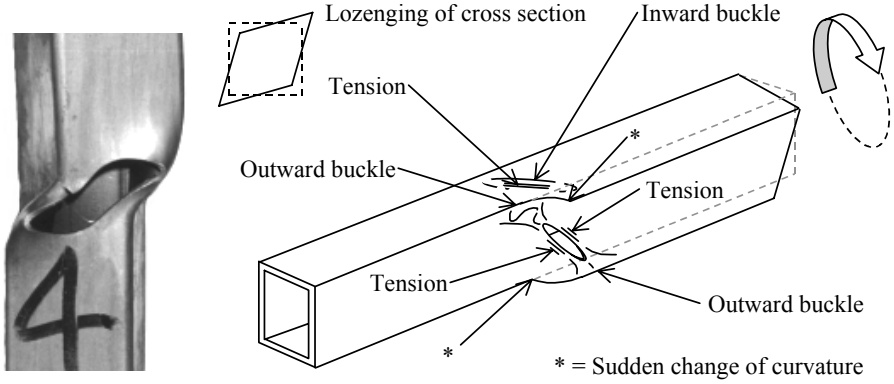

Figure 6-14: Failure of type II specimens

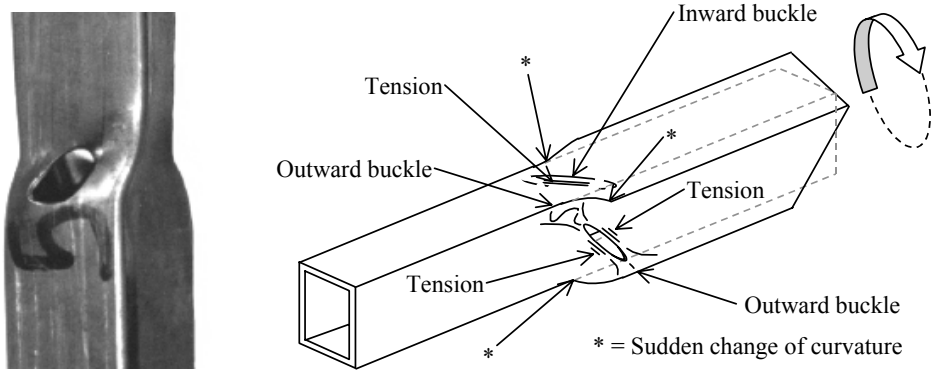

Figure 6-15: Failure of type III specimens

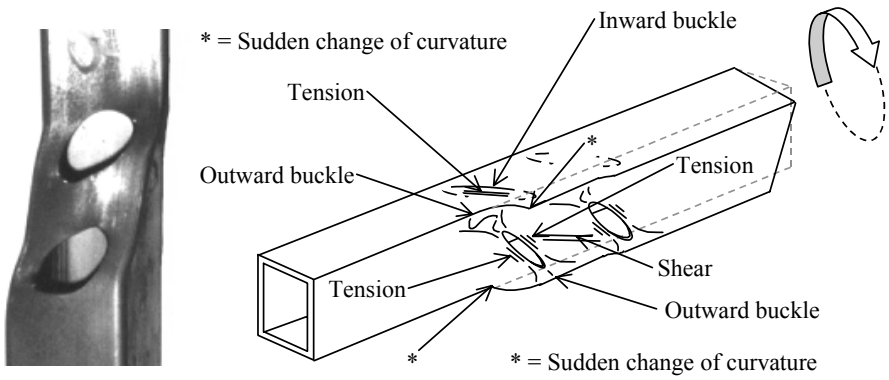

Figure 6-16: Failure of type IV specimens

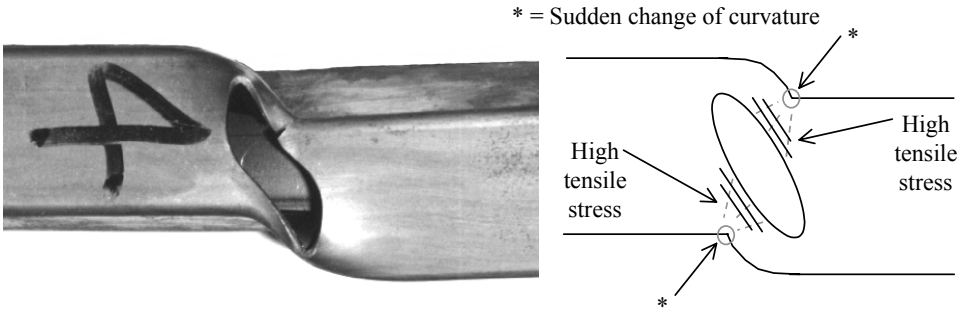

Figure 6-17: Regions of high tensile stress around the hole

6.4 A comparison of experimental results and analytical predictions

6.4.1 Introduction

The laboratory tests were modelled using the ABAQUS v5.8.1 FEA program (Section 2.3). Models included both material and geometric non-linearity and contained between 3100 and 5900 four-noded shell elements (S4R). The FE models were based on the actual measured dimensions of the test specimens and included the corner radii of the tube. The support conditions and were modelled by defining constraint equations to describe the permitted displacements in the nodal degrees of freedom. Type IV specimens were not included in the analytical modelling.

The Finite Element models were calibrated against the experimental observations by comparing torque-rotation histories (torsional stiffness and capacity) and deformed shapes. In some instances, additional features of the failure mechanism could be identified such as localised high tensile stress (evident as visible local tensile failure of the material).

6.4.2 Deformed shapes

The deformed shapes obtained from the FE models match closely those observed during the laboratory testing (Figure 6-18 through Figure 6-22 are typical).

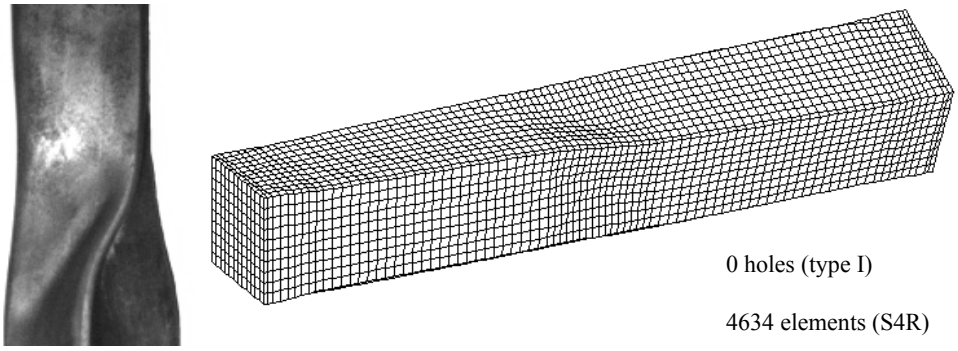

Figure 6-18: Displaced shape (type I)

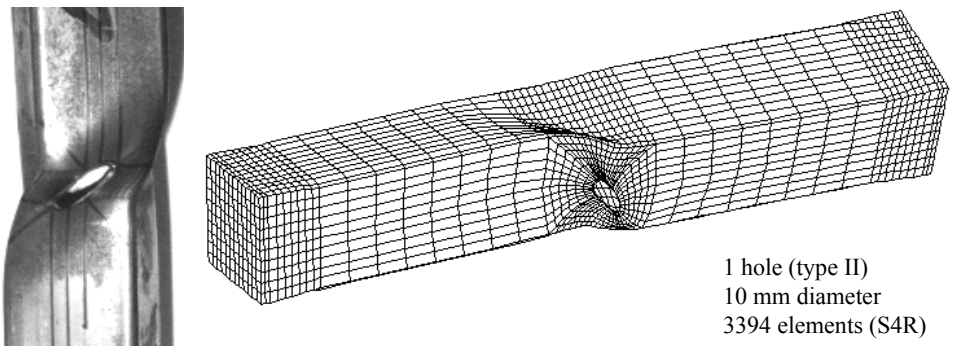

Figure 6-19: Displaced shape (type II 10 mm dia)

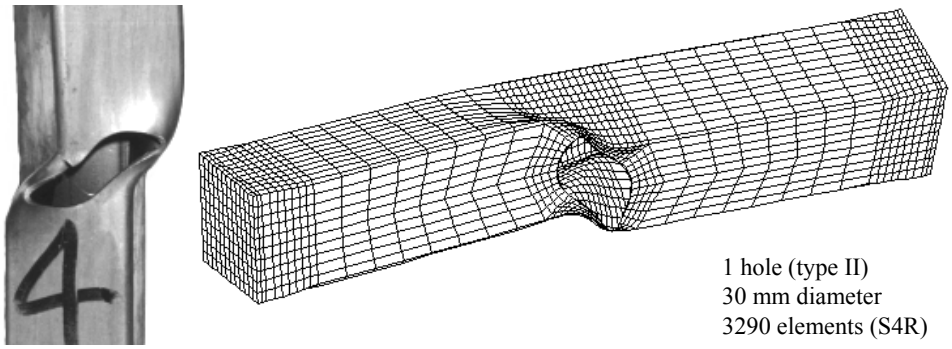

Figure 6-20: Displaced shape (type II 30 mm dia)

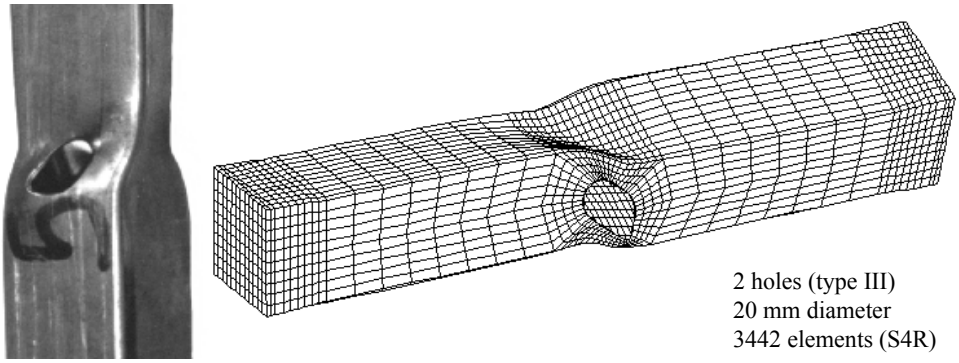

Figure 6-21: Displaced shape (type III 20 mm dia)

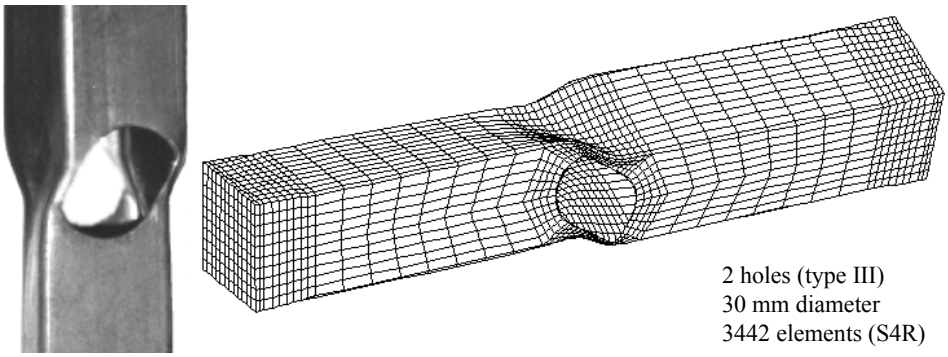

Figure 6-22: Displaced shape (type III 30 mm dia)

6.4.3 Torque-rotation relationships

The maximum torques predicted by the FE models and those measured in the tests are listed in Table 6-6. The agreement between the FE predictions and the measured values is extremely good with a maximum difference of only 3%, with FE tending to under-predict the maximum torque in most cases. The good agreement is true for the entire torque-rotation relationship (Figure 6-23, Figure 6-24 and Figure 6-25) with FE correctly modelling the onset of non-linearity, the maximum torque and the plastic collapse. The largest difference occurred for the plastic collapse of the unperforated specimens, which was particularly sensitive to the mesh density.

The correct prediction of the torque at yield and maximum torque for the unperforated specimens and the specimens with small holes is in direct contrast to the poor agreement obtained at full-scale (Section 5.5)

The initial elastic stiffnesses were difficult to measure accurately in the laboratory due to limitations of the testing method, but the FE models were used to obtain indirect measures (Table 6-7). The reduction in stiffness is slight for small holes, but becomes important for holes larger than $\Phi = 0.44$. Sections with two holes are less stiff than sections with a single hole of corresponding diameter.

The FE predictions of elastic stiffness are significantly lower (up to 50%) than the experimentally measured values. This is partly due to the low values of Young's modulus used in the FE material models. Young's modulus is difficult to measure accurately using a tensile test, particularly when the coupons are very thin. Although the tensile tests indicated values of Young's modulus in the order of 180 kN/mm^2, when the deflection of a 5.5 m span of the cold-formed tube was measured in bending tests, the Young's modulus was calculated to be 214 kN/mm^2. In the

absence of the opportunity to obtain more reliable material property data, the tensile test results (with low E values) were used in the theoretical and FE models.

The boundary conditions in the FE models were found to be important for unsymmetrical cases. Figure 6-26 shows how, for a single hole diameter, three FE models can give very different results depending on the boundary conditions at the ends of the specimen. When the boundary conditions are fixed in both transverse directions at both ends (labelled 'fixed'), the specimen is able to reach a higher value of peak torque than if the boundary conditions are pinned (labelled 'pinned'). Fixed boundary conditions resist the tendency of the unsymmetrical specimens to bend at high twist. Their influence is more significant for the small-scale specimens than the full-scale torsion specimens (Section 5.6.8) because the values of twist are higher and the specimens are shorter (in relation to section depth). The true condition is that each end is pinned in one transverse direction and fixed in the other and that the pinned axes at each end are perpendicular (labelled 'cross-pinned'). This condition represents the experimental situation, where the driving flats on each specimen were initially mutually perpendicular (to prevent accidental transmission of bending to the specimen). The cross-pinned condition reaches a maximum torque between that of the pinned and fixed cases, but is able to maintain the torque with increasing twist.

Table 6-6: Maximum torque (average experimental and FE)

Type	Number of specimens tested	Hole diameter		Maximum torque		
		D (mm)	Φ	Av exp (% of T_{max})	FE (% of T_{max})	Difference (%)
I (control)	6	-	-	102.7	104.3	1.52
II	2	5	0.15	100.6	101.5	0.84
(one hole)	2	10	0.30	94.60	94.90	0.30
	2	15	0.44	81.87	83.61	1.75
	2	20	0.59	67.87	67.76	-0.12
	2	25	0.74	52.83	52.58	-0.25
	2	30	0.89	46.88	45.04	-1.84
III	2	5	0.15	100.76	99.48	-1.28
(two holes)	2	10	0.30	93.06	90.13	-2.94
	2	15	0.44	79.77	79.23	-0.53
	2	20	0.59	64.72	63.05	-1.67
	2	25	0.74	49.33	47.45	-1.88
	2	30	0.89	35.55	33.75	-1.80

Note: T_{max} is the theoretical capacity of the unperforated section (Table 6-5)

Table 6-7: Elastic stiffness from Finite Element (average over 240 mm length)

	Finite Element elastic stiffness (% of theory unperforated)								
Hole diameter (mm)	0	1	2	5	10	15	20	25	30
Hole size ratio, Φ	0	0.03	0.06	0.15	0.30	0.44	0.59	0.74	0.89
No holes (type I)	98.18	-	-	-	-	-	-	-	-
Ono hole (type II)	-	98.17	98.15	98.02	97.41	96.02	93.10	86.68	65.15
Two holes (type III)	-	98.17	98.13	97.84	96.63	93.92	88.50	77.49	56.12

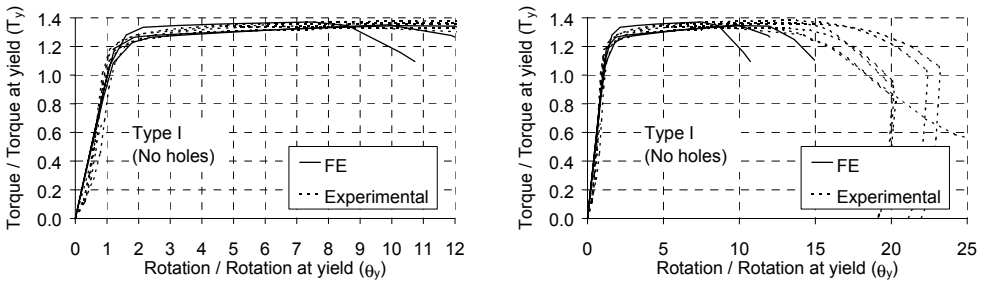

Figure 6-23: FE and experimental for type I specimens (no holes)

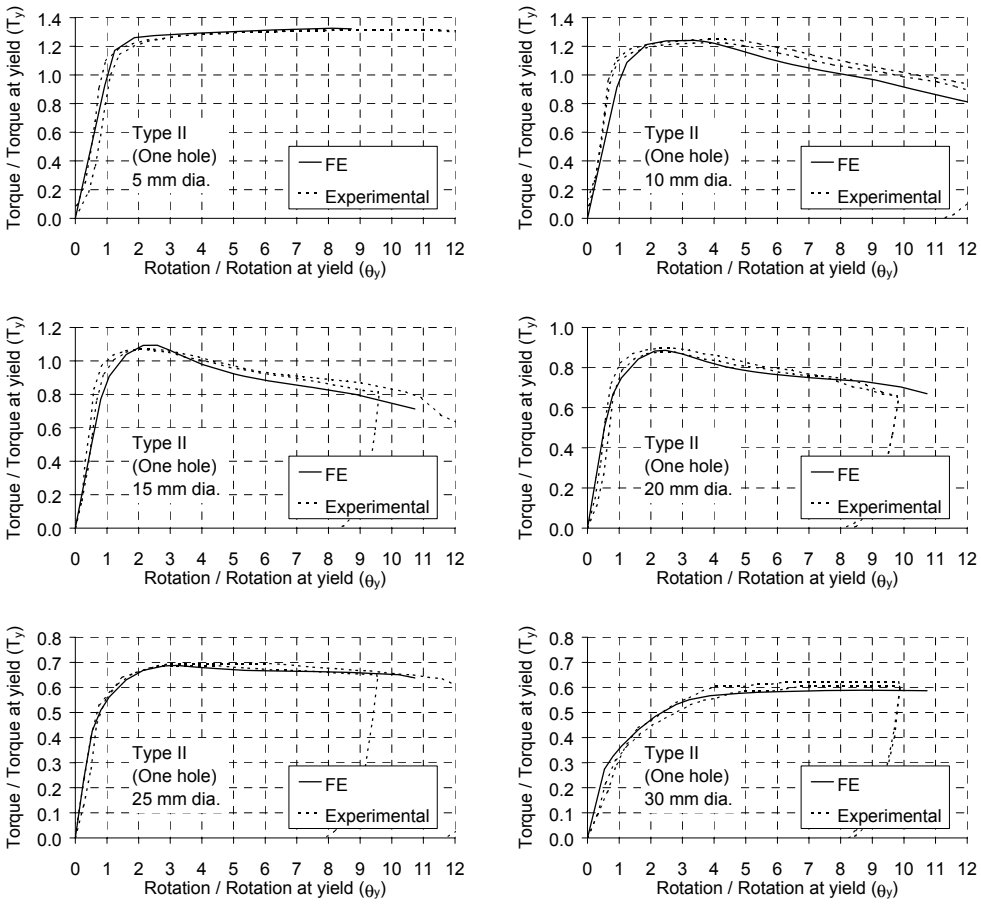

Figure 6-24: FE and Experimental for type II specimens (one hole)

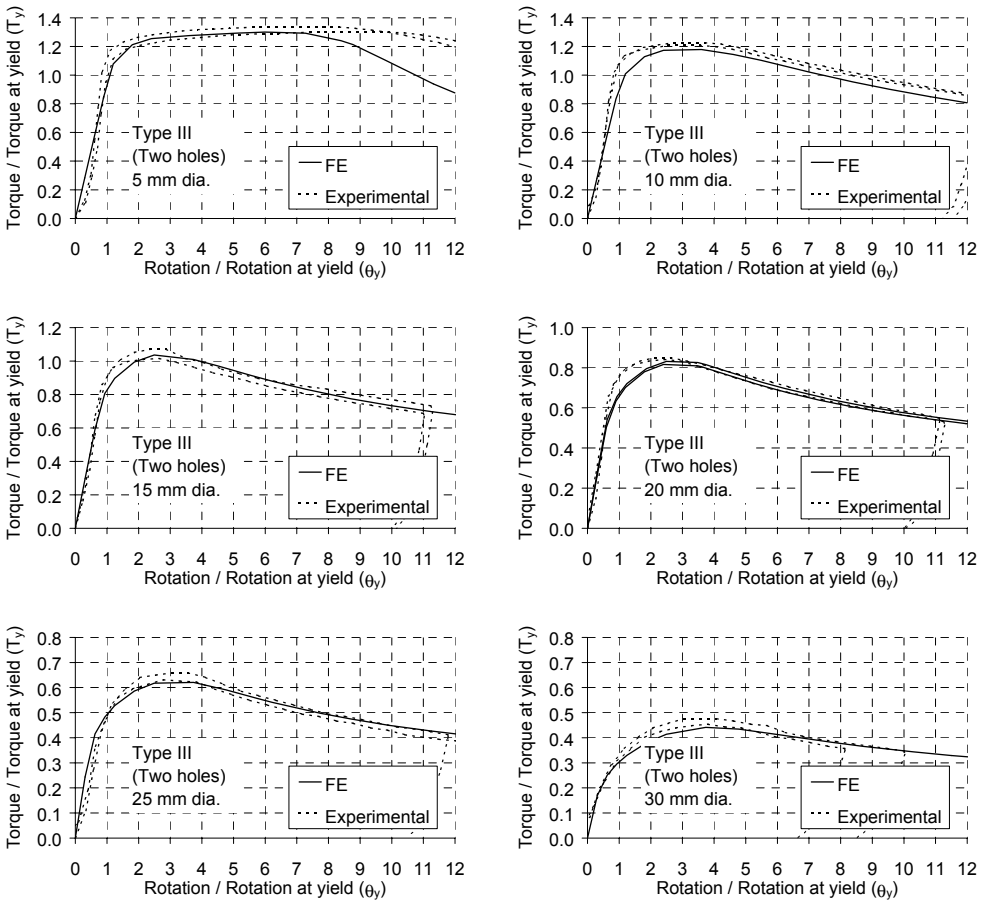

Figure 6-25: FE and experimental for type III specimens (two holes facing)

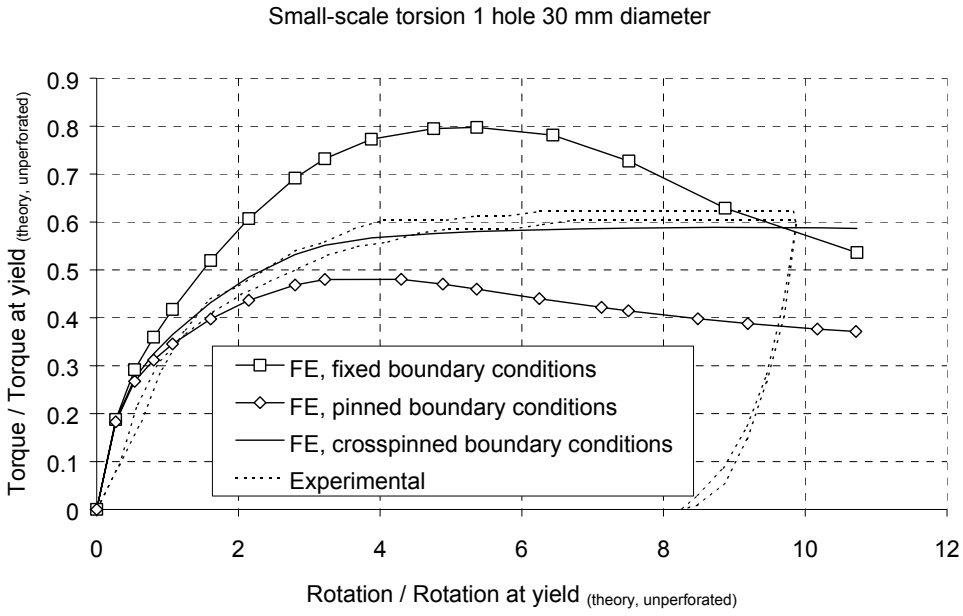

Figure 6-26: The influence of boundary conditions

6.5 Stress distributions

A number of FE models with an increased mesh density (up to 10500 elements) were used to study stress distributions. Figure 6-27 and Figure 6-28 show typical surface distribution of von Mises stress around a small hole, and large hole respectively. In the figures, the von Mises stress is plotted in terms of the stress concentration factor for torsion ($\psi_{torsion}$). The stress concentration factor for torsion is defined as the ratio of the maximum von Mises stress in the unperforated zone, to the maximum von Mises stress which would be present in an equivalent unperforated beam at the same torque. The torque is such that the maximum von Mises stress in the perforated zone is in the elastic range. The values obtained are listed in Table 6-8.

The FE study showed that the stress distribution in the web of an RHS with two holes is nearly identical to that in the web of an RHS with a single hole of equal diameter. Even small holes caused stress concentrations, but the highest stresses were generated by the largest holes. In all cases, in the elastic range, the disturbance of the otherwise uniform stress flow caused by the hole was limited to a short distance on either side of the hole. The locations of the highest stress in the FE models coincided with the locations in the experimental specimens where the metallurgical effects of high stress were most evident.

Table 6-8: Concentration factors for Von Mises stress

	Stress concentration factor ($\psi_{torsion}$)								
Hole diameter (mm)	0	1	2	5	10	15	20	25	30
Hole size ratio, Φ	0	0.03	0.06	0.15	0.30	0.44	0.59	0.74	0.89
No holes (type I)	1.03	-	-	-	-	-	-	-	-
Ono hole (type II)	-	1.72	1.93	2.22	2.55	3.14	4.15	6.28	12.29
Two holes (type III)	-	1.72	1.93	2.22	2.55	3.15	4.16	6.30	12.29

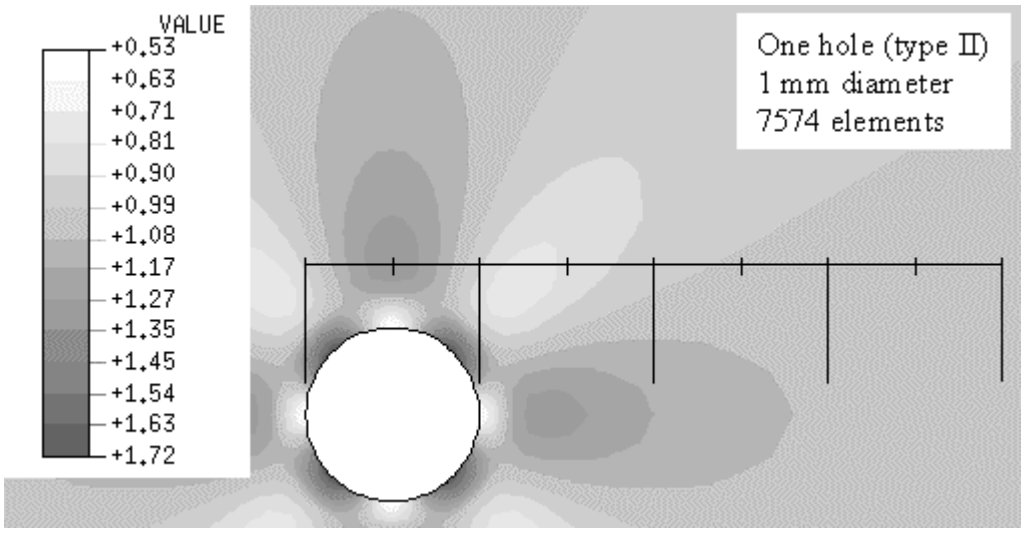

Figure 6-27: Concentration factors for Von Mises stress around a small hole

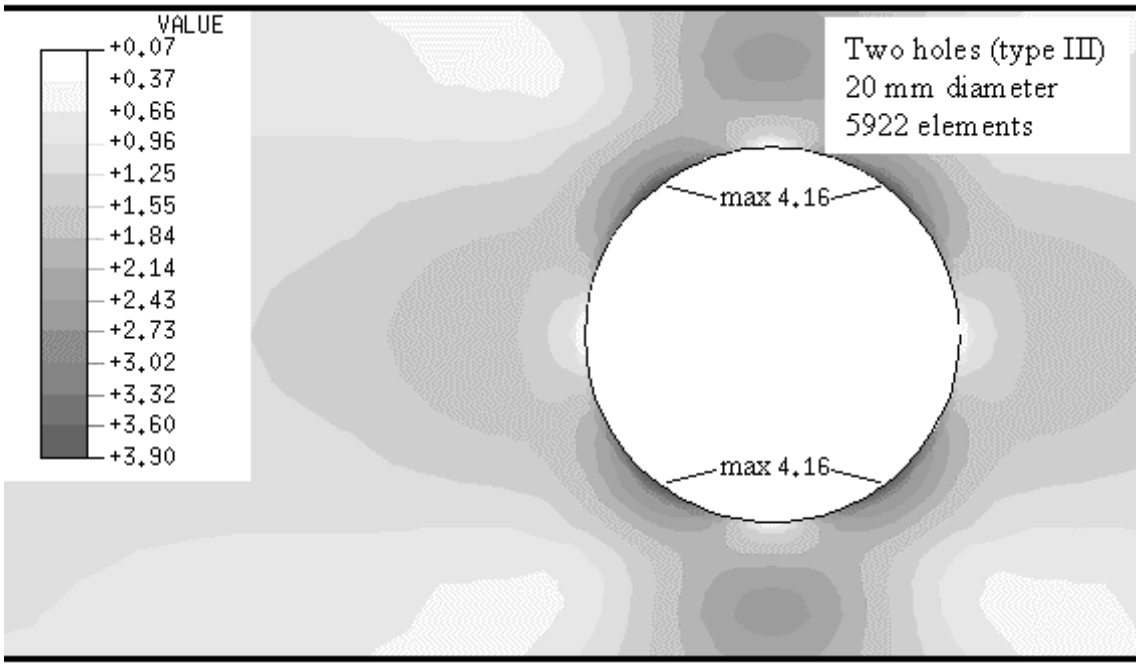

Figure 6-28: Concentration factors for Von Mises stress around a large hole

6.6 Concluding remarks

The small-scale experimental investigation showed the extent to which circular openings in the walls of square-section steel tube can have a significant influence on the torsional capacity and stiffness of the section.

A single-sided circular opening reduced the ultimate torsional capacity by as much as 70%. A small opening (Φ less than 0.2) did not reduce ultimate capacity or stiffness, but did reduce the extent of plastic deformation at peak torque. A larger opening (Φ greater than 0.3) reduced significantly both ultimate capacity and stiffness, and resulted in non-linear behaviour with asymmetry causing secondary bending effects at high twist due to differential shear in the webs.

A double-sided circular opening was found to have a similar effect to that of a single sided opening of equal diameter having a capacity slightly lower (0 to 10%). The symmetry of the condition meant there were no bending effects at high twist although there was a more rapid loss of post failure stiffness.

The sections with web openings behaved in a largely non-linear manner. The presence of the hole(s) and associated stress concentrations constituted a flexible zone about which the majority of twist occurred, and this was found to govern the nature of the failure mechanism.

FE models were calibrated against the experimental observations by comparing torque-rotation histories and deformed shapes. The deformed shapes obtained from the FE models match closely those observed during the laboratory testing, as do the torque-rotation relationships. The agreement between the FE predictions and the measured values of maximum torque is extremely good with a maximum difference of only 3%. This is particularly encouraging as it extends confidence in the use of small-scale testing for studying a wider range of parameters than can be investigated in expensive full-scale torsion tests.

The following Chapter, describes how the FE models, calibrated against the experimental data obtained in the small and full-scale experimental studies, were used in a parametric study in order to develop the preliminary design recommendations for perforated RHS.

7 Parametric study and design recommendations

7.1 Introduction

This Chapter contains recommendations for the design of hot-finished steel Rectangular Hollow Sections (RHS) with circular web openings under the actions of torsion, bending and shear. Equations are given permitting the calculation of static resistance, subject to specified limitations of web slenderness. The recommendations are presented in a form that allows integration with modern design codes and reference is made to parallel procedures in BS 5950-1:1990 and Eurocode 3 (EC3). The recommendations are justified by the findings of an analytical parametric study (also presented in this Chapter) using Finite Element (FE) models calibrated by laboratory testing (Chapters 3, 4, 5 and 6).

In the case of torsion, laboratory tests indicated lower resistances than those predicted by the theory underlying the prevailing design procedures (Section 5.4). Design recommendations based on current practice are provided here, as the experimental results are not yet fully understood.

The actions of torsion, bending and shear are isolated before proposals are made about the treatment of combinations of these actions. At each step, the justification for each recommendation is outlined with reference to analytical and experimental data. Finally, the design procedure is summarised, and the potential for further development of design guidance is discussed.

The terminology and symbols have been selected to maintain consistency with EC3, although the use of the decimal point for numerical values has been retained. Some additional subscripts and symbols not found in EC3 are introduced for clarity. Part 2 of Annex N in EC3 deals with the design of I-beams with individual web openings and provided a useful model for a design procedure concerned with web openings in RHS.

The 1993 version of EC3 refers to steel grades Fe 430 and Fe 510 in accordance with BS EN 10025:1990. Here, use is made of the revised terminology specified by BS EN 10025:1993 and more particularly BS EN 10210-1:1994, which applies specifically to hot-finished hollow sections. Fortunately, for the purposes of design, the equivalence between codes is elementary (Table 7-1).

Table 7-1: Equivalence of material grades for design

BS 4360:1990	BS EN 10025:1990	BS EN 10210-1:1994
Design grade 43	Fe 430	S275
Design grade 50	Fe 510	S355

7.2 Scope and limitations

The scope of the design advice is limited to tubes of constant wall thickness, with circular holes placed at mid-depth in the webs. Two cases of perforated section are considered, depending on whether just one web, or both webs contain holes (Figure 1-8). These cases are termed ‘one hole’ and ‘two holes’ and, for the purposes of design, are compared with unperforated sections (‘unperforated’ or ‘no holes’). In the case of the doubly perforated RHS, the two holes are of equal diameter, and are situated symmetrically with one in each web.

The topic of elastic instability is briefly discussed, but no attempt has been made to provide rules for determining the limits of stability for use in design. It is clear that such a system of stability classification is necessary, but there is insufficient experimental evidence to form generalised conclusions from this research. A study of stability limits would be, by necessity, more detailed than this broader, and more fundamental, investigation would allow.

Perforations have the effect of concentrating deformations in one location and therefore higher strains develop than in equivalent unperforated sections. Because of this, strain hardening plays a much more important role in the development of the ultimate resistance of a perforated section than an unperforated section. In the absence of an opportunity to study the importance of strain hardening in sufficient detail, the design recommendations here must remain conservative, and neglect any strengthening effect that results from strains exceeding the yield stress of the material.

These design recommendations apply principally to hot-finished steel RHS of grades S275J2H and S355J2H since they are based largely upon experimental work performed on those materials. Much of what follows is also applicable to other materials, such as cold-formed steel and aluminium. However, no advice is given regarding the particular properties of these materials, or how the behaviour of RHS produced from them differs, in general, to hot-finished steel RHS.

Standard section sizes for hot-finished RHS are specified by BS EN 10210-2:1997. The principal European producers roll the whole range, and commonly include additional sizes based on other national and international standards. Reference here is restricted to sections covered by the European Standard, but the

design recommendations proposed are applicable to any section size, provided the limitations accompanying the rules are met.

BS EN 10210-2:1997 prescribes a standard nominal corner profile, which relates the internal and external radii to the section thickness. Although most producers roll their own corner profiles (within the permitted tolerances) the section properties quoted in technical documentation are calculated from the nominal corner profile (and the equations[3] given in BS EN 10210-2:1997). For unperforated sections, the difference is negligible. The corner profile has a small influence upon the behaviour of RHS with large holes (Φ greater than 0.9) but the affect is too slight to merit inclusion here. The nominal corner profile (or a close approximation) was used in the parametric study.

BS EN 10210-2:1997 specifies a standard range of 267 different RHS, within which are 24 different depths and eight different aspect ratios (Table 7-2). Sections range from 20 mm to 500 mm in depth and from 2 mm to 20 mm in thickness. Web slenderness ranges from 4.5 to 55.3. Of the standard sections, 180 (67%) have a web slenderness less than or equal to 22.0, but the majority of these are at the small end of the scale (150 have depths of 200 mm or less).

While it is possible to use the standard sections with the depth and width transposed, thereby giving seven additional aspect ratios less than 1.0, it is uncommon in practice. The scope of this document is limited to aspect ratios within in the standard range (between 1.0 and 2.0).

[3] The equations in BS EN 10210-2:1997 are also given in Appendix C.

Table 7-2: RHS in the European Standard range

Aspect ratio	Number of different sections	Number of different depths	Number with web slenderness less than or equal to 22.0
1.00	131	22	98
1.40	7	1	1
1.44	7	1	3
1.50	27	4	20
1.67	28	5	18
1.75	6	1	4
1.80	19	3	9
2.00	42	7	27

7.3 General design procedure

The size of an RHS can be described by three parameters. The common method is to identify the depth, width and wall thickness (Figure 1-10). An alternative method is also used here, which uses the three parameters that control the structural behaviour: aspect ratio (α), section depth (h) and web slenderness (λ_{web}). As in the foregoing Chapters, a fourth parameter, the hole size ratio (Φ), is used to indicate the size of the perforation. Aspect ratio is defined by Equation 7-1, slenderness by Equation 1-1 and Equation 1-2, and hole size ratio by Equation 1-3.

$$\alpha = h/b$$

Equation 7-1

The design of an RHS with web perforations can be facilitated by considering an idealised member consisting of a number of perforated and unperforated sub-members. The sub-members can be designed individually using the existing rules for unperforated sub-members, and the new recommendations for perforated sub-members. Multiple perforations must be placed at sufficient

distances apart to ensure there is no detrimental interaction. The permissible spacing of holes is based on the notion of zones of influence, which are discussed later in this Chapter. This is the same approach as the one used in Annex N of EC3, which deals with the design of I-section beams with web openings.

The design recommendation for bending is based partly on the strength limit state approach used in Annex N of EC3. The EC3 approach was modified to include a maximum stress component for when a yield based serviceability criterion is also required (such as in BS 5950-1:1990).

A yield based serviceability approach is recommended for design in shear and torsion. Web openings in RHS under the action of shear or torsion induce large stresses and a serviceability approach based on a maximum stress criterion results in a large reduction in design capacity. Unperforated RHS are naturally strong in both shear and torsion and large reductions in design shear and torsion capacity may not necessarily result in a requirement for a larger section. However, it is likely that a strength limit state approach coupled with a displacement based serviceability limit will result in a more economical method of design. Unfortunately, there was insufficient time available to develop fully this approach within this project.

The stress based design recommendations presented in this Chapter are based on the observation of stress distributions obtained from a parametric FE study. In the following sections, the locations of raised stress will be referenced to the regions labelled ①, ② and ③ in Figure 7-2. The regions are:

① The top surface of the upper flange above the opening and the bottom surface of the lower flange below the opening

② The edge of the opening at the top and bottom

③ The four locations where the edge of the opening meets the diagonals

In design, a factor of safety is normally included in the expression for design resistance. In EC3 this safety factor is referred to as a 'partial material factor' and is denoted by the symbol γ_{M0}. In the following discussions, where the design resistance of an unperforated RHS or a perforated I-beam is mentioned, the reference is to the value produced by the code expressions when the factor of safety is unity.

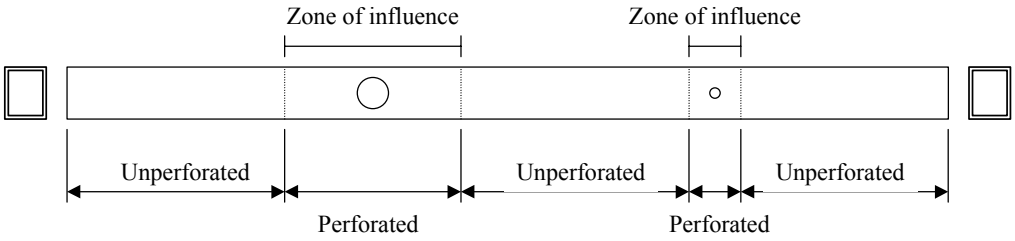

Figure 7-1: Perforated and unperforated sub-members

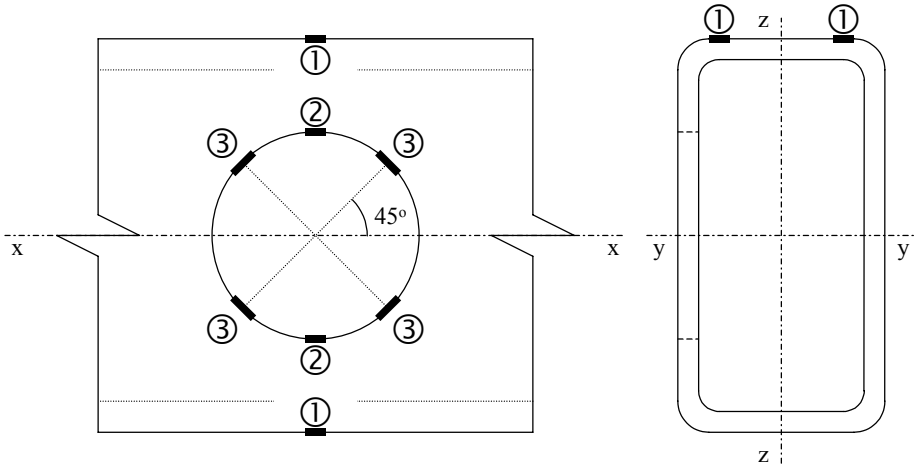

Figure 7-2: Locations for stress concentration

7.4 The parametric Finite Element study

The design recommendations presented in this Chapter were formulated with regard to knowledge obtained from a parametric FE study. Perforated and unperforated RHS of varying dimensions were modelled using the ABAQUS v5.8.1 FEA program (Section 2.3). Models included material and geometric non-linearity and each contained between 3200 to 5700 four-noded shell elements (S4R). The sensitivity of the solutions to meshes and element types was studied to ensure that the findings of the parametric study were reliable. The FE models were calibrated against the results of laboratory tests of perforated and unperforated RHS in torsion, bending and shear (Chapters 3 to 6).

Three section sizes where chosen to investigate the full load-displacement response (resistance and ductility) for each action (116 models in total). The three sizes had the same web slenderness (22.0) as the sections used in the experimental study and had aspect ratios (1.0, 1.5 and 2.0) representing the range of European standard sizes (BS EN 10210-2:1997).

A standardised material model was used in the study (Table 7-3 and Table 7-4). The standardised material has typical yield plateau and strain hardening behaviour (Section 2.2). The material fits the criteria for both S275 and S355 grades, being at the lower boundary of S355 and the upper boundary of S275. The models included strain hardening because the parametric study was designed to investigate the behaviour of actual perforated RHS in service. For purely design purposes, it would have been more appropriate to use a simple elastic, perfectly plastic material definition.

A larger number of models were displaced in the elastic range to study stress distributions and concentrations over a wider range of section size (66 models for bending, 84 models for shear and 73 models for torsion). The models contained the full definition of the non-linear material used in the full plastic parametric study, but the displacement steps were reduced to keep stresses within the elastic range. Geometrical non-linearity was also accounted for, but its influence was insignificant for such small deflections. Elastic parametric models contained more elements than plastic parametric models to ensure reliable stress concentration data.

All the parametric models were based on the same generic mesh definition. The boundary conditions (Table 7-5 and Figure 7-3) were selected to re-create the typical conditions of RHS beams in service (RHS beams bolted between columns). Actions were induced by controlling the displacements at the ends of the RHS. Fixed and active boundary conditions were achieved by linking (via mathematical relationships) the displacement of the cross-section at each end, to the displacement of a single node.

Models used to study the action of bending (Figure 7-4a) were displaced at the ends by rotations about the horizontal transverse axis. The rotations were equal in magnitude, but opposite in direction, to produce a uniform bending moment over whole length of the beam. Since the bending moment was uniform, no external shear forces were produced. Models were long (2.5 m) to ensure that the end effects did not interfere with the behaviour of the perforated zone.

Models used to study the action of shear (Figure 7-4b) were also displaced at the ends by rotations about the horizontal transverse axis. The rotations were equal in magnitude, and in direction, to produce a uniform shear force over whole length of the beam, with zero bending moment in the middle (the perforated zone). Models

in the full plastic study were short (0.7 m) to ensure that bending failure did not occur at the ends. However, the high shear resistance meant that only RHS with large openings could be caused to fail in shear without any bending failure. In addition, the short length meant that some interaction between the end effects and the perforated zone was unavoidable. Elastic parametric models were longer in length (2.0 m) and were used to study holes of all sizes without end effect interaction or bending failure.

Models used to study the action of torsion (Figure 7-4c) were displaced at the ends by rotations about the longitudinal axis. The rotations were equal in magnitude, but opposite in direction, to produce a uniform torsional moment over whole length of the beam. No external shear forces or bending moments were applied. Models were long (2.0 m) to ensure that the end effects did not interfere with the behaviour of the perforated zone.

Table 7-3: Material model for parametric study

	f_{y1} (N/mm^2)	E (kN/mm^2)	$\lambda_{plateau}$	$E_{plateau}$ (kN/mm^2)	λ_{ESHF}	f_u (N/mm^2)	ε_u (%)	ν
Material model for parametric FE	360.0	205.0	13.0	0.0	0.20	510.0	16.0	0.3

Note 1: Typical material based on observation of tensile tests of steel from RHS (Appendix D)
Note 2: Refer to Section 2.2 for definitions of quantities

Table 7-4: ABAQUS material model for parametric study

*ELASTIC		
205540.3	,	0.3
*PLASTIC		
360.63	,	0
368.85	,	0.022493
403.30	,	0.028912
461.61	,	0.048132
530.81	,	0.085696
591.60	,	0.145542
624.24	,	0.199087

Table 7-5: Boundary conditions for parametric FE models

Model type		Axis 1 (longitudinal)		Axis 2 (horizontal transverse)		Axis 3 (vertical transverse)	
		Translation	Rotation	Translation	Rotation	Translation	Rotation
Bending	End 1	Free	Fixed	Fixed	Active, $+\theta$	Fixed	Fixed
	End 2	Fixed	Fixed	Fixed	Active, $-\theta$	Fixed	Fixed
Shear	End 1	Free	Fixed	Fixed	Active, $+\theta$	Fixed	Fixed
	End 2	Fixed	Fixed	Fixed	Active, $+\theta$	Fixed	Fixed
Torsion	End 1	Free	Active, $+\theta$	Fixed	Fixed	Fixed	Fixed
	End 2	Fixed	Active, $-\theta$	Fixed	Fixed	Fixed	Fixed

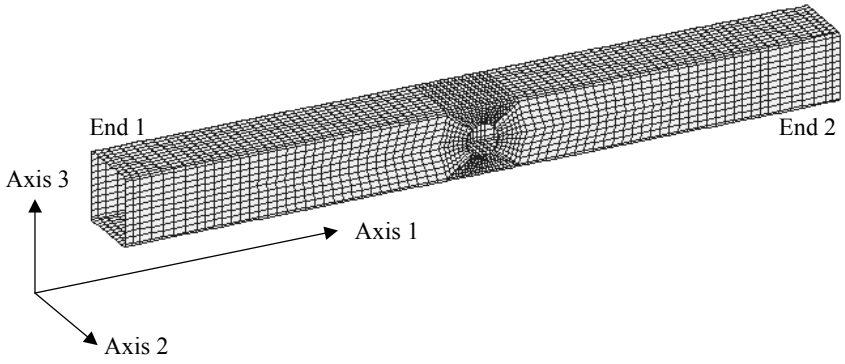

Figure 7-3: Model coordinate axes

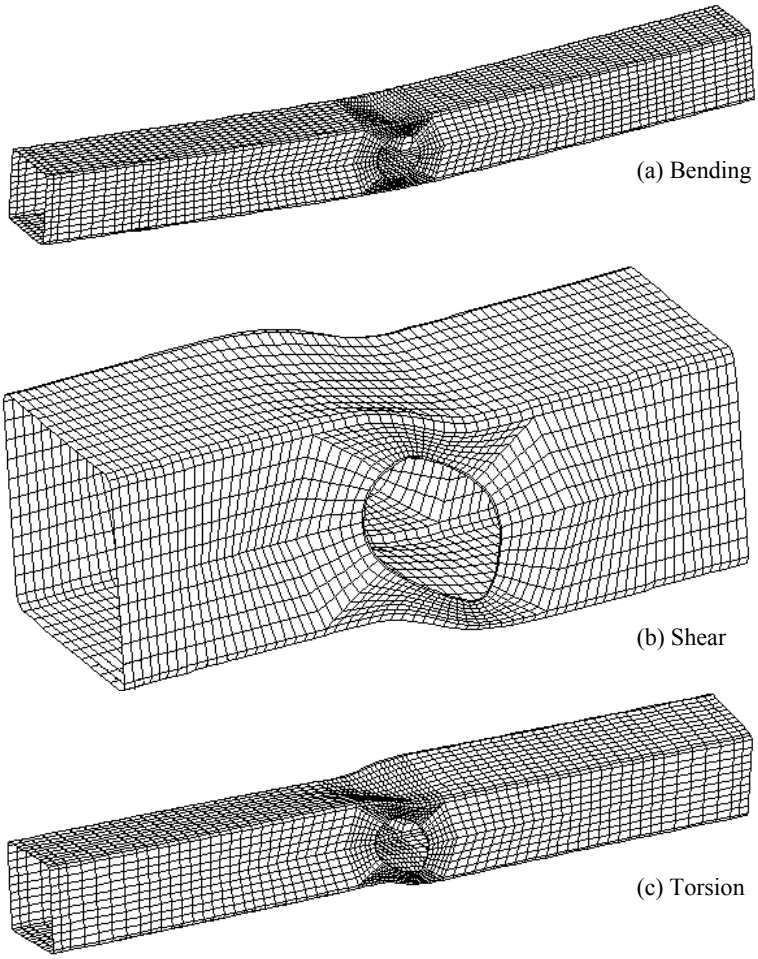

Figure 7-4: Finite Element meshes for parametric investigation

7.5 Bending

7.5.1 Introduction

When designing a beam in bending using EC3 or BS 5950 (which both use the limit state approach) the first step is the classification of the cross-section. The section classification gives an indication of the expected performance (Figure 7-5) of the beam with respect to the elements of the cross-section that are in compression and hence determines the method of design.

Class 1 (plastic) cross-sections as those that can develop the plastic moment of resistance (M_p) and can form a plastic hinge with a rotation capacity sufficient for plastic design (allowing for the redistribution of moment within a structure). Class 1 sections have a long plateau of rotation, where the plastic hinge can form without the occurrence of local buckling.

Class 2 (compact) cross-sections are those that can develop the plastic moment of resistance (M_p), but have limited rotation capacity once this is reached (due to local buckling), and are not suitable for plastic design.

Class 3 (semi-compact) cross-sections are those in which the calculated stress at the extreme fibre of the member can reach its yield strength, but in which local buckling prevents the development of the plastic moment of resistance (M_p). Class 3 sections may only be designed in the elastic range up to the design yield stress (elastic moment M_e). The behaviour of class 3 sections does not necessarily have to be linear up to the yield point.

Class 4 (slender) cross sections are those for which it is necessary to make allowances for the effect of local buckling when determining the moment of

resistance. Class 4 sections can buckle locally before reaching the elastic moment (M_e).

The treatment of the various classifications of section in EC3 is similar to that in BS 5950 with one significant exception. The design of class 4 sections in EC3 proceeds by an effective area method rather than one of reduced stresses as in BS 5950. The effective area method results in a more realistic and economical design (Joannides et al 1993).

For sections of class 1 and 2 there is no requirement for further checking for local buckling, although only class 1 sections may be used at plastic hinges. Restrictions on use of class 3 and class 4 sections ensure that local buckling is considered in design.

In practice, the classification of a section is determined by limits of web and flange slenderness, with a modification for the grade of material (Clauses 5.3 of EC3 and 3.5 of BS 5950). A section can be described by the individual classifications of the web and flange, or by the classification of the cross-section as a whole. For bending, with the neutral axis at mid-depth, all the RHS in the European standard range have class 1 webs for both S275 and S355 steel grades (EC3 or BS 5950 limits). The flange classification varies from class 1 to class 4.

Although the determination of class 1 cross-sections in design is determined by geometric ratios, the actual definition of class 1 behaviour is based on rotation capacity (R). Rotation capacity is defined by Equation 7-2 where κ is the curvature at which the moment falls below M_p and κ_p is the curvature at which the plastic moment is reached assuming an elastic flexural rigidity (Equation 7-3). Eurocode 3 requires $R \geq 3$ for plastic design, but some standards require $R \geq 4$, particularly those covering seismic regions.

$$R = \kappa / \kappa_p - 1$$

Equation 7-2

$$\kappa_p = M_p / EI$$

Equation 7-3

The current web slenderness limits for RHS classification are based on tests of I-sections where more work has been done on plastic design, but flanges in RHS have different support conditions than those in I-sections. Flange slenderness limits for RHS have been studied by a number of investigators (e.g. Dwyer and Galambos (1965), Korol and Hudoba (1972), Hasan and Hancock (1988), and Zhao and Hancock (1991)).

Recent research has resulted in cause to doubt the design code treatments of RHS classification, and the way in which flanges and webs are treated in isolation without consideration of interaction (Zhao and Hancock (1990) and (1992), Wilkinson and Hancock (1997)). There has also been some cause to reflect on the plastic performance of hot-finished sections, which might be considered to be compromised by the yield plateau (Sedlacek et al (1998)). To add to the confusion the Australian standard AS 4100 actually requires a sizeable yield plateau ($\lambda_{plateau} \geq 6$) as part of the material ductility requirement for plastic classification.

Once a section has been classified, its design moment of resistance (elastic or plastic) is calculated using equations based on beam bending theory. To comply with the ultimate limit state requirement, the factored load (EC3 refers to this as the design load) must be less than the design moment of resistance (with a reduction factor for safety). Both codes have two approaches: one for bending coexistent with

high shear, and one for bending coexistent with low shear load. Design for bending about one axis with low shear load is dealt with in Clauses 4.2.5 of BS 5950 and 5.4.5.2 of EC3. The design of RHS with web openings under the action of shear and bending is dealt with later in Section 7.8.

In EC3, the moment of resistance is calculated using Equation 7-4 for sections of classes 1 and 2 and Equation 7-5 for sections of class 3. Elastic and plastic section moduli are denoted by $W_{el,y}$ and $W_{pl,y}$ respectively, f_y is the yield strength (Table 3.1 of EC3) and γ_{M0} is the material partial factor (a safety factor). Class 4 sections are dealt with differently using area reduction factors. Section 7.5.3 contains analogous expressions that can be used to calculate the design moment of resistance for RHS with web openings.

$$M_{c,y,Rd} = M_{pl,y,Rd} = W_{pl,y} f_y / \gamma_{M0}$$

Equation 7-4

$$M_{c,y,Rd} = M_{el,y,Rd} = W_{el,y} f_y / \gamma_{M0}$$

Equation 7-5

For the serviceability limit state, the deflection of the beam must be limited so as not to impair the strength or efficiency of the structure. Normally this is done by checking that the calculated deflection is within the limiting values recommended in the codes (Clauses 4.2 of EC3 and 2.5.1 of BS 5950). Deflection limits in BS 5950 are for imposed loads only, while EC3 considers deflections arising from both dead and imposed loads. In BS 5950, the strength clause (Clause 4.2.5) prohibits plasticity at working load so deflections can be calculated by elastic methods. There is no such clause in EC3 and calculations of deflection must allow for plasticity.

Section 7.5.4 contains expressions that allow the calculation of the elastic deflection under bending of RHS with web openings.

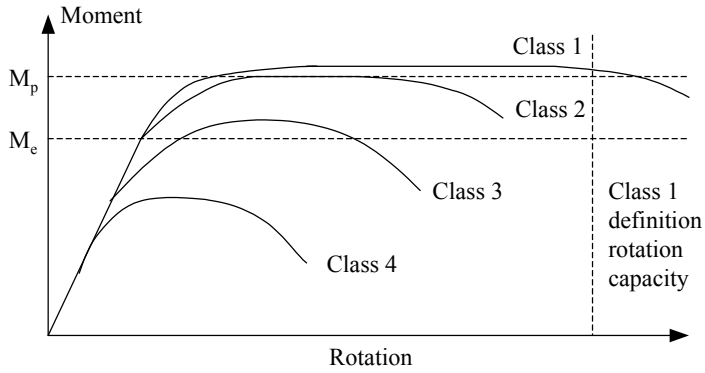

Figure 7-5: Cross-section classifications and moment-rotation relationship

7.5.2 Concentration factors for elastic stress

The distribution of elastic bending stresses around an opening is shown schematically in Figure 7-6. Examples of FE contour plots of von Mises stress are shown in Figure 7-7. The stress distribution in the web of an RHS with one hole is nearly identical to that in the web of an RHS with two holes. Small differences occur due to asymmetry, but are too slight to merit discussion here.

An RHS without an opening (Figure 7-6a) will have a linear distribution of stress as predicted by Euler-Bernoulli-Parent beam bending theory. Under a uniform bending moment, the cross-sections at all points along the beam remain plane. The bending stress in a longitudinal fibre is proportional to the perpendicular distance from the neural axis. Yield occurs when the stress in the extreme fibres reaches the yield stress (f_y).

A small circular opening on the neutral axis (Figure 7-6b) will disturb the uniform system of stress, causing longitudinal warping of the cross-section (planes no longer remain plane). Longitudinal stress close to the neutral axis is interrupted by the opening and must flow around it, raising the stress above and below the opening (location ② in Figure 7-2). Longitudinal stress closer to the flanges is less disturbed by the flow of stress around the hole and bending stress distant from the neutral axis returns to the same linear distribution of stress present in the unperforated beam, remote from the opening. Since the highest stresses are present at the extreme fibres, yield occurs simultaneously with yield in the unperforated beam. The higher stresses around the opening compensate for the reduced second moment of area and the moment at yield is not reduced by the presence of the hole.

An opening of a particular size (Figure 7-6c) will raise the stress above and below the opening (location ② in Figure 7-2), to the same magnitude as that at the extreme fibres (location ① in Figure 7-2). This size of hole is, here, termed the 'critical hole size', and marks the boundary between small holes that do not reduce the moment at yield and large holes that do.

Holes larger than the critical hole size (Figure 7-6d) raise the stress above and below the opening to values larger than the bending stress at the extreme fibre of the unperforated beam distant from the opening. Stress in the flanges immediately above and below the hole is also raised by the proximity to the hole (the reduction in second moment of area), but yield occurs in the webs first and the moment at yield is reduced.

A beam with a large opening that does not produce a stress concentration effect (such as a very long elongated hole with a gradual change in cross-section) has a linear stress distribution (Figure 7-6e). The stress distribution at the opening is

analogous to that in the unperforated section, but higher stresses (in all longitudinal fibres) will result for a particular bending moment because of the reduced second moment of area. A beam with a circular hole large enough to remove the entire web at the central cross-section behaves in a similar way, because the flow of concentrated stress is confined to the webs (although stress in the corner radii becomes very high).

A number of FE models (66) have been used to study the stress concentrations around openings in the webs of RHS in pure bending. The models used in the parametric study are shown diagrammatically in Figure 7-8. Stress concentrations were found to be dependent on hole size and web slenderness, but not aspect ratio. The web may be considered as a rectangular beam acting as an element of the whole beam. The dependence of stress concentration on the web slenderness is analogous to the dependence upon thickness, of the stress concentration around a circular hole in an infinite strip in bending (as considered by investigators such as Isida (1952) and Peterson (1974)).

The FE models were used to obtain a representative sample of stress concentration factors for bending. The stress concentration factor for bending, $\Psi_{bending}$, is defined as the ratio of the maximum von Mises stress in the perforated beam (at any location) against the maximum von Mises stress in the unperforated beam. The two maximum stresses are compared at the same bending moment and the moment is such that both maximum stresses are in the elastic range.

The stress concentration factors obtained from the FE study were approximated by an empirical mathematical function, which was fitted to the data using a least squares method (Equation 7-6). For the 66 models included in the study, the maximum differences (in absolute terms) between the empirical function

and the FE values were 0.14 (empirical value less than FE value) and 0.07 (empirical value greater than FE value). The square root of the average square error is 0.04. The actual stress concentration data from the FE study is presented in Appendix E.

$$\psi_{bending} = \text{Maximum}\left[\left(-\frac{\lambda_{web}^2}{439.2}+\frac{\lambda_{web}}{5.916}+1.5054\right)\Phi+\frac{\lambda_{web}^2}{1200}-\frac{\lambda_{web}}{14.16}-0.3288\,,1\right]$$

Equation 7-6

The empirical function for stress concentration factor is shown graphically in Figure 7-9. Stress concentration factors increase with increasing hole size and are larger for more slender webs. The function is valid only for hole size ratios between 0 and 0.9 and for web slendernesses between 9.0 and 32.0. The function actually reduces slightly at the extreme limit of slenderness (λ_{web} > 29.0): this is a consequence of its empirical nature and is not indicative of true behaviour.

Holes smaller than the critical hole size ratio (see above) have stress concentration factors of unity. The critical hole size is represented by the intersection of the stress concentration function with the plane $\Psi_{bending}$ = 1 (Figure 7-10).

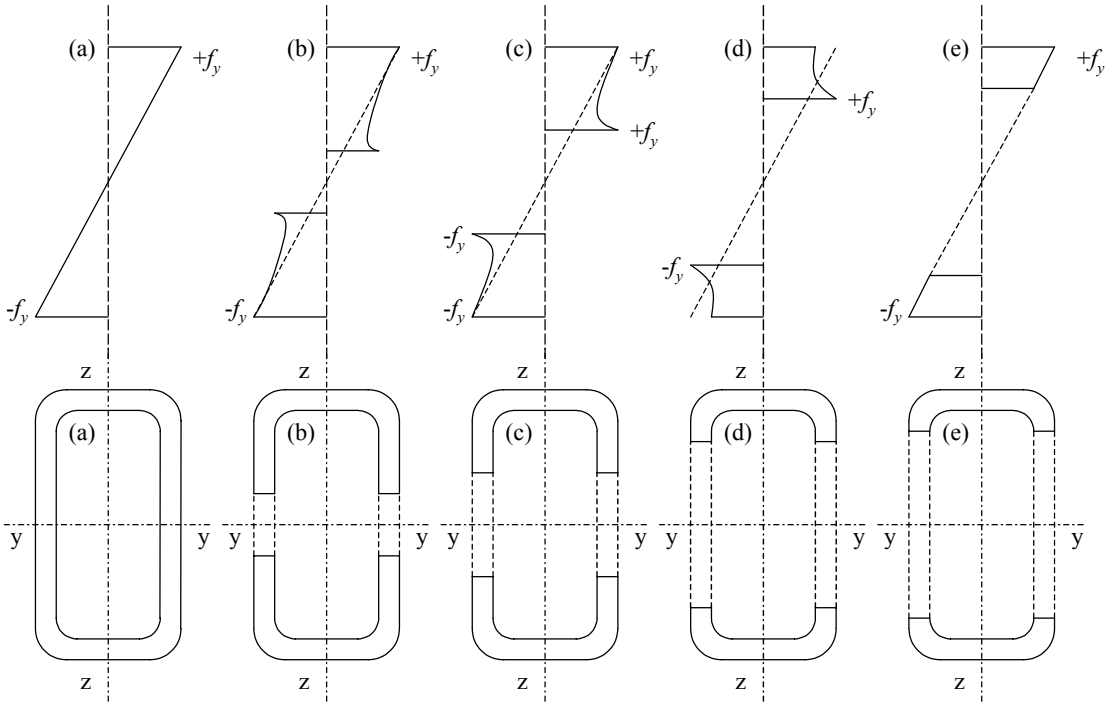

Figure 7-6: Distribution of elastic bending stress

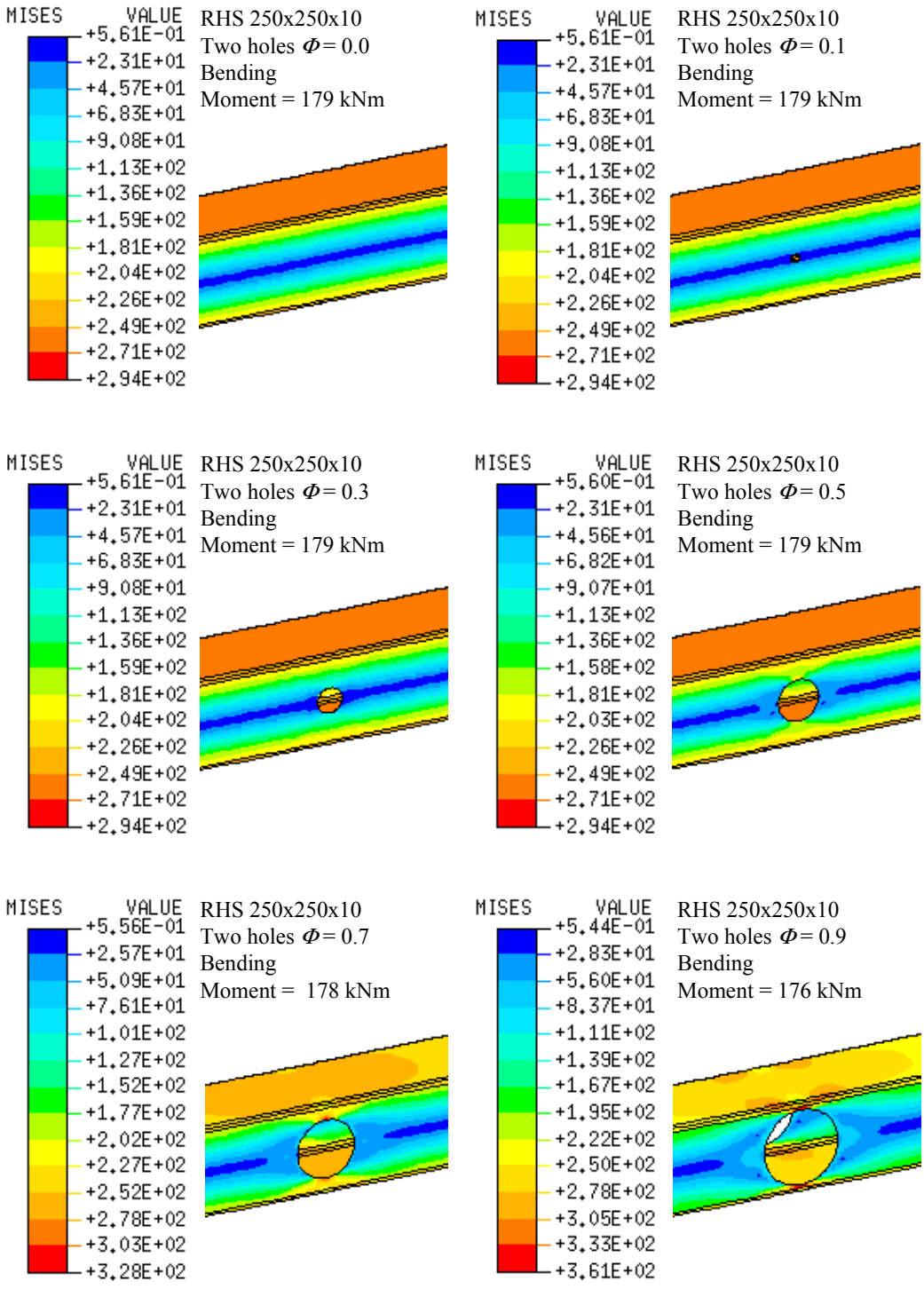

Figure 7-7: Distribution of von Mises stress for RHS 250x250x10 in bending

Von Mises stress plotted on external surface
(Original in colour)

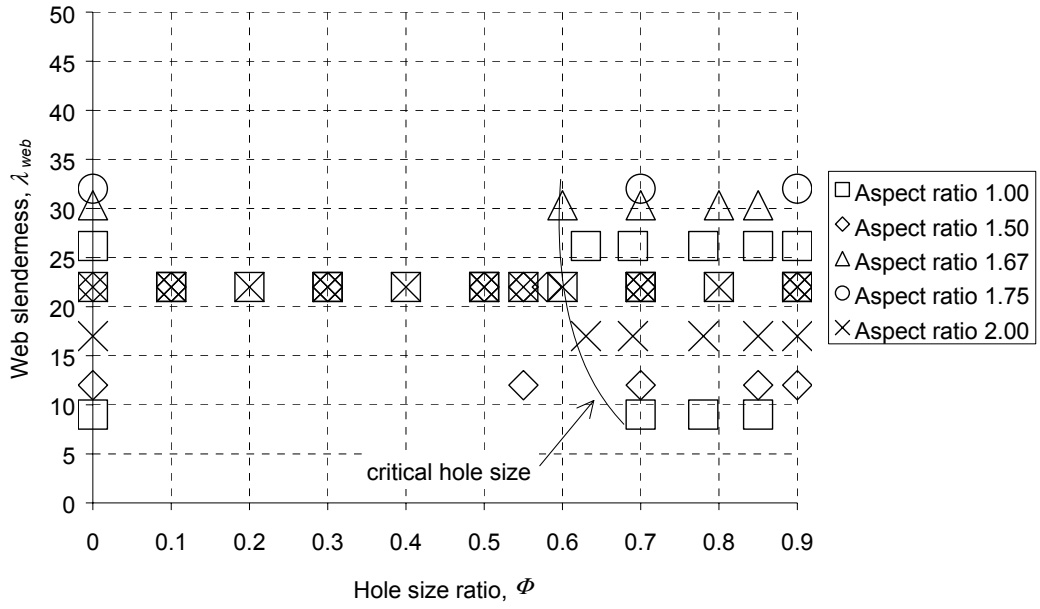

Figure 7-8: Parametric sampling for bending

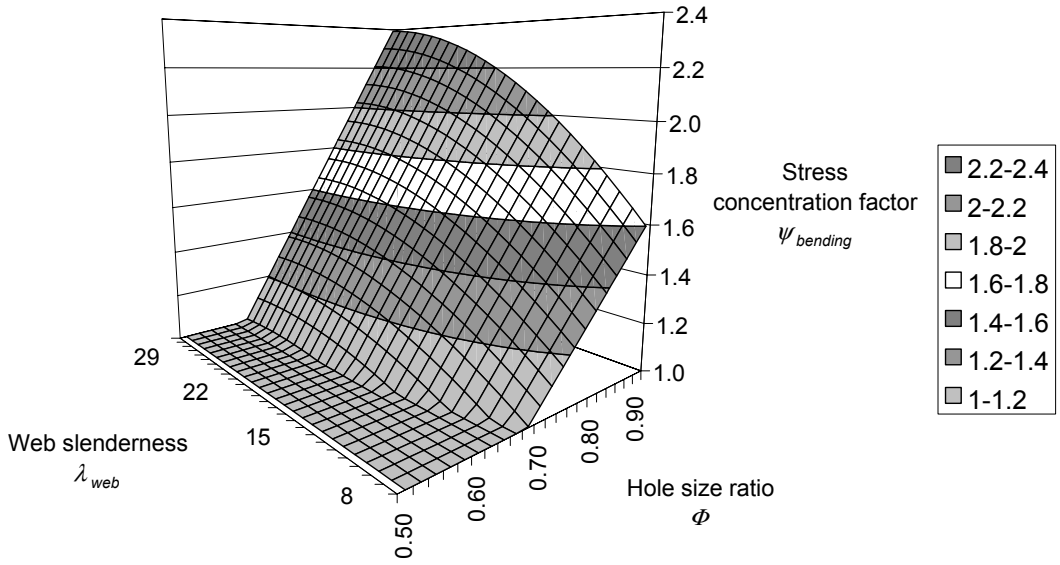

Figure 7-9: Stress concentration factors for bending

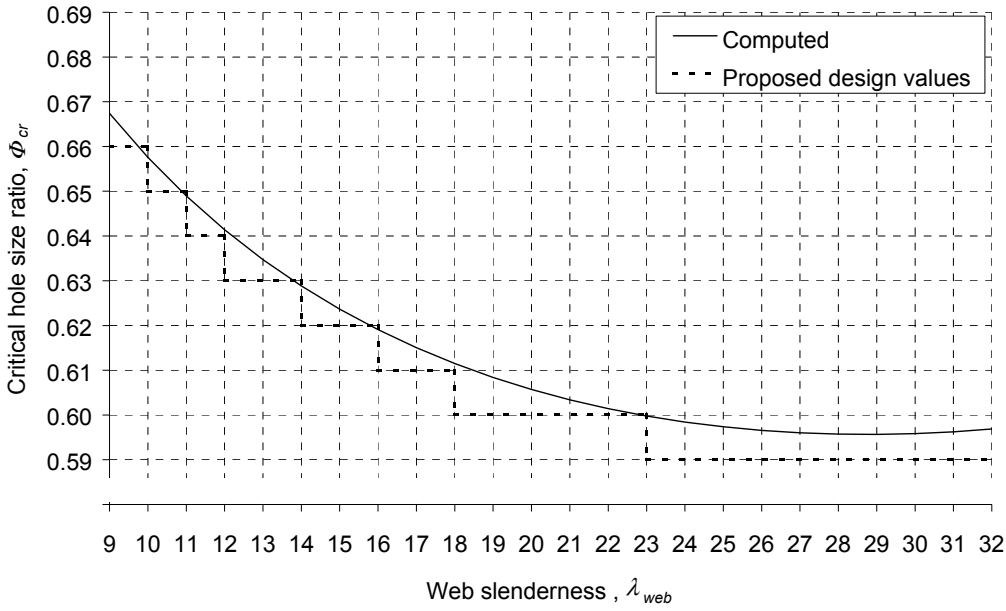

Figure 7-10: Critical hole size ratio for bending

7.5.3 Resistance

While it is clear that a system of stability classification is necessary for design, there is insufficient experimental evidence to form generalised conclusions from this research. However, a number of preliminary observations can be made based on this study and on parallel design procedures for I-sections with web openings. The proposed expressions for calculation of resistance which follow, are based on the premise that elastic instability will not occur.

Class 1 sections differ from class 2 sections by having sufficient rotation capacity for plastic design. However, plastic design is not practicable for perforated sections (no flame cut edges or punched holes: Clause 7.3 of EC3). The critical requirements for classification therefore lie at the boundary between class 2 and class 3 behaviour, which governs the design resistance (elastic or plastic), and the

boundary between class 3 and class 4 behaviour, which marks the point where elastic stability must be considered.

Annex N of EC3 deals with the design of I-section beams with web openings and specifies that the flange of the unperforated section must be of class 1 or class 2 (Clause N.1.7.1). It is recommended that this specification be adopted for RHS, as class 3 flanges will be susceptible to flange buckling. Clause N.1.7.1 also specifies that the web should be of class 1, 2, or 3, but this requirement is not critical for RHS where webs are of class 1 for the entire standard European range.

Clause N.2.1.4 of Annex N deals with the calculation of design resistance, and gives two approximate methods. The first method is for sections of class 1 and class 2, and is based on the plastic capacity. Equation N.10b in the code is based on the plastic section modulus of the reduced section (for RHS: Equation 7-7 and Equation 7-8). The analogous expressions for the plastic moment of resistance of perforated RHS are Equation 7-9 (for one hole) and Equation 7-10 (for two holes).

$$W_{pl,y,1hole} = W_{pl,y,unperf} - tr^2$$

Equation 7-7

$$W_{pl,y,2holes} = W_{pl,y,unperf} - 2tr^2$$

Equation 7-8

$$M_{pl,y,Rd,1hole} = M_{pl,y,Rd,unperf}\left(1 - \frac{tr^2}{W_{pl,y,unperf}}\right)$$

Equation 7-9

$$M_{pl,y,Rd,2holes} = M_{pl,y,Rd,unperf}\left(1 - \frac{2tr^2}{W_{pl,y,unperf}}\right)$$

Equation 7-10

The second method in clause N.2.1.4 of Annex N is for class 3 sections and is based on the elastic capacity. Equation N.10d in the code is based on the elastic section modulus of the reduced section. However, the examination of stress distributions (Section 7.5.2) has shown that holes smaller than the critical hole size ratio (Φ_{cr}) do not reduce the elastic bending capacity (hence Equation 7-11).

For RHS with holes larger than the critical hole size, the reduced section expression produces a more economical design than the maximum stress approach. The capacity can be reduced by an appropriate proportion towards the fully perforated capacity (when $\Phi = 1$, Figure 7-6e) as shown diagrammatically in Figure 7-11. The mathematical expressions are Equation 7-12 (for one hole) and Equation 7-13 (for two holes).

$$M_{el,y,Rd,1hole} \text{ or } M_{el,y,Rd,2holes} = M_{el,y,Rd,unperf} = f_y W_{el,y,unperf}$$

For $\Phi \le \Phi_{cr}$

Equation 7-11

$$M_{el,y,Rd,1hole} = M_{el,y,Rd,unperf} - \left(M_{el,y,Rd,unperf} - f_y \left(W_{el,y,unperf} - \frac{t(h-3t)^3}{6h} \right) \right) \left(\frac{\Phi - \Phi_{cr}}{1 - \Phi_{cr}} \right)$$

For $\Phi > \Phi_{cr}$

Equation 7-12

$$M_{el,y,Rd,2holes} = M_{el,y,Rd,unperf} - \left(M_{el,y,Rd,unperf} - f_y \left(W_{el,y,unperf} - \frac{t(h-3t)^3}{3h} \right) \right) \left(\frac{\Phi - \Phi_{cr}}{1 - \Phi_{cr}} \right)$$

For $\Phi > \Phi_{cr}$

Equation 7-13

The expressions for elastic moment above do not predict the moment at which first yield occurs. Actual material yield occurs at a lower moment due to stress concentrations at the opening. However, the area of yielded material is small, and does not influence the behaviour of the beam as a whole. In this instance, the elastic moment defines the extent of the linear region of the behaviour of the whole beam.

A section without strain hardening is incapable of achieving a moment greater than its plastic moment of resistance. For an unperforated hot-finished section, the strains required for strain hardening are large and correspond to enormous curvatures (hence Sedlacek et al (1998)). However, the presence of the opening in a perforated RHS induces high strains by focusing displacements in the flexible zone. Consequently, the strain hardening behaviour has a significant role in the plastic performance.

Although strain hardening is not considered in design (here or in Annex N), it has, in practice, a significant effect on the plastic capacity of a perforated section. Strain hardening increases the ductility of the section allowing it to reach a higher maximum moment, as is shown by example in Figure 7-12. In the figure, the moment has been reduced to a dimensionless ratio against the theoretical elastic moment of the unperforated section. Curvature has been reduced to a dimensionless ratio against the theoretical curvature of the unperforated section at yield. The curvature is an average measure made along the whole beam and is therefore dependent on the length.

For sections of classes 1 and 2, the maximum moment is limited by the inelastic stability of the elements of the cross-section in compression. The principal buckling mechanisms are arching of the compression cee (Figure 7-13a) and

buckling of the compression flange (Figure 7-13b). Flange buckling occurs for squarer RHS where the flange slenderness is greater and is similar to flange buckling in unperforated sections. Larger holes reduce the stabilising influence of the web and induce flange buckling at lower curvatures. Arching of the compression cee occurs for more oblong RHS with larger holes. Both mechanisms of plastic collapse were observed in the experimental study (Chapter 3). Sections with single holes also experience arching (Figure 7-14a), and this can induce sympathetic buckling of the unperforated web (Figure 7-14b).

The moment-curvature relationships for the three sizes of RHS used in the plastic parametric study are shown in Figure 7-15 through Figure 7-20. Moment and curvature are reduced to non-dimensional ratios in the same way as in Figure 7-12.

The reductions in the elastic capacity (global rather than first yield) due to perforations are small (less than 25%) as the webs contribute a minor part of the elastic section modulus. Small holes remove small amounts of material close to the neutral axis and the reduction in elastic capacity is correspondingly small. The elastic capacities of the three sections as determined by FE are plotted in Figure 7-21 and Figure 7-22. The elastic capacities as determined by the design expressions (Equation 7-12 and Equation 7-13) are also plotted. The FE elastic capacities are, in all cases, greater than the design expressions predict.

The maximum moments achieved by the three sections as determined by FE are plotted in Figure 7-23 and Figure 7-24. The plastic moments of resistance as determined by the design expressions (Equation 7-9 and Equation 7-10) are also plotted.

All three RHS chosen for the full plastic study were capable of generating the plastic moment of resistance and, therefore, can be described as class 2. The

three sizes have the same web slenderness (22.0), and since they have aspect ratios at both ends of the standard European range, indicate that all standard sections with web slendernesses less than 22.0 will also be class 2.

Strain hardening has the effect of increasing the maximum capacity moment beyond the design values and FE models without strain hardening in the material model have maximum moments equal to the design values (Figure 7-25).

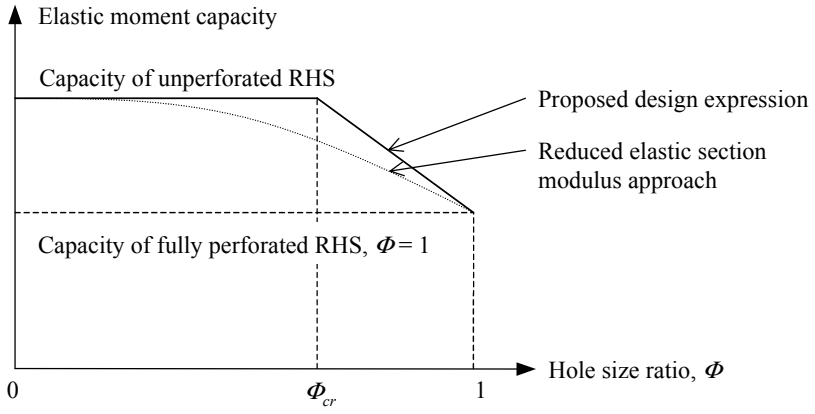

Figure 7-11: Elastic moment capacity

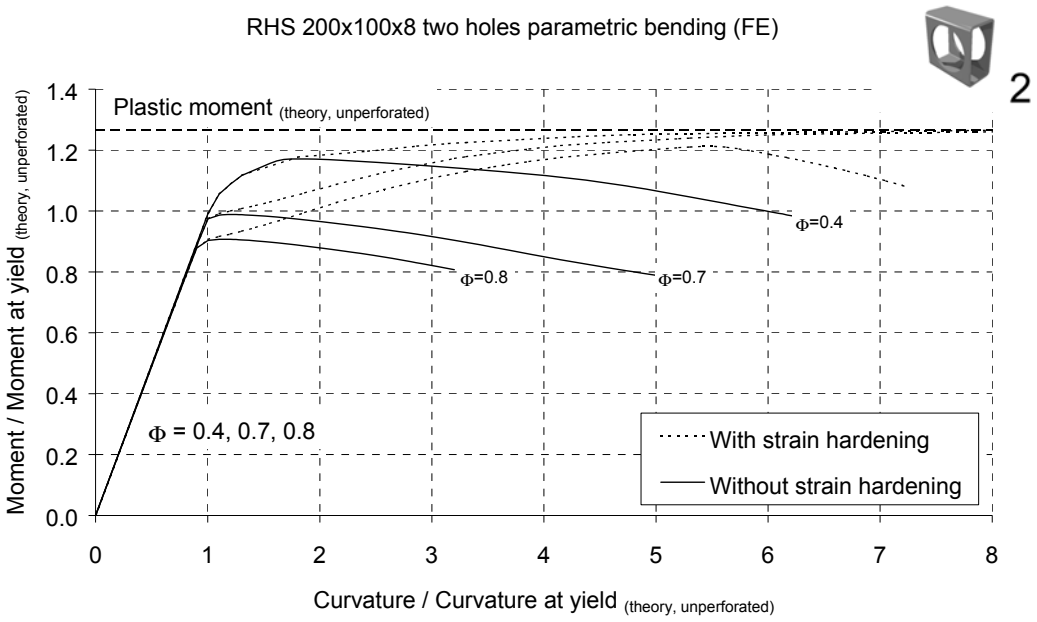

Figure 7-12: The significance of strain hardening for beam ductility

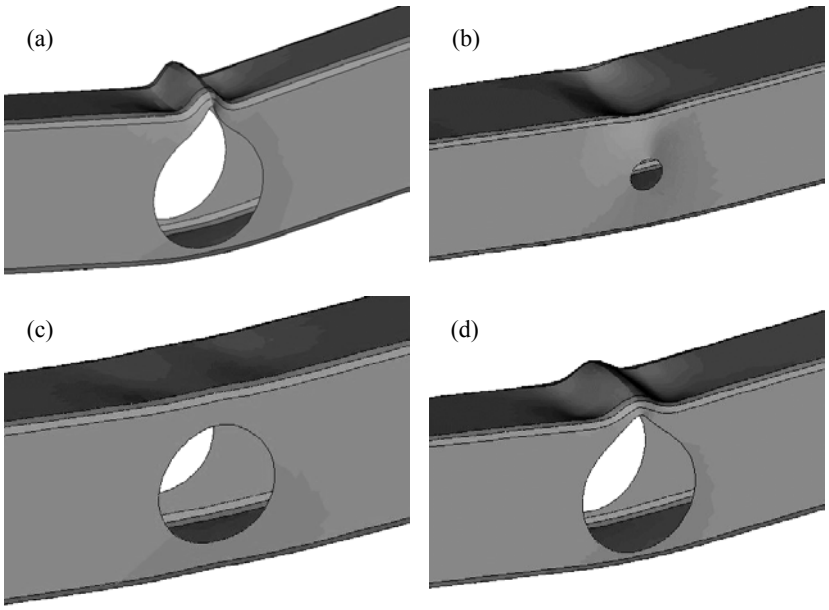

Figure 7-13: Distortions under the action of bending (two holes)

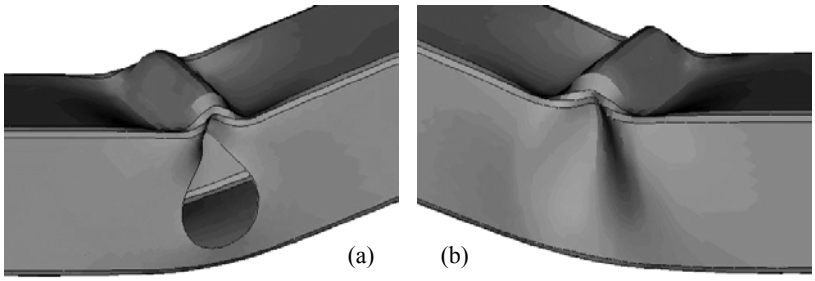

Figure 7-14: Distortions under the action of bending (one hole)

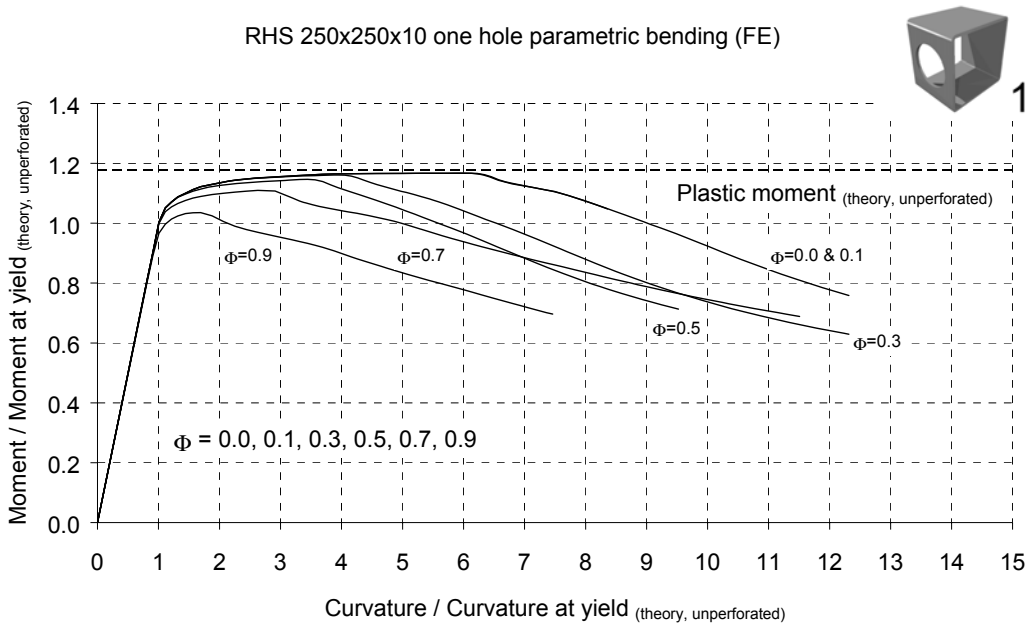

Figure 7-15: Moment-curvature relationship for RHS 250x250x10 one hole

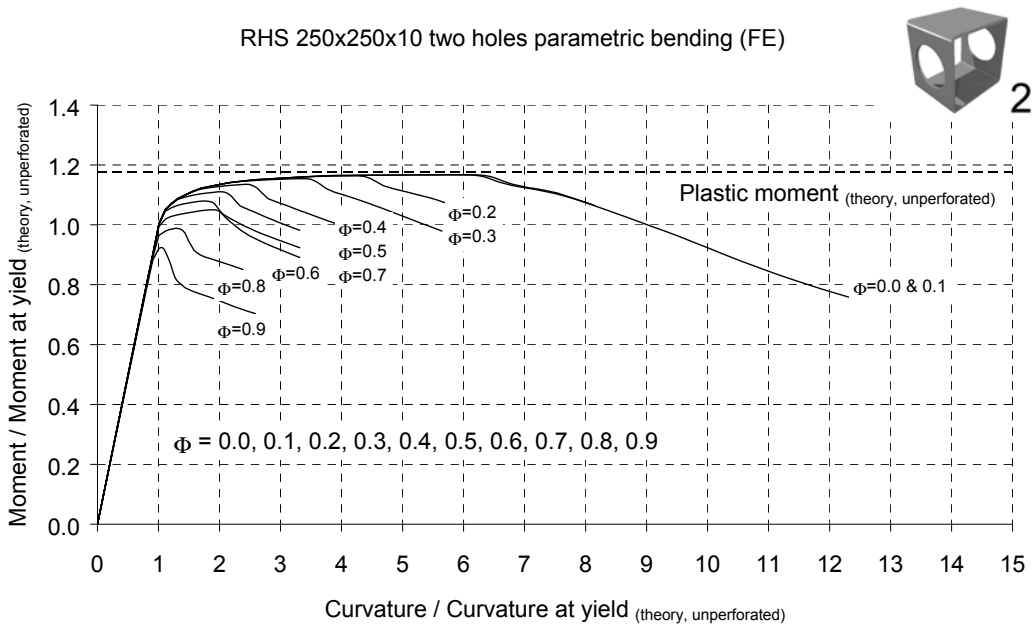

Figure 7-16: Moment-curvature relationship for RHS 250x250x10 two holes

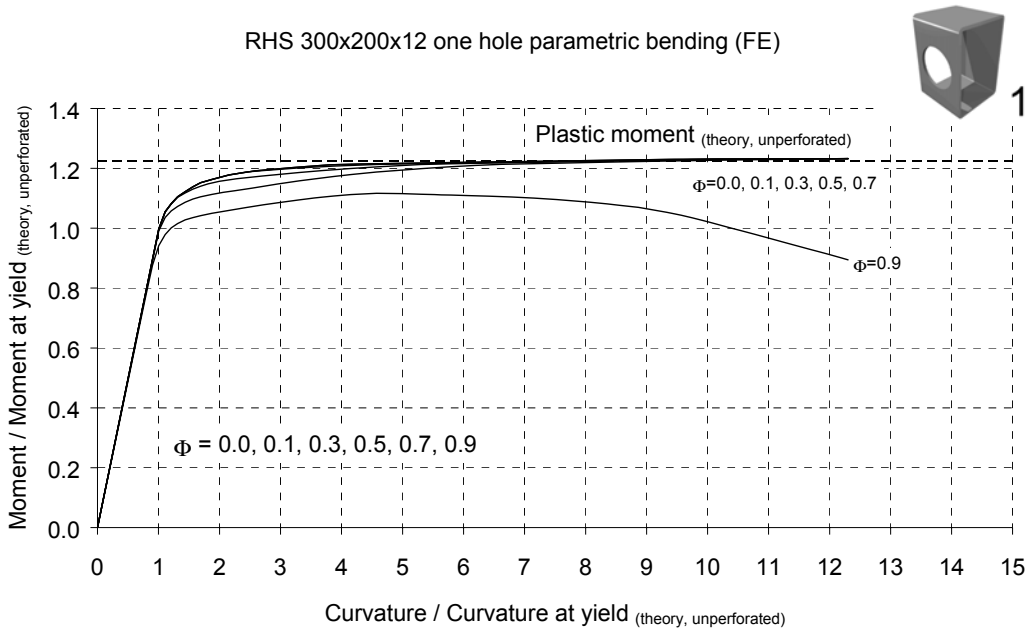

Figure 7-17: Moment-curvature relationship for RHS 300x200x12 one hole

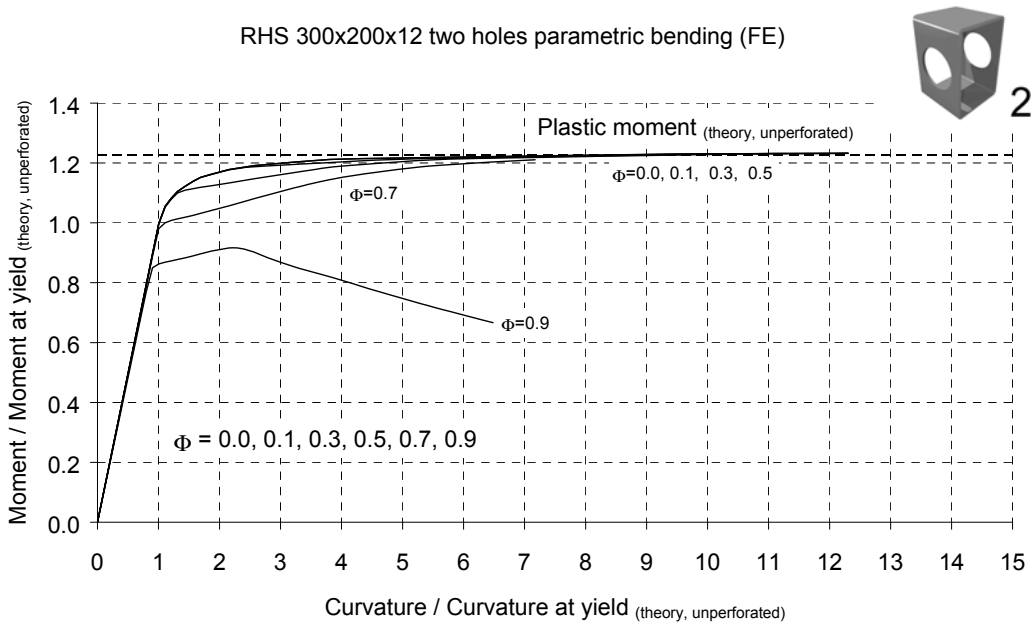

Figure 7-18: Moment-curvature relationship for RHS 300x200x12 two holes

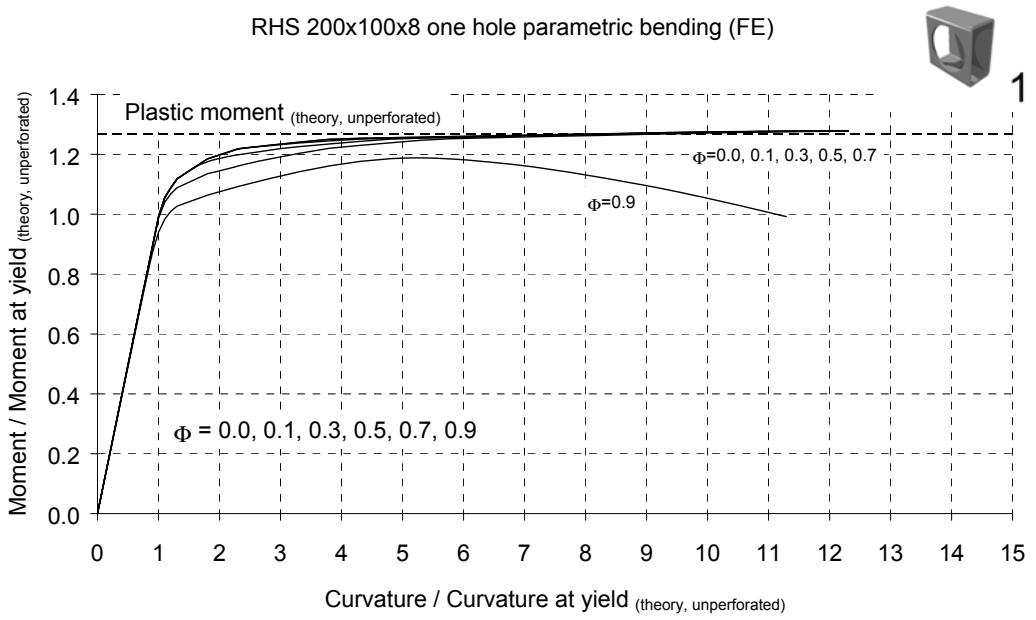

Figure 7-19: Moment-curvature relationship for RHS 200x100x8 one hole

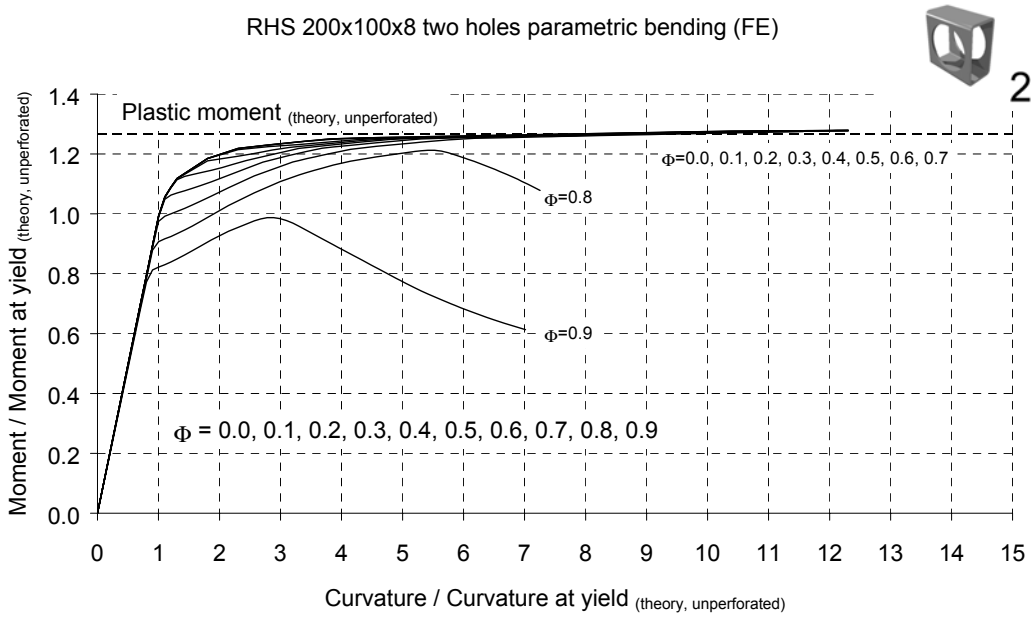

Figure 7-20: Moment-curvature relationship for RHS 200x100x8 two holes

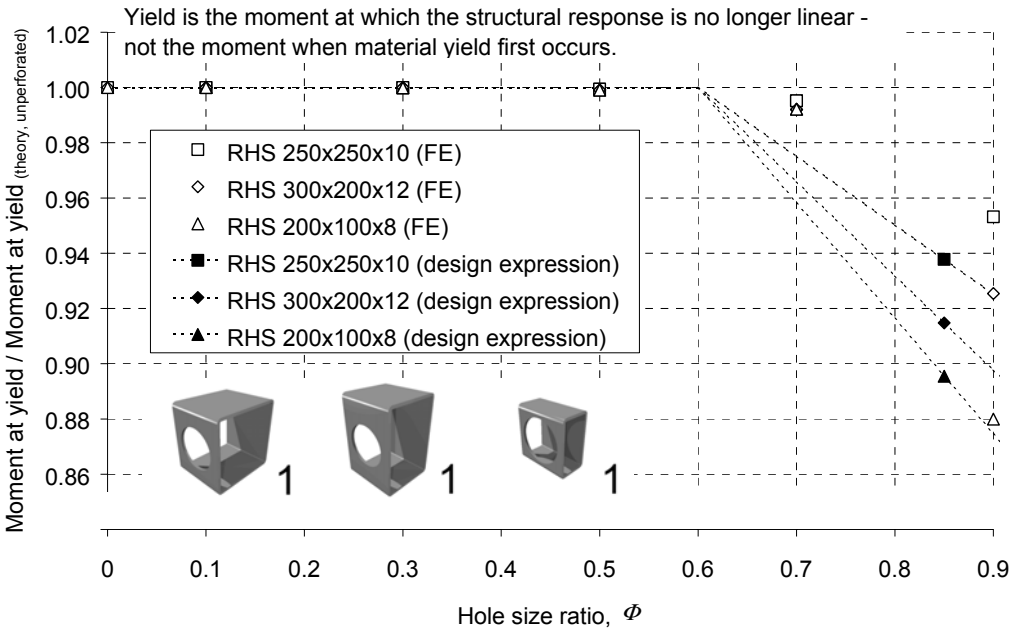

Figure 7-21: Yield in bending for sections with one hole (FE and design)

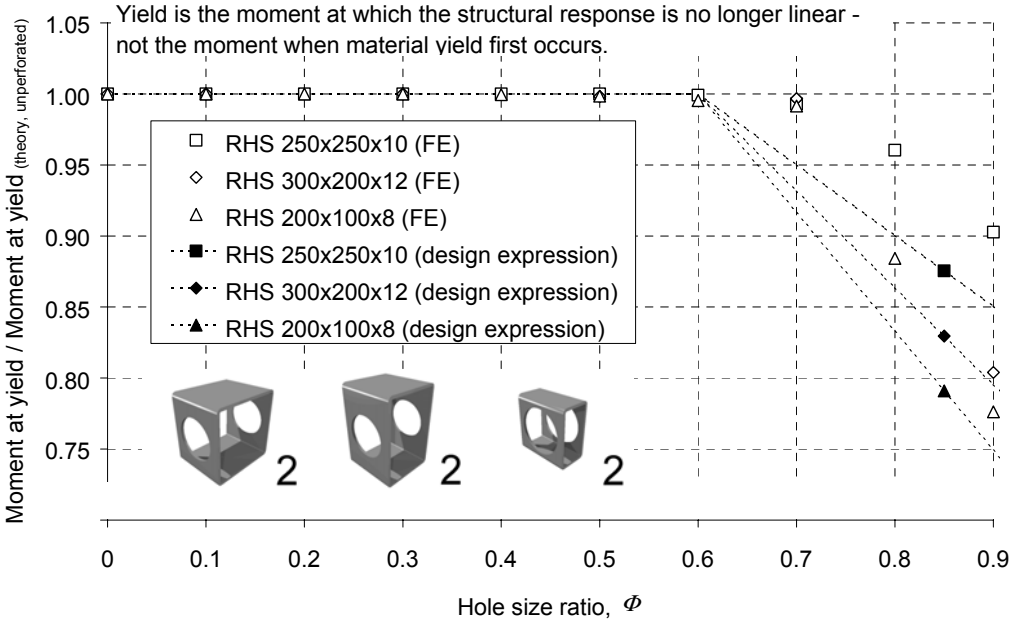

Figure 7-22: Yield in bending for sections with two holes (FE and design)

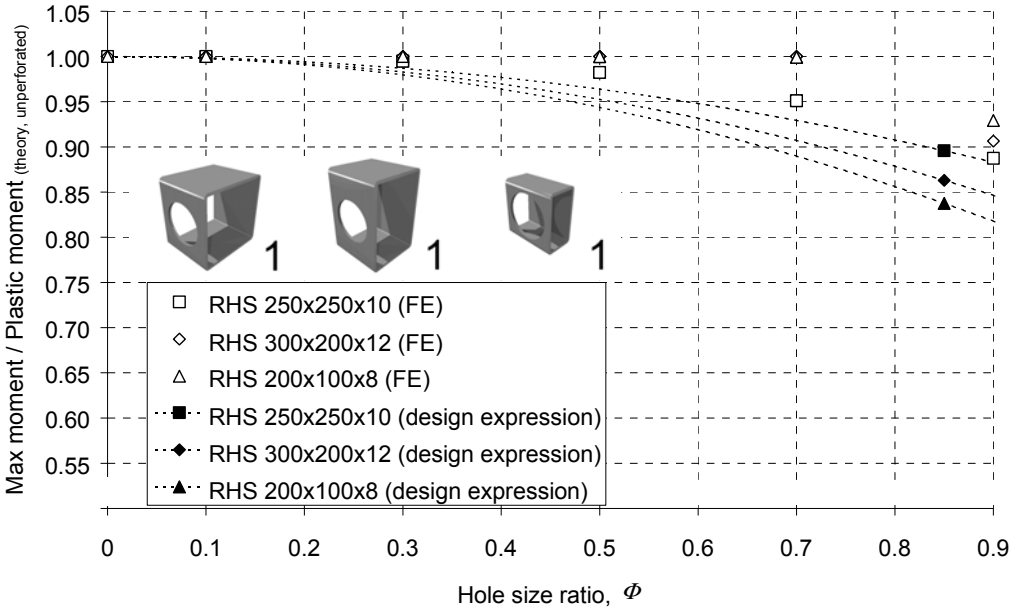

Figure 7-23: Maximum moment for sections with one hole (FE and design)

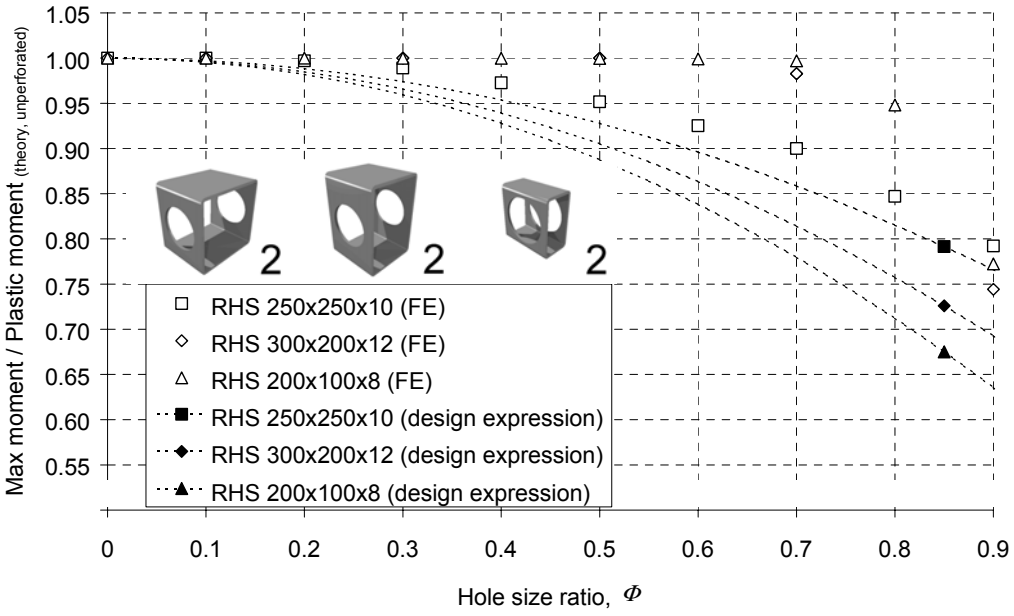

Figure 7-24: Maximum moment for sections with two holes (FE and design)

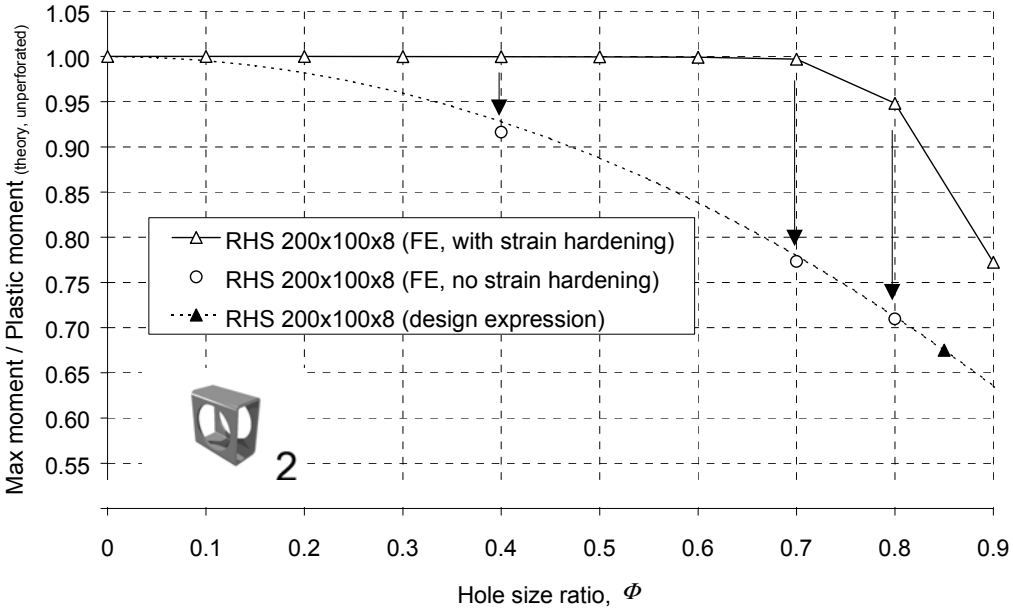

Figure 7-25: Maximum moment without strain hardening

7.5.4 Deflection

Clause N.2.3 of Annex N in EC3 deals with the deflection of I-beams with single perforations. The clause states that the deflection should be calculated from the overall bending deformation of the unperforated beam and the additional deformation of the perforated part, but does not provide a method by which this might be achieved. The requirements of clause N.2.3 when transposed to the bending deformation of a perforated RHS are:

(1) The additional deformation of the perforated beam should be determined taking into account:

- The effect of global bending on the overall deformation of the perforated cross-section

- The effect of localised bending deformation of the top and bottom cees

(2) The deformations due to the presence of the web opening should be analysed taking slope compatibility at the ends of the opening into account

In the elastic range, the displaced shape of a perforated RHS in bending can be calculated as follows:

(1) By treating the perforated zone as a sub-member of one hole diameter in length with a reduction in the stiffness proportional to the reduction in the second moment of area at the central cross-section

(2) By taking slope compatibility at the ends of the perforated zone into account

The displaced shape calculated by this method is a good match for the displaced shape produced by FE (e.g. Figure 7-26) but the resulting deflections are only slightly larger than for an unperforated beam (Table 7-6). Short beams and beams with multiple perforated zones are most affected, but the additional deflection for a 2.5 m beam with a single perforated zone is less than 5%.

Table 7-6: Deflection in bending

Section	Hole size ratio, Φ	One hole		Two holes	
		Deflection (% of unperforated)		Deflection (% of unperforated)	
		FE	Calculation	FE	Calculation
RHS 250x250x10	0.1	99.98	100.00	99.97	100.00
RHS 250x250x10	0.2	-	-	99.98	100.01
RHS 250x250x10	0.3	99.99	100.01	99.99	100.03
RHS 250x250x10	0.4	-	-	100.02	100.09
RHS 250x250x10	0.5	100.05	100.11	100.11	100.22
RHS 250x250x10	0.6	-	-	100.27	100.46
RHS 250x250x10	0.7	100.27	100.42	100.65	100.88
RHS 250x250x10	0.8	-	-	101.35	101.55
RHS 250x250x10	0.9	101.21	101.20	102.64	102.60
RHS 200x100x8	0.1	99.98	100.00	99.96	100.00
RHS 200x100x8	0.2	-	-	99.97	100.01
RHS 200x100x8	0.3	99.99	100.02	99.99	100.04
RHS 200x100x8	0.4	-	-	100.06	100.12
RHS 200x100x8	0.5	100.52	100.15	100.21	100.30
RHS 200x100x8	0.6	-	-	100.52	100.65
RHS 200x100x8	0.7	102.06	100.59	101.12	101.26
RHS 200x100x8	0.8	-	-	102.22	102.29
RHS 200x100x8	0.9	102.24	101.72	104.33	104.01
RHS 300x200x12	0.1	99.98	100.00	99.96	100.00
RHS 300x200x12	0.3	99.99	100.02	99.98	100.05
RHS 300x200x12	0.5	100.10	100.18	100.19	100.37
RHS 300x200x12	0.7	100.48	100.70	101.10	101.48
RHS 300x200x12	0.9	102.06	102.01	102.88	104.53

Note: Elastic defection of a 2.5 m beam in pure bending

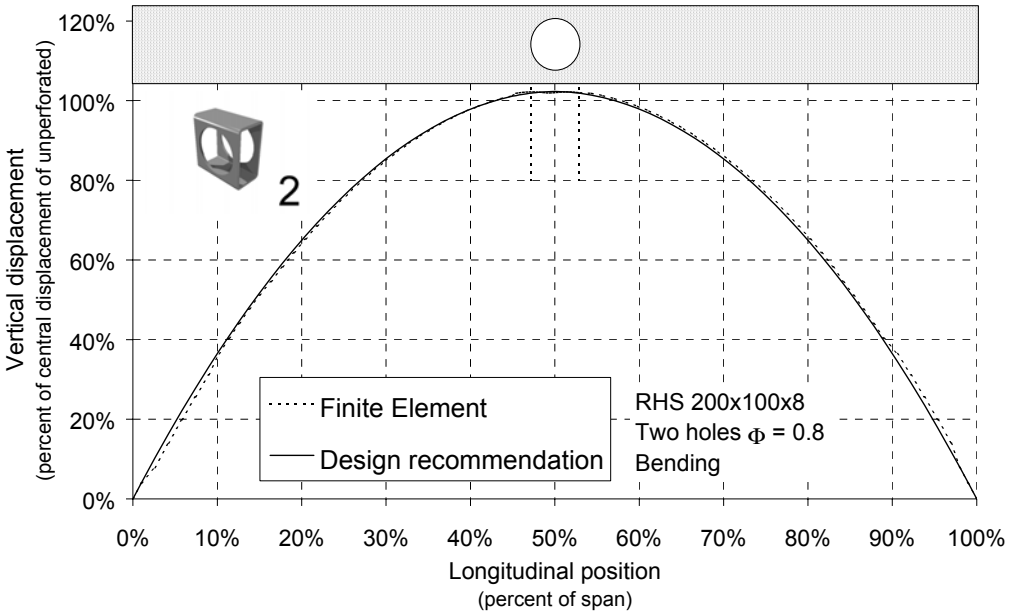

Figure 7-26: Bending displacement of RHS 200x100x8 two holes 140.8 mm dia

7.5.5 Zone of influence

The zone of influence is the length of the RHS over which the web opening influences the stress distribution, and hence marks the boundary between the perforated and unperforated zones (Figure 7-1). In the elastic range, the zone of influence for bending has been observed to extend a distance in the order of one hole diameter on either side of the edge of the hole. Consequently, the zone is approximately three diameters in length (e.g. Figure 7-7).

Openings placed in the same web at sufficient separations, such that the zones of influence do not overlap, will not cause the stress distributions to interact, and hence will not cause a further reduction in resistance (provided there is no instability e.g. web post buckling).

In Clause N.2.1.1 of Annex N (EC3) the allowable clear width between circular holes in I-beams is dependent on the shear force but the minimum value is one and a half diameters.

7.5.6 Design recommendation for calculation of resistance

It has been observed that RHS with web slenderness less than or equal to 22.0 can be treated as class 2 sections. For the present, it is recommended that a conservative approach be adopted for perforated RHS with more slender webs: treating them as class 3 sections. Very slender sections are likely to exhibit class 4 behaviour. Since perforated sections are not practicable for plastic design, there is no requirement for a class 1 definition.

If all plasticity is to be avoided, the elastic bending capacity can be calculated using Equation 7-14, where γ_{MBen1} and γ_{MBen2} are possible partial safety factors. The stress concentration factor for bending ($\psi_{bending}$) can be found from Table 7-7. The expression is valid for hole size ratios between 0 and 0.9 and for web slendernesses between 10.0 and 34.0, but does not allow for class 4 behaviour.

$$M_{el,y,Rd,1hole} \text{ or } M_{el,y,Rd,2holes} = \frac{M_{el,y,Rd,unperf}}{\left(\psi_{bending} + \gamma_{MBen1}\right) \times \gamma_{MBen2}}$$

Equation 7-14

Alternatively, the design elastic moment for sections with holes larger than the critical size (Table 7-8) can be calculated using Equation 7-15 for sections with one hole, and Equation 7-16 for sections with two holes, where γ_{M0} is a possible partial safety factor. The design elastic moment for sections with holes smaller than

the critical hole size is equal to the design elastic moment of the unperforated section.

$$M_{el,y,Rd,1hole} = \frac{M_{el,y,Rd,unperf} - \left(M_{el,y,Rd,unperf} - f_y \left(W_{el,y,unperf} - \frac{t(h-3t)^3}{6h} \right) \right) \left(\frac{\Phi - \Phi_{cr}}{1 - \Phi_{cr}} \right)}{\gamma_{M0}}$$

Equation 7-15

$$M_{el,y,Rd,2holes} = \frac{M_{el,y,Rd,unperf} - \left(M_{el,y,Rd,unperf} - f_y \left(W_{el,y,unperf} - \frac{t(h-3t)^3}{3h} \right) \right) \left(\frac{\Phi - \Phi_{cr}}{1 - \Phi_{cr}} \right)}{\gamma_{M0}}$$

Equation 7-16

The design plastic moment of can be calculated using Equation 7-17 for sections with one hole, and Equation 7-18 for sections with two holes, where γ_{M0} is a possible partial safety factor.

$$M_{pl,y,Rd,1hole} = \frac{M_{pl,y,Rd,unperf}}{\gamma_{M0}} \left(1 - \frac{tr^2}{W_{pl,y,unperf}} \right)$$

Equation 7-17

$$M_{pl,y,Rd,2holes} = \frac{M_{pl,y,Rd,unperf}}{\gamma_{M0}} \left(1 - \frac{2tr^2}{W_{pl,y,unperf}} \right)$$

Equation 7-18

Table 7-7: Stress concentration factors for bending, $\psi_{bending}$

Hole size ratio, Φ	Web slenderness, λ_{web}						
	10	14	18	22	26	30	34
<=0.575	1.00	1.00	1.00	1.00	1.00	1.00	1.00
0.600	1.00	1.00	1.00	1.00	1.01	1.02	1.01
0.625	1.00	1.00	1.05	1.10	1.12	1.13	1.12
0.650	1.00	1.07	1.15	1.20	1.23	1.24	1.24
0.675	1.05	1.16	1.24	1.30	1.34	1.36	1.35
0.700	1.13	1.24	1.34	1.41	1.45	1.47	1.47
0.725	1.20	1.33	1.43	1.51	1.56	1.58	1.58
0.750	1.27	1.41	1.53	1.61	1.67	1.70	1.70
0.775	1.35	1.50	1.62	1.72	1.78	1.81	1.81
0.800	1.42	1.59	1.72	1.82	1.89	1.92	1.93
0.825	1.50	1.67	1.81	1.92	2.00	2.04	2.04
0.850	1.57	1.76	1.91	2.02	2.10	2.15	2.16
0.875	1.65	1.84	2.00	2.13	2.21	2.26	2.28
0.900	1.72	1.93	2.10	2.23	2.32	2.38	2.39

Note: Values obtained from Equation 7-6

Table 7-8: Critical hole size ratio for bending, Φ_{cr}

Web slenderness, λ_{web}	10-11	11-12	12-14	14-16	16-18	18-23	23-32
Critical hole size ratio, Φ_{cr}	0.65	0.64	0.63	0.62	0.61	0.60	0.59

Note: Values obtained from Figure 7-10

7.6 Shear

7.6.1 Introduction

Clauses 5.5.1 of EC3 and 4.2.3 of BS 5950 deal with the shear resistance of unperforated beams. The design value of shear force must be less than the plastic shear resistance ($V_{pl,Rd}$) defined by Equation 7-19.

$$V_{pl,Rd} = \frac{A_v f_y}{\sqrt{3} \times \gamma_{M0}}$$

Equation 7-19

The plastic shear resistance is the product of the shear stress at yield ($0.6f_y$ in BS 5950) and the shear area (A_v) modified by a material partial safety factor (γ_{M0}). The shear area is defined by Equation 7-20 (Table 5.16 in EC3 and Clause 4.2.3d of BS 5950), where A is the total area of the cross-section. The shear area is therefore the area of the flat part of the webs (that used to calculate web slenderness and hole size ratio) and a portion of area of the radii.

$$A_v = Ah / (b + h)$$

Equation 7-20

RHS are much stronger in shear than other types of section as they have two relatively thick webs. In practice, the shear resistance is so high that it is rarely critical for design, as can be illustrated by the following generalised example.

A cantilever loaded at the unsupported end by a point load is subject to uniform shear force and has a maximum bending moment at the supported end, that is equal to the product of the load and span. A critical cantilever length may be defined as that at which the shear resistance is equal to the shear force and the elastic bending resistance is equal to the maximum bending moment. For an RHS, this critical length (l_{cr}) is given by Equation 7-21. This expression is based on a simple calculation that assumes the cross-section remains plane regardless of the high shear forces and short span.

$$\frac{l_{cr}}{h} = \frac{\sqrt{3}\left(bh^3 - (b-2t)(h-2t)^3\right)}{12t(h-t)h^2}$$

Equation 7-21

The critical cantilever length for the sizes of RHS in the standard European range (BS EN 10210) is shown in Figure 7-27. The critical length increases with increasing slenderness, but reaches a limit (Equation 7-22) which is dependent only on aspect ratio. Any beam under any system of loads with a span longer than twice the critical cantilever length can never be made to fail in shear as it will fail in bending first. Since the maximum critical length (for $\alpha = 1$) is only 1.16 times the section depth, the shear resistance is rarely critical in practice.

$$\left(\frac{l_{cr}}{h}\right)_{\max} = \frac{0.866}{\alpha} + 0.289$$

Equation 7-22

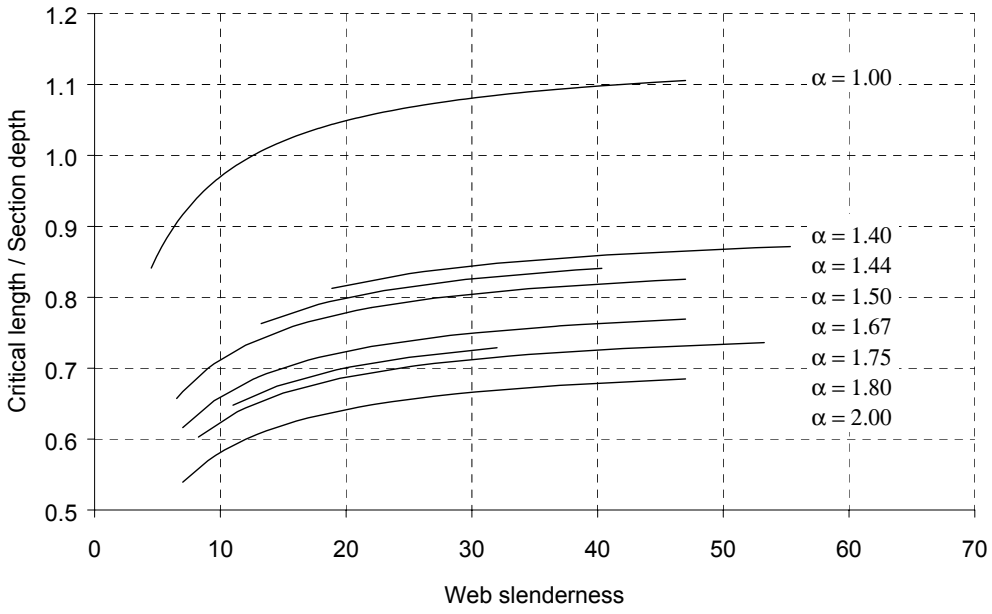

Figure 7-27: Critical cantilever length for shear

7.6.2 Concentration factors for elastic stress

An RHS without an opening in the web in pure shear will have 'top hat' distribution of elastic shear stress (Figure 7-28) similar in shape to the distribution of shear stress in an I-section. A small circular opening on the neutral axis will disturb the system of stress where it is most uniform, and produce a stress pattern similar to that around a hole in an infinite plate in pure shear. Stress is raised at four points around the edge of the hole (location ③ in Figure 7-2). Larger holes raise the stress further, as less web is available to transmit the shear across the width of the hole.

A number of FE models (84) have been used to study the stress concentrations around openings in the webs of RHS in shear with zero bending moment at the location of the hole. The models used in the parametric study are shown diagrammatically in Figure 7-29. Stress concentrations were found to be dependent on hole size and web slenderness, but not aspect ratio. The dependence of stress concentration on the web slenderness is analogous to the dependence upon thickness of the stress concentration around a circular hole in an infinite plate in pure shear. The FE contour plots of von Mises stress shown in Figure 7-30 are typical of the stress patterns observed.

The FE models were used to obtain a representative sample of stress concentration factors for shear. The stress concentration factor for shear, Ψ_{shear}, is defined by Equation 7-23 and is the ratio of the plastic shear resistance of the unperforated beam to the shear force at first yield for the perforated beam. The shear force (V) is such that the maximum von Mises stress in the perforated RHS ($\sigma_{Mises,Max}$) is in the elastic range.

$$\psi_{shear} = \frac{\sigma_{Mises,Max}}{\sqrt{3}V} A_v$$

Equation 7-23

The stress distribution in the web of an RHS with one hole is similar to that in the web of an RHS with two holes, although maximum stresses are slightly lower, particularly for large holes. To simplify the parametric study, a conservative approach was used and stress concentration factors were obtained for sections with two holes, to be applied also to sections with one hole.

The stress concentration factors obtained from the FE study were approximated by an empirical mathematical function, which was fitted to the data using a least squares method (Equation 7-24). For the models (with two holes) included in the study, the maximum differences (in absolute terms) between the empirical function and the FE values were 0.76 (empirical value less than FE value) and 2.01 (empirical value greater than FE value). The square root of the average square error was 0.44. The actual stress concentration data from the FE study is presented in Appendix E.

$$\psi_{shear} = \left(\frac{1}{1-\Phi} - 1\right)\left(0.02705\lambda_{web} - 1.149\Phi^2 + 0.152\Phi + 1.573\right) + 2$$

Equation 7-24

The empirical function for stress concentration factor is shown graphically in Figure 7-31. Stress concentration factors increase with increasing hole size and are larger for more slender webs. The function is valid for hole size ratios between 0 and 0.9 and for web slendernesses between 9.5 and 47.0.

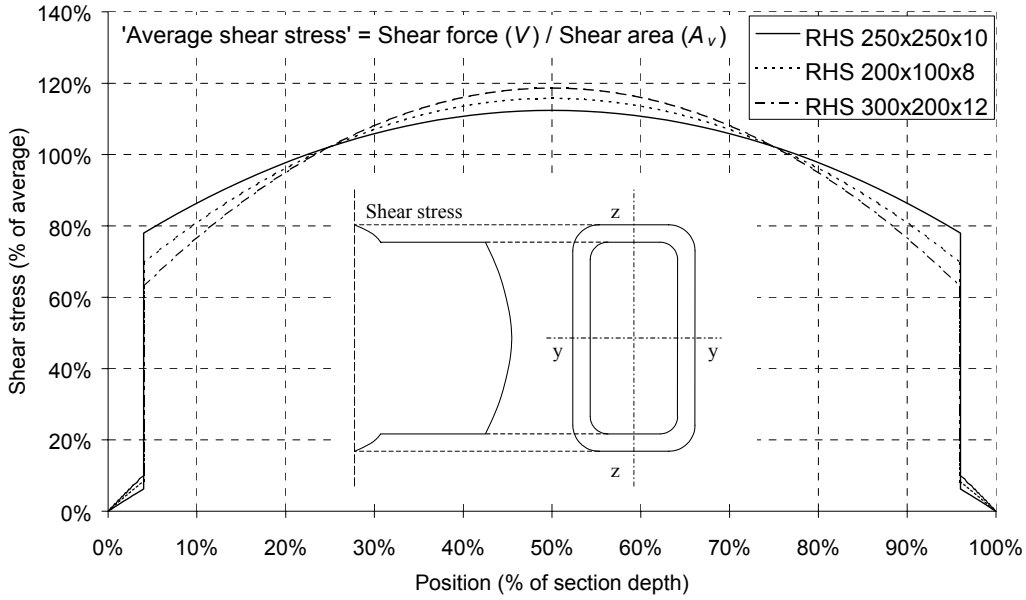

Figure 7-28: Distribution of elastic shear stress

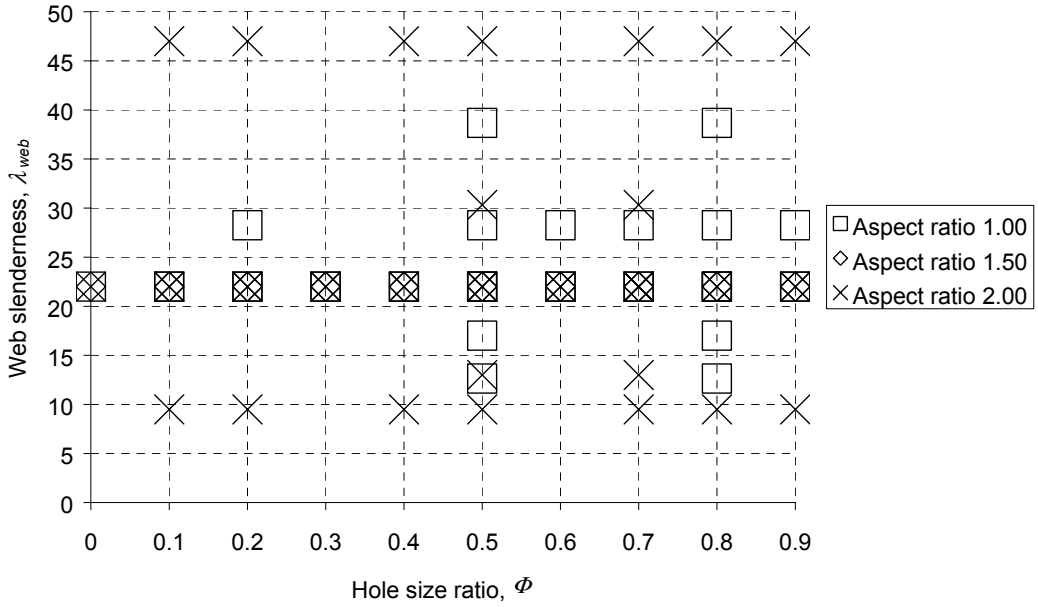

Figure 7-29: Parametric sampling for shear

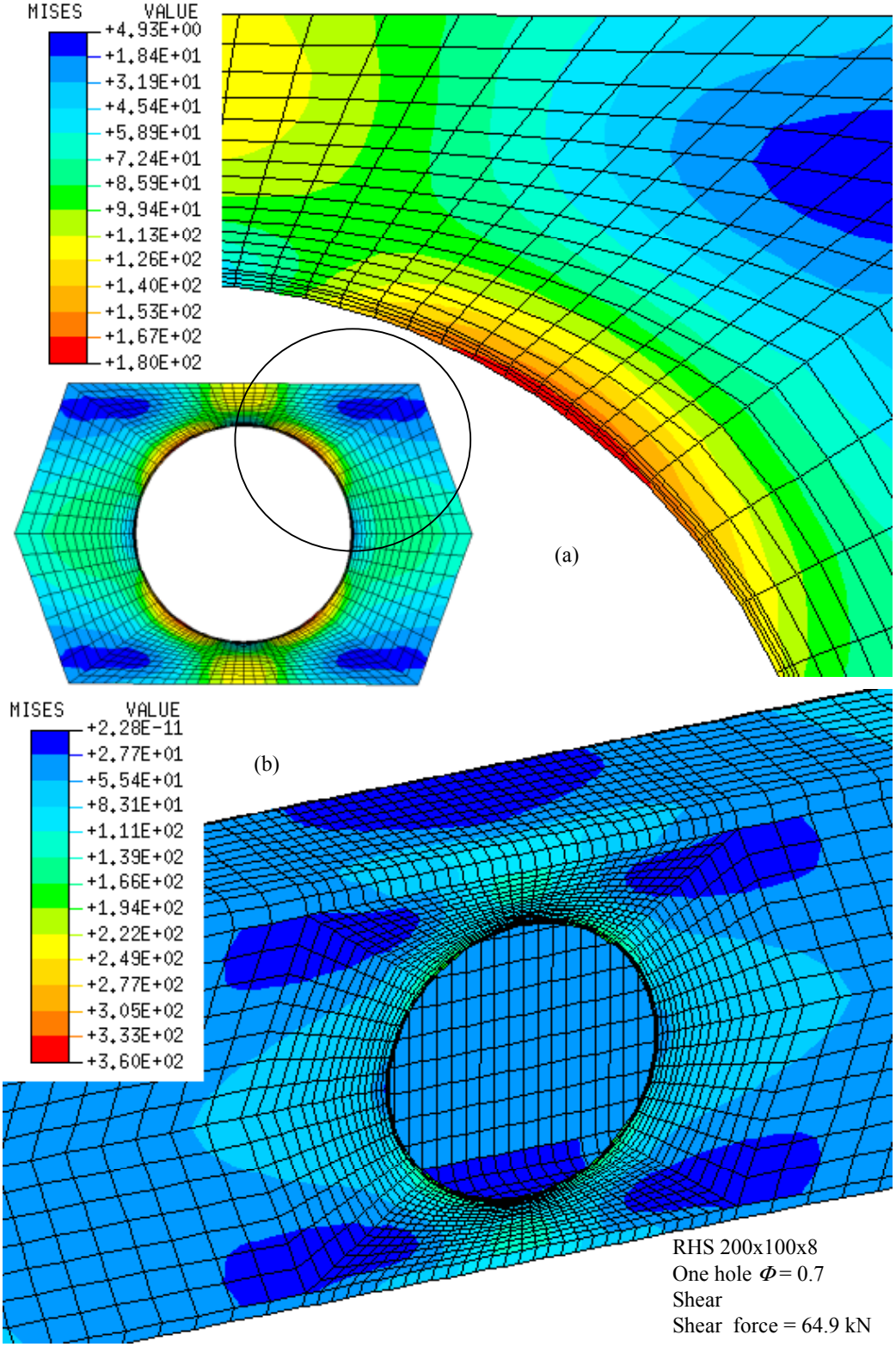

Figure 7-30: Distribution of von Mises stress for RHS 200x100x8 in shear

Von Mises stress plotted on external surface
(Original in colour)

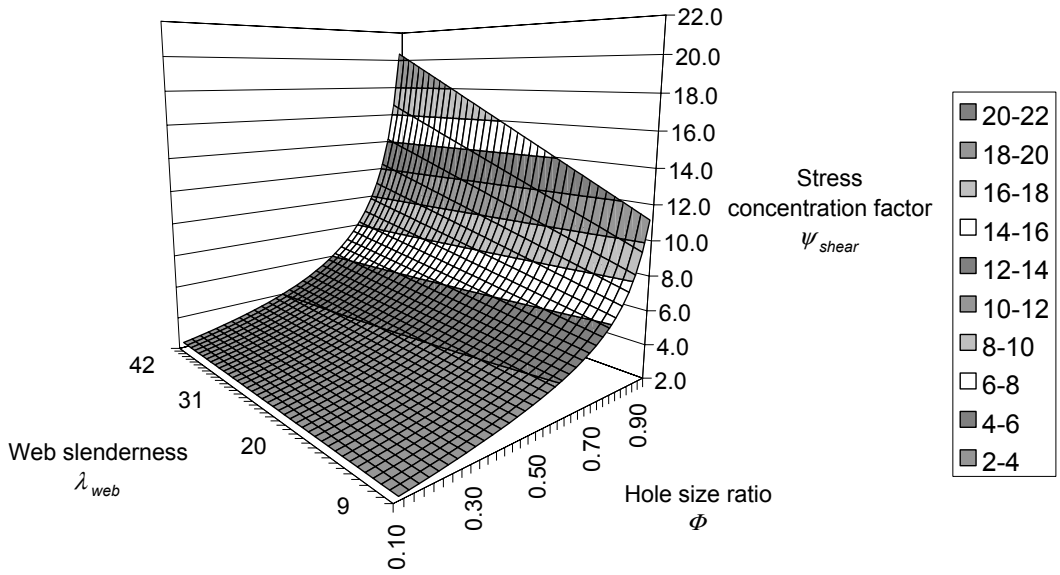

Figure 7-31: Stress concentration factors for shear

7.6.3 Resistance

In BS 5950, clause 4.2.4 states that the shear stress in sections with web openings significantly larger than those required for fasteners should be calculated from first principles assuming elastic behaviour. The clause imposes a maximum limit on shear stress that is higher (17%) than the design shear yield stress.

In EC3, the shear resistance of I-beams with individual web openings is dealt with in clause N.2.1.3 of Annex N. The clause provides an equation (N.7c) for calculation of the plastic shear resistance of I-beams with circular web openings that is based on the reduced shear area. The clause also provides an equation for the calculation of shear buckling resistance (N.8b).

The stress concentration factors determined in the previous section can be used to determine the shear resistance based on a maximum stress criterion (as in BS 5950). If stress is limited to the design yield stress, the yield based shear resistance

of the perforated section can be determined by dividing the plastic shear resistance of the unperforated section by the stress concentration factor (Equation 7-25).

$$V_{el,y,Rd,1hole} \text{ or } V_{el,y,Rd,2holes} = V_{pl,y,Rd,unperf} \Big/ \psi_{shear}$$

Equation 7-25

An alternative approach based on the reduced section (similar to than in Annex N of EC3 but less sophisticated) is to base the shear resistance of the perforated RHS on a simple ratio of the portion of remaining web at the centre of the hole (Equation 7-26). This approach results in a higher resistance than the maximum stress approach for all hole sizes, but means that there is some plasticity present at design loads.

$$V_{el,y,Rd,1hole} \text{ or } V_{el,y,Rd,2hole} = (1-\Phi) \times V_{pl,y,Rd,unperf}$$

Equation 7-26

Only sections with large holes ($\Phi \geq 0.6$) were used for the full plastic parametric FE study as sections with small holes were too strong to be failed in shear. The shear force-displacement plots are shown in Figure 7-32 through Figure 7-37. The non-dimensional ratio of shear force against the plastic shear capacity of the unperforated section is plotted on the ordinate axis and shear angle is plotted on the abscissa. The shear angle is the angle between the original longitudinal axis of the RHS and the displaced longitudinal axis at each end. The shear angle is dimensional and is dependent on the length of the beam. The shear resistance calculated from Equation 7-26 is also plotted and shown as a circle symbol on the corresponding data series.

For the range of sections chosen for the full plastic parametric study, the shear resistance based on the reduced section is less than the shear force at the onset of non-linearity. However, sections with more slender webs may be susceptible to the Vierendeel shear failure mechanism and shear resistance may have to be reduced accordingly. The relative thickness of the webs means that RHS are more resistant to Vierendeel shear failure than I-sections and a consideration of the mechanism may not be necessary in practice.

The Vierendeel shear force can be estimated using an equivalent rectangular opening (Figure 7-38a) and plastic stress block for the hinges (Figure 7-38b) as previously used in allowable stress design (e.g. Constrado document Cl/SfB 1968 'Holes in beam webs'). Alternatively a more sophisticated method for calculating internal forces and moments may be employed such as the one used in Clause N.3.3.2.3 of Annex N (for beams with multiple circular openings).

The shear resistance of a section with one hole is larger than the shear resistance of the same section with two holes, particularly for squarer sections. In the unperforated zone, the webs each carry the same amount of shear force. However, in the perforated zone, the torsional and lozenging rigidity of the box shape allows the unperforated web to carry a greater portion of the shear force than the perforated web. This effect is exaggerated by the boundary conditions and short span used in the parametric FE models. Asymmetry induces internal torsional and lozenging forces that, for high plastic shear loads in longer spans, can cause distortion of the cross-section at some considerable distance from the hole. In design, the distortion of the cross-section is of much less importance than the (much larger) vertical deformations across the hole.

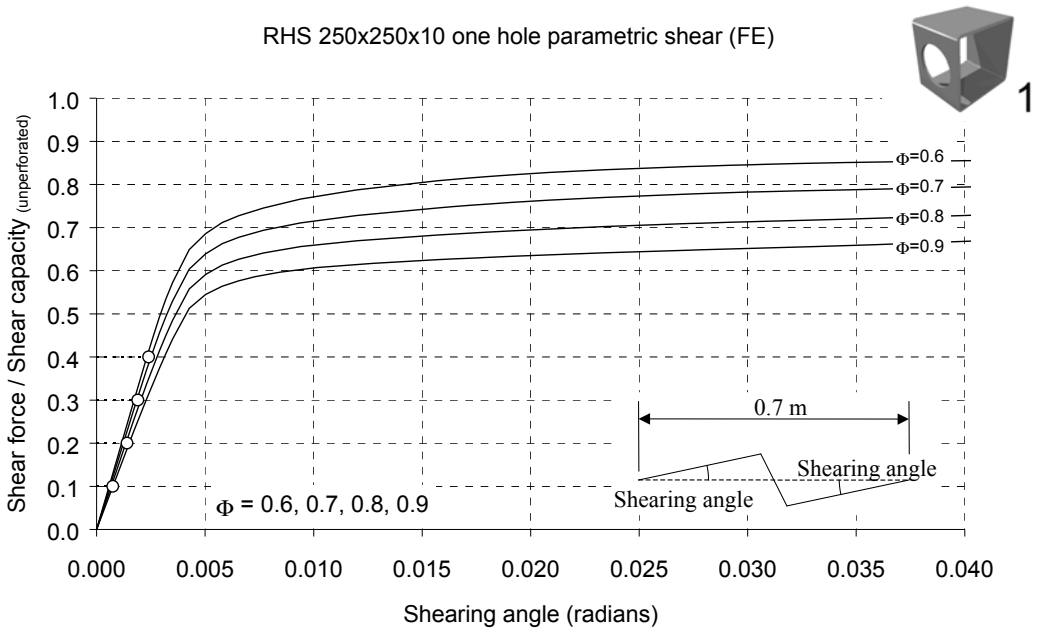

Figure 7-32: Shear force-shearing angle relationship for RHS 250x250x10 one hole

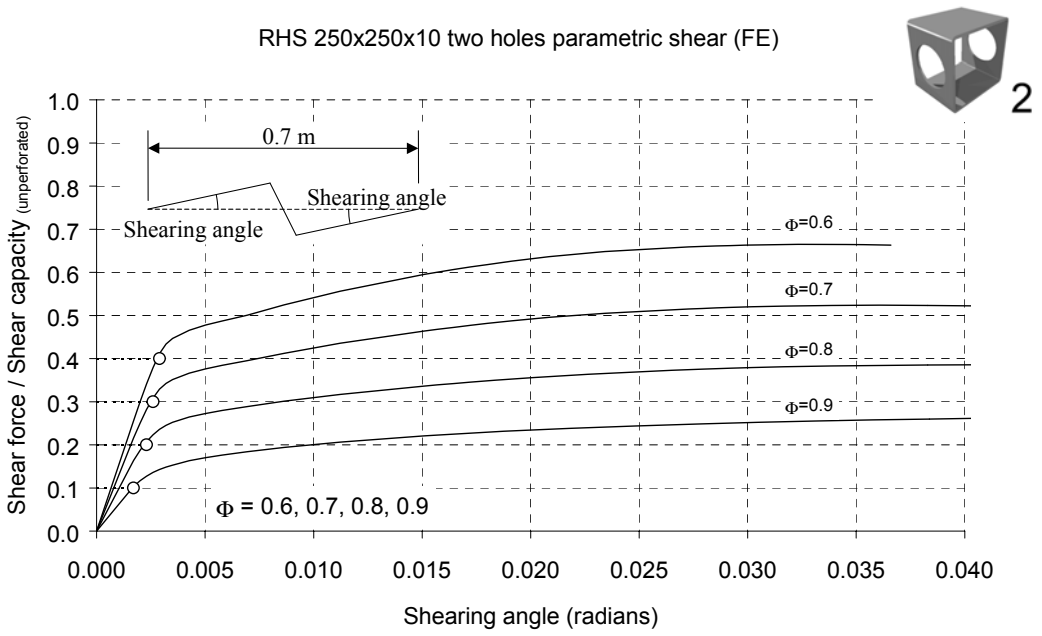

Figure 7-33: Shear force-shearing angle relationship for RHS 250x250x10 two holes

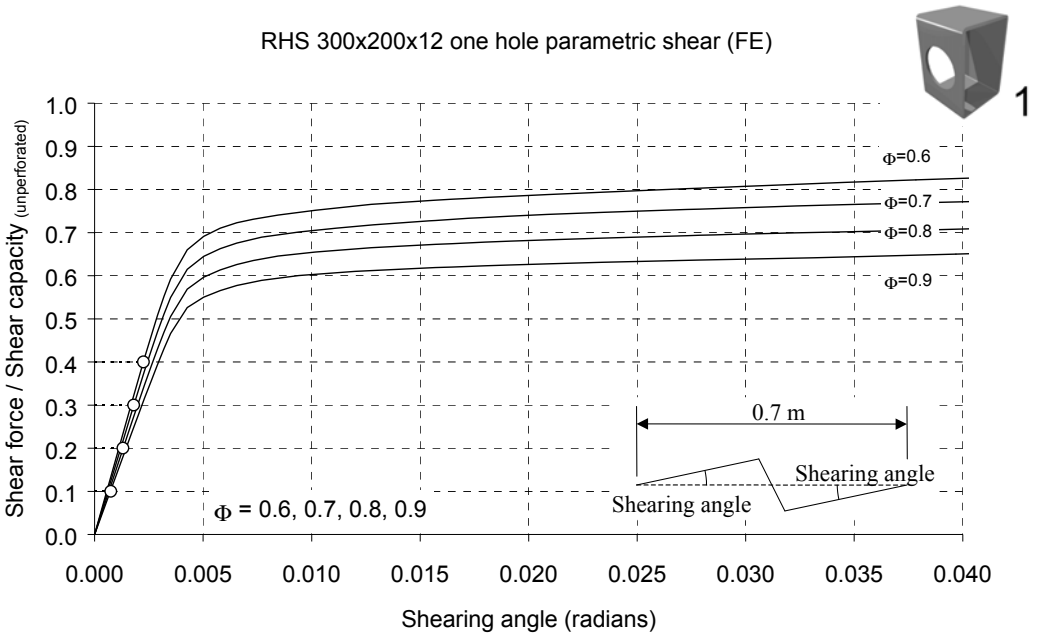

Figure 7-34: Shear force-shearing angle relationship for RHS 300x200x12 one hole

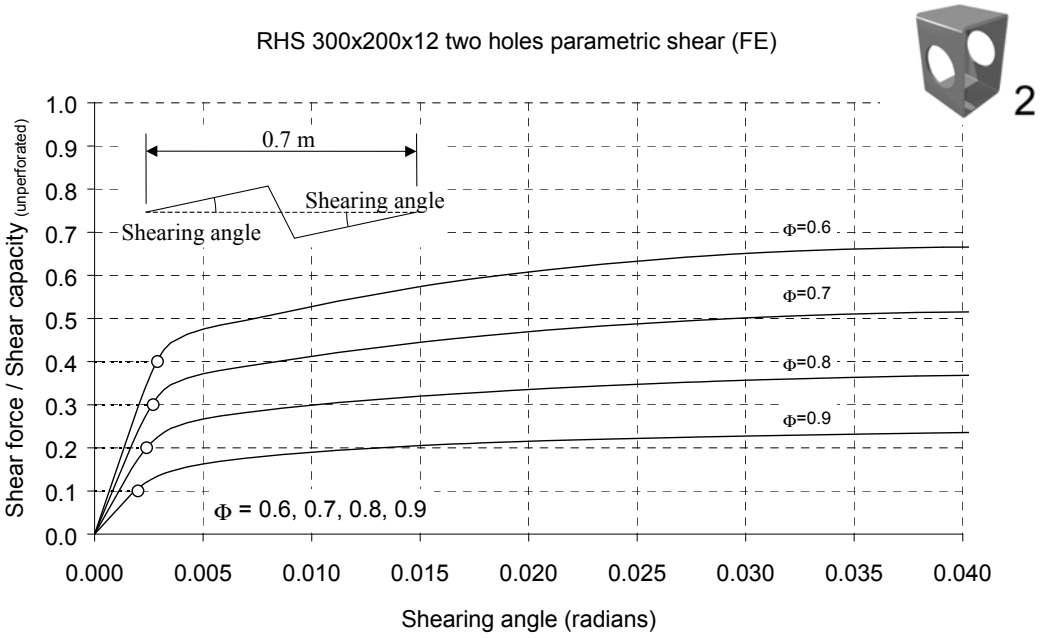

Figure 7-35: Shear force-shearing angle relationship for RHS 300x200x12 two holes

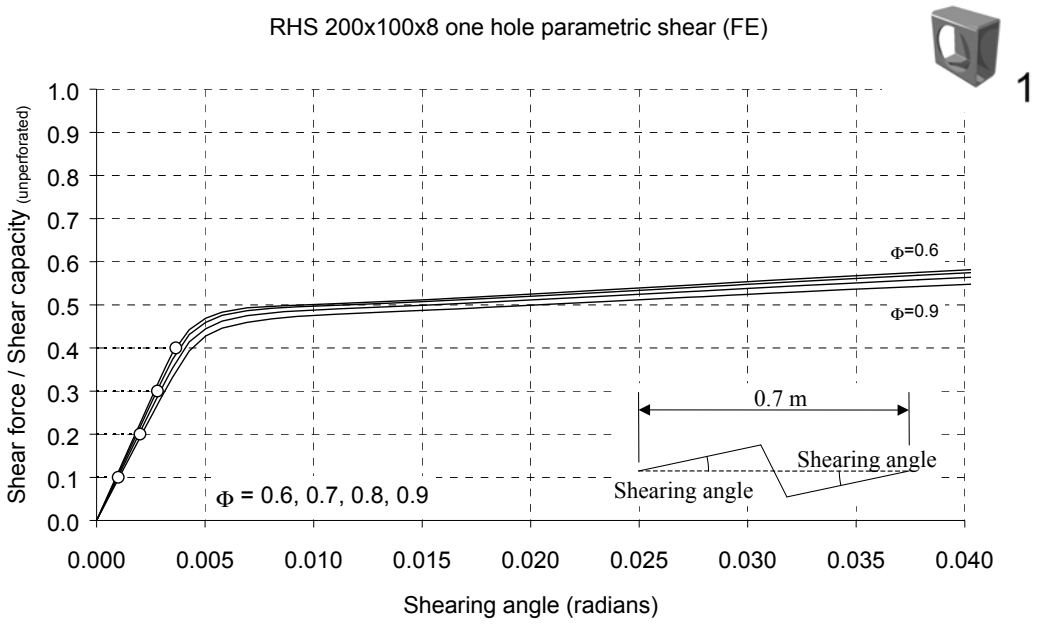

Figure 7-36: Shear force-shearing angle relationship for RHS 200x100x8 one hole

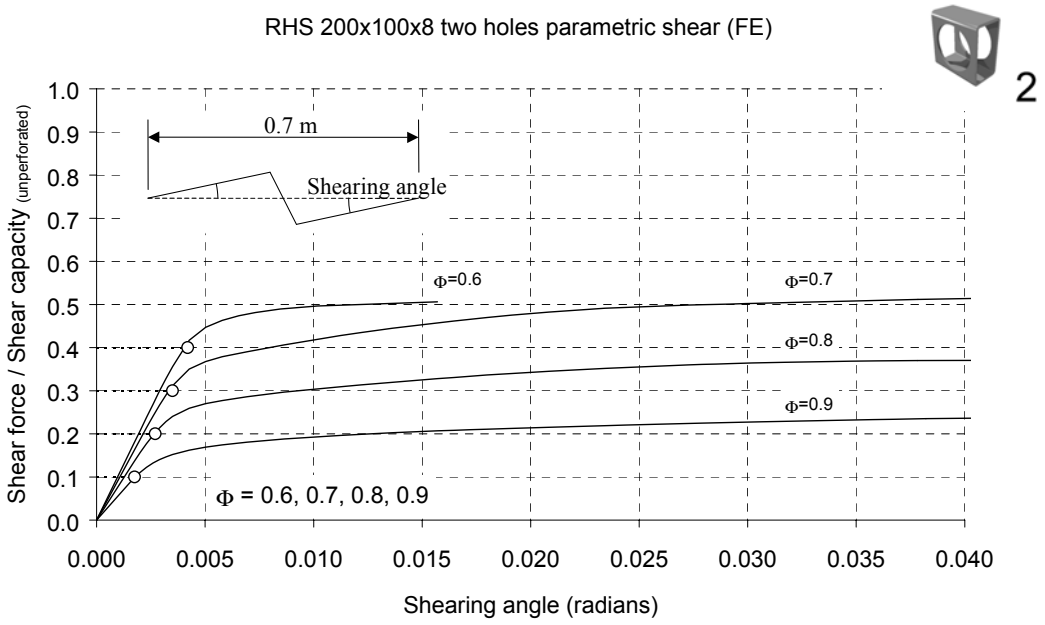

Figure 7-37: Shear force-shearing angle relationship for RHS 200x100x8 two holes

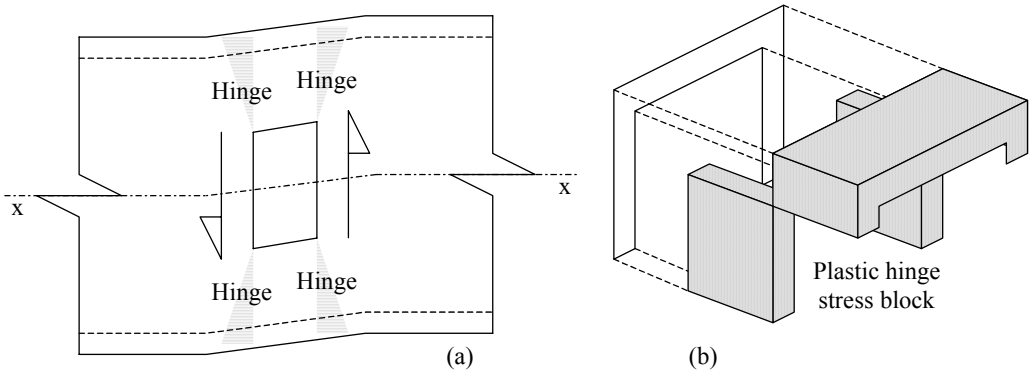

Figure 7-38: The vierendeel mechanism of shear failure

7.6.4 Deflection

Clause N.2.3 of Annex N in EC3 deals with the deflection of I-beams with single perforations. The clause states that the calculation should include a component of the shear deformation across the opening. Shear deformation at extreme displacements, for RHS with large openings ($\Phi \geq 0.6$) takes the form shown in Figure 7-39 and is similar for sections with similar hole sizes, regardless of the aspect ratio.

If the shear resistance is calculated according to a maximum elastic stress criterion, the strains at design loads will be limited to the elastic range and shear deformation will be small enough to be neglected.

The deformation of the perforated zone is crucial in design, as displacements are concentrated over a short length. The displaced shape shown in Figure 7-40 is typical of the shear deformation of RHS with large holes. If a reduced shear area approach is adopted for design, a reliable method of calculating the vertical

displacement across the width of the hole must be developed as an accompanying serviceability limit.

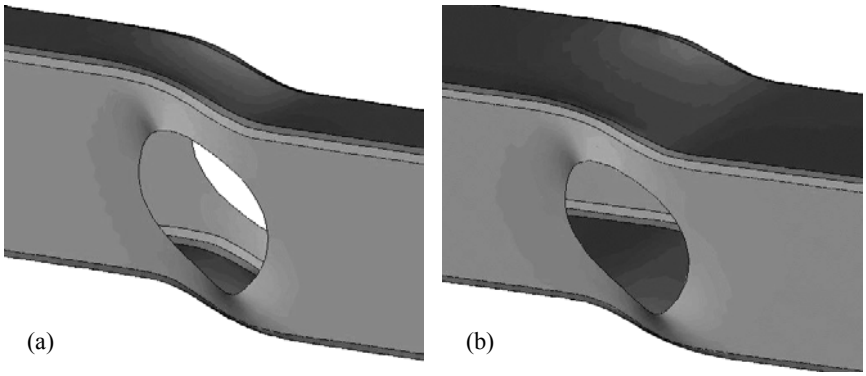

Figure 7-39: Distortions under the action of shear

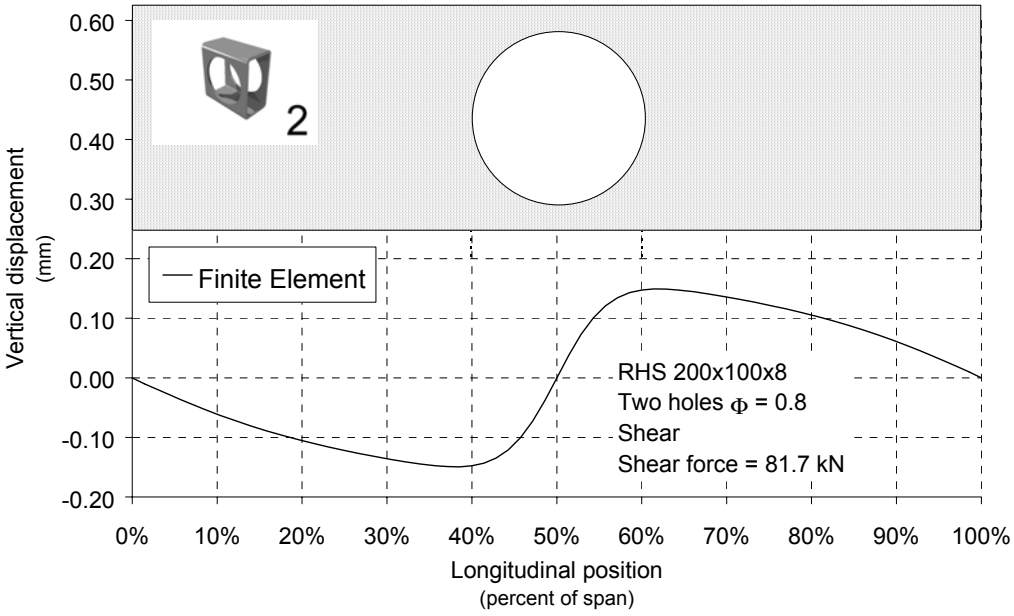

Figure 7-40: Shear displacement of RHS 200x100x8 two holes 140.8 mm dia

7.6.5 Zone of influence

The zone of influence describes the length of the RHS over which the web opening influences the stress distribution, and hence marks the boundary between the perforated and unperforated zones (Figure 7-1). In the elastic range, the zone of influence for shear has been observed to extend a distance in the order of one hole diameter on either side of the edge of the hole. Consequently, the zone is approximately three diameters in length.

Openings placed in the same web at sufficient separations, such that the zones of influence do not overlap, will not cause the stress distributions to interact, and hence will not cause a further reduction in resistance (provided there is no instability).

7.6.6 Design recommendation for calculation of resistance

The shear capacity based on a yield criterion can be calculated using Equation 7-27, where γ_{MShe1} and γ_{MShe2} are possible partial safety factors. The stress concentration factor for shear (ψ_{shear}) can be found from Table 7-9. The expression is valid for hole size ratios between 0 and 0.9 and for web slendernesses between 10.0 and 46.0, but does not allow for instability of the cross-section (such as shear buckling of the webs).

$$V_{el,y,Rd,1hole} \text{ or } V_{el,y,Rd,2holes} = \frac{V_{pl,y,Rd,unperf}}{(\psi_{shear} + \gamma_{MShe1}) \times \gamma_{MShe2}}$$

Equation 7-27

An alternative shear capacity based on a simplified reduced shear area approach can be calculated from Equation 7-28. This does not allow for instability of the cross-section or shear failure by the Vierendeel mechanism, and requires a displacement based serviceability criterion to be useful in design.

$$V_{el,y,Rd,1hole} \text{ or } V_{el,y,Rd,2holes} = \frac{V_{pl,y,Rd,unperf}\left(1-\Phi\right)}{\gamma_{M0}}$$

Equation 7-28

For both approaches, the shear capacity of RHS with one hole is taken to be the same as the shear capacity of an RHS with two holes.

Table 7-9: Stress concentration factors for shear, ψ_{shear}

Hole size ratio, Φ	Web slenderness, λ_{web}									
	10	14	18	22	26	30	34	38	42	46
0.1	2.21	2.22	2.23	2.24	2.25	2.27	2.28	2.29	2.30	2.31
0.2	2.46	2.48	2.51	2.54	2.57	2.59	2.62	2.65	2.67	2.70
0.3	2.77	2.81	2.86	2.90	2.95	3.00	3.04	3.09	3.14	3.18
0.4	3.15	3.22	3.29	3.36	3.44	3.51	3.58	3.65	3.72	3.80
0.5	3.63	3.74	3.85	3.96	4.07	4.17	4.28	4.39	4.50	4.61
0.6	4.28	4.44	4.61	4.77	4.93	5.09	5.26	5.42	5.58	5.74
0.7	5.24	5.49	5.74	5.99	6.25	6.50	6.75	7.00	7.26	7.51
0.8	6.92	7.35	7.78	8.22	8.65	9.08	9.52	9.95	10.38	10.81
0.9	11.45	12.42	13.39	14.37	15.34	16.32	17.29	18.26	19.24	20.21

Note: Values obtained from Equation 7-24

7.7 Torsion

7.7.1 Introduction

Rules for design of members in torsion can be found in Annex G of EC3. BS 5950 does not contain any specific rules for torsion although British Steel publication TD 365, 'SHS Design to BS 5950 Part 1' contains a short section for torsional design of RHS. The Steel Construction Institute also provides advice for the design of members in torsion (Nethercot et al 1989).

Clause G.2 of Annex G (EC3) states that designing to resist loads by torsion is not usually an efficient method of load transfer and should be avoided wherever practicable. The clause recommends the use of hollow sections or box girders where torsion is unavoidable because box sections are more efficient at transmitting torsional loads than open sections. The design rules in Annex G are applicable only to members with class 1, 2 or 3 cross-sections, and where the webs are not susceptible to shear buckling.

The total internal torque in a thin walled member under the action of torsion is the sum of Saint-Venant torsion and the warping torsion, but the torsional rigidity of RHS is very large compared to the warping rigidity and design may proceed by neglecting warping torsion, without any loss of accuracy (Section 2.5.3).

The plastic torsional capacity (T_{pl}) of an unperforated RHS can be calculated by considering the flow of plastic shear around the cross-section (Equation 7-29). The full plastic torque is only reached at large angles of twist and design is normally based on the elastic torsional capacity (T_{el}). The elastic torsional capacity is proportional to the torsional modulus constant (C_t) and can be calculated from

Equation 7-30. The shear stress at the external surface (τ_o) is proportional to the applied torque (T) and inversely proportional to the torsional modulus constant (Equation 7-31).

$$T_{pl} = \frac{Af_y}{2\sqrt{3}(b+h)}\left(h(b-t)+b(h-t)\right)$$

Equation 7-29

$$T_{el} = f_y C_t \Big/ \sqrt{3}$$

Equation 7-30

$$\tau_o = T/C_t$$

Equation 7-31

The total angle of torsional twist (θ) is proportional to the length of the member (L) and the applied torque (T) and is inversely proportional to the shear modulus of the material (G) and the torsional inertia constant (I_t). The total angle of twist (Equation 7-32) and the twist per unit length are both important for the serviceability limit state, but permissible values will be depend on the structure being designed.

$$\theta = \frac{TL}{GI_t}$$

Equation 7-32

Annex G of EC3 gives formulae for the calculation of torsional constants, but not for box sections. However, formulae for calculation of the torsional inertia constant and torsional modulus constant for RHS can be found in Annex A of BS EN 10210 part 2 (see also Section 2.5 and Appendix C).

FE models of unperforated RHS closely match theoretical predictions using the BS EN 10210 values for the torsional constants. However, full-scale tests conducted as part of this research project indicate elastic and plastic capacities below (12 to 20%) those predicted by Equation 7-29 and Equation 7-30 (Section 5.4). FE models of perforated sections were considerably more successful at predicting behaviour in the laboratory (Section 5.4).

7.7.2 Concentration factors for elastic stress

An unperforated RHS in pure torsion will have a (reasonably) uniform distribution of elastic shear stress that varies through the thickness and is greater (typically 20 to 30%) on the external surface (Section 2.5.2). A small circular opening on the neutral axis will disturb the system of stress and produce a stress pattern similar to that around a hole in an infinite plate in pure shear (See also Section 6.5). Stress is raised at four points around the edge of the hole (location ③ in Figure 7-2). Larger holes raise the stress further as less web is available to transmit the shear across the width of the hole.

A number of FE models (73) have been used to study the stress concentrations around openings in the webs of RHS under the action of uniform external torsion. The models used in the parametric study are shown diagrammatically in Figure 7-41. Stress concentrations were found to be dependent on hole size and web slenderness, but not aspect ratio. The dependence of stress concentration on the web slenderness is analogous to the dependence upon thickness, of the stress concentration around a circular hole in an infinite plate in pure shear. The FE contour plots of von Mises stress shown in Figure 7-43 are typical of the stress patterns observed.

The FE models were used to obtain a representative sample of stress concentration factors for torsion. The stress concentration factor for torsion, $\Psi_{torsion}$, is defined as the ratio of the maximum von Mises stress in the unperforated beam, to the maximum von Mises stress in the perforated beam. The torque is such that the maximum von Mises stress in the perforated RHS is in the elastic range. The stress distribution in the web of an RHS with one hole is nearly identical to that in the web of an RHS with two holes, although the maximum stress is slightly higher for sections with two holes for large diameters.

The stress concentration factors obtained from the FE study were approximated by an empirical mathematical function, which was fitted to the data using a least squares method (Equation 7-33). For the models included in the study, the maximum differences between the empirical function and the FE values were 1.03 (empirical value less than FE value) and 1.25 (empirical value greater than FE value). The square root of the average square error was 0.23. The actual stress concentration data from the FE study is presented in Appendix E.

$$\psi_{torsion} = \left(\frac{1}{1-\Phi} - 1\right)\left(0.038\lambda_{web} - 4.847\Phi^2 + 6.562\Phi - 1.734\right) + 2$$

Equation 7-33

The empirical function for stress concentration factor is shown graphically in Figure 7-42. Stress concentration factors increase with increasing hole size and are larger for slender webs. The function is valid for hole size ratios between 0 and 0.9 and for web slendernesses between 13.0 and 38.7.

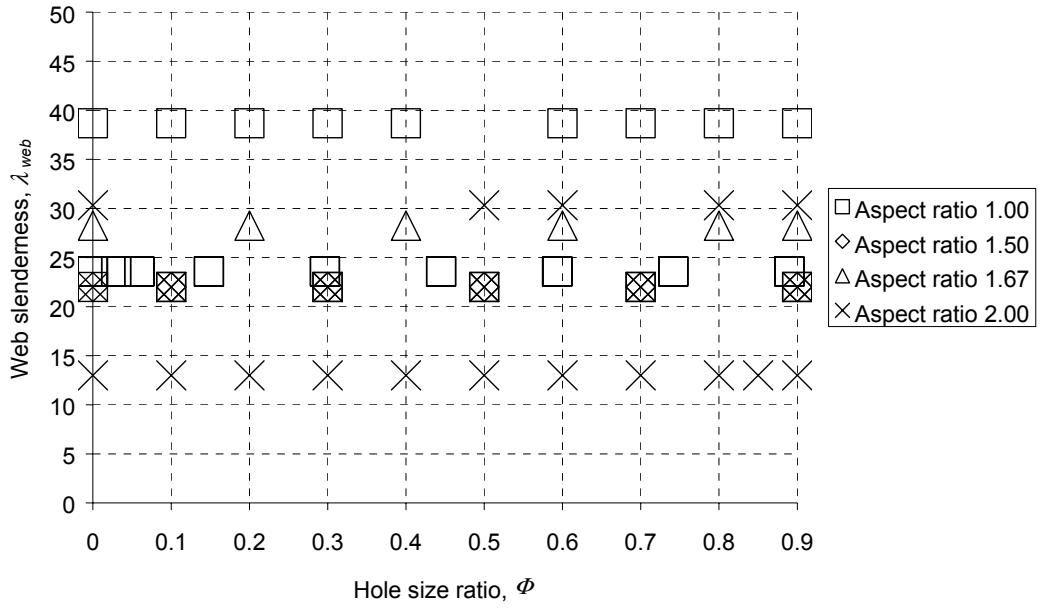

Figure 7-41: Parametric sampling for torsion

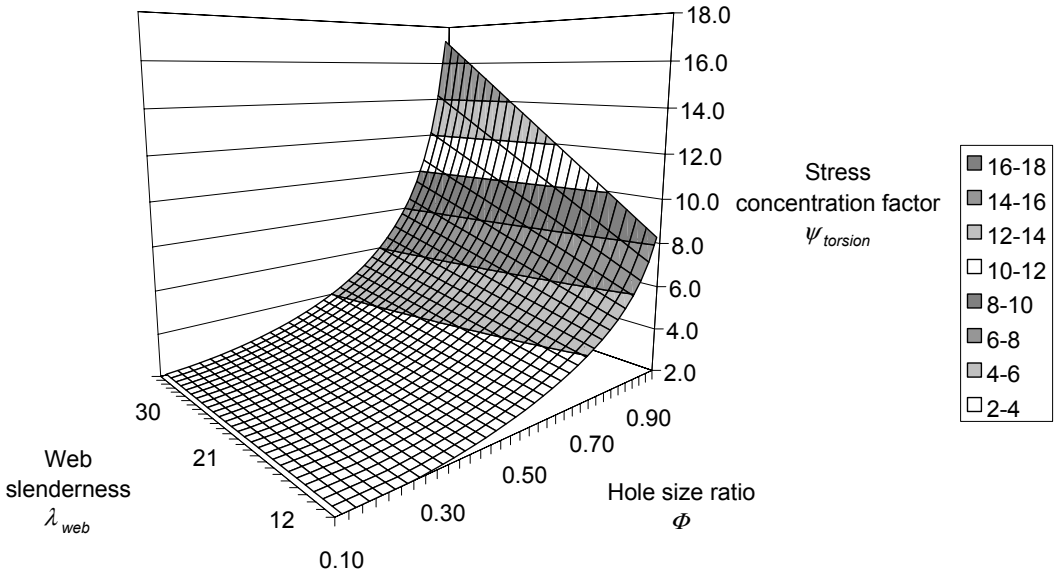

Figure 7-42: Stress concentration factors for torsion

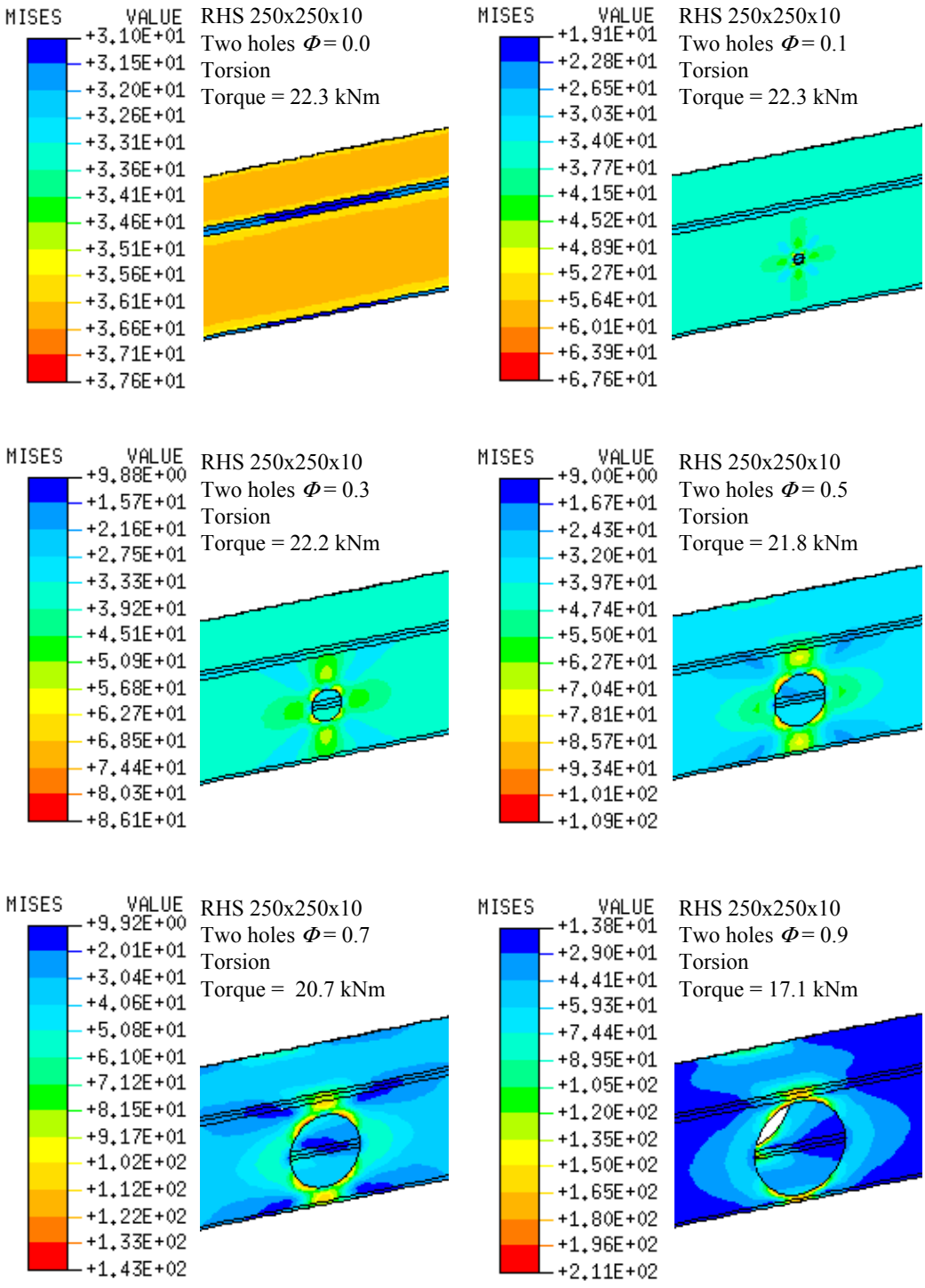

Figure 7-43: Distribution of von Mises stress for RHS 250x250x10 in torsion

Von Mises stress plotted on external surface
(Original in colour)

7.7.3 Resistance

The stress concentration factors determined in the previous section can be used to determine the torsional resistance based on a maximum stress criterion. If stress is limited to the design yield stress, the yield based torsional resistance of the perforated section can be determined by dividing the elastic torsional capacity of the unperforated section by the stress concentration factor (Equation 7-34).

$$T_{el,Rd,1hole} \text{ or } T_{el,Rd,2holes} = T_{el,Rd,unperf} \,/\, \psi_{torsion}$$

Equation 7-34

An alternative approach based on the reduced section (similar to that for shear) is to base the torsional resistance of the perforated RHS on a simple ratio of the portion of remaining web at the centre of the hole (Equation 7-35). This approach results in a higher resistance than the maximum stress approach for all hole sizes, but means that there is some plasticity present at design loads.

$$T_{el,Rd,1hole} \text{ or } T_{el,Rd,2hole} = (1-\Phi) \times T_{el,Rd,unperf}$$

Equation 7-35

The torque-rotation plots obtained from the full plastic parametric study are shown in Figure 7-44 through Figure 7-49. The non-dimensional ratio of torque against the elastic torsional capacity of the unperforated section is plotted on the ordinate axis. The non-dimensional ratio of the total rotation against the rotation at yield of the unperforated section is plotted on the abscissa. The total rotation is the sum of the rotations across the perforated and unperforated parts and is dependent on

the member length. The torsional resistance calculated from Equation 7-35 is also plotted and shown as a circle symbol on the corresponding data series.

For the range of sections chosen for the full plastic parametric study, the torsional resistance based on the reduced section is less than the torque at the onset of non-linearity. However, sections with more slender webs may be susceptible to a mechanism of failure similar to Vierendeel shear failure and torsional resistance may have to be reduced accordingly. This type of failure can be evaluated with yield line analysis. Maximum plastic torque may be evaluated by the same method, but is unlikely to be useful in design, as, for most applications, high twist is likely to cause a loss of structural integrity before plastic collapse of the member occurs.

Maximum torques are shown in Figure 7-50 and Figure 7-51. For small holes and unperforated sections, the maximum torque is equal to the theoretical plastic torque (Equation 7-29). Strain hardening is unable to generate higher torques, as plastic strains are relatively small. Large holes reduce the elastic capacity by a significant amount, but the reduction in maximum torque is comparatively low. This is partly due to strain hardening, which is able to develop due to the enormous strains that result from the gross torsional twist across the hole.

The ultimate torsional resistance of a section with one hole is larger than the ultimate torsional resistance of the same section with two holes. In the perforated zone, the torsional and lozenging rigidity of the box shape allows the unperforated web to carry a greater portion of the shear flow than the perforated web. Asymmetry induces internal torsional and lozenging forces that, for high plastic torsional loads, can cause distortion of the cross-section at some considerable distance from the hole. In design, the distortion of the cross-section is of much less importance than the angular deformation across the hole.

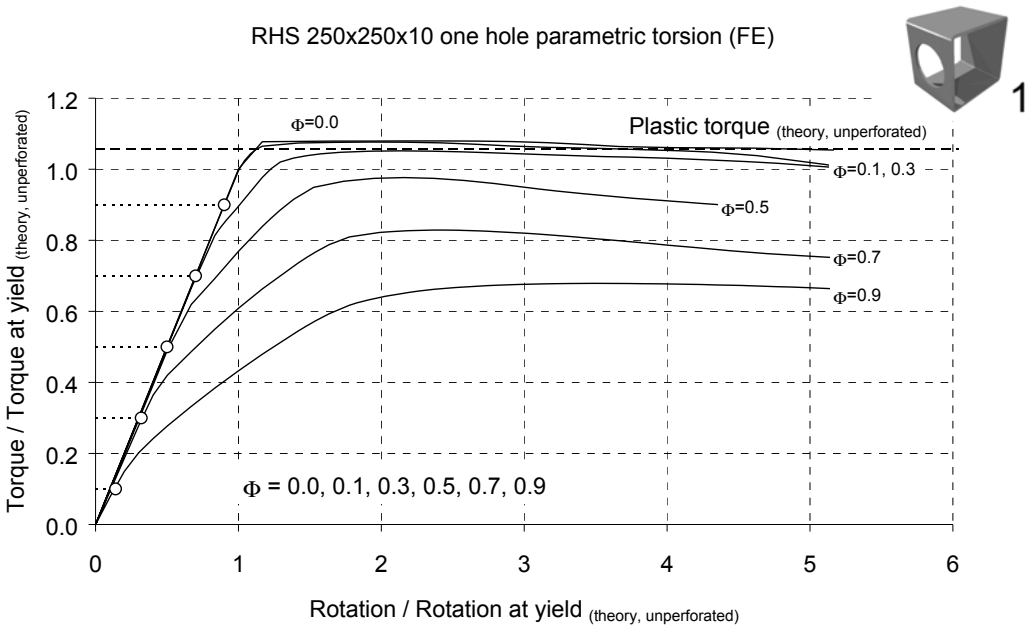

Figure 7-44: Torque-rotation relationship for RHS 250x250x10 one hole

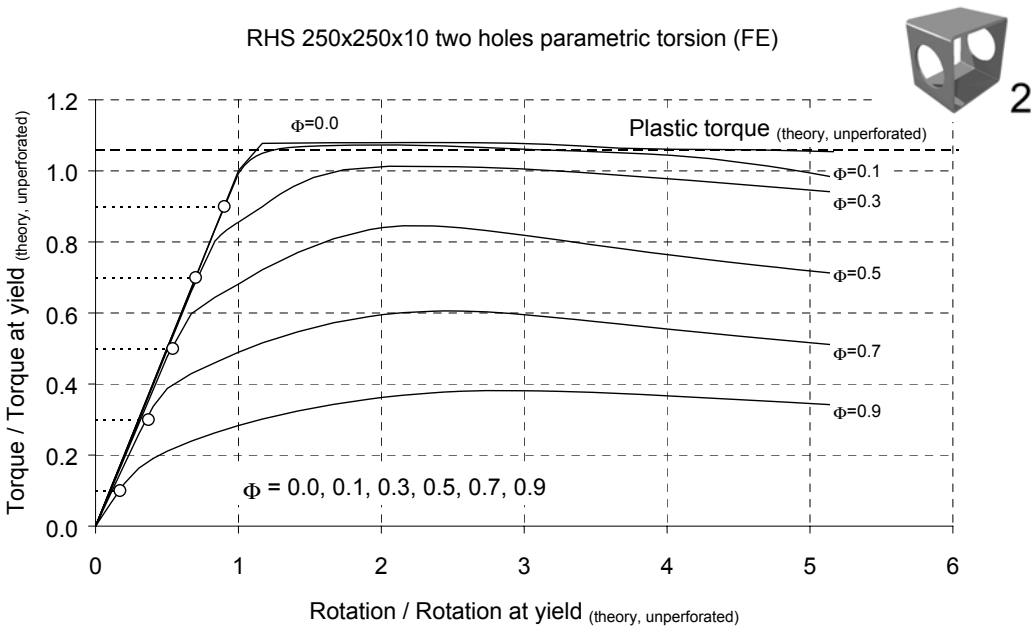

Figure 7-45: Torque-rotation relationship for RHS 250x250x10 two holes

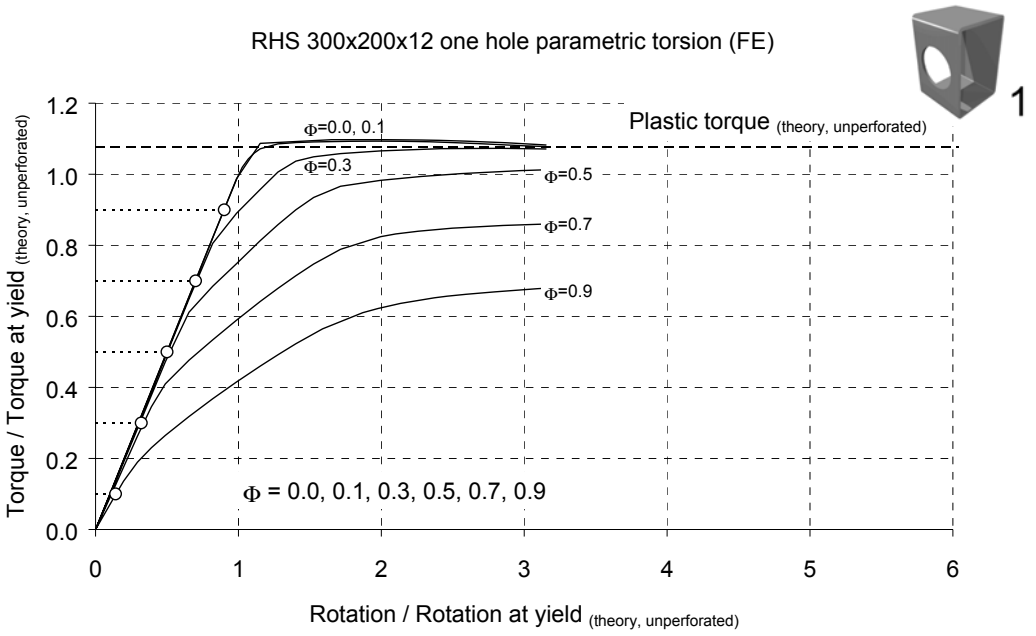

Figure 7-46: Torque-rotation relationship for RHS 300x200x12 one hole

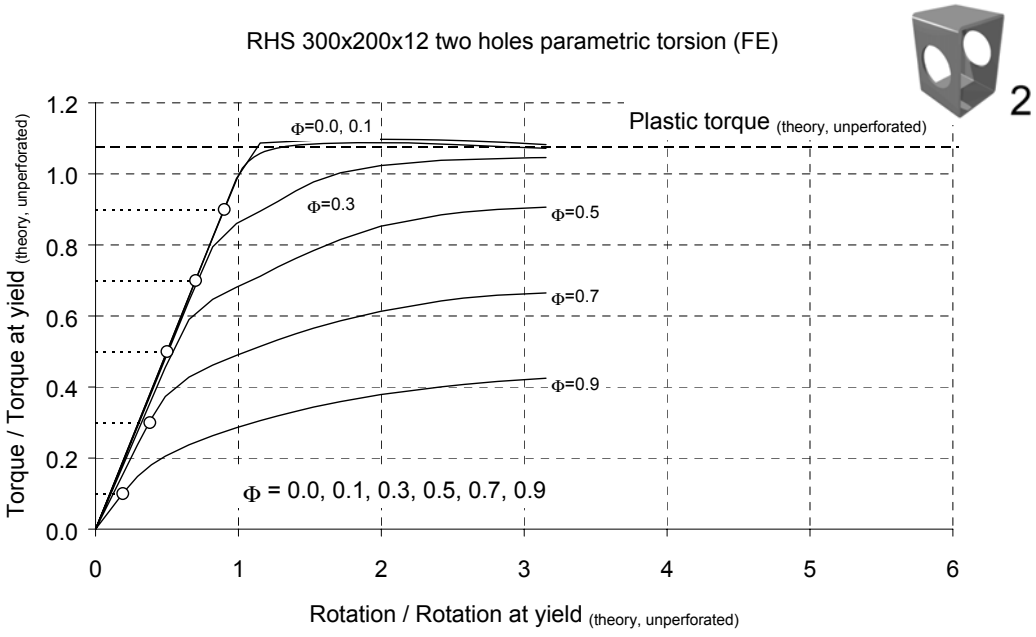

Figure 7-47: Torque-rotation relationship for RHS 300x200x12 two holes

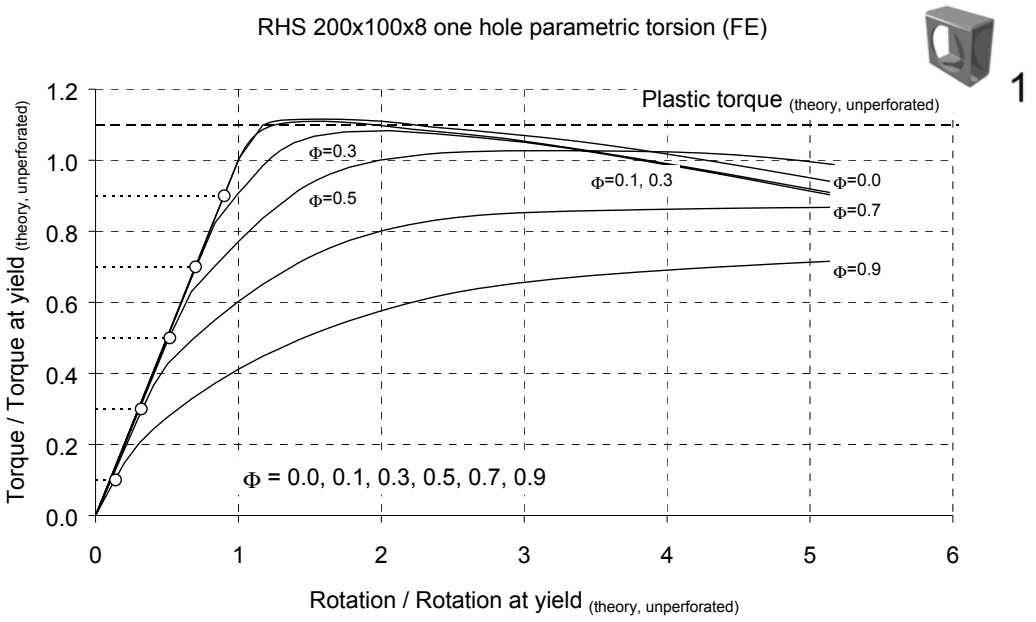

Figure 7-48: Torque-rotation relationship for RHS 200x100x8 one hole

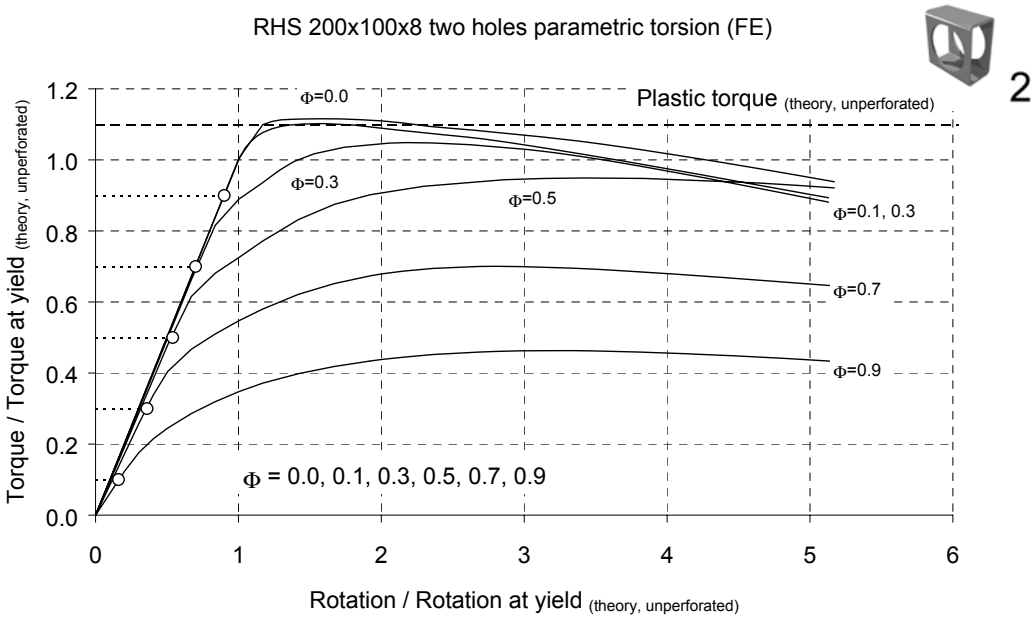

Figure 7-49: Torque-rotation relationship for RHS 200x100x8 two holes

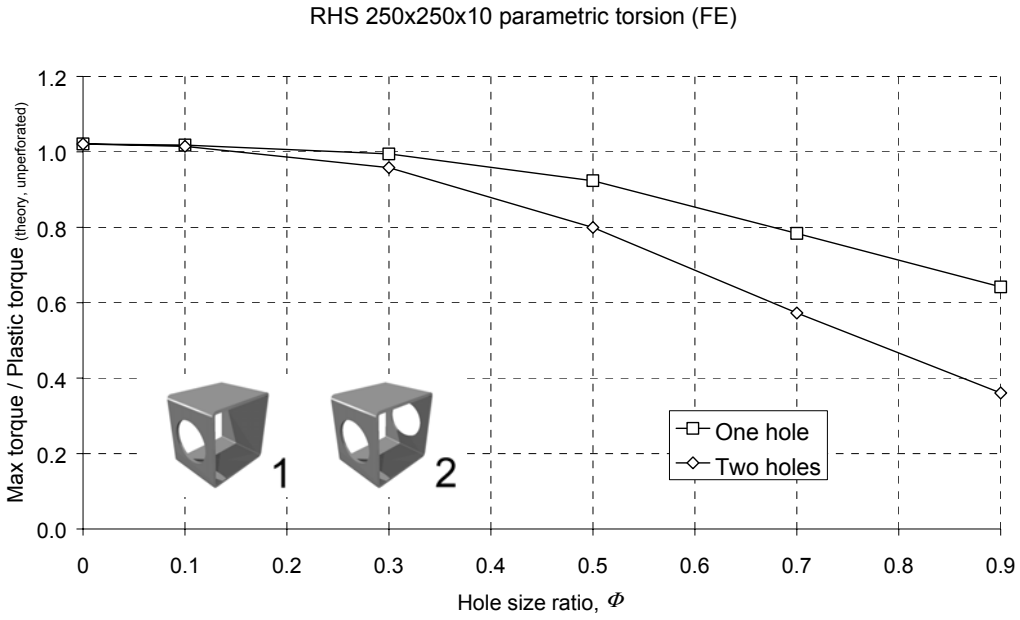

Figure 7-50: Maximum torque for RHS 250x250x10

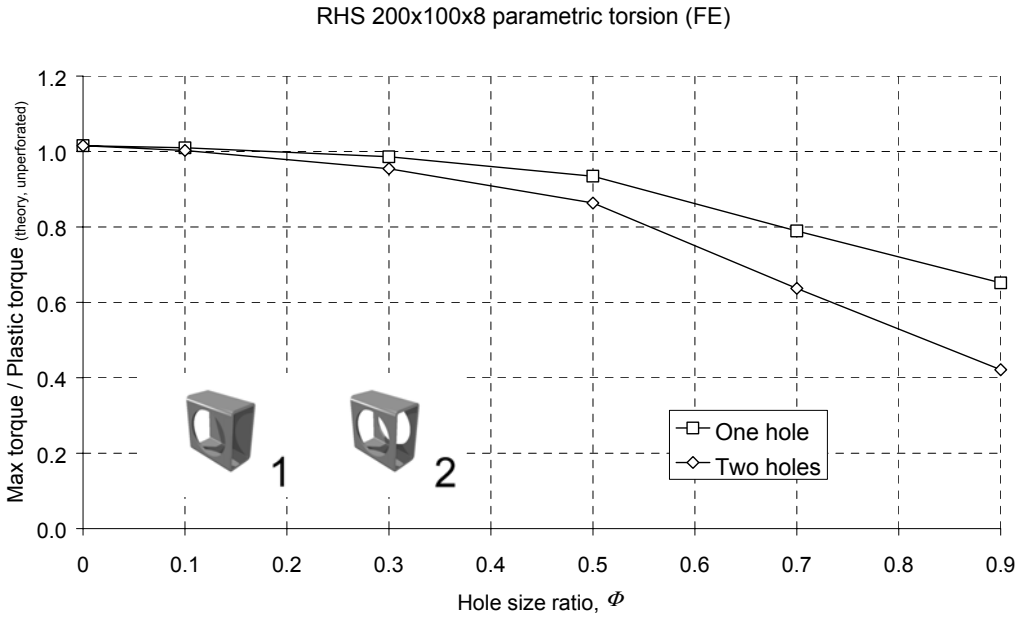

Figure 7-51: Maximum torque for RHS 200x100x8

7.7.4 Deflection

Torsional deformation at extreme displacements, for perforated RHS, takes the form shown in Figure 7-52 and, for small diameters is similar for sections with similar hole sizes, regardless of the aspect ratio (Figure 7-52a and b). For large holes, oblong sections distort through shearing of the flanges (Figure 7-52c), while square sections distort through shearing of the webs (Figure 7-52d).

If the torsional resistance is calculated according to a maximum elastic stress criterion, the strains at design loads will be limited to the elastic range and the additional angular deformation across the width of the hole will be small enough to be neglected.

As for members in shear, the deformation of the perforated zone is crucial in design, as displacements are concentrated over a short length. The displaced shapes shown in Figure 7-53 and Figure 7-54 are typical of the torsional deformation of RHS with web openings. If a reduced area approach is adopted for design, a reliable method of calculating the angular displacement across the width of the hole must be developed as an accompanying serviceability limit.

In the elastic range, the total twist (θ) can be calculated from the sum of the twist in the unperforated and perforated parts. The twist across the perforated zone can be estimated by applying a reduced stiffness over a length equal to the depth of section. For a member with one perforated zone the total twist can be estimated from Equation 7-36. The stiffness reduction factor ($\rho_{torsion}$) given in Equation 7-37, and as described by Equation 7-36, is conservative for all the sections chosen for the fully plastic parametric study (Figure 7-55).

$$\theta = \frac{T \times (L - h)}{I_t \times G} + \frac{T \times h \times \rho_{torsion}}{I_t \times G}$$

Equation 7-36

$$\rho_{torsion} = 1/(1 - \Phi)$$

Equation 7-37

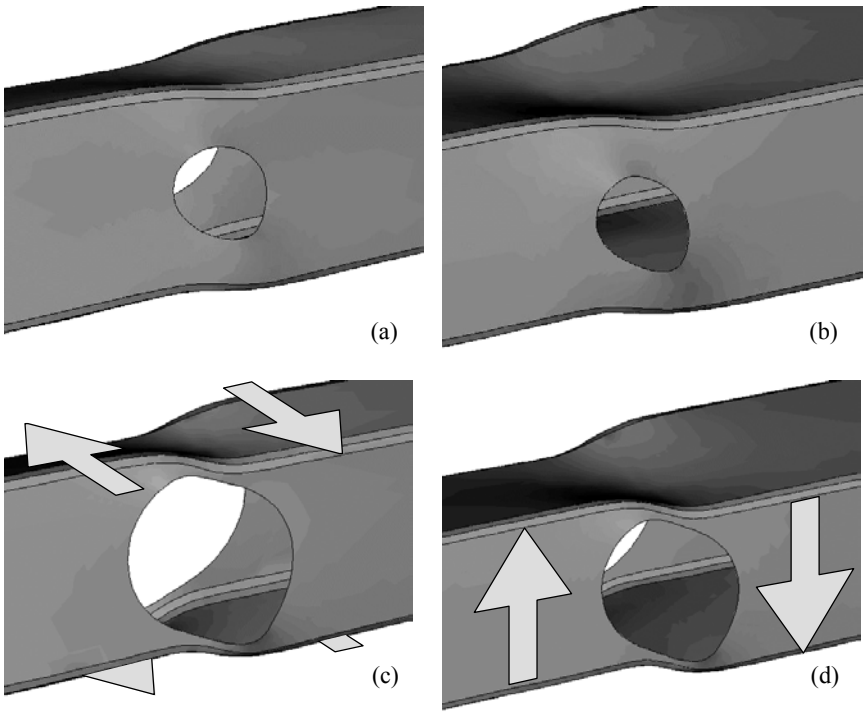

Figure 7-52: Distortions under the action of torsion

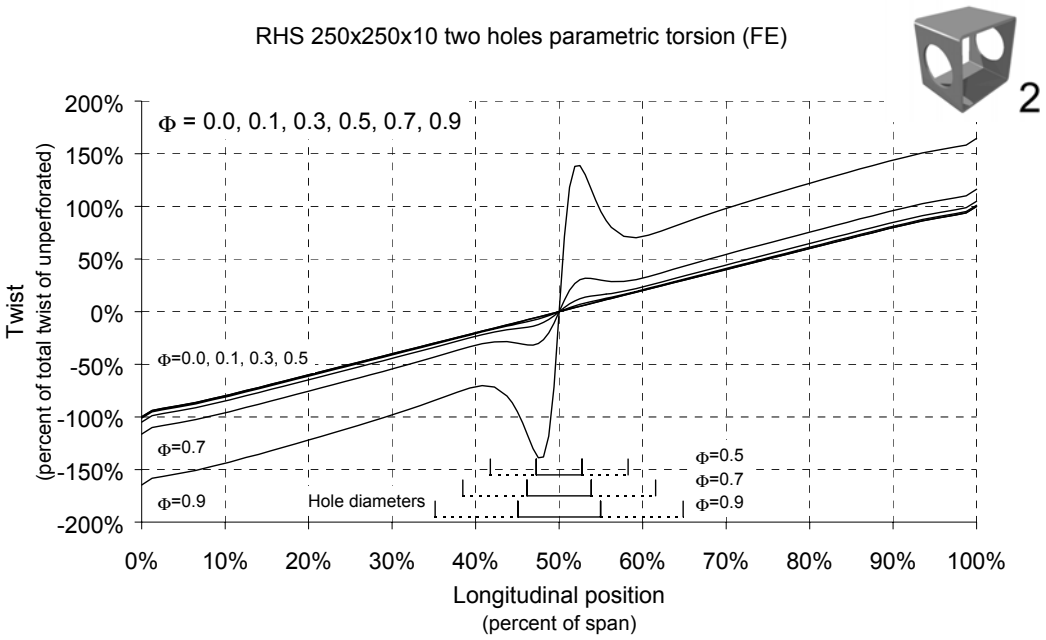

Figure 7-53: Torsional twist of RHS 250x250x10 two holes

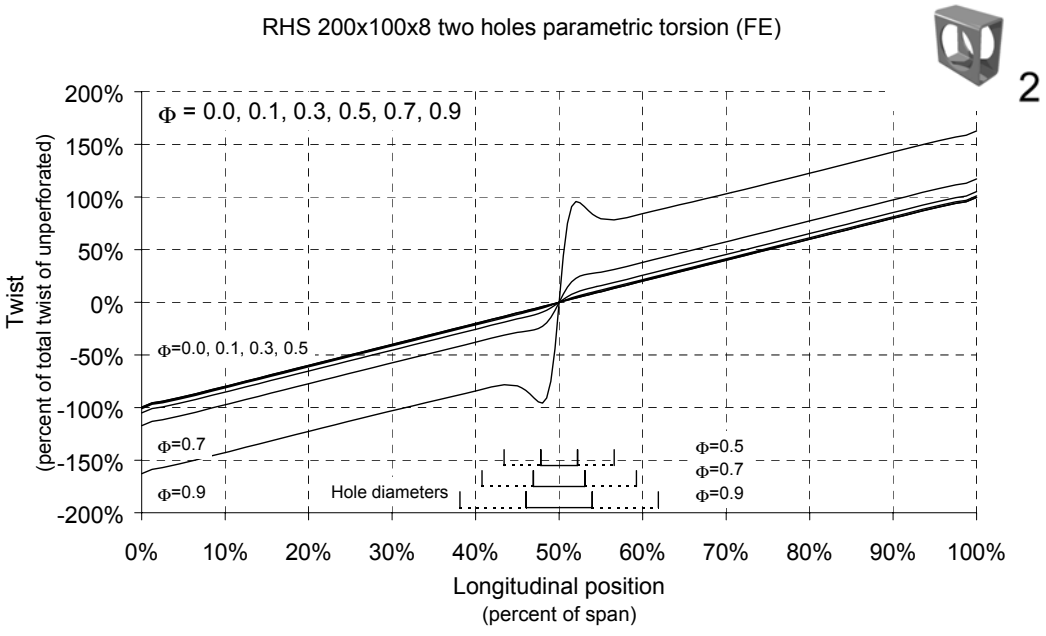

Figure 7-54: Torsional twist of RHS 200x100x8 two holes

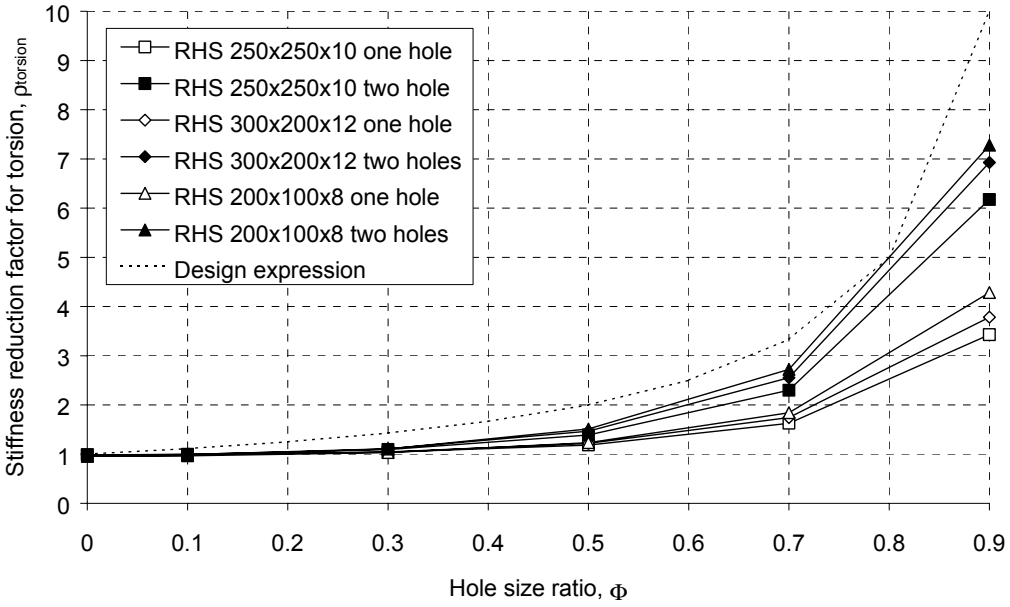

Figure 7-55: Stiffness reduction factors for torsion

7.7.5 Zone of influence

The zone of influence describes the length of the RHS over which the web opening influences the stress distribution, and hence marks the boundary between the perforated and unperforated zones (Figure 7-1). In the elastic range, the zone of influence for torsion has been observed to extend a distance in the order of two hole diameters on either side of the edge of the hole. Consequently, the zone is approximately five diameters in length (e.g. Figure 7-43).

Openings placed in the same web at sufficient separations, such that the zones of influence do not overlap, will not cause the stress distributions to interact, and hence will not cause a further reduction in resistance (provided there is no instability).

7.7.6 Design recommendation for calculation of resistance

The elastic torsion capacity can be calculated using Equation 7-38, where γ_{MTor1} and γ_{MTor2} are possible partial safety factors. The stress concentration factor for shear ($\psi_{torsion}$) can be found from Table 7-10. The expression is valid for hole size ratios between 0 and 0.9 and for web slendernesses between 14.0 and 38.0, but does not allow for instability of the cross-section.

$$T_{el,Rd,1hole} \text{ or } T_{el,Rd,2holes} = \frac{T_{el,Rd,unperf}}{\left(\psi_{torsion} + \gamma_{MTor1}\right) \times \gamma_{MTor2}}$$

Equation 7-38

An alternative torsional capacity based on a simplified reduced area approach can be calculated from Equation 7-39. This does not allow for instability of the cross-section or failure by a torsional Vierendeel mechanism, and requires a displacement based serviceability criterion to be useful in design.

$$T_{el,Rd,1hole} \text{ or } T_{el,Rd,2holes} = \frac{T_{pl,Rd,unperf}\left(1 - \Phi\right)}{\gamma_{M0}}$$

Equation 7-39

For both approaches, the torsional capacity of RHS with one hole is taken to be the same as the torsional capacity of an RHS with two holes.

Table 7-10: Stress concentration factors for torsion, $\psi_{torsion}$

Hole size ratio, Φ	Web slenderness, λ_{web}						
	14	18	22	26	30	34	38
0.1	1.93	1.95	1.97	1.98	2.00	2.02	2.04
0.2	1.98	2.02	2.06	2.09	2.13	2.17	2.21
0.3	2.14	2.21	2.27	2.34	2.40	2.47	2.53
0.4	2.43	2.53	2.63	2.74	2.84	2.94	3.04
0.5	2.87	3.02	3.17	3.32	3.48	3.63	3.78
0.6	3.49	3.71	3.94	4.17	4.40	4.63	4.85
0.7	4.37	4.73	5.08	5.44	5.79	6.14	6.50
0.8	5.78	6.39	7.00	7.61	8.21	8.82	9.43
0.9	9.00	10.37	11.74	13.10	14.47	15.84	17.21

Note: Values obtained from Equation 7-33

7.8 Combinations

7.8.1 Introduction

Torsion and shear force both produce shear stress in a member while bending produces longitudinal direct stress. If deflections are small enough (no geometric non-linearity), the resulting system of stress is the combination (superposition) of the three systems of stress that would be present for each individual action. The shear stress resulting from the torsion combines with the shear stress due to the shear force and the direct stress due to the bending to produce an increased von Mises stress in the member. Therefore, a perforated RHS subject to a combination of actions can be designed by the superposition of the stresses calculated by the reduced area method introduced above.

Clause G.5 in Annex G of EC3 deals with design of unperforated RHS in combined flexure and bending. The shear stress due to shear force and the shear stress due to torsion are combined by additive superposition (Equation G.46d), but

the bending resistance is not reduced unless the combined shear stress (as a von Mises equivalent) represents more than half of the design yield strength (Equation G.47d). This approach is similar to the approach used when designing for a member in shear and bending.

When torsion is coexistent with bending, design should allow for the effect of the torsional rotation of the cross-section relative to its unloaded position. A beam under the action of bending about its major axis will, when twisted by the action of torsion be obliged to bend about its minor axis also. Similarly, the bending deformations resulting from the bending about the major and minor axes may have an influence on the torsional loading of the beam. Clause G.5 of EC3 provides procedures for design that allow for the second order effects due to the rotational and translational deformations. The procedure for perforated RHS outlined below is a simplified treatment with no explicit allowance for second order effects.

7.8.2 Design recommendation for calculation of resistance

In the case of an eccentrically loaded beam, such as a slim floor edge beam, the principal structural action is that of bending. Hence, a convenient approach for design is one that reduces the bending capacity to allow for coexistent shear force and torsion. One way to achieve this is to use a reduced yield stress ($f_{y,reduced}$) in the bending resistance calculation (plastic and elastic moment capacity, perforated and unperforated) to allow for the coexistent shear stress. Equation 7-40 is based on the von Mises model for yield and a simplified reduced area calculation for shear stress due to shear force ($V_{y,Sd}$) and torque (T_{Sd}). Since bending capacity is proportional to yield stress, the ratio of the bending capacity in pure bending to the bending capacity with coexistent shear and torsion is the same as the ratio f_y / $f_{y,reduced}$ (leading to Figure 7-56, or Figure 7-57 for only two actions). Equation 7-41 is for the special

case of an RHS with one hole where the shear force opposes the torsional shear in the perforated web. Additional calculations are required to ensure that failure will not occur by a Vierendeel shear mode (torsional or shear) or by instability of the cross-section. The parametric FE study indicates that instability and the Vierendeel shear mode will not occur if the web slenderness is less than 22.0.

$$f_{y,reduced} = \sqrt{f_y^2 - 3\left(\frac{V_{y,Sd}}{(1-\Phi)A_v} + \frac{T_{Sd}}{(1-\Phi)C_t}\right)^2}$$

Equation 7-40

$$f_{y,reduced} = MIN\left(\sqrt{f_y^2 - 3\left(\frac{V_{y,Sd}}{(1-\Phi)A_v} - \frac{T_{Sd}}{(1-\Phi)C_t}\right)^2}, \sqrt{f_y^2 - 3\left(\frac{V_{y,Sd}}{A_v} + \frac{T_{Sd}}{C_t}\right)^2}\right)$$

Equation 7-41

As with the individual actions, the reduced area method for resistance calculation for combined actions requires a displacement based serviceability criterion to be useful in design.

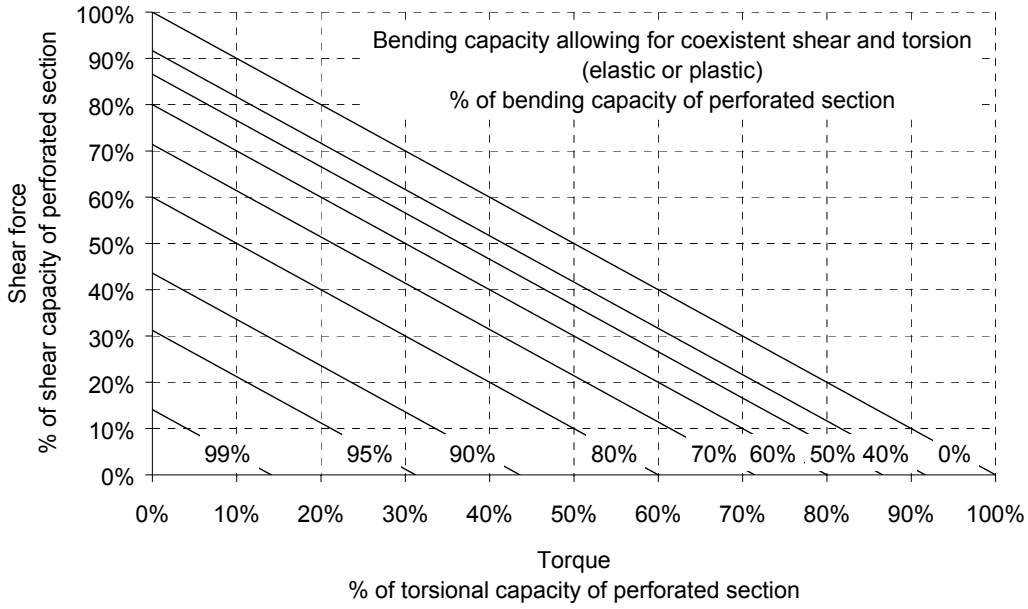

Figure 7-56: Contours of bending capacity with coexistent shear and torsion

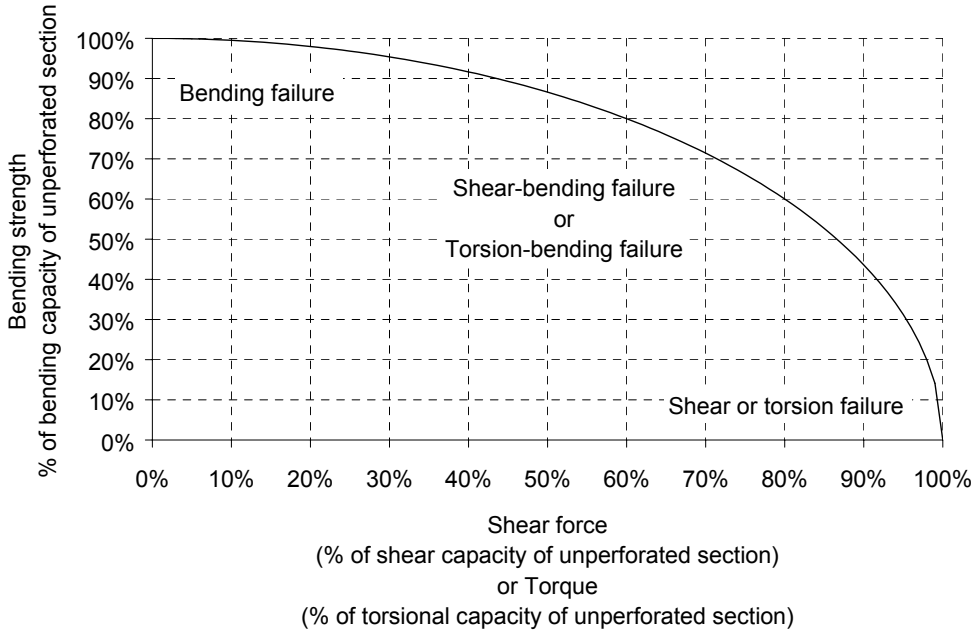

Figure 7-57: Bending capacity with coexistent shear or torsion

7.9 Concluding remarks

A number of design recommendations have been proposed which have been developed and justified by the findings of a parametric FE study. Expressions for resistance based on a simplified reduced area approach have been shown to be reliable when instability of the cross-section is not critical. Empirical expressions for the prediction of concentration factors for elastic stress have been developed for when all plasticity is to be avoided.

The recommendations are intended to form the basis for the development of design rules, but the following areas require additional investigation in order for the recommendations to be useful for design:

1) An extended fully plastic parametric FE study to cover the full range of web slenderness. The identification of stability limits and suitable models for Vierendeel mechanisms in shear and torsion. The identification of sections with unstable cross-sections at elastic loads is particularly important.
2) An extended fully plastic parametric FE study to cover combinations of actions to confirm the recommendations for the treatment of perforated RHS beams with coexistent shear and torsion.
3) Additional laboratory testing to calibrate the FE models where instability of the cross-section and Vierendeel mechanisms are critical.
4) The development of reliable expressions for displacement and twist (including localised deformation) for elastic and plastic loads (serviceability).
5) An experimental and FE study to develop rules for checking the stability of perforated RHS members (e.g. lateral torsional buckling).

The following extensions to the scope would produce a wider and more generally applicable set of design rules:

1) The inclusion of axial forces, bending about the minor axis and shear force parallel to the flanges.
2) The inclusion of alternative common shapes for openings (e.g. rectangular and extended circular).
3) Provision for closely spaced multiple perforations.
4) Provision for staggered and eccentric openings.

It may also be useful to consider the design of reinforcement and stiffeners for situations where the reduction in resistance or stiffness due to an opening is unacceptable. Possible schemes for reinforcement and stiffening of perforated RHS are shown in Figure 7-58. The schemes are based on the reinforcement of circular openings in I-sections (see EC3 Annex N clause N.2.1.5) although the closed shape of the RHS presents the additional practical problem of limited access for welding.

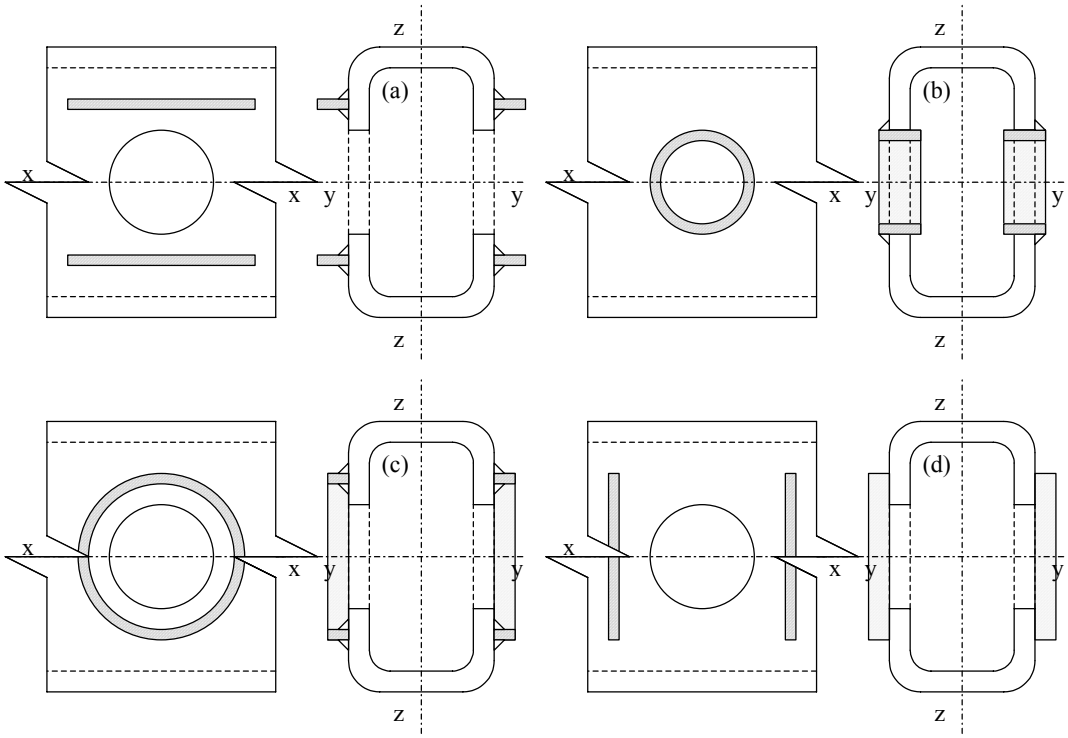

(a) Longitudinal stiffener or reinforcement (b) Ring stiffener
(c) Circular reinforcement (d) Transverse reinforcement

Figure 7-58: Possible stiffening or reinforcement of web openings

8 Conclusions

8.1 Introduction

The primary aim of this project was to study the behaviour of Rectangular Hollow Sections (RHS) with web openings, and to develop the basis for a set of design rules for perforated RHS edge beams. To this end, the fundamental structural behaviour of RHS with web openings was examined by an investigation that combined analytical study with both small and full-scale testing. Representative laboratory tests were conducted to provide sufficient data for Finite Element (FE) models to be calibrated. The FE models were then used to study the behaviour in greater detail, over a wider range of parameters. This Chapter summarises the various stages of the project and ends with a synopsis of the conclusions and a brief critical analysis of the project as a whole.

8.2 Laboratory testing and calibration of Finite Element models

8.2.1 Four-point bending (bending)

A series of 13 full-scale four-point bending tests were conducted on two sizes of RHS to assess the effect of web openings upon structural performance in uniform bending. During the tests, the moment and average curvature were

measured. In 12 tests, strains on the external surface of the flanges and webs were also measured.

The results of the tests showed that the reduction in the bending capacity due to the web openings was as much as 30%, and that the openings caused no measurable reduction in elastic stiffness. The reductions in bending capacity were comparable to the reductions in the elastic and plastic section moduli at the location of the hole. In some tests, the web openings were observed to decrease the plastic stability of the cross-section causing a reduction in the rotation capacity.

The experimental results were compared with FE predictions and a close agreement was observed in terms of displaced shapes, elastic stiffnesses and strains in the elastic range. The experimental moment-curvature relationships matched those predicted by the FE models, although the FE tended to under-predict the bending resistance by around 10%.

8.2.2 Three-point bending (shear)

A series of six full-scale three-point bending tests were conducted on two sizes of RHS to assess the effect of web openings upon structural performance in combined shear and bending. During the tests, the shear force, bending moment and displacement were measured. In all six tests, strains on the external surface of the flanges and webs were also measured.

The results of the tests showed that the reduction in the shear capacity due to the web openings was as much as 85%, and that the openings caused a significant reduction in the shear stiffness of the perforated zone. The reductions in shear capacity were comparable to the reductions in the cross-sectional area of the webs at the location of the hole.

The experimental results were compared with FE predictions and a close agreement was observed in terms of displaced shapes, elastic stiffnesses and strains in the elastic range. The experimental shear force-displacement relationships closely matched those predicted by the FE models with a maximum difference of only 5%.

8.2.3 Full-scale torsion

A series of 14 full-scale torsion tests were conducted on two sizes and grades of RHS to assess the effect of web openings upon structural performance in torsion. During the tests, the torque and angle of twist were measured. In six tests, strains on the external surface of the webs were also measured.

The experimental results showed that large holes cause a significant reduction in both torsional capacity (up to 60%) and stiffness (up to 40%). The reduction in stiffness was due to the perforated zone being much more flexible than the unperforated beam, and severe deformations in this region were observed. The reductions in capacity were comparable to the reductions in the cross-sectional area of the perforated web.

The experimental results were compared with FE predictions and good agreement was observed in terms of displaced shapes, elastic stiffness and strains in elastic range. Experimental torque-rotation relationships matched closely those predicted by the FE models in some cases, but were significantly different in others. The largest difference between the FE predictions of torsional resistance and experimental results occurred for the specimens without web openings. Theoretical predictions of the torsional resistance of the unperforated sections were close to the FE predictions.

The experimental method was re-examined in detail and the experimental measurements were found to be valid. One explanation (that appears to fit most of

the available evidence) is that the steel does not always comply with the von Mises failure criterion. Evidence of similar behaviour is present in the results of full-scale testing of hot-finished RHS by Marshall (1972). Further experimental investigation is required to investigate this phenomenon as it has important implications for design.

8.2.4 Small-scale torsion

A series of 35 small-scale torsion tests was conducted on one size of cold-formed steel tube to assess the effect of web openings of various diameters upon structural performance in torsion. During the tests, the torque and angle of twist were measured.

The experimental results showed that large web openings caused a significant reduction in both torsional capacity and stiffness (as observed in the full-scale torsion tests). The holes with the greatest diameter caused the biggest reduction in resistance and stiffness and resulted in plastic deformation at lower twist. Small holes caused only a small reduction in the torsional resistance and stiffness, but reduced the torsional ductility of the member.

Various plastic collapse mechanisms were observed that were dependent on the size and arrangement of holes, as it was possible to apply larger rotations with the small-scale torsion testing apparatus than the full-scale apparatus.

A small number of tests showed how two holes in the same web were able to interact if close enough together. The interaction between two openings caused a further reduction in resistance than that resulting from one hole alone.

The experimental results were compared with FE predictions and good agreement was observed in terms of displaced shapes and collapse mechanisms. Experimental torque-rotation relationships matched closely those predicted by the

FE models in all cases (including specimens without holes), but there were large differences between measurements and predictions of elastic stiffness due, in part, to the testing method. The FE models also showed that, for unsymmetrical cases, the boundary conditions (at the ends) have a large influence upon the torsional behaviour of short members.

8.3 The parametric Finite Element study

8.3.1 Bending

Parametric FE models of three different sizes of RHS, with web openings of various diameters, were used to study the structural performance of RHS in pure bending. Moment-curvature relationships were obtained and stress distributions were observed. In all cases, the RHS were thick enough to prevent elastic instability of the flange and web.

The presence of the web opening was observed to cause an increased von Mises stress in the webs above the opening, due to the reduced section moduli and the stress concentrating effect of the change in cross-section. For small holes, the increased stress above the hole balanced the effect of the reduction in elastic section modulus and the moment at yield was not reduced. For large holes, the raised stress was higher than the stress in the flanges and the moment at first yield was reduced by the presence of the hole. The structural performance of the member was seen to be unaffected by small areas of yielding material and, for design purposes, some plasticity at working loads may be permissible. An empirical formula for the prediction of maximum von Mises stress was developed and formulae for the

calculation of elastic and plastic moments, based on reduced area calculations, were proposed.

The long yield plateau, characteristic of hot finished steel, prevented strain hardening in the unperforated sections. In contrast, the high strains present in perforated sections were able to generate sufficiently strain hardened stresses to maintain increasing resistance at high curvatures. The ultimate resistance of perforated members was observed to be increased by strain hardening and limited by the stability of the compression flange and compression cee above the hole.

The stiffness of a member with a single perforated zone was seen to be reduced slightly by the presence of large openings, but the reduction is small enough to be neglected in design with no compromise in safety.

8.3.2 Shear

Parametric FE models of three different sizes of RHS, with web openings of various diameters, were used to study the structural performance of RHS in high shear. Shear force-deformation relationships were obtained and stress distributions were observed. In all cases, the RHS were thick enough to prevent elastic instability of the flange and web.

As with bending, the presence of the web opening was observed to cause an increased von Mises stress in the webs at the edge of the opening, in this case due to the reduced shear area and the stress concentrating effect of the change in cross-section. The shear capacity and stiffness were seen to be reduced by all but the smallest of openings, and the consequences of the increased flexibility of the perforated zone for serviceability were seen to be important for design. For shear, the structural performance of the member was seen to be governed by small areas of yielding material and, for design purposes, plasticity at working loads is likely to be

undesirable. An empirical formula for the prediction of maximum von Mises stress was developed and a formula for the calculation of the shear force at yield, based on a reduced area calculation, was proposed. The high shear resistance of unperforated members means that large reductions in shear resistance may not be critical in design.

The high strains present in perforated sections were able to generate sufficiently strain hardened stresses to maintain increasing shear resistance beyond the first yield.

8.3.3 Torsion

Parametric FE models of three different sizes of RHS, with web openings of various diameters, were used to study the structural performance of RHS in uniform torsion. Torque-twist relationships were obtained and stress distributions were observed. In all cases, the RHS were thick enough to prevent elastic instability of the flange and web.

The presence of the web opening was observed to cause an increased von Mises stress in the webs at the edge of the opening, due to the reduced area of cross-section and the stress concentrating effect of the change in cross-section. The torsional resistance and stiffness were seen to be reduced by all but the smallest of openings, and the consequences of the increased flexibility of the perforated zone for serviceability were seen to be important for design. The structural performance of the member was seen to be governed by small areas of yielding material and, for design purposes, plasticity at working loads may be undesirable. An empirical formula for the prediction of maximum von Mises stress was developed and a formula for the calculation of the torque at yield, based on a reduced area calculation, was proposed.

The long yield plateau, characteristic of hot finished steel, prevented strain hardening in the unperforated sections. In contrast, the high strains present in perforated sections were able to generate sufficiently strain hardened stresses to maintain increasing resistance beyond the twist at first yield.

8.4 Concluding remarks

In all but one category of tests, good agreement was achieved between experimentally measured quantities and the corresponding FE predictions, allowing parametric investigations to be conducted using the calibrated FE models. Preliminary design advice was formulated based on the results of the parametric study and laboratory tests. Aspects requiring further investigation or development were identified (Sections 5.7 and 7.9).

The full-scale torsion tests produced some unexpected results with measured capacities significantly lower than those predicted by FE and torsion theory. Attempts were made to determine the cause of this behaviour and a number of possibilities were eliminated. Although the anomalous results have not yet been fully explained, evidence of similar behaviour in previous research was discovered.

The primary aim of the project was to develop the basis for a set of design rules for perforated RHS in combined torsion, bending and shear. The preliminary design rules were formulated, but problems with a testing machine and unexpected torsion test results meant that more experimental work was conducted than originally planned.

8.5 Lists of conclusions

8.5.1 Bending of perforated RHS (without elastic instability)

- For both perforated and unperforated sections, the results of four-point bending tests can be adequately modelled using the FE technique (resistance, stiffness, displaced shapes, collapse mechanisms, and strains in the elastic range). [Section 3.5]
- Unperforated sections behave as predicted by conventional (Euler-Bernoulli-Parent) beam bending theory (resistance, stiffness and strains in the elastic range). [Section 3.4]
- Perforations cause an increased von Mises stress in the webs above the opening, due to the reduced section moduli and the stress concentrating effect of the change in cross-section. [Section 7.5.2]
- If the hole is smaller than a certain size (the 'critical hole size'), the increased stress above the hole balances the effect of the reduction in the elastic section modulus, and the moment at yield is not reduced. [Section 7.5.3]
- For holes larger than the critical hole size, the raised stress is higher than the stress in the flanges, and the moment at first yield is reduced by the presence of the hole. [Section 7.5.3]
- The critical hole size and the maximum von Mises stress can be approximated by empirical equations. [Section 7.5.2]
- Bending capacity can be conservatively predicted by an approximate method based on the reduced elastic and plastic section moduli at the location of the hole. [Section 7.5.3]

- The ultimate resistance of perforated members is increased by strain hardening and is limited by the stability of the compression flange and compression cee above the hole. [Section 7.5.3]
- The bending resistance of a section with two web openings is lower than that of a section with one opening of the same diameter. [Section 7.5.3]
- The stiffness of a member with a single perforated zone is reduced slightly by the presence of large openings, but the reduction is small enough to be neglected in design with no compromise in safety. [Sections 3.5 and 7.5.4]
- In the elastic range, the zone of influence extends a distance in the order of one hole diameter on either side of the edge of the hole. [Section 7.5.5]

8.5.2 Shearing of perforated RHS (without elastic instability)

- For both perforated and unperforated sections, the results of three-point bending tests can be adequately modelled using the FE technique (resistance, stiffness, displaced shapes, collapse mechanisms, and strains in the elastic range). [Section 4.5]
- Perforations cause an increased von Mises stress in the webs around the opening, due to the reduced shear area and the stress concentrating effect of the change in cross-section. [Section 7.6.2]
- The stress distribution in the web of an RHS with one hole is similar to that in the web of an RHS with two holes, although the maximum stress is slightly lower, particularly for large holes. [Section 7.6.2]
- The maximum von Mises stress can be approximated by an empirical equation. [Section 7.6.2]
- In shear, the structural performance of the member is governed by small areas of yielding material and, for design purposes, plasticity at working loads is likely to be undesirable. [Section 7.6.3]

- Asymmetry induces internal torsional and lozenging forces that, for high plastic shear loads in longer spans, can cause distortion of the cross-section at some considerable distance from the hole. [Sections 4.4, 4.5 and 7.6.3]
- Shear capacity can be conservatively predicted by an approximate method based on the reduced shear area at the location of the hole. [Section 7.6.3]
- The ultimate resistance of perforated members is increased by strain hardened stresses (due to extreme deformations in the perforated zone). [Section 7.6.3]
- The shear capacity and stiffness are reduced by all but the smallest of openings, and the consequences of the increased flexibility of the perforated zone for serviceability are important for design. [Sections 7.6.4 and 7.6.6]
- The high shear resistance of unperforated members means that large reductions in shear resistance may not be critical in design. [Section 7.6.1]
- In the elastic range, the zone of influence extends a distance in the order of one hole diameter on either side of the edge of the hole. [Section 7.6.5]

8.5.3 Torsion of perforated RHS (without elastic instability)

- In some cases, for both perforated and unperforated sections, the results of torsion tests can be adequately modelled using the FE technique (resistance, stiffness, displaced shapes, collapse mechanisms, and strains in the elastic range). However, the FE models used in this project did not produce accurate predictions for some of the laboratory tests. [Sections 5.5 and 6.4]
- In terms of resistance, unperforated sections do not appear to behave as predicted by conventional thick wall torsion theory, although stiffness and elastic shear can be correctly predicted. [Sections 5.5 and 5.6.9]
- Perforations cause an increased von Mises stress in the webs around the opening, due to the reduced cross-sectional area and the stress concentrating effect of the change in cross-section. [Sections 6.5 and 7.7.2]

- The stress distribution in the web of an RHS with one hole is similar to that in the web of an RHS with two holes, although maximum stresses are slightly lower, particularly for large holes. [Sections 6.5 and 7.7.2]
- The maximum von Mises stress can be approximated by an empirical equation. [Section 7.7.2]
- In torsion, the structural performance of the member is governed by small areas of yielding material and, for design purposes, plasticity at working loads is likely to be undesirable. [Section 7.7.3]
- Asymmetry induces internal lozenging forces that, for high plastic torques, can cause distortion of the cross-section at some considerable distance from the hole. [Sections 6.4.2 and 7.5.3]
- Torsional capacity (in FE at least) can be conservatively predicted by an approximate method based on the reduced web area at the location of the hole. [Section 7.7.3]
- The ultimate resistance of perforated members is increased by strain hardened stresses (due to extreme deformations in the perforated zone). [Section 7.7.3]
- The torsional capacity and stiffness are reduced by all but the smallest of openings, and the consequences of the increased flexibility of the perforated zone for serviceability are important for design. [Sections 7.7.3 and 7.7.4]
- In the elastic range, the zone of influence extends a distance in the order of two hole diameters on either side of the edge of the hole. [Section 7.7.5]

Appendices

Merely corroborative detail, intended to give artistic verisimilitude to an otherwise bald and unconvincing narrative.

W.S. Gilbert, 1885
The Mikado, (Act II)

Table of contents

Table of Contents	II
List of Figures	III
List of Tables	IV
A. Calibration of the Avery torsion testing machine	VI
A.1 Introduction	VI
A.2 Details of the testing machine	VII
A.3 Measurement of torque	VII
A.4 Measurement of twist	XIII
B. Sensitivity of sectional properties	XVII
C. Formulae for the calculation of the properties of cross-section	XXV
D. Material properties	XXIX
D.1 Introduction	XXIX
D.2 Material properties RHS 250x250x10 grade S275J2H bar number 1	XXX
D.3 Material properties RHS 250x250x10 grade S275J2H bar number 2	XXXII
D.4 Material properties RHS 250x250x10 grade S275J2H bar number 3	XXXIV
D.5 Material properties RHS 200x100x8 grade S275J2H bar number 1	XXXVI
D.6 Material properties RHS 200x100x8 grade S275J2H bar number 2	XXXVIII
D.7 Material properties RHS 200x100x8 grade S275J2H bar number 3	XL
D.8 Material properties RHS 150x150x6.3 grade S275J2H bar number 1	XLII
D.9 Material properties RHS 200x100x8 grade S355J2H bar number 1	XLIV
D.10 Material properties RHS 150x150x6.3 grade S355J2H bar number 1	XLVI
D.11 Statistical analysis of material properties	XLVIII
E. Stress concentration factors (Finite Element)	LII
F. Calibration of testing equipment	LVIII
F.1 Introduction	LVIII
F.2 The Instron testing machine	LVIII
F.3 The Zwick testing machine	LIX
F.4 The Denison testing machine	LIX

List of figures

Figure A-1: Test piece dimensions XI
Figure A-2: Torque-rotation relationship XII
Figure A-3: The material model and tensile test results XII
Figure A-4: Experimental measurements of elastic torsional stiffness XVI
Figure B-1: Sensitivity to section width (RHS 200x100x8) XVIII
Figure B-2: Sensitivity to section width (RHS 250x250x10) XVIII
Figure B-3: Sensitivity to section height (RHS 200x100x8) XIX
Figure B-4: Sensitivity to section height (RHS 250x250x10) XIX
Figure B-5: Sensitivity to section thickness (RHS 200x100x8) XX
Figure B-6: Sensitivity to section thickness (RHS 250x250x10) XX
Figure B-7: Sensitivity to external corner radius (RHS 200x100x8) XXI
Figure B-8: Sensitivity to external corner radius (RHS 250x250x10) XXI
Figure B-9: Sensitivity to internal corner radius (RHS 200x100x8) XXII
Figure B-10: Sensitivity to internal corner radius (RHS 250x250x10) XXII
Figure B-11: Sensitivity to yield stress (any section) XXIII
Figure B-12: Sensitivity to Young's modulus (any section) XXIII
Figure B-13: Sensitivity to Poisson's ratio (any section) XXIV
Figure D-1: Typical values of percentage energy error XLIX
Figure D-2: Typical values of plateau ratio XLIX
Figure D-3: Typical values of post yield stiffness L
Figure D-4: Typical values of elliptical strain hardening factor L
Figure D-5: Typical values of strain at maximum force LI
Figure D-6: Plateau ratio and post yield stiffness LI

List of tables

Table A-1: Torsion test results summary X
Table A-2: Tension test results summary X
Table A-3: Summary of comparison with theoretical and FE predictions X
Table A-4: Stiffness of the testing machine (K_{ends}) XV
Table D-1: Tensile test results for RHS 250x250x10 grade S275J2H bar #1 XXX
Table D-2: Material model for RHS 250x250x10 grade S275J2H bar #1 XXXI
Table D-3: ABAQUS material model (RHS 250x250x10 grade S275J2H bar #1) XXXI
Table D-4: Tensile test results for RHS 250x250x10 grade S275J2H bar #2 XXXII
Table D-5: Material model for RHS 250x250x10 grade S275J2H bar #2 XXXIII
Table D-6: ABAQUS material model (RHS 250x250x10 grade S275J2H bar #2) XXXIII
Table D-7: Tensile test results for RHS 250x250x10 grade S275J2H bar #3 XXXIV
Table D-8: Material model for RHS 250x250x10 grade S275J2H bar #3 XXXV
Table D-9: ABAQUS material model (RHS 250x250x10 grade S275J2H bar #3) XXXV
Table D-10: Tensile test results for RHS 200x100x8 grade S275J2H bar #1 XXXVI
Table D-11: Material model for RHS 200x100x8 grade S275J2H bar #1 XXXVII
Table D-12: ABAQUS material model (RHS 200x100x8 grade S275J2H bar #1) XXXVII
Table D-13: Tensile test results for RHS 200x100x8 grade S275J2H bar #2 XXXVIII
Table D-14: Material model for RHS 200x100x8 grade S275J2H bar #2 XXXIX
Table D-15: ABAQUS material model (RHS 200x100x8 grade S275J2H bar #2) XXXIX
Table D-16: Tensile test results for RHS 200x100x8 grade S275J2H bar #3 XL
Table D-17: Material model for RHS 200x100x8 grade S275J2H bar #3 XLI
Table D-18: ABAQUS material model (RHS 200x100x8 grade S275J2H bar #3) XLI
Table D-19: Tensile test results for RHS 150x150x6.3 grade S275J2H bar #1 XLII
Table D-20: Material model for RHS 150x150x6.3 grade S275J2H bar #1 XLIII
Table D-21: ABAQUS material model (RHS 150x150x6.3 grade S275J2H bar #1) XLIII
Table D-22: Tensile test results for RHS 200x100x8 grade S355J2H bar #1 XLIV
Table D-23: Material model for RHS 200x100x8 grade S355J2H bar #1 XLV
Table D-24: ABAQUS material model (RHS 200x100x8 grade S355J2H bar #1) XLV
Table D-25: Tensile test results for RHS 150x150x6.3 grade S355J2H bar #1 XLVI
Table D-26: Material model for RHS 150x150x6.3 grade S355J2H bar #1 XLVII
Table D-27: ABAQUS material model (RHS 150x150x6.3 grade S355J2H bar #1) XLVII
Table E-1: FE stress concentration factors for bending (part 1 of 2) LII
Table E-2: FE stress concentration factors for bending (part 2 of 2) LIII

Table E-3: FE stress concentration factors for shear (part 1 of 2) LIV
Table E-4: FE stress concentration factors for shear (part 2 of 2) LV
Table E-5: FE stress concentration factors for torsion (part 1 of 2) LVI
Table E-6: FE stress concentration factors for torsion (part 2 of 2) LVII

A. Calibration of the Avery torsion testing machine

A.1 Introduction

The torsion testing machine used in the small-scale study (Chapter 6) is employed principally for undergraduate teaching and, unlike the equipment used in the full-scale experimental work (Chapters 3, 4 and 5), is not calibrated regularly to National Standards (Appendix F).

The original role of the small-scale torsion tests was that of exploratory study, preliminary to the full-scale testing programme. At the time of testing, the uncertain accuracy of the results was not regarded as significant, because the principal aim was to gain a qualitative understanding of the torsional behaviour of perforated RHS. However, the results proved to be particularly informative and the matter of accuracy became important after the tests were complete. This Appendix contains a short description of the methods employed to verify the accuracy of the experimental results.

A.2 Details of the testing machine

Description	Avery "Reverse torsion testing machine" (Figure 6-1)
	Type 6609 CGG Number E61981
Load ranges	0 - 15000 inch lb in 50 inch lb divisions (calibrated)
(Dial readout)	0 - 7500 inch lb in 20 inch lb divisions (not calibrated)
	0 - 3000 inch lb in 10 inch lb divisions (not calibrated)
	0 - 1500 inch lb in 5 inch lb divisions (not calibrated)
	Note: 1 inch lb is equivalent to 0.113 Nm
Speed ranges	90 degrees per minute (not checked)
(Both directions)	30 degrees per minute (not checked)
	10 degrees per minute (checked)
	$3^1/_3$ degrees per minute (checked)

Date of calibration 17th July 1997

A.3 Measurement of torque

To investigate the accuracy of the torsion rig torque gauge, two (nominally identical) steel test pieces of solid circular cross-section were tested at angular velocities of $3^1/_3$ degrees and 10 degrees per minute. Torque-rotation histories of the two tests were compared with numerical predictions based on established torsion formulae and a simple Finite Element (FE) model. Tensile tests provided values for the material properties used in the calculations.

The approximate dimensions of the torsion test pieces are given in Figure A—1a. The driving flats on each specimen were initially mutually perpendicular to restrict transmission of any bending that may result due to any accidental asymmetry of test pieces.

Both specimens were initially tested at an angular velocity of $3^1/_3$ degrees per minute and then unloaded at the same speed. The specimens were then reloaded at

10 degrees per minute until a steady value of torque was obtained. The 15,000 inch lb. (1700 Nm) scale was used for both tests. The torsion tests on the two specimens are referred to as 'test A' and 'test B'.

The approximate dimensions of the tension test pieces are given in Figure A—1b. Tensile tests were conducted on a 200 kN Zwick machine with a 50 mm gauge length extensometer. The tension tests on the two specimens are referred to as 'test 1' and 'test 2'.

Tensile test piece dimensions are specified in accordance with BS EN 10002-1:1990. The tensile test pieces were turned from the same steel bar as the torsion specimens.

Table A—1 gives a summary of the torsion test results. Complete torque-rotation histories can be seen in Figure A—2. Table A—2 gives a summary of the tension test results.

The torsion tests were modelled using an ABAQUS v5.5.1 (Section 2.3) FE model consisting of a single three-noded quadratic beam element (B32) of circular cross-section[4]. The material model is shown in Figure A—3. The results were also compared with predictions based on torsion theory (Section 2.5). The torque at yield (T_{el}) was calculated using Equation A—1. The maximum torque (T_{max}) was calculated using Equation A—2. The elastic stiffness was calculated using Equation A—3.

[4] The formulation of the beam element used in the FE study is also based on torsion theory, and is able to model plastic yielding as it moves inwards from the outside of the cross-section.

$$T_{el} = \frac{1}{2\sqrt{3}} \pi r^3 f_y$$

Equation A—1

$$T_{\max} = \frac{2}{3\sqrt{3}} \pi r^3 f_u$$

Equation A—2

$$\frac{T}{\theta} = \frac{E \pi r^4}{4L(1+\upsilon)}$$

Equation A—3

Where

E = Young's modulus (208.6 kN/mm2)

f_y = Yield stress (580 N/mm2)

f_u = Tensile strength (620 N/mm2)

L = Gauge length (108 mm)

r = Radius of bar (10 mm)

T = Torque

T_{el} = Torque at yield

T_{max} = Maximum torque

υ = Poisson's ratio (assumed to be 0.3)

The torque-rotation histories from the torsion tests are compared with the FE and theoretical predictions in Figure A—2. The comparisons are summarised in Table A—3. The measurements of maximum torque and torque at yield are sufficiently close to the predictions to conclude that the testing machine is correctly

indicating the torque. The experimental measurement of stiffness is lower than the predictions, due to the flexibility of the testing machine (Section A.4).

Table A—1: Torsion test results summary

Test	Initial stiffness (Nm per degree)	Torque at yield T_{el} (Nm)	Maximum torque T_{max} (Nm)
Test A	118.8	491.6	728.9
Test B	115.3	474.6	748.1
Mean	117.0	483.1	738.5
Standard deviation	2.5	12.0	13.6
(% of mean)	(2.1%)	(2.5%)	(1.8%)

Table A—2: Tension test results summary

Test	Young's modulus E (kN/mm^2)	0.1% proof stress (N/mm^2)	0.2% proof stress (N/mm^2)	Tensile strength f_u (N/mm^2)
Test 1	209.8	576.0	579.2	626.5
Test 2	207.2	573.4	581.9	623.6
Mean	208.5	574.7	580.6	625.1
Standard deviation	1.8	1.8	1.9	2.1
(% of mean)	(0.9%)	(0.3%)	(0.3%)	(0.3%)

Table A—3: Summary of comparison with theoretical and FE predictions

Test	Initial stiffness (Nm per degree)	Torque at yield T_{el} (Nm)	Maximum torque T_{max} (Nm)
Theoretical	202.2	523.2	745.8
(% of theoretical)	(100.0%)	(100.0%)	(100.0%)
Finite Element	195.0	500.0	747.5
(% of theoretical)	(96.4%)	(95.6%)	(100.2%)
Average experimental	117.0	483.1	758.5
(% of theoretical)	(57.9%)	(92.3%)	(101.7%)

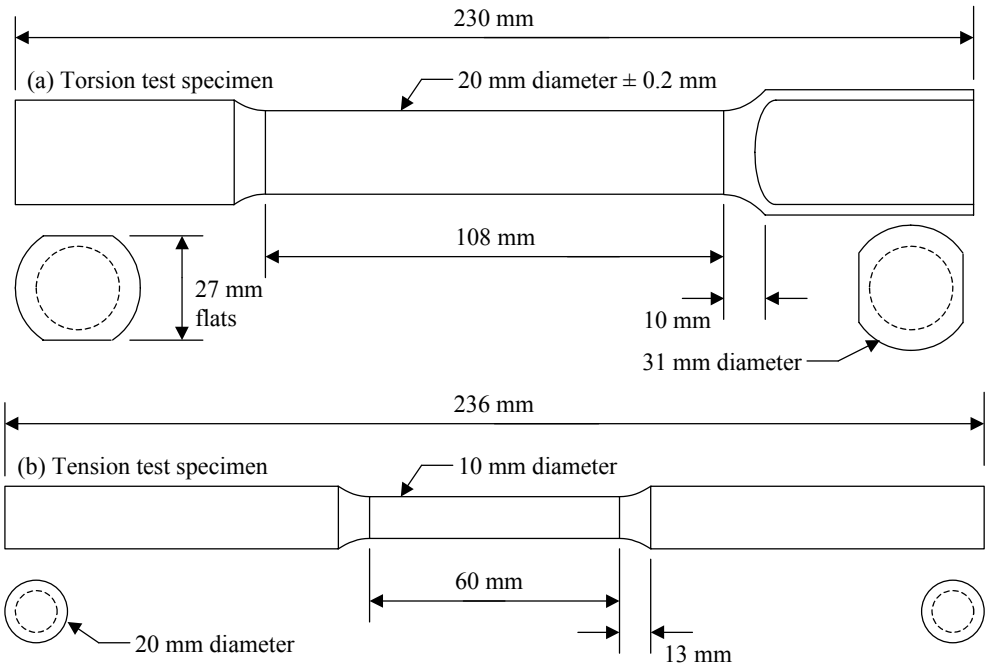

Figure A—1: Test piece dimensions

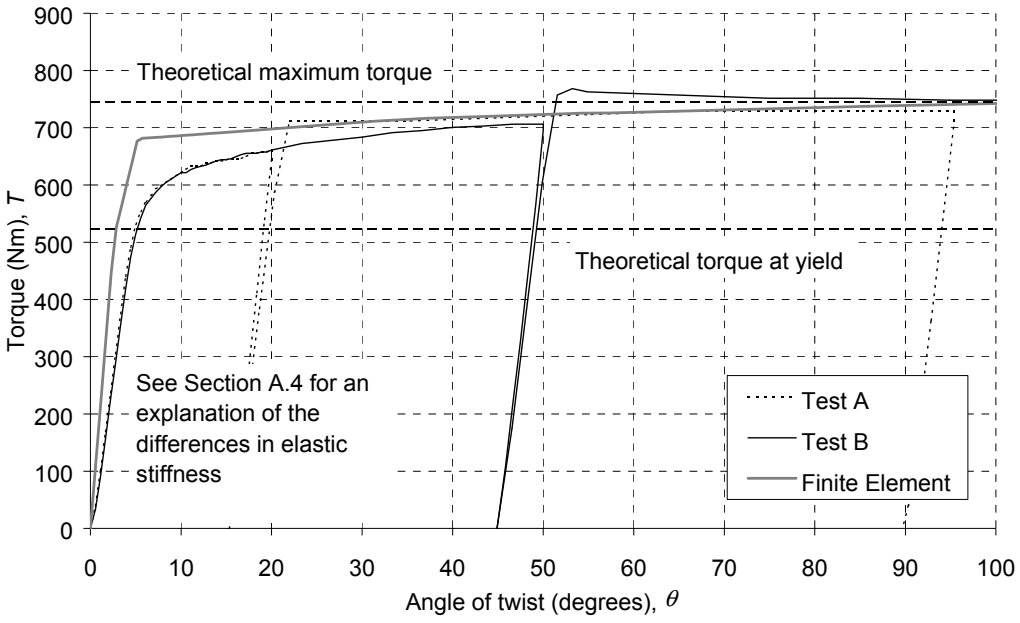

Figure A—2: Torque-rotation relationship

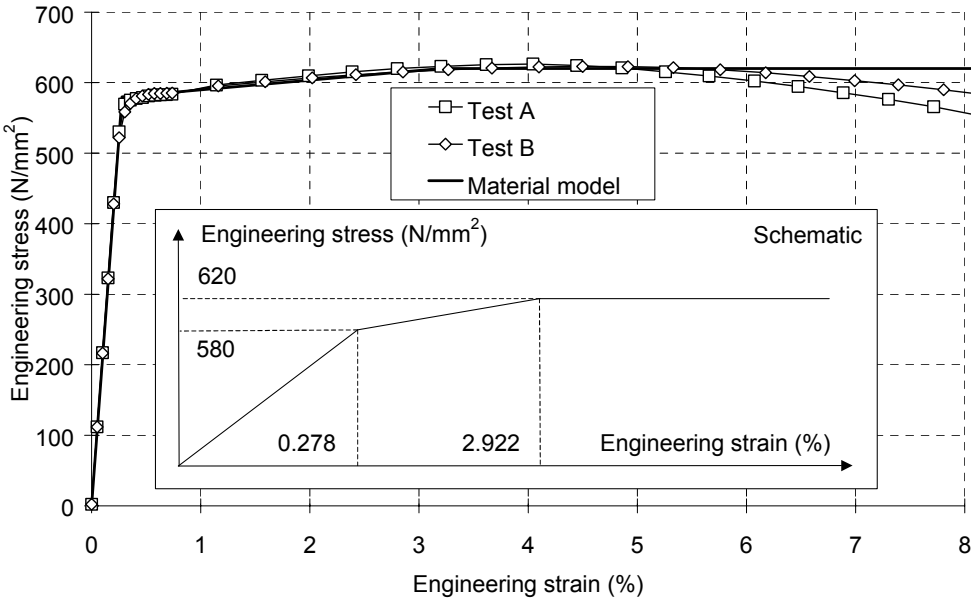

Figure A—3: The material model and tensile test results

A.4 Measurement of twist

The angle of twist in the small-scale torsion tests was measured by timing the machine while it applied a rotation at the constant angular velocity of $3^1/_3$ degrees per minute. This method allowed the tests to be conducted quickly, by a single operator, but it lacked the accuracy that could be achieved by measuring the twist of the specimen directly. Similar tests, such as those conducted by Marshall (1972) and Moore and Clark (1952), made use of optical devices[5], and twists were measured very accurately, but to the detriment of the simplicity of the experimental set-up and rate of testing.

The largest error that resulted as a consequence of the chosen method of twist measurement was that the total rotation also included the rotation that occurred outside the gauge length of the specimen. Rotation occurred outside the gauge length due to a combination of the deformation of the devices that serve to hold the specimen in place and the rotation that occurred at the 'fixed' end, where some movement was necessary in order to measure the torque. Consequently, the uncorrected experimental results appeared to show that the specimens were significantly less stiff than predicted by torsion theory and FE analysis. The circular bars tested in order to calibrate the torque measurement showed a similar error (Table A—3), in this case due entirely to the rotation at the 'fixed' end where the torque is transmitted to the mechanical torque measuring device. Since the elastic portion of these two experimental measurements is linear (Figure A—2), it can be

[5] See Fenner (1965) for a description of an optical twist meter.

deduced that the rotation of the torque measuring device is proportional to the torque.

A retrospective correction was applied to the original experimental results to remove the error due to the rotational flexibility of the testing apparatus. The factor of correction was obtained by measuring the flexibility experimentally, as described below.

If the rotation stiffness of the testing apparatus (K_{ends}) is assumed to be elastic and proportional to the applied torque (T) then the total twist (θ) can be described by Equation A—4. In the equation, L is the gauge length, G is the shear modulus of the steel and I_t is the torsional inertia constant of the material.

$$\theta = \frac{TL}{I_t G} + \frac{T}{K_{ends}}$$

Equation A—4

Since it was not possible to test a specimen with a zero gauge length, the stiffness of the testing apparatus was obtained by testing specimens of various gauge lengths. Angles of twist for different lengths were compared at different values of elastic torque and, at each, a value of K_{ends} was obtained by a least squares fit (Table A—4). The final value of K_{ends} was obtained by taking the average of the measurements of K_{ends} at the different torques.

The results were a good match with the model described by Equation A—4, and this was borne out by the strong linear fit with the experimental results (correlation coefficient = 0.93). However, the retrospective altering of results is an additional source of error that is best avoided whenever possible. Ideally, the twist over the gauge length would have been measured directly, but this would have

required a complicated experimental set-up, and unfortunately, was not a practical approach for this investigation.

The elastic torsional stiffness of the cold-formed tube was very difficult to measure experimentally. This was due partly to the errors in the measurement of twist, but also due to difficulties in reading the torque scale accurately when the needle was moving, and the difficulties in measuring the Young's modulus of the thin tube material. Following the application of the correction factor, the experimental measurements of torsional stiffness were 50% higher than the theoretical predictions (Figure A—4). However, comparisons of the corrected experimental results and the FE predictions for the perforated specimens were extremely good (Section 6.4.3).

Table A—4: Stiffness of the testing machine (K_{ends})

Torque (Nm)	Twist at the ends (^{o})	K_{ends} (Nm/^{o})
100	0.4361	229.31
200	0.8722	229.31
300	1.3084	229.29
400	1.7445	229.29
500	2.1806	229.29
600	2.6167	229.30
	Average	229.30

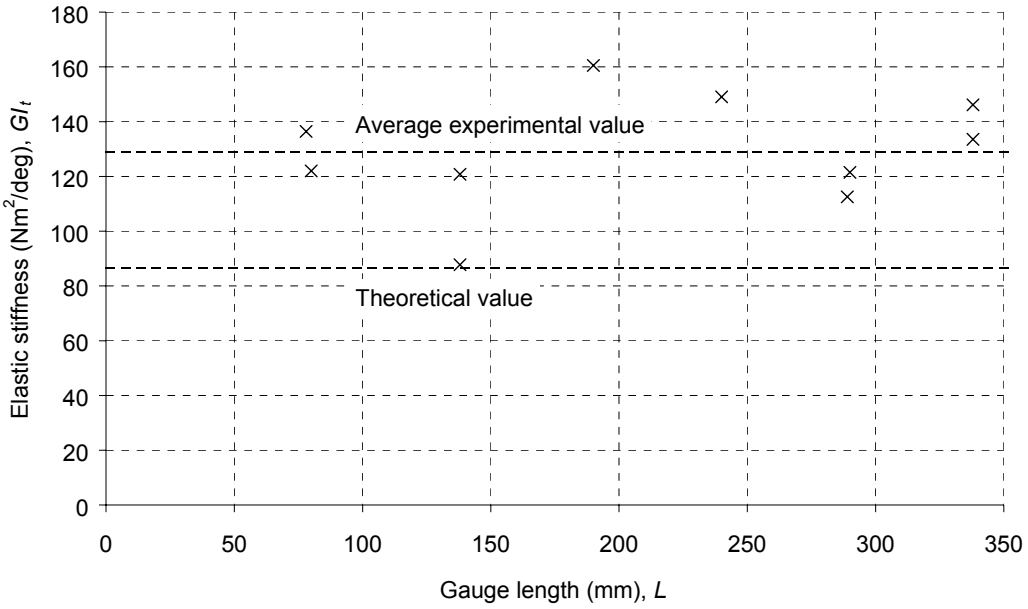

Figure A—4: Experimental measurements of elastic torsional stiffness

B. Sensitivity of sectional properties

The following figures (Figure B—1 through Figure B—13) illustrate the sensitivity of various sectional properties (unperforated) to small changes in the dimensions of the cross-section and the properties of the material.

The figures show that accurate measurements of the principal dimensions (width, height and thickness) are necessary for accurate calculation of the sectional properties. The dimensions of the corners are much less important, and accurate measurements (which are difficult to make) are not necessary for accurate calculation of the sectional properties. However, the internal radius of the corner is very important when calculating stress concentrations in the case of torsion (Section 2.5).

Of all the principal material properties, the yield stress is the most important as it has a direct influence on all the sectional properties. In this investigation, the yield stress was measured accurately using multiple direct tensile tests on coupons in accordance with BS 10002-1:1990 (Appendix D). Young's modulus is more difficult to measure accurately in a tensile test, but only influences stiffness. Poisson's ratio is very difficult to measure, but only influences torsional stiffness slightly. In this investigation, the Poisson's ratio was assumed to be 0.3 (a typical value for steel) and no attempt was made to measure it directly.

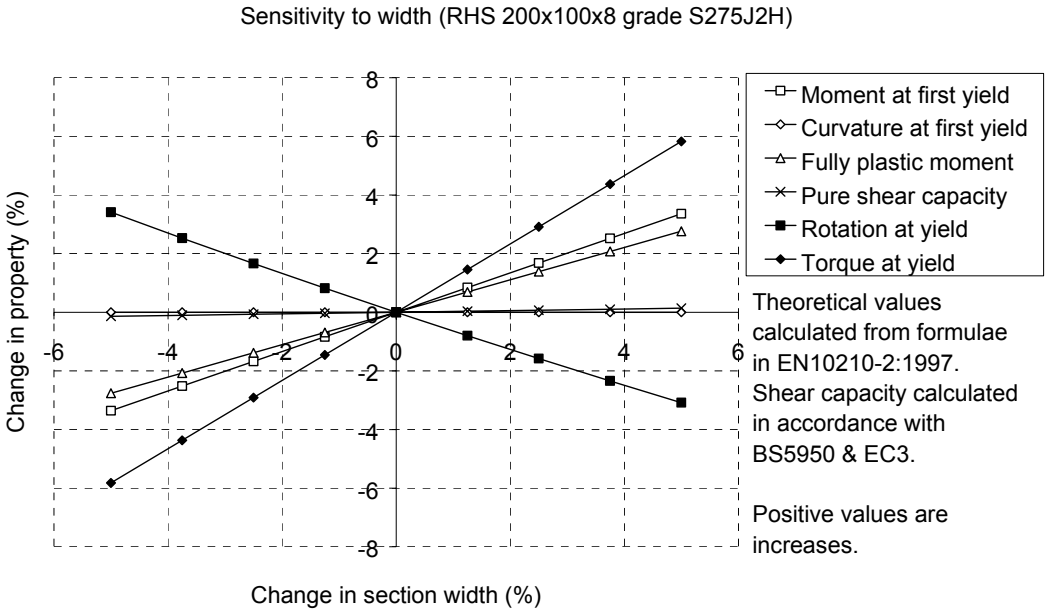

Figure B—1: Sensitivity to section width (RHS 200x100x8)

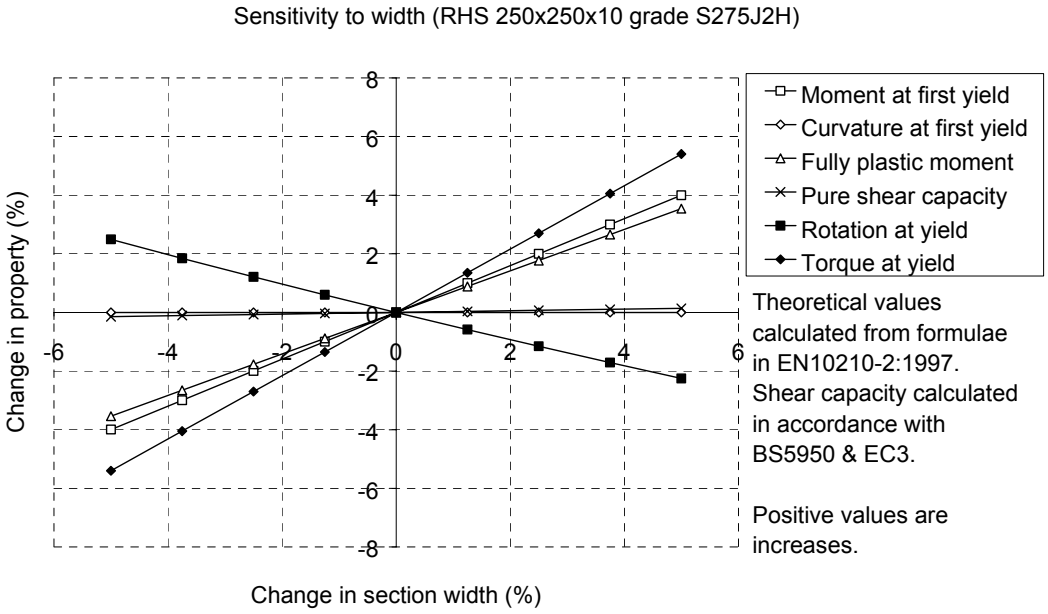

Figure B—2: Sensitivity to section width (RHS 250x250x10)

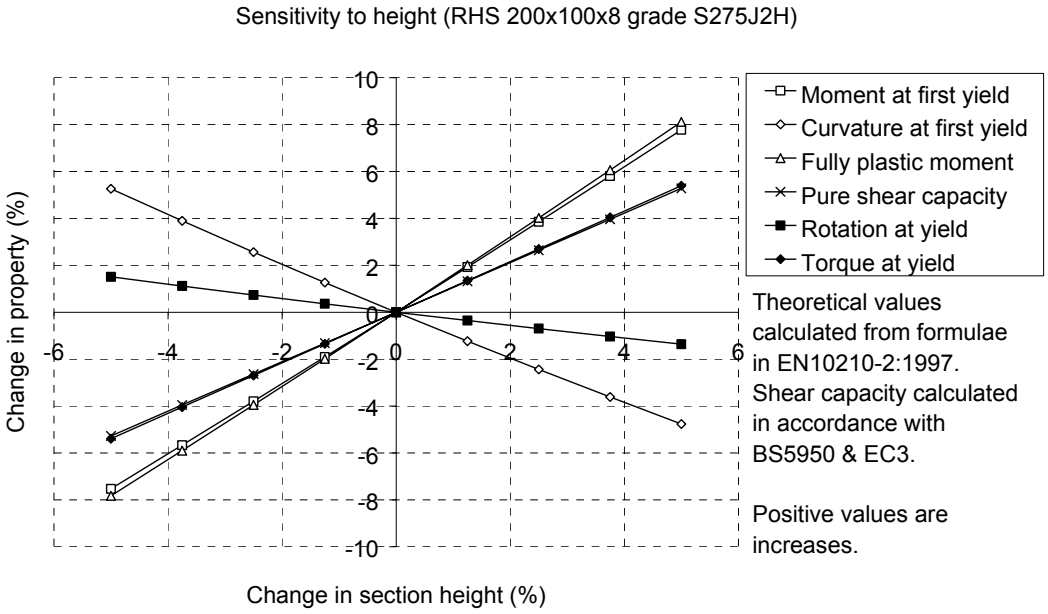

Figure B—3: Sensitivity to section height (RHS 200x100x8)

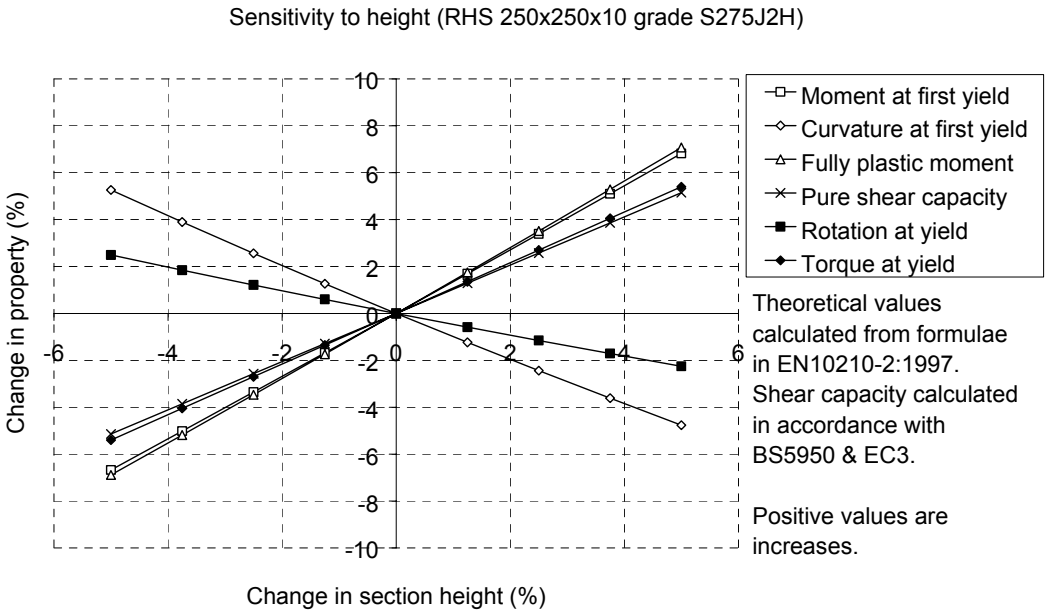

Figure B—4: Sensitivity to section height (RHS 250x250x10)

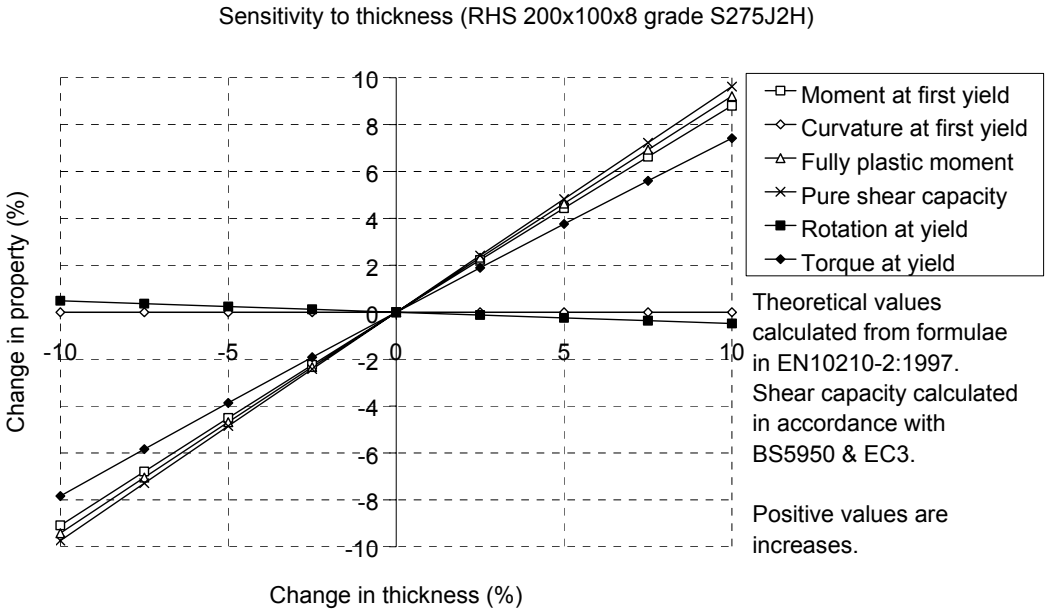

Figure B—5: Sensitivity to section thickness (RHS 200x100x8)

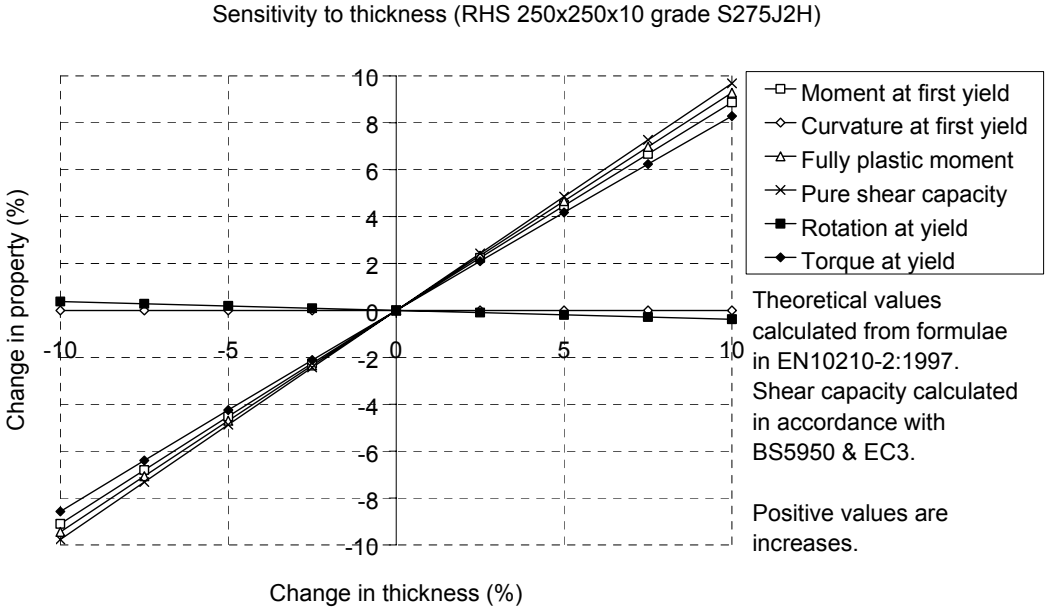

Figure B—6: Sensitivity to section thickness (RHS 250x250x10)

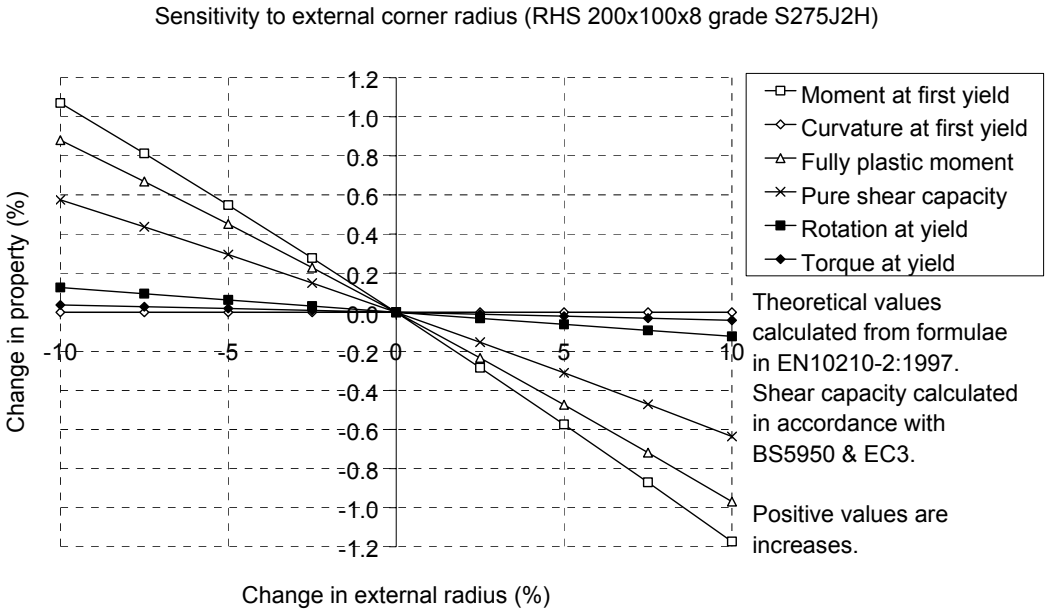

Figure B—7: Sensitivity to external corner radius (RHS 200x100x8)

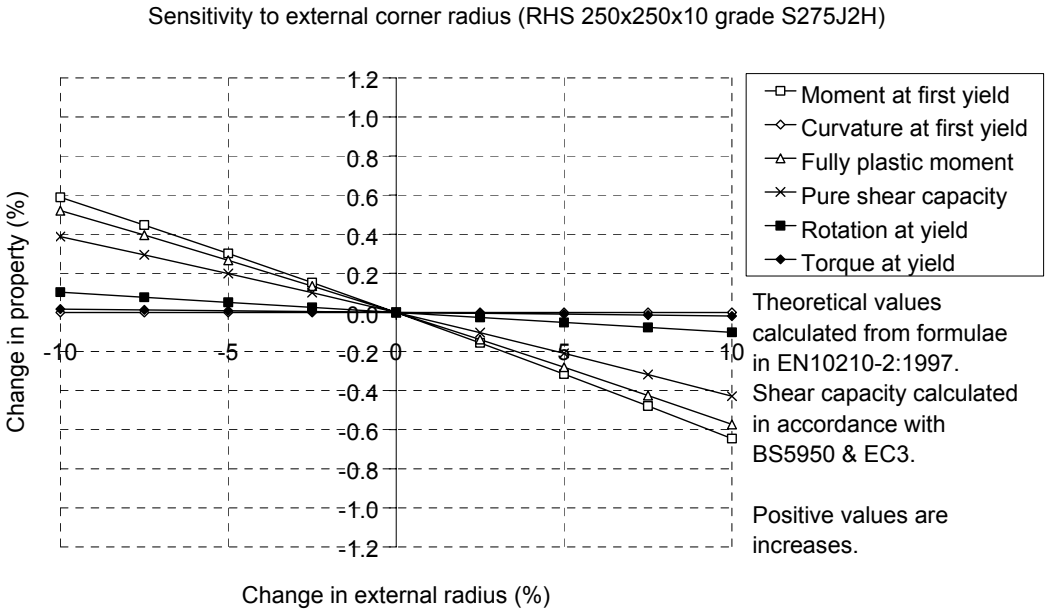

Figure B—8: Sensitivity to external corner radius (RHS 250x250x10)

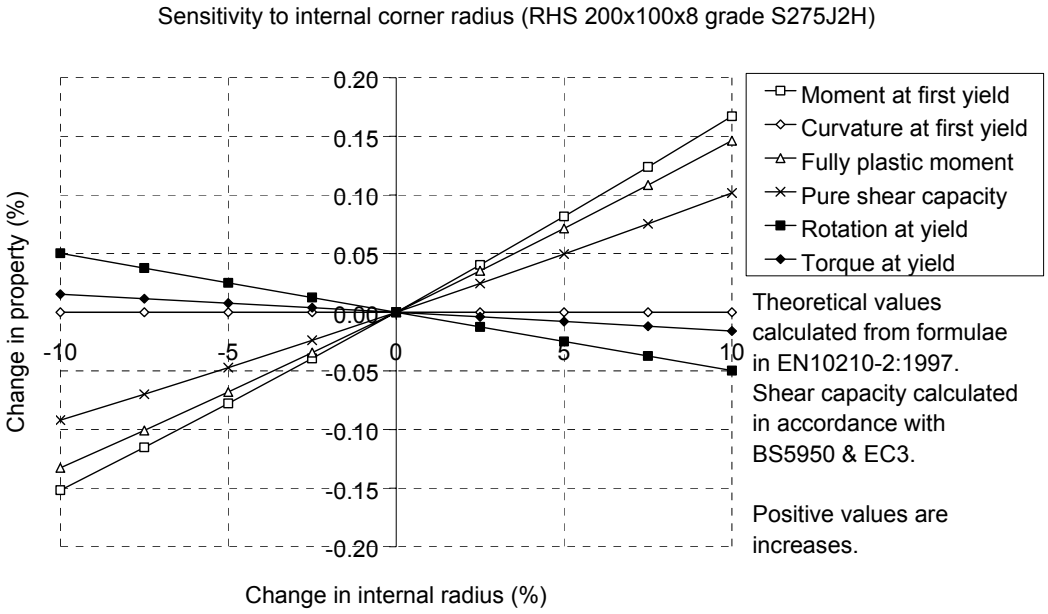

Figure B—9: Sensitivity to internal corner radius (RHS 200x100x8)

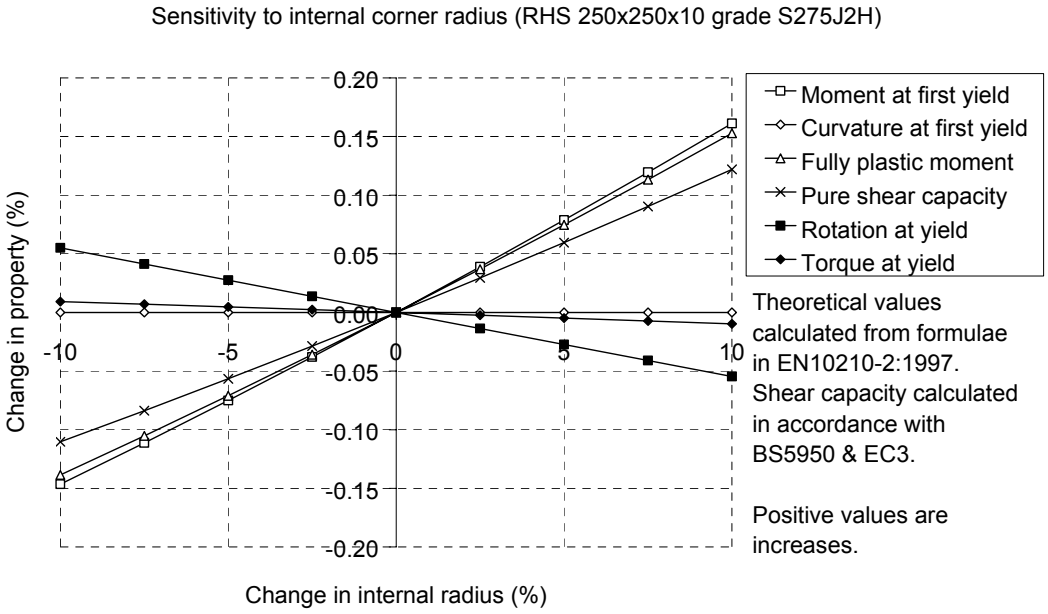

Figure B—10: Sensitivity to internal corner radius (RHS 250x250x10)

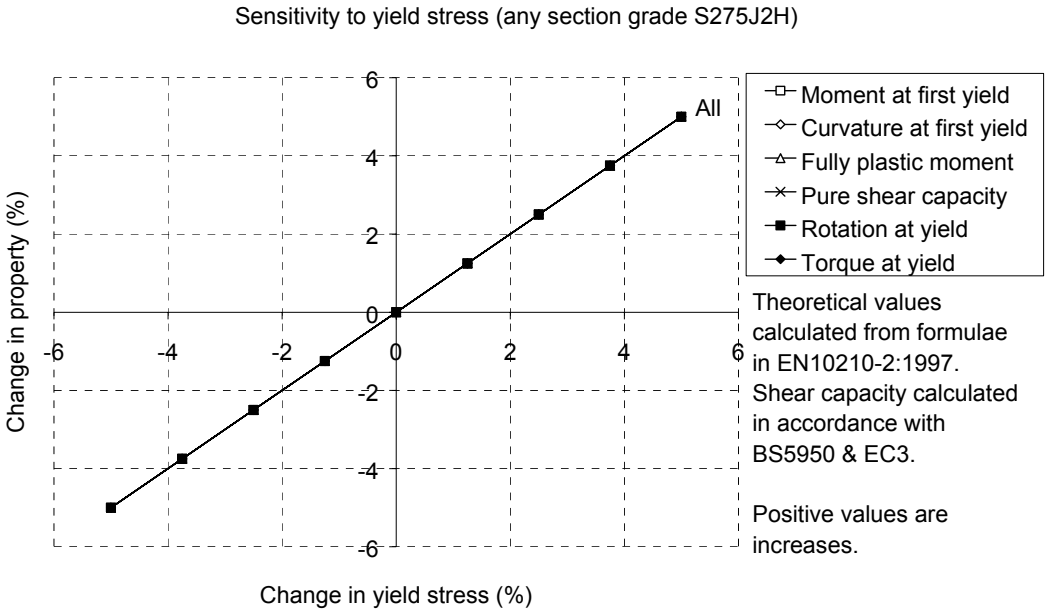

Figure B—11: Sensitivity to yield stress (any section)

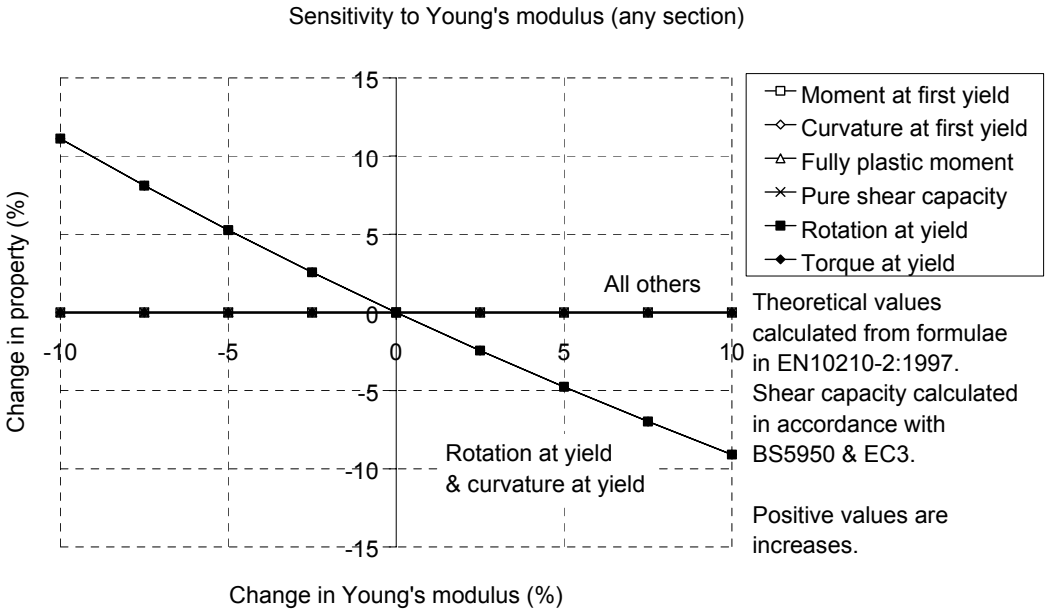

Figure B—12: Sensitivity to Young's modulus (any section)

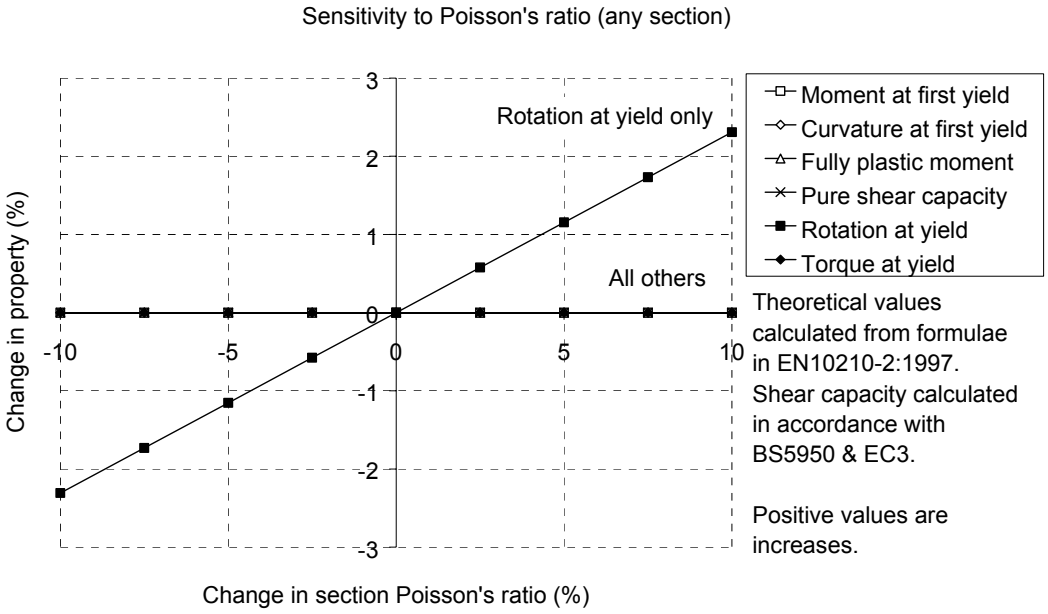

Figure B—13: Sensitivity to Poisson's ratio (any section)

C. Formulae for the calculation of the properties of cross-section

The following formulae for geometric properties are given in Annex A of BS EN 10210-2:1997. Some of the symbols have been changed to maintain consistency with the main body of this Thesis. Dimensions of the cross-section are as defined in Figure 1-9 and Figure 1-10.

Nominal corner radii

$$r_o = 1.5t$$

Equation C—1

$$r_i = 1.0t$$

Equation C—2

Cross-sectional area

$$A = 2t\left(b + h - 2t\right) - \left(4 - \pi\right)\left(r_o^2 - r_i^2\right)$$

Equation C—3

Second moment of area (major axis)

$$I_y = \frac{bh^3}{12} - \frac{\left(b - 2t\right)\left(h - 2t\right)^3}{12} - 4\left(I_{\zeta\zeta} + A_\zeta h_\zeta^2\right) + 4\left(I_{\xi\xi} + A_\xi h_\xi^2\right)$$

Equation C—4

Radius of gyration (major axis)

$$i_y = \sqrt{\frac{I_y}{A}}$$

Equation C—5

Elastic section modulus (major axis)

$$W_{el,y} = \frac{2I_y}{h}$$

Equation C—6

Plastic section modulus (major axis)

$$W_{pl,y} = \frac{bh^2}{4} - \frac{(b-2t)(h-2t)^2}{4} - 4A_\zeta h_\zeta + 4A_\xi h_\xi$$

Equation C—7

Torsional inertia constant

$$I_t = t^3 \frac{h_c}{3} + 2KA_h$$

Equation C—8

Note: The above equation for torsional inertia constant is the same as the equation given in Appendix B of BS 5950-1:1990 (lateral torsional buckling) with an allowance for the radii of the corners.

Torsional modulus constant

$$C_t = \frac{I_t}{t + K/t}$$

Equation C—9

Where

$$A_{\zeta} = \left(1 - \pi/4\right) r_o^2$$

Equation C—10

$$A_{\xi} = \left(1 - \pi/4\right) r_i^2$$

Equation C—11

$$h_{\zeta} = \frac{h}{2} - \left(\frac{10 - 3\pi}{12 - 3\pi}\right) r_o$$

Equation C—12

$$h_{\xi} = \frac{h - 2t}{2} - \left(\frac{10 - 3\pi}{12 - 3\pi}\right) r_i$$

Equation C—12

$$I_{\zeta\zeta} = \left(\frac{1}{3} - \frac{\pi}{16} - \frac{1}{3\left(12 - 3\pi\right)}\right) r_o^4$$

Equation C—13

$$I_{\xi\xi} = \left(\frac{1}{3} - \frac{\pi}{16} - \frac{1}{3\left(12 - 3\pi\right)}\right) r_i^4$$

Equation C—14

Mean perimeter

$$h_c = 2\left(\left(b - t\right) + \left(h - t\right)\right) - 2R_c\left(4 - \pi\right)$$

Equation C—15

Area enclosed by mean perimeter

$$A_h = (b-t)(h-t) - R_c^2(4-\pi)$$

Equation C—16

$$K = \frac{2A_h t}{h_c}$$

Equation C—17

$$R_c = \frac{r_o + r_i}{2}$$

Equation C—18

Roark (Young 1989) gives an alternative formula for calculation of the torsional inertia constant for an RHS with sharp re-entrant corners (Equation C—19). The formula is strictly only accurate for infinitely thin sections and, for typical RHS, is between 5% and 1% lower than the BS EN 10210 value (Figure 2-21).

$$I_{t,no\,radii,Roark} = \frac{2t(b-t)^2(h-t)^2}{b+h-2t}$$

Equation C—19

Roark (Young 1989) also gives an alternative formula for calculation of the torsional modulus constant for an RHS with sharp re-entrant corners (Equation C—20). The formula is only accurate for infinitely thin sections and, for typical RHS, is between 5% and 25% higher than the BS EN 10210 value (Figure 2-22).

$$C_{t,no\,radii} = 2t(h-t)(b-t)$$

Equation C—20

D. Material properties

D.1 Introduction

The properties of the nine hot finished bars, used in the full-scale testing component of this research, are summarised in Tables D—1 to D—27. The properties were measured by uniaxial tensile testing in accordance with BS EN 10002–1:1990, with the exception of the four coupons indicated below. Material models for the bars were determined by averaging the results of at least four coupons from each (two from each end of the bar), using the scheme outlined in Section 2.2.

One coupon was tested at a very low rate of strain (0.5% strain per minute) in order to verify that the yield stress and subsequent plateau were unaffected by a slow strain rate. No differences were observed in the stress-strain behaviour of the coupon with the low strain rate, and the other coupons taken from the same bar (See coupon code 200b in Table D—16).

Three coupons with shortened parallel lengths were tested to confirm that the steel in the Rectangular Hollow Section (RHS) was isotropic. The parallel lengths of the three coupons were inclined at 0.0^{o}, 22.5^{o} and 45.0^{o} to the longitudinal axes of the RHS. No differences were observed in the stress-strain behaviour of the three coupons (See coupon codes Ang00, Ang22 and Ang 45 in Table D—19).

D.2 Material properties RHS 250x250x10 grade S275J2H bar number 1

Table D—1: Tensile test results for RHS 250x250x10 grade S275J2H bar #1

Coupon ID code	B1	B2	B3	B4	B5	B6	Mean [①]
Parallel length (mm)	125	125	125	125	125	125	-
Thickness (mm)	9.70	9.71	9.77	9.64	9.67	9.68	9.70 [0.5%]
Width (mm)	8.04	8.13	7.95	7.95	7.92	7.93	-
Proportionality factor	5.66	5.63	5.67	5.71	5.71	5.71	-
Upper yield (N/mm^2) R_{eH}	349	359	349	364	402	363	364 [5.4%]
Lower yield (N/mm^2) R_{eL}	342	352	348	359	366	327	349 [3.9%]
Suitability of fit (% energy error) K	0.15	0.14	0.20	0.15	0.21	0.23	0.18 [21%]
Yield stress (N/mm^2) f_{y1}	342.2	357.1	346.6	351.4	362.0	327.1	347.7 [3.6%]
Young's modulus (kN/mm^2) E	211.0	210.8	202.3	212.5	208.2	215.1	210.0 [2.1%]
Plateau ratio $\lambda_{plateau}$	9.5	9.1	16.3	26.0	13.8	13.8	14.8 [42%]
Post yield stiffness (kN/mm^2) $E_{plateau}$	0.61	-0.02	0.83	1.61	-0.51	0.59	0.52 [140%]
Elliptical strain Hardening factor λ_{ESHF}	0.21	0.17	0.27	0.42	0.14	0.21	0.24 [42%]
Tensile strength (N/mm^2) f_u	461.2	469.6	463.5	476.7	460.9	450.7	463.8 [1.9%]
Strain at maximum force (%) ε_u	14.8	14.5	15.7	16.2	16.2	16.4	15.6 [5.2%]
Strain at fracture (%)	22.1	22.4	25.3	25.7	26.2	26.8	24.8 [8.1%]

Note 1: Refer to Section 2.2
Note 2: ① denotes the standard deviation as a percentage of the mean value

Table D—2: Material model for RHS 250x250x10 grade S275J2H bar #1

Section size Grade	K (%)	f_{y1} (N/mm^2)	E (kN/mm^2)	$\lambda_{plateau}$	$E_{plateau}$ (kN/mm^2)	λ_{ESHF}	f_u (N/mm^2)	ε_u (%)
RHS 250x250x10 grade S275J2H	1.48	347.7	210.0	14.8	0.52	0.24	463.8	15.6

Note: Refer to Section 2.2

Table D—3: ABAQUS material model (RHS 250x250x10 grade S275J2H bar #1)

```
*ELASTIC
 210520.0 ,      0.3
*PLASTIC
   348.28 ,        0
   369.77 , 0.023990
   392.82 , 0.030203
   435.08 , 0.048735
   487.43 , 0.084932
   536.24 , 0.142637
   565.22 , 0.195143
```

Note: Refer to Sections 2.2.5 & 2.3.7

D.3 Material properties RHS 250x250x10 grade S275J2H bar number 2

Table D—4: Tensile test results for RHS 250x250x10 grade S275J2H bar #2

Coupon ID code	La	Lb	Loe1	Loe2	Low1	Low2	Mean [①]
Parallel length (mm)	125	125	125	125	125	125	-
Thickness (mm)	9.66	9.66	9.66	9.57	9.74	10.17	9.74 [2.2%]
Width (mm)	7.86	7.91	7.89	7.93	7.84	7.97	-
Proportionality factor	5.74	5.72	5.73	5.74	5.72	5.55	-
Upper yield (N/mm^2) R_{eH}	365	335	374	384	412	345	369 [7.6%]
Lower yield (N/mm^2) R_{eL}	331	320	351	358	357	334	342 [4.6%]
Suitability of fit (% energy error) K	0.26	0.23	0.21	0.28	0.22	0.26	0.25 [10%]
Yield stress (N/mm^2) f_{y1}	327.9	323.2	356.3	366.0	357.3	328.9	343.2 [5.4%]
Young's modulus (kN/mm^2) E	199.7	199.6	210.1	198.0	202.5	175.9	197.6 [5.8%]
Plateau ratio $\lambda_{plateau}$	15.3	12.5	9.2	11.4	16.0	13.0	12.9 [19%]
Post yield stiffness (kN/mm^2) $E_{plateau}$	0.36	0.19	0.47	-0.56	0.18	0.61	0.21 [197%]
Elliptical strain Hardening factor λ_{ESHF}	0.22	0.25	0.25	0.19	0.17	0.22	0.22 [15%]
Tensile strength (N/mm^2) f_u	464.3	451.6	481.7	479.7	473.0	458.0	468.0 [2.6%]
Strain at maximum force (%) ε_u	16.6	16.1	14.9	16.0	16.4	15.7	15.9 [3.8%]
Strain at fracture (%)	27.7	26.9	24.8	29.4	28.9	27.1	27.5 [5.9%]

Note 1: Refer to Section 2.2
Note 2: ① denotes the standard deviation as a percentage of the mean value

Table D—5: Material model for RHS 250x250x10 grade S275J2H bar #2

Section size Grade	K (%)	f_{y1} (N/mm^2)	E (kN/mm^2)	$\lambda_{plateau}$	$E_{plateau}$ (kN/mm^2)	λ_{ESHF}	f_u (N/mm^2)	ε_u (%)
RHS 250x250x10 grade S275J2H	3.16	343.2	197.6	12.9	0.21	0.22	468.0	15.9

Note: Refer to Section 2.2

Table D—6: ABAQUS material model (RHS 250x250x10 grade S275J2H bar #2)

```
*ELASTIC
  198159.6 ,       0.3
*PLASTIC
    343.84 ,         0
    356.30 ,  0.022041
    383.54 ,  0.028487
    431.47 ,  0.047738
    489.69 ,  0.085326
    542.65 ,  0.145171
    572.49 ,  0.198557
```

Note: Refer to Sections 2.2.5 & 2.3.7

D.4 Material properties RHS 250x250x10 grade S275J2H bar number 3

Table D—7: Tensile test results for RHS 250x250x10 grade S275J2H bar #3

Coupon ID code	Lne1	Lne2	Lnw1	Lnw2	Mean [①]
Parallel length (mm)	125	125	125	125	-
Thickness (mm)	10.16	10.09	10.46	10.17	10.22 [1.6%]
Width (mm)	7.99	8.11	8.00	7.97	-
Proportionality factor	5.55	5.53	5.47	5.55	-
Upper yield (N/mm^2) R_{eH}	383	368	375	388	378 [2.4%]
Lower yield (N/mm^2) R_{eL}	355	352	362	374	361 [2.8%]
Suitability of fit (% energy error) K	0.25	0.22	0.18	0.27	0.23 [17%]
Yield stress (N/mm^2) f_{y1}	360.9	350.2	361.1	384.2	364.1 [3.9%]
Young's modulus (kN/mm^2) E	210.1	200.0	206.2	199.5	204.0 [2.5%]
Plateau ratio $\lambda_{plateau}$	10.6	9.8	8.9	14.7	11.0 [24%]
Post yield stiffness (kN/mm^2) $E_{plateau}$	-0.44	0.67	0.82	0.17	0.31 [187%]
Elliptical strain Hardening factor λ_{ESHF}	0.28	0.30	0.29	0.20	0.27 [18%]
Tensile strength (N/mm^2) f_u	488.8	486.8	493.5	491.1	490.0 [0.6%]
Strain at maximum force (%) ε_u	15.0	14.6	14.5	15.9	15.0 [4.3%]
Strain at fracture (%)	24.0	24.4	26.1	27.7	25.6 [6.7%]

Note 1: Refer to Section 2.2
Note 2: ① denotes the standard deviation as a percentage of the mean value

Table D—8: Material model for RHS 250x250x10 grade S275J2H bar #3

Section size Grade	K (%)	f_{y1} (N/mm^2)	E (kN/mm^2)	$\lambda_{plateau}$	$E_{plateau}$ (kN/mm^2)	λ_{ESHF}	f_u (N/mm^2)	ε_u (%)
RHS 250x250x10 grade S275J2H	1.23	364.1	204.0	11.0	0.31	0.27	490.0	15.0

Note: Refer to Section 2.2

Table D—9: ABAQUS material model (RHS 250x250x10 grade S275J2H bar #3)

*ELASTIC		
204505.8	,	0.3
*PLASTIC		
364.75	,	0
378.05	,	0.019353
403.20	,	0.025509
450.97	,	0.043881
510.10	,	0.079796
563.60	,	0.137105
593.03	,	0.187853

Note: Refer to Sections 2.2.5 & 2.3.7

D.5 Material properties RHS 200x100x8 grade S275J2H bar number 1

Table D—10: Tensile test results for RHS 200x100x8 grade S275J2H bar #1

Coupon ID code	A1	A3	A4	Ca	Cb	S	Mean [①]
Parallel length (mm)	85	85	85	85	85	85	-
Thickness (mm)	7.70	7.70	7.81	7.89	7.84	7.69	7.77 [1.1%]
Width (mm)	9.87	9.98	10.07	10.05	9.98	9.90	-
Proportionality factor	5.74	5.70	5.64	5.61	5.65	5.73	-
Upper yield (N/mm^2) R_{eH}	377	363	352	377	448	346	377 [9.8%]
Lower yield (N/mm^2) R_{eL}	346	345	340	336	350	344	343 [1.4%]
Suitability of fit (% energy error) K	0.33	0.34	0.44	0.29	0.27	0.23	0.32 [23%]
Yield stress (N/mm^2) f_{y1}	341.1	336.6	371.7	374.7	358.7	349.7	355.4 [4.4%]
Young's modulus (kN/mm^2) E	185.7	205.9	193.6	205.2	204.6	202.0	199.5 [4.1%]
Plateau ratio $\lambda_{plateau}$	16.7	14.0	10.6	13.4	12.3	13.2	13.4 [15%]
Post yield stiffness (kN/mm^2) $E_{plateau}$	1.11	0.54	-1.66	-0.64	-0.53	0.78	-0.07 [high]
Elliptical strain Hardening factor λ_{ESHF}	0.25	0.22	0.11	0.07	0.10	0.28	0.17 [high]
Tensile strength (N/mm^2) f_u	471.0	471.0	473.5	482.4	477.1	489.6	477.4 [1.5%]
Strain at maximum force (%) ε_u	16.5	16.3	15.7	16.3	16.1	16.1	16.2 [1.6%]
Strain at fracture (%)	28.7	29.6	28.9	27.4	27.7	29.1	28.6 [3.0%]

Note 1: Refer to Section 2.2
Note 2: ① denotes the standard deviation as a percentage of the mean value

Table D—11: Material model for RHS 200x100x8 grade S275J2H bar #1

Section size Grade	K (%)	f_{y1} (N/mm^2)	E (kN/mm^2)	$\lambda_{plateau}$	$E_{plateau}$ (kN/mm^2)	λ_{ESHF}	f_u (N/mm^2)	ε_u (%)
RHS 200x100x8 grade S275J2H	1.21	355.4	199.5	13.4	-0.07	0.17	477.4	16.2

Note: Refer to Section 2.2

Table D—12: ABAQUS material model (RHS 200x100x8 grade S275J2H bar #1)

```
*ELASTIC
 200037.3 ,       0.3
*PLASTIC
    356.03 ,         0
    362.90 ,  0.023456
    393.12 ,  0.029921
    442.24 ,  0.049268
    500.97 ,  0.087044
    554.64 ,  0.147170
    585.53 ,  0.201217
```

Note: Refer to Sections 2.2.5 & 2.3.7

D.6 Material properties RHS 200x100x8 grade S275J2H bar number 2

Table D—13: Tensile test results for RHS 200x100x8 grade S275J2H bar #2

Coupon ID code	A2	Soe1	Soe2	Sow1	Sow2	Mean [①]
Parallel length (mm)	85	125	125	125	125	-
Thickness (mm)	7.85	7.66	7.73	7.73	7.66	7.73 [1.0%]
Width (mm)	10.01	9.89	9.95	9.87	9.93	-
Proportionality factor	5.64	5.74	5.70	5.72	5.73	-
Upper yield (N/mm^2) R_{eH}	405	362	342	339	335	356 [8.2%]
Lower yield (N/mm^2) R_{eL}	351	343	339	334	325	338 [2.9%]
Suitability of fit (% energy error) K	0.29	0.23	0.23	0.34	0.28	0.27 [16%]
Yield stress (N/mm^2) f_{y1}	345.3	325.4	343.1	337.8	323.7	335.1 [3.0%]
Young's modulus (kN/mm^2) E	181.8	180.6	183.5	162.8 (ignored)	171.6 (ignored)	182.0 [0.8%]
Plateau ratio $\lambda_{plateau}$	12.1	12.3	7.2	12.9	13.7	11.7 [22%]
Post yield stiffness (kN/mm^2) $E_{plateau}$	-0.08	0.26	0.65	0.53	1.16	0.50 [92%]
Elliptical strain Hardening factor λ_{ESHF}	0.09	0.20	0.26	0.20	0.28	0.21 [35%]
Tensile strength (N/mm^2) f_u	471.1	457.9	486.9	482.5	478.9	475.5 [2.4%]
Strain at maximum force (%) ε_u	16.1	16.1	15.0	16.7	16.2	16.0 [3.9%]
Strain at fracture (%)	28.3	28.3	26.2	26.7	26.9	27.3 [3.5%]

Note 1: Refer to Section 2.2
Note 2: Values of Young's modulus for coupons Sow1 and Sow2 ignored (extensometer fault)
Note 3: ① denotes the standard deviation as a percentage of the mean value

Table D—14: Material model for RHS 200x100x8 grade S275J2H bar #2

Section size Grade	K (%)	f_{y1} (N/mm^2)	E (kN/mm^2)	$\lambda_{plateau}$	$E_{plateau}$ (kN/mm^2)	λ_{ESHF}	f_u (N/mm^2)	ε_u (%)
RHS 200x100x8 grade S275J2H	2.53	335.1	182.0	11.7	0.50	0.21	475.5	16.0

Note: Refer to Section 2.2

Table D—15: ABAQUS material model (RHS 200x100x8 grade S275J2H bar #2)

*ELASTIC		
182458.1	,	0.3
*PLASTIC		
335.67	,	0
353.91	,	0.021088
383.61	,	0.027588
434.77	,	0.047034
496.30	,	0.085019
551.62	,	0.145492
582.07	,	0.199061

Note: Refer to Sections 2.2.5 & 2.3.7

D.7 Material properties RHS 200x100x8 grade S275J2H bar number 3

Table D—16: Tensile test results for RHS 200x100x8 grade S275J2H bar #3

Coupon ID code	Sne1	Sne2	Snw1	Snw2	200a	200b	Mean [①]
Parallel length (mm)	125	125	125	125	125	125	-
Thickness (mm)	7.73	7.79	7.79	7.83	7.88	7.88	7.82 [0.8%]
Width (mm)	9.91	9.91	9.85	9.90	12.48	12.46	-
Proportionality factor	5.71	5.69	5.71	5.68	5.04	5.05	-
Upper yield (N/mm^2) R_{eH}	347	344	344	355	348	350	348 [1.2%]
Lower yield (N/mm^2) R_{eL}	344	337	341	341	321	313	333 [3.8%]
Suitability of fit (% energy error) K	0.21	0.20	0.27	0.29	0.35	0.33	0.28 [23%]
Yield stress (N/mm^2) f_{y1}	344.2	338.8	344.1	350.5	327.6	319.9	337.5 [3.4%]
Young's modulus (kN/mm^2) E	198.2	192.3	187.9	202.5	181.9	186.5	191.6 [4.0%]
Plateau ratio $\lambda_{plateau}$	14.8	14.1	11.7	14.1	13.7	12.8	13.5 [8.1%]
Post yield stiffness (kN/mm^2) $E_{plateau}$	1.01	1.63	0.34	-0.21	-0.12	-0.20	0.42 [182%]
Elliptical strain Hardening factor λ_{ESHF}	0.27	0.27	0.24	0.20	0.16	0.11	0.21 [31%]
Tensile strength (N/mm^2) f_u	476.6	474.9	480.4	472.9	460.5	456.0	470.2 [2.1%]
Strain at maximum force (%) ε_u	16.2	15.9	16.1	16.6	17.1	17.8	16.6 [4.4%]
Strain at fracture (%)	26.6	27.4	26.9	29.0	29.4	30.9	28.4 [5.9%]

Note 1: Refer to Section 2.2
Note 2: Coupon 200b tested at low strain rate (0.5% strain per minute)
Note 3: ① denotes the standard deviation as a percentage of the mean value

Table D—17: Material model for RHS 200x100x8 grade S275J2H bar #3

Section size Grade	K (%)	f_{y1} (N/mm^2)	E (kN/mm^2)	$\lambda_{plateau}$	$E_{plateau}$ (kN/mm^2)	λ_{ESHF}	f_u (N/mm^2)	ε_u (%)
RHS 200x100x8 grade S275J2H	0.96	344.4	195.2	13.7	0.71	0.25	476.2	16.2

Note: Refer to Section 2.2

Table D—18: ABAQUS material model (RHS 200x100x8 grade S275J2H bar #3)

```
*ELASTIC
 195757 ,      0.3
*PLASTIC
 344.97 ,        0
 370.77 ,  0.023636
 395.89 ,  0.030102
 442.39 ,  0.049390
 499.98 ,  0.087039
 553.14 ,  0.146972
 583.92 ,  0.200968
```

Note: Refer to Sections 2.2.5 & 2.3.7

D.8 Material properties RHS 150x150x6.3 grade S275J2H bar number 1

Table D—19: Tensile test results for RHS 150x150x6.3 grade S275J2H bar #1

Coupon ID code	150a	150b	150c	150d	150e	150f	Ang00	Ang22	Ang45	Mean [①]
Parallel length (mm)	125	125	125	125	125	125	65	65	65	-
Thickness (mm)	6.08	6.11	6.10	6.07	6.09	6.10	5.96	5.95	5.94	6.04 [1.2%]
Width (mm)	12.44	12.38	12.41	12.42	12.41	12.44	12.49	12.49	12.47	-
Proportionality factor	5.75	5.75	5.75	5.76	5.75	5.74	5.80	5.80	5.81	-
Upper yield (N/mm^2) R_{eH}	368	372	381	328	315	353	339	332	330	347 [6.6%]
Lower yield (N/mm^2) R_{eL}	329	336	328	308	312	316	323	321	324	322 [2.8%]
Suitability of fit (% energy error) K	0.29	0.37	0.37	0.33	0.28	0.43	0.25	0.26	0.24	0.31 [21%]
Yield stress (N/mm^2) f_{y1}	339.6	345.8	344.0	315.9	312.6	335.0	325.3	321.8	323.8	329.3 [3.7%]
Young's modulus (kN/mm^2) E	196.3	196.2	188.3	191.0	208.0	208.1	208.5	189.6	186.8	191.9 [4.1%]
Plateau ratio $\lambda_{plateau}$	15.8	19.6	18.1	16.4	15.1	15.1	11.7	13.8	12.6	15.3 [16%]
Post yield stiffness (kN/mm^2) $E_{plateau}$	-0.26	-0.19	-0.35	0.28	0.38	-0.82	-0.08	0.24	0.03	-0.09 [high]
Elliptical strain hardening factor λ_{ESHF}	0.11	0.15	0.11	0.11	0.14	0.20	0.14	0.18	0.17	0.15 [22%]
Tensile strength (N/mm^2) f_u	456.3	462.3	459.2	451.6	454.9	457.8	469.8	468.5	470.7	461.2 [1.5%]
Strain at maximum force (%) ε_u	17.5	18.5	18.7	18.1	17.5	17.1	19.1	19.0	19.2	18.3 [4.3%]
Strain at fracture (%)	29.2	29.5	29.1	29.0	28.4	28.0	32.9	33.4	32.7	30.3 [7.0%]

Note 1: Refer to Section 2.2
Note 2: Coupon Ang00 inclined at 0.0^o to longitudinal axis of tube
Note 3: Coupon Ang22 inclined at 22.5^o to longitudinal axis of tube
Note 4: Coupon Ang45 inclined at 45.0^o to longitudinal axis of tube
Note 5: ① denotes the standard deviation as a percentage of the mean value

Table D—20: Material model for RHS 150x150x6.3 grade S275J2H bar #1

Section size Grade	K (%)	f_{y1} (N/mm^2)	E (kN/mm^2)	$\lambda_{plateau}$	$E_{plateau}$ (kN/mm^2)	λ_{ESHF}	f_u (N/mm^2)	ε_u (%)
RHS 150x150x6.3 grade S275J2H	1.02	329.3	195.2	16.7	-0.16	0.14	457.0	17.9

Note: Refer to Section 2.2

Table D—21: ABAQUS material model (RHS 150x150x6.3 grade S275J2H bar #1)

```
*ELASTIC
 195678.2 ,        0.3
*PLASTIC
   329.86 ,          0
   336.62 ,  0.027677
   369.97 ,  0.034711
   421.48 ,  0.055755
   482.65 ,  0.096743
   538.72 ,  0.161711
   571.40 ,  0.220436
```

Note: Refer to Sections 2.2.5 & 2.3.7

D.9 Material properties RHS 200x100x8 grade S355J2H bar number 1

Table D—22: Tensile test results for RHS 200x100x8 grade S355J2H bar #1

Coupon ID code	Tt5	Tt6	Tt7	Tt8	Mean [①]
Parallel length (mm)	125	125	125	125	-
Thickness (mm)	8.00	7.73	7.95	8.03	7.93 [1.7%]
Width (mm)	10.06	10.10	10.05	10.11	-
Proportionality factor	5.57	5.66	5.59	5.55	-
Upper yield (N/mm^2) R_{eH}	384	380	395	377	384 [2.1%]
Lower yield (N/mm^2) R_{eL}	371	372	371	369	371 [0.3%]
Suitability of fit (% energy error) K	0.32	0.44	0.23	0.50	0.37 [33%]
Yield stress (N/mm^2) f_{y1}	381.3	380.9	382.7	382.7	381.9 [0.3%]
Young's modulus (kN/mm^2) E	219.6	211.6	200.6	200.7	208.1 [4.5%]
Plateau ratio $\lambda_{plateau}$	7.5	8.9	6.4	5.7	7.1 [19%]
Post yield stiffness (kN/mm^2) $E_{plateau}$	0.23	0.20	-0.37	-0.41	-0.09 [high]
Elliptical strain hardening factor λ_{ESHF}	0.27	0.27	0.23	0.23	0.25 [8.8%]
Tensile strength (N/mm^2) f_u	526.4	519.4	526.8	522.2	523.7 [0.7%]
Strain at maximum force (%) ε_u	13.5	13.5	13.7	13.3	13.5 [1.3%]
Strain at fracture (%)	21.2	20.5	22.8	21.7	21.6 [4.5%]

Note 1: Refer to Section 2.2
Note 2: ① denotes the standard deviation as a percentage of the mean value

Table D—23: Material model for RHS 200x100x8 grade S355J2H bar #1

Section size Grade	K (%)	f_{y1} (N/mm^2)	E (kN/mm^2)	$\lambda_{plateau}$	$E_{plateau}$ (kN/mm^2)	λ_{ESHF}	f_u (N/mm^2)	ε_u (%)
RHS 200x100x8 grade S355J2H	0.71	380.9	203.1	7.0	-0.09	0.24	523.7	12.9

Note: Refer to Section 2.2

Table D—24: ABAQUS material model (RHS 200x100x8 grade S355J2H bar #1)

```
*ELASTIC
 203631.8 ,      0.3
*PLASTIC
   381.65 ,        0
   385.43      0.013002
   415.80 ,    0.018471
          ,    0.034870
   535.91      0.067075
   591.45 ,    0.118765
   636.53 ,    0.192000
```

Note: Refer to Sections 2.2.5 & 2.3.7

D.10 Material properties RHS 150x150x6.3 grade S355J2H bar number 1

Table D—25: Tensile test results for RHS 150x150x6.3 grade S355J2H bar #1

Coupon ID code	Tt1	Tt2	Tt3	Tt4	Mean [①]
Parallel length (mm)	125	125	125	125	-
Thickness (mm)	5.78	6.05	5.69	5.65	5.79 [3.1%]
Width (mm)	13.02	12.77	12.66	12.64	-
Proportionality factor	5.76	5.69	5.89	5.92	-
Upper yield (N/mm^2) R_{eH}	411	404	414	413	411 [1.1%]
Lower yield (N/mm^2) R_{eL}	403	396	404	401	401 [0.9%]
Suitability of fit (% energy error) K	0.31	0.42	0.37	0.49	0.40 [18%]
Yield stress (N/mm^2) f_{y1}	406.0	405.7	405.8	401.2	404.7 [0.6%]
Young's modulus (kN/mm^2) E	172.5	230.8	199.9	205.2	202.1 [12%]
Plateau ratio $\lambda_{plateau}$	6.9	9.2	6.8	5.8	7.2 [20%]
Post yield stiffness (kN/mm^2) $E_{plateau}$	0.01	-0.29	0.01	1.05	0.20 [301%]
Elliptical strain Hardening factor λ_{ESHF}	0.34	0.33	0.35	0.34	0.34 [2.6%]
Tensile strength (N/mm^2) f_u	547.3	541.4	543.4	546.7	544.7 [0.5%]
Strain at maximum force (%) ε_u	13.5	13.4	13.0	12.6	13.1 [3.0%]
Strain at fracture (%)	21.8	22.9	20.4	18.9	21.0 [8.3%]

Note 1: Refer to Section 2.2
Note 2: ① denotes the standard deviation as a percentage of the mean value

Table D—26: Material model for RHS 150x150x6.3 grade S355J2H bar #1

Section size Grade	K (%)	f_{y1} (N/mm^2)	E (kN/mm^2)	$\lambda_{plateau}$	$E_{plateau}$ (kN/mm^2)	λ_{ESHF}	f_u (N/mm^2)	ε_u (%)
RHS 150x150x6.3 grade S355J2H	0.98	404.7	199.9	7.1	0.13	0.34	544.7	13.1

Note: Refer to Section 2.2

Table D—27: ABAQUS material model (RHS 150x150x6.3 grade S355J2H bar #1)

```
*ELASTIC
 200524.8 ,      0.3
*PLASTIC
   405.50 ,        0
   413.24 ,  0.014222
   438.97 ,  0.019725
   491.95 ,  0.036169
   558.53 ,  0.068438
   616.18 ,  0.120229
   659.19 ,  0.187487
```

Note: Refer to Sections 2.2.5 & 2.3.7

D.11 Statistical analysis of material properties

In order to determine a suitable material model for use in the parametric Finite Element study (Chapter 7), a statistical analysis of the tensile test results was performed. Figures D—1 to D—6 show typical values of the quantities defined in Section 2.2. Figures D—1 to D—5 are for grade S275J2H steel, while Figure D—6 also includes data for grade S355J2H steel. The material model used in the parametric Finite Element study is shown in Table 7-3.

Additional data were added following tests on hot finished RHS provided kindly by Moayad Omair (The School of the Built Environment, Coventry University, UK), and analysis of tensile test data provided kindly by Tim Wilkinson (The Department of Civil Engineering, University of Sydney, Australia).

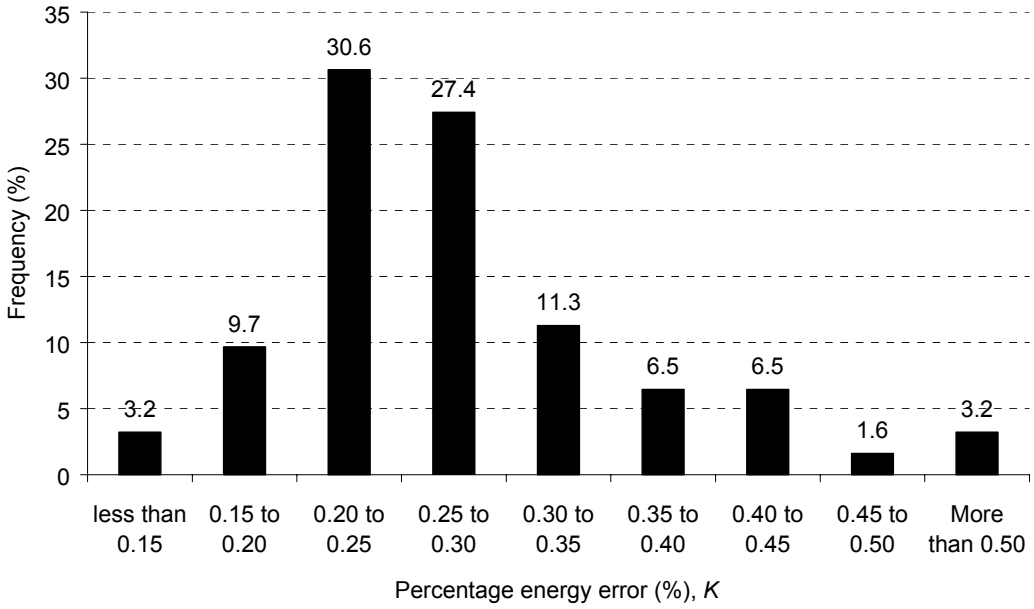

Figure D—1: Typical values of percentage energy error

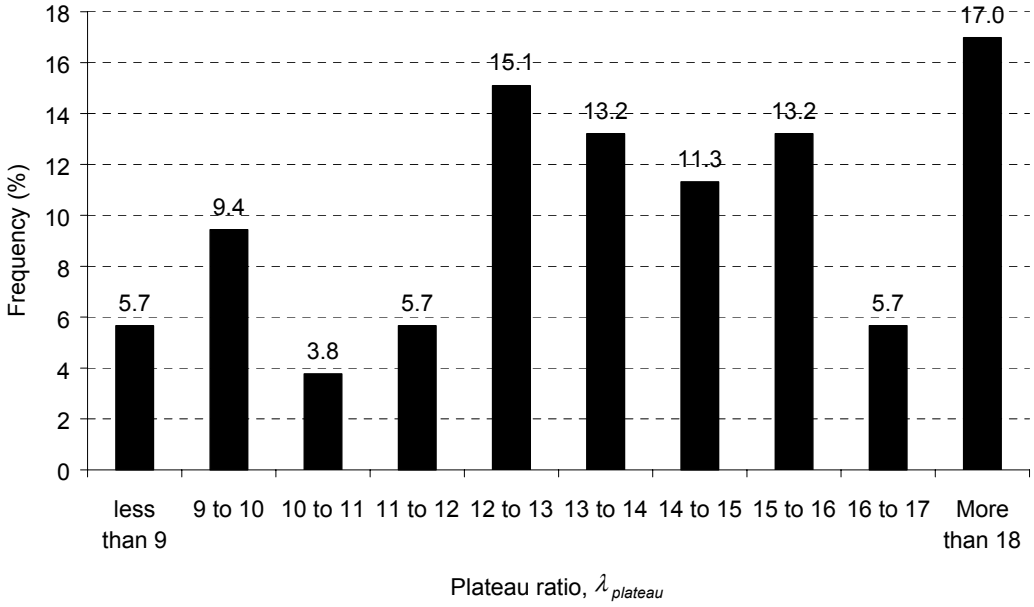

Figure D—2: Typical values of plateau ratio

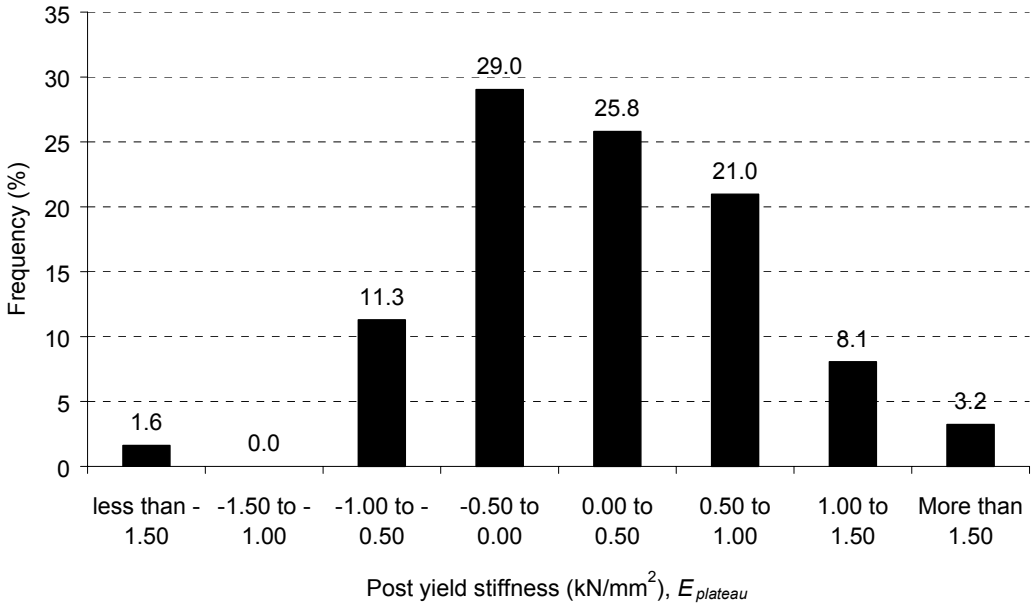

Figure D—3: Typical values of post yield stiffness

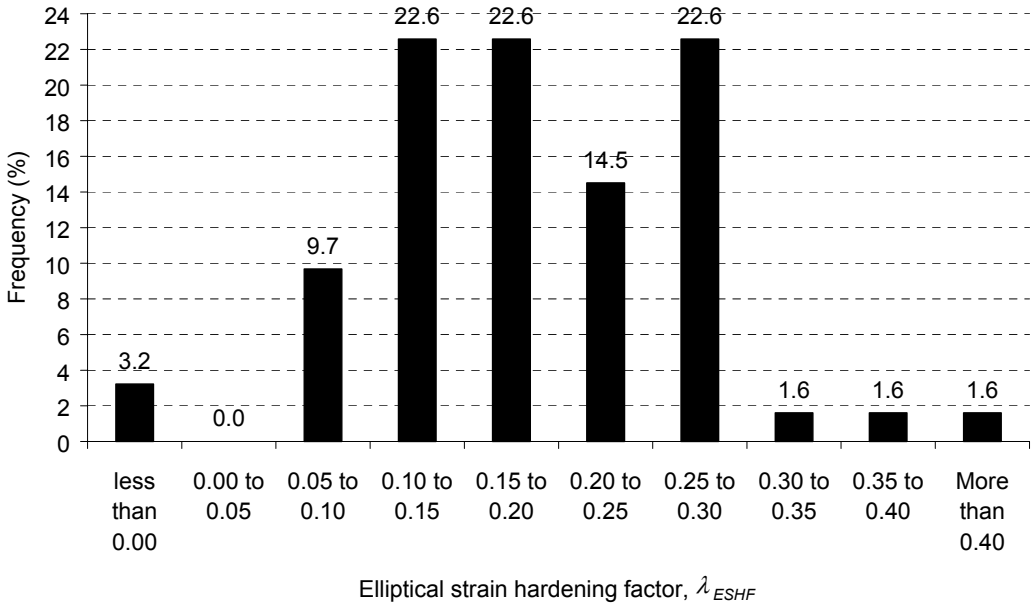

Figure D—4: Typical values of elliptical strain hardening factor

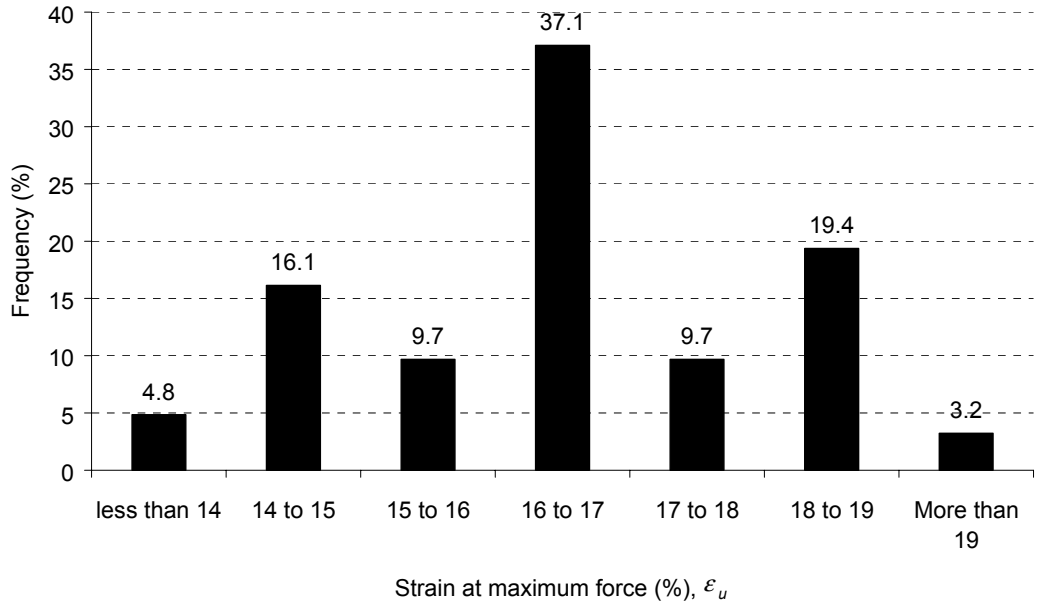

Figure D—5: Typical values of strain at maximum force

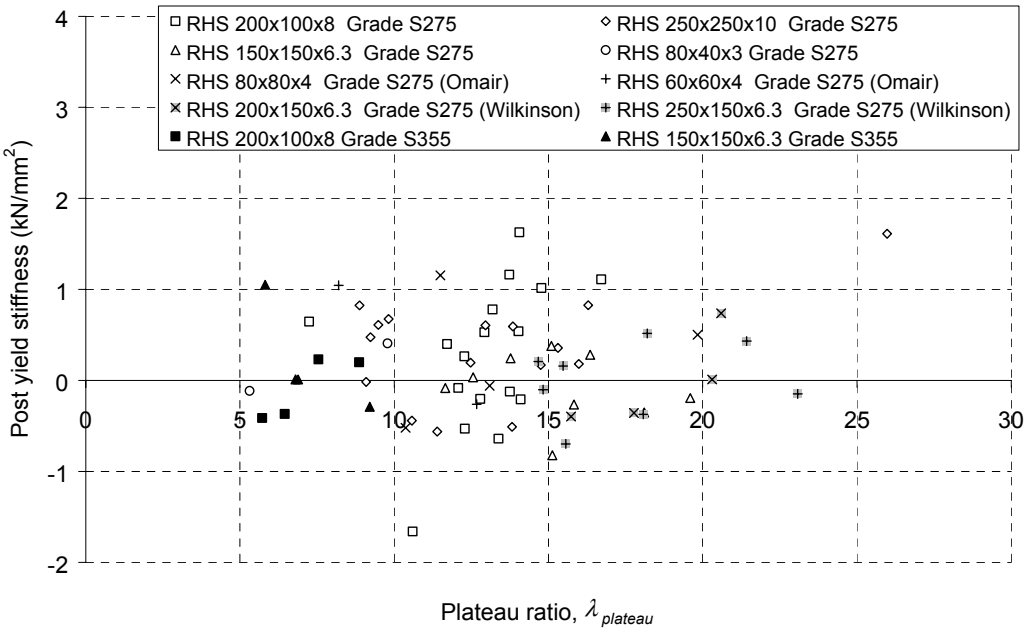

Figure D—6: Plateau ratio and post yield stiffness

E. Stress concentration factors (Finite Element)

Table E—1: FE stress concentration factors for bending (part 1 of 2)

Section	Number of holes	Hole size ratio, Φ	Stress concentration factor, $\psi_{bending}$		
			FE	Fit	Difference (Fit – FE)
150x150x12.5	1	0.70	1.09	1.09	0.00
150x150x12.5	1	0.85	1.46	1.52	0.06
150x150x12.5	2	0.78	1.29	1.32	0.03
250x250x10	1	0.10	1.00	1.00	0.00
250x250x10	1	0.30	1.00	1.00	0.00
250x250x10	1	0.50	1.00	1.00	0.00
250x250x10	1	0.55	1.00	1.00	0.00
250x250x10	1	0.70	1.39	1.41	0.02
250x250x10	1	0.90	2.23	2.23	0.00
250x250x10	2	0.10	1.00	1.00	0.00
250x250x10	2	0.20	1.00	1.00	0.00
250x250x10	2	0.30	1.00	1.00	0.00
250x250x10	2	0.40	1.00	1.00	0.00
250x250x10	2	0.50	1.01	1.00	-0.01
250x250x10	2	0.60	1.10	1.00	-0.10
250x250x10	2	0.70	1.38	1.41	0.02
250x250x10	2	0.80	1.75	1.82	0.07
250x250x10	2	0.90	2.20	2.23	0.03
350x350x12	1	0.78	1.73	1.80	0.07
350x350x12	2	0.63	1.21	1.15	-0.07
350x350x12	2	0.69	1.39	1.41	0.02
350x350x12	2	0.85	2.05	2.11	0.06
350x350x12	2	0.90	2.30	2.33	0.03
120x80x8	1	0.55	1.00	1.00	0.00
120x80x8	1	0.85	1.67	1.67	0.00
120x80x8	2	0.70	1.21	1.19	-0.03
120x80x8	2	0.90	1.83	1.83	0.00
300x200x12	1	0.10	1.00	1.00	0.00
300x200x12	1	0.30	1.00	1.00	0.00
300x200x12	1	0.50	1.00	1.00	0.00
300x200x12	1	0.55	1.00	1.00	0.00
300x200x12	1	0.70	1.39	1.41	0.01
300x200x12	1	0.90	2.28	2.23	-0.05

Table E—2: FE stress concentration factors for bending (part 2 of 2)

Section	Number of holes	Hole size ratio, Φ	Stress concentration factor, $\psi_{bending}$		
			FE	Fit	Difference (Fit – FE)
300x200x12	2	0.10	1.00	1.00	0.00
300x200x12	2	0.30	1.00	1.00	0.00
300x200x12	2	0.50	1.01	1.00	-0.01
300x200x12	2	0.55	1.01	1.00	-0.01
300x200x12	2	0.58	1.05	1.00	-0.05
300x200x12	2	0.70	1.40	1.41	0.01
300x200x12	2	0.90	2.27	2.23	-0.04
200x120x6	1	0.80	1.91	1.93	0.02
200x120x6	2	0.60	1.16	1.02	-0.14
200x120x6	2	0.70	1.47	1.47	0.00
200x120x6	2	0.85	2.17	2.15	-0.02
140x80x4	1	0.70	1.48	1.47	-0.01
140x80x4	2	0.90	2.51	2.39	-0.12
200x100x10	1	0.78	1.61	1.61	0.00
200x100x10	2	0.63	1.13	1.06	-0.08
200x100x10	2	0.69	1.31	1.28	-0.03
200x100x10	2	0.85	1.93	1.87	-0.06
200x100x10	2	0.90	2.16	2.06	-0.10
200x100x8	1	0.10	1.00	1.00	0.00
200x100x8	1	0.30	1.00	1.00	0.00
200x100x8	1	0.50	1.01	1.00	-0.01
200x100x8	1	0.70	1.41	1.41	-0.01
200x100x8	1	0.90	2.33	2.23	-0.10
200x100x8	2	0.10	1.00	1.00	0.00
200x100x8	2	0.20	1.00	1.00	0.00
200x100x8	2	0.30	1.00	1.00	0.00
200x100x8	2	0.40	1.00	1.00	0.00
200x100x8	2	0.50	1.01	1.00	-0.01
200x100x8	2	0.55	1.01	1.00	-0.01
200x100x8	2	0.60	1.11	1.00	-0.11
200x100x8	2	0.70	1.41	1.41	0.00
200x100x8	2	0.80	1.81	1.82	0.01
200x100x8	2	0.90	2.34	2.23	-0.11

Table E—3: FE stress concentration factors for shear (part 1 of 2)

Section	Number of holes	Hole size ratio, Φ	Stress concentration factor, ψ_{shear}		
			FE	Fit	Difference (Fit – FE)
250x250x16	2	0.50	3.62	3.70	0.09
250x250x16	2	0.80	7.56	7.20	-0.36
250x250x12.5	2	0.50	3.74	3.82	0.08
250x250x12.5	2	0.80	8.35	7.68	-0.67
250x250x10	1	0.10	2.36	2.24	-0.12
250x250x10	1	0.20	2.59	2.54	-0.05
250x250x10	1	0.30	2.84	2.90	0.06
250x250x10	1	0.40	3.22	3.36	0.14
250x250x10	1	0.50	3.76	3.96	0.19
250x250x10	1	0.60	4.51	4.77	0.26
250x250x10	1	0.70	5.67	5.99	0.32
250x250x10	1	0.80	7.66	8.22	0.55
250x250x10	1	0.90	10.97	14.37	3.39
250x250x10	2	0.10	2.36	2.24	-0.12
250x250x10	2	0.20	2.59	2.54	-0.05
250x250x10	2	0.30	2.86	2.90	0.05
250x250x10	2	0.40	3.25	3.36	0.11
250x250x10	2	0.50	3.83	3.96	0.12
250x250x10	2	0.60	4.68	4.77	0.09
250x250x10	2	0.70	6.13	5.99	-0.14
250x250x10	2	0.80	8.98	8.22	-0.76
250x250x10	2	0.90	14.37	14.37	-0.01
250x250x8	2	0.20	2.64	2.58	-0.06
250x250x8	2	0.50	3.91	4.13	0.22
250x250x8	2	0.60	4.78	5.02	0.24
250x250x8	2	0.70	6.34	6.39	0.04
250x250x8	2	0.80	9.50	8.89	-0.60
250x250x8	2	0.90	14.58	15.89	1.31
250x250x6	2	0.50	3.98	4.41	0.43
250x250x6	2	0.80	10.05	10.02	-0.03
300x200x12	1	0.10	2.42	2.24	-0.18
300x200x12	1	0.20	2.66	2.54	-0.12
300x200x12	1	0.30	2.91	2.90	-0.01
300x200x12	1	0.40	3.27	3.36	0.09
300x200x12	1	0.50	3.79	3.96	0.16
300x200x12	1	0.60	4.49	4.77	0.28
300x200x12	1	0.70	5.49	5.99	0.51
300x200x12	1	0.80	7.10	8.22	1.12
300x200x12	1	0.90	9.44	14.37	4.93

Table E—4: FE stress concentration factors for shear (part 2 of 2)

Section	Number of holes	Hole size ratio, Φ	Stress concentration factor, ψ_{shear}		
			FE	Fit	Difference (Fit – FE)
300x200x12	2	0.10	2.42	2.24	-0.18
300x200x12	2	0.20	2.66	2.54	-0.12
300x200x12	2	0.30	2.93	2.90	-0.02
300x200x12	2	0.40	3.31	3.36	0.05
300x200x12	2	0.50	3.89	3.96	0.07
300x200x12	2	0.60	4.72	4.77	0.05
300x200x12	2	0.70	6.11	5.99	-0.11
300x200x12	2	0.80	8.88	8.22	-0.66
300x200x12	2	0.90	14.15	14.37	0.22
200x100x16	2	0.10	2.16	2.20	0.05
200x100x16	2	0.20	2.45	2.45	0.00
200x100x16	2	0.40	3.25	3.14	-0.11
200x100x16	2	0.50	3.54	3.62	0.08
200x100x16	2	0.70	5.15	5.20	0.06
200x100x16	2	0.80	6.71	6.86	0.16
200x100x16	2	0.90	9.31	11.32	2.01
200x100x12.5	2	0.50	3.72	3.71	0.00
200x100x12.5	2	0.70	5.56	5.43	-0.14
200x100x8	1	0.10	2.48	2.24	-0.24
200x100x8	1	0.20	2.73	2.54	-0.19
200x100x8	1	0.30	2.99	2.90	-0.09
200x100x8	1	0.40	3.36	3.36	0.00
200x100x8	1	0.50	3.90	3.96	0.06
200x100x8	1	0.60	4.62	4.77	0.15
200x100x8	1	0.70	5.72	5.99	0.28
200x100x8	1	0.80	7.35	8.22	0.87
200x100x8	1	0.90	9.88	14.37	4.49
200x100x8	2	0.10	2.48	2.24	-0.24
200x100x8	2	0.20	2.73	2.54	-0.19
200x100x8	2	0.30	2.99	2.90	-0.09
200x100x8	2	0.40	3.37	3.36	-0.01
200x100x8	2	0.50	3.95	3.96	0.01
200x100x8	2	0.60	4.77	4.77	0.00
200x100x8	2	0.70	6.12	5.99	-0.12
200x100x8	2	0.80	8.83	8.22	-0.62
200x100x8	2	0.90	15.06	14.37	-0.69
200x100x6	2	0.50	4.05	4.18	0.13
200x100x6	2	0.70	6.40	6.52	0.12
200x100x4	2	0.10	2.71	2.32	-0.39
200x100x4	2	0.20	2.89	2.71	-0.18
200x100x4	2	0.40	3.53	3.81	0.28
200x100x4	2	0.50	4.16	4.63	0.48
200x100x4	2	0.70	6.70	7.57	0.87
200x100x4	2	0.80	10.24	10.92	0.68
200x100x4	2	0.90	20.46	20.45	-0.01

Table E—5: FE stress concentration factors for torsion (part 1 of 2)

Section	Number of holes	Hole size ratio, Φ	Stress concentration factor, $\psi_{torsion}$		
			FE	Fit	Difference (Fit – FE)
250x250x10	1	0.10	1.85	1.97	0.11
250x250x10	1	0.30	2.39	2.27	-0.11
250x250x10	1	0.50	3.19	3.17	-0.02
250x250x10	1	0.70	5.22	5.08	-0.14
250x250x10	1	0.90	12.17	11.74	-0.44
250x250x10	2	0.10	1.85	1.97	0.11
250x250x10	2	0.30	2.39	2.27	-0.12
250x250x10	2	0.50	3.24	3.17	-0.07
250x250x10	2	0.70	5.35	5.08	-0.27
250x250x10	2	0.90	12.76	11.74	-1.03
38x38x1.43	1	0.03	1.72	1.98	0.26
38x38x1.43	1	0.06	1.93	1.97	0.04
38x38x1.43	1	0.15	2.22	2.00	-0.21
38x38x1.43	1	0.30	2.55	2.29	-0.26
38x38x1.43	1	0.44	3.14	2.90	-0.24
38x38x1.43	1	0.59	4.15	3.97	-0.19
38x38x1.43	1	0.74	6.28	5.91	-0.37
38x38x1.43	1	0.89	12.29	11.40	-0.89
38x38x1.43	2	0.03	1.72	1.98	0.26
38x38x1.43	2	0.06	1.93	1.97	0.04
38x38x1.43	2	0.15	2.22	2.00	-0.21
38x38x1.43	2	0.30	2.55	2.29	-0.26
38x38x1.43	2	0.44	3.15	2.90	-0.25
38x38x1.43	2	0.59	4.19	3.97	-0.23
38x38x1.43	2	0.74	6.30	5.91	-0.39
38x38x1.43	2	0.89	12.29	11.40	-0.89
250x250x6	2	0.10	2.19	2.04	-0.15
250x250x6	2	0.20	2.36	2.21	-0.15
250x250x6	2	0.30	3.04	2.54	-0.50
250x250x6	2	0.40	2.94	3.06	0.12
250x250x6	2	0.60	4.46	4.89	0.43
250x250x6	2	0.70	6.10	6.56	0.46
250x250x6	2	0.80	9.37	9.53	0.17
250x250x6	2	0.90	17.43	17.44	0.01
300x200x12	1	0.10	1.83	1.97	0.14
300x200x12	1	0.30	2.41	2.27	-0.14
300x200x12	1	0.50	3.08	3.17	0.10
300x200x12	1	0.70	5.03	5.08	0.05
300x200x12	1	0.90	11.25	11.74	0.49
300x200x12	2	0.10	1.83	1.97	0.14
300x200x12	2	0.30	2.35	2.27	-0.08
300x200x12	2	0.50	3.15	3.17	0.02
300x200x12	2	0.70	5.21	5.08	-0.13
300x200x12	2	0.90	11.74	11.74	-0.01

Table E—6: FE stress concentration factors for torsion (part 2 of 2)

Section	Number of holes	Hole size ratio, Φ	Stress concentration factor, $\psi_{torsion}$		
			FE	Fit	Difference (Fit – FE)
250x150x8	2	0.20	2.26	2.11	-0.15
250x150x8	2	0.40	2.79	2.79	0.00
250x150x8	2	0.60	4.21	4.30	0.09
250x150x8	2	0.80	8.40	7.95	-0.46
250x150x8	2	0.90	13.93	13.87	-0.06
200x100x12.5	1	0.60	3.31	3.43	0.12
200x100x12.5	1	0.80	5.76	5.63	-0.13
200x100x12.5	2	0.10	1.84	1.93	0.09
200x100x12.5	2	0.20	2.02	1.97	-0.05
200x100x12.5	2	0.30	2.18	2.13	-0.05
200x100x12.5	2	0.40	2.38	2.41	0.03
200x100x12.5	2	0.50	2.71	2.83	0.12
200x100x12.5	2	0.70	4.20	4.28	0.08
200x100x12.5	2	0.85	6.41	6.74	0.33
200x100x12.5	2	0.90	7.41	8.66	1.25
200x100x8	1	0.10	1.82	1.97	0.14
200x100x8	1	0.30	2.34	2.27	-0.06
200x100x8	1	0.50	3.06	3.17	0.11
200x100x8	1	0.70	5.04	5.08	0.04
200x100x8	1	0.90	11.50	11.74	0.23
200x100x8	2	0.10	1.82	1.97	0.14
200x100x8	2	0.30	2.33	2.27	-0.06
200x100x8	2	0.50	3.12	3.17	0.05
200x100x8	2	0.70	5.13	5.08	-0.05
200x100x8	2	0.90	10.88	11.74	0.85
200x100x6	1	0.60	4.15	4.42	0.27
200x100x6	1	0.80	8.36	8.26	-0.09
200x100x6	2	0.50	3.38	3.49	0.11
200x100x6	2	0.90	13.94	14.59	0.64

F. Calibration of testing equipment

F.1 Introduction

The load indicating devices of the testing machines used in the course of this research project are calibrated annually in accordance with National Standards. The classifications at the time of testing are listed in the following Sections.

The Instron machine was used in the three and four-point loading tests (compression), and the Zwick machine was used for tensile testing of coupons. The Denison machine was used to calibrate the load cells used in the full-scale torsion tests. The accuracy of the Avery torsion testing machine used for the small-scale tests is discussed in Appendix A.

F.2 The Instron testing machine

2000 kN Instron servo hydraulic testing machine with autoranging facility
Machine type 8500 Serial Number H0468
Verified in compression as a grade 0.5 testing machine from 2000 kN to 50 kN
In accordance with BS 1610-1:1992 and NAMAS Technical Policy Statement 10
Edition 2 (May 1996) using equipment calibrated to BS 1610-2:1985.

F.3 The Zwick testing machine

200 kN Zwick testing machine with autoranging facility
Machine type 1484 Serial Number 116431
Verified in tension as a grade 0.5 testing machine from 200 kN to 2 kN
In accordance with BS EN 10002-2:1992 and NAMAS Technical Policy Statement 10 Edition 2 (May 1996) using equipment calibrated to BS 1610-2:1985.

F.4 The Denison testing machine

3000 kN Denison compression testing machine with analogue scale
Machine type T60CT Serial Number 29411
Verified in tension as a grade 1.0 testing machine from 6 kN to 3000 kN
In accordance with BS 1610-1:1992 and NAMAS Technical Policy Statement 10 Edition 2 (May 1996) using equipment calibrated to BS 1610-2:1985 and BS EN 10002-3:1995

References

Abramyan, B.L., "*Torsion and bending of prismatic rods of hollow rectangular section*", National Advisory Committee for Aeronautics, Technical Memorandum 1319, November **1951**.

ASM, "*Materials handbook*", 9th Edition, Volume 8 "*Mechanical testing*", American Society for Metals, **1985**.

Brendt, R., "*Kritische bemerkungen zur drehungselastizität*", Zeitschrift des Vereines Deutscher Ingenieure, Vol. 40, pp 785-790 and pp 785-817, **1896**.

Byrne, J.G., and Carré, B.A., "*Torsional stress concentrations at rounded corners of Rectangular Hollow Sections*", Journal of Mechanical Engineering Science, Vol. 4, No. 4, pp 334-340, **1962**.

Cook, R.D, Malkus, D.S. and Plesha, M.E., "*Concepts and applications of finite element analysis*", Wiley, 3rd Edition, **1988**.

Coulomb, C. A. de, "*Histoire de l'Académie 1784*", Paris, pp 229-269, **1787**.

Dally, J.W. and Riley, W.F., "*Experimental stress analysis*", McGraw-Hill, 3rd Edition, **1991**.

Dwyer, T.J. and Galambos, T.V., "*Plastic Behaviour of Tubular Beam-Columns*", American Society of Civil Engineers, Journal of the Structural Division, Vol. 91, No. ST4, pp 153-168, **1965**.

El Darwish, I.A. and Johnson, B.G., "*Torsion of structural shapes*", American Society of Civil Engineers, Journal of the Structural Division, Vol. 91, No. ST1, pp 203-27, **1965**.

Fenner, A.J., "*Mechanical testing of materials*", George Newnes, **1965**.

Griffith, A.A. and Taylor, G.I., "*The use of soap films in solving torsion problems*", Technical Reports of the British Advisory Committee for Aeronautics, Vol. 3, No. 333, pp 901-938, June **1917**.

Hasan, S.W. and Hancock, G.J., "*Plastic Bending Tests of Cold-Formed Rectangular Hollow Sections*", Research Report, No. R586, School of Civil and Mining Engineering, The University of Sydney, Australia, **1988**.

Hohenmser, G.I, and Prager, W., "*The mechanics of the plastic deformation of mild steel*", R.T.P. Translation number 2468, British Ministry of Aircraft Production, **1932**.

Huber, M.T., "*Czasoprismo Technizne*", Lwóv, **1904**.

Isida, M., "*On the Bending of an Infinite Strip with an Eccentric Circular Hole*", Proceedings of the 2nd Japanese Congress of Applied Mechanics, **1952**.

Joannides, F., Weller, A. and Gwynn, J., "*Structural Steelwork, basic design to ENV 1993-1-1:1992 (prestandard) Eurocode 3, Design of Steel Structures, Part 1.1 General rules and rules for buildings*", Parthenon Press, Dublin, **1993**.

Just, D.J. and Walley, J., "*Torsion of solid and hollow rectangular beams*", American Society of Civil Engineers, Journal of the Structural Division, Vol. 105, No. 9, pp 1789-1804, September **1979**.

Kármán, T. von, and Chien, W.Z., "*Torsion with variable twist*", J Aero Sci, Vol. 13, No. 10, pp 503-510, **1946**.

Kazic, M. and Dong, S.B., "*Analysis of restrained torsion*", American Society of Civil Engineers, Journal of Engineering Mechanics, Vol. 116, No. 4, pp 870-891, April **1990**.

Korol, R.M. and Hudoba, J., "*Plastic Behaviour of Hollow Structural Sections*", American Society of Civil Engineers, Journal of the Structural Division, Vol. 98, No. ST5, pp 1007-1023, **1972**.

Lawson, R.M. and Mullett, D.L.,"*Slim floor construction using deep decking*", Steel Construction Institute, Ref. SCI-P-127, **1993**.

Lawson, R.M., Mullett, D.L. and Rackham, J.W.,"*Design of asymmetric Slimflor beams using deep composite decking*", Steel Construction Institute, Ref. SCI-P-175, **1997**.

Lode, W., Z. Physik, Vol 36, p 913, **1926**.

Lode, W., "*Der Einfluss der mittleren Hauptspannung auf das Fliessen der Metalle*". Forsch. –Arb. Geb. Ing. –Wes., VDI-Verlag G.M.b.H, Berlin, Heft 303, **1928**.

Lyse, I. and Johnson, B.G., "*Structural beams in torsion*", Transactions of the American Society of Civil Engineers, Vol. 101, pp 857-926, **1936**.

Marciniak, Z., "*Aspects of metal formability*", Metal working research group, McMaster University, Ontario, Canada, pp 84-91, **1973**.

Marin, J., "*Working stresses for members subjected to compound loads*", Product Engineering, Vol 8 no 5, p 169, **1937**.

Marshall, J., "*Derivation of Torsional Formulas for Multiply Connected Thick-Walled Rectangular Sections*", Journal of Applied Mechanics, pp 399-402, June **1970**.

Marshall, J., "*Torsional behaviour of structural rectangular hollow sections*", The Structural Engineer, No. 8, Vol. 49, pp 375-379, August **1971**.

Marshall, J., "*Aspects of torsion of structural rectangular hollow sections*", Ph.D. thesis, University of Strathclyde, **1972**.

Megson, T.H.G., "*Aircraft structures for engineering students*", Edward Arnold, 2nd Edition, **1990**.

Mises, R. von, "*Gottingen Nachrichten*", Math. – Phys. Klasse, p 582, **1913**.

Miyauchi, K., "*Stress-strain relationships in simple shear testing on in-plane deformation for various steel sheets*", 13th Congress of the International deep drawing research group, Melbourne, Australia, pp 360-371, February **1984**.

Moore, R.L. and Paul, D.A., "*Torsion tests of 24S-T Aluminum Alloy Noncircular Bar and Tubing*", National Advisory Committee for Aeronautics, Technical Note 885, **1943**.

Moore, R.L. and Paul, D.A., "*Observations on the behavior of some noncircular aluminum alloy sections loaded to failure in torsion*", National Advisory Committee for Aeronautics, Technical Note 1097, March **1947**.

Moore, R.L. and Clark, J.W., "*Torsion, compression and bending tests of tubular sections machined from 75S-T6 rolled round rod*", National Advisory Committee for Aeronautics, Research Memorandum 52125, November **1952**.

Mullett, D.L., "*Slim floor design and construction*", Steel Construction Institute, Ref. SCI-P-110, **1992**.

Mullett, D.L., Ogden, R.G. and Kerry, J., "*Design of structural hollow sections for edge beams in Slimflor construction*", Report to British Steel (Tubes and Pipes), Steel Construction Institute, Doc RT481, Draft 01, **1995**.

Mullett, D.L., "*Design of RHS Slimflor edge beams*", Steel Construction Institute, Ref. SCI-P-169, **1997**.

Nádai, A., "*Plasticity – A mechanics of the state of matter*", 6th (English) edition, Engineering societies monographs, McGraw-Hill, pp 93-96, **1931**.

Navier, L. M. H., "*Résumé des leçons données à l'école des ponts et chaussées sur l'application de la mécanique à l'établissement des constructions et des machines*", 1st Ed, Paris, **1826**.

Navier, L. M. H., "*Résumé des leçons données à l'école des ponts et chaussées sur l'application de la mécanique à l'établissement des constructions et des machines*", 3rd Ed, Paris, with notes and appendices by Saint-Venant, **1864**.

Nethercot, D.A., Salter, P.R. and Malik, A.S., "*Design of members subjected to combined bending and torsion*", Steel Construction Institute, Ref. SCI-P-057, **1989**.

Nitzche, R.N. and Miller, R.E., "*Torsion and flexure of closed thin-walled beams*", American Society of Civil Engineers, Journal of the Engineering Mechanics Division, Vol. 102, No. 1, pp 189-193, September **1979**.

Peterson, R.E., "*Stress Concentration Factors*", John Wiley and Sons, **1974**.

Prandtl, L., "*Zur torsion von prismatischen stäben*", Physik. Z. Vol. 4, p 758, 1903. See also Anthes, Dinglers Polytech. J. p 342, **1906**.

Ridley-Ellis, D.J., Davies, G. and Owen, J.S., "*Fundamental behaviour of rectangular hollow sections with web openings*", Presented at the 8th International Symposium on Tubular Structures, Singapore, August **1998**.

Roark, R.J., "*Formulas for stress and strain*", McGraw-Hill, **1938**.

Rockey, K.C, Evans, H.R, Griffiths, D.W. and Nethercot, D.A., "*The finite element method - a basic introduction for engineers*", Collins, 2nd Edition, **1986**.

Saint-Venant, A. J. C. B. Count de, "*De la Torsion des Prismes – Extrait du Tome XIV des Mémoires Presentés par divers Savants a l'Académie des Sciences*", Vol. 14, **1855**.

Savin, G.N., "*Stress concentration around holes*", Pergamon, **1961**.

Schulz, M. and Filippou, F.C., "*Generalized warping torsion formulation*", American Society of Civil Engineers, Journal of Engineering Mechanics, Vol. 124, No. 3, pp 339-347, March **1998**.

Sedlacek, G., Dahl, N., Stranghöner, B., Kalinowski, B., Rondal, J. and Boeraeve, Ph., "*Investigation of the rotation behaviour of hollow section beams*", European Commission report (technical steel research) EUR 17994, **1998**.

Shanley, F.R., "*Strength of Materials*", McGraw-Hill, **1957**.

Smith, F.A., Thomas, F.M. and Smith, J.O., "*Torsional analysis of heavy box beams in structures*", American Society of Civil Engineers, Journal of the Structural Division, Vol. 96, No. ST3, pp 613-635, **1970**.

Stang, A.H., Ramberg, W. and Back, G., "*Torsion tests of tubes*", National Advisory Committee for Aeronautics, Technical Report 601, **1937**.

Taylor, G.I. and Quinney, H., "*The plastic distortion of metals*", Phil. Trans. Roy. Soc., Ser. A. Vol. 230, London, pp 323-362, November **1931**.

Thomas, F.M., "*An analysis of the effects due to restrained warping of thick walled box beams and I-beams subject to torsion*", Ph.D. thesis, University of Ilinois at Urbana, **1969**.

Timoshenko, S.P., "*Strength of materials, Part 1: Elementary theory and problems*", D. Van Nostrand, 2rd Edition, **1941**(a).

Timoshenko, S.P., "*Strength of materials, Part 2: Advanced theory and problems*", D. Van Nostrand, 2rd Edition, **1941**(b).

Timoshenko, S.P., "*Strength of materials, Part 1: Elementary theory and problems*", D. Van Nostrand, 3rd Edition, **1955**.

Timoshenko, S.P. and Goodier, J.N., "*Theory of elasticity*", McGraw-Hill, 3rd Edition, **1970**.

Trahair, N.S. and Bradford, M.A., "*The behaviour and design of structures to AS 4100*", E & FN Spon, 3rd Edition, **1998**.

Wilkinson, T. and Hancock, G.J., "*Tests to investigate the web slenderness limits for cold-formed RHS in bending*", The Mechanics of Structures and Materials, Proceedings of the 15th Australasian Conference on the Mechanics of Structures and Materials, Melbourne, Australia, (Balkema, publ.), (Grzebieta, Al-Mahaidi & Wilson editors), pp 559-564, December **1997**.

Willems, N. Easley, J.T. and Rolfe, S.T., "*Strength of materials*", McGraw-Hill, p 316, **1981**.

Young, W.C., "*A practical approach to theoretical stress analysis – or where do you find it in Roark and how do you use it effectively*", Society for experimental mechanics, **1982**.

Young, W.C., "*Roark's formulas for stress and strain*", McGraw-Hill, 6th Edition, **1989**.

Zhao X.L. and Hancock G.J., "*T-Joints in Rectangular Hollow Sections Subject to Combined Actions*", American Society of Civil Engineers, Journal of Structural Engineering, Vol. 117, No. 8, pp 2258-2277, **1990**.

Zhao X.L. and Hancock G.J., "*Tests to Determine Plate Slenderness Limits for Cold-Formed Rectangular Hollow Sections of Grade C450*", Steel Construction, Journal of Australian Institute of Steel Construction, Vol. 25, No. 4, pp 2-16, November **1991**.

Zhao X.L. and Hancock G.J., "*Square and Rectangular Hollow Sections Subject to Combined Actions*", American Society of Civil Engineers, Journal of Structural Engineering, Vol. 118, No. 3, pp 648-668, **1992**.

Zienkiewicz, O.C. and Taylor, R.L., "*The finite element method*", McGraw-Hill, 4th Edition, **1994**.

Standards and technical design documents

British Steel publication TD 365, "*SHS Design to BS 5950 Part 1*", British Steel Tubes and Pipes, **1994**.

BS 1610-1:1992, "*Materials testing machines and force verification equipment*", Part 1: "*Specification for the grading of the forces applied by materials testing machines when used in the compression mode*", British Standards Institution, **1992**.

BS 1610-2:1985, "*Materials testing machines and force verification equipment*", Part 2: "*Specification for the grading of equipment used for the verification of the forces applied by materials testing machines*", British Standards Institution, **1985**.

BS 4360:1990, "*Specification for weldable structural steels*", British Standards Institution, **1990**.

BS 5950-1:1990, "*Structural use of steelwork in building*", Part 1: "*Code of practice for design in simple and continuous construction, hot rolled sections*", British Standards Institution, **1990**.

BS EN 10002-1:1990, "*Tensile testing of metallic materials*", Part 1: "*Method of test at ambient temperatures*", British Standards Institution, **1990**.

BS EN 10002-2:1992, "*Tensile testing of metallic materials*", Part 2: "*Verification of the force measuring system of the tensile testing machine*", British Standards Institution, **1992**.

BS EN 10002-3:1992, "*Tensile testing of metallic materials*", Part 3: "*Calibration of force proving instruments used for the verification of uniaxial testing machines*", British Standards Institution, **1995**.

BS EN 10025:1990, "*Specification for hot rolled products of non-alloy structural steels and their technical delivery conditions*", British Standards Institution, **1990**.

BS EN 10025:1993, "*Hot rolled products of non-alloy structural steels. Technical delivery conditions*", British Standards Institution, **1993**.

BS EN 10210-1:1994, "*Hot finished structural hollow sections of non-alloy and fine grain structural steels*", Part 1: "*Technical delivery requirements*", British Standards Institution, **1994**.

BS EN 10210-2:1997, "*Hot finished structural hollow sections of non-alloy and fine grain structural steels*", Part 2: "*Tolerances, dimensions and sectional properties*", British Standards Institution, **1997**.

Constrado document Cl/SfB 1968, "*Holes in beam webs. Allowable stress design*", Constructional Steel Research and Development Organisation, **1977**.

Eurocode 3, "*Design of Steel Structures*", Part 1.1: "*General Rules and Rules for buildings*", ENV 1993-1-1:1992, European Committee for Standardization, UK version, British Standards Institution, **1992**.

Papers and project reports

Ridley-Ellis D. J., Owen J. S. and Davies G., "Flexural behaviour of Rectangular Hollow Sections with circular side wall openings." Submitted for presentation at the 9th International Symposium on Tubular Structures, Düsseldorf (Germany), April **2001**.

Ridley-Ellis D. J., Davies G. and Owen J. S., "Fundamental behaviour of rectangular hollow sections with web openings." Presented at the 8th International Symposium on Tubular Structures, Singapore, August **1998**.

Ridley-Ellis D. J., Davies G. and Owen J. S., "Rectangular Hollow Sections as Slim Floor edge beams." Trends and developments in building, TEMPUS JEP 11297, Iasi (Romania), May **1998**.

(Further papers in preparation)

Ridley-Ellis D. J., Owen J. S. and Davies G., "*Recommendations for the design of hot-finished steel Rectangular Hollow Sections with circular web openings; Torsion, bending and shear.*" Report to Corus Tubes, Report no: SC2000-011, School of Civil Engineering, The University of Nottingham, July **2000**.

Ridley-Ellis D. J., Owen J. S. and Davies G., "*Torsion-testing of Rectangular Hollow Sections with web openings; A summary of experimental procedure, apparatus and results and a quantitative comparison of experimental observations with theoretical and Finite Element predictions.*" Report to Corus Tubes, Report no: SC2000-010, School of Civil Engineering, The University of Nottingham, March **2000**.

Ridley-Ellis D. J., Owen J. S. and Davies G., "*A mathematical approximation of the stress-strain relationship of steel from hot finished Rectangular Hollow Sections.*" Internal Report, Report no: SC2000-008, School of Civil Engineering, The University of Nottingham, February **1999**.

Errata